

Mathematics of Generative AI

Michael Chertkov

Applied Mathematics, University of Arizona, Tucson, AZ 85721, USA

December 24, 2025

Contents

1 Linear Algebra (of AI)	10
1.1 Foundations of Representing Data	10
1.1.1 Vectors	10
1.1.2 Matrices: Representing Linear Transformations.	11
1.1.3 Convolution: Bridging Linear Algebra and Applications in AI	13
1.1.4 Tensors: The Generalization	14
1.1.5 Applications in Generative AI – Mechanics of Transformers	21
1.2 Matrix Decompositions	27
1.2.1 Singular Value Decomposition	27
1.2.2 Reduced Representation of a Single Data Point with SVD	30
1.2.3 Eigen-Decomposition	34
1.2.4 Connecting SVD and ED for Symmetric Positive-Definite Matrices . .	35
2 Calculus and Differential Equations (in AI)	38
2.1 Automatic Differentiation	38
2.1.1 Forward vs. Reverse Mode AD	39
2.2 Differential Equations: Foundations and Links to AI	43
2.2.1 Ordinary Differential Equations (ODEs) – Primer	44
2.2.2 Regression – Direct and ODE-Based	46
2.2.3 Second-Order ODE	51
2.3 System of Linear ODEs	54
2.3.1 Homogeneous ODEs	55
2.3.2 Inhomogeneous ODEs	57
2.3.3 Dynamics over Graph	59
2.3.4 Time-Ordered Exponential	62
3 Optimization (in AI)	65
3.1 Starting Example — Logistic Regression	66
3.1.1 The Logistic Regression Model	66
3.1.2 Linear Logistic Regression and Its Limitations	67
3.1.3 Why Linear Logistic Regression Fails for Non-Linearly Separable Data	67
3.1.4 Gradient Descent for Logistic Regression: The Vector Field	68
3.1.5 Nonlinear Logistic Regression via Feature Engineering	70
3.2 Convex Optimization – Primer	71
3.2.1 Variety of (Non-Convex) Landscapes	71

3.2.2	Convexity: A Guiding Light in AI Optimization	74
3.2.3	Convexity of Logistic Regression	75
3.2.4	Constrained Optimization and Lagrange Multipliers	76
3.3	Gradient Descent and Its Essential AI Variants	77
3.3.1	Gradient Descent (GD)	77
3.3.2	Stochastic Gradient Descent (SGD)	78
3.3.3	Momentum-Based Methods	78
3.3.4	Projected Gradient Descent (PGD)	79
3.3.5	Adaptive Learning Rate Methods	79
3.3.6	Why the Second-Order Methods are no go in AI?	84
3.4	Regularization & Sparsity	85
3.4.1	Compressed Sensing and Sparse Optimization	86
3.4.2	Regularization and Its Importance in AI	88
3.4.3	Sparsity for Inference Acceleration	89
3.5	(*) Optimization of Transformers – GenAI Example	90
3.5.1	Loss Function and Optimization Objective	91
3.5.2	Optimization Process: From Backpropagation to SGD Variants	91
3.5.3	How Does the Loss Function Handle Growing Input Sequences?	91
3.5.4	Ongoing Advances in Transformer Optimization	95
4	Neural Networks & Deep Learning	99
4.1	Neural Network Mechanics	100
4.1.1	Perceptron – Historical Remark	100
4.1.2	NN with a Single Fully Connected Hidden Layer	101
4.1.3	Interpolation vs. Extrapolation: Polynomial Regression vs Neural Networks	104
4.1.4	Simple Convolutional Neural Network	107
4.2	Neural Architectures	111
4.2.1	From CNN to ResNet – the Power of Skip Connections	113
4.2.2	From Residual Networks to Neural ODEs: A 2D Spiral Example	118
4.3	Universal Geometric Principles of Deep Learning	123
4.3.1	Discovery of Flat Regions in the Energy Landscape	123
4.3.2	Dynamic Selection of Low-Dimensional Manifolds in Deep Networks	127
4.4	Further Reading and Roadmap to the Rest of the Book	130
5	Probability and Statistics	135
5.1	Primer for Probability Spaces & Random Variables	137
5.1.1	Probability Spaces: The Foundation	138
5.1.2	Random Variables	139
5.1.3	Expectation and Moments	140
5.1.4	Data-Driven Probability: Empirical Distributions	140
5.1.5	Transformations of Random Variables	142
5.1.6	A First Normalizing Flow in 1D	143
5.2	Transforming Probability Distributions	144
5.2.1	Change of Variables in One Dimension	144

5.2.2	From Spiky to Smooth: Kernel Density Estimation	145
5.2.3	From Gaussian to Arbitrary Distributions: Normalizing Flows	147
5.2.4	Normalizing Flows and Optimal Transport (Preview)	148
5.3	Multivariate Random Variables	149
5.3.1	Random Vectors, Joint Distributions, and Independence	150
5.3.2	Algebraic and Linear Operations on Random Vectors	151
5.3.3	Multivariate Gaussian Distributions	152
5.3.4	Empirical Multivariate Statistics	154
5.4	From Aggregate Behavior to Rare Events	156
5.4.1	The Central Limit Theorem: Weak Form	156
5.4.2	Large Deviations: Tail Form of the CLT	158
5.4.3	When CLT Fails: Heavy Tails and Stable Laws	159
5.4.4	Rare Events in Many Trials: The Poisson Limit	160
5.4.5	Beyond Sums: Extreme Value Theorems	162
6	Entropy and Information Theory	166
6.1	Conditional Probability and Bayes' Rule	167
6.1.1	Conditional Probability, Joint Laws, and Bayes' Rule	167
6.1.2	Discrete Bayes in a Toy Medical Diagnosis Model	168
6.1.3	Exploring Test Quality: Sensitivity and Specificity	169
6.1.4	From Naïve Bayes to Neural Networks	170
6.2	Entropy: Quantifying Uncertainty	173
6.2.1	Definition and Interpretations of Entropy	174
6.2.2	Mutual Information	176
6.2.3	KL Divergence: Comparing Distributions	179
6.2.4	Cross-Entropy and Its Connection to KL Divergence	181
6.2.5	Wasserstein Distance: Geometry of Probability Distributions	183
6.3	Information Theory and Neural Networks	186
6.3.1	Source Coding Theorem (Lossless Compression)	187
6.3.2	Neural Networks as Encoding Schemes	189
6.3.3	Autoencoders and Nonlinear Compression	190
6.3.4	The Information Bottleneck Principle and U-Net as a Nonlinear Compressor	193
6.3.5	Channel Coding Theorem and Its Application to Neural Networks	195
6.3.6	Efficient Memory and Neural Network Storage	197
7	Stochastic Processes	201
7.1	Exact Sampling	202
7.1.1	Inverse Transform Sampling	202
7.1.2	Exact Sampling from Multivariate Distributions via Chain Rule	205
7.2	Importance Sampling and its Applications	206
7.2.1	General Formulation of Importance Sampling	206
7.2.2	Importance Sampling for Posterior Estimation	207
7.2.3	Adaptive Importance Sampling and the Cross-Entropy Method	209
7.3	Diffusion and Brownian Motion	213

7.3.1	Diffusion from Brownian Motion	213
7.3.2	From the Stochastic Differential Equation to the Path Integral	214
7.3.3	Generalization: Diffusion with Drift Induced by a Potential	219
7.4	Markov Chains	223
7.4.1	Global Balance and Detailed Balance	224
7.4.2	Perron–Frobenius Theorem, Spectral Gap, and Mixing on Graphs	226
7.4.3	Arrow of Time and Dynamic Programming	228
7.5	Markov Chains Meet Sampling: MCMC	230
7.5.1	Gibbs Sampling (Warm-up: Ising / RBM Conditionals)	231
7.5.2	Metropolis–Hastings (Local Moves and Detailed Balance)	231
7.5.3	Restricted Boltzmann Machines as Bipartite Ising Models	231
7.5.4	Gibbs vs. Local MH (Glauber-Style) in an RBM	233
7.5.5	Contrastive Divergence: Truncated MCMC for Learning	234
7.6	Beyond Markov via Auto-Regressive Modeling	235
7.6.1	Randomness in Next-Token Generation	235
7.6.2	Auto-Regressive Models as Expanding Markov Chains	236
8	Energy Based (Graphical) Models	239
8.1	Inference	240
8.1.1	Graphical Models	241
8.1.2	Variational Methods	245
8.1.3	Neural Decoding of Low-Density Parity-Check Codes	253
8.1.4	Variational Auto-Encoders	256
8.2	Learning	259
8.2.1	Likelihood	260
8.2.2	Local Methods: Pseudo-Log-Likelihood and Interaction Screening . . .	264
8.2.3	Restricted Boltzmann Machines: Learning with Latent Variables . . .	267
8.2.4	From Graphical Models to Graph Neural Networks	271
9	Synthesis	275
9.1	Score-Based Diffusion Models	277
9.1.1	Bridge Diffusion	281
9.2	A Unified View: Generative Models as Diffusions	286
9.2.1	GANs as Implicit Diffusion Models	287
9.2.2	Normalizing Flows as Deterministic Transport	291
9.2.3	Variational Autoencoders as Diffusion Models	293
9.3	Diffusion Models and Dynamic Phase Transitions	297
9.3.1	U-Turn Diffusion as a Dynamical Probe	297
9.3.2	Dynamic Phase Transients and High-Dimensional Theory	298
9.3.3	Perspective and Open Directions	300
9.4	From MDP to Reinforcement Learning	301
9.4.1	Markov Decision Processes	302
9.4.2	Reinforcement Learning	303
9.4.3	Agentic AI as Iterated Planning and Policy Improvement	304
9.4.4	Maximum Entropy Reinforcement Learning	310

9.5	Path–Integral Diffusion	315
9.5.1	From stochastic optimal control to Path–Integral Diffusion	316
9.5.2	Three levels of integrability	317
9.5.3	Sample-based and Importance Sampling Representations	318
9.5.4	Sensitivity Minimization via Adaptive Path Integral Diffusion	319
9.5.5	Navigation via Guided PID	320
9.5.6	Open Challenges and Research Directions	321
9.6	Sampling Decisions	322
9.6.1	Markovian Sampling Decision	323
9.6.2	Generative Flow Networks in a Nutshell	327
9.6.3	Decision Flow: an Integrable, Auto-Regressive Extension of Markovian Sampling	328
9.7	Path Forward	331
9.7.1	Work in Progress (by the author) and Open Directions	331
9.7.2	Further Ideas on a Grand Unification of Generative Models	332
9.7.3	Downstream Applications: Where the Mathematics of AI Meets the Real World	333

Introduction to the "Mathematics of Generative AI"

This book aims to build a clear and modern bridge between the rapidly evolving practice of Generative AI and the mathematical principles that underlie it. Its primary audience is *advanced STEM undergraduates, graduate students, and research-minded AI practitioners* who have seen core undergraduate mathematics (linear algebra, differential equations, probability, optimization) but now seek an integrated view of how these ideas power state-of-the-art generative models. Rather than treating mathematics and AI as separate subjects, the book presents them as a single, mutually reinforcing narrative – mathematics illuminated by AI, and AI clarified through mathematics.

What Makes This Book Different?

Most applied mathematics textbooks build upward: fundamentals first, applications last. This book takes a more fluid and strategically timed approach. While we do *not* open with full Generative AI (GenAI) case studies or advanced architectures, we introduce the motivating phenomena of modern GenAI – diffusion models, transformers, high-dimensional representation learning – *as soon as the relevant mathematical groundwork is in place*. In this way, the appearance of each AI example is synchronized with the mathematical ideas that illuminate it. This “application-aligned” route helps the reader maintain a sense of purpose: every mathematical concept is introduced because it is **required** to understand an insight, mechanism, or algorithm that matters today. Since the field of GenAI is a moving target, the book emphasizes not completeness but **relevance**, focusing on mathematical structures that currently shape research frontiers.

A Selective Approach to Mathematical Foundations

Generative AI relies on a remarkably broad mathematical toolkit: linear algebra, optimization, stochastic calculus, variational principles, statistical mechanics, and more. This book does *not* attempt a comprehensive survey. Instead, it takes a *curated, selective approach*, choosing mathematical ideas that directly empower the reader to understand diffusion models, denoising, score matching, autoencoders, transformers, and the stochastic control/transport interpretations that unify many of these themes. The emphasis throughout is on *conceptual clarity* and *practical utility*: What does this piece of mathematics buy us in GenAI? Why does this identity, inequality, or operator show up again and again? Where rigorous treatments would distract from intuition, we point the reader to standard references and keep the exposition focused on insight and mechanism.

Learning by Doing

The book follows a *learning-by-doing* philosophy. Each chapter contains exercises that blend:

- core mathematical manipulations;
- conceptual questions that probe understanding;

- exploratory tasks based on recent AI techniques;
- computational experiments in Python.

Many readers find that intuition for generative models develops most naturally through *experimentation* – visualizing diffusions, probing loss surfaces, inspecting denoisers, and comparing implementations. The book therefore encourages curiosity, creativity, and iterative experimentation as essential complements to theory.

This philosophy is concretely implemented through *tight integration with computational resources*. All theoretical examples, exercises, and the majority of the figures presented in the text are computationally realized via linked Jupyter/Python notebooks. This seamless integration allows the reader to immediately test concepts, visualize complex functions, and modify models. As a continuously evolving resource, the current version of the living book (pdf file), along with the complete collection of notebooks organized by chapter, are maintained and updated on our public repository: <https://github.com/mchertkov/Mathematics-of-Generative-AI-Book>.

Computational Exploration: Scope and Intent

The computational components accompanying many exercises are intentionally lightweight: small, transparent scripts designed to run on an ordinary laptop. Their purpose is to illuminate ideas – not to reproduce production – scale training and inference pipelines. Topics such as distributed training, large-scale optimization, or multi-GPU pipelines are beyond the scope of this book and are better learned in specialized courses or through dedicated self-study. Our computational aim here is to support mathematical insight, not engineering.

Acknowledgments

The December 2025 edition of this living book reflects the insight and generosity of many colleagues, collaborators, and students. Their contributions – ranging from lectures and notes to code and exercises – shaped the material in ways that a single author could not.

Robert Ferrando – a graduate student in Applied Mathematics at the University of Arizona and my co-instructor for Math 496T/Spring 2025 at University of Arizona – deserves special thanks. Robert advised me on countless technical points, delivered two guest lectures, and compiled the complete set of exercise solutions in the Spring of 2025. His insight, enthusiasm, and talent for explaining subtle ideas were indispensable; without his help these notes would not have come to life.

I am equally grateful to my colleagues **Jason Aubrey** and **Arvind Suresh** for sharing their relevant notes and offering timely advice as the material of Math496T evolved. Arvind also contributed two guest lectures on practical neural-network implementation in PYTORCH, enriching the applied component of the course.

Heartfelt thanks go to the **Math 496T students**. Their curiosity, sharp questions, and vigilant spotting of errors shaped the exposition and pushed the project far beyond what a single author could achieve.

AI-assisted tools (including large language models) are also used in the preparation and editing of the text. Their role is acknowledged as part of modern mathematical and computational practice, and their contributions – while carefully curated – help accelerate iteration and broaden perspective.

A Living and Collaborative Resource – Envisioning the Future

This text is deliberately designed as a *living book*, updated through regular teaching cycles, research developments, and feedback from students and colleagues across academia, national laboratories, and industry.

The Mathematics of Generative AI will continue to evolve alongside the field itself. As diffusion models, score-based samplers, reinforcement-learning formulations, and transformer-based architectures continue to advance, new editions of this book will incorporate the emerging mathematics that supports them. Readers are warmly invited to participate by:

- proposing new exercises, illustrations, and computational explorations;
- suggesting clarifications or alternative explanations;
- summarizing recent research papers for inclusion;
- sharing implementations or extensions of the included notebooks.

These who contribute improvements – whether conceptual, computational, or expository – will be acknowledged as collaborators in this ongoing effort. The hope is that this book becomes not just a resource but a community project: a shared effort to understand the mathematical ideas driving the most transformative technological development of our time.

Chapter 1

Linear Algebra (of AI)

1.1 Foundations of Representing Data

1.1.1 Vectors

A vector is an ordered collection of numbers (or elements) that can represent points, directions, or quantities in space. Mathematically, a vector in n -dimensional real space is represented as:

$$v = [v_1, v_2, \dots, v_n]^\top \in \mathbb{R}^n$$

where v_i are the components of the vector; n is dimensionality of the vector; $[v_1, v_2, \dots, v_n]$ is the notation we use for the row-vector; and $^\top$ is the transposition turning raw vector to column vector and vice versa. Later in the text, we will use the same notation, such as v , interchangeably for both a row vector and a column vector. Any potential ambiguities will be explicitly clarified when they arise.

Key Operations:

- **Addition:** $(u + v)_i = u_i + v_i$, u and v are vectors of the same dimensionality
- **Scalar multiplication:** $(cv)_i = cv_i$, where c is a scalar
- **Product:** $uv^\top = \sum_{i=1}^n u_i v_i$, where u and v are co-dimensional vectors
- **Norm:** $\|v\| = \sqrt{vv^\top}$

Vectors are used to represent data points (e.g., pixel intensities in an image, word embeddings in NLP) or transformations (e.g., directions of gradients in optimization).

1.1.2 Matrices: Representing Linear Transformations.

A matrix is a 2D array of numbers that generalizes vectors to multiple dimensions. A matrix $A \in \mathbb{R}^{m \times n}$ can be represented as:

$$A = \begin{bmatrix} A_{11} & A_{12} & \cdots & A_{1n} \\ A_{21} & A_{22} & \cdots & A_{2n} \\ \vdots & \vdots & \ddots & \vdots \\ A_{m1} & A_{m2} & \cdots & A_{mn} \end{bmatrix}$$

Key Operations:

- **Addition:** Element-wise addition (for matrices with the same dimensions) –

$$(A + B)_{ij} = A_{ij} + B_{ij}.$$

- **Element-Wise Multiplication:** The element-wise (Hadamard) product of matrices A and B (with the same dimensions) is denoted by \odot and computed as:

$$(A \odot B)_{ij} = A_{ij}B_{ij}.$$

- **Multiplication:** Matrix-vector and matrix-matrix multiplication –

$$(AB)_{ij} = \sum_{k=1}^n A_{ik}B_{kj}, \quad (Av)_i = \sum_{j=1}^n A_{ij}v_j,$$

where the inner dimensions of A and B must match.

- **Transpose:** The transpose of a matrix is defined as:

$$(A^\top)_{ij} = A_{ji}.$$

- **Inverse:** The inverse of a square and invertible matrix A , denoted as A^{-1} , satisfies:

$$AA^{-1} = A^{-1}A = I,$$

where I is the identity matrix, defined as $I_{ii} = 1$ and $I_{ij} = 0$ for $i \neq j$.

Why do we associate matrices with linear algebra? Because matrices serve as fundamental tools for representing linear transformations in a general form. A $n \times m$ dimensional matrix acting on a m -dimensional vector represents **linear** transformations such as rotations, rescaling, and projections of the vector:

1. Rotation: For example, a 3D rotation matrix around the z -axis by an angle θ (in radians) is given by:

$$R_z(\theta) = \begin{bmatrix} \cos \theta & -\sin \theta & 0 \\ \sin \theta & \cos \theta & 0 \\ 0 & 0 & 1 \end{bmatrix}.$$

If we apply the matrix to the unit vector aligned with the x -axis, $R_z(\theta)[1, 0, 0]^\top$, the result is the unit vector rotated by the angle θ in the (x, y) -plane.

2. Re-scaling: A re-scaling transformation adjusts the magnitude of vectors along specified axes. For example, the following matrix rescales vectors in the x - and y -directions by factors s_x and s_y , respectively:

$$S = \begin{bmatrix} s_x & 0 \\ 0 & s_y \end{bmatrix}.$$

Applying this matrix to a vector $x = [x, y]^\top$ results in:

$$y = Sx = \begin{bmatrix} s_x x \\ s_y y \end{bmatrix}.$$

For example, if $s_x = 2$ and $s_y = 0.5$, the vector $[1, 2]^\top$ is transformed into:

$$y = \begin{bmatrix} 2 & 0 \\ 0 & 0.5 \end{bmatrix} \begin{bmatrix} 1 \\ 2 \end{bmatrix} = \begin{bmatrix} 2 \\ 1 \end{bmatrix}.$$

3. Projection: A projection transformation maps vectors onto a subspace. For example, a projection onto the x -axis in 2D is given by the matrix:

$$P_1 = \begin{bmatrix} 1 & 0 \\ 0 & 0 \end{bmatrix}.$$

Applying this matrix to a vector $[x, y]^\top$ gives:

$$y = P_1 x = \begin{bmatrix} 1 & 0 \\ 0 & 0 \end{bmatrix} \begin{bmatrix} x \\ y \end{bmatrix} = \begin{bmatrix} x \\ 0 \end{bmatrix}.$$

This operation removes the second y -component of the vector, effectively projecting it onto the first x -axis.

Similarly, projection onto the y -axis can be achieved using:

$$P_2 = \begin{bmatrix} 0 & 0 \\ 0 & 1 \end{bmatrix}.$$

Summarizing/rephrasing – any linear map $\mathcal{L} : \mathbb{R}^n \rightarrow \mathbb{R}^m$ can be uniquely expressed in terms of a matrix $A \in \mathbb{R}^{m \times n}$ such that for any vector $x \in \mathbb{R}^n$, the image $\mathcal{L}(x)$ is given by $\mathcal{L}(x) = Ax$. This representation encapsulates the aforementioned essential operations like scaling, rotations, and projections, and is indispensable in various applications, from solving systems of linear equations to encoding (some) transformations in Neural Networks (NN). Moreover, matrices also facilitate iterative processes, such as those encountered in diffusion models, where repeated applications of matrix multiplications are key to de-noising and generating data.

Exercise 1.1.1 (Matrix Multiplication and Elliptical Dynamics). (a) Consider $x_0 = (a, 0)^\top$, a column vector in 2D. Design a 2×2 matrix A such that its repeated application to x_0 :

$$x_t = A^t x_0, \quad t = 1, 2, \dots,$$

results in all x_t lying on an ellipse with a semi-axis ratio of a/b . Here, A^t represents the matrix A raised to the power t , meaning t -fold matrix multiplication.

- (b) Can you ensure that as $t \rightarrow \infty$, the trajectory of x_t covers the entire ellipse? In other words, is it possible to design A such that the process explores all points on the ellipse in the limit of infinite iterations?

1.1.3 Convolution: Bridging Linear Algebra and Applications in AI

Convolution is a fundamental operation in linear algebra and signal processing, playing a pivotal role in many applications, including modern AI architectures. Here, we introduce convolution and demonstrate its relevance in practical settings, particularly its compactness and efficiency compared to other forms of linear transformations.

Convolution combines two inputs f and g , producing an output that reflects their interaction. In a one-dimensional case, for functions f and g defined on \mathbb{R} , the convolution $(f * g)(t)$ is defined as:

$$(f * g)(t) = \int_{-\infty}^{\infty} f(\tau)g(t - \tau) d\tau.$$

In discrete settings, such as in linear algebra – where discreteness is represented via indices – convolution is often applied to vectors or matrices.

Convolution should be viewed as a particular form of a linear transformation. Consider the following example: the convolution of the vector $x \in \mathbb{R}^n$ and a kernel (filter) $k \in \mathbb{R}^m$, where $m < n$, resulting in $y \in \mathbb{R}^{n-m+1}$:

$$y_i = \sum_{j=1}^m k_j \cdot x_{i+j-1}, \quad i = 1, 2, \dots, n - m + 1.$$

This operation can be represented as a structured matrix-vector multiplication, where matrix $A(k)$ acts on x to produce y :

$$y = A(k) \cdot x, \quad A(k) = \begin{bmatrix} k_1 & 0 & \cdots & 0 \\ k_2 & k_1 & \cdots & 0 \\ \vdots & k_2 & \ddots & \vdots \\ k_m & \vdots & \cdots & k_1 \\ 0 & k_m & \ddots & \vdots \\ \vdots & 0 & \cdots & k_m \end{bmatrix}.$$

In this formulation, each entry y_i of the output vector y is obtained by computing the dot product of the kernel k with a corresponding window of the input vector x . This emphasizes that convolution is fundamentally a linear transformation that is computationally efficient and compact.

Example 1.1.1 (Convolutional Neural Networks). *Let us discuss a fundamental building block of Convolutional Neural Networks (CNNs): the linear part of a single convolutional layer. While a full CNN architecture typically involves multiple convolutional, pooling, and fully connected layers, here we restrict our discussion to the operation of a single convolutional layer to illustrate its role in feature extraction.*

Consider an input image $x \in \mathbb{R}^{n \times n}$. A convolutional filter $k \in \mathbb{R}^{m \times m}$ slides across x , producing the output:

$$y_{i,j} = \sum_{h,w=1}^m k_{h,w} \cdot x_{i+h-1,j+w-1}, \quad i,j = 1, \dots, n-m+1.$$

Example 1.1.2 (Image to Tensor). Consider a grayscale image $x \in \mathbb{R}^{4 \times 4}$ and a filter $k \in \mathbb{R}^{2 \times 2}$:

$$x = \begin{bmatrix} 1 & 2 & 3 & 0 \\ 4 & 5 & 6 & 1 \\ 7 & 8 & 9 & 0 \\ 1 & 0 & 2 & 3 \end{bmatrix}, \quad k = \begin{bmatrix} 1 & 0 \\ 0 & -1 \end{bmatrix}.$$

The convolution of x with the filter k becomes:

$$\begin{aligned} y &= \begin{bmatrix} (1 \cdot 1 + 2 \cdot 0 + 4 \cdot 0 + 5 \cdot -1) & (2 \cdot 1 + 3 \cdot 0 + 5 \cdot 0 + 6 \cdot -1) & (3 \cdot 1 + 0 \cdot 0 + 6 \cdot 0 + 1 \cdot -1) \\ (4 \cdot 1 + 5 \cdot 0 + 7 \cdot 0 + 8 \cdot -1) & (5 \cdot 1 + 6 \cdot 0 + 8 \cdot 0 + 9 \cdot -1) & (6 \cdot 1 + 1 \cdot 0 + 9 \cdot 0 + 0 \cdot -1) \\ (7 \cdot 1 + 8 \cdot 0 + 1 \cdot 0 + 0 \cdot -1) & (8 \cdot 1 + 9 \cdot 0 + 0 \cdot 0 + 2 \cdot -1) & (9 \cdot 1 + 0 \cdot 0 + 2 \cdot 0 + 3 \cdot -1) \end{bmatrix} \\ &= \begin{bmatrix} -4 & -4 & 2 \\ -4 & -4 & 6 \\ 7 & 6 & 6 \end{bmatrix}. \end{aligned}$$

We can also re-state this operation as a linear transformation without index shifts:

$$\begin{aligned} y_{i,j} &= \sum_{i',j'=1}^4 A_{i,j,i',j'} x_{i',j'}, \quad i,j = 1, \dots, 3, \\ A_{i,j,i',j'} &= \begin{cases} k_{i'-i+1,j'-j+1}, & \text{if } 1 \leq i' - i + 1 \leq m \text{ and } 1 \leq j' - j + 1 \leq m, \\ 0, & \text{otherwise.} \end{cases} \end{aligned}$$

Two remarks are in order. First, notice that the number of operations required to express elements of matrix y via matrix x in the form of a linear transformation is larger than in the form of a convolution (4 vs. 2). This emphasizes that convolution, when possible, can be a much more compact representation than a general linear transformation.

Second, A in the last formula is an example of a new type of object – a tensor – which we will discuss in the next subsection.

1.1.4 Tensors: The Generalization

The word "tensor" originates from the Latin word tendere, which means "to stretch." The term was introduced into mathematics and physics to describe objects that generalize the notion of scalars, vectors, and matrices to higher dimensions – we also call it rank or order – capturing properties related to "stretching" or "deformation."

A tensor \mathcal{T} of rank k can be represented as:

$$\mathcal{T} \in \mathbb{R}^{d_1 \times d_2 \times \dots \times d_k}$$

where d_i is the size along the i -th dimension.

Rank:

- Scalars: Rank 0.
- Vectors: Rank 1.
- Matrices: Rank 2.
- Higher-rank tensors: $k \geq 3$.

Representation

Tensors are particularly powerful tools for representing multi-dimensional data. The following example and exercise demonstrates their application in representing RGB images, video clips, and NLP embeddings.

Machine Learning Tensors vs. Mathematical Tensors

The word *tensor* is used in two different ways in mathematics, physics, and machine learning. Because this book moves between formal linear algebra and practical implementations (NumPy, PyTorch, JAX), it is important to clarify the distinction.

1. Classical Tensors (Multilinear Algebra). In its classical mathematical meaning, a tensor is a *multilinear object*:

$$T \in V^{\otimes r} \otimes (V^*)^{\otimes s}.$$

A rank- (r, s) tensor transforms according to specific rules under changes of basis. Examples include scalars, vectors, covectors, bilinear forms, stress tensors, and curvature tensors.

The defining characteristic is:

A mathematical tensor obeys coordinate transformation laws.

2. Tensors in Machine Learning (Multi-Index Arrays). In modern ML libraries (NumPy, PyTorch, TensorFlow, JAX), a *tensor* is simply a **numerical array** with shape

$$(d_1, d_2, \dots, d_k).$$

No geometric structure or transformation law is assumed. For example: - Images: $\mathbb{R}^{H \times W \times 3}$, - Video clips: $\mathbb{R}^{H \times W \times 3 \times T}$, - Embedding batches: $\mathbb{R}^{L \times D}$, are all called “tensors” in the ML sense.

Thus:

In ML practice: tensor = multi-dimensional numerical array.

3. Why This Distinction Matters Here. Throughout this book, unless clearly indicated otherwise, the word *tensor* refers to the ML meaning (a multi-index array). This is the natural and useful notion for: - image and video data representations, - neural-network computations, - attention mechanisms, - batch processing and automatic differentiation.

The classical, multilinear-algebraic notion reappears later when discussing continuous-time models, differential operators, or geometry-driven aspects of diffusion processes.

Example 1.1.3. Representing RGB Images: Theory and Implementation

RGB images are commonly represented as tensors in $\mathbb{R}^{H \times W \times 3}$, where:

- H : Height of the image (number of rows),
- W : Width of the image (number of columns),
- 3: The three color channels: Red, Green, and Blue.

For instance, a color image of size 256×256 may be represented as a tensor

$$\mathcal{T} \in \mathbb{R}^{256 \times 256 \times 3}.$$

Each pixel channel typically stores an 8-bit intensity value between 0 and 255. Figure 1.1 illustrates the three views used in this exercise: the original grayscale MNIST image, its RGB version obtained via a colormap, and the extracted green channel whose average intensity we compute below.

Theoretical Formulation.

- To extract the green channel (second slice along the third dimension):

$$\mathcal{T}_{\text{green}} = \mathcal{T}[:, :, 2].$$

- To compute the average green-channel intensity:

$$\text{avg_green} = \frac{1}{HW} \sum_{i=1}^H \sum_{j=1}^W \mathcal{T}_{i,j,2}.$$

See the accompanying Jupyter notebook `Ex1-1-1image.ipynb` for the full computational workflow.

Exercise 1.1.2 (Tensor Representation of Video Clips and NLP Embeddings). In this exercise we extend the tensor viewpoint of Example 1.1.3 (RGB images) to (1) videos represented as four-dimensional arrays and (2) sequences of word embeddings represented as matrices. Throughout Chapter 1, the term “tensor” refers to a multidimensional numerical array used in applied machine learning practice – not necessarily to a multi-linear-algebra tensor.

1. Videos as 4D tensors: $\mathbb{R}^{H \times W \times 3 \times T}$

A video of resolution 1920×1080 , recorded at 30 fps for 10 seconds, may be represented as

$$\mathcal{T} \in \mathbb{R}^{1080 \times 1920 \times 3 \times 300},$$

where $\mathcal{T}_{i,j,c,t}$ denotes the intensity of pixel location (i, j) , color channel $c \in \{1, 2, 3\}$, in frame t .

Exercise 1.1.1: RGB representation and green channel

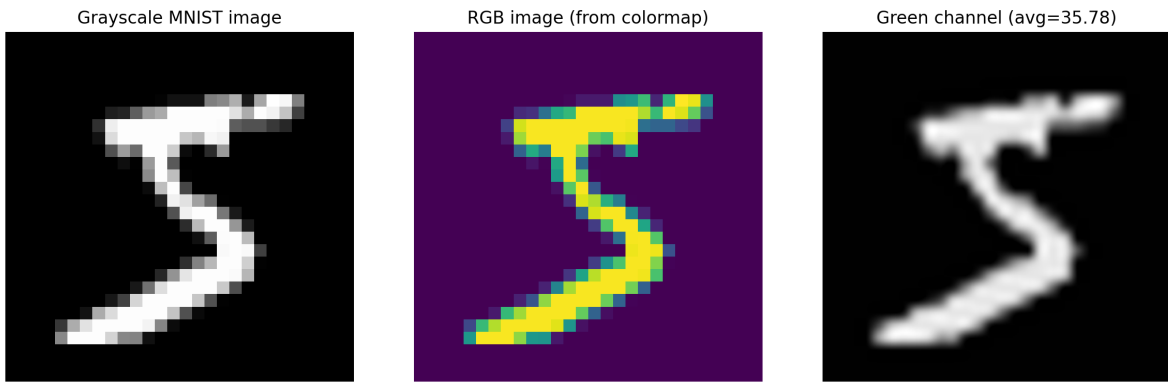


Figure 1.1: Three-panel illustration for Example 1.1.1. **Left:** Original MNIST grayscale image. **Middle:** RGB image obtained via a colormap. **Right:** Extracted green channel, annotated with its average intensity. These views illustrate the tensor representation of images and motivate the extraction-and-averaging operations defined in the exercise.

Pixel Intensity. Two common summaries of RGB brightness are:

$$I_{\text{grayscale}} = 0.2989R + 0.5870G + 0.1140B, \quad I_{\text{average}} = \frac{R + G + B}{3}.$$

Tasks:

- (a) Propose a formula for the mean grayscale intensity over all pixels and all frames whose timestamps lie in the interval $[t_1, t_2]$. (Assume frame t corresponds to time $t/30$ seconds.)
- (b) How would this mean intensity change if only the green channel G is used, instead of the grayscale combination of R, G, B ?

2. **Word embeddings as 2D and 3D tensors:** $\mathbb{R}^{D \times L}$

A sentence of length L may be represented by a matrix of word embeddings $\mathcal{T} \in \mathbb{R}^{D \times L}$, obtained by multiplying an embedding matrix $E \in \mathbb{R}^{D \times V}$ by one-hot word encodings. For example, if ‘‘cat’’ is the third word in the vocabulary, then

$$\text{Embedding(cat)} = E_{:,3}.$$

Tasks:

- (a) Write a formula for the weighted average embedding

$$e_{\text{avg}} = \sum_{i=1}^L w_i \mathcal{T}_{:,i}, \quad w_i \geq 0, \quad \sum_{i=1}^L w_i = 1.$$

- (b) Suggest how to choose the weight vector w to emphasize a particular position in the sequence (e.g., the first or last word).

(c) Suppose the weights depend on embedding dimension d and position i , yielding weights $w_{d,i}$. How does the formula for the weighted embedding change?

Note. Only theoretical reasoning and formulas are required; no code is needed.

Tensor Operations: Direct Product and Contraction-Based Product

Tensors serve as versatile tools for representing and manipulating multi-dimensional data. In this subsection, we focus on two fundamental tensor operations: the **direct product**, which creates higher-rank tensors, and the **contraction-based product**, which generalizes matrix multiplication by summing over shared indices. These operations are widely used in applications ranging from physics to modern AI.

The **direct product**, or tensor product, combines two tensors to produce a higher-rank tensor. Let $\mathcal{T}_1 \in \mathbb{R}^{d_1 \times \dots \times d_k}$ and $\mathcal{T}_2 \in \mathbb{R}^{d_{k+1} \times \dots \times d_{k+m}}$. Their direct product $\mathcal{T}_1 \otimes \mathcal{T}_2 \in \mathbb{R}^{d_1 \times \dots \times d_k \times d_{k+1} \times \dots \times d_{k+m}}$ is defined element-wise as:

$$(\mathcal{T}_1 \otimes \mathcal{T}_2)_{i_1, \dots, i_{k+m}} = (\mathcal{T}_1)_{i_1, \dots, i_k} \cdot (\mathcal{T}_2)_{i_{k+1}, \dots, i_{k+m}}.$$

The rank of the resulting tensor is the sum of the ranks of the input tensors, making it a powerful operation for constructing multi-linear expressions.

The **contraction-based product** reduces the rank of the resulting tensor by summing over one or more shared indices between the input tensors. This operation generalizes the familiar matrix product. For example, if $\mathcal{T}_1 \in \mathbb{R}^{d_1 \times d_2 \times d_3}$ and $\mathcal{T}_2 \in \mathbb{R}^{d_3 \times d_4}$, contracting the third index of \mathcal{T}_1 with the first index of \mathcal{T}_2 gives:

$$\mathcal{T}_{i_1, i_2, i_4} = \sum_{i_3=1}^{d_3} (\mathcal{T}_1)_{i_1, i_2, i_3} \cdot (\mathcal{T}_2)_{i_3, i_4}.$$

This operation reduces the rank of the resulting tensor by the number of contracted indices.

Examples of Tensor Operations:

- **Direct Product of Vectors:** Consider two vectors $u \in \mathbb{R}^n$ and $v \in \mathbb{R}^m$. Their direct product is a rank-2 tensor (or matrix):

$$u \otimes v = A \in \mathbb{R}^{n \times m}, \quad A_{ij} = u_i v_j.$$

This operation constructs a bi-linear representation of the two vectors without reducing dimensionality.

- **Contraction with a Vector:** Given a rank-3 tensor $\mathcal{T} \in \mathbb{R}^{d_1 \times d_2 \times d_3}$ and a vector $v \in \mathbb{R}^{d_3}$, contracting the third index of \mathcal{T} with v yields:

$$\mathcal{M}_{i_1, i_2} = \sum_{i_3=1}^{d_3} \mathcal{T}_{i_1, i_2, i_3} \cdot v_{i_3}.$$

The result is a rank-2 tensor (or matrix). For instance, if \mathcal{T} represents time-series data across multiple sensors, contracting with v can aggregate measurements across channels.

- **Contraction with a Matrix:** Let $A \in \mathbb{R}^{d_3 \times d_4}$. Contracting the third index of \mathcal{T} with the first index of A gives:

$$\mathcal{T}'_{i_1, i_2, i_4} = \sum_{i_3=1}^{d_3} \mathcal{T}_{i_1, i_2, i_3} \cdot A_{i_3, i_4}.$$

Here, A acts as a linear transformation on the third dimension of \mathcal{T} .

Here are some worked examples of tensor operations.

Example 1.1.4 (Direct Product of Vectors). *Let \mathbf{u} and \mathbf{v} be two vectors:*

$$\mathbf{u} = \begin{bmatrix} 1 \\ 2 \end{bmatrix}, \quad \mathbf{v} = \begin{bmatrix} 3 \\ 4 \end{bmatrix}$$

The **direct product** (or *tensor product*) $\mathbf{u} \otimes \mathbf{v}$ results in a higher-dimensional tensor, which in this case is a 2×2 matrix. According to the definition of the direct product, each element of the resulting tensor is formed by multiplying each element of \mathbf{u} with each element of \mathbf{v} :

$$\mathbf{u} \otimes \mathbf{v} = \begin{bmatrix} 1 \\ 2 \end{bmatrix} \otimes \begin{bmatrix} 3 \\ 4 \end{bmatrix} = \begin{bmatrix} 1 \cdot 3 & 1 \cdot 4 \\ 2 \cdot 3 & 2 \cdot 4 \end{bmatrix} = \begin{bmatrix} 3 & 4 \\ 6 & 8 \end{bmatrix}$$

Thus, the result of the direct product is a 2×2 matrix:

$$\begin{bmatrix} 3 & 4 \\ 6 & 8 \end{bmatrix}$$

This is a rank-2 tensor, where the dimensions correspond to the input vectors \mathbf{u} and \mathbf{v} .

Example 1.1.5 (Direct Product of Matrices). *Let A and B be two matrices:*

$$A = \begin{bmatrix} 1 & 2 \\ 3 & 4 \end{bmatrix}, \quad B = \begin{bmatrix} 5 & 6 \\ 7 & 8 \end{bmatrix}$$

The direct product $A \otimes B$ is a higher-order tensor in $\mathbb{R}^{2 \times 2 \times 2 \times 2}$, whose (i, j, k, l) entry is the (i, j) entry of A times the (k, l) entry of B .

Example 1.1.6 (Contraction of Two Matrices). *Let's take two matrices A and B :*

$$A = \begin{bmatrix} a_{11} & a_{12} \\ a_{21} & a_{22} \end{bmatrix}, \quad B = \begin{bmatrix} b_{11} & b_{12} \\ b_{21} & b_{22} \end{bmatrix}$$

The tensor contraction (matrix multiplication) is done by summing over the common index k :

$$A \cdot B = \sum_k a_{ik} b_{kj}$$

So, for matrices, this looks like:

$$A \cdot B = \begin{bmatrix} a_{11}b_{11} + a_{12}b_{21} & a_{11}b_{12} + a_{12}b_{22} \\ a_{21}b_{11} + a_{22}b_{21} & a_{21}b_{12} + a_{22}b_{22} \end{bmatrix}$$

Example 1.1.7 (Contraction on Higher-Dimensional Tensors). *Let's consider two tensors T and S :*

$$T_{ijk} = \begin{bmatrix} T_{111} & T_{112} \\ T_{121} & T_{122} \end{bmatrix}, \quad S_{klm} = \begin{bmatrix} S_{111} & S_{112} \\ S_{121} & S_{122} \end{bmatrix}$$

The contraction of T and S over the index k is:

$$T_{ij} \circ S_{jlm} = \sum_k T_{ijk} S_{klm}$$

Thus, the result of contracting along the index k will produce a new tensor with indices i , j , and m . The resulting tensor is:

$$T \circ S = \begin{bmatrix} T_{111}S_{111} + T_{112}S_{211} & T_{111}S_{112} + T_{112}S_{212} \\ T_{121}S_{111} + T_{122}S_{211} & T_{121}S_{112} + T_{122}S_{212} \end{bmatrix}$$

To see how to perform these tensor operations in Python using the `torch` package, please refer to the Jupyter notebook `TensorOperations.ipynb`.

Exercise 1.1.3 (Einstein Summation and Computational Efficiency). *Einstein Summation Notation (ESN) provides a compact, index-based way to express tensor operations, directly translating into efficient GPU kernels. This exercise tests your ability to translate between traditional summation and ESN, and addresses core efficiency concerns in modern deep learning hardware.*

1. **ESN Translation:** Express the following two fundamental operations using Einstein Summation Notation:

- (1) The matrix-vector product $y = Ax$, where $A \in \mathbb{R}^{m \times n}$ and $x \in \mathbb{R}^n$.
- (2) The squared Frobenius norm of a matrix A : $\|A\|_F^2 = \sum_{i=1}^m \sum_{j=1}^n A_{ij}^2$.

2. **Contraction Dimensionality:** Given the tensor contraction $C_{ikl} = A_{ij}B_{jkl}$, assuming all dimensions are D :

- What is the rank (number of indices) of the resulting tensor C ?
- What is the final dimensionality of C (e.g., $\mathbb{R}^{d_1 \times d_2 \times \dots}$)?

3. **Hardware Efficiency:** In GPU programming, why is **memory contiguity** (how elements are stored and accessed in memory) often more important for overall performance than the theoretical Floating-point OPeration count (FLOPs)?

To check your ESN logic against practical implementation, refer to the Jupyter notebook `TensorOperations.ipynb`.

Convolution vs Tensor Operations

While convolution, discussed above in Section 1.1.3, is sometimes conflated with the tensor product or contraction, it has distinct characteristics:

- **Tensor Product:** Combines two tensors $\mathcal{T}_1 \in \mathbb{R}^{d_1 \times d_2}$ and $\mathcal{T}_2 \in \mathbb{R}^{d_3 \times d_4}$ into a higher-dimensional tensor $\mathcal{T}_1 \otimes \mathcal{T}_2 \in \mathbb{R}^{d_1 \times d_2 \times d_3 \times d_4}$.
- **Contraction:** Reduces the dimensionality of tensors by summing over shared indices, e.g., the matrix product AB contracts indices of $A \in \mathbb{R}^{n \times m}$ and $B \in \mathbb{R}^{m \times p}$ to yield $C \in \mathbb{R}^{n \times p}$.
- **Convolution:** Applies a kernel in a sliding window manner, emphasizing locality and weight sharing.

From Data Structures to Architecture: The Role of Tensors

We have established the core building blocks of data representation: vectors, matrices for transformations, and tensors as the high-dimensional generalization. All Generative AI models, from simple CNNs to complex Transformers, operate exclusively on these tensor structures. The next step is to see how these elements – specifically the concepts of vector projection and attention – are woven together to create the complex, multi-layered mechanisms in the *Transformer* model.

1.1.5 Applications in Generative AI – Mechanics of Transformers

Vector Representations and Matrix Transformations in Generative Diffusion Models

In generative diffusion models, data points are represented as vectors and undergo a sequence of matrix transformations to progressively refine noisy inputs into meaningful outputs, such as generating new images. This iterative de-noising process can be described as:

$$x_{t+1} = A_t x_t + b_t, \quad t = 0, \dots, T,$$

where:

- x_0 is the noisy input that initializes the de-noising process.
- x_T is the final generated image or output.
- $A_t \in \mathbb{R}^{n \times n}$ is a transformation matrix.
- $b_t \in \mathbb{R}^n$ is a bias term.

The transformation matrix A_t and bias term b_t are nonlinear functions of x_t and t , often incorporating stochastic components such as Wiener noise and Neural Networks (NNs). These parameters are learned during training to effectively model the complex dynamics of the de-noising process. This framework enables the generation of high-quality synthetic data by iteratively refining the noise over time.

High-Dimensional Feature Interactions with Tensors in Transformers:

The transformer architecture, introduced in 2017 by Vaswani et al. in their seminal work 'Attention is All You Need' [1], revolutionized AI by leveraging self-attention mechanisms and feed-forward layers to model complex dependencies across input sequences. For a detailed and intuitive explanation of the underlying principles, readers are referred to the online tutorial <https://jalammar.github.io/illustrated-transformer/>, which provides visual insights into the architecture.

Transformers are foundational in modern generative AI, leveraging tensors to model dependencies across tokens in a sequence. These tokens are processed through a combination of linear tensor operations (index contractions, including convolutions) and nonlinear functions to predict the next token in a sequence.

Tokens and Their Role in Sequence Generation: The input sequence is represented as a matrix $X = \{t_1, t_2, \dots, t_n\} \in \mathbb{R}^{n \times d}$, where n is the sequence length, $t_i \in \mathbb{R}^d$ is the embedding of the i -th token, and d is the embedding dimension. The process of predicting the next token t_{n+1} involves evolving a "token-to-be-predicted" vector $\hat{t}_{n+1} \in \mathbb{R}^d$, which stabilizes over iterative applications of the transformer mechanism.

1. **Embedding and Initialization:** The vector $\hat{t}_{n+1}^{(0)}$ is initialized, typically as the "average" of the embeddings:

$$\hat{t}_{n+1}^{(0)} = \frac{1}{n} \sum_{i=1}^n t_i, \quad \hat{t}_{n+1}^{(0)} \in \mathbb{R}^d.$$

2. **Attention Mechanism and Update:** The matrix of known tokens $X \in \mathbb{R}^{n \times d}$ interacts with $\hat{t}_{n+1}^{(k)} \in \mathbb{R}^d$ through the self-attention mechanism. At each step k , the matrices of queries (Q), keys (K), and values (V) are computed as:

$$Q = \hat{t}_{n+1}^{(k)} W_Q, \quad K = X W_K, \quad V = X W_V,$$

where $W_Q, W_K, W_V \in \mathbb{R}^{d \times d}$ are learned weight matrices, and $\hat{t}_{n+1}^{(k)}$ should be treated as a row vector (check the dimensionality of the vector-matrix product to convince yourself of this). Here, $Q \in \mathbb{R}^d$ is the query vector for the token-to-be-predicted; $K, V \in \mathbb{R}^{n \times d}$ are the key and value matrices for the known tokens.

The attention weights are calculated using the softmax function as:

$$\alpha_i^{(k)} = \text{softmax} \left(\frac{Q \cdot K}{\sqrt{d}} \right)_i := \frac{\exp \left(\frac{QK_{i,:}^\top}{\sqrt{d}} \right)}{\sum_{j=1}^n \exp \left(\frac{QK_{j,:}^\top}{\sqrt{d}} \right)} \in [0, 1],$$

where $K_{i,:}$ denotes the i th row of K , which is transposed to become the i th column of K^\top , and appears as a column vector in the computation of $\alpha_i^{(k)}$.¹ These weights

¹The softmax in computing $\alpha_i^{(k)}$ may also be applied by computing QK^\top/\sqrt{d} first, and then applying $e^{x_i}/\sum_i e^{x_i}$ to each component of the resulting vector.

represent the importance of each known token t_i in predicting t_{n+1} . The aggregated output is obtained by contracting the attention weights with the value vectors:

$$z^{(k)} = \sum_{i=1}^n \alpha_i^{(k)} V_i, \quad z^{(k)} \in \mathbb{R}^d.$$

Note that the attention mechanism – arguably the most important part of the transformer construction – incorporates both linear transformations and nonlinear operations, enabling the model to capture complex relationships in the data.

- 3. Nonlinear Transformation + Normalization:** The aggregated output $z^{(k)}$ undergoes a nonlinear transformation to update $\hat{t}_{n+1}^{(k)}$:

$$\hat{t}_{n+1}^{(k+1)} = \text{LayerNorm}(\sigma(W_2\sigma(W_1 z^{(k)}) + b)),$$

where:

- $W_1, W_2 \in \mathbb{R}^{d \times d}$ are learned weight matrices,
- $b \in \mathbb{R}^d$ is a bias vector,
- $\sigma(\cdot)$ is a point-wise activation function, such as Gaussian Error Linear Unit (GELU), defined as:

$$\sigma(x) = x \cdot \Phi(x),$$

where $\Phi(x) = \frac{1}{2} \left(1 + \text{erf}\left(\frac{x}{\sqrt{2}}\right) \right)$ is the cumulative distribution function of a standard Gaussian.

Layer Normalization ensures stability during iterations and is defined as:

$$\text{LayerNorm}(x) = \frac{x - \mu}{\sqrt{\sigma^2 + \epsilon}} \odot \gamma + \beta,$$

where:

- $\mu = \frac{1}{d} \sum_{i=1}^d x_i$ is the mean of the input x ,
- $\sigma^2 = \frac{1}{d} \sum_{i=1}^d (x_i - \mu)^2$ is the variance of the input,
- $\gamma, \beta \in \mathbb{R}^d$ are learnable parameters for scaling and shifting,
- ϵ is a small constant to ensure numerical stability,
- \odot denotes element-wise multiplication.

This combination of nonlinear transformations and normalization ensures that the model learns stable and expressive representations at each iteration.

- 4. Multi-Head Attention:** To capture diverse patterns in the input data, transformers employ multi-head attention, which divides the embeddings into multiple subspaces (or heads), allowing the model to focus on different aspects of the data simultaneously.

The following construct serves as a unified extension of steps 1–3 described above, adapted for the case where multi-head attention is applied.

Each head independently computes attention, and the outputs are concatenated and projected back into the original dimension:

$$Q_h = \hat{t}_{n+1}^{(k)} W_Q^h, \quad K_h = X W_K^h, \quad V_h = X W_V^h, \quad h = 1, \dots, H,$$

where H is the number of attention heads, $Q_h, K_h, V_h \in \mathbb{R}^{n \times d_h}$, and $W_Q^h, W_K^h, W_V^h \in \mathbb{R}^{d \times d_h}$ are learned weight matrices for head h . The dimension of each head is $d_h = \frac{d}{H}$.

The attention weights for each head are computed as:

$$\alpha_{i,h}^{(k)} = \text{softmax}_i \left(\frac{Q_h K_h^\top}{\sqrt{d_h}} \right), \quad \alpha_{i,h}^{(k)} \in [0, 1],$$

where $\alpha_{i,h}^{(k)}$ is component of a tensor representing the importance (or attention) of the i -th token in the sequence relative to the query vector for head h . Here, $Q_h \in \mathbb{R}^{1 \times d_h}$ and $K_h \in \mathbb{R}^{n \times d_h}$ interact to produce $\alpha_h^{(k)} \in \mathbb{R}^{n \times 1}$, encoding relationships between the query and all tokens in the sequence.

The transition from the attention weights $\alpha_h^{(k)}$ to the aggregated output $z_h^{(k)}$ can be understood as a **tensor embedding process**:

$$z_h^{(k)} = \sum_{i=1}^n \alpha_{i,h}^{(k)} V_{h,i}, \quad z_h^{(k)} \in \mathbb{R}^{d_h}.$$

Here, $V_h \in \mathbb{R}^{n \times d_h}$ is the value matrix, and each $V_{h,i} \in \mathbb{R}^{d_h}$ represents the embedding of the i -th token for head h . The operation combines the attention weights $\alpha_{i,h}^{(k)}$ with the embeddings $V_{h,i}$, effectively projecting the sequence-level relationships (encoded in $\alpha_h^{(k)}$) back into the token embedding space of dimension d_h . This embedding process embeds **token relationships** as weighted contributions to the output vector, thereby incorporating context into the representation.

The final multi-head attention output is obtained by concatenating the outputs from all heads:

$$z^{(k)} = \text{Concat}(z_1^{(k)}, z_2^{(k)}, \dots, z_H^{(k)}) W_O \in \mathbb{R}^d, \quad W_O \in \mathbb{R}^{(d_1+d_2+\dots+d_H) \times d}.$$

Here, $\text{Concat}(\cdot) \in \mathbb{R}^{d_1+d_2+\dots+d_H}$ is projected back to the original embedding dimension d via W_O . This ensures that the multi-head attention captures diverse contextual features across multiple subspaces of the token embeddings while preserving the original dimensionality of the data.

After the multi-head attention mechanism computes the aggregated output $z^{(k)}$, it undergoes a nonlinear transformation (see above) to refine and update the representation of the token-to-be-predicted, $\hat{t}_{n+1}^{(k+1)}$.

5. Convergence and Stabilization: The iterations in k proceed until $\hat{t}_{n+1}^{(k)}$ converges to a stable vector $\hat{t}_{n+1}(X)$. The stabilized vector is then used to compute the probabilities of the next token over the vocabulary:

$$p(t_{n+1}|X) = \text{softmax}(W_{\text{out}}\hat{t}_{n+1}(X) + b_{\text{out}}),$$

where $W_{\text{out}} \in \mathbb{R}^{d \times v}$ projects the embedding to the vocabulary size v (enumerating all valid tokens); and $b_{\text{out}} \in \mathbb{R}^v$ is bias vector.

Exercise 1.1.4 (Multi-Head Attention with Prescribed Weights and Ternary Alphabet). Consider a sequence of tokens $\{t_1, t_2, t_3\}$ embedded as

$$X = \begin{bmatrix} 1 & 2 \\ 3 & 4 \\ 5 & 6 \end{bmatrix} \in \mathbb{R}^{3 \times 2},$$

where $n = 3$ (sequence length) and $d = 2$ (embedding dimension). The tokens t_1, t_2, t_3 correspond to three states in the vocabulary $\mathcal{A} = \{a, b, c\}$, with:

$$t_1 \rightarrow a, \quad t_2 \rightarrow b, \quad t_3 \rightarrow c.$$

These embeddings represent features associated with each state and will guide the computation of the next token in the sequence, t_4 . Assume the transformer has two, $H = 2$, attention heads with the following prescribed weights:

$$\begin{aligned} W_Q^1 &= \begin{bmatrix} 1 & 0 \\ 0 & 1 \end{bmatrix}, & W_K^1 &= \begin{bmatrix} 1 & 1 \\ 1 & -1 \end{bmatrix}, & W_V^1 &= \begin{bmatrix} 1 & 0 \\ 0 & 1 \end{bmatrix}, \\ W_Q^2 &= \begin{bmatrix} 0 & 1 \\ 1 & 0 \end{bmatrix}, & W_K^2 &= \begin{bmatrix} 1 & -1 \\ -1 & 1 \end{bmatrix}, & W_V^2 &= \begin{bmatrix} 2 & 0 \\ 0 & 2 \end{bmatrix}. \end{aligned}$$

The token-to-be-predicted $\hat{t}_4 \in \mathbb{R}^2$ is initialized as:

$$\hat{t}_4^{(0)} = \frac{1}{3}(t_1 + t_2 + t_3) = \begin{bmatrix} 3 \\ 4 \end{bmatrix}.$$

1. Query, Key, and Value Computation: Compute the query vector Q_h , key matrix K_h , and value matrix V_h for each head $h = 1, 2$ using:

$$Q_h = \hat{t}_4^{(0)} W_Q^h, \quad K_h = X W_K^h, \quad V_h = X W_V^h.$$

2. Attention Weights: Compute the attention weights $\alpha_{i,h}$ for each token $i = 1, 2, 3$ and each head $h = 1, 2$ using:

$$\alpha_{i,h} = \text{softmax}_i \left(\frac{Q_h \cdot K_h^\top}{\sqrt{d_h}} \right), \quad \text{where } d_h = d/H = 1.$$

3. **Aggregated Output per Head:** Compute the aggregated output $z_h^{(0)}$ for each head $h = 1, 2$ using:

$$z_h^{(0)} = \sum_{i=1}^n \alpha_{i,h} V_{h,i}.$$

4. **Multi-Head Attention Output:** Concatenate $z_1^{(0)}$ and $z_2^{(0)}$, and project back to the original dimension $d = 2$ using:

$$z^{(0)} = \text{Concat}(z_1^{(0)}, z_2^{(0)}) W_O, \quad W_O = \begin{bmatrix} 1 & 0 \\ 0 & 1 \\ 0 & 1 \\ 1 & 0 \end{bmatrix}.$$

5. **Nonlinear Transformation:** Verify the updated value of $\hat{t}_4^{(1)}$ after applying the non-linear transformation:

$$\hat{t}_4^{(1)} = \text{LayerNorm} \left(\text{ReLU} \left(W_2 \text{ReLU}((W_1 z^{(0)})^\top) + b \right) \right),$$

where $W_1 = \begin{bmatrix} 1 & 0 \\ 0 & 1 \end{bmatrix}$, $W_2 = \begin{bmatrix} 1 & 0 \\ 0 & 1 \end{bmatrix}$, $b = \begin{bmatrix} 0 \\ 0 \end{bmatrix}$, and $\text{ReLU}(x) = \max(0, x)$ (ReLU activation). When computing LayerNorm, assume that γ and β are constant vectors of all 1's and all 0's, respectively.

6. **Stabilization:** Perform parts 1-5 once more on $\hat{t}_4^{(1)}$ and compute the "stabilized" \hat{t}_4 . (Actual stabilization of $\hat{t}_4^{(k)}$ to \hat{t}_4 would happen at $k \rightarrow \infty$.)

7. **Probabilistic Step:** Recall that the vocabulary (alphabet) is ternary – $\mathcal{A} = \{a, b, c\}$ – and compute the probabilities of the next token using the softmax function:

$$\begin{aligned} p(t_4 = a | t_1, t_2, t_3) &= \frac{\exp((W_{out}\hat{t}_4)_1)}{\sum_{j=1}^3 \exp((W_{out}\hat{t}_4)_j)}, \\ p(t_4 = b | t_1, t_2, t_3) &= \frac{\exp((W_{out}\hat{t}_4)_2)}{\sum_{j=1}^3 \exp((W_{out}\hat{t}_4)_j)}, \\ p(t_4 = c | t_1, t_2, t_3) &= \frac{\exp((W_{out}\hat{t}_4)_3)}{\sum_{j=1}^3 \exp((W_{out}\hat{t}_4)_j)}, \end{aligned}$$

where

$$W_{out} = \begin{bmatrix} 1 & 0 \\ 0 & 1 \\ 1 & -1 \end{bmatrix} \in \mathbb{R}^{3 \times 2}.$$

Compute these probabilities explicitly and explain how the output distribution depends on the attention mechanism and token embeddings.

This exercise demonstrates the application of multi-head attention with explicit tensor operations and a ternary vocabulary, showcasing the transformer's ability to model dependencies across tokens.

Pivoting from Representation to Structure: The Power of Decompositions

Section 1.1 focused on defining the algebraic objects – vectors, matrices, and tensors – that *represent* data and *execute* core AI operations like convolution and attention. However, simply representing data is not enough. To compress, analyze, and gain insight into the geometric structure of this high-dimensional data, we need powerful tools. Matrix decompositions, specifically the Singular Value Decomposition (SVD) and Eigen-Decomposition (ED), provide the mathematical framework for breaking down complex matrices into simpler, interpretable components, which is the focus of Section 1.2.

1.2 Matrix Decompositions

1.2.1 Singular Value Decomposition

Singular Value Decomposition (SVD) is a powerful linear algebra technique that can be applied to a batch of data points to extract a reduced-dimensional representation for individual data points. It works by identifying principal directions of variation in the data and allows projecting each data point onto a smaller set of basis vectors while retaining most of the relevant information.

Consider a dataset represented as a matrix $X \in \mathbb{R}^{n \times d}$, where n is the number of data points and d is the dimensionality of each data point. We assume that $n > d$. The Singular Value Decomposition (SVD) of X is given by:

$$X = USV^\top,$$

where:

- $U \in \mathbb{R}^{n \times n}$ is the left singular matrix, whose columns form an orthonormal basis for the space spanned by the rows of X .
- $S \in \mathbb{R}^{n \times d}$ is a diagonal matrix containing the singular values, which indicate the significance of the corresponding directions.
- $V \in \mathbb{R}^{d \times d}$ is the right singular matrix, whose columns form an orthonormal basis for the space spanned by the columns of X .

Both U and V are orthogonal matrices, meaning $U^\top = U^{-1}$ and $V^\top = V^{-1}$, and therefore they are invertible.

Steps to Compute SVD:

The key property of the SVD is that the columns of V (right singular vectors) are the eigenvectors of $X^\top X$, and the squares of the singular values σ_i^2 are the eigenvalues of $X^\top X$:

$$X^\top X = VS^\top U^\top USV^\top = VS^\top SV^\top$$

$$= V \begin{bmatrix} \sigma_1 & 0 & \cdots & 0 & 0 & \cdots & 0 \\ 0 & \sigma_2 & \cdots & 0 & 0 & \cdots & 0 \\ \vdots & \vdots & \ddots & \vdots & \vdots & \ddots & \vdots \\ 0 & 0 & \cdots & \sigma_d & 0 & \cdots & 0 \end{bmatrix} \begin{bmatrix} \sigma_1 & 0 & \cdots & 0 \\ 0 & \sigma_2 & \cdots & 0 \\ \vdots & \vdots & \ddots & \vdots \\ 0 & 0 & \cdots & \sigma_d \\ 0 & 0 & \cdots & 0 \\ \vdots & \vdots & \ddots & \vdots \end{bmatrix} V^\top = V \text{diag}(\sigma_1^2, \dots, \sigma_d^2) V^\top,$$

where we took into account the orthogonality of U .

Values of the diagonal matrix are conventionally ordered in **descending** order, with the largest singular values appearing first:

$$\sigma_1^2 \geq \cdots \geq \sigma_d^2.$$

Since $X^\top X \in \mathbb{R}^{d \times d}$ is symmetric and positive semi-definite (as it is constructed as the product of a matrix and its transpose), it has real, non-negative eigenvalues $\lambda_1 \geq \lambda_2 \geq \cdots \geq \lambda_d \geq 0$ and an orthonormal set of eigenvectors v_1, v_2, \dots, v_d ². Therefore, by computing the eigenvalues and eigenvectors of $X^\top X$, we can directly obtain the singular values ($\sigma_i = \sqrt{\lambda_i}$) and the right singular vectors (the columns of V).

Once the singular values and V are determined, the left singular vectors (columns of U) can be computed using the following relation:

$$XV = US.$$

Expanding this for each singular vector v_i of V :

$$Xv_i = \sigma_i u_i,$$

where σ_i is the singular value corresponding to v_i , and u_i is the left singular vector. Thus:

$$u_i = \frac{1}{\sigma_i} Xv_i \quad \text{for } \sigma_i \neq 0.$$

The matrix U can then be constructed by normalizing u_i for all i .

For singular values corresponding to $\sigma_i = 0$, the remaining columns of U can be completed to form an orthonormal basis for \mathbb{R}^m .

²The symmetry of $X^\top X$ ensures that it can be diagonalized by an orthogonal matrix, as guaranteed by the spectral theorem. The spectral theorem states that any real symmetric matrix can be decomposed as $V\Lambda V^\top$, where V is an orthogonal matrix whose columns are the eigenvectors of the matrix, and Λ is a diagonal matrix whose entries are the corresponding real eigenvalues. The positive semi-definiteness of $X^\top X$ follows from the fact that for any vector $z \in \mathbb{R}^d$, the quadratic form $z^\top X^\top X z = \|Xz\|^2 \geq 0$, meaning all eigenvalues of $X^\top X$ are non-negative. This guarantees that Λ has only non-negative entries. The orthonormal eigenvectors correspond to the standard diagonalization of symmetric matrices, meaning that $X^\top X$ can be rewritten as $V\Lambda V^\top$, where V is an orthogonal matrix ($V^\top V = I$) and Λ is a diagonal matrix containing the eigenvalues of $X^\top X$. The fact that V is orthogonal ensures that the eigenvectors form an orthonormal basis of \mathbb{R}^d .

Summary of Steps:

1. Compute $X^\top X$ and find its eigenvalues λ_i and eigenvectors v_i .
2. The singular values are $\sigma_i = \sqrt{\lambda_i}$.
3. Construct V from the eigenvectors v_i of $X^\top X$.
4. Compute U using $U = \frac{1}{\sigma_i}XV$, normalizing the columns as needed.
5. Assemble S , U , and V to complete the SVD: $X = USV^\top$.

Exercise 1.2.1 (Finding the SVD of a Simple Matrix). *Find SVD of the matrix:*

$$X = \begin{bmatrix} 1 & 0 & 0 & 0 & 2 \\ 0 & 0 & 3 & 0 & 0 \\ 0 & 0 & 0 & 0 & 0 \\ 0 & 4 & 0 & 0 & 0 \end{bmatrix}.$$

Exercise 1.2.2 (SVD for Matrix Completion: Low-Rank Approximation and Prediction). *Matrix completion is a classical application of the Singular Value Decomposition (SVD). Suppose we observe a partially filled user – item rating matrix $R \in \mathbb{R}^{m \times n}$, where rows correspond to users, columns to items, and entries represent observed ratings. Missing entries are denoted by ?.*

A small illustrative example is:

$$R = \begin{bmatrix} 5 & ? & 3 & 1 \\ 4 & 2 & ? & ? \\ ? & 5 & 4 & ? \\ 1 & ? & 2 & 3 \end{bmatrix}.$$

The core idea of SVD-based matrix completion is that user preferences and item attributes often lie near a low-rank subspace. Thus, one approximates R by retaining only the leading k singular values:

$$R_k \approx U_k S_k V_k^\top, \quad k \ll \min(m, n).$$

Missing entries are then predicted using the reconstructed approximation R_k .

Tasks.

1. **Low-rank approximation.** Assume the full matrix R were known. (a) Write explicitly how to obtain its truncated SVD $R_k = U_k S_k V_k^\top$. (b) Explain why keeping only the top k singular values amounts to projecting R onto the subspace of maximal variance.
2. **Predicting missing entries.** Suppose we only observe the entries that are not ?. Describe a procedure (theoretical, not computational) for estimating the missing entries using:

$$\min_{X \in \mathbb{R}^{m \times n}} \|P_\Omega(X - R)\|_F^2 \quad \text{subject to} \quad \text{rank}(X) \leq k,$$

where P_Ω is the projection onto observed entries.

Explain why alternating between (i) filling missing entries using the current X , and (ii) recomputing a rank- k SVD of X , converges to a low-rank completion.

3. **Interpretation.** In the movie-rating context, explain the meaning of the factors U_k , S_k , V_k :
- What do the rows of U_k represent?
 - What do the columns of V_k represent?
 - Why does low-rank structure correspond to the existence of “latent” genres or user preference dimensions?
4. **Optional (conceptual): Connection to the Netflix Prize.** Briefly summarize why low-rank methods (including SVD-based ones) historically performed well for large-scale recommendation systems such as the Netflix dataset.

Note. This exercise is theoretical; no code implementation is required. The goal is to connect the SVD to a widely used practical application that depends on low-rank structure, prediction, and latent representation learning.

1.2.2 Reduced Representation of a Single Data Point with SVD

Let $X \in \mathbb{R}^{n \times d}$ be a dataset whose rows $x_i \in \mathbb{R}^d$ represent individual data points. A central goal in data analysis and machine learning is to obtain a low-dimensional representation $z_i \in \mathbb{R}^k$, with $k \ll d$, such that z_i preserves the most informative geometric structure of x_i . This is essential in applications involving compression, denoising, and feature extraction. The Singular Value Decomposition (SVD) of X ,

$$X = USV^\top,$$

provides a principled way to construct such reduced representations. The columns of V are right singular vectors, representing principal directions of variability in the dataset, while the singular values $\sigma_1 \geq \sigma_2 \geq \dots$ quantify how much variance is captured in each direction. To reduce the dimensionality of a single point x_i , we project it onto the top k singular directions:

$$z_i = x_i V_k,$$

where $V_k \in \mathbb{R}^{d \times k}$ contains the first k columns of V . The reduced vector $z_i \in \mathbb{R}^k$ captures the dominant features of x_i while ignoring lower-variance structure.

Example 1.2.1 (Dimensionality Reduction on MNIST). To illustrate these concepts, the accompanying Python notebook `MNIST-SVD.ipynb` performs SVD on a small batch of MNIST digits (flattened into vectors in \mathbb{R}^{784}). Each image is centered by subtracting the batch mean, and the SVD of the resulting data matrix is computed.

Fig. 1.2 provides a visual summary:

1. the mean image of the batch,
2. the first two right singular vectors (“eigendigits”),
3. rank- k reconstructions of a sample image for $k = 5, 20, 50$.

These reconstructions demonstrate how increasing the number of retained components improves the fidelity of the approximation, with coarse global structure captured by small k and finer details emerging as k grows.

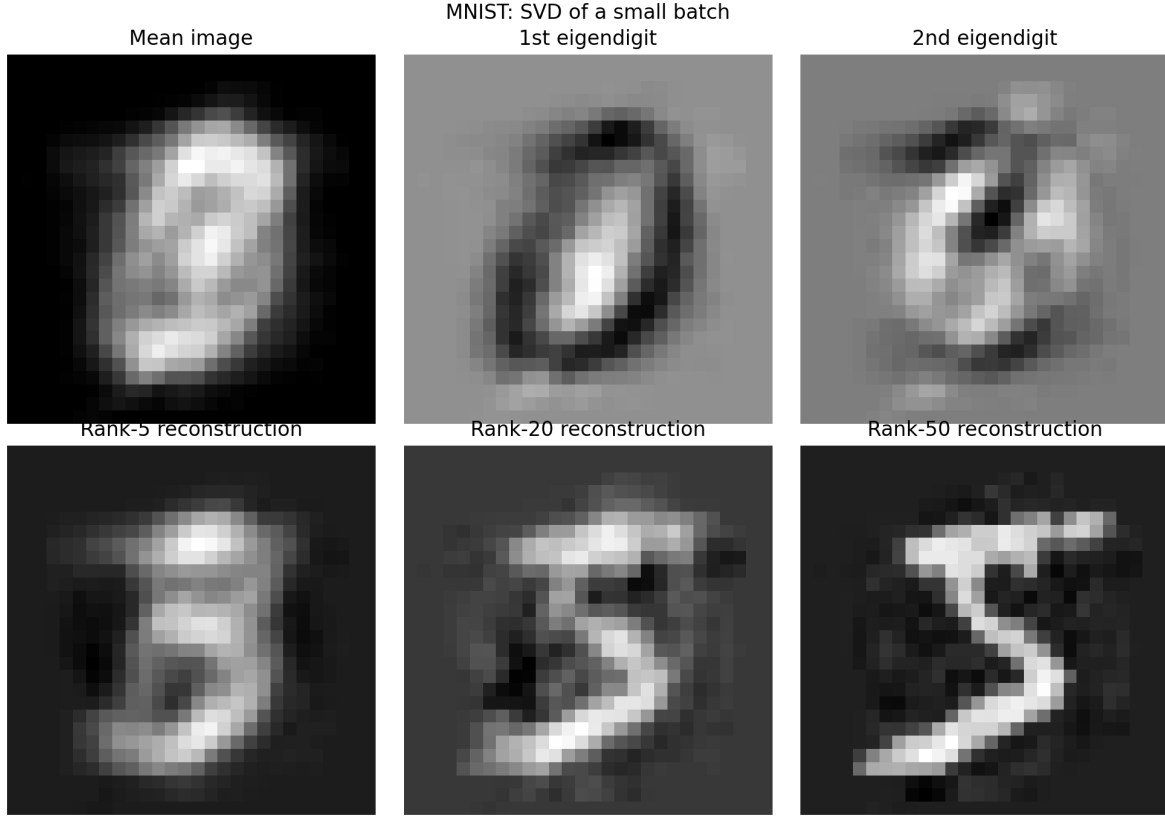


Figure 1.2: Mean image, principal directions, and rank- k reconstructions. Top row: mean image and the first two principal directions (eigen-digits) obtained from the SVD of a small MNIST batch. Bottom row: reconstructions of a sample digit using rank-5, rank-20, and rank-50 approximations. The leading singular vectors capture large-scale geometric patterns and strokes typical of handwritten digits.

Spectral Diagnostics and Interpretability Beyond reconstructions, the singular value spectrum provides insight into the intrinsic dimensionality and structure of image datasets. The rich spectral analysis in Fig. 1.3 shows four complementary views:

1. **Single-batch spectrum** (upper left): normalized singular values exhibit rapid decay, reflecting a strong low-rank structure typical of handwritten digits.
2. **Multiple random batches** (upper right): several spectra computed from different random subsets of MNIST. Their remarkable alignment indicates that the dominant principal directions are stable across samples—an important empirical fact that justifies using SVD on small batches.
3. **Per-digit spectra** (lower left): classes differ in intrinsic geometric complexity. For example, the digit “1” exhibits a sharper spectral decay, reflecting its nearly one-dimensional structure, while digits such as “8” or “2” require more components to capture curved strokes.

4. **Cumulative variance curve** (lower right): the curve

$$E_k = \frac{\sum_{j=1}^k \sigma_j^2}{\sum_{j=1}^d \sigma_j^2}$$

quantifies how quickly variance is captured. For MNIST, a modest number of singular directions (typically $k \approx 40\text{--}60$) already explains the vast majority of variance.

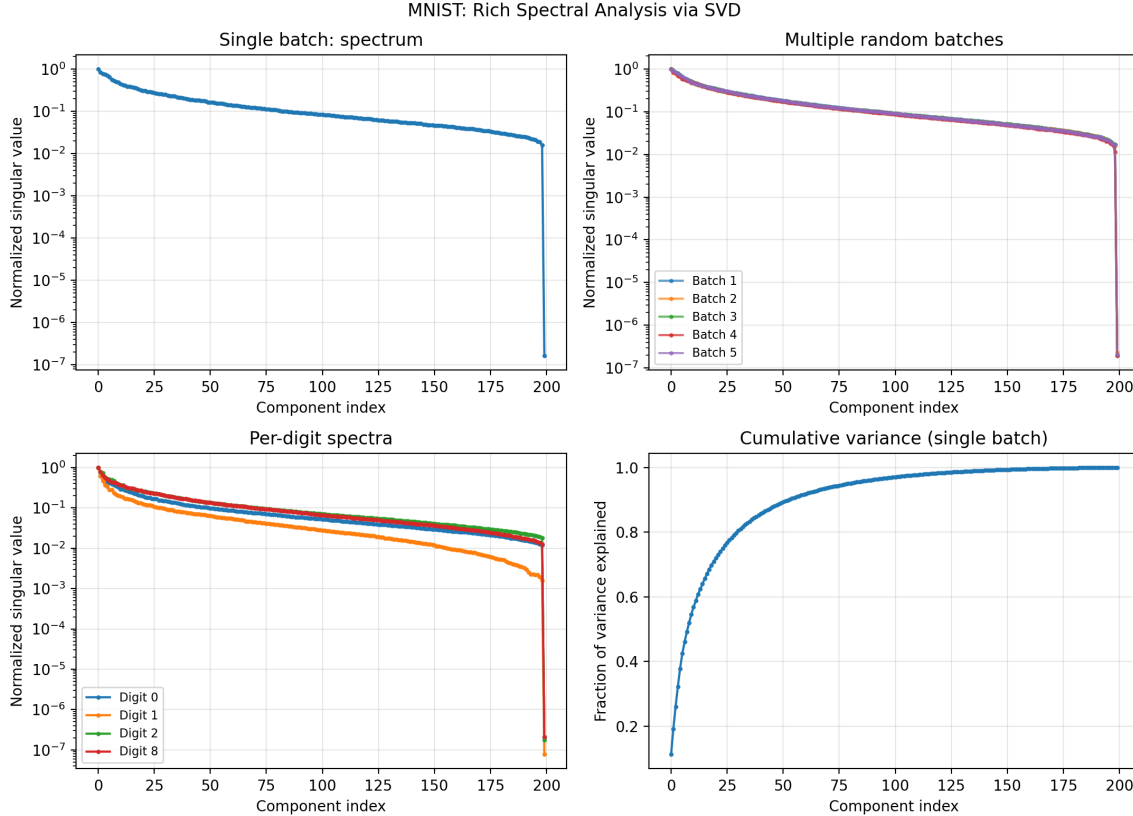


Figure 1.3: **MNIST: rich spectral analysis via SVD.** Upper left: spectrum from a single batch. Upper right: spectra from multiple random batches, demonstrating spectral stability across samples. Lower left: per-digit spectra for digits $\{0, 1, 2, 8\}$, revealing differences in geometric complexity. Lower right: cumulative variance curve for a canonical batch, showing that a relatively small number of components captures most of the dataset's structure.

Key Properties

- **Dimensionality Reduction:** The projection $z_i = x_i V_k$ compresses data from d to k dimensions while preserving dominant directions.
- **Information Retention:** Singular values quantify explained variance; keeping the first k singular vectors ensures that the reduced representation retains most of the dataset's structure.

- **Interpretability:** Eigendigits reveal meaningful global patterns (strokes, spatial templates) learned directly from the data.
- **Spectral Stability:** Similar spectra across random batches and characteristic differences across digit classes highlight both the universality and the specificity of data-driven structure in MNIST.

Why SVD Matters for Generative AI

Although the Singular Value Decomposition (SVD) is introduced in this chapter as a linear-algebraic tool for dimensionality reduction, it plays a conceptual role throughout modern Generative AI. This sidebar highlights several reasons why understanding SVD helps in interpreting and designing generative models of AI.

1. Covariance, Gaussian Geometry, and Whitening. The starting point for diffusion models and many Variation Auto Encoders (VAE) discussed later in the book is a Gaussian reference distribution. The covariance matrix admits an eigen-decomposition:

$$\Sigma = V\Lambda V^\top,$$

and SVD reveal the principal axes along which the data varies. Whitening and preconditioning — routine steps in deep learning — depend on this diagonalization. Understanding these transformations clarifies why diffusion models prefer isotropic priors and why Gaussian scores have the form $\nabla_x \log p(x) = -\Sigma^{-1}(x - \mu)$.

2. Intrinsic Dimension and Spectral Decay. A rapidly decaying singular spectrum indicates that the dataset lies near a low-dimensional manifold. This observation connects directly to the practice of:

- choosing small latent dimensions in VAEs,
- using Low-Rank Approximations (LORA) in transformers,
- compressing neural representations without significant performance loss.

SVD thus provides the first quantitative measure of *intrinsic dimension*.

3. Conditioning, Stiffness, and Gradient Scales. Diffusion models evolve probability densities along continuous-time paths. Low-variance directions (small singular values) correspond to stiff directions in the reverse-time Stochastic Ordinary Differential Equation (SODE), often requiring careful noise schedules or preconditioning. Interpreting these stiff modes through SVD gives intuition about why some data manifolds are harder to sample than others.

4. Score Approximation and Data Geometry. The score of the data distribution, $\nabla_x \log p_{\text{data}}(x)$, plays a central role in score-based generative modeling. For Gaussian data, SVD shows that the score has larger magnitude in low-variance directions, explaining why diffusion models denoise anisotropically even with isotropic noise.

5. Low-Rank Structure in Attention Mechanisms. Although not expressed through SVD explicitly, the attention matrices in transformers frequently exhibit approximate low-rank structure. This has enabled:

- spectral compression,
- linear-attention variants,
- efficient fine-tuning (LoRA),
- structured low-rank updates in large models.

Understanding SVD prepares the reader for these ideas in later chapters.

Overall: SVD is more than a tool for dimensionality reduction. It provides a geometric lens through which many aspects of generative modeling become clearer: the structure of data manifolds, conditioning of sampling processes, Gaussian reference models, and the spectral behavior of network representations. This makes SVD a cornerstone concept for the mathematics of modern Generative AI.

1.2.3 Eigen-Decomposition

Eigen-Decomposition (ED) is a fundamental matrix factorization technique applicable to square matrices. Given a square matrix $A \in \mathbb{R}^{d \times d}$, eigen-decomposition expresses A in terms of its eigenvalues and eigenvectors. An eigenvalue-eigenvector pair (λ, v) satisfies the equation:

$$Av = \lambda v,$$

where $\lambda \in \mathbb{C}$ is the eigenvalue, and $v \in \mathbb{C}^d$ is the corresponding eigenvector³. The eigenvectors represent directions that remain invariant under the linear transformation defined by A , and the eigenvalues describe the scaling along these directions.

In the general case, A may have complex eigenvalues and eigenvectors, even if the entries of A are real. This occurs when A has non-symmetric or non-diagonalizable properties, such as in rotations or other non-conservative transformations. Eigenvalues can be repeated (degenerate) or distinct, and not all square matrices are guaranteed to have a full set of linearly independent eigenvectors. However, for matrices that are diagonalizable (no zero eigenvalues), ED expresses A as:

$$A = Q\Lambda Q^{-1},$$

where:

- $Q \in \mathbb{C}^{d \times d}$ contains the eigenvectors of A as columns.
- $\Lambda \in \mathbb{C}^{d \times d}$ is a diagonal matrix with the eigenvalues of A on its diagonal.

³Here, \mathbb{C} represents the system of complex numbers. While in this living book we primarily work with the system of real numbers, \mathbb{R} , which is naturally a subset of the system of complex numbers, we introduce complex numbers to highlight their generality. This generality is particularly valuable in the context of the ED, where complex eigenvalues and eigenvectors often arise even for real-valued matrices.

1.2.4 Connecting SVD and ED for Symmetric Positive-Definite Matrices

The relationship between SVD and ED becomes apparent when considering symmetric positive-definite matrices, such as the aforementioned covariance matrix of a dataset: $\Sigma = \frac{1}{n}X^\top X$. The covariance matrix $\Sigma \in \mathbb{R}^{d \times d}$ is symmetric and positive semi-definite, meaning its eigenvalues are non-negative. Eigen-decomposition of Σ yields:

$$\Sigma = V\Lambda V^\top,$$

where:

- V contains the eigenvectors of Σ (the principal directions of the data).
- Λ contains the eigenvalues of Σ (the variance explained by each principal direction).

For symmetric positive-definite matrices, the eigenvalues in Λ are equivalent to the squared singular values from the SVD of X . Thus, for such matrices:

$$\Sigma = VS^2V^\top,$$

establishing that SVD and ED are closely related.

Exercise 1.2.3 (Comparing SVD and ED). *Consider the symmetric positive-definite matrix (covariance matrix):*

$$\Sigma = \begin{bmatrix} 4 & 2 \\ 2 & 3 \end{bmatrix}.$$

1. *Compute the ED of Σ :*

$$\Sigma = V\Lambda V^\top,$$

where Λ contains eigenvalues and V contains eigenvectors. Perform this computation manually or using software.

2. *Compute the SVD of Σ :*

$$\Sigma = US^2U^\top,$$

where S contains singular values ($\sqrt{\lambda_i}$). Perform this computation manually or using software.

3. *Verify the relationship between eigenvalues (Λ) and singular values (S).*

Example 1.2.2 (Graphs and the Graph Laplacian). *Symmetric matrices naturally arise in the study of graphs, particularly through the graph Laplacian, which encodes important structural properties of the graph. Consider an undirected graph $G = (V, E)$, where V is the set of nodes and E is the set of edges. Let $n = |V|$ denote the number of nodes.*

The adjacency matrix $A \in \mathbb{R}^{n \times n}$ of G is defined as:

$$A_{ij} = \begin{cases} 1, & \text{if there is an edge between nodes } i \text{ and } j, \\ 0, & \text{otherwise.} \end{cases}$$

The degree matrix $D \in \mathbb{R}^{n \times n}$ is a diagonal matrix where D_{ii} equals the degree of node i , defined as $D_{ii} = \sum_{j=1}^n A_{ij}$.

The graph Laplacian $L \in \mathbb{R}^{n \times n}$ is then given by:

$$L = D - A.$$

- **Symmetry and Semi-Definiteness:** L is symmetric and positive semi-definite.
- **Eigenvalues:** The eigenvalues of L provide insight into the structure of G :
 - The smallest eigenvalue is always 0.
 - The multiplicity of the 0 eigenvalue corresponds to the number of connected components in the graph.

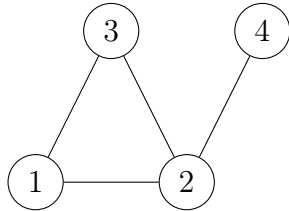


Figure 1.4: An example graph with 4 nodes. Nodes 1, 2, and 3 form a triangle, and node 4 is connected to node 2.

Exercise 1.2.4 (Understanding the Graph Laplacian). Consider the graph shown in Figure 1.4. Perform the following tasks:

1. Write down the adjacency matrix A for the graph.
2. Compute the degree matrix D .
3. Derive the graph Laplacian $L = D - A$.
4. Find the eigenvalues of L and verify the multiplicity of the 0 eigenvalue.
5. Use the eigenvectors corresponding to the smallest two nonzero eigenvalues to embed the graph in a 2D space. Discuss how the embedding reflects the structure of the graph.

From Static Structure to Dynamic Change

Chapter 1 provided the essential algebraic toolkit for high-dimensional data: the geometry of vectors, the mechanics of transformations, and the analysis offered by SVD and ED. Crucially, *Linear Algebra describes the static state and structure of data*. However, for an AI model to learn, adapt, and generate new content, it must change its internal weights – a process that involves movement and optimization. To model this dynamic change, we must shift from algebra to calculus. Chapter 2 will introduce

Automatic Differentiation (AD), the foundational technique for calculating the direction of change (the gradient), and *Differential Equations*, the mathematical language which is used (in particular) for modeling change over time.

Chapter 2

Calculus and Differential Equations (in AI)

2.1 Automatic Differentiation

Automatic differentiation (AD) is the backbone of modern scientific computing and machine learning. Its central idea is simple but powerful: *a complex function is nothing more than a composition of elementary operations, and the chain rule can be applied systematically and efficiently.* AD differs from symbolic differentiation (which often produces large expressions) and from numerical finite differences (which suffer from truncation and rounding errors). Instead, AD evaluates derivatives *exactly up to machine precision* while keeping the computational cost controlled.

Today, AD powers all major deep-learning frameworks, including PYTORCH, TENSORFLOW, and JAX. In this section we introduce the core principles of AD, illustrate them through a computational graph for a simple multivariate function, and then show how modern AD systems compute gradients efficiently in practice.

Example 2.1.1 (Decomposing a Function into a Directed Acyclic Graph). *Consider the scalar function*

$$f(x_1, x_2) = \frac{\sin(x_1 + x_2)}{x_1}.$$

To expose AD's structure, we rewrite the computation as a sequence of elementary operations:

$$w_1 = x_1, \quad w_2 = x_2, \quad w_3 = w_1 + w_2, \quad w_4 = \sin(w_3), \quad w_5 = \frac{w_4}{w_1}. \quad (2.1)$$

These steps form a Directed Acyclic Graph (DAG), also called a computational graph. Each node carries a value computed from its parents, while each edge encodes the dependency structure. This viewpoint is fundamental to AD: instead of differentiating the full expression for f symbolically, AD applies the chain rule locally along the edges of the graph. During forward execution, values flow from inputs to output; in reverse mode (backpropagation), sensitivities propagate from the output back to all inputs. Fig. 2.1 visualizes both modes. Differentiating f means expressing the differential

$$df = dw_5 = \partial_{x_1} f dx_1 + \partial_{x_2} f dx_2.$$

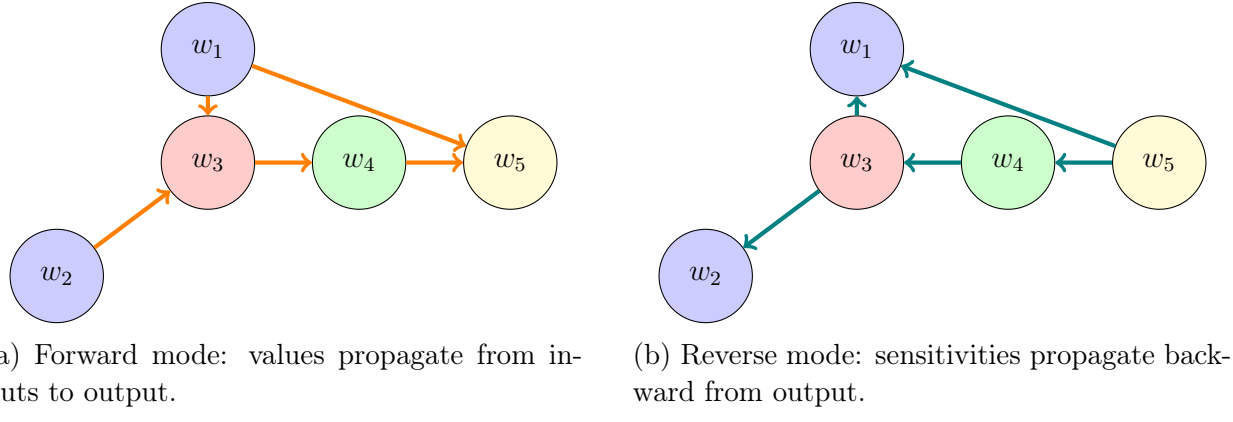


Figure 2.1: Forward-mode (left) and reverse-mode (right) propagation on the computational graph of $f(x_1, x_2) = \sin(x_1 + x_2)/x_1$. Orange arrows illustrate the flow of primal values in forward execution; teal arrows illustrate the flow of adjoints (gradients) in backpropagation.

Using chain-rule expansions along the graph gives

$$\begin{aligned} dw_5 &= \frac{\partial w_5}{\partial w_1} dw_1 + \frac{\partial w_5}{\partial w_4} dw_4, \\ dw_4 &= \frac{\partial w_4}{\partial w_3} dw_3, \\ dw_3 &= \frac{\partial w_3}{\partial w_1} dw_1 + \frac{\partial w_3}{\partial w_2} dw_2. \end{aligned}$$

After substitution, one obtains the explicit gradient formulas:

$$\partial_{x_1} f = \frac{\partial w_5}{\partial w_1} + \frac{\partial w_5}{\partial w_4} \frac{\partial w_4}{\partial w_3} \frac{\partial w_3}{\partial w_1}, \quad \partial_{x_2} f = \frac{\partial w_5}{\partial w_4} \frac{\partial w_4}{\partial w_3} \frac{\partial w_3}{\partial w_2}. \quad (2.2)$$

2.1.1 Forward vs. Reverse Mode AD

The computational graph in Fig. 2.1 highlights the two fundamental modes of automatic differentiation. Both modes apply the chain rule locally along the graph, but they differ in the direction in which derivatives are propagated, and therefore in their computational costs.

Forward Mode (many inputs \rightarrow few outputs). Forward mode propagates differentials *with* the computational graph—from inputs toward the output. For each input direction dx_i , forward mode computes the associated chain of partial derivatives all the way to the output. This makes it efficient when:

$$(\# \text{ of inputs}) \ll (\# \text{ of outputs}).$$

Typical use cases include:

- sensitivity analysis of models with a small number of parameters;

- Jacobian–vector products;
- probing which input features influence a model’s prediction.

Conceptually, forward mode answers: “*If I nudge some inputs, how does the output change?*”

Reverse Mode (one or few outputs → many inputs). Reverse mode propagates sensitivities *against* the graph—from the (often scalar) output back to all inputs. Instead of computing all derivatives for all inputs *independently*, reverse mode reuses intermediate adjoints, making it dramatically more efficient when:

$$(\# \text{ of outputs}) \ll (\# \text{ of inputs}).$$

This is the case when training neural networks, where the loss is a scalar and the number of parameters ranges from millions to tens of billions. Reverse mode therefore underlies backpropagation.

Conceptually, reverse mode answers: “*How does this particular output depend on every input or parameter?*”

Forward vs. Reverse: summary of complexity. Let $n = \#\text{inputs}$ and $m = \#\text{outputs}$. Then:

$$\text{Forward mode cost} \sim \mathcal{O}(n), \quad \text{Reverse mode cost} \sim \mathcal{O}(m).$$

Thus:

Scenario	Preferred AD mode
$n \ll m$	Forward mode
$m \ll n$	Reverse mode (backprop)

Common pitfalls in interpreting AD.

- **AD is not symbolic differentiation.** AD never constructs or simplifies algebraic expressions; it differentiates the *execution trace* of a program.
- **AD is not finite differences.** AD is exact to machine precision—there is no truncation error from numerical differencing.
- **Forward vs. reverse are not interchangeable.** They compute the same mathematical derivatives but have vastly different runtime and memory characteristics.
- **Reverse-mode AD must store intermediates.** Backprop requires access to all intermediate values, which is why memory usage grows with model depth. Techniques such as check-pointing and recomputation address this.

The next example shows how modern AD systems (here in PYTORCH) use reverse-mode AD in practice and how their performance compares to finite differences.

Example 2.1.2 (AD in Practice via Python and PyTorch). *We provide a Jupyter/Python notebook AD.ipynb that illustrates three core aspects of AD:*

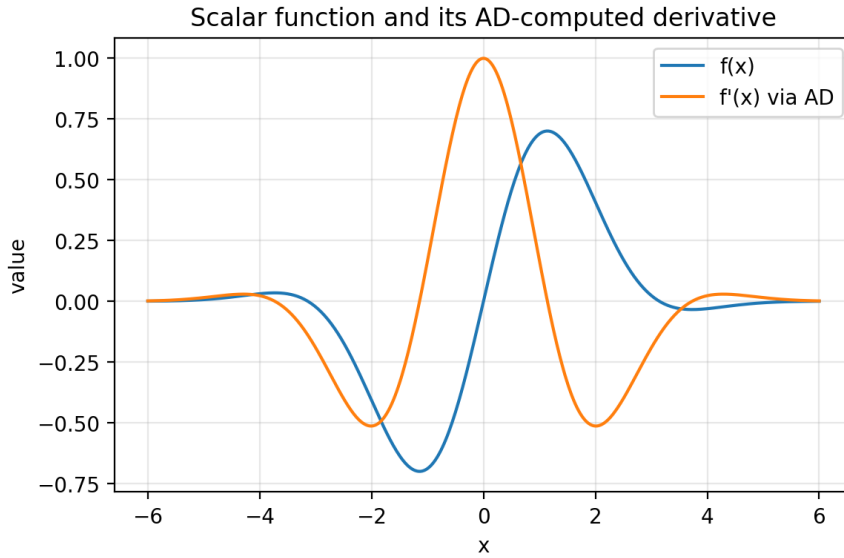


Figure 2.2: Scalar function $f(x) = \sin(x)e^{-x^2/5}$ and its derivative $f'(x)$ computed via reverse-mode AD in PyTorch. Generated by `AD.ipynb`.

1. **Automatic differentiation of a 1D function.** We evaluate the scalar function

$$f(x) = \sin(x) e^{-x^2/5}$$

on a grid and compute $f'(x)$ using reverse-mode AD. Fig. 2.2 shows both curves.

2. **Gradient computation for a multivariate function.** For the function

$$k(x, y, z) = x^2y + yz + z^3,$$

the notebook compares the analytic gradient with the PyTorch AD gradient.

3. **Runtime scaling: finite differences vs. reverse-mode AD.** For a d -dimensional function, finite differences require d function evaluations, while reverse-mode AD requires only one backward pass. The runtime comparison in Fig. 2.3 illustrates this difference on a log-log scale.

All figures are automatically saved in the `figs/` directory.

Why Automatic Differentiation Matters for Modern Generative AI

Automatic differentiation (AD) is not just a technical tool for computing gradients – it is one of the mathematical *pillars* of modern Generative AI. Almost every contemporary model, from diffusion models to transformers to large vision–language systems, relies critically on AD in several ways:

- **Training deep networks.** Reverse-mode AD (backpropagation) enables efficient optimization of models with millions or billions of parameters by computing

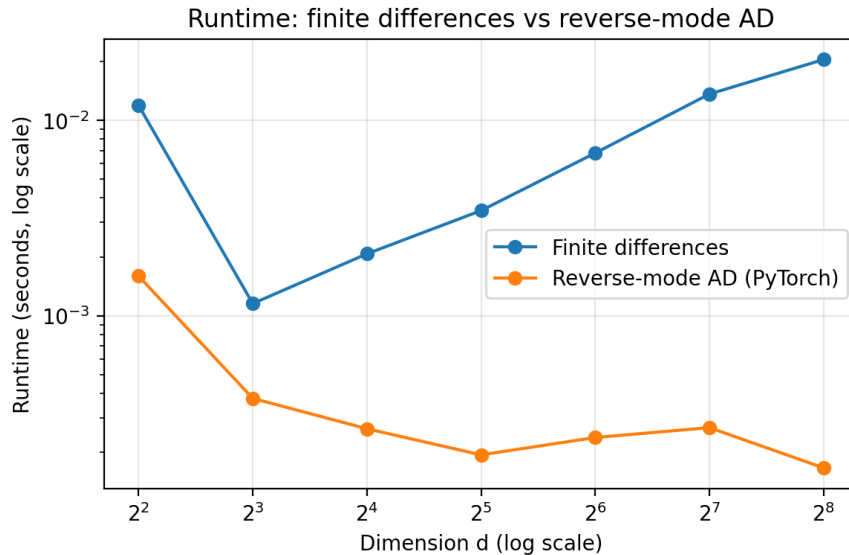


Figure 2.3: Runtime comparison between finite differences and PyTorch reverse-mode AD for increasing dimension d . Reverse-mode AD scales dramatically better. Generated by `AD.ipynb`.

the gradient of a scalar loss in a single backward sweep.

- **Learning vector fields for generation.** Diffusion models, flow-matching models, and continuous normalizing flows all require gradients of log-densities or vector fields. These gradients are learned by minimizing squared-error losses whose evaluation depends directly on AD.
- **Score estimation.** In score-based generative modeling, the objective is to regress onto $\nabla_x \log p_t(x)$. AD makes it possible to differentiate through neural networks that parameterize the score, the noise schedule, or the drift of a reverse-time SDE.
- **Differentiating through ODE/SDE solvers.** Many modern samplers differentiate through numerical ODE or SDE integrators. AD is essential for implicit layers, neural ODEs, and diffusion-based likelihood estimation.
- **Architectural design and meta-learning.** Transformer attention maps, activation functions, normalization layers, and even optimizers (e.g., Adam) are differentiable components whose internal gradients must be computed automatically for end-to-end learning.

In short, understanding AD is understanding how modern generative models *learn*, *optimize*, and *evolve* during training. It is one of the hidden engines enabling the scalability and performance of today’s systems.

Exercise 2.1.1 (The Chain Rule, Backpropagation, and AD in Practice). *This exercise*

bridges the theoretical application of the Chain Rule (Backpropagation) with its practical implementation using PyTorch’s Automatic Differentiation (AD).

1. **Theoretical Backpropagation Derivation.** Consider a simple two-layer network $f(x) = W_2\sigma(W_1x)$, where $W_1 \in \mathbb{R}^{h \times d}$, $W_2 \in \mathbb{R}^{m \times h}$, and $\sigma(\cdot)$ is an element-wise activation function.
 - (a) Write the full Jacobian $J = \frac{\partial f}{\partial x}$ as a product of matrix and diagonal matrix Jacobians.
 - (b) If L is a scalar loss function, use the chain rule to derive the gradient $\frac{\partial L}{\partial W_1}$ in terms of W_2 , the derivative σ' , and the loss gradient $\frac{\partial L}{\partial f}$. This is the essence of backpropagation.
2. **Computational Graph and Gradient Verification.** This part builds on the computational examples in the notebook `AD.ipynb`.
 - (a) **Constructing a DAG:** Consider the function $h(x, y) = \ln(x^2 + y^2) + \sin((x + y)^2)$. Construct a computational graph (DAG) for h by introducing intermediate variables and then compute ∇h manually using reverse-mode AD.
 - (b) **PyTorch Verification:** Modify the function $k(x, y, z) = x^2y + yz + z^3$ by adding a new nonlinearity, e.g., replace z^3 with $\tanh(z^3)$ or add a term such as $x \exp(y)$. Compute the analytic gradient and verify it against PyTorch AD.
3. **Hardware and Scaling Insight.**
 - (a) **Forward vs. Reverse Mode Scaling:** Use the runtime-comparison cell in `AD.ipynb` and extend it to dimensions $d = 512, 1024, 2048$ (if your machine allows). Plot the results and comment on the scaling of finite differences versus automatic differentiation.
 - (b) **Gradient Stability:** What is the fundamental problem (related to the product of Jacobians) that the backpropagation algorithm introduces in very deep networks, leading to the vanishing/exploding gradient problem? Briefly discuss how one simple technique, like gradient clipping, helps mitigate this issue.

2.2 Differential Equations: Foundations and Links to AI

Following our exploration of Automatic Differentiation, which provides the instantaneous rate of change (the gradient), we now turn to *Differential Equations* – the language used to describe change and dynamics over time. While classical deep learning focused on static mapping from input to output, the frontier of Generative AI, including Diffusion Models, Flow Matching, and Neural ODEs, fundamentally relies on modeling continuous-time dynamics. This section first reviews the mathematical foundations of Ordinary Differential Equations (ODEs) using symbolic methods. We then bridge this classical view to the modern AI challenge of *learning dynamics from data* (ODE-based regression), and finally examine the structure and solution of higher-order systems on the example of the second order ODEs.

2.2.1 Ordinary Differential Equations (ODEs) – Primer

An Ordinary Differential Equation (ODE) is an equation involving derivatives of a function with respect to a single independent variable:

$$\frac{dx}{dt} = f(x, t), \quad x \in \mathbb{R}^n, \quad t \in \mathbb{R}. \quad (2.3)$$

Often, a shorthand notation is used where \dot{x} represents $\frac{dx}{dt}$.

ODEs play a crucial role in modeling time-dependent phenomena across science and engineering, including motion, heat transfer, and population dynamics.

Integration: The Simplest Case $\dot{x} = f(t)$

Let us begin with the simplest case where $n = 1$ and the right-hand side f does not depend on x . In this case, Eq. (2.3) becomes:

$$\frac{dx}{dt} = f(t).$$

Integrating this equation gives the symbolic solution:

$$x(t) = \int f(t) dt + \text{const.} \quad (2.4)$$

The integral on the right-hand side is called an indefinite integral or anti-derivative. While differentiation is straightforward and always produces elementary expressions for well-defined functions, *integration is inherently more challenging*. In many cases, the anti-derivative of $f(t)$ cannot be expressed in terms of elementary functions. This distinction highlights the complexity of integration, which remains a significant area of mathematical study and justifies the need for numerical methods.

Exercise 2.2.1. Consider two “integrable” examples :

$$\frac{dx}{dt} = \begin{cases} \sin(at), & (I); \\ \exp(at), & (II), \end{cases}$$

where $a \in \mathbb{R}$.

1. Solve these ODEs analytically, fixing the integration constant such that $x(0) = x_0$.
2. Analyze the asymptotic behavior of the solutions as $t \rightarrow +\infty$, considering the dependence on the initial condition x_0 and the parameter a . Does the solution grow, decay, or remain bounded?

Autonomous ODEs: $\dot{x} = f(x)$

Another important one-dimensional case arises when f depends only on x (and not explicitly on t). This is referred to as an *autonomous ODE*. The equation can often be solved by separating variables:

$$\frac{dx}{f(x)} = dt.$$

Integrating both sides yields an implicit solution:

$$\int \frac{dx}{f(x)} = t + \text{const.}$$

As with the previous case, the anti-derivatives involved may or may not have elementary function forms. For autonomous systems, the focus shifts to qualitative analysis, such as the existence and stability of fixed points.

Exercise 2.2.2.

$$\frac{dx}{dt} = \begin{cases} \sin(ax), & (I); \\ \exp(ax), & (II), \end{cases}$$

where $a \in \mathbb{R}$.

1. Solve these ODEs analytically, fixing the integration constant such that $x(0) = x_0$.
2. Analyze the asymptotic behavior of the solutions as $t \rightarrow +\infty$, considering the dependence on x_0 and a .
3. Explore the existence of fixed points. If they exist, analyze their stability under small perturbations of the initial condition $x(0)$.
4. Design a function $f(x)$ such that the ODE serves as a binary classifier, separating the domain $x > 0$ and $x < 0$. Modify the function to create a time-evolving boundary (e.g., oscillatory behavior).

Symbolic Programming: Addressing Non-Integrable ODEs

The most general one-dimensional equation, where $f(x, t)$ is an arbitrary function of both x and t , is typically not integrable. We cannot present the solution explicitly or even implicitly in terms of algebraic equation(s). This challenge opens the door to two primary methodological avenues: *symbolic methods* and *approximation techniques*. We first discuss the former.

Symbolic programming (SP) focuses on representing mathematical expressions as abstract symbols and manipulating them algebraically. The analytic form of the integral in Eq. (2.4) exemplifies this approach. SP contrasts sharply with differential programming techniques like Automatic Differentiation (AD), which we discussed in the preceding section. While AD is universally applicable and excels in numerical computation, symbolic integration is constrained by fundamental limitations: many integrals and more generally equations simply cannot be expressed in terms of elementary functions. However, when such a closed-form

symbolic representation *does* exist – for instance, when an integral can be expressed via elementary or easily tabulable functions – this representation becomes extraordinarily efficient, bypassing the need for computationally costly numerical solvers and providing exact mathematical insight.

Role of Symbolic Programming in AI

While Automatic Differentiation (AD) and numerical methods form the basis of training in AI, the role of *Symbolic AI* is growing rapidly, driven by the increasing need for interpretation and rigor in Generative AI models. This resurgence is primarily seen in two areas:

- 1. Scientific Discovery:** Modern AI is increasingly employed for *symbolic regression*, where the objective shifts from merely predicting data to discovering the underlying governing physical law (such as an ODE or PDE) in a closed, analytic form. This leverages the inherent exactness and interpretability of symbolic expressions.
- 2. Reasoning and Interpretability:** Integrating symbolic solvers with Large Language Models (LLMs) allows generative models to perform complex mathematical and logical reasoning with *guaranteed correctness*. This ability overcomes the hallucination issues inherent in purely probabilistic models, which are often constructed without any application-specific *inductive* bias. The powerful synergy between numerical generation (AD) and logical verification (SP) is crucial for building reliable and trustworthy AI systems.

The second approach to solving non-integrable ODEs – powerful *approximation* techniques, such as linearizations – is discussed later in Section 2.3 (in the context of higher-dimensional systems).

2.2.2 Regression – Direct and ODE-Based

An important feature of the ODE (2.3) is that once the function $f(x, t)$ is known and the initial condition $x(0)$ is fixed, the solution $x(t)$ at $t > 0$ (of the so-called Cauchi, initial value problem) is unique and well-defined, even if finding it analytically is challenging. However, what if $f(x, t)$ is unknown, but we have access to a sequence of measurements $x(t_1), x(t_2), \dots$ at specific times t_1, t_2, \dots ?

This setting is called *regression*¹. The goal is to predict the dynamics of $x(t)$ given an initial condition $x(0)$ and the observed sequence of measurements.

In this subsection, we explore two fundamentally different approaches:

- 1. Direct regression:** Learn $x(t)$ directly as a function of t .

¹Mathematical regression is called regression because it originated in studies, by statistician Galton in the late 19th century, involving the tendency of data to revert toward the mean, or *regress*. Galton was studying the relationship between the heights of parents and their children.

- 2. ODE-based regression:** Learn $f(x, t)$ from the data using the structure of the ODE.
It is a continuous time version of the so-called auto-regression.

To illustrate the benefits of ODE-based regression, we consider the example of an over-damped oscillator.

Over-Damped Oscillator

Consider the one-dimensional linear ODE, commonly referred to as the *over-damped oscillator*:

$$\dot{x}(t) = -\gamma x(t) + g(t), \quad (2.5)$$

where:

- $x(t)$ is the state variable at time t ,
- $\gamma > 0$ is the damping coefficient, ensuring an over-damped response,
- $g(t)$ is an external forcing term.

This ODE models systems where the state responds slowly to external inputs due to significant damping. Such dynamics are common in physics and engineering, and they provide a foundation for understanding time-dependent processes in AI, such as optimization and NN dynamics.

Direct Regression vs. ODE-Based Regression

1. **Direct Regression:** Directly fit $x(t)$ using a chosen regression model (e.g., polynomial basis, splines). While straightforward, this approach often struggles with noisy data and fails to uncover underlying dynamics.
2. **ODE-Based Regression:** Instead of fitting $x(t)$, ODE-based regression estimates the parameters γ and $g(t)$ in Eq. (2.5) – which is our equations based – quantitative – model in this example. By leveraging the structure of the ODE, this approach offers:
 - A dynamic relationship between $\dot{x}(t)$ and $x(t)$, reducing over-fitting risks.
 - Robustness to noisy measurements of $x(t)$.
 - Improved generalization to cases where $g(t)$ is complex or time-varying, and also to the ranges of t under-represented or missing in training.
 - Natural incorporation of the initial condition $x(0)$.

Example 2.2.1. *Direct vs ODE-based Regressions* Assume the true dynamics are governed by:

$$\dot{x}(t) = -2x(t) + \sin(t), \quad x(0) = 1,$$

which is a special case of Eq. (2.5). The analytical solution of the equation is:

$$x(t) = e^{-2t} + \frac{1}{\sqrt{5}} (\sin(t) - 2 \cos(t)). \quad (2.6)$$

We simulate $x(t)$ at discrete times $t_i = 0, 0.1, \dots, 5$, adding Gaussian noise $\epsilon_i \sim \mathcal{N}(0, \sigma^2)$, $x(t_i) \rightarrow x(t_i) + \epsilon_i$ to mimic measurement errors.

Direct Regression: Fit the noisy data $x(t)$ by a polynomial of degree d $P(t) = a_0 + a_1 t + a_2 t^2 + \dots + a_d t^d$ solving a least-square optimization problem:

$$\min_{a_0, \dots, a_d} \sum_{i=1}^N (x_i - P(t_i))^2.$$

(We will give more details on the underlying optimization scheme in the chapter devoted to optimization.) While this approach approximates the trajectory, it cannot reveal γ or $g(t)$.

ODE-Based Regression: Using numerical differentiation, estimate $\dot{x}(t)$ and fit $-\gamma x(t) + g(t)$ using the structure of Eq. (2.5). Specifically, we do it in two steps:

1. Since the data consists of discrete observations, the time derivative dx/dt is estimated using finite differences: $\dot{x}_i \approx (x_{i+1} - x_{i-1})/(t_{i+1} - t_{i-1})$, $i = 1, \dots, N-1$.
2. This numerical derivative is then used to set up and solve the least-square optimization problem:

$$(\gamma^*, g_1^*, \dots, g_N^*) = \arg \min_{\gamma, g_1, \dots, g_N} \sum_{i=1}^{N-1} (\dot{x}_i + \gamma x_i - g_i)^2.$$

This approach not only captures the dynamics but also enables parameter estimation – $\gamma^*, g_1^*, \dots, g_N^*$.

This example is implemented in the accompanying notebook `regression.ipynb`. The resulting trajectories from direct and ODE-based regression are illustrated in Figs. 2.4, 2.5.

Exercise 2.2.3 (Regression and Parameter Estimation for a New ODE). This exercise explores the fundamental advantages of learning underlying dynamics (ODE-based regression) compared to simple function approximation (direct regression) when dealing with noisy, time-series data.

Consider the following ordinary differential equation:

$$\dot{x}(t) = -\gamma x(t) + \cos(2t), \quad x(0) = 2.$$

You are given noisy measurements of the trajectory $x(t)$ and are asked to estimate the parameter γ , whose true value is -3 . Use the provided notebook `regression-python.ipynb` to implement and compare both regression methods.

1. **Conceptual Advantage: Why \dot{x} over $x(t)$?**

- (a) Explain the fundamental mathematical reason why trying to fit the instantaneous rate of change $\dot{x}(t)$ is less susceptible to integration error and systematic bias than trying to fit the trajectory $x(t)$ directly, especially when the data contains additive noise.
- (b) Based on your explanation, hypothesize which method (ODE-based or Direct) should yield a more accurate estimate of the parameter γ and why.

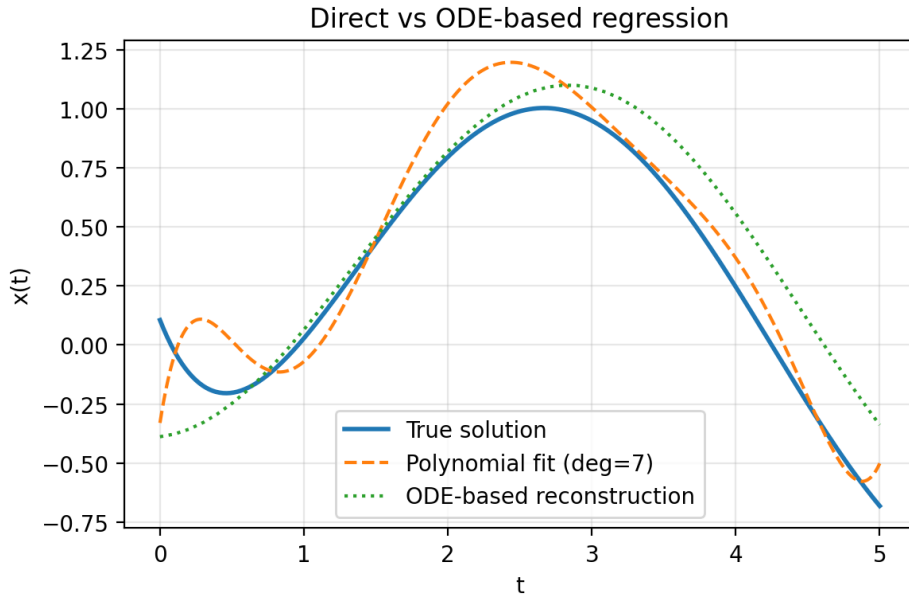


Figure 2.4: Direct polynomial regression vs. ODE-based regression for the over-damped oscillator. The ODE-based fit exploits the dynamical structure and typically generalizes better, especially away from the training window or under higher noise. Generated by `regression.ipynb`.

2. Computational Comparison of Methods: Modify the notebook as necessary to accommodate this new example. Analyze the performance of direct regression and ODE-based regression methods under different levels of additive noise in the data (e.g., consider noise levels $\sigma = 0.1, 0.5, 1$). Compare the following metrics:

- (a) The accuracy of the estimated parameter γ .
- (b) The fidelity of the reconstructed trajectory over the full time domain.

Provide a detailed discussion of your findings, ensuring they support or refute your hypothesis from part 1(b).

3. Heuristic Refinement of γ : The estimation relies on optimization. Without using black-box optimization software (i.e., focusing on the mathematical model), propose a heuristic approach to refine the estimated parameter γ . For example, this might involve iterative adjustments based on the residuals of the ODE constraint or analyzing the discrepancy between the model and the data at specific points. Evaluate the effectiveness of your heuristic by comparing the refined parameter to the true value ($\gamma = -3$) and discussing its advantages and limitations.

Additional Notes: When implementing the ODE-based regression, ensure you properly incorporate the influence of the known forcing term $\cos(2t)$ in your model. Explain any modifications made to the notebook and how they address the specific challenges of this example.

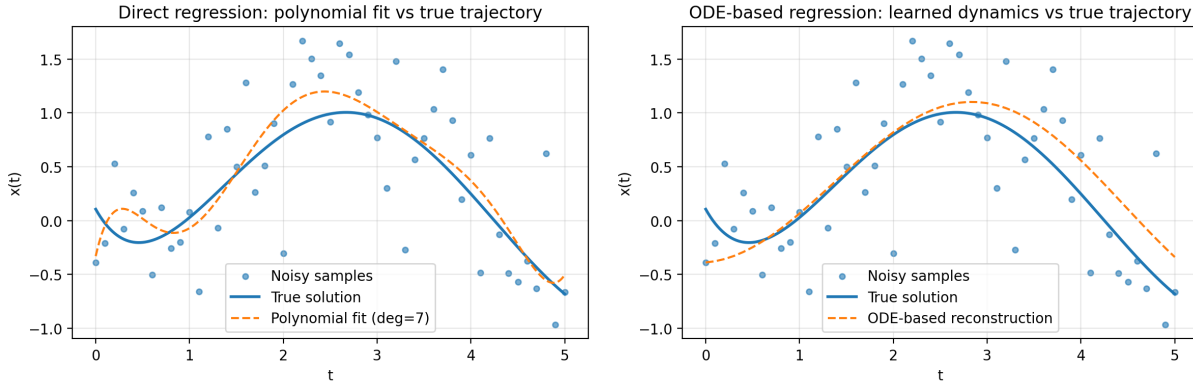


Figure 2.5: Left: direct polynomial regression fit to noisy data. Right: ODE-based regression using the structure $\dot{x}(t) \approx -\gamma x(t) + \sin t$. Both figures generated by `regression.ipynb`.

Neural ODEs and Continuous-Time Auto-Regression

The over-damped oscillator regression example illustrates a simple but very general idea: instead of fitting the trajectory $t \mapsto x(t)$ directly, we fit the *dynamics*

$$\dot{x}(t) = f(x(t), t; \theta)$$

and then *generate* trajectories by integrating the learned vector field forward in time. This viewpoint appears repeatedly in modern *generative*- and *representation*-learning models.

In a *Neural ODE*, the right-hand side $f(x, t; \theta)$ is represented by a neural network. Given observations of trajectories (or a loss that depends on the final state), one learns the parameters θ so that the solution of $\dot{x} = f(x, t; \theta)$ matches the data or minimizes the loss. *Residual networks* (ResNets) can be interpreted as discrete-time approximations of such continuous-time dynamics.

Continuous-time auto-regression. Classical auto-regressive models predict future values x_{t+1} from past values (x_t, x_{t-1}, \dots) via a discrete recurrence. Learning $f(x, t; \theta)$ instead corresponds to a *continuous-time* version of auto-regression: once the dynamics are known, the entire future trajectory is obtained by solving the ODE, not by iterating an explicit discrete map.

From ODEs to generative flows. In likelihood-based generative modeling, *continuous normalizing flows* use ODEs of the form

$$\dot{x}(t) = f(x(t), t; \theta)$$

to transport a simple reference distribution (e.g., a Gaussian) into a complex target distribution. Both the transformation of samples and the evolution of log-densities are governed by the learned vector field f . This connects directly to the finite-dimensional ODE examples in this section.

Later chapters will revisit these ideas in higher dimensions and in stochastic settings (SDEs, diffusion models, and path-integral viewpoints), where the learned dynamics become the core mechanism for sampling and generation.

2.2.3 Second-Order ODE

In Eq. (2.3), x is a state variable of dimension n , and the equation is first-order in derivatives. However, the concepts of order (with respect to derivatives) and dimensionality of the state space n are interrelated and can often be traded off. Let us illustrate this with a second-order one-dimensional ODE:

$$\frac{d^2x}{dt^2} + \gamma \frac{dx}{dt} + f(x) = 0, \quad x(t) \in \mathbb{R}. \quad (2.7)$$

By introducing a two-dimensional state variable $y(t) = (x(t), \dot{x}(t))$, where $\dot{x}(t) = \frac{dx}{dt}$, the second-order ODE can be rewritten as a system of first-order ODEs:

$$\frac{dy}{dt} = \frac{d}{dt} \begin{bmatrix} y_1 \\ y_2 \end{bmatrix} = \begin{bmatrix} y_2 \\ -\gamma y_2 - f(y_1) \end{bmatrix}.$$

This reformulation not only simplifies numerical and analytical approaches to solving the equation but also provides geometric insight into the system's behavior by analyzing trajectories in the two-dimensional phase space.

The second-order ODE in Eq. (2.7) (or equivalently the system of first-order ODEs) significantly enriches the variety of possible solution behaviors. For example, if we choose $f(x) = \omega^2 x$, the equation becomes:

$$\frac{d^2x}{dt^2} + \gamma \frac{dx}{dt} + \omega^2 x = 0,$$

which describes the dynamics of a *damped harmonic oscillator*.

Solving the Damped Harmonic Oscillator

To solve the damped harmonic oscillator, assume a solution of the form $x(t) = e^{\lambda t}$. Substituting into the equation gives the characteristic equation:

$$\lambda^2 + \gamma\lambda + \omega^2 = 0.$$

The roots of this quadratic equation are:

$$\lambda_{1,2} = -\frac{\gamma}{2} \pm \sqrt{\frac{\gamma^2}{4} - \omega^2}.$$

The nature of the solution depends on the discriminant $\Delta = \frac{\gamma^2}{4} - \omega^2$:

- **Over-damped Case ($\Delta > 0$):** The roots $\lambda_{1,2}$ are real and distinct, leading to a solution of the form:

$$x(t) = C_1 e^{\lambda_1 t} + C_2 e^{\lambda_2 t}.$$

The motion decays monotonically without oscillations.

- **Critically Damped Case ($\Delta = 0$):** The roots $\lambda_{1,2}$ are real and equal, leading to a solution:

$$x(t) = (C_1 + C_2 t) e^{-\frac{\gamma}{2} t}.$$

This represents the fastest decay to equilibrium without oscillation.

- **Under-damped Case ($\Delta < 0$):** The roots $\lambda_{1,2}$ are complex conjugates, $\lambda_{1,2} = -\frac{\gamma}{2} \pm i\sqrt{\omega^2 - \frac{\gamma^2}{4}}$, leading to an oscillatory solution:

$$x(t) = e^{-\frac{\gamma}{2}t} (C_1 \cos(\omega_d t) + C_2 \sin(\omega_d t)),$$

where $\omega_d = \sqrt{\omega^2 - \frac{\gamma^2}{4}}$ is the damped angular frequency.

Phase Portrait and Conservation Law(s)

Let us now see how the solution looks from the two-dimensional perspective, that is, by simultaneously considering both the coordinate x of the harmonic oscillator and its rate of change — the velocity \dot{x} . This leads to the notion of the *phase portrait*, which offers a convenient and intuitive way of visualizing the dynamics. Let us illustrate this on a slightly more general case than the harmonic oscillator. Instead of the linear Hookean force $-\omega^2 x$, we will introduce a potential force of general position, while simplifying the setup by discussing the undamped case:

$$\frac{d^2x}{dt^2} = -\frac{dU(x)}{dx}, \quad (2.8)$$

where $U(x)$ is the potential energy associated with the force $f(x) = -\frac{dU(x)}{dx}$. In the case of the harmonic potential, $U(x) = \frac{1}{2}\omega^2 x^2$, Eq. (2.8) describes sustained oscillations without decay.

In general, for any bounded-from-below potential $U(x)$ (i.e., $\forall x, U(x) > \text{const}$), Eq. (2.8) represents a *conservative dynamical system*. These systems are termed *conservative* because, even if Eq. (2.8) cannot be solved analytically for arbitrary $U(x)$, we can establish a conservation law. Specifically, the total energy $E(x, \dot{x}) = U(x) + \frac{1}{2}\dot{x}^2$ is conserved:

$$\dot{x} \frac{d}{dt} \dot{x} + \frac{d\dot{x}}{dt} \frac{d}{d\dot{x}} U(x) = 0 \Rightarrow \frac{d}{dt} \left(\frac{1}{2}\dot{x}^2 + U(x) \right) = 0,$$

thus proving $\frac{d}{dt}E(x, \dot{x}) = 0$.

The phase portraits shown in Fig. 2.6 are generated by the Jupyter/Python notebook `double-well.ipynb`, which computes the total energy $E(x, \dot{x})$ on a grid and plots its level sets.

Double-Well Potential: Dynamics and Phase Portraits

A double-well potential is a classic example of a nonlinear system with rich dynamics. The potential is given by:

$$U(x) = \frac{x^4}{4} - \frac{x^2}{2}, \quad (2.9)$$

which has two minima at $x = \pm 1$ and a local maximum at $x = 0$. This potential models systems with bistable states, such as a particle trapped in two wells separated by a barrier. The corresponding equation of motion is:

$$\frac{d^2x}{dt^2} = -\frac{dU(x)}{dx} = -x^3 + x. \quad (2.10)$$

Phase Portraits in Different Regimes. The phase portraits for the double-well potential illustrate the rich dynamics of the system. Depending on the initial energy, the trajectories exhibit distinct behaviors:

- **Low Energy:** For energies below the barrier height ($E < \frac{1}{4}$), the particle remains confined to one of the wells. The phase portrait consists of closed orbits around $x = \pm 1$.
- **Barrier-Crossing Energy:** At the critical energy $E = \frac{1}{4}$, the particle reaches the top of the barrier at $x = 0$ and can transition between wells.
- **High Energy:** For $E > \frac{1}{4}$, the particle explores the entire potential landscape, crossing between wells repeatedly.

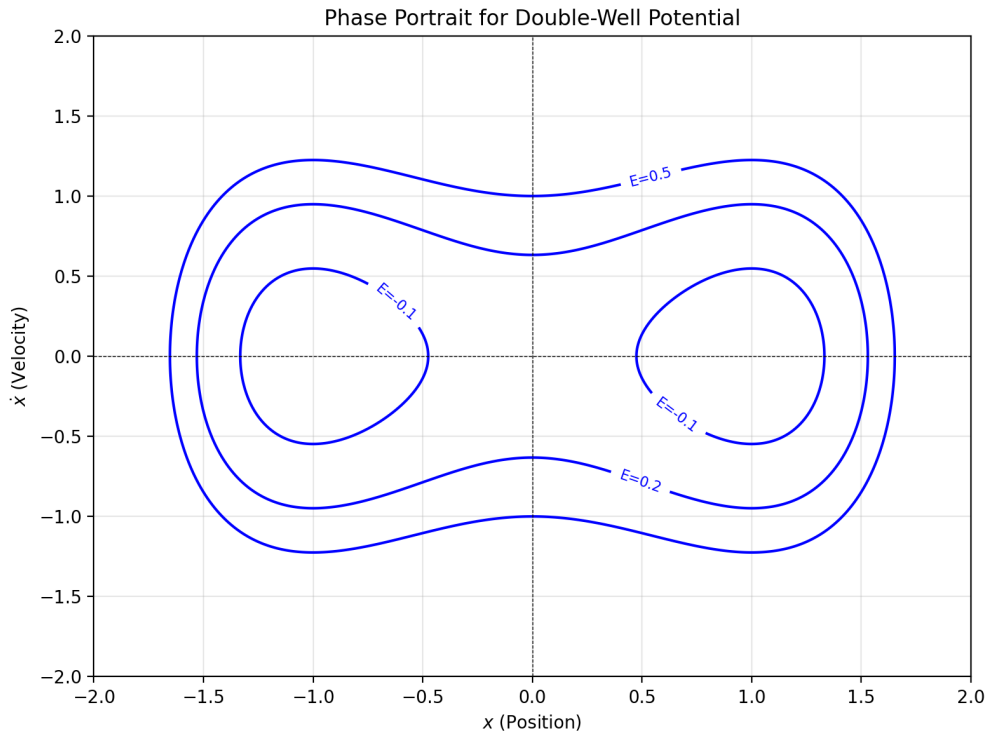


Figure 2.6: Phase portraits for the double-well potential $U(x) = \frac{1}{4}x^4 - \frac{1}{2}x^2$ at different energy levels. Contours of constant total energy $E(x, \dot{x})$ are shown in the (x, \dot{x}) plane. Generated by `double-well.ipynb`.

Damped Dynamics in the Double-Well Potential

Adding damping to the double-well system introduces energy dissipation, leading to relaxation into one of the potential wells. The equation of motion becomes:

$$\frac{d^2x}{dt^2} + \gamma \frac{dx}{dt} - x + x^3 = 0, \quad (2.11)$$

where $\gamma > 0$ represents the damping coefficient. The dynamics depend on the initial condition and the value of γ :

- **Low Damping ($\gamma \ll 1$):** The system exhibits oscillatory behavior before settling into one of the wells.
- **High Damping ($\gamma \gg 1$):** The system relaxes monotonically into one of the wells without oscillations.

This damped double-well system is widely used in physics – e.g., tunneling phenomena – and machine learning – e.g., modeling binary classification. In the latter case the two wells correspond to two distinct states or classes, with the damping term ensuring convergence to a stable state.

Exercise 2.2.4 (Damped Double-Well and Nonlinear Classification). *Consider the damped double-well system given by Eq. (2.11):*

1. *Numerically simulate the system for $\gamma = 0.1$, $\gamma = 1$, and $\gamma = 5$, with initial conditions $x(0) = 0.5$ and $\dot{x}(0) = 0$. Plot the trajectories $x(t)$. (You may use and modify the Python/Jupyter notebook `double-well.ipynb`, which was used to generate Fig. 2.6.)*
2. *Generate the phase portraits for each γ . Interpret the impact of damping on the trajectories in the (x, \dot{x}) -space.*
3. *Discuss the relevance of this system to nonlinear classification. Suppose $x > 0$ corresponds to one class and $x < 0$ corresponds to another. How does the damping influence the classification boundary and convergence?*
4. *Extend the system to a time-dependent classification boundary given by $x(t) = \cos(\omega t)$. Simulate the dynamics and discuss the implications for adaptive classification.*

From Low-Dimensional Dynamics to High-Dimensional AI

The analysis of second-order ODEs and the phase portrait method have shown how low-dimensional systems can exhibit rich, interpretable dynamics, such as oscillations and bistable states. However, in the realm of Generative AI, the challenge is typically reversed: we deal with extremely *high-dimensional* state vectors (e.g., millions of parameters or pixel values), where the governing dynamics are nearly always *nonlinear*. Since analytical solutions are impossible and direct numerical simulations of complex nonlinear systems are too slow at scale, we must rely on powerful approximation techniques. A cornerstone of these techniques is *linearization*. The remainder of this section pivots to the study of *Systems of Linear ODEs*, which, despite their simplicity, provide the fundamental mathematical machinery for understanding the local behavior, stability, and evolution of the vast, high-dimensional dynamical systems inherent in modern AI models.

2.3 System of Linear ODEs

Ordinary Differential Equations (ODEs) play a foundational role in understanding the dynamics of many systems in Artificial Intelligence (AI). They provide a mathematical framework for describing how quantities evolve over time in contexts such as optimization, data processing, and machine learning models. Some notable examples include:

- **Gradient Descent Dynamics:** The gradient descent algorithm, a cornerstone of optimization, can be viewed as a discrete approximation to a continuous gradient flow:

$$\frac{dx}{dt} = -\nabla f(x),$$

where $f(x)$ is the objective function being minimized.

- **Neural Network (NN) Training:** The training dynamics of NNs can often be modeled using ODEs, particularly in the case of continuous-time gradient flows, enabling theoretical insights into optimization and convergence behavior.

In practical AI applications, such as the examples above, the ODEs of interest typically involve high-dimensional vectors and are often nonlinear. However, as discussed in the previous section, solving nonlinear ODEs analytically is generally infeasible, even in one dimension. This necessitates the use of approximation methods and computational techniques, many of which rely on linearization of the equations.

Given the centrality of these challenges, this section focuses on systems of high-dimensional linear ODEs. By understanding linear systems, we build a foundation for tackling more complex nonlinear dynamics through approximation and computational strategies.

2.3.1 Homogeneous ODEs

We aim to solve a system of linear Ordinary Differential Equations (ODEs) that describes the time evolution of the vector $x \in \mathbb{R}^n$:

$$\frac{dx}{dt} = Ax, \quad (2.12)$$

where $A \in \mathbb{R}^{n \times n}$ is a fixed, time-independent matrix. The system is subject to the initial condition

$$x(0) = x_0.$$

When $n = 1$, A is a scalar, and the solution is straightforward:

$$x(t) = \exp(tA)x_0. \quad (2.13)$$

Remarkably, this solution generalizes to the case of $n > 1$, where $\exp(tA)$ is the *matrix exponential*, defined as:

$$\exp(tA) = \sum_{k=0}^{\infty} \frac{(tA)^k}{k!}.$$

The series converges for any finite-dimensional square matrix A , ensuring the matrix exponential is well-defined. Substituting $x(t) = \exp(tA)x_0$ into Eq. (2.12) verifies that this indeed satisfies the equation:

$$\frac{dx}{dt} = A \exp(tA)x_0 = Ax(t).$$

Example 2.3.1 (Linear Diffusion on a Short 1D Grid). *A simple but instructive instance of Eq. (2.12) arises from a finite-difference discretization of the 1D heat equation on a short spatial grid. Let $x(t) \in \mathbb{R}^n$ collect the temperature at n grid points, and consider*

$$\dot{x}(t) = Ax(t),$$

where $A \in \mathbb{R}^{n \times n}$ is the discrete Laplacian with (approximate) Neumann boundary conditions:

$$A_{ii} = -2, \quad A_{i,i+1} = A_{i,i-1} = 1, \quad i = 2, \dots, n-1,$$

with suitable edge modifications at $i = 1$ and $i = n$.

Starting from a spiky initial condition (all zeros except a single large entry in the middle), the solution $x(t)$ evolves by progressively smoothing out the spike as heat diffuses along the grid. This illustrates how a matrix with negative diagonal and positive off-diagonal entries can generate a contracting semigroup $x(t) = \exp(tA)x_0$ that drives the system toward a more uniform state.

Fig. 2.7 shows snapshots $x(t)$ at several times, while Fig. 2.8 displays the full space–time evolution as a heatmap. Both figures are generated by the Python notebook `linear_systems.ipynb`.

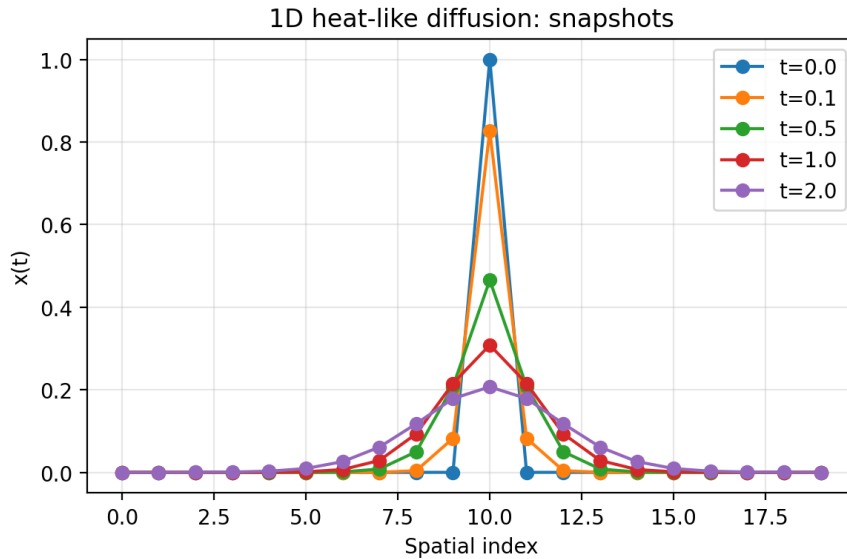


Figure 2.7: Snapshots of the state $x(t)$ for the 1D discrete heat equation on a short grid, starting from a single spike. Over time the profile smooths out, illustrating diffusion governed by a linear system $\dot{x} = Ax$. Generated by `linear_systems.ipynb`.

Exercise 2.3.1 (Properties of the Matrix Exponential). *Prove that:*

1. if $AB - BA = 0$, then $\exp(A + B) = \exp(A)\exp(B) = \exp(B)\exp(A)$;
2. if $\det(P) \neq 0$, then $\exp(PAP^{-1}) = P\exp(A)P^{-1}$;
3. $\det(\exp(A)) = \exp(\text{Tr}(A))$. In your proof, you may assume that A is diagonalizable. For an extra challenge – prove the statement without the assumption that A is diagonalizable.

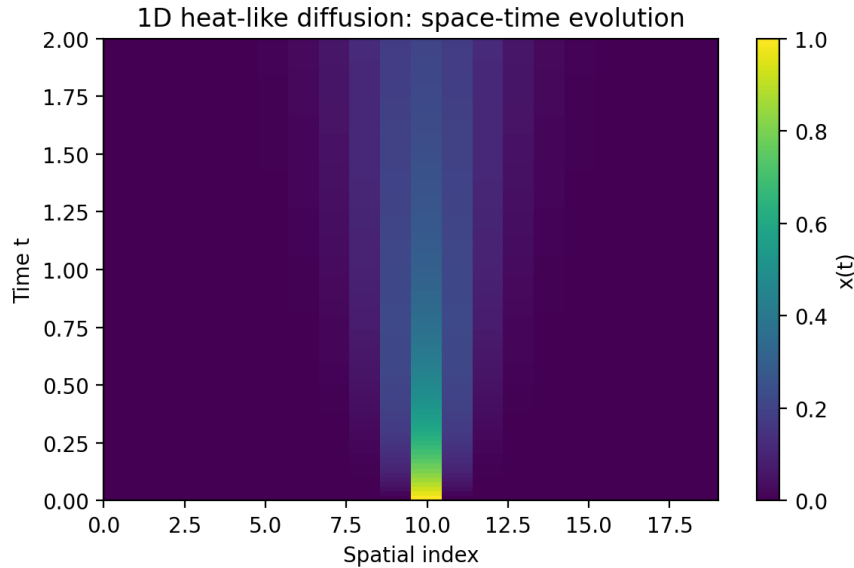


Figure 2.8: Space–time evolution of the 1D heat-like system from Example 2.3.1. The vertical axis is time and the horizontal axis is the spatial index. The initial spike spreads out as heat diffuses across the grid. Generated by `linear_systems.ipynb`.

2.3.2 Inhomogeneous ODEs

Now consider the generalization to an inhomogeneous system:

$$\frac{dx}{dt} = Ax + b(t),$$

where $b(t) \in \mathbb{R}^n$ is a time-dependent vector. The solution method leverages the linear structure of Eq. (2.13). Substituting $x(t) = \exp(tA)\tilde{x}(t)$ into the inhomogeneous equation leads to an ODE for $\tilde{x}(t)$:

$$\frac{d\tilde{x}}{dt} = \exp(-tA)b(t).$$

This equation is straightforward to integrate, and reversing the substitution yields the solution:

$$x(t) = \exp(tA)x_0 + \int_0^t \exp((t-\tau)A)b(\tau) d\tau,$$

where the first term solves the homogeneous equation, and the second term accounts for the inhomogeneous component.

Case of Constant b : If $b(t) = b$ is constant, the time-dependent integral simplifies, resulting in the algebraic expression:

$$x(t) = \exp(tA)x_0 + A^{-1}(\exp(tA) - I)b, \quad (2.14)$$

which expresses the solution using elementary matrix functions (exponential and inverse).

Example 2.3.2 (Forced Linear System in \mathbb{R}^3). Consider the system

$$\dot{x}(t) = Ax(t) + b, \quad x(t) \in \mathbb{R}^3,$$

with a stable matrix $A \in \mathbb{R}^{3 \times 3}$ (all eigenvalues have negative real part) and a constant forcing vector b . In this setting, Eq. (2.14) predicts that the solution is a sum of a transient term $\exp(tA)x_0$ and a steady-state term

$$\bar{x} = -A^{-1}b,$$

to which all trajectories converge as $t \rightarrow \infty$.

The notebook `linear_systems.ipynb` constructs such an A and b , integrates the ODE numerically, and overlays the time series of each component $x_i(t)$ with its corresponding steady-state value \bar{x}_i . As shown in Fig. 2.9, the trajectories exhibit an initial transient followed by convergence to the constant equilibrium \bar{x} .

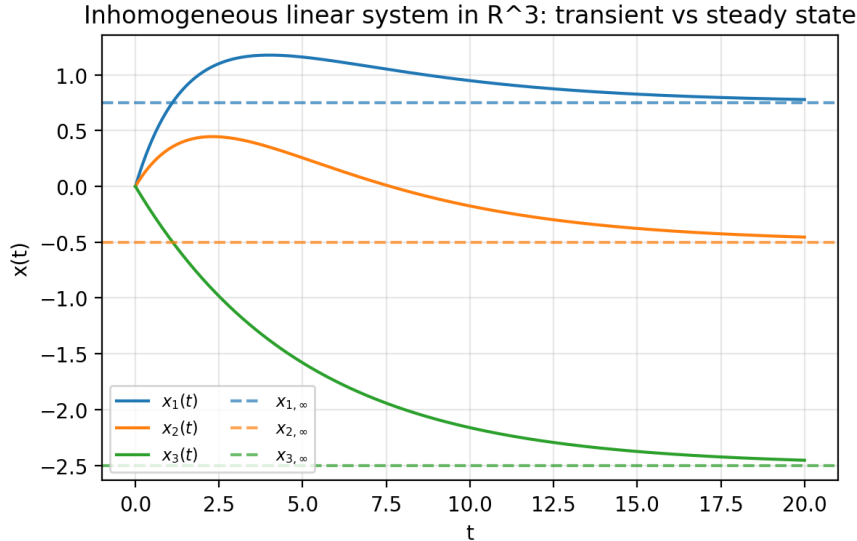


Figure 2.9: Forced linear system in \mathbb{R}^3 : components $x_1(t), x_2(t), x_3(t)$ (solid lines) and their steady-state values \bar{x}_i (dashed lines). All trajectories converge to the equilibrium $\bar{x} = -A^{-1}b$. Generated by `linear_systems.ipynb`.

To explore the solution further, we use the Eigenvalue Decomposition (ED) of A :

$$A = Q\Lambda Q^{-1},$$

where $Q \in \mathbb{R}^{n \times n}$ is an invertible matrix whose columns are the eigenvectors of A , and $\Lambda = \text{diag}(\lambda_1, \lambda_2, \dots, \lambda_n)$ is a diagonal matrix containing the eigenvalues of A .

For symmetric matrices, Q is orthogonal ($Q^{-1} = Q^\top$), and the eigenvalues are real but may be positive, negative, or zero. For non-symmetric matrices, Q is not necessarily orthogonal, and the eigenvalues may be complex.

Substituting the ED of A into $\exp(A)$, we find:

$$\begin{aligned}\exp(tA) &= \sum_{k=0}^{\infty} \frac{(tA)^k}{k!} = \sum_{k=0}^{\infty} \frac{t^k}{k!} \underbrace{Q\Lambda Q^{-1} \cdots Q\Lambda Q^{-1}}_{k \text{ times}} = Q \left(\sum_{k=0}^{\infty} \frac{(t\Lambda)^k}{k!} \right) Q^{-1} = Q \exp(t\Lambda) Q^{-1} \\ &= Q [\text{diag}(\exp(t\lambda_1), \dots, \exp(t\lambda_n))] Q^{-1},\end{aligned}$$

then arriving at the following simplification of Eq. (2.14)

$$x(t) = \exp(tA)x_0 + Q \left[\text{diag} \left(\frac{\exp(t\lambda_1) - 1}{\lambda_1}, \dots, \frac{\exp(t\lambda_n) - 1}{\lambda_n} \right) \right] Q^{-1} b.$$

What if A^{-1} Does Not Exist? If A is singular, meaning that one or more eigenvalues $\lambda_i = 0$, the above formula remains valid. The key lies in handling the term $(\exp(t\lambda_i) - 1)/\lambda_i$ for $\lambda_i = 0$. Using L'Hôpital's rule, we resolve the limit

$$\lim_{\lambda_i \rightarrow 0} \frac{\exp(t\lambda_i) - 1}{\lambda_i} = t.$$

This shows that the ED-based approach is robust and well-defined, even when A^{-1} does not exist.

Exercise 2.3.2. If we use SVD (and not ED as above) working with Eq. (2.14), does it lead to a simplification? To validate your answer consider, $A = \begin{bmatrix} 2 & 1 \\ 1 & -1 \end{bmatrix}$, derive ED and SVD for the matrix and see if either of the two allows to simplify $\exp(tA)$. (Hint: Pay attention to the sign of the eigen-values.)

2.3.3 Dynamics over Graph

For a symmetric matrix A with stochastic-like properties – e.g., a *graph Laplacian*, where *stochastic* does not imply randomness but rather refers to a structure in which all matrix elements are non-negative and each row sums to unity – the non-negativity of eigenvalues plays a crucial role in governing the system's behavior. Specifically, the non-negative spectrum of A ensures that the system's dynamics, described by the evolution matrix $\exp(-tA)$, asymptotically relaxes to an equilibrium state. This equilibrium corresponds to the eigenvector associated with the zero eigenvalue of A and it is reached in the limit $t \rightarrow \infty$.

This property is widely utilized in applications such as community detection and clustering algorithms, where the dynamics governed by the graph Laplacian can reveal the underlying structure of the data or network. The gradual relaxation highlights the separation of clusters, aiding in their identification.

Example 2.3.3 (Consensus Dynamics on a Ring Graph). Consider a simple undirected graph with $n = 5$ nodes arranged in a ring. The adjacency matrix A has entries $A_{ij} = 1$ if nodes i and j are neighbors on the ring and 0 otherwise. The degree matrix D is diagonal with $D_{ii} = \sum_j A_{ij}$, and the graph Laplacian is $L = D - A$.

We study the consensus dynamics

$$\dot{x}(t) = -Lx(t),$$

with an arbitrary initial condition $x(0) = x_0 \in \mathbb{R}^5$. Because L is positive semi-definite and has a single zero eigenvalue corresponding to the constant vector, the solution $x(t)$ converges to a consensus state where all components are equal:

$$x_i(t) \rightarrow \bar{x} = \frac{1}{n} \sum_{j=1}^n x_j(0), \quad t \rightarrow \infty.$$

The notebook `graph_dynamics.ipynb` simulates this ODE using a forward Euler scheme. Fig. 2.10 shows the node values $x_i(t)$ versus time, while Fig. 2.11 visualizes the initial and final states on the ring. The final configuration clearly illustrates convergence to a uniform consensus.

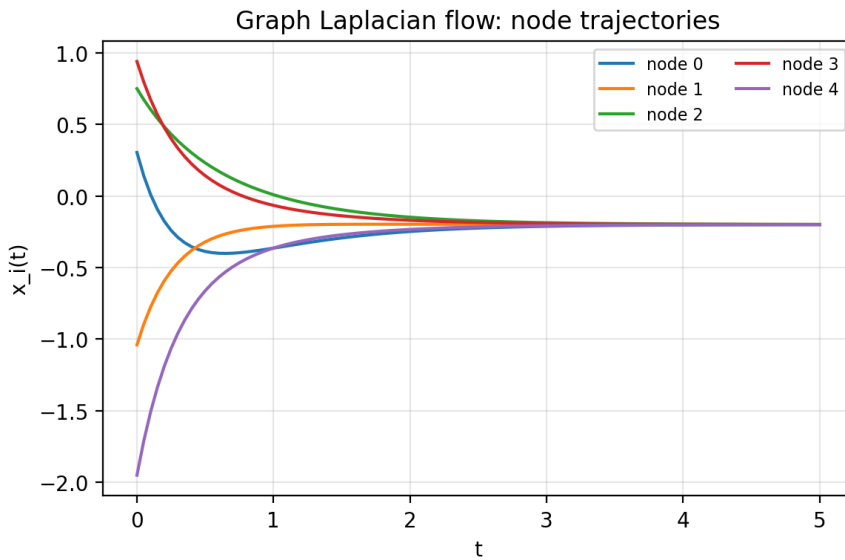


Figure 2.10: Consensus dynamics on a 5-node ring: trajectories of each node value $x_i(t)$ under $\dot{x} = -Lx$. All states converge to a common value (consensus). Generated by `graph_dynamics.ipynb`.

Exercise 2.3.3 (Analyzing Linear ODEs on Graphs). This exercise focuses on understanding and solving linear ODEs using graph-based dynamics.

1. **Graph-Laplacian Dynamics:** Consider a graph with n nodes and a symmetric weighted adjacency matrix A . Let the degree matrix D be diagonal with entries $D_{ii} = \sum_j A_{ij}$. The graph Laplacian is defined as $L = D - A$.

- (a) Write the ODE governing the evolution of node values $x(t)$:

$$\frac{dx(t)}{dt} = -Lx(t),$$

in components.

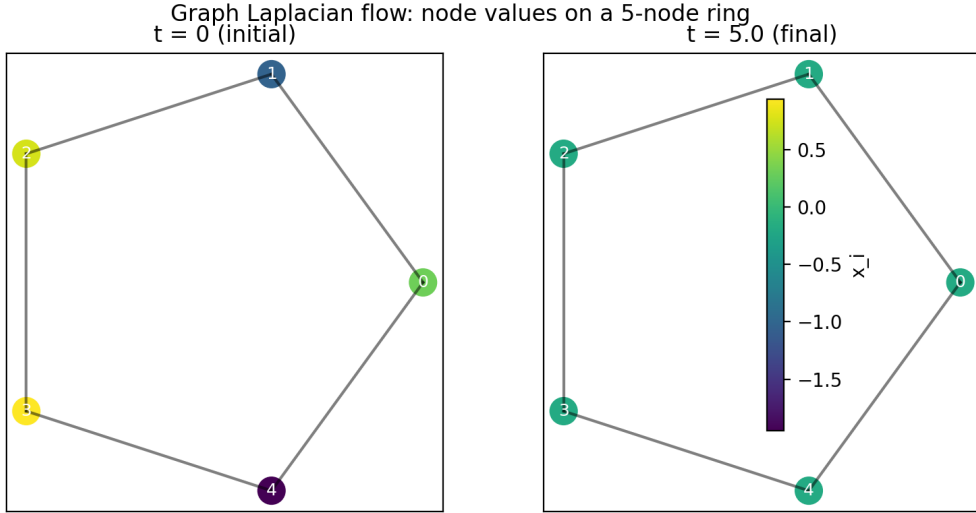


Figure 2.11: Graph representation of consensus dynamics on a 5-node ring. Left: node values at $t = 0$; right: node values at a large time t , after consensus is reached. Nodes are placed on a circle and colored according to their scalar state value. Generated by `graph_dynamics.ipynb`.

- (b) Solve the ODE analytically using eigen-decomposition for an initial condition $x(0)$.
 - (c) Discuss the long-term behavior of $x(t)$ in terms of the eigenvalues of L .
2. **Example with a Small Graph:** Consider a graph with 3 nodes and the adjacency matrix:
- $$A = \begin{bmatrix} 0 & 1 & 1 \\ 1 & 0 & 1 \\ 1 & 1 & 0 \end{bmatrix}.$$
- (a) Compute the degree matrix D and the graph Laplacian L .
 - (b) Solve the ODE $\frac{dx(t)}{dt} = -Lx(t)$ for $x(0) = [1, 0, 0]^\top$.
 - (c) Plot $x(t)$ for $t \in [0, 10]$ and interpret the results.

3. **Energy and Gradient Flow:** Consider the quadratic energy function:

$$f(x) = \frac{1}{2}x^\top Lx.$$

- (a) Derive the gradient flow ODE: $\frac{dx(t)}{dt} = -\nabla f(x)$.
- (b) Simulate the gradient flow numerically for the graph given above. Compare the numerical solution to the analytical solution obtained using ED.
- (c) Discuss the role of eigenvalues in determining the dynamics of $x(t)$.

2.3.4 Time-Ordered Exponential

Let us now discuss solution of $\dot{x} = Ax$, where $x \in \mathbb{R}^n$ and $A(t) \in \mathbb{R}^{n \times n}$, in the case where $A = A(t)$ is time-dependent. For $n = 1$, the solution is straightforward: the matrix exponential $\exp(tA)$ is replaced by: $\exp\left(\int_0^t A(t') dt'\right)$. However, it is also straightforward to check by substitution that for $n > 1$, this expression is incorrect in general, and specifically when the matrix function $A(t)$ evaluated at two different moments of time, t_1 and t_2 , do not commute. To account for this matrix non-commutativity, we replace the matrix exponential with the so-called *time-ordered exponential*. Unlike the case of time-independent A , this object cannot be expressed as a simple function of $A(t)$ and should be viewed as defined in terms of a Taylor series:

$$\begin{aligned}\mathcal{T} \exp\left(\int_0^t A(t') dt'\right) &= I + \int_0^t A(t_1) dt_1 + \int_0^t \int_0^{t_1} A(t_1)A(t_2) dt_2 dt_1 + \dots \\ &= \sum_{n=0}^{\infty} \int_0^t \dots \int_0^{t_{n-1}} A(t_1)A(t_2) \dots A(t_n) dt_n \dots dt_1,\end{aligned}\quad (2.15)$$

where \mathcal{T} indicates time-ordering, ensuring that matrices $A(t_1), A(t_2), \dots$ are multiplied in the correct chronological order, with earlier times appearing to the right.

Example 2.3.4 (Naive vs Time-Ordered Exponential for a Rotating System). *To visualize the difference between a naive exponential and the true time-ordered evolution, consider the 2D system*

$$\dot{x}(t) = A(t)x(t), \quad A(t) = \begin{bmatrix} 0 & -\omega(t) \\ \omega(t) & 0 \end{bmatrix}, \quad \omega(t) = 1 + 0.5 \sin t.$$

For each fixed t , the matrix $A(t)$ generates a rotation with instantaneous angular velocity $\omega(t)$. However, the matrices $A(t_1)$ and $A(t_2)$ do not commute at different times because $\omega(t)$ changes.

The notebook `timeordered.ipynb` compares:

- the true solution, obtained by time-stepping with small increments (approximating the time-ordered exponential), and
- a naive solution that treats the integral $\int_0^t \omega(\tau) d\tau$ as a single effective rotation angle and applies a simple rotation matrix of that angle.

Fig. 2.12 shows the components $x_1(t), x_2(t)$ over time for both solutions, while Fig. 2.13 compares the corresponding trajectories in phase space. The discrepancy between the two curves illustrates how ignoring time ordering can lead to noticeable errors when the generators $A(t)$ do not commute.

Exercise 2.3.4. Let $A(t) \in \mathbb{R}^{n \times n}$ be a continuous, time-dependent matrix defined for $t \in [0, T]$ and defined by Eq. (2.15).

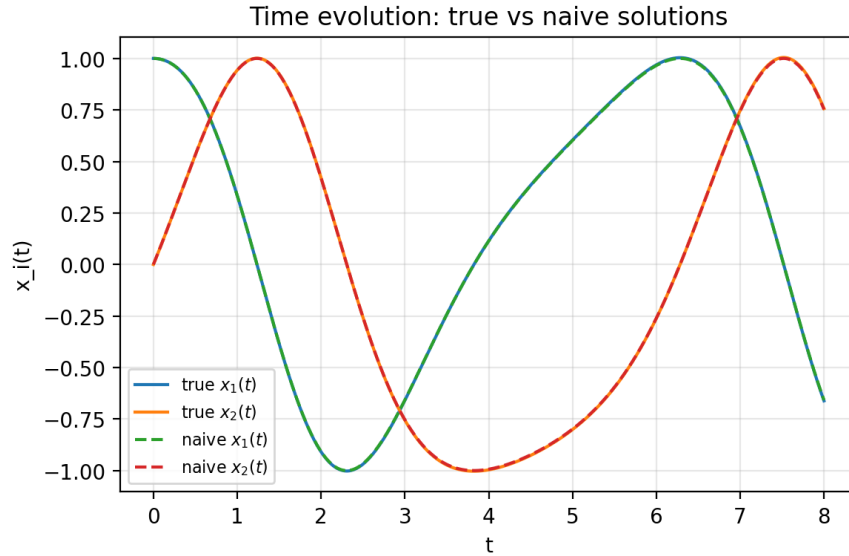


Figure 2.12: Time evolution of $x_1(t)$ and $x_2(t)$ for the true (time-stepped) solution and the naive exponential solution that ignores time ordering. The mismatch shows the effect of non-commuting $A(t)$. Generated by `timeordered.ipynb`.

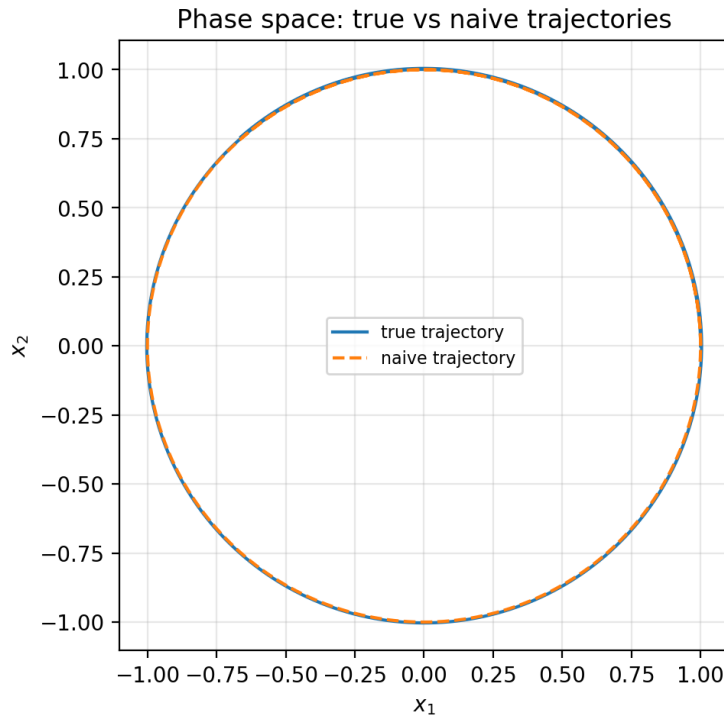


Figure 2.13: Phase-space trajectories $(x_1(t), x_2(t))$ for the true time-ordered dynamics and the naive approximation. Even though both are rotations in the plane, the paths diverge due to the time dependence of $\omega(t)$. Generated by `timeordered.ipynb`.

1. Prove that the Taylor expansion for the time-ordered exponential satisfies the differential equation:

$$\frac{d}{dt} \mathcal{T} \exp \left(\int_0^t A(t') dt' \right) = A(t) \mathcal{T} \exp \left(\int_0^t A(t') dt' \right),$$

with the initial condition:

$$\mathcal{T} \exp \left(\int_0^0 A(t') dt' \right) = I.$$

Hint: Expand the Taylor series term by term and verify the differential equation by differentiating under the integral sign. Use the fact that the limits of the integrals enforce time-ordering.

2. Consider the time-dependent matrix:

$$A(t) = \begin{bmatrix} 0 & -t \\ t & 0 \end{bmatrix}.$$

Compute the time-ordered exponential explicitly for $t \in [0, T]$ up to the second-order term of the Taylor series:

$$\mathcal{T} \exp \left(\int_0^T A(t') dt' \right) \approx I + \int_0^T A(t_1) dt_1 + \int_0^T \int_0^{t_1} A(t_1) A(t_2) dt_2 dt_1.$$

The Mathematics of Dynamics and the Path to Optimization

This chapter established the two core mathematical engines of modern AI: **Automatic Differentiation (AD)**, which provides the instantaneous gradient, and **Differential Equations**, which model the evolution of a system over continuous time.

The final section on linear systems, particularly the formula for the Time-Ordered Exponential, concludes our exploration of how high-dimensional dynamics are solved. Critically, these dynamics are directly linked to optimization: the core algorithm of **Gradient Descent** is simply a discrete approximation of the continuous **Gradient Flow** ODE, $\dot{x} = -\nabla f(x)$.

Moving to Optimization: We have the tool (the gradient, provided by AD) and the language (ODEs, for dynamics). The next step is to use the gradient iteratively to find minima. However, this is where the computational limits of high-dimensional AI become the primary design constraint. In the next chapter we will put these skills at work to analyze complex energy landscapes subject to optimization, in particular building the practical, first-order optimization algorithms (SGD, Adam) that dominate modern machine learning.

Chapter 3

Optimization (in AI)

Overview

Optimization underpins most advances in Artificial Intelligence (AI). Whether training a Neural Network (NN), fine-tuning a transformer, or building a generative diffusion model, optimization is at the heart of creating, training, and performing inference with these models. In this chapter, we focus on the principles and techniques of unconstrained optimization, a dominant paradigm in modern AI, where the complexity of the problem is encapsulated entirely in the energy (or loss) landscape.

Why Optimization in AI?

AI workflows involve three major stages:

1. **Model Creation:** Formulating the model structure and the optimization problem.
2. **Training:** Optimizing over parameters of the model using a fixed dataset.
3. **Inference:** Finding optimal states or predictions with parameters already fixed trained and with optimization over the model state space with the energy function (landscape) fixed or evolving in the (algorithmic) time.

Of these, the training stage demands the most computational resources, as it involves optimizing a super high-dimensional, continuous parameter space. Modern state-of-the-art AI models often contain billions or even trillions of parameters (of the underlying neural networks), making scalability and efficiency critical. This is why optimization methods in AI primarily focus on:

- **Continuous Spaces:** Most models have continuous parameters.
- **Single-Objective Optimization:** Only one objective (e.g., minimizing loss) is considered.
- **First-Order Methods:** Gradients (but not second derivatives) are used to ensure scalability (as evaluating Jacobians – second order derivatives - scales quadratically with the number of parameters, and thus not feasible).

- **Unconstrained Settings:** Constraints are avoided, accounted in the loss/cost function via the so-called Lagrange multiplier methodology to allow efficient use of the Automatic Differentiation (AD) - see Section 2.1, or used as guard rails within the first order methods.

Other optimization paradigms, such as discrete optimization or higher-order methods, are occasionally employed but primarily as supplements (for pre-processing or down-stream tasks) to improve scalability, robustness, or accuracy.

3.1 Starting Example — Logistic Regression

Optimization is at the core of modern AI. Virtually every supervised-learning task – from logistic regression to large-scale deep learning – requires adjusting model parameters to *minimize a loss function* computed over a dataset. For a Neural Network (NN) $f_\theta(x)$, the standard learning problem takes the form

$$\theta^* = \arg \min_{\theta} \frac{1}{N} \sum_{i=1}^N \mathcal{L}(f_\theta(x_i), y_i), \quad (3.1)$$

where $\{(x_i, y_i)\}_{i=1}^N$ is the dataset, \mathcal{L} is a loss (e.g., MSE or cross-entropy), and θ are the parameters to be optimized.

Neural Networks will be studied in depth in Chapter 4. Here, to build intuition for optimization in a simple yet realistic setting, we focus on a classical model: *Logistic Regression* (LR). Despite its simplicity, LR already illustrates many important ideas: convex loss functions, decision boundaries, linear separability, feature engineering, and the geometry of optimization landscapes.

3.1.1 The Logistic Regression Model

In its simplest 2D form, logistic regression has parameters $\omega = (b, \omega_1, \omega_2)$, and predicts the probability of class $y = 1$ via

$$\hat{y}_{LR}(x, \omega) = \sigma(b + \omega_1 x_1 + \omega_2 x_2), \quad \sigma(z) = \frac{1}{1 + e^{-z}}, \quad (3.2)$$

where $x = (x_1, x_2) \in \mathbb{R}^2$ and σ is the sigmoid activation function ¹.

¹The sigmoid function was originally introduced in the 19th century by the Belgian mathematician Pierre François Verhulst (1838) in the context of population growth modeling. He used it to describe how growth starts rapidly but slows as it approaches a natural limit due to constrained resources. In modern AI and machine learning, the sigmoid function is often called the logistic function, as it smoothly interpolates between 0 and 1, making it useful for probability estimation and binary classification. The term "logistic" comes from the Greek word *logistikos* (λογιστικός), meaning "skilled in calculation" or "rational reasoning." Though originally referring to mathematical logic, its adoption in this context likely reflects the function's role in making smooth, calculated transitions between discrete states – 0 and 1.

Given labeled samples $\{(x_i, y_i)\}_{i=1}^N$, the parameters are estimated by solving

$$\omega^* = \arg \min_{\omega} \frac{1}{N} \sum_{i=1}^N \mathcal{L}_{LR}(x_i, y_i, \omega), \quad (3.3)$$

with the *binary cross-entropy loss*

$$\mathcal{L}_{LR}(x_i, y_i, \omega) = - \left[y_i \log \hat{y}_{LR}(x_i, \omega) + (1 - y_i) \log(1 - \hat{y}_{LR}(x_i, \omega)) \right]. \quad (3.4)$$

Why cross-entropy? Cross-entropy measures the *information mismatch* between predicted probabilities and true labels:

- confident and correct predictions \rightarrow loss ≈ 0 ,
- confident and wrong predictions \rightarrow loss $\rightarrow \infty$
- uncertain predictions (≈ 0.5) \rightarrow moderate loss.

A full information-theoretic interpretation will appear later in Chapter 5.

3.1.2 Linear Logistic Regression and Its Limitations

Define the linear feature map

$$\phi_{LR}(x) = (1, x_1, x_2)^\top.$$

After training, the decision rule is

$$y_{LR}(x, \omega^*) = \begin{cases} 1, & (\omega^*)^\top \phi_{LR}(x) \geq 0, \\ 0, & (\omega^*)^\top \phi_{LR}(x) < 0. \end{cases} \quad (3.5)$$

Thus the decision boundary is the *hyperplane*

$$(\omega^*)^\top \phi_{LR}(x) = 0.$$

Conclusion: Logistic regression is always a linear classifier. Its separator in feature space is a straight line (in 2D), a plane (in 3D), or, more generally, a hyperplane.

3.1.3 Why Linear Logistic Regression Fails for Non-Linearly Separable Data

Many real-world datasets are not linearly separable. The XOR dataset provides the simplest illustration:

$$(0, 0) \rightarrow 0, \quad (0, 1) \rightarrow 1, \quad (1, 0) \rightarrow 1, \quad (1, 1) \rightarrow 0.$$

No single straight line can separate the classes. Thus *linear LR fails* because:

- it can only produce monotonic decision functions,
- its decision boundary is always linear.

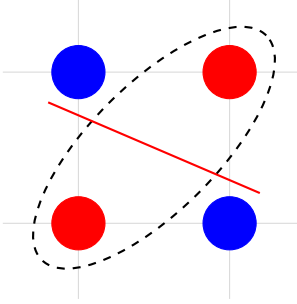


Figure 3.1: XOR dataset: the dashed nonlinear separator works; a linear separator (red) fails. Linear logistic regression cannot solve XOR.

3.1.4 Gradient Descent for Logistic Regression: The Vector Field

Optimization algorithms such as Gradient Descent (GD) operate by iteratively updating the parameter vector ω in the direction of steepest descent of the loss. For logistic regression, the loss landscape is smooth and convex, making it an ideal setting to visualize the *vector field* of the gradient.

Studying this vector field is especially useful because:

- it reveals how optimization “flows” toward the optimum;
- it highlights anisotropy in curvature (directions of flatness vs. sharpness);
- it provides a geometric viewpoint on why GD converges reliably for LR;
- it introduces the dynamical-systems perspective foundational for continuous-time optimization, Neural ODEs, and diffusion models.

Setup (2D visualization). To produce a 2D visualization, we restrict attention to a logistic regression model with two parameters, keeping the bias fixed:

$$\omega = (\omega_1, \omega_2).$$

Given data points (x_i, y_i) , the loss is

$$\mathcal{L}(\omega) = -\frac{1}{N} \sum_{i=1}^N \left[y_i \log \sigma(\omega^\top x_i) + (1 - y_i) \log (1 - \sigma(\omega^\top x_i)) \right].$$

The gradient has closed form:

$$\nabla_\omega \mathcal{L}(\omega) = \frac{1}{N} \sum_{i=1}^N (\sigma(\omega^\top x_i) - y_i) x_i.$$

Gradient Flow Interpretation. Consider the continuous-time gradient flow ODE

$$\frac{d\omega}{dt} = -\nabla_{\omega}\mathcal{L}(\omega).$$

This ODE defines a vector field over the (ω_1, ω_2) -plane. Arrows point toward decreasing loss, and their magnitude encodes the steepness. For convex logistic regression, all trajectories converge to the unique optimum ω^* .

Example 3.1.1 (Linear Regression Gradient Field). *The accompanying notebook `LR-gradient-field.ipynb` constructs a simple 2D dataset, computes the gradient field on a grid, plots the loss contours, projects gradient flow trajectories, and performs discrete gradient descent for comparison with the continuous field.*

Fig. 3.2 shows a typical output: contour lines of the loss together with gradient arrows and a GD trajectory.

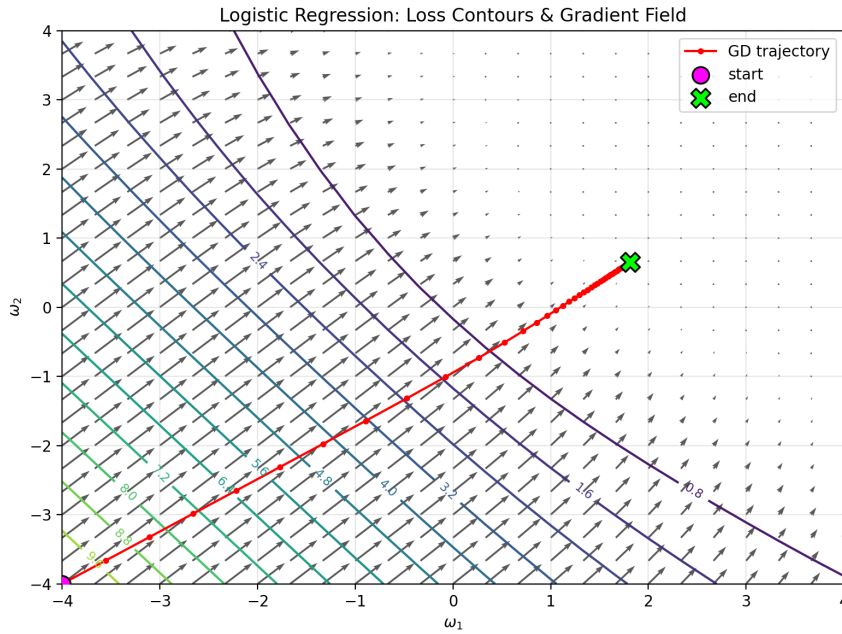


Figure 3.2: Loss-level sets and gradient vector field for 2D logistic regression. Arrows point toward decreasing loss; the red curve shows a discrete GD trajectory. Generated by `LR-gradient-field.ipynb`.

Exercise 3.1.1 (Exploring Optimization Dynamics). *Using the notebook `LR-gradient-field.ipynb`:*

1. *Visualize the loss contours and vector field for different datasets (linearly vs. nonlinearly separable).*
2. *Compare continuous gradient flow trajectories with discrete GD and SGD. How does stochasticity change the trajectories?*

3. Increase the learning rate and observe instability in discrete GD. Relate this to the curvature of the loss landscape.
4. Add a bias parameter b (making the parameter space 3D) and visualize 2D slices. Discuss how the additional degree of freedom alters convergence.

3.1.5 Nonlinear Logistic Regression via Feature Engineering

A classical strategy – predating neural networks – is to enrich the feature map. Introduce a *quadratic feature map*

$$\phi_Q(x) = (x_1, x_2, x_1^2, x_2^2, x_1 x_2)^\top.$$

The nonlinear logistic regression model becomes

$$P(y = 1 \mid x, \omega) = \sigma((\phi_Q(x))^\top \omega),$$

which is trained by the same convex optimization problem as in Eq. (3.3), but with $\phi_{LR}(x)$ replaced by $\phi_Q(x)$.

The resulting decision boundary

$$(\phi_Q(x))^\top \omega^* = 0$$

is a *quadratic curve*: ellipse, parabola, hyperbola, etc.

Key advantages of nonlinear features:

- nonlinear decision boundaries,
- feature–feature interactions,
- ability to handle non-linearly separable datasets.

Example 3.1.2 (Linear vs. Quadratic Logistic Regression). *We visualize these ideas using the notebook LogReg+NN-supervised-2D.ipynb. The dataset consists of two classes forming an elliptically shaped separation boundary.*

The comparison clearly shows:

- *The linear model learns the best straight-line separator – but it is fundamentally mismatched.*
- *The quadratic model learns a curved boundary that perfectly aligns with the data geometry.*

This example demonstrates the power of nonlinear features:

Nonlinearity in the feature space enables linear models to solve non-linear classification problems.

Exercise 3.1.2 (Exploring Logistic Regression with Polynomial Features). *Using the notebook LogReg2D.ipynb:*

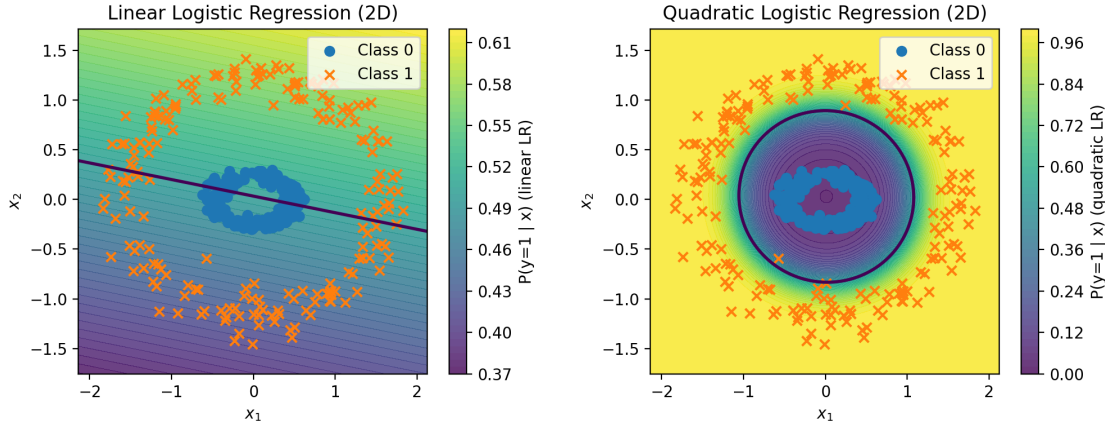


Figure 3.3: Left: linear logistic regression fails to separate classes with elliptic structure. Right: quadratic logistic regression succeeds by learning a curved boundary. Both plots generated by `LogReg2D.ipynb`.

1. Train both linear and quadratic logistic regression models. Compare classification accuracy, loss decay, and decision boundaries.
2. Perform a sensitivity analysis: perturb one entry of ω^* while holding others fixed, and plot how the loss changes.
3. Extend the feature map to include cubic terms. Visualize the resulting boundary and discuss overfitting tendencies.

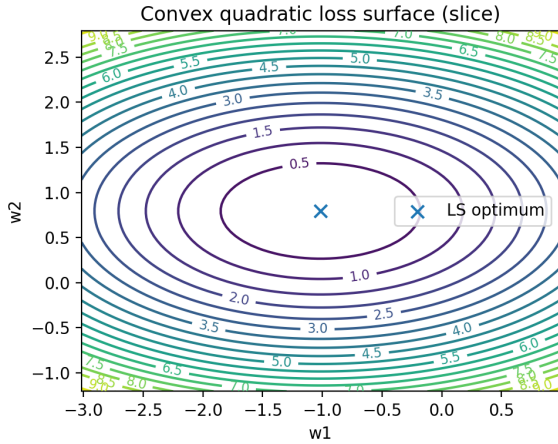
3.2 Convex Optimization – Primer

Optimization is at the heart of modern AI. Whether training a neural network, fitting a regression model, or solving a reinforcement learning problem, we repeatedly search for parameters that minimize a loss function. Yet the difficulty of this search strongly depends on the *shape* of the loss landscape, and that shape is governed by **convexity** (or lack of it). Convex optimization problems enjoy beautiful mathematical guarantees: every local minimum is a global minimum, gradient descent converges reliably, and duality theory offers deep structural insights. In contrast, most AI models — in particular neural networks — lead to *non-convex* landscapes with many flat regions, narrow valleys, and saddle points. Understanding convexity therefore provides a clean baseline from which we can appreciate the complexity of non-convex optimization in AI.

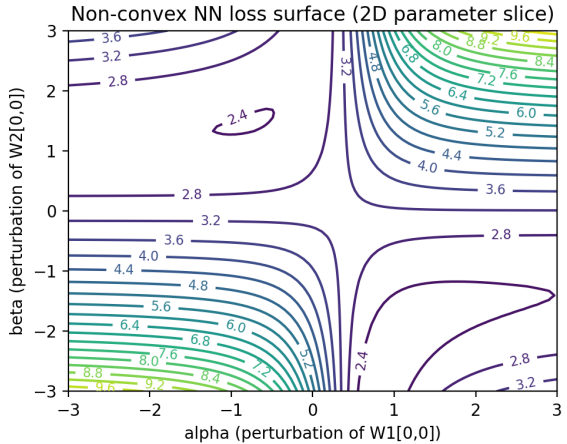
3.2.1 Variety of (Non-Convex) Landscapes

Optimization landscapes encountered in AI typically include:

- **Global minima:** Ideal convergence points where the loss is smallest.



(a) Convex quadratic loss landscape.



(b) Non-convex neural network loss landscape.

Figure 3.4: Convex vs non-convex loss landscapes. Both contour plots are produced by the notebook `Convex_vs_NonConvex_Landscapes.ipynb`. **Left:** The mean-squared error of a linear regression model, shown as a function of its two parameters (w_1, w_2), forms a strictly convex quadratic bowl with a unique global minimizer. **Right:** A two-parameter slice of the loss surface of a tiny one-hidden-layer neural network. The resulting landscape exhibits non-convex features such as distorted level sets, saddle-like regions, and multiple attraction basins. These differences illustrate why convex optimization behaves predictably, while neural-network training encounters the full complexity of non-convex geometry.

- **Local minima:** Stationary points that are not global minima. In high dimensions, most local minima of large neural networks are “good enough” and often comparable to the global minimum.
- **Saddle points:** Points where curvature is positive in some directions and negative in others. These dominate high-dimensional non-convex landscapes.
- **Flat regions (plateaus):** Regions where gradients vanish or are very small, causing slow optimization.
- **Narrow valleys:** Curvature varies dramatically across directions, forcing small learning rates and slowing gradient methods.

Even simple two-layer neural networks display many of these features. Convex optimization provides tools and intuition that help us navigate and mitigate such difficulties.

Example 3.2.1 (Convex vs non-convex loss landscapes). *To visualize the difference between convex and non-convex optimization problems, consider the Jupyter/Python notebook `Convex_vs_NonConvex_Landscapes.ipynb`. The notebook constructs and compares two loss landscapes:*

- *A convex quadratic loss corresponding to least-squares linear regression in 2D. We fit a linear model $\hat{y}(x; w) = w_1 x_1 + w_2 x_2$, to a small synthetic dataset. The resulting mean-squared error loss $L_{\text{lin}}(w_1, w_2)$ is a strictly convex quadratic function of the parameters.*

Its level sets are ellipses, and there is a unique global minimizer. The contour plot of this loss, as a function of (w_1, w_2) , is shown on the left panel of Fig. (3.4).

- A **non-convex loss** arising from a tiny one-hidden-layer neural network. We keep most parameters fixed and vary only two of them (for example, one weight in the hidden layer and one weight in the output layer). Evaluating the mean-squared error as a function of these two parameters defines a 2D slice of the full NN loss landscape. This slice exhibits multiple valleys, saddle-like regions, and non-elliptic level sets, illustrating non-convex behavior. The corresponding contour plot is shown on the right panel of Fig. (3.4).

Comparing the two figures highlights a key structural difference:

- In the convex quadratic case, the loss landscape is “bowl-shaped,” with smooth, nested ellipses and a single global minimum.
- In the neural network case, the same least-squares objective becomes non-convex in the parameters, showing distorted contours, flat regions, and directions of negative curvature.

Exercise 3.2.1 (Gradient Descent Trajectories in Convex and Non-Convex Landscapes). This exercise complements Example 3.2.1 and the Jupyter/Python notebook `Convex_vs_NonConvex_Landscapes.ipynb`. Extend the notebook as follows.

1. Gradient Descent on the Convex Quadratic.

- Implement vanilla gradient descent on the convex quadratic loss used in the linear-regression part of the notebook.
- Choose several distinct initial parameter vectors $(w_1^{(0)}, w_2^{(0)})$ and run gradient descent from each.
- On top of the convex contour plot `figs/convex_quadratic_loss_contours.png`, overlay the corresponding gradient-descent trajectories in the (w_1, w_2) -plane.
- Comment on your observations: do all trajectories converge smoothly to the same global minimizer? How does the step size (learning rate) influence the path and speed of convergence?

2. Gradient Descent on the Non-Convex Neural-Network Loss.

- Reuse the tiny one-hidden-layer neural network from the notebook and implement gradient descent (or basic SGD) on the full parameter vector.
- At each iteration, project the current parameter vector onto the 2D slice used in the contour plot (for example, by expressing the current values of the two perturbed parameters as (α, β) corresponding to $W_1[0, 0]$ and $W_2[0, 0]$).
- Overlay the resulting trajectory in the (α, β) -plane on top of the non-convex contour plot `figs/nonconvex_nn_loss_contours.png`.

- (d) Compare the resulting paths for several different initializations of the full parameter vector. Do the trajectories converge to the same region or to different local minima?

3. Effect of Learning Rate and Noise.

- (a) Vary the learning rate in both the convex and non-convex experiments above. How do too-small and too-large learning rates manifest in the trajectories (e.g., very slow progress, overshooting, or divergence)?
- (b) Add small random perturbations (noise) to the gradient updates to mimic stochastic gradient descent. In the non-convex case, can you observe situations where noise helps the trajectory escape shallow minima or saddle-like regions?
- (c) Summarize your findings: contrast the behavior of gradient-based methods in the convex quadratic landscape versus the non-convex neural-network landscape. Relate your observations to the general discussion of convex vs. non-convex optimization in this section.

To summarize, the numerical experiments and visualizations in Example 3.2.1 and Exercise 3.2.1 illustrate a fundamental phenomenon: in convex landscapes, optimization behaves in a predictable and robust way, whereas in non-convex landscapes even simple models exhibit multiple valleys, plateaus, and dramatically different trajectories depending on initialization. These geometric differences explain why convex problems are mathematically tractable, while non-convex problems such as those arising in neural networks are considerably more challenging.

This motivates a deeper look at what convexity actually is and why it guarantees such favorable optimization behavior. We now formally introduce the mathematical notion of convexity and outline the key structural properties that make convex optimization the cornerstone of modern optimization theory.

3.2.2 Convexity: A Guiding Light in AI Optimization

Although AI optimization problems are generally non-convex, convexity is central to understanding how and why optimization works.

Convex Functions. A function $f : \mathbb{R}^n \rightarrow \mathbb{R}$ is convex if

$$f(\alpha x + (1 - \alpha)y) \leq \alpha f(x) + (1 - \alpha)f(y), \quad \forall x, y, \alpha \in [0, 1]. \quad (3.6)$$

Convexity ensures that every local minimum is global.

Strict Convexity. If the inequality in Eq. (3.6) is strict for $x \neq y$, the minimizer is unique.

Second-Order Characterization. A twice differentiable function is convex iff its Hessian is positive semi-definite:

$$v^\top H_f(x)v \geq 0 \quad \forall v.$$

If the Hessian is positive definite, the function is strictly convex.

Convex Constraints. A feasible set \mathcal{C} is convex if

$$\alpha x + (1 - \alpha)y \in \mathcal{C}$$

for all $x, y \in \mathcal{C}$. Convex constraints preserve the favorable geometric structure of the problem.

Duality. Convex problems admit powerful dual formulations, relating the structure of constraints to the structure of the objective. Duality provides:

- computational advantages,
- sensitivity analysis,
- natural connections to Lagrangian methods.

First-Order Methods. Gradient descent and its variants (SGD, momentum, Adam, AdaGrad, RMSProp – all to be discussed below) form the backbone of modern ML optimization. In convex problems, gradient descent is guaranteed to converge to the global minimum; in strictly convex problems, convergence is linear.

3.2.3 Convexity of Logistic Regression

Logistic Regression (LR), introduced in Section 3.1, is a notable example of a convex optimization problem in machine learning, even when nonlinear feature maps are used.

Recall the objective:

$$\omega^* = \arg \min_{\omega} \sum_{i=1}^N \mathcal{L}_{\text{LR}}(y_i, \hat{y}(x_i, \omega)), \quad (3.7)$$

$$\hat{y}(x, \omega) = \frac{1}{1 + \exp(-\phi(x)^\top \omega)}, \quad \mathcal{L}_{\text{LR}}(y, \hat{y}) = -\log(\hat{y}^y (1 - \hat{y})^{1-y}). \quad (3.8)$$

Convexity follows from:

1. The logistic loss is convex in \hat{y} .
2. The mapping $\omega \mapsto \phi(x)^\top \omega$ is affine.
3. A nonnegative weighted sum of convex functions is convex.

From Linear Programming to Primal and Dual. It is instructive to transform logistic regression into a Linear Programming (LP) approximation. Introducing slack variables t_i enforcing

$$t_i \geq \mathcal{L}_{\text{LR}}(y_i, \hat{y}(x_i, \omega)),$$

and approximating the convex log-loss via a piecewise linear lower envelope yields the LP relaxation:

$$\min_{\omega, t} \sum_{i=1}^N t_i, \quad \text{s.t. } t_i \geq a_k(y_i) \phi(x_i)^\top \omega + b_k(y_i), \quad \forall i, k.$$

Such LP formulations are effective for interpretability and robustness analysis, though not competitive with gradient-based methods for modern high-dimensional models.

3.2.4 Constrained Optimization and Lagrange Multipliers

Many AI problems involve constraints (fairness, robustness, regularization). The Lagrangian method provides a systematic approach to such problems:

$$\mathcal{L}(x, \lambda) = f(x) + \lambda^\top g(x),$$

where $g(x) \leq 0$ encodes constraints. Optimality is characterized by the Karush–Kuhn–Tucker (KKT) conditions.

Support Vector Machines (SVM) exemplify constrained convex optimization, forming an ideal entry point for primal–dual optimization. The soft margin SVM solves:

$$\min_{w, b, \xi \geq 0} \frac{1}{2} \|w\|^2 + C \sum_{i=1}^N \xi_i, \quad \text{s.t. } y_i(w^\top x_i + b) \geq 1 - \xi_i.$$

SVMs are closely related to logistic regression but optimize *hinge loss* instead of log-loss.

Example 3.2.2 (Primal–dual derivation of a two-point SVM). *For a toy dataset*

$$\{([1, 1], +1), ([−1, −1], −1)\},$$

one obtains the dual optimization problem:

$$\max_{0 \leq \lambda_i \leq C} \sum_{i=1}^2 \lambda_i - \frac{1}{2} \sum_{i,j} \lambda_i \lambda_j y_i y_j (x_i^\top x_j), \quad \sum_i \lambda_i y_i = 0.$$

Solving this by hand yields the optimal separating hyperplane.

Exercise 3.2.2. *Derive the dual formulation above using the Lagrangian and KKT conditions. Then:*

1. *Explicitly solve for the optimal multipliers λ .*
2. *Recover w and b .*
3. *Create a Jupyter notebook that visualizes the decision boundary for a larger synthetic 2D dataset.*
4. *Study the effect of varying C on the margin.*

From Optimization Landscapes to Optimization Algorithms

The preceding section emphasized the *geometry* of optimization problems: convexity, curvature, constraints, and the qualitative structure of loss landscapes. Before turning to specific algorithms, it is helpful to understand how geometry informs the design of practical methods.

- In a strongly convex landscape, plain gradient descent already enjoys global con-

vergence with a predictable rate, and algorithmic complexity is well understood.

- In non-convex problems—such as neural networks or transformers—the landscape contains flat regions, ridges, anisotropy, and poorly conditioned directions. Here, curvature varies dramatically across coordinates and layers.
- This mismatch between *local geometry* and a *uniform step size* motivates the introduction of momentum, coordinate-wise scaling, normalization layers, and adaptive learning rates.

Thus, gradient-based algorithms should not be viewed as abstract update rules but as tools designed to cope with the geometric distortions arising in modern AI models. The methods introduced next – GD, SGD, momentum, RMSProp, Adam, and their variants – can be interpreted as increasingly sophisticated attempts to adapt the update step to the underlying curvature.

3.3 Gradient Descent and Its Essential AI Variants

Gradient descent is the backbone of optimization in AI, enabling efficient model training by minimizing loss functions. However, AI optimization problems present unique challenges, including high-dimensionality, non-convex landscapes, and large datasets. To address these challenges, several gradient descent variants have been developed, each offering advantages in different settings.

This section introduces key first-order optimization methods, discussing their theoretical foundations in convex settings before transitioning to their practical application in AI, particularly in Deep Learning (DL).

3.3.1 Gradient Descent (GD)

Gradient Descent (GD) iteratively updates the vector of parameters θ_t in the discrete time, $t = 0, \dots$ based on the negative gradient of the loss function over θ_t :

$$\theta_{t+1} = \theta_t - \eta \nabla_{\theta_t} \sum_{i=1}^N \mathcal{L}(x_i, \theta_t), \quad (3.9)$$

where $(x_i | i = 1, \dots, N)$ is the Ground Truth (GT) data set with N samples. (Recall over-damped relaxation in a potential we have discussed in Chapter 2.) For a convex and L -smooth function, GD converges at a rate of $O(1/T)$ for general convex functions and $O(1/T^2)$ for strongly convex functions with an optimal step size η . Here the number of iterations T required to reach an error ϵ depends on the problem dimension n (in the context of AI training – on the number of parameters), with typical dependencies being $T = O(n \log(1/\epsilon))$ for well-conditioned convex problems. This dependence worsens with high-dimensional ill-conditioned problems.

GD was first introduced by Augustin-Louis Cauchy (1847) and later formalized for convex optimization by Yurii Nesterov (1983) [2, 3].

3.3.2 Stochastic Gradient Descent (SGD)

SGD approximates GD by computing noisy gradient estimates over randomly chosen batches:

$$\theta_{t+1} = \theta_t - \eta \nabla_{\theta_t} \sum_{i \in \text{batch}} \mathcal{L}(x_i, \theta_t),$$

where batch is updated frequently (possibly at each iteration step) at random, that is stochastically – thus the name. SGD reduces per-iteration computational cost and enables large-scale learning but converges at a slower rate of $O(1/\sqrt{T})$ in expectation. A key consideration in SGD is batch size. Worst case analysis suggests that an optimal batch size, balancing computational efficiency and variance reduction, scales as $O(N)$. However, in practice the batch size is much smaller than the number of GT samples, therefore resulting in gain in efficiency. The method was pioneered by Robbins and Monro (1951) and refined for ML by Léon Bottou (1998) [4].

3.3.3 Momentum-Based Methods

Momentum methods incorporate past increments to accelerate convergence by simulating the behavior of a dynamical system with inertia. The classical Polyak Heavy-Ball Method (Polyak, 1964) follows the update rule:

$$\theta_{t+1} = \theta_t + \beta(\theta_t - \theta_{t-1}) - \eta \nabla_{\theta_t} \sum_i \mathcal{L}(x_i, \theta_t), \quad (3.10)$$

where β is the momentum coefficient, controlling how much of the past increment is retained; η is the step size; $\mathcal{L}(x_i, \theta)$ is the loss function evaluated at data point x_i . The heavy-ball method can be interpreted as a damped second-order system in continuous time, where momentum reduces oscillations and accelerates convergence.

Nesterov (1983) introduced an accelerated momentum-based method:

$$\theta_{t+1} = \theta_t + \beta(\theta_t - \theta_{t-1}) - \eta \nabla_{\theta_t} \sum_i \mathcal{L}(x_i, \theta_t + \beta(\theta_t - \theta_{t-1})), \quad (3.11)$$

where the key difference is that the gradient is evaluated at an anticipated point $\theta_t + \beta(\theta_t - \theta_{t-1})$, rather than at θ_t .

For a smooth and strongly convex objective the heavy-ball Polyak's method achieves $O(1/T)$ convergence in T iterations under well-tuned parameters, which is however not as fast typically as the optimal $O(1/T^2)$ rate achieved by Nesterov's acceleration.

The main distinction between heavy-ball and standard gradient descent lies in their behavior for ill-conditioned problems: the heavy-ball method can exhibit faster practical convergence despite its theoretical rate.

Exercise 3.3.1. Mechanical Interpretation of Momentum Methods: Consider the equations of motion for a damped oscillator discussed in the previous chapter. Provide a mechanical interpretation for the Polyak heavy-ball and the Nesterov Accelerated Method. Further, consider the following extensions:

- *Pen-and-paper derivation:* Derive the continuous-time ODE limit of Polyak’s and Nesterov’s methods and discuss their implications for optimization.
- *Phase space analysis:* Sketch the phase portraits (velocity vs. position) for both methods and explain the impact of momentum on the trajectory.
- *Parameter tuning:* Given a convex quadratic function, analyze how choosing different values of β affects convergence and stability.

3.3.4 Projected Gradient Descent (PGD)

In constrained optimization, a key challenge is ensuring that iterates remain within a feasible set \mathcal{C} . One widely used approach is Projected Gradient Descent (PGD), which enforces constraints by projecting the updated iterate back onto the feasible set after each gradient step. The PGD update rule is:

$$\theta_{t+1} = \text{Proj}_{\mathcal{C}}(\theta_t - \eta \nabla_{\theta_t} \sum_i \mathcal{L}(x_i, \theta_t)).$$

This ensures that each iterate θ_t remains within \mathcal{C} while descending along the gradient of the objective function. The projection operator $\text{Proj}_{\mathcal{C}}(\cdot)$ finds the closest point in \mathcal{C} to the updated parameter, maintaining feasibility.

PGD is guaranteed to converge under mild assumptions. When the loss function is convex and Lipschitz-smooth, and the constraint set \mathcal{C} is convex, PGD converges at a rate of $O(1/T)$ for general convex functions and $O(\exp(-\mu T))$ for strongly convex functions with $\mu > 0$. These guarantees ensure that PGD remains an effective tool for constrained optimization. PGD has its roots in classical projection methods for constrained convex optimization, with early developments appearing in the work of *Bertsekas (1976)* and later refined in studies such as *Nesterov (2004)* and *Beck and Teboulle (2009)*. PGD has since been widely used in applications ranging from machine learning to signal processing and robust optimization.

3.3.5 Adaptive Learning Rate Methods

Optimization methods with *adaptive learning rates* dynamically adjust step sizes based on past gradient information. Such approaches have become central in modern deep learning, where high dimensionality, heterogeneous curvature, and sparsity patterns necessitate learning-rate schedules more flexible than the fixed-step schemes used in classical gradient descent.

Below we review three foundational adaptive methods – **AdaGrad**, **RMSProp**, and **Adam** – highlighting their mathematical structure, historical origins, and practical implications.

AdaGrad (Adaptive Gradient Algorithm). AdaGrad [5] modifies standard gradient descent, Eq. (3.9), by assigning each parameter θ_α its own time-dependent learning rate:

$$\eta_\alpha^{(t)} = \frac{\eta}{\sqrt{G_\alpha^{(t)} + \epsilon}}, \quad G_\alpha^{(t)} = \sum_{t'=1}^t \left(\partial_{\theta_\alpha^{(t')}} \sum_i L(x_i, \theta^{(t')}) \right)^2.$$

Since $G_\alpha^{(t)}$ accumulates the squared gradients over time, directions with frequent large gradients receive progressively smaller step sizes. AdaGrad is particularly effective for sparse or highly anisotropic problems, but its monotonically growing accumulator can cause learning rates to shrink excessively, slowing convergence at later stages.

RMSProp (Root Mean Square Propagation). RMSProp, introduced by Tieleman and Hinton in a lecture note [6], mitigates AdaGrad's diminishing-step-size problem by replacing the cumulative sum with an exponentially decaying moving average:

$$\begin{aligned} G_\alpha^{(t+1)} &= \beta G_\alpha^{(t)} + (1 - \beta) \left(\partial_{\theta_\alpha^{(t)}} \sum_i L(x_i, \theta^{(t)}) \right)^2, \\ \theta_\alpha^{(t+1)} &= \theta_\alpha^{(t)} - \eta \frac{\partial_{\theta_\alpha^{(t)}} \sum_i L(x_i, \theta^{(t)})}{\sqrt{G_\alpha^{(t+1)}} + \epsilon}. \end{aligned}$$

The exponential decay prevents $G_\alpha^{(t)}$ from diverging, making RMSProp a stable and widely used optimizer for non-stationary or noisy gradient regimes, especially in deep learning.

Adam (Adaptive Moment Estimation). Adam [7] combines the ideas of AdaGrad and RMSProp with momentum by tracking both first and second moments of the gradient:

$$\begin{aligned} m_\alpha^{(t+1)} &= \beta_1 m_\alpha^{(t)} + (1 - \beta_1) \partial_{\theta_\alpha^{(t)}} \sum_i L(x_i, \theta^{(t)}), \\ G_\alpha^{(t+1)} &= \beta_2 G_\alpha^{(t)} + (1 - \beta_2) \left(\partial_{\theta_\alpha^{(t)}} \sum_i L(x_i, \theta^{(t)}) \right)^2, \\ \hat{m}_\alpha^{(t+1)} &= \frac{m_\alpha^{(t+1)}}{1 - \beta_1^t}, \quad \hat{G}_\alpha^{(t+1)} = \frac{G_\alpha^{(t+1)}}{1 - \beta_2^t}, \\ \theta_\alpha^{(t+1)} &= \theta_\alpha^{(t)} - \eta \frac{\hat{m}_\alpha^{(t+1)}}{\sqrt{\hat{G}_\alpha^{(t+1)}} + \epsilon}. \end{aligned}$$

Adam has become the de-facto standard optimizer in deep learning due to its fast empirical convergence, robustness to hyperparameter choices, and efficiency in stochastic settings. Despite subtle issues with theoretical convergence (now well understood), its practical performance has made it ubiquitous across modern neural network applications.

Example 3.3.1 (Adaptive Optimizers on a Non-Convex ReLU Landscape). *To illustrate the qualitative differences between AdaGrad, RMSProp, and Adam on a genuinely non-convex optimization problem, consider the Jupyter/Python notebook `adaptive_relu_2D.ipynb`. The dataset consists of two classes in \mathbb{R}^2 :*

- points inside a disk of radius R (label 1),
- points outside the disk (label 0).

This makes the optimization landscape of the classification problem strongly non-convex even in low dimension. A tiny neural network

$$x \mapsto f_\theta(x) = W_2 \sigma(W_1 x + b_1) + b_2, \quad \sigma(z) = \max(z, 0),$$

is trained using binary cross-entropy loss. Because the ReLU network with a small hidden layer cannot represent a true circular boundary, the model learns a piecewise linear polygonal approximation to the circle.

Optimizer Comparison at Hidden Dimension $H = 2$. Figs. 3.5–3.6 show the performance of the three optimizers when the hidden layer width is $H = 2$.

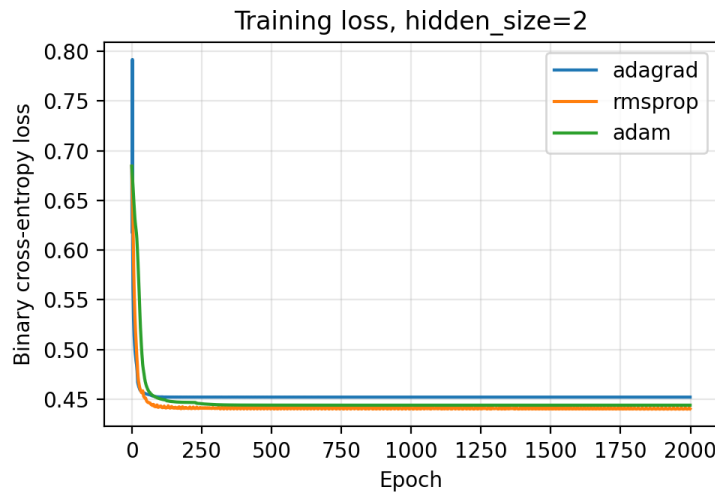


Figure 3.5: Training loss for AdaGrad, RMSProp, and Adam on the non-convex ReLU ring-classification task with $H = 2$. AdaGrad descends very quickly at first but plateaus higher. Adam exhibits (presumably due to oscillations) a slower progress. RMSProp shows the most stable and lowest long-run loss.

Observations.

- **AdaGrad:** Converges quickly initially due to large effective learning rates on under-utilized parameters, but its learning rate decays rapidly and becomes too conservative. As a result, optimization slows dramatically and the model underfits.
- **Adam:** Exhibits oscillatory behavior and a somewhat noisy trajectory in this small-scale setting; this is consistent with known issues where Adam may overshoot due to accumulated first moments when curvature is highly anisotropic.
- **RMSProp:** Performs the best. It balances adaptivity and stability, avoids AdaGrad's vanishing steps, and avoids Adam's oscillatory behavior.

Width Sweep: $H = 2, 4, 8, 32$ with RMSProp.

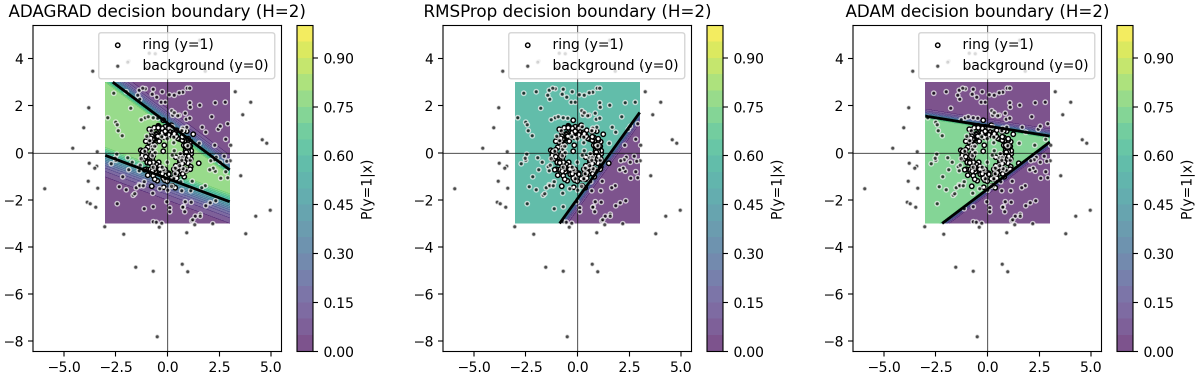


Figure 3.6: Decision boundaries (white curves) for AdaGrad (left), RMSProp (center), and Adam (right). All boundaries are triangular, reflecting that $H = 2$ ReLU units can produce only three linear segments. This demonstrates the expressivity bottleneck at small width: optimizer choice cannot overcome representational limits of the network. RMSProp produces the most symmetric and stable triangle.

To understand the geometry induced by width, the notebook increases the number of hidden ReLU units. A network with H ReLUs can represent decision boundaries as a polygon with at most H linear segments.

Figures 3.7–3.8 visualize this transition from triangle → polygon → nearly circular boundary.

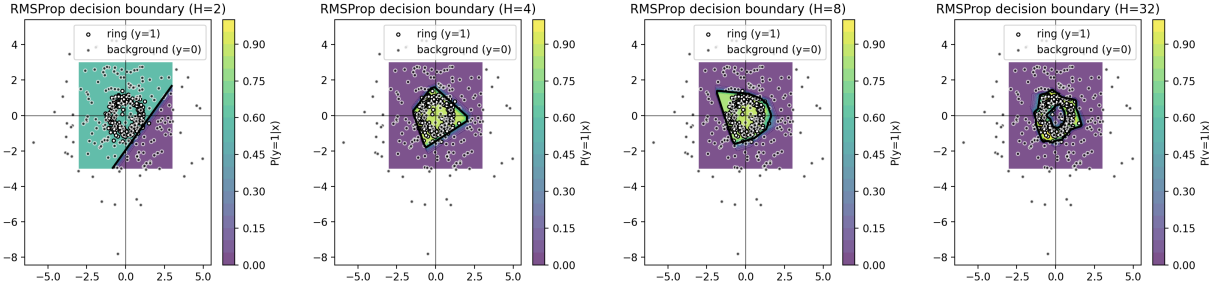


Figure 3.7: Decision boundaries for RMSProp as hidden width increases. **Left to right:** $H = 2$ (triangle), $H = 4$ (quadrilateral), $H = 8$ (octagon-like polygon), $H = 32$ (nearly circular). Increased width increases the number of linear regions, approximating the circle with growing fidelity.

Key Takeaways.

- *Width limits representational capacity: small H forces polygonal boundaries; large H approximates smooth shapes.*
- *Optimizers behave differently in low-dimensional non-convex problems: RMSProp is stable, AdaGrad collapses to tiny steps, Adam oscillates.*
- *The notebook provides a clean sandbox for observing expressivity vs. optimization effects in a controlled low-dimensional model.*

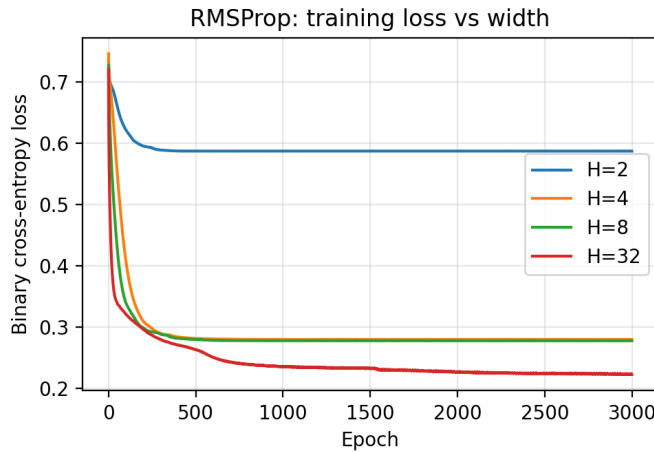


Figure 3.8: Training loss for RMSProp as a function of iteration for different hidden widths. Larger width models achieve lower final loss and more stable convergence.

Exercise 3.3.2 (Optimizer Behavior in a Non-Convex ReLU Model). *Using the notebook `adaptive_relu_2D.ipynb`, extend the analysis from Example 3.3.1 through the following tasks.*

1. **Optimizer Sensitivity Study.** For the three optimizers (AdaGrad, RMSProp, Adam):

- (a) explore learning rates $\eta \in \{10^{-1}, 10^{-2}, 10^{-3}, 10^{-4}\}$,
- (b) run multiple random initializations,
- (c) plot mean and variance of the loss curves.

Discuss which optimizer is most robust to hyperparameters and initialization.

2. **Expressivity and Geometry.** For widths $H \in \{2, 4, 8, 16, 32, 64\}$:

- (a) train with RMSProp,
- (b) extract the decision boundary,
- (c) compute a measure of “circularity” (e.g., variance of boundary radius).

Verify empirically that the boundary converges from triangle \rightarrow polygon \rightarrow smooth circle.

3. **Optimizer–Expressivity Interaction.** Pick $H = 8$ and compare how AdaGrad, RMSProp, and Adam differ in:

- boundary smoothness,
- convergence rate,
- stability across random seeds.

Explain why optimizers interact differently with the same network architecture.

4. ***Challenging Regimes.*** Increase noise by adding label flips or Gaussian perturbations to inputs. Which optimizer is most robust? Which boundary shape distorts the least?

Include all plots and provide a short written report summarizing insights about:

- optimizer dynamics,
- expressivity-limited non-convexity,
- geometry of learned decision boundaries.

The Indispensability of First-Order Methods

The algorithms we have discussed so far in this section are fundamentally *first-order methods* because their search directions rely primarily on the computation of the first derivative (the gradient) of the optimization objective. While simple, these techniques are the indispensable workhorses that allow us to navigate the complex, high-dimensional loss landscapes of Generative AI.

However, their pervasive use raises a critical question: If second-order methods offer theoretically superior convergence speed by incorporating curvature information, why do we rely solely on the simple gradient? The answer lies in the computational limitations and scale of the Hessian matrix, which we address in the following subsection.

3.3.6 Why the Second-Order Methods are no go in AI?

The pervasive use of first-order methods like Gradient Descent and Adam in large-scale AI is not a matter of choice, but necessity. While Automatic Differentiation (AD) handles first-order derivatives (gradients) with remarkable efficiency, extending the same logic to second-order derivatives in high-dimensional spaces introduces a fundamental, insurmountable bottleneck. This bottleneck explains why virtually all state-of-the-art Generative AI models are trained using first-order methods and ignore the theoretically superior second-order methods (like Newton's method).

The second-order derivative information is captured by the *Hessian matrix*, H . For an optimization objective $L(W)$ (like a loss function in neural network training) depending on a parameter vector W with P elements, the Hessian is a matrix of all second partial derivatives:

$$H_{ij} = \frac{\partial^2 L}{\partial W_i \partial W_j}, \quad \text{where } H \in \mathbb{R}^{P \times P}.$$

The Hessian is crucial because it provides local curvature information about the loss landscape. This curvature information is what allows second-order optimization methods (like Newton's method) to converge quadratically (extremely fast) near a minimum by adapting the search direction to the shape of the function.

However, the cost of utilizing the Hessian becomes prohibitive for modern AI uses. The core issue is scaling:

- **Storage Complexity:** For a generative model with P parameters, the Hessian matrix H has P^2 elements. Since P can reach 10^{11} (billions), storing the P^2 values requires an infeasible amount of memory (scaling as $\mathcal{O}(P^2)$).

- **Inversion Complexity:** The full Newton step requires computing the inverse of the Hessian, H^{-1} , which scales as $\mathcal{O}(P^3)$ and is computationally impossible for realistic values of P .

While methods exist to compute the Hessian-Vector Product (HVP) efficiently ($\mathcal{O}(P)$) without explicitly forming H , the full Hessian required for global optimization remains the *Second-Order Cost Trap*. This hard limit forces us to rely on the simpler, less informed gradient direction, which necessitates more sophisticated techniques (momentum, adaptive learning rates) to navigate the complex, high-dimensional loss landscapes of modern AI.

Exercise 3.3.3 (Computational Cost and Properties of the Hessian). *This exercise explores the computational limitations and optimization insights associated with the Hessian matrix, $H = \nabla^2 L(W)$.*

1. **Complexity Analysis.** If a typical large language model has $P \approx 10^{11}$ parameters (e.g., 100 billion):
 - (a) Calculate the memory (in bytes, assuming 4-byte floats) required just to store the Hessian matrix $H \in \mathbb{R}^{P \times P}$. Why does this immediately rule out its use?
 - (b) What is the computational complexity (in terms of P) required to invert H (i.e., to implement the full Newton update)? State the complexity using Big O notation.
2. **Optimization Insight.** In low dimensions, Newton's method (which uses H^{-1}) finds optimal solutions faster than Gradient Descent. Why? Specifically, what information about the loss landscape, provided by the Hessian, allows Newton's method to choose a more effective direction and step size than the simple negative gradient?
3. **The Problem of Saddle Points.**
 - (a) The critical points of the loss function $L(W)$ are defined by $\nabla L(W) = 0$. Describe the necessary and sufficient conditions on the eigenvalues of the Hessian, $\lambda_i(H)$, that define a saddle point.
 - (b) Why do saddle points pose a significantly greater obstacle to training large neural networks than local minima, particularly in high-dimensional space? (Hint: Think about the number of dimensions/directions that lead away from the critical point.)

3.4 Regularization & Sparsity

In the previous sections of the chapter, we analyzed optimization methods without assuming much about the structure of the underlying optimization problem. The worst-case analysis often dominates theoretical discussions, leaving significant room for practical improvements when special structural properties exist in the problem. One such property is sparsity, which arises naturally in various AI applications and can be exploited to improve both training and inference efficiency.

This section introduces sparsity as an essential concept in AI optimization, covering:

- The motivation for sparsity: Why it arises and how it can be leveraged.
- Compressed sensing: A theoretical (and also practical) framework for exploiting sparsity.
- The link between ℓ_0 and ℓ_1 regularization, convex relaxation, and Linear Programming (LP).
- The role of sparsity in AI models, including training DNNs and accelerating inference.
- Practical implementations, including a computational exercise on sparsity-based regularization in NNs.

3.4.1 Compressed Sensing and Sparse Optimization

Compressed sensing (CS) is a paradigm that exploits the fact that many high-dimensional signals and datasets have an underlying sparse structure. The fundamental insight is that *under-determined linear systems, which appear to be ill-posed, can still be solved uniquely when the true solution is sparse*.

Historical Context and AI Relevance: The theory of compressed sensing was pioneered by Candes, Romberg, and Tao (2006) and Donoho (2006), who showed that a sparse signal can be recovered from far fewer observations than traditionally required by the Nyquist-Shannon sampling theorem. The connection to AI arises in several contexts:

- In **deep learning**, sparsity is used in weight pruning and feature selection.
- In **optimization**, sparsity reduces the effective problem dimensionality, improving efficiency.
- In **inference acceleration**, sparse representations allow for faster computations at runtime.

Mathematical Formulation: Consider an underdetermined system:

$$Ax = b, \quad A \in \mathbb{R}^{m \times n}, \quad m \ll n. \quad (3.12)$$

The system has infinitely many solutions unless additional constraints are imposed. If we know that x is sparse, meaning that only a few of its components are nonzero, we can attempt to recover it by solving:

$$\min_x \|x\|_0 \quad \text{s.t.} \quad Ax = b, \quad (3.13)$$

where $\|x\|_0$ is the shortcut for the l_0 "norm" (which is not actually a norm, as it does not satisfy the "homogeneity" property $\|ax\| = |a|\|x\|$ required for norms) of the vector x , that is

$$\|x\|_0 = \sum_{i=1,\dots,n} \begin{cases} 1, & x_i = 0 \\ 0, & \text{otherwise.} \end{cases}$$

However, this ℓ_0 minimization problem is combinatorial and computationally intractable (that is number of steps required is exponential in n). A major breakthrough in compressed sensing is that relaxing ℓ_0 to ℓ_1 norm, which consists of summing up the absolute values of each component of x , leads to a convex optimization problem, which can be solved efficiently:

$$\min_x \sum_{i=1}^n |x_i| \quad \text{s.t.} \quad Ax = b. \quad (3.14)$$

This reformulation can be efficiently solved using **Linear Programming** (LP), linking sparsity to convex optimization techniques discussed earlier.

Why ℓ_1 Regularization Works?

A fundamental insight behind the success of ℓ_1 minimization is that the ℓ_1 norm promotes sparsity while remaining convex. Intuitively:

- Unlike the ℓ_2 norm, which penalizes large deviations evenly, the ℓ_1 norm favors solutions where many elements are exactly zero.
- Under suitable conditions (such as the Restricted Isometry Property, RIP), the ℓ_1 minimization recovers the same sparse solution as the ℓ_0 problem with high probability. (And this is where the asymptotic, $n \rightarrow \infty$, theory by Candes, Romberg, and Tao (2006) [8] plays a crucial role.)

A Geometric Perspective: The difference between ℓ_1 and ℓ_2 regularization can be understood through the geometry of their constraint regions and how they interact with the level sets of the loss function.

Let us illustrate this with a simple two-dimensional constrained optimization problem:

$$\begin{aligned} \ell_2 : \quad & \arg \min_x (x_1^2 + x_2^2) \quad \text{s.t.} \quad x_1 + 2x_2 = 1 \\ \ell_1 : \quad & \arg \min_x (|x_1| + |x_2|) \quad \text{s.t.} \quad x_1 + 2x_2 = 1. \end{aligned}$$

This setup captures a fundamental contrast: when minimizing the ℓ_2 norm, the optimal solution has small but nonzero values for both x_1 and x_2 , while minimizing the ℓ_1 norm promotes sparsity by forcing one component to be exactly zero.

As shown in Fig. (3.9):

- The **red line** represents the constraint $x_1 + 2x_2 = 1$, restricting the feasible solutions.
- The **blue dashed circles** represent level sets of the ℓ_2 loss function. The optimal solution occurs where the smallest blue circle touches the constraint, leading to small but nonzero values for both x_1 and x_2 .
- The **green dashed squares (rotated)** represent level sets of the ℓ_1 loss function. The optimal solution is at a corner, where either x_1 or x_2 is exactly zero. This illustrates why ℓ_1 regularization induces sparsity.

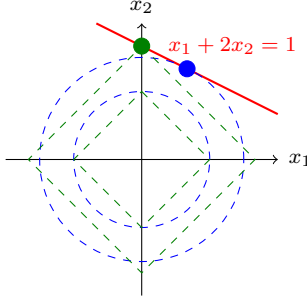


Figure 3.9: **Geometric interpretation of ℓ_1 vs. ℓ_2 regularization.** The red line represents the constraint $x_1 + 2x_2 = 1$, which restricts feasible solutions. The blue dashed circles are level sets of the ℓ_2 loss, with the **largest circle touching the constraint** at $(1/5, 2/5)$, leading to **small but nonzero values** for both x_1 and x_2 . The green dashed squares represent the level sets of the ℓ_1 loss, with the **largest square touching the constraint** at $(0, 1/2)$, enforcing a **sparse solution** where one coordinate is exactly zero. Smaller dashed contours are shown to illustrate suboptimal solutions. For a live demonstration of this geometric interpretation, please see

<https://www.desmos.com/calculator/1unxjbr3bm>.

3.4.2 Regularization and Its Importance in AI

Sparse Regularization in Machine Learning: Many modern AI models incorporate sparsity-inducing regularization. A common approach is **Lasso regression**, where the loss function includes an ℓ_1 penalty:

$$\min_w \sum_{i=1}^N \mathcal{L}(y_i, f_w(x_i)) + \lambda \|w\|_1. \quad (3.15)$$

This enforces sparsity in w , effectively selecting a subset of relevant features.

In **Neural Networks**, sparsity constraints are used to prune weights, reducing model size without significant loss of accuracy.

Example 3.4.1 (Image Denoising via Total Variation). *Total Variation (TV) regularization is one of the classical and most widely used approaches for image denoising. Given a noisy observation*

$$w = v + \xi,$$

where v is the clean image and ξ is noise, the TV restoration problem seeks

$$u^* = \arg \min_u \left[\frac{1}{2} \|u - w\|_2^2 + \lambda \sum_{(i,j) \sim (i',j')} \sqrt{\varepsilon^2 + (u_{ij} - u_{i'j'})^2} \right].$$

The first term enforces fidelity to the observed image, and the second term enforces spatial smoothness, penalizing local differences between neighboring pixels. This corresponds to the isotropic TV norm with a small smoothing parameter ε used to make the functional differentiable.

Gradient Flow Interpretation. The minimizer u^* can be found by gradient descent on the energy

$$E(u) = \frac{1}{2} \|u - w\|_2^2 + \lambda \sum_{(i,j) \sim (i',j')} \sqrt{\varepsilon^2 + (u_{ij} - u_{i'j'})^2}.$$

For each pixel,

$$\frac{du_{ij}}{dt} = -\frac{\partial E}{\partial u_{ij}} = w_{ij} - u_{ij} - \lambda \sum_{(i',j') \sim (i,j)} \frac{u_{ij} - u_{i'j'}}{\sqrt{\varepsilon^2 + (u_{ij} - u_{i'j'})^2}}.$$

This PDE is discretized and integrated numerically. A small step size is required for stability when λ is large, reflecting the stiff nature of the TV term, as discussed previously in Section 3.3.1.

Worked Example. We apply isotropic TV denoising to a 64×64 binary image of the letter “U”. Three levels of Gaussian noise with standard deviations $\sigma \in \{0.05, 0.15, 0.30\}$ are added, and TV denoising is performed for several values of the regularization parameter $\lambda \in \{0.0, 0.5, 1.5, 4.0\}$.

Figure 3.10 shows the resulting multi-panel comparison:

- top row: original and noisy images,
- subsequent rows: restored images for increasing λ .

As expected:

- small λ produces mild denoising while preserving edges,
- moderate λ removes noise effectively but begins to round corners,
- large λ oversmooths, yielding a blurry but very clean image.

Energy Decay During Optimization. The energy $E(u(t))$ decreases monotonically along the gradient flow. This behavior is illustrated in Figure 3.11, which shows the decay of the objective for several values of λ . Larger regularization produces a stiffer system and therefore a slower (despite stable) decay under explicit gradient descent.

The complete Python implementation generating both figures is available in the accompanying Jupyter notebook `ImageRestoration_TV.ipynb`, and students are encouraged to experiment with different values of λ , noise levels, and numerical solvers (explicit Euler, midpoint, implicit schemes).

3.4.3 Sparsity for Inference Acceleration

Motivation: Once a model is trained, inference should be fast. One approach to accelerating inference is to reduce the number of active parameters used in the forward pass.

Sparsity-Based Compression: A natural idea is to store only the most informative directions, identified during training. Specifically:

- Track gradients during training and identify key weight directions.
- Construct a low-dimensional subspace for inference.
- Project new inputs onto this space for efficient computation.

This reduces computational cost while maintaining accuracy.

Exercise 3.4.1. (*) Sparse Projection for Faster Inference²

In this exercise, we explore a dimensionality reduction strategy for trained Neural Networks (NN) to enhance inference efficiency:

- Train a NN on the MNIST dataset.
- Identify the most significant weight vectors utilized during training.
- Construct a compressed subspace based on these important weights and project test inputs onto this subspace.
- Evaluate the trade-off between speedup and accuracy, analyzing the impact of the compression.

This approach investigates how targeted sparsification can maintain performance while reducing computational overhead, contributing to efficient model deployment.

In conclusion (for this section): Sparsity is a powerful principle in AI optimization. Whether through compressed sensing, ℓ_1 -based regularization, or inference acceleration, sparsity enables efficient computation and improved generalization. By leveraging structured sparsity, we can develop AI models that are both accurate and computationally efficient.

3.5 (*) Optimization of Transformers – GenAI Example

³ In Section 1.1.5, we introduced the multi-head transformer model to illustrate key concepts of tensor operations, such as multiplications and convolutions, combined with nonlinear transformations. Here, we conclude the chapter on optimization by focusing on how transformers are trained – framing this as a non-convex optimization problem in state-of-the-art AI.

Training a transformer involves optimizing its weight matrices $\{W_Q, W_K, W_V\}$ in the attention layers, as well as the parameters in the feed-forward layers. We will use θ for an aggregated notation for all the adjustable parameters used to train a transormer. Given the large-scale nature of transformer models and their highly non-convex optimization landscape, sophisticated optimization techniques are essential to ensure convergence.

²The asterisk (*) indicates that this is a bonus exercise – challenging and optional, potentially requiring significant effort and creativity. Completing this exercise may even contribute to an original publication. The topic of inference acceleration is crucial, as it relies on innovation rather than massive computational resources. See [9, 10, 11, 12] and references therein.

³Sections marked with an asterisk (*) are optional and can be skipped on a first reading without loss of continuity.

3.5.1 Loss Function and Optimization Objective

The training objective for **transformers** typically involves minimizing the **cross-entropy** loss — \mathcal{L} , which we define later in the text — accumulated (sum over) all the input data. This optimization problem is non-convex due to:

- The hierarchical composition of multiple nonlinear transformations (e.g., self-attention, softmax, feedforward layers).
- The presence of highly non-linear residual connections and layer normalization.

Notably the high-dimensional parameter space makes global optimization intractable, thus motivating researchers to look for efficient heuristics, in particular based on Stochastic Gradient Based iterative algorithms.

3.5.2 Optimization Process: From Backpropagation to SGD Variants

Training transformers relies on **Back-Propagation** and **Stochastic Gradient**-based optimization methods. As discussed in Section 2.1, **Automatic Differentiation** (AD) plays a crucial role in computing gradients efficiently. There, we introduced both Forward and **Reverse Mode AD** and noted that Reverse Mode AD is preferable for minimizing the loss function in machine learning models. This preference arises because we need to compute the gradient of a scalar-valued loss function with respect to a high-dimensional vector of parameters (weight matrices), making Reverse Mode AD computationally efficient.

The gradient of the loss function with respect to each component of θ . Given the high-dimensional nature of transformers, simple gradient descent is inadequate due to slow convergence and instability in optimization. Instead, adaptive optimization techniques such as Adam are typically employed. By leveraging Reverse Mode AD and adaptive gradient-based methods, transformer models efficiently navigate the complex, non-convex loss landscape to achieve effective training.

3.5.3 How Does the Loss Function Handle Growing Input Sequences?

The training of transformers for sequence prediction involves handling dynamically growing input sequences. At each training step, the model processes progressively larger input segments while predicting the next token. The loss function — typically cross-entropy loss — is computed over multiple overlapping sub-sequences.

Consider a sequence of tokens:

$$[t_1, t_2, t_3, t_4, t_5].$$

During training, the model is presented with progressively increasing input sequences:

$$\begin{aligned} \text{Input: } [t_1] &\rightarrow \text{Target: } [t_2], \\ \text{Input: } [t_1, t_2] &\rightarrow \text{Target: } [t_3], \\ \text{Input: } [t_1, t_2, t_3] &\rightarrow \text{Target: } [t_4], \\ \text{Input: } [t_1, t_2, t_3, t_4] &\rightarrow \text{Target: } [t_5]. \end{aligned}$$

At each step, the model makes a prediction for the next token, and the loss function evaluates how well the predicted distribution aligns with the true target.

Summing Over Different Input Lengths: The total loss for a sequence of length T is computed as:

$$\mathcal{L}(\theta) = - \sum_{i=1}^T \log p_\theta(t_{i+1}|t_1, \dots, t_i), \quad (3.16)$$

where $p_\theta(t_{i+1}|t_1, \dots, t_i)$ is the predicted probability of the next token, and θ is a collective notation for all the parameters we adjust to train the transformer (see Section 1.1.5).

The model is trained to minimize this sum over all input subsequences with respect to θ , reinforcing its ability to predict tokens based on growing contexts. This dynamic approach allows transformers to efficiently learn dependencies in sequences and generalize effectively to unseen data.

Connector: From Optimization Theory to Transformers

The adaptive optimizers introduced above (momentum methods, RMSProp, Adam, and their variants) were not designed with transformers in mind – yet they became the backbone of modern large-scale transformer training. Why?

Transformers present a highly *anisotropic*, *layer-coupled*, and *poorly conditioned* optimization landscape. Gradients vary in scale across attention heads, feed-forward blocks, embeddings, and normalization layers. As a consequence:

- coordinate-wise scaling (as in RMSProp/Adam) helps navigate directions of extremely uneven curvature;
- momentum smooths out high-variance gradients that arise even in full-batch regimes due to architectural depth;
- the geometry of attention introduces directions in which naive gradient descent makes excessively large steps.

The tiny transformer experiment that follows illustrates these effects on a much smaller scale: although the model is toy-sized, the same optimization pathologies and sensitivities already appear. In this way, the example serves as a bridge from classical optimizer theory to the practical realities of training modern neural architectures.

Example 3.5.1 (Tiny Transformer Optimization). *In this example we make the abstract discussion of transformer optimization concrete by training a very small character-level transformer on the toy string*

"hello world. this is a simple transformer example."

using the companion Jupyter/PyTorch notebook `tiny-transformer.ipynb`.

We tokenize at the character level, build overlapping windows of fixed length $L = 5$, and train the transformer to predict the next character in each window. More precisely, if x_1, \dots, x_T

denotes the encoded character sequence, we form input–target pairs

$$(x_i, \dots, x_{i+L-1}) \mapsto (x_{i+1}, \dots, x_{i+L}), \quad i = 1, \dots, T - L.$$

The model is a minimal encoder–decoder transformer with an embedding layer, a few self–attention and feed–forward blocks, and a final linear layer projecting to logits over the vocabulary. We compare three optimizers:

- Stochastic Gradient Descent (SGD),
- Adam,
- RMSProp.

Fig. 3.12 shows the evolution of the mean per–token training loss for all three methods. A striking observation is that RMSProp does not perform well in this setting: the loss initially increases and then drifts back toward its starting value, showing little meaningful progress. Adam, on the other hand, converges quickly and achieves the lowest loss, while SGD improves steadily but slowly.

This behavior highlights a pedagogically important point: even on a tiny problem, transformer training is highly non–convex and sensitive to hyperparameters and initialization. For the particular model and learning rates used here, RMSProp can effectively “freeze” after a few large early gradients, producing little further learning. Adam’s two–moment normalization makes it more robust to such early steps.

Beyond the global loss, we can inspect how difficult each position in the length–5 window is to predict. Figure 3.13 shows the mean per–position loss at the final epoch. Some positions are systematically easier or harder, reflecting both the geometry of the data (e.g., spaces and punctuation) and the internal inductive biases of the transformer. The optimizers induce different profiles, again demonstrating that optimization and data structure are intertwined. Finally, Fig. 3.14 displays the confusion matrix of the best–performing optimizer (Adam). The strong diagonal indicates accurate predictions, while off–diagonal structure reveals consistent confusions (e.g., between space, period, and some letters). Even this tiny transformer has learned a meaningful next–character model, and the confusion structure provides a useful qualitative diagnostic.

The notebook `tiny-transformer.ipynb` contains the full implementation and produces all three figures. Students are encouraged to run and modify it.

Exercise 3.5.1 (Exploring Optimizers and Data Geometry in Tiny Transformers). *Using the companion notebook `tiny-transformer.ipynb` as a starting point, explore how optimization, model architecture, and data geometry interact in this tiny transformer.*

1. **Change the training text.** Replace the toy string “hello world. this is a simple transformer example.” with a different short text (natural language or a structured synthetic string).
 - Retrain with SGD, Adam, and RMSProp using the same hyperparameters and regenerate Fig. 3.12.

- Compare the new loss curves to the original ones. Does RMSProp behave differently on a different dataset? When does Adam retain its advantage?
2. **Vary the window length.** Modify `sequence_length` (e.g., $L = 3$ and $L = 8$) and repeat the experiment.
- Regenerate the per-position loss plot (analogous to Fig. 3.13). How does the difficulty profile change with L ?
 - Interpret how the receptive field and context length interact with optimizer behavior.
3. **Hyperparameter sensitivity of RMSProp.** RMSProp performed poorly in the example above.
- Reduce its learning rate (e.g., to `lr = 0.001` or `0.0005`) and repeat the training.
 - Compare the resulting curves to Adam and SGD. When (if ever) does RMSProp become competitive?
 - Discuss why RMSProp can “freeze” after large early gradients, and how this differs from Adam’s two-moment updates.
4. **Analyze confusion matrices.** For each modified setup, compute the confusion matrix of the best-performing optimizer.
- Compare how structure, spaces, and punctuation influence confusion.
 - Relate changes in confusion structure to both optimization behavior and the data distribution.

Summarize your findings, including regenerated versions of the three figures and a discussion of how small transformers expose the sensitivity of adaptive optimizers in non-convex settings.

Connector: Optimization as a Moving Target

The behavior observed in the tiny-transformer example highlights a fundamental truth about modern deep learning: *optimization is not a solved problem*. Performance depends delicately on architectural choices, initialization, normalization, learning-rate scales, and the interaction between model geometry and optimizer dynamics.

This sensitivity is amplified in large-scale transformers, where depth, attention mechanisms, long-range dependencies, and mixture-of-experts routing all interact to produce highly structured but challenging loss surfaces. As a result, optimizer design has become an active research frontier, tightly coupled to systems considerations (memory, throughput), modeling innovations (compression, structure), and new inference paradigms (multi-token prediction, speculative decoding).

The final subsection outlines several representative directions in which this frontier is evolving, illustrating how optimization, architecture, and hardware co-design now advance together.

3.5.4 Ongoing Advances in Transformer Optimization

Research on transformer optimization continues to evolve at a remarkable pace, driven by the need for faster training, lower memory footprint, and more efficient inference. Rather than a single dominant direction, progress now unfolds simultaneously across multiple fronts—including architectural innovations, algorithmic refinements, and new approaches to compression and sampling. The diversity of methods reflects a growing recognition that scalable transformer training is fundamentally a systems, architecture, and optimization problem at once.

A few representative examples (among many) illustrate these active trends:

- **DeepSeek-V3** [13]: Introduces low-rank join compression of attention keys and values, a refined mixture-of-experts design, and multi-token prediction to enable partial parallelization in generation. These ideas exemplify the broader movement toward *compression-aware training* and improved utilization of hardware bandwidth.
- **Titans** [14]: Proposes a long-short-term memory reinterpretation of attention, where attention handles short-term dependencies and recurrent structure preserves long-term information. This reflects a wider effort to bring *Recurrent Neural Network (RNN)-style recurrence and transformer-style attention* into closer alignment, thereby reducing memory costs while retaining expressivity.
- **Transformer²** [15]: Uses Singular-Value Decomposition (SVD) and Adaptive Importance Sampling (AIS) to accelerate optimization. This contributes to a growing class of *factorization- and sampling-based* approaches that seek to reduce training-time overhead by acting directly at the level of weight matrices or gradient estimation.

Many related themes are developing in parallel: structured sparsity, dynamic token routing, long-context approximations, improved optimizers tailored to attention geometry, mixture-of-experts scaling laws, and multi-token or speculative decoding strategies aimed at reducing inference latency. The field is highly dynamic, and no single idea has yet emerged as definitive. Instead, transformer optimization has become an active, rapidly shifting research frontier in which architectural changes, algorithmic insights, and systems-level constraints continually reshape one another.

TV-regularized image denoising: clean, noisy, and denoised images

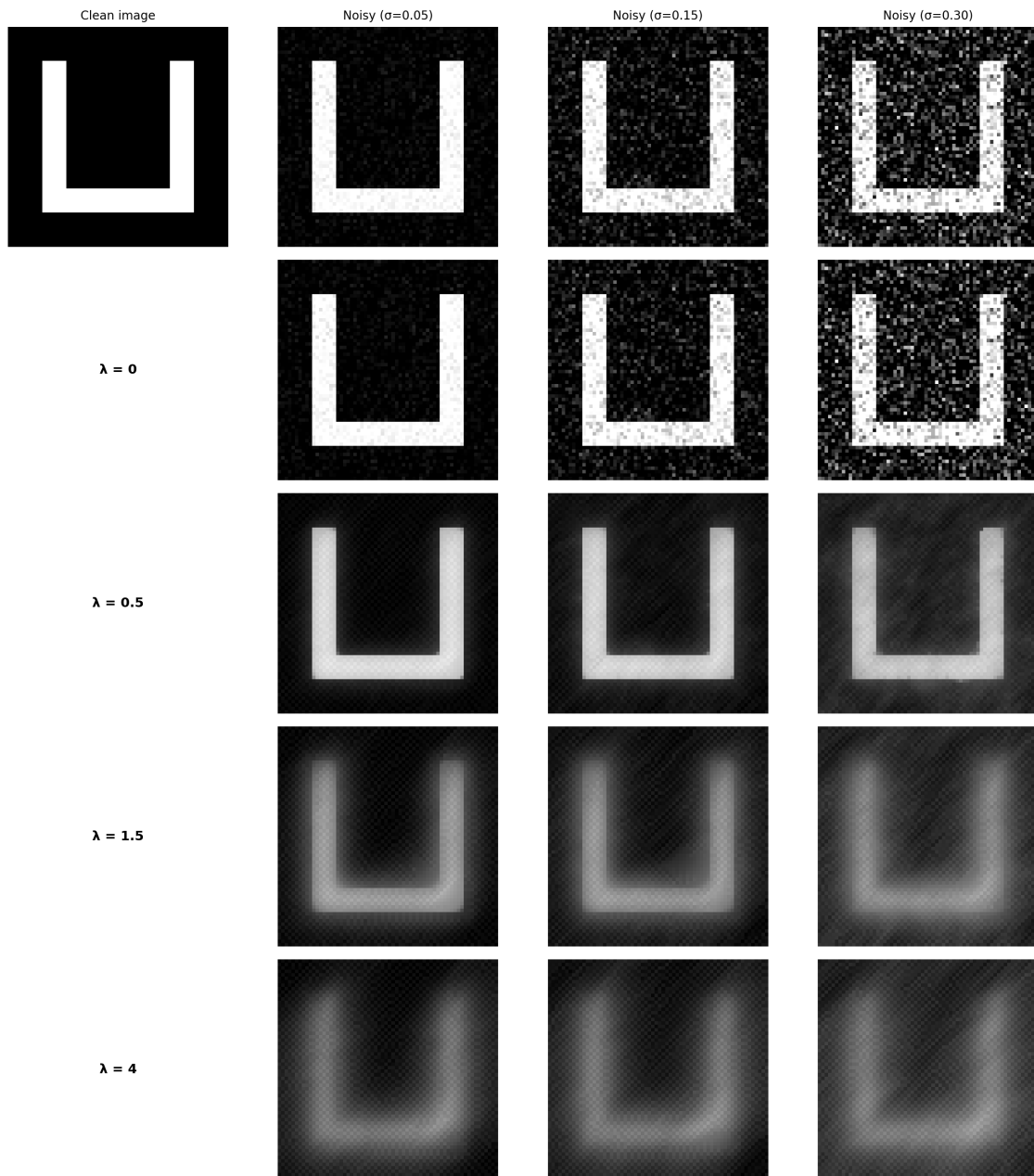


Figure 3.10: Total Variation denoising on a 64×64 image of the letter “U” for multiple noise levels (columns) and regularization parameters λ (rows). Larger values of λ produce stronger smoothing.

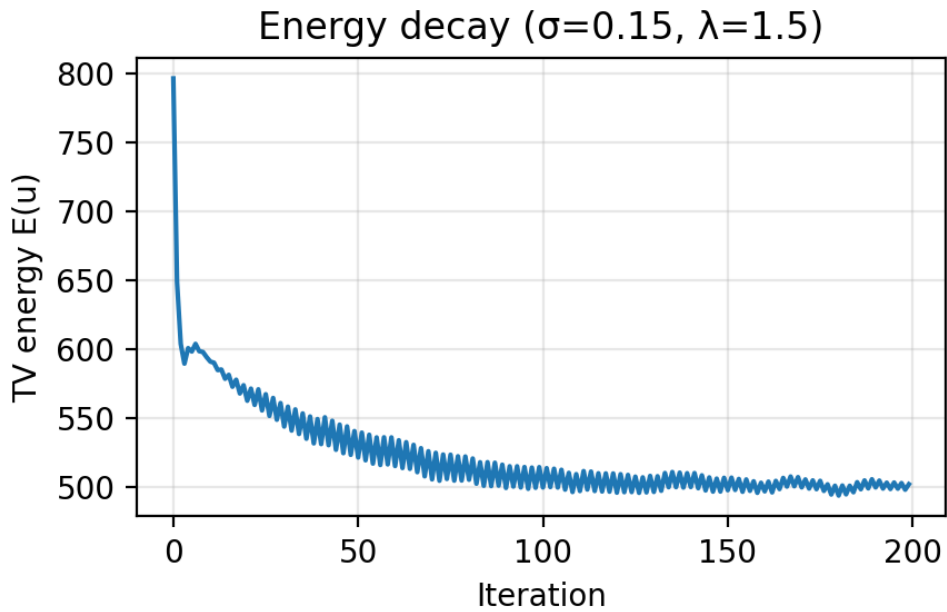


Figure 3.11: Energy $E(u(t))$ as a function of iteration during TV denoising. Each curve corresponds to a different λ . Larger λ results in a stiffer gradient flow and slower decay.

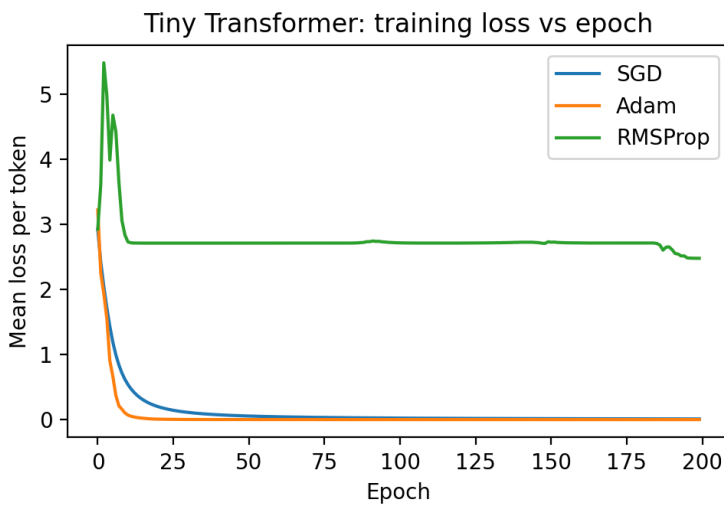


Figure 3.12: Tiny transformer: mean per-token training loss versus epoch for three optimizers (SGD, Adam, RMSProp) on the toy character-level sequence "hello world. this is a simple transformer example." Adam and RMSProp converge faster and reach a lower loss than vanilla SGD.

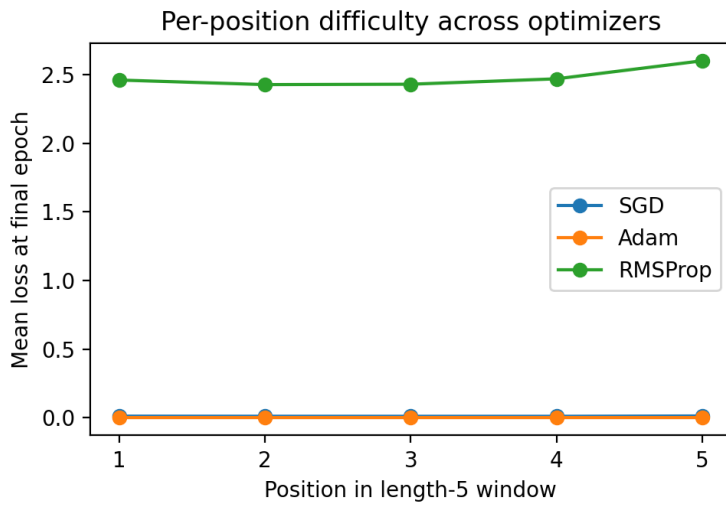


Figure 3.13: Mean per-position loss at the final epoch for each optimizer, as a function of position in the length-5 input window. Some positions are consistently easier or harder to predict, reflecting both data geometry and the optimization dynamics.

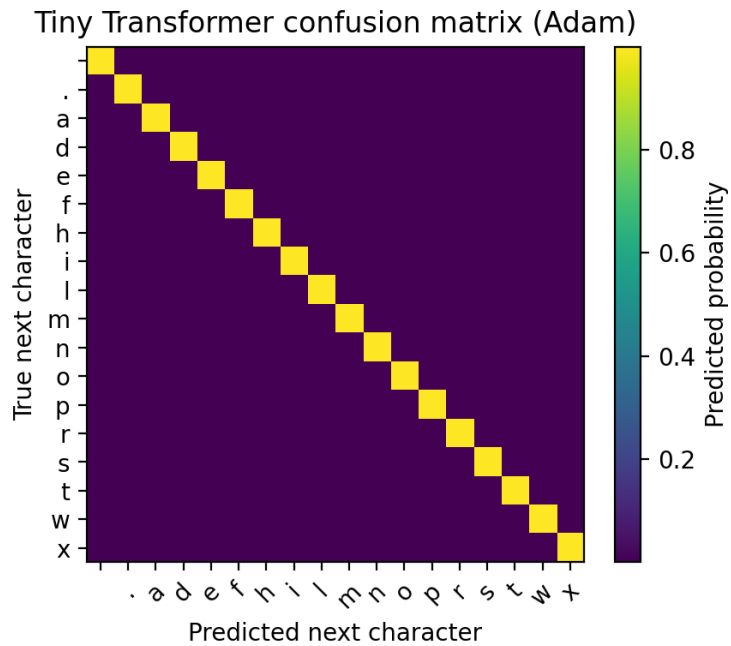


Figure 3.14: Confusion matrix for the best–performing optimizer (lowest final mean loss). Rows correspond to true next characters and columns to predicted characters; entries show the average predicted probability. The strong diagonal indicates accurate predictions, while off–diagonal structure reveals systematic confusions (e.g., between spaces, punctuation, and certain letters).

Chapter 4

Neural Networks & Deep Learning

We begin this chapter by situating neural networks within the mathematical framework developed in Chapters 1,2,3. The aim is to make explicit how the core ingredients of deep learning – representation of data, dynamical evolution through layers, and optimization of parameters – connect to earlier material:

1. **Data as vectors, matrices, and tensors (Chapter 1).** Neural networks process inputs that are represented as vectors or higher-order tensors. The linear components of each layer (affine maps, convolutions, embeddings) are direct applications of the matrix and tensor transformations introduced in Section 1.1.
2. **Layers as discrete-time dynamical systems (Chapter 2).** Each neural-network layer applies a transformation of the form

$$x_{k+1} = \sigma(W_k x_k + b_k),$$

and thus defines a discrete-time dynamical system. Residual and skip connections relate this directly to the ODE viewpoint of Section 2.2, where

$$x_{k+1} \approx x_k + h f_\theta(x_k)$$

resembles an explicit Euler step. This dynamical interpretation later serves as a bridge to Neural ODE models and, ultimately, to diffusion-based generative models.

3. **Training as optimization (Chapter 3).** Neural-network training is formulated as an empirical-risk minimization problem, where one seeks parameters θ minimizing a *loss function*:

$$\min_{\theta} \frac{1}{N} \sum_{i=1}^N \mathcal{L}(f_\theta(x_i), y_i).$$

This viewpoint extends the optimization framework of Sections 2.2.2–3.1 and incorporates *regularization* techniques such as sparsity (Section 3.4) that control model complexity and improve generalization.

4. **Gradient-based training algorithms.** The parameter updates used in deep learning—stochastic gradient descent, momentum, and adaptive methods—are direct descendants of the gradient-descent variants introduced in Section 3.3. Thus, the evolution of parameters during training can itself be viewed as a dynamical system in parameter space, influenced by noise, step size, and curvature of the loss landscape.
5. **Neural networks as nonlinear extensions of classical supervised-learning models.** Logistic regression (Section 3.1) is the simplest example of a neural network: a single affine layer followed by a nonlinearity. In contrast, deep networks compose many such transformations, enabling vastly richer decision boundaries and more complex feature hierarchies. The notebook associated with Exercise 3.1.2 illustrated how multilayer networks can represent intricate 2D boundaries and illuminated the geometry of the loss surface.

Purpose and scope of this chapter. Neural networks are among the most expressive and computationally effective function approximators available today. In this chapter, we introduce their mathematical structure and interpret them as layered compositions of linear transformations and nonlinear activations. Our emphasis is on supervised learning, with a focus on classification, where the goal is to learn a mapping $x \mapsto y$ from high-dimensional inputs to discrete class labels. Training proceeds by minimizing an appropriate loss function — typically the cross-entropy loss — over labeled data.

Along the way, we highlight architectural innovations (convolutions, residual connections, Neural ODEs) and structural principles (representation learning, energy landscapes) that set the stage for later chapters on probabilistic modeling, information theory, graphical models, and generative diffusion processes.

4.1 Neural Network Mechanics

In this section, we move from the abstract optimization and dynamical-systems viewpoints of Chapters 1,2,3 to the concrete mechanics of Neural Networks (NNs). Our focus is on how relatively simple and compact NNs can be used as flexible function approximators for supervised learning, and on how their parameters are trained by gradient-based methods. We proceed in three steps:

1. Start from the historical single-layer *perceptron*, which can be viewed as both a primitive model of a neuron and a special case of logistic regression.
2. Introduce a neural network with a single fully connected hidden layer and interpret it as an automatically learned nonlinear feature map.
3. Compare this NN to logistic regression with manually engineered nonlinear features on a two-dimensional classification task, using the accompanying Jupyter notebook.

4.1.1 Perceptron – Historical Remark

We begin with the simplest single-layer architecture (with no hidden layers) and one of the earliest artificial NN models — the **Perceptron**, introduced by Frank Rosenblatt in

1958 [16]. The name “Perceptron” reflects its **biologically inspired** design: Rosenblatt aimed to develop a mathematical model that mimicked, in highly simplified form, how neurons in the brain perceive and process information.

A perceptron takes an input vector $x \in \mathbb{R}^d$, computes a linear score $w^\top x + b$, and then applies a threshold nonlinearity to decide between two classes:

$$\hat{y} = \text{sign}(w^\top x + b).$$

Training consists of iteratively adjusting w and b based on misclassified examples, which can be interpreted as a primitive gradient-like update (compare with Chapter 3.3).

Despite its historical importance, the perceptron has a major limitation: it can only learn **linearly separable** problems. In their seminal work, Minsky and Papert (1969) [17] showed that a single-layer perceptron **cannot solve linearly non-separable problems**, such as the **XOR problem** (already discussed in the context of logistic regression with linear feature vectors in Section 3.1).

This limitation served as a turning point. It highlighted the need for more expressive architectures — in particular, **multi-layer** neural networks with hidden layers and nonlinear activations — and for efficient training algorithms, culminating in the **backpropagation** method. These developments opened the way to modern deep learning, where many layers are stacked to form highly expressive nonlinear maps.

4.1.2 NN with a Single Fully Connected Hidden Layer

We now revisit the two-dimensional classification problem introduced in Exercise 3.1.2. There, we examined logistic regression and saw that with a *linear* feature vector it cannot separate data sets of XOR type or other nonlinearly separable patterns. Introducing **nonlinear feature vectors** (e.g., polynomial features) can remedy this limitation, but at the price of explicit feature engineering.

In this subsection, we demonstrate how a neural network can address the same problem **at least as efficiently**, while learning its own nonlinear features. The simplest architecture that already exhibits this behavior is a **single-hidden-layer, fully connected neural network**.

Logistic Regression with Nonlinear Features vs. NN with a Hidden Layer

Before turning to a concrete example, it is useful to summarize the conceptual similarities and differences between these two approaches:

- **Similarity:** Both methods introduce nonlinearity to go beyond linear decision boundaries. Logistic regression achieves this via nonlinear feature maps $\phi(x)$, while an NN introduces nonlinearity through activation functions in the hidden layer.
- **Difference:** Logistic regression with nonlinear features requires **explicit feature engineering** (e.g., manually adding polynomial or radial basis transformations). By contrast, an NN with a hidden layer **learns** an internal feature transformation through its hidden neurons and parameters.

From the perspective of Chapters 1–3, both can be viewed as:

- compositions of linear maps (matrices) and nonlinearities (activation functions),
- trained by gradient-based optimization of a loss function (typically cross-entropy),
- but differing in whether the feature map is hand-designed or learned.

Example 4.1.1. *2D Classifier with a Fully Connected Single-Hidden-Layer NN.* In the Jupyter/PyTorch notebook `LogReg+NN-supervised-2D.ipynb`, we study a two-dimensional classification task in which the ground-truth labels are determined by membership in the union of two overlapping circles in \mathbb{R}^2 .

Data generation. Points $x = (x_1, x_2) \in \mathbb{R}^2$ are sampled uniformly in a square domain. Two circles of radius r are centered at $(-\text{offset}, 0)$ and $(+\text{offset}, 0)$. A point is labeled $y = 1$ if it lies inside at least one of the circles, and $y = 0$ otherwise.

Neural-network architecture. The implemented NN consists of:

- a **2D input layer** for (x_1, x_2) ,
- a **hidden layer with 10 neurons**, using the hyperbolic tangent activation function \tanh ,
- a **single output neuron** producing a scalar logit; applying the sigmoid $\sigma(z) = 1/(1 + e^{-z})$ yields the estimated probability of class $y = 1$.

Training. The network parameters are trained using the binary cross-entropy loss and the Adam optimizer (see Section 3.3) over several thousand epochs. The training loss as a function of epochs shows a good convergence behavior (decay, temporary-saturation and then decay).

Decision boundary. After training, the learned decision boundary of the NN is visualized in the left panel of Fig. 4.1, which shows the estimated probability of class 1 across the input domain. For comparison, the logistic regression model with polynomial features is visualized in the right panel of Fig. 4.1. Both are overlaid on the training data.

Observation. Both models are capable of approximating the nonlinearly separable boundary. The key difference is conceptual:

- Logistic regression relies on an explicit polynomial feature map chosen by the model designer.
- The NN learns its own internal representation through the hidden layer, with the feature map encoded in its weights and activations.

This illustrates the shift from manual feature engineering to learned representations.

Exercise 4.1.1 (Comparing Logistic Regression and a Single-Hidden-Layer NN). Use the notebook `LogReg+NN-supervised-2D.ipynb` to perform the following steps.

1. **Implement and train both models.**

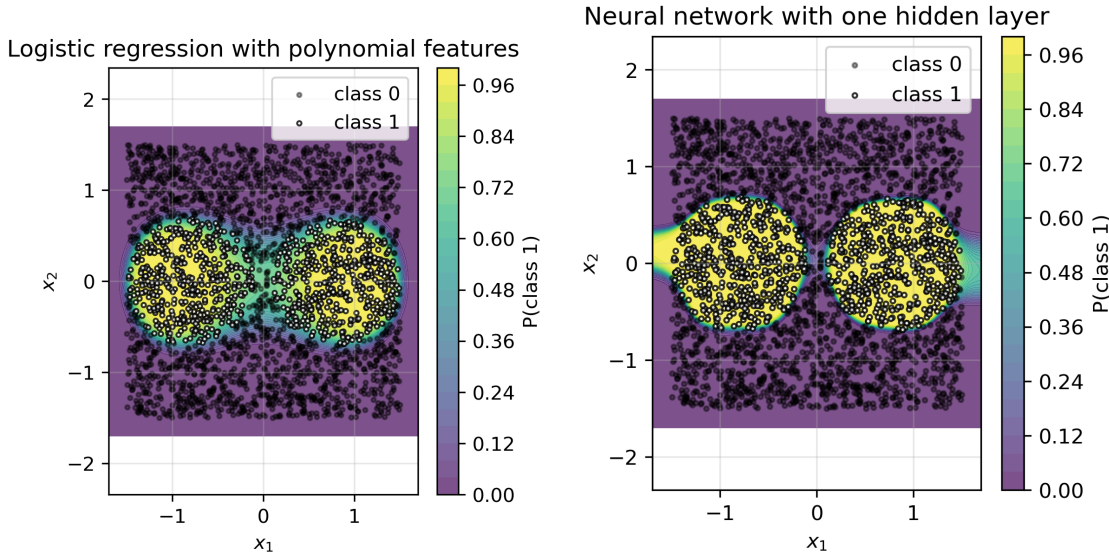


Figure 4.1: Left: Decision boundary learned by logistic regression with degree-4 polynomial features. The color encodes the predicted probability of class 1. Right: Decision boundary learned by the neural network with one hidden layer. The network learns a flexible nonlinear separation that closely matches the ground-truth two-circle structure.

- (a) Train logistic regression with a polynomial feature expansion of degree d (e.g., $d = 2, 3, 4$).
- (b) Train the single-hidden-layer NN with 10 hidden units and tanh activation, using binary cross-entropy loss and the Adam optimizer.

2. Quantitative comparison.

- Record training and test accuracies for both models.
- Compare how the results change as you vary the polynomial degree in logistic regression and the number of hidden units in the NN.

3. Qualitative comparison of decision boundaries.

- Reproduce and inspect figures similar to Figs. 4.1.
- Comment on regions where the models differ significantly from the ground truth.

4. Discussion.

- Under what conditions does logistic regression with polynomial features perform comparably to the NN?
- When does the NN provide a clear advantage in terms of approximation quality or robustness to hyperparameter choices?
- Relate your observations to the role of learned representations discussed later in this chapter.

From Hand-Crafted Features to Learned Representations

A key transition from classical machine learning to modern neural networks lies in **where the nonlinearity comes from**. Logistic Regression with polynomial or radial features relies on an *explicitly engineered* feature map $x \mapsto \phi(x)$, chosen by the model designer. Its expressive power is determined entirely by this choice.

In contrast, a neural network introduces a *learned* nonlinear feature map through its hidden layers:

$$x \longmapsto h(x) = \sigma(W_1 x + b_1),$$

where the weights and biases are optimized jointly with the classifier. Thus, the representation itself adapts to the data. This shift has profound consequences:

- Feature engineering is replaced by **representation learning**.
- Model capacity scales by adding layers or neurons rather than manually expanding the feature set.
- Optimization (Chapter 3) becomes central – not only for fitting a classifier, but for shaping the internal geometry of learned features.

In the simple 2D example above, both approaches succeed, but the neural network **learns its own features**, illustrating on a small scale the principle that underlies modern deep architectures – ResNets, Transformers, and diffusion-model backbones explored later in this book.

4.1.3 Interpolation vs. Extrapolation: Polynomial Regression vs Neural Networks

In this subsection we analyze **overfitting** (or its surprising absence) in the *interpolation regime* by studying a simple one-dimensional regression problem $f : \mathbb{R} \rightarrow \mathbb{R}$. We compare two families of models:

- **Polynomial regression** of increasing degree.
- A **single-hidden-layer fully connected neural network**, as introduced in Section 4.1.2.

Both are trained on a small number of data points in a bounded interval, and then evaluated both inside this interval (interpolation) and outside (extrapolation). The experiments are implemented in the Jupyter/PyTorch notebook `InterPoly-vs-NN.ipynb`.

Example 4.1.2. *Interpolation vs Extrapolation in 1D: Polynomials and a Neural Network*
We consider a smooth non-polynomial target function

$$f(x) = e^{-x^2} \cos(3x), \quad x \in \mathbb{R}.$$

A small training set of $n_{\text{train}} = 5$ points $\{(x_i, y_i)\}_{i=1}^{n_{\text{train}}}$ is sampled uniformly in the interval $[-1, 1]$, with $y_i = f(x_i)$. This interval is the **interpolation region**. We then examine model

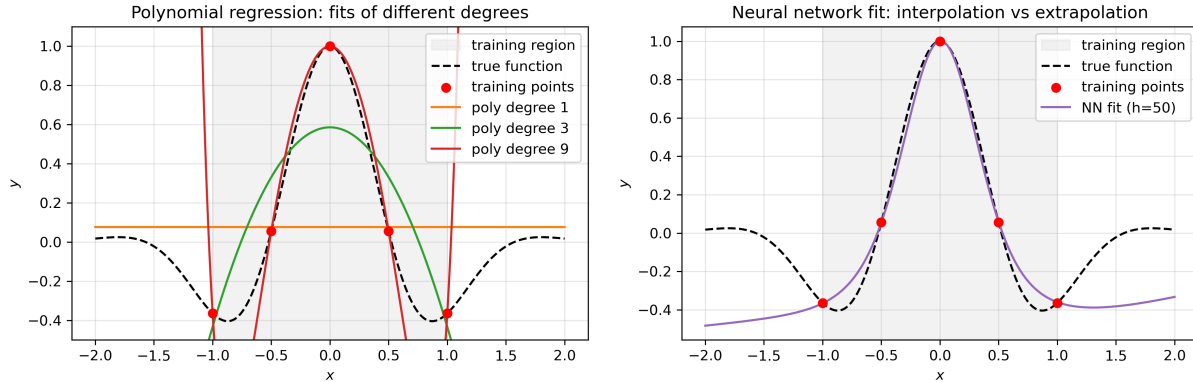


Figure 4.2: Left: Polynomial regression for degrees $d = 1, 3, 9$ trained on the same 5 data points (red) in the interval $[-1, 1]$ (shaded). For $d = 9 > n_{\text{train}} - 1$, the polynomial interpolates all training points but develops strong oscillations, especially near the edges and outside the training region. Right: Neural-network fit (solid curve) versus the true function (dashed) and training points (red). Inside the training region $[-1, 1]$ (shaded), the NN provides a smooth interpolation without oscillations, even though the number of parameters ($2h + 2$) greatly exceeds the number of data points. Outside $[-1, 1]$, however, the NN also fails to follow the true function, illustrating limited extrapolation.

behavior on a wider domain $[-2, 2]$, which includes both interpolation and extrapolation regions.

Polynomial regression. Given the training data $\{(x_i, y_i)\}$, we fit a polynomial of degree d ,

$$P_d(x; w) = w_0 + w_1 x + \cdots + w_d x^d,$$

by minimizing the mean squared error (MSE)

$$\mathcal{L}(w) = \frac{1}{n_{\text{train}}} \sum_{i=1}^{n_{\text{train}}} (P_d(x_i; w) - y_i)^2.$$

Left panel in Fig. 4.2 shows polynomial fits of degrees $d \in \{1, 3, 9\}$ over the wide interval $[-2, 2]$.

Overfitting in the interpolation regime. From the left panel of Fig. 4.2 we observe:

- For **low degree** ($d = 1$), P_d is too rigid to approximate f well; it underfits even inside the training interval.
- For **moderate degree** ($d = 3$), P_d fits the data reasonably in the interpolation region and behaves smoothly.
- For **high degree** ($d = 9 > n_{\text{train}} - 1$), the polynomial can pass exactly through all training points but exhibits sharp oscillations between them and near the boundary of $[-1, 1]$. This is a classical form of overfitting or memorization.

Neural network with one hidden layer. We now consider a simple fully connected neural network with one hidden layer:

$$\hat{y}(x) = W_{out} \tanh(W_{hidden}x + b_{hidden}) + b_{out}.$$

Here $W_{hidden} \in \mathbb{R}^{h \times 1}$, $W_{out} \in \mathbb{R}^{1 \times h}$, and h is the number of hidden neurons (we take, e.g., $h = 50$). The total number of trainable parameters is $2h + 2$, which can be much larger than n_{train} .

The network is trained using the MSE loss and the Adam optimizer, as in Section 3.3. The learned fit on $[-2, 2]$ is shown in the right panel of Fig. 4.2.

Key observations.

- In the **interpolation regime** (inside $[-1, 1]$), high-degree polynomials tend to overfit and oscillate, while the neural network produces a much smoother fit, despite being heavily overparameterized.
- In the **extrapolation regime** (outside $[-1, 1]$), both models deviate substantially from the true function; increasing polynomial degree or the number of hidden units does not automatically improve extrapolation.

This illustrates that neural networks can generalize smoothly in the interpolation regime, even with far more parameters than data points, yet still share the fundamental limitation that neither model extrapolates reliably without additional structure or prior knowledge.

Exercise 4.1.2 (Interpolation, Overfitting, and Extrapolation). Use the notebook *InterPoly-vs-NN.ipynb* to explore the following questions.

1. Varying polynomial degree.

- Fix $n_{train} = 5$ and vary the degree d (e.g., $d = 1, 3, 5, 9, 15$).
- For each d , plot $P_d(x)$ together with $f(x)$ and the training points on $[-2, 2]$.
- Identify the smallest d for which you observe pronounced oscillations in the interpolation region.

2. Varying network width.

- Fix the number of training points and vary the number of hidden neurons h (e.g., $h = 5, 20, 50, 100$).
- For each h , record the final training loss and plot the NN fit on $[-2, 2]$.
- Compare how the smoothness of the NN fit depends on h .

3. Interpolation vs extrapolation.

- For a representative polynomial degree (e.g., $d = 9$) and network width (e.g., $h = 50$), compare the approximation error inside $[-1, 1]$ and outside.
- Discuss why both models fail to capture $f(x)$ reliably outside the training region, despite excellent performance inside.

4. Inductive bias.

- Relate your observations to the notion of inductive bias: what kinds of functions are favored by high-degree polynomials vs one-hidden-layer NNs?
- How might these biases change when we move to deeper architectures (multi-layer NNs, ResNets) discussed later in this chapter?

4.1.4 Simple Convolutional Neural Network

The fully connected NN layer, which was the building block in the preceding subsections, is deliberately *structure-agnostic*: it treats all input coordinates as unrelated. In many practical settings, however, we *do* know something about the structure of the data. For images, for example, it is natural to assume that *nearby pixels are more strongly related than distant ones*, and that the same local pattern (such as an edge or corner) may appear anywhere in the image.

Convolutional Neural Networks (CNNs) exploit exactly this kind of prior structure:

- They connect each neuron only to a *local receptive field* in the previous layer, enforcing **locality**.
- They *reuse the same filter weights* across all locations, implementing **weight sharing** and a form of translation equivariance.

These design choices dramatically reduce the number of parameters compared to fully connected layers and lead to architectures that are particularly effective for images. We introduced discrete convolutions already in Section 1.1.3; here we see how they appear inside a concrete NN architecture.

Network construction (architecture). Consider an input image $x \in \mathbb{R}^{H \times W \times C}$ with height H , width W , and C channels (for MNIST, $H = W = 28$, $C = 1$). A single convolutional layer with K filters $F_k \in \mathbb{R}^{f \times f \times C}$ produces K feature maps $z_k \in \mathbb{R}^{H \times W}$ via

$$z_k(i, j) = \sigma \left(\sum_{m=0}^{f-1} \sum_{n=0}^{f-1} \sum_{c=1}^C x_c(i+m, j+n) F_k(m, n, c) + b_k \right), \quad k = 1, \dots, K,$$

where $\sigma(\cdot)$ is a point-wise nonlinearity (e.g., ReLU) and b_k is a bias term. In practice, we often include padding and striding to control the spatial resolution.

A typical CNN block alternates:

- **Convolution + nonlinearity**: local feature extraction with shared parameters.
- **Pooling** (e.g., max pooling): local down-sampling that reduces spatial resolution while keeping the number of channels.

After several such blocks, the feature maps are flattened and fed into one or more *fully connected* layers that produce class logits.

In our running example we use the following small CNN:

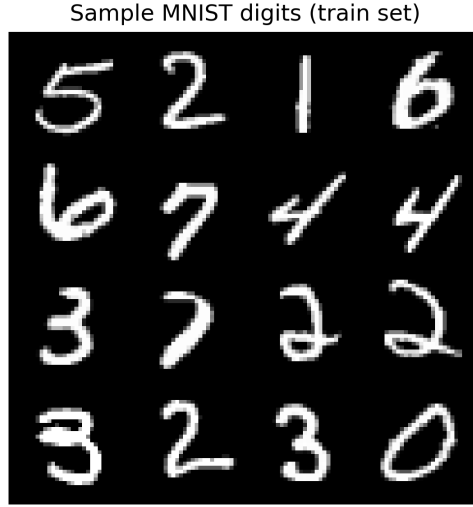


Figure 4.3: Sample MNIST digits from the training set (grayscale 28×28 images). Each image is labeled with a digit 0–9. Figure generated by the notebook `cnn-simple-MNIST.ipynb`.

- **Conv layer 1:** $1 \rightarrow 16$ channels, 3×3 kernels, padding 1 (keeps 28×28).
- **MaxPool 1:** 2×2 pooling $\Rightarrow 14 \times 14 \times 16$.
- **Conv layer 2:** $16 \rightarrow 32$ channels, 3×3 kernels, padding 1 (keeps 14×14).
- **MaxPool 2:** 2×2 pooling $\Rightarrow 7 \times 7 \times 32$.
- **Fully connected head:** flatten to a vector of size $7 \cdot 7 \cdot 32 = 1568$, apply a dense layer with 128 hidden units and ReLU, then a final dense layer with 10 outputs (class logits).

Fig. 4.3 shows example MNIST digits that serve as inputs to this architecture.

Optimization: training with cross-entropy and mini-batch SGD. The CNN is trained as a multi-class classifier. For a given input x and label $y \in \{0, \dots, 9\}$, the network produces logits $\ell_y(x; \theta)$ and class probabilities via the softmax

$$p(y | x, \theta) = \frac{\exp(\ell_y(x; \theta))}{\sum_{y'} \exp(\ell_{y'}(x; \theta))}.$$

The standard **cross-entropy loss** for one sample is

$$L(\theta; x, y) = -\log p(y | x, \theta).$$

For a mini-batch \mathcal{B} , the batch loss is

$$L_{\text{batch}}(\theta) = \frac{1}{|\mathcal{B}|} \sum_{(x_i, y_i) \in \mathcal{B}} L(\theta; x_i, y_i).$$

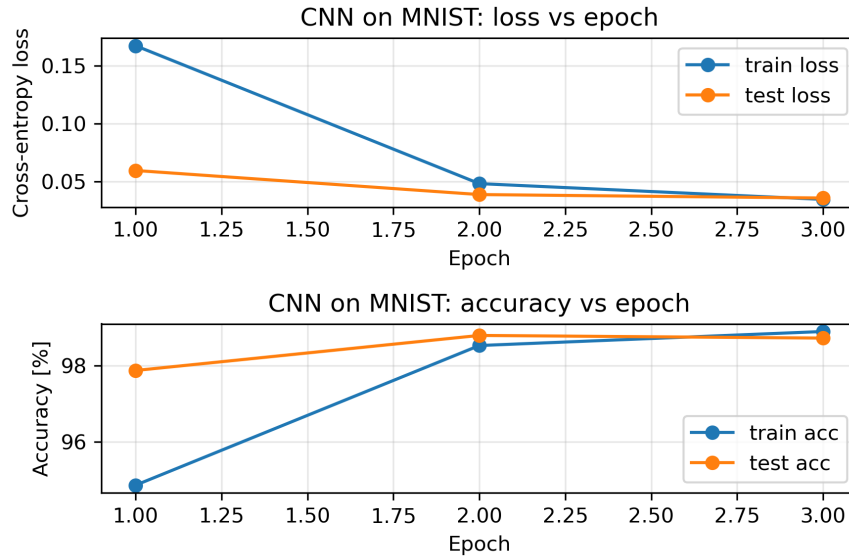


Figure 4.4: Training and test loss (top) and accuracy (bottom) versus epoch for the simple CNN on MNIST. The model quickly reaches high accuracy, illustrating the effectiveness of convolutional architectures on structured image data.

Training consists of solving

$$\min_{\theta} L_{\text{batch}}(\theta)$$

approximately using a gradient-based optimizer. In practice, we update θ iteratively using mini-batch SGD or one of its variants (e.g., Adam) as in Section 3.3:

$$\theta \leftarrow \theta - \eta \nabla_{\theta} L_{\text{batch}}(\theta).$$

Gradients are computed efficiently via reverse-mode automatic differentiation (AD), introduced in Section 2.1.

In the notebook `cnn-simple-MNIST.ipynb` we train the above CNN using Adam and record both training and test loss/accuracy across epochs. The resulting learning curves are shown in Fig. 4.4.

Inference. Once trained, the CNN defines a mapping $x \mapsto p(y | x, \theta)$ from images to class probabilities. For a new test image x , the network performs a forward pass and outputs $p(y | x, \theta)$; the predicted class is

$$\hat{y} = \arg \max_{y \in \{0, \dots, 9\}} p(y | x, \theta).$$

Even our small CNN achieves strong accuracy on the MNIST test set; however, it still makes mistakes. Fig. 4.5 shows representative misclassified digits, which are useful for diagnosing model limitations and dataset ambiguities. We will study MNIST misclassifications again in Chapter 6, using information-theoretic diagnostics to understand how and why different models diverge in their uncertainty and predictions.

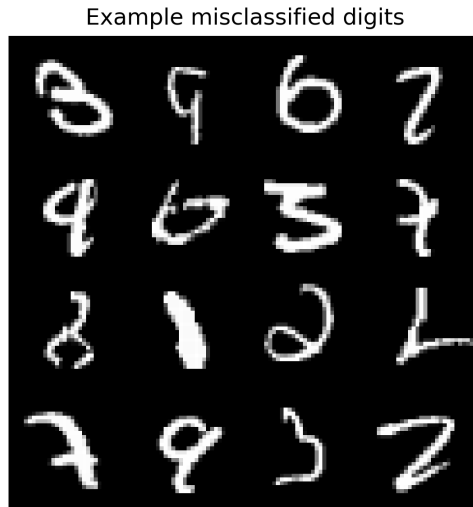


Figure 4.5: Example misclassified MNIST digits (true labels vs predicted labels are shown in the notebook output). Such examples highlight the limits of the learned representation and the importance of architecture, data quality, and optimization.

Principles for choosing the number of channels. The number of channels (filters) in a CNN controls how many distinct feature types the network can represent at each layer. There is no closed-form rule for the optimal number of channels; instead, several empirical principles are used:

1. **Shallow layers: low-level features.** Early layers detect simple patterns (edges, corners, textures). A moderate number of channels (e.g., 16–64) is typically sufficient to capture such local structures.
2. **Deeper layers: abstract features.** As depth increases and spatial resolution decreases (due to pooling or striding), layers need more channels to represent a richer variety of high-level patterns (object parts, whole digits, faces, . . .). Many successful architectures increase channel counts with depth (e.g., $32 \rightarrow 64 \rightarrow 128 \rightarrow 256$).
3. **Computational budget.** More channels mean more parameters and higher computational cost. Choices must balance accuracy with runtime and memory, especially in resource-constrained environments.
4. **Dataset complexity.** Simple datasets like MNIST can be handled with relatively few channels (e.g., 16 and 32 in this example). Complex datasets (e.g., ImageNet) benefit from deeper networks with hundreds of channels per layer.
5. **Empirical tuning and architectural templates.** Popular CNN architectures (AlexNet, VGG, ResNet, . . .) provide practical templates. A common heuristic is to roughly *double* the number of channels whenever the spatial resolution is halved.

These rules of thumb are widely used in practice but still lack full theoretical justification, making them a natural target for future theory.

Exercise 4.1.3 (Exploring the Impact of Filter Count and Size in a CNN). *Using the Jupyter/PyTorch notebook `cnn-simple-MNIST.ipynb`, investigate how varying the number of filters and the filter size affects CNN performance on MNIST.*

1. Vary the number of filters.

- *Modify the first and second convolutional layers to use different channel counts (e.g., (8, 16), (16, 32), (32, 64)).*
- *For each configuration, train the network for the same number of epochs and record training and test accuracy.*
- *Discuss the trade-off between model capacity and overfitting/underfitting: larger models fit the training data better but may generalize worse if the dataset is small.*

2. Vary the filter size.

- *Change the kernel size from 3×3 to 5×5 or 7×7 , adjusting padding as needed to preserve spatial dimensions.*
- *Compare classification accuracy and training time for different kernel sizes.*
- *Analyze how larger kernels affect the effective receptive field and whether they improve or degrade performance on MNIST.*

3. Convergence behavior.

- *For each architectural variant, plot training and test loss across epochs (as in Fig. 4.4).*
- *Compare convergence speed and final accuracy as a function of channel count and kernel size.*

4. Summary.

- *Summarize your findings about how filter number and size influence expressiveness, overfitting, and computational cost.*
- *Discuss how these lessons might change when moving from MNIST to more complex datasets or to deeper CNNs such as ResNets.*

4.2 Neural Architectures

We have already experimented with the MNIST database – a collection of small handwritten digit images that has become one of the most widely used benchmarks for testing ideas in Convolutional Neural Networks (CNNs). Indeed, MNIST was a central example in one of the earliest and most influential works that helped shape the modern Deep Learning (DL) era: LeCun et al. (1998) [18]. That work demonstrated, in a convincing and scalable way, how CNNs can exploit the **spatial structure** of image data through three key architectural principles:

- **Local receptive fields** (nearby pixels are more correlated than distant ones),
- **Weight sharing** (translational equivariance),
- **Hierarchical feature extraction** (from edges to shapes to semantic content).

These ideas established the basic architectural template that would guide deep-learning research for two decades.

The AlexNet turning point. Although CNNs were known earlier, the breakthrough that triggered the explosive growth of deep learning came with AlexNet [19]. Its impact derived not only from its convolutional components but from the demonstration that *deep* and *heterogeneous* architectures – consisting of multiple convolutional layers, interleaved pooling, and fully connected layers – could be trained reliably at scale using **GPU acceleration**. AlexNet effectively launched the *scaling era of Deep Learning*, showing that performance improves dramatically when models, data, and compute are scaled in tandem. This insight underlies virtually all contemporary state-of-the-art systems.

Beyond AlexNet: major architectural milestones. Several architectural innovations following AlexNet have shaped modern DL and influenced the development of contemporary generative AI. Each is rooted in a distinct inductive bias and contributes new mathematical insights or optimization strategies.

- **Autoencoders [20]:** Autoencoders provide a foundational framework for nonlinear **compression** and **representation learning**. In contrast to the linear PCA–SVD compression methods discussed in Section 1.2.4, autoencoders learn *nonlinear* low-dimensional latent spaces, enabling tasks such as denoising, generative modeling, and unsupervised feature discovery.
- **U-Net [21]:** Originally developed for medical image segmentation, U-Net introduced a novel **encoder–decoder** geometry enhanced by **skip connections** that preserve fine-scale spatial information. This architecture remains a backbone for many modern high-resolution image-to-image models and serves as a precursor to the U-shaped architectures used in diffusion models.
- **ResNet [22]:** ResNet introduced **residual (skip) connections**, addressing the vanishing-gradient bottleneck and enabling the stable training of networks with hundreds or thousands of layers. This development is essential for understanding the continuous-depth limit of neural networks, which leads naturally to **Neural ODEs** and diffusion-model architectures discussed later.
- **Transformers [1]:** Transformers replace convolutional locality with a flexible, global **self-attention mechanism**. Initially a revolution in Natural Language Processing, Transformers have since migrated to computer vision (e.g., Vision Transformers, ViTs), where they challenge the dominance of CNNs by removing fixed spatial inductive biases and enabling dynamic, data-driven receptive fields.

Each of these architectures is tied to a core mathematical theme: nonlinear approximation, hierarchical representation learning, compression, and optimization under increasingly large parameter budgets. Autoencoders and U-Nets reappear in Section 6.3.4, where we connect them to information-theoretic views of compression. Transformers were already introduced in Chapters 1–2 and will be revisited in later chapters devoted to the synthesis of modern generative AI.

Focus of this section. In the remainder of this section we will examine **ResNet** and its continuous-depth interpretation, leading naturally into the mathematics of **Neural ODEs**. These architectures introduce new perspectives on depth, stability, optimization, and expressivity—concepts that form the backbone of contemporary generative modeling frameworks, including diffusion models and flow-based models, which we encounter in later chapters. Before diving into ResNet, it is worth emphasizing a broader practical point: *architectural design is an exercise in balancing model capacity, computational constraints, data availability, and inductive bias*. Modern state-of-the-art neural architectures often contain **billions of parameters**, making choices of depth, width, locality, normalization, and parameter sharing essential both for model generalization and for computational feasibility.

4.2.1 From CNN to ResNet – the Power of Skip Connections

The step from a plain CNN to a ResNet may look minor architecturally, but it has had a *major* impact on practice. The key idea is to make each layer (or block) learn a *residual* correction on top of an identity map, rather than a full transformation from scratch.

A basic **Residual Block** (RB) in a ResNet consists, schematically, of two convolutional layers plus an identity (skip) connection:

$$\text{RB}(x) = \sigma\left(\text{BN}\left(F_2\left(\sigma(\text{BN}(F_1(x)))\right)\right) + x\right),$$

where

- F_1 and F_2 are convolutional layers,
- $\text{BN}(\cdot)$ is batch normalization,
- $\sigma(\cdot)$ is a pointwise nonlinearity (e.g. ReLU),
- the *skip connection* is the additive $+x$ term.

Without the skip connection, we would simply have $\text{RB}(x) \approx g(x)$ for some nonlinear g ; with the skip, the block instead learns $x \mapsto x + f(x)$, where f is typically “small” in a suitable sense.

Continuous-depth perspective and ODE analogy. Recall from Chapter 2 that a standard generic deep network, *without any skip-connection restriction*, can be written as a composition of layer maps

$$h_L = F_L \circ F_{L-1} \circ \cdots \circ F_1(h_0),$$

where h_0 is the input and each F_ℓ represents a generic nonlinear transformation. In this form, successive layers may differ substantially, and no notion of an underlying continuous dynamics is implied.

To make a continuous-depth interpretation meaningful, one must **restrict the class of layer maps**. In particular, suppose that each layer is *close to the identity* and can be written as

$$F_\ell(h) = h + \Delta t f(h, \theta_\ell),$$

where $\Delta t > 0$ is a small step size and f is a learned vector field. This assumption corresponds precisely to introducing skip connections and leads to the residual update rule

$$h_{\ell+1} = h_\ell + \Delta t f(h_\ell, \theta_\ell). \quad (4.1)$$

If we now imagine the number of layers L to be large, with $\Delta t = 1/L$, the discrete index ℓ may be replaced by a continuous depth variable $t \in [0, 1]$. In this limit, the residual network converges to the ordinary differential equation

$$\frac{dh(t)}{dt} = f(h(t), \theta(t)), \quad (4.2)$$

where $h(t)$ denotes the feature representation at depth t and $\theta(t)$ represents the continuously varying parameters.

From this viewpoint, ResNet architectures can be interpreted as forward Euler discretizations of an underlying continuous-time dynamical system in feature space. Each residual block performs a *small* step along the learned vector field, moving from h_t to $h_t + \Delta t f(h_t, \theta_t)$. Empirically, such residual updates

- ease optimization in very deep networks,
- mitigate vanishing and exploding gradients (since Jacobians remain close to the identity),
- establish a natural bridge to continuous-time dynamics and Neural ODE models.

We will return to this ODE-based viewpoint in Section 4.2.2.

Batch Normalization. Most modern ResNet implementations also use **Batch Normalization** (BN) inside each block to stabilize training. For an intermediate pre-activation z , BN computes

$$\text{BN}(z) = \gamma \frac{z - \mu}{\sqrt{\sigma^2 + \epsilon}} + \beta,$$

where μ and σ^2 are the mini-batch mean and variance; γ, β are learnable scale and shift parameters; and $\epsilon > 0$ is a small constant. BN keeps activation statistics more stable across layers and epochs, which in turn supports deeper architectures and larger learning rates.

ResNet-9 as a small residual architecture. Full-scale ResNets used in computer vision (ResNet-18, -34, -50, ...) are deep CNNs built from many residual blocks. For didactic purposes and toy problems, smaller variants such as *ResNet-9* are often used. These retain the essential pattern

$$(\text{Conv} + \text{BN} + \text{ReLU}) \rightarrow (\text{Residual blocks}) \rightarrow (\text{Global pooling} + \text{classifier}),$$

while drastically reducing depth and parameter count. In image applications, ResNet-9 uses convolutional residual blocks; in our 2D spiral example below we adopt the same skip-connection pattern but in a fully connected feature space.

Example 4.2.1 (Residual Network on a 2D Spiral Dataset). *To illustrate the effect of skip connections on optimization and decision geometry, we consider a synthetic 2D classification task where three classes form spiral arms in \mathbb{R}^2 . The corresponding Jupyter/PyTorch notebook is `ResNet9-Spiral.ipynb`.*

- **Data.** We generate $N = 3n$ points (x_i, y_i) with $x_i \in \mathbb{R}^2$ and $y_i \in \{0, 1, 2\}$, where each class follows a noisy spiral arm. The resulting dataset is not linearly separable and features highly curved decision boundaries; see the left panel of Fig. 4.6.
- **Architecture.** The model is a small fully connected ResNet-style network:
 1. an input linear layer mapping $\mathbb{R}^2 \rightarrow \mathbb{R}^{64}$, followed by ReLU;
 2. four residual blocks acting in \mathbb{R}^{64} , each of the form

$$h \mapsto \sigma(h + g(h)),$$

where g is a two-layer MLP with optional batch normalization;

3. a final linear layer mapping \mathbb{R}^{64} to 3 class logits.

This mirrors the ResNet pattern in a low-dimensional feature space.

- **Training.** We train the network with cross-entropy loss and the Adam optimizer over a moderate number of epochs, recording the training loss and accuracy curves; see Fig. 4.7. The network quickly attains high classification accuracy on the spirals.
- **Decision regions.** After training, we evaluate the classifier on a dense grid in the (x_1, x_2) -plane and color each point by the predicted class. The right panel of Fig. 4.6 shows that the residual network learns a smooth but nontrivial partition of the plane that wraps around the spiral arms.

Fig. 4.7 also shows a snapshot of gradient norms across layers for a single mini-batch, which we use as a baseline in the exercise below.

Exercise 4.2.1 (Effect of Skip Connections in a ResNet-style Network). *Building on Example 4.2.1 and the notebook `ResNet9-Spiral.ipynb`, investigate the role of skip connections in training the spiral classifier.*

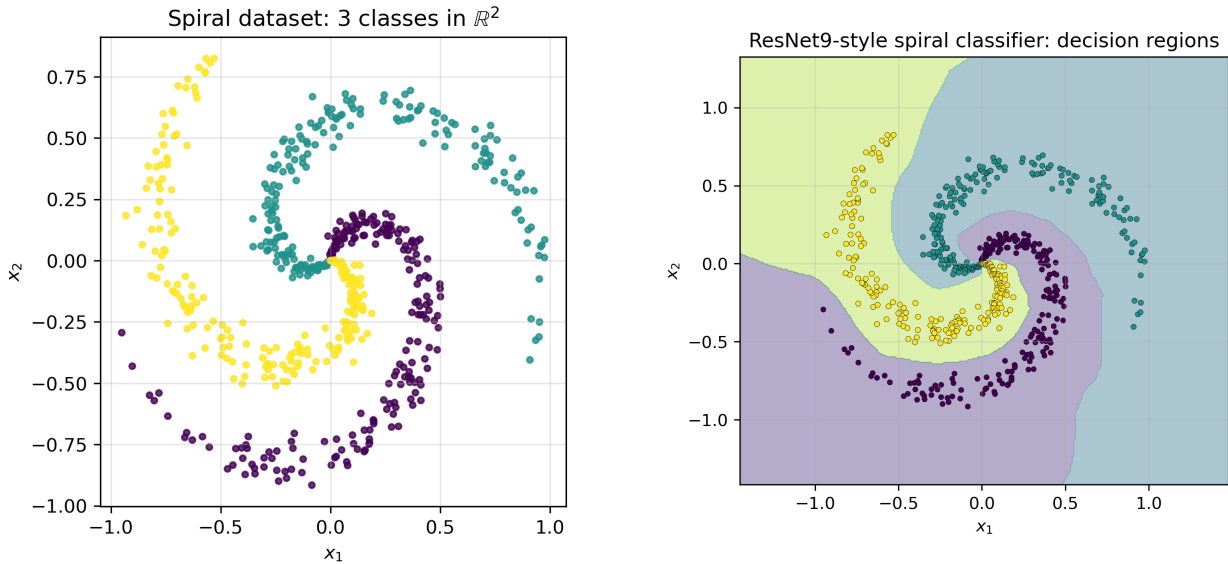


Figure 4.6: **Left:** Spiral dataset in \mathbb{R}^2 (three classes). **Right:** Decision regions learned by the ResNet-style model from Example 4.2.1. Figures generated by `ResNet9-Spiral.ipynb`.

1. **Remove skip connections.** Modify the model so that residual blocks become plain two-layer Multi-Layer-Perceptron (MLP) blocks, i.e., replace

$$h \mapsto \sigma(h + g(h))$$

by

$$h \mapsto \sigma(g(h)).$$

Train this non-residual network under the same conditions (optimizer, learning rate, number of epochs) and compare its training loss and accuracy curves to those in Fig. 4.7.

2. **Decision boundaries.** For the non-residual network, recompute and plot the decision regions in the (x_1, x_2) -plane, as in Fig. 4.6. Compare the shapes of the learned decision boundaries with and without skip connections.
3. **Gradient flow.** For both models (with and without skip connections), compute gradient norms for each layer using a single mini-batch (as in the notebook) and plot them on a log scale. Discuss how skip connections influence the distribution of gradient norms across depth and how this relates to the vanishing-gradient phenomenon.
4. **Summary.** Summarize your observations:
 - How does removing skip connections affect training stability and convergence?
 - How do skip connections impact gradient flow quantitatively (via gradient norms) and qualitatively (via optimization behavior)?
 - How do these findings support the ODE-based interpretation $h_{t+1} = h_t + f(h_t, \theta_t)$ as a sequence of small, stable updates?

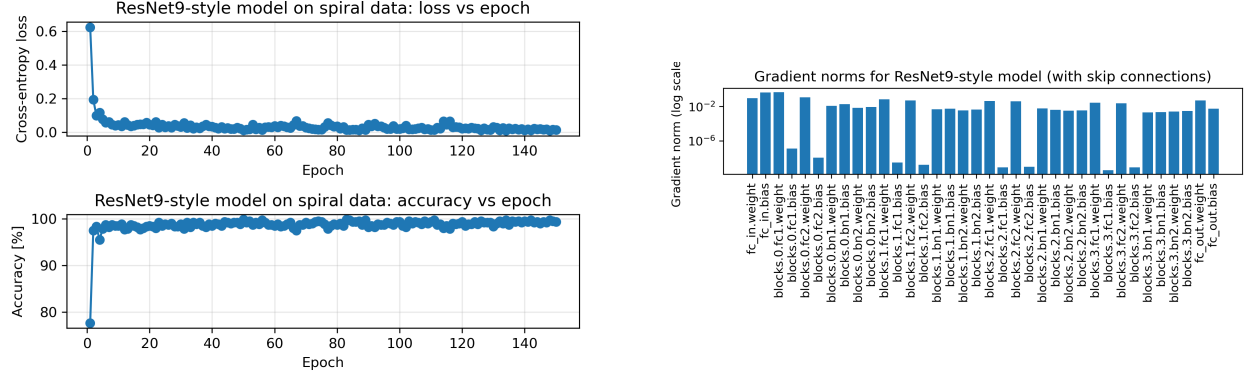


Figure 4.7: **Left:** Training loss and accuracy versus epoch for the ResNet-style model on the spiral dataset. **Right:** Gradient norms of individual layers (log scale) for a single mini-batch, illustrating how gradients propagate through the residual architecture.

From Discrete Layers to Continuous Depth

Residual Networks (ResNets) introduce *skip connections* that reinterpret each layer as a small *incremental update* rather than a full transformation. This idea allows a deep network to evolve its representation gradually, layer by layer. When we view the layer index as a discretized “time” variable, the residual update

$$h_{k+1} = h_k + f_\theta(h_k) \Delta t$$

resembles an explicit Euler step for an ordinary differential equation (ODE). This observation motivates a conceptual shift:

- Rather than stacking finitely many discrete layers, we may imagine a **continuous-depth model** governed by an ODE $\dot{h}(t) = f_\theta(h(t))$.
- The architecture of the network is now encoded in the choice of vector field f_θ and the numerical solver used to integrate it.
- Training requires differentiating *through the ODE solver*, giving rise to the **Neural ODE** framework.

Thus the small modification introduced by skip connections in ResNets opens a direct path to treating deep networks as continuous-time dynamical systems. The next subsection develops this perspective and illustrates it on a simple but instructive example: learning the dynamics of a 2D spiral.

4.2.2 From Residual Networks to Neural ODEs: A 2D Spiral Example

Residual networks can be viewed as an explicit Euler discretization of a continuous-depth evolution. Recall the residual update

$$h_{k+1} = h_k + \Delta t f_\theta(h_k), \quad k = 0, \dots, K-1, \quad (4.3)$$

which, in the limit $\Delta t \rightarrow 0$ and $K \rightarrow \infty$ at fixed final time T , suggests an underlying ordinary differential equation (ODE)

$$\frac{dh(t)}{dt} = f_\theta(h(t)), \quad h(0) = h_0, \quad (4.4)$$

with $h(t)$ playing the role of a “continuous layer index”. The Neural ODE viewpoint replaces the discrete stack of residual blocks by such a continuous-depth evolution, and delegates the role of the “network architecture” to the choice of vector field f_θ and the numerical ODE solver used to approximate (4.4).

From discriminative mappings to generative dynamics

The transition from residual networks to Neural ODEs is not merely a change in how *depth* is modeled; it also signals a conceptual shift in what the model represents. Standard residual networks are typically trained in a **discriminative** setting, where the goal is to map an input h_0 to a target output through a finite sequence of layers. In contrast, Neural ODEs promote a *dynamical* viewpoint: the model defines a continuous-time flow in feature space, and learning amounts to shaping the vector field f_θ so that entire trajectories exhibit desired behavior. This perspective naturally extends from fitting individual input–output pairs to modeling the evolution of *distributions* under learned dynamics—an idea that lies at the heart of modern **generative models**.

At this stage, however, the dynamics (4.4) is fully deterministic: given an initial condition $h(0)$, the trajectory $h(t)$ is uniquely determined. The genuinely generative models studied in the later chapters of this book – including diffusion models, score-based methods, and stochastic control formulations – will instead rely on *stochastic* differential equations, where randomness plays a central and essential role.

In practice, one chooses a parameterized vector field $f_\theta : \mathbb{R}^d \rightarrow \mathbb{R}^d$ and solves (4.4) with a standard ODE integrator. The simplest choice is explicit Euler,

$$h_{k+1} = h_k + \Delta t f_\theta(h_k),$$

but higher-order schemes such as Runge–Kutta methods, or adaptive solvers such as Dormand–Prince, are equally natural. The key algorithmic idea of Neural ODEs [23] is to *differentiate through the solver* in order to back-propagate from a loss defined at the terminal time T (or along the entire trajectory) back to the parameters θ .

2D spiral setup. To illustrate these ideas in a tangible, low-dimensional setting, we consider a decaying spiral trajectory in \mathbb{R}^2 given by

$$x_{\text{true}}(t) = e^{-\alpha t} \begin{bmatrix} \cos(\omega t) \\ \sin(\omega t) \end{bmatrix}, \quad t \in [0, T], \quad (4.5)$$

with $\alpha > 0$ and $\omega > 0$. We sample (4.5) on a uniform grid $0 = t_0 < t_1 < \dots < t_N = T$ and corrupt the samples with small Gaussian noise, obtaining $\{x_k^{\text{noisy}}\}_{k=0}^N$. The task is then to learn a Neural ODE whose solution trajectory $x_\theta(t)$ matches these noisy observations.

The accompanying notebook `NeuralODE-Spiral.ipynb` implements this example using a fixed-step fourth-order Runge–Kutta (RK4) solver and a small neural network $f_\theta : \mathbb{R}^2 \rightarrow \mathbb{R}^2$. The initial condition is taken from the first noisy observation, $x_\theta(0) = x_0^{\text{noisy}}$, and the loss is the mean squared error over the entire time grid:

$$\mathcal{L}(\theta) = \frac{1}{N+1} \sum_{k=0}^N \|x_\theta(t_k) - x_k^{\text{noisy}}\|_2^2. \quad (4.6)$$

The network parameters θ are trained with Adam, while gradients are obtained by automatic differentiation through the RK4 integrator. Fig. 4.8 shows the underlying noiseless spiral, the noisy data, and the fitted Neural ODE trajectory; the right panel reports the training loss as a function of iteration.

A particular advantage of the dynamical viewpoint is that we can easily *extrapolate* beyond the training horizon $[0, T]$ by integrating (4.4) further in time. This reveals the inductive bias imposed by the learned vector field f_θ : in some parameter regimes the learned dynamics continues to spiral inward in a physically plausible way, while in others it may deviate or develop spurious oscillations. The extrapolation behavior is illustrated in Fig. 4.9.

Example 4.2.2 (Neural ODE fit of a 2D spiral). *The notebook `NeuralODE-Spiral.ipynb` constructs a 2D decaying spiral in \mathbb{R}^2 , corrupts it with Gaussian noise, and then learns a Neural ODE drift f_θ so that the RK4 solution $x_\theta(t)$ matches the noisy data. The drift is represented by a two-layer MLP with tanh nonlinearities. Training is carried out with Adam by backpropagating through the RK4 solver. The example exposes three important aspects of Neural ODEs:*

1. *The continuous-depth viewpoint: the “depth” variable k of a residual network is replaced by a continuous time variable t , and the model is specified by a vector field f_θ .*
2. *The role of the numerical solver: changing the ODE integrator (Euler vs. RK4 vs. adaptive methods) changes the effective model class.*
3. *Trajectory-level supervision: the loss is defined over the entire time series $\{x_\theta(t_k)\}$, not just at a single terminal state.*

Exercise 4.2.2 (Discrete vs. continuous depth on the spiral). *Using the same spiral dataset and time grid as in `NeuralODE-Spiral.ipynb`, construct a discrete-time model in the spirit of a residual network, e.g. by learning a map $g_\phi : \mathbb{R}^2 \rightarrow \mathbb{R}^2$ and iterating*

$$x_{k+1} = x_k + g_\phi(x_k), \quad k = 0, \dots, N-1.$$

Train ϕ to minimize the same trajectory loss as in (4.6), and compare:

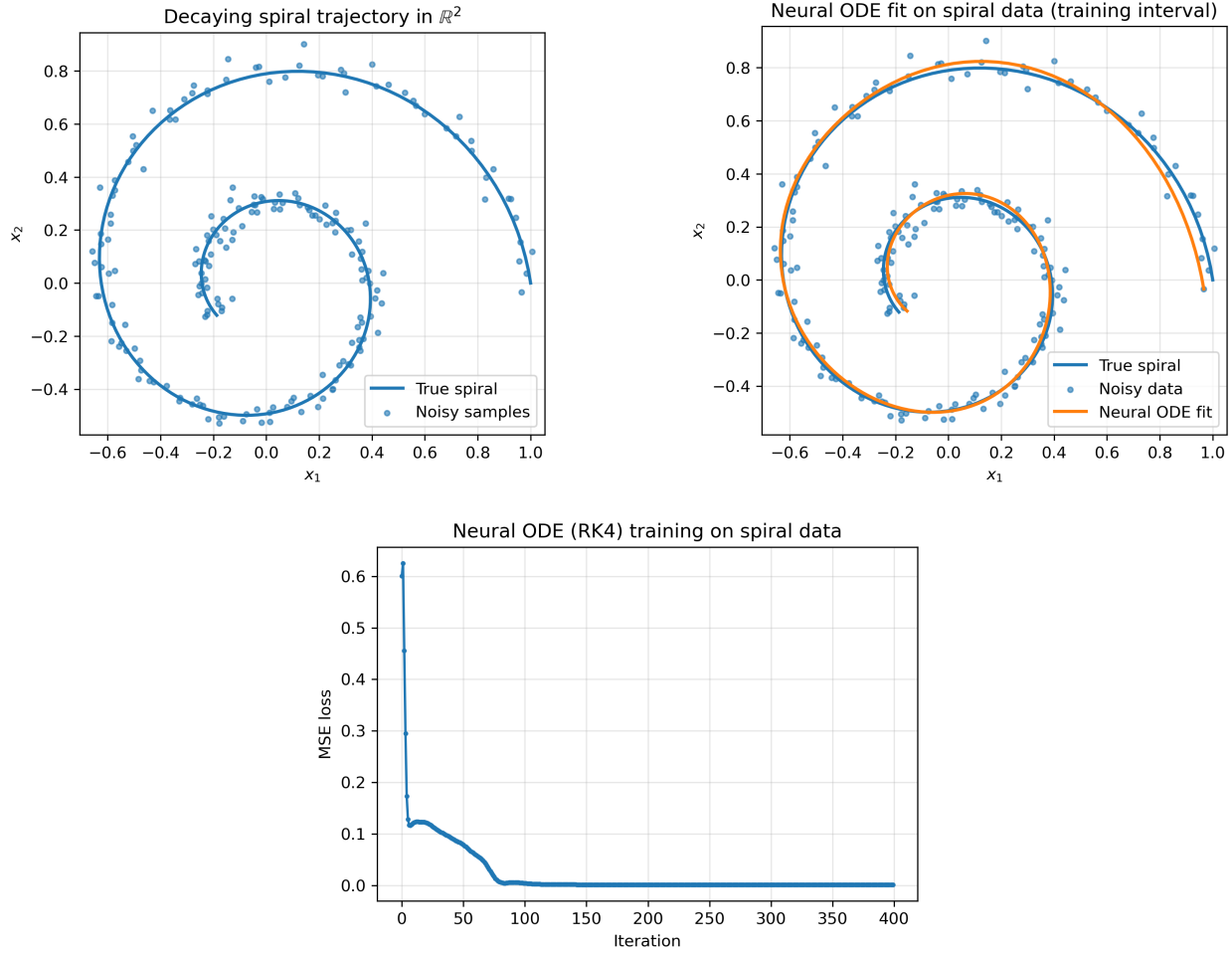


Figure 4.8: Top left: ground truth spiral trajectory (4.5) (solid curve) and noisy observations (dots). Top right: Neural ODE trajectory $x_\theta(t)$ fitted using a fixed-step RK4 solver, superimposed on the data. Bottom: training loss (4.6) versus optimization iteration. Generated by the notebook `NeuralODE-Spiral.ipynb`.

1. *Quality of fit on the training interval $[0, T]$.*
2. *Extrapolation behavior beyond T .*
3. *Sensitivity of the learned dynamics to changes in the number of steps N (while keeping T fixed), for both the discrete and the continuous models.*

Discuss in which regimes the discrete residual model behaves similarly to the continuous Neural ODE, and where they differ qualitatively, both in terms of trajectory geometry and stability.

Adaptive solvers and the adjoint equation. In practice, Neural ODE implementations almost always rely on *adaptive* time-stepping, so that the solver chooses its own internal step sizes in order to control a local error estimate. This is illustrated in the companion notebook

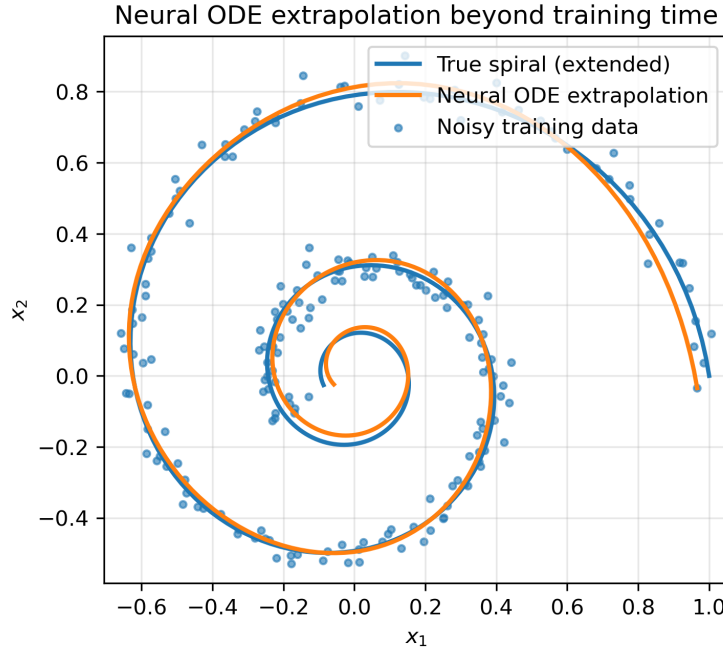


Figure 4.9: Extrapolation of the learned Neural ODE beyond the training window. Solid curve: ground truth spiral extended to a longer time interval; dashed curve: extrapolated Neural ODE trajectory. Noisy training data are shown as dots near the origin. Generated by `NeuralODE-Spiral.ipynb`.

`NeuralODE-Adjoint-Spiral.ipynb`, which replaces the fixed-step RK4 integrator with a simple adaptive RK scheme based on step-doubling. The resulting model $x_\theta(t)$ still fits the noisy spiral (see Fig. 4.10), but now the number and size of solver steps depend on both the data and the current parameters θ .

From the variational perspective developed earlier in this chapter, gradients with respect to the initial condition and the parameters can be expressed in terms of an *adjoint state* $\lambda(t)$ solving a companion ODE backward in time. For a terminal loss

$$L = \frac{1}{2} \|x(T) - x_{tar}\|_2^2 \quad (4.7)$$

with x_{tar} fixed, the adjoint $\lambda(t)$ obeys

$$\dot{\lambda}(t) = -(\partial_x f_\theta(x(t)))^\top \lambda(t), \quad \lambda(T) = x(T) - x_{tar}. \quad (4.8)$$

The notebook `NeuralODE-Adjoint-Spiral.ipynb` computes $\lambda(t)$ for the trained spiral model and verifies numerically that $\lambda(0)$ coincides with the gradient of L with respect to the initial state $x(0)$:

$$\lambda(0) \approx \nabla_{x(0)} L, \quad (4.9)$$

in agreement with the general adjoint theory for ODE-constrained optimization. Fig. 4.11 shows the time evolution of the adjoint components $\lambda_1(t)$ and $\lambda_2(t)$ along the spiral.

Exercise 4.2.3 (From backpropagation to adjoint dynamics). *Starting from the implementation in `NeuralODE-Adjoint-Spiral.ipynb`, extend the code so that the adjoint state $\lambda(t)$*

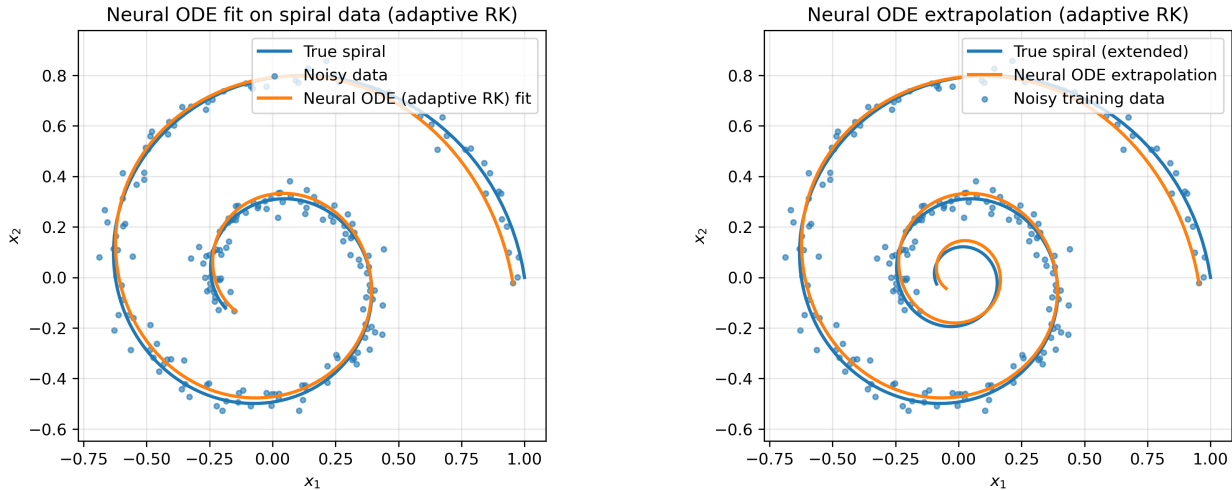


Figure 4.10: Left: Neural ODE fit of the spiral using an adaptive-step RK solver. Right: extrapolation of the adaptive solver beyond the training window. Generated by `NeuralODE-Adjoint-Spiral.ipynb`.

is used not only to recover $\nabla_{x(0)} L$ but also to assemble an approximation of the gradient $\nabla_\theta L$ via the continuous-time formula

$$\nabla_\theta L = \int_0^T \lambda(t)^\top \partial_\theta f_\theta(x(t)) dt.$$

Compare the resulting gradient vector to the one obtained by automatic differentiation through the adaptive solver, both in norm and direction. Discuss numerical issues that arise (such as the need to recompute the forward trajectory or to store it in memory) and relate them to the trade-offs in full-fledged Neural ODE implementations.

From architectures to universal phenomena in deep learning

The progression $CNN \rightarrow ResNet \rightarrow Neural\ ODE$ revealed how architectural innovations increasingly impose structure on the transformations performed by a network: locality and equivariance in CNNs, stability and incremental updates in ResNets, and continuous-depth flows in Neural ODEs.

However, many striking behaviors of modern neural networks *do not depend on architecture at all*. Across CNNs, MLPs, Transformers, autoencoders, and ODE-based models, we repeatedly observe:

- optimization trajectories that preferentially settle in **flat**, high-volume minima;
- internal representations that collapse onto **low-dimensional manifolds**;
- implicit regularization induced by SGD, normalization layers, and network width.

In the following Section we analyze these effects through simple but revealing experiments which move us from *how networks are built* to *why trained networks behave the way they do*.

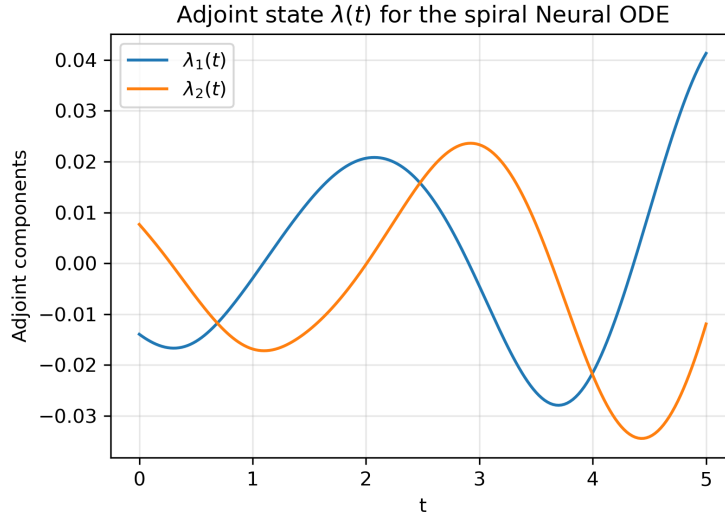


Figure 4.11: Adjoint state $\lambda(t)$ for the spiral Neural ODE, obtained by integrating the adjoint ODE (4.8) backward in time from the terminal condition $\lambda(T) = x(T) - x_{tar}$. The value $\lambda(0)$ matches the gradient of the terminal loss with respect to the initial condition. Generated by `NeuralODE-Adjoint-Spiral.ipynb`.

4.3 Universal Geometric Principles of Deep Learning

Having traced the evolution of architectures from CNNs to ResNets and finally to Neural ODEs, we now turn to a different – but equally fundamental—perspective: the *architecture-independent* geometric principles that govern how neural networks learn. Despite operating in extremely high-dimensional parameter and activation spaces, trained networks consistently exhibit two remarkable phenomena. First, the dynamics of stochastic gradient descent bias solutions toward *flat, high-volume minima* in the loss landscape, a property closely tied to stability and generalization. Second, the internal representations of deep networks collapse onto *low-dimensional manifolds*, revealing an implicit form of structured compression. The two subsections that follow examine these emergent behaviors in detail—first through the lens of SGD-induced flat minima, and then through PCA- and activation-based analyses of the intrinsic dimensionality of learned representations.

4.3.1 Discovery of Flat Regions in the Energy Landscape

The geometry of the loss landscape plays a critical role in determining a model’s generalization ability [24]. Stochastic Gradient Descent (SGD) tends to converge to **flat regions** in the energy landscape, which correspond to solutions that are robust to small perturbations in the data or model parameters. **Flat minima** are associated with better generalization, while **sharp minima** often lead to overfitting. The emergence of flat minima is influenced by the interaction between the **learning rate**, **batch size**, and the **controlled stochasticity** of SGD.

Example 4.3.1 (Neural-network decoding, SGD noise, and the geometry of minima). *To*

explore the highlighted feature of SGD in a setting that is both analytically simple and conceptually rich, we consider a three-bit **error-correcting code**. Let $x = (x_1, x_2, x_3)$ be a binary vector constrained by a single parity check

$$x_1 + x_2 + x_3 \equiv 0 \pmod{2}.$$

The valid codewords are

$$(0, 0, 0), (1, 1, 0), (1, 0, 1), (0, 1, 1).$$

One of these four codewords is transmitted through an additive noisy channel, yielding a corrupted observation

$$y = x + \text{noise},$$

where $y \in \mathbb{R}^3$ and the noise is Gaussian. A small fully connected neural network is then trained to decode y and recover the most probable original codeword.

Setup. We consider a feedforward neural-network decoder

$$\phi_\theta : \mathbb{R}^3 \rightarrow [0, 1]^3$$

(with one hidden layer and three output logits) is trained to recover x from y using a bit-wise binary cross-entropy loss.

SGD noise via batch size. To study the influence of stochasticity, we train the same network using three batch sizes:

$$\text{batch} \in \{4, 32, \text{full batch}\},$$

all with the same learning rate. The accompanying notebook `NN-Decoding.ipynb` records:

- **Training loss trajectories.** Small batches produce noisy, spike-filled loss curves, whereas large batches have smoother, more monotone behavior.
- **Approximate Hessian eigenvalues** near the final solution. The Hessian is computed on a small subset of the training data via automatic differentiation.
- **Local two-dimensional slices** of the loss landscape obtained by probing the loss on a random 2D affine subspace through the solution.

What the results show. Fig. 4.12 summarizes representative outcomes. The most striking feature is the behavior of the training loss trajectories. Small batches produce visibly noisy dynamics: the loss fluctuates substantially from one step to the next and exhibits characteristic “spikes”—temporary increases in loss caused by high-variance gradient estimates. Batch size 32 displays a milder version of this phenomenon, with smaller oscillations and fewer spikes. In contrast, full-batch gradient descent follows a smooth, nearly monotone path, reflecting its low-variance updates. These differences illustrate a core principle of SGD: **optimization noise is controlled by batch size**, and this noise directly shapes the geometry of the optimization trajectory long before convergence.

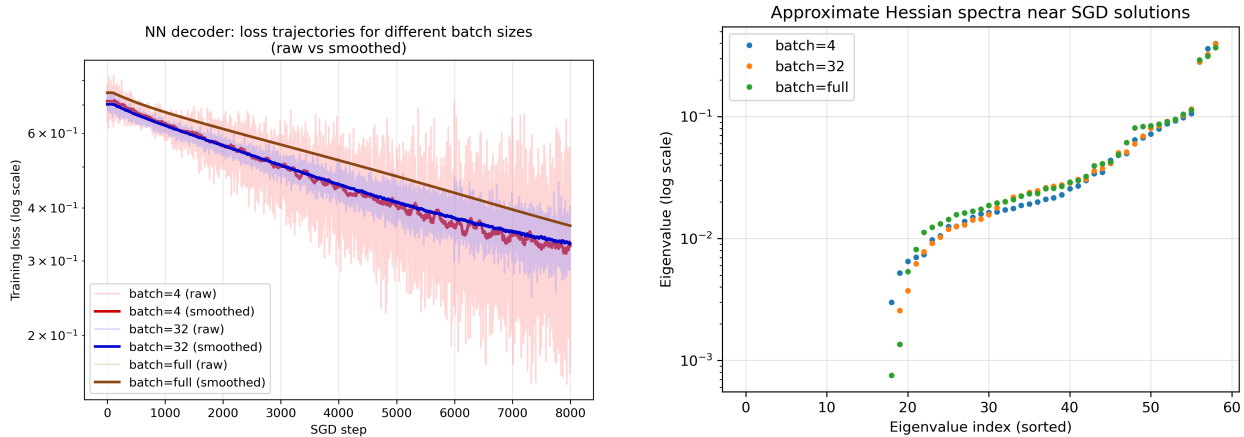


Figure 4.12: **Left:** Training loss (log scale) for different batch sizes. Small batches exhibit high-variance trajectories with distinct spikes; large batches produce smoother curves. **Right:** Approximate Hessian spectra near the trained solutions. In this small decoding task, all three runs converge to minima with remarkably similar curvature, illustrating that batch-size effects on flatness are problem-dependent and may be subtle in low-dimensional settings. Generated by `NN-Decoding.ipynb`.

By comparison, the curvature profiles near convergence show much subtler differences. Although small-batch SGD is often associated with flatter minima in large modern networks, the Hessian spectra for this tiny model—with only 59 parameters and a highly constrained decoding task—are remarkably similar across batch sizes. This is not surprising: in low-dimensional settings with strong inductive structure, the optimizer is effectively guided into the same broad basin regardless of the stochasticity level. Thus, while the trajectory-level effects of batch size are clearly visible, the curvature-level effects may remain muted in such small toy examples.

Local loss slices. A two-dimensional slice of the loss around the solution (Fig. 4.13) reveals a gently curved, broad basin. Such slices are helpful for visualizing qualitative geometry, even when Hessian spectra are not dramatically different.

Key observations. Even this small example illustrates essential conceptual points:

- Smaller batches induce noisy, irregular optimization trajectories with characteristic spikes.
- Flat minima do not always show sharply separated curvature signatures—especially in small models.
- Hessian spectra, loss slices, and trajectories together give a more complete picture of the loss landscape than any single metric.

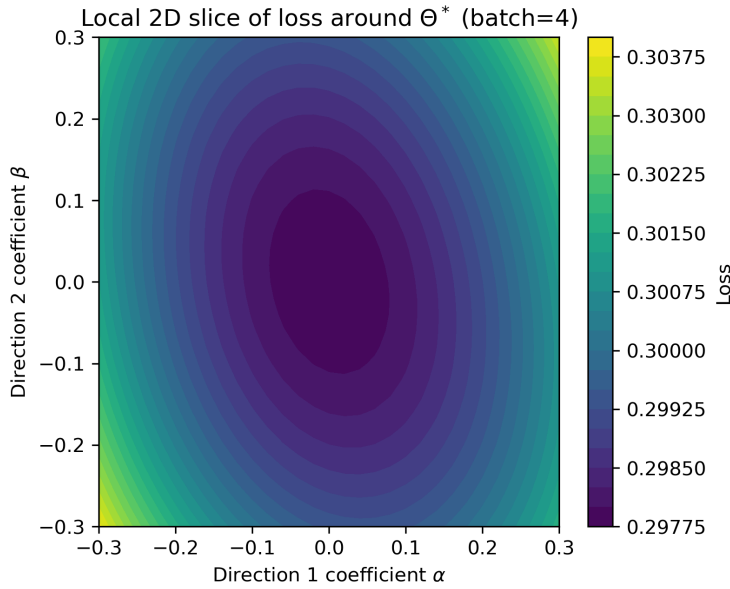


Figure 4.13: Two-dimensional slice of the loss landscape around a solution obtained with batch size 4. The basin is broad and smooth, characteristic of a flat minimum in this low-dimensional example. Despite different SGD noise levels, all batch sizes converge to geometrically similar regions in this task.

Trajectory Noise vs. Curvature Effects

Small-batch SGD leaves a strong signature on the *optimization trajectory* – its noisy, spike-ridden path reflects high-variance gradient estimates. However, in small neural networks with strong inductive bias, this stochasticity does not necessarily translate into visibly different *curvature profiles* near the final solution: the optimizer is drawn into the same broad basin regardless of batch size.

This illustrates a general principle: **SGD’s noise strongly shapes the path by which a solution is reached, but its effect on the local geometry of that solution depends on model scale and problem complexity.** Larger models and more flexible loss landscapes exhibit much richer curvature differences across batch sizes.

Exercise 4.3.1 (Exploring SGD dynamics and curvature in a toy decoding problem). *Extend the notebook `NN-Decoding.ipynb` to deepen your understanding of how SGD interacts with the loss landscape.*

1. **Batch size, learning rate, and flatness.** Compute the Hessian eigenvalue spectra for several combinations of batch size and learning rate. Compare:

- the number of small eigenvalues (e.g., $\lambda < 10^{-2}$);
- the largest eigenvalues.

Is there any detectable trend? Discuss why flatness differences may or may not appear in such a small model.

2. **Convergence behavior.** Plot loss trajectories for each configuration. Compare:

- convergence speed,
- variance of the trajectory,
- frequency and magnitude of spikes.

How does SGD noise influence the qualitative shape of the optimization path?

3. **Local geometry via contour slices.** For several trained solutions (different batch sizes or learning rates), generate 2D loss slices. Compare their shapes and relate them to Hessian spectra.
4. **Effect of model size.** Increase the number of hidden units. Does a higher-dimensional parameter space reveal clearer curvature differences between batch sizes? At what model size do you begin to see distinct spectral signatures?

Support your conclusions with:

- Hessian eigenvalue plots,
- loss trajectories,
- 2D loss contour plots.

4.3.2 Dynamic Selection of Low-Dimensional Manifolds in Deep Networks

A recurring theme in modern deep learning is that, despite operating in extremely high-dimensional parameter and activation spaces, neural networks *implicitly restrict their computations to low-dimensional manifolds*. Empirical and theoretical studies [25] suggest that during training, networks organize data into structured, low-rank representations, effectively using only a small subset of the available degrees of freedom. This emergent reduction of intrinsic dimensionality is deeply related to how neural networks generalize.

These ideas connect naturally to concepts introduced earlier in the book:

- Chapter 1 introduced PCA and SVD as tools for identifying dominant directions of variation.
- Section 4.1.4 showed how CNNs extract increasingly abstract hierarchical features.
- Section 4.2.1 on ResNets and Section 4.2.2 on Neural ODEs emphasized smoothness, stability, and low-complexity transformations.

In this subsection, we use PCA to directly visualize how a trained CNN organizes MNIST digits into a compact, low-dimensional manifold inside its intermediate layers. This provides geometric intuition for hierarchical feature extraction and generalization.

Example 4.3.2 (Low-dimensional structure in CNN activation manifolds). *A small CNN trained on MNIST produces high-dimensional activations:*

- the first convolutional layer has $16 \times 28 \times 28$ features,
- the second convolutional layer has $32 \times 14 \times 14$ features,
- the first fully connected layer has 128 features.

These spaces are far too high-dimensional to visualize directly. However, PCA (defined via SVD in Chapter 1) allows us to extract the dominant variance directions and project activations into two or three dimensions.

Using the notebook `CNN-MNIST-PCA.ipynb`, we:

- train a CNN for several epochs,
- collect activations from multiple layers for a subset of test images,
- flatten each activation tensor into a feature vector,
- perform PCA, compute explained-variance curves, and visualize PC1–PC2 scatter plots.

Left panel of Fig. 4.14 shows the PCA projection for the **first convolutional layer**. Even at this early stage, the network partially separates digits into clusters, indicating that the CNN has already started constructing a task-dependent embedding.

Fig. 4.15 shows explained-variance curves for three layers. The number of principal components needed to capture most of the variance decreases with depth—empirical evidence of representation compression.

Finally, right panel of Fig. 4.14 shows PCA for the **fully connected layer**. The clusters become significantly tighter and more separable, reflecting the network’s progression from pixel-level detail to abstract digit identity.

Why PCA exposes hidden geometry in neural networks

Deep networks tend to compress information into a small number of dominant directions in activation space. PCA reveals this compression: if a handful of components explain most of the variance, then activations lie near a **low-dimensional manifold**. Crucially, this structure is not hand-designed—it emerges dynamically during training as part of deep learning’s implicit regularization.

Exercise 4.3.2 (Exploring learned low-dimensional manifolds). Using `CNN-MNIST-PCA.ipynb`, investigate how deep networks compress and structure information.

1. **Layer-wise PCA.** Compute PCA for each of the layers shown above. How does the intrinsic dimensionality evolve with depth?
2. **Effect of nonlinearities.** Compare PCA before and after ReLU in the convolutional layers. How does the activation function reshape the manifold?
3. **Class geometry.** Which digits separate cleanly in the PCA plane? Which overlap? Relate this to difficulty of classification.

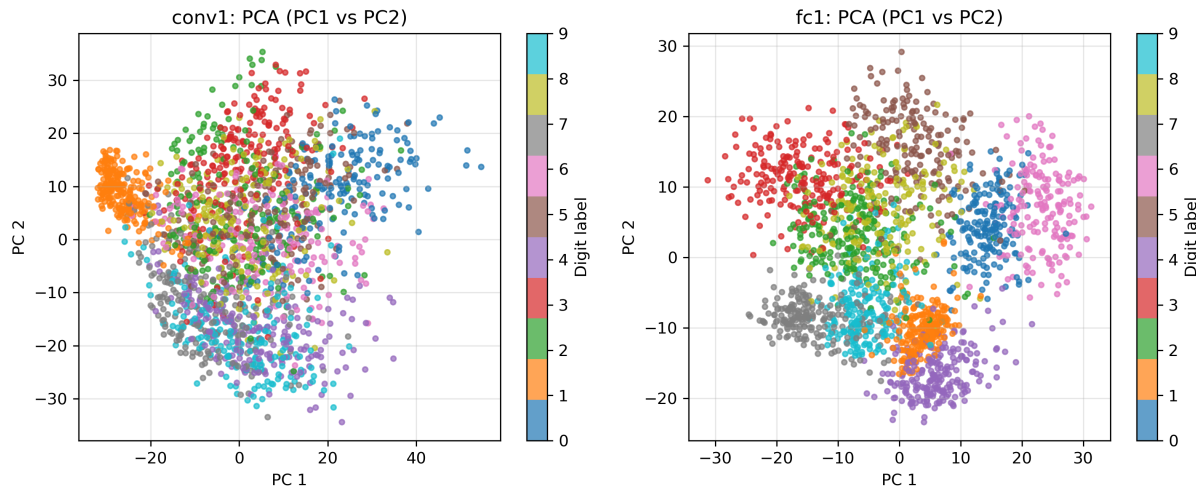


Figure 4.14: **PCA of activations in the first convolution (left) and last hidden (right) layers.** Left – first layer: Even early in the network, the CNN organizes digits into a moderately structured manifold. Points represent MNIST test images projected onto the first two principal components and are colored by digit label. Right – last (hidden) layer: Digit classes now form tight, well-separated geometric clusters in the top two principal components. This illustrates the emergence of a low-dimensional manifold encoding digit identity. Figure generated by `CNN-MNIST-PCA.ipynb`.

4. **Compression vs. memorization.** Train on a reduced dataset (e.g., 1 000 images). Does the PCA spectrum become flatter, indicating less compression?
5. **Depth and abstraction.** Compare PCA scatter plots of the first convolutional layer, second convolutional layer, and fully connected layer. How does the manifold evolve from pixel space to abstract concept space?

Support your findings with:

- PCA scatter plots,
- explained-variance curves,
- layer-wise comparisons of intrinsic dimensionality.

Computational Companion Notebooks

To complement the mathematical exposition of this Section (and more generally Chapter), three optional Jupyter notebooks are provided in the Companion Notebook Collection accompanying this book. They allow the reader to explore empirically the transition from discrete architectures (CNNs, ResNets) to continuous-depth models (Neural ODEs), as well as the geometric principles described in this Section.

`ResNet9-MNIST.ipynb` and `ResNet18-MNIST.ipynb` illustrate how skip-connections modify optimization dynamics and progressively approximate continuous-time flows.

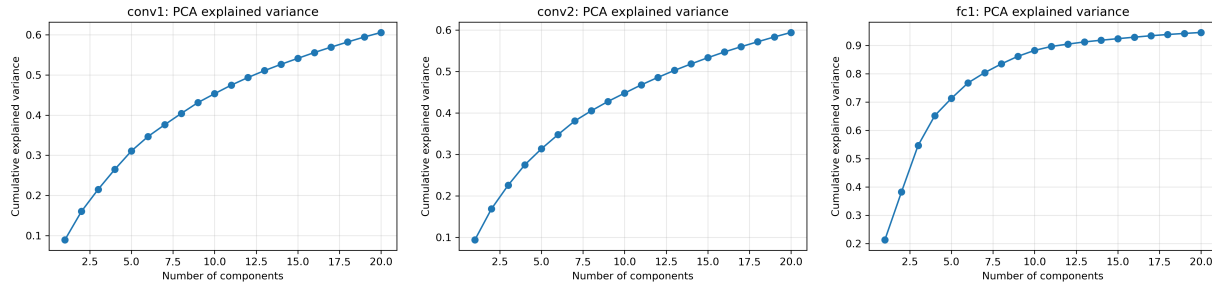


Figure 4.15: **Explained-variance curves for PCA across layers.** Deeper layers exhibit earlier saturation of variance with the number of components, indicating strong dimensionality compression. Only a small number of principal components are needed to capture most of the structure in the activations.

`Sharp-vs-Flat.ipynb` provides an implementation-level view of loss-landscape geometry, complementing the conceptual discussion of flat regions and low-dimensional manifolds discussed above.

These notebooks are optional and exploratory: they are designed to reinforce intuition.

4.4 Further Reading and Roadmap to the Rest of the Book

Further Reading

We conclude this chapter by noting that learning from ODE-based or more generally *operator-based* data structures has become a major research direction that extends far beyond the Neural ODE framework. Many of the ideas predate the modern deep learning era, yet they continue to shape state-of-the-art methods through the integration of domain knowledge, physics, and mathematical structure.

The earliest use of **artificial neural networks for solving differential equations** appeared in [26], where NN-based trial solutions were used to satisfy boundary conditions and approximate ODE/PDE solutions. This line of work was revitalized two decades later by Raissi, Perdikaris, and Karniadakis [27] under the name **Physics-Informed Neural Networks (PINNs)**, which incorporate differential operators directly into the loss function. PINNs exploit the governing equations to regularize learning, often improving sample efficiency and enabling limited extrapolation.

Another early direction involves **equation-free modeling** and data-driven coarse-graining [28], in which high-fidelity simulators are used only to estimate local dynamical behavior. This allowed researchers to learn reduced-order dynamics without ever writing down the full equations.

Symbolic approaches have also contributed to data-driven discovery of dynamics. **Symbolic regression** methods [29] search for compact analytical expressions explaining observed trajectories, while the **Sparse Identification of Nonlinear Dynamics (SINDy)** framework [30] uses sparse regression to recover interpretable differential equations from time-series

data. These approaches demonstrate how incorporating sparsity and interpretability priors can significantly reduce the hypothesis space.

A more recent family of methods — **neural operators** — aims to learn *mappings between infinite-dimensional function spaces*, such as

$$\mathcal{G} : f(x) \mapsto u(x),$$

where u solves a PDE with input field f . Unlike PINNs, which approximate *solutions*, neural operators approximate *solution operators*, enabling rapid evaluation for many different inputs. Two widely used architectures are:

- **DeepONet** [31], based on the universal approximation theorem for operators, which decomposes the mapping into “branch” and “trunk” networks and can learn nonlinear operators from data.
- **Fourier Neural Operators (FNO)** [32], which learn integral operators using convolution kernels represented in the Fourier domain. FNOs scale extremely well and have become a foundation for scientific machine learning in CFD, climate modeling, materials science, and more.

Neural operators represent a natural extension of Neural ODEs: they learn not just trajectories, but entire *families* of dynamical solutions. They provide a powerful interface between scientific computing and generative AI, while retaining mathematical structure such as translation symmetries and convolutional integral kernels.

Together, these approaches illustrate a broader principle: **learning improves significantly when augmented with physics, structure, sparsity, or operator priors**. Standard neural networks excel at interpolation within the observed domain but often fail to extrapolate meaningfully. Methods such as Neural ODEs, PINNs, SINDy, symbolic regression, and neural operators help overcome this limitation by embedding additional structure into the optimization problem, providing bridges between black-box machine learning and interpretable, equations-aware modeling.

Software Tools

For state-of-the-art, research-grade software that leverages neural networks for ODEs, PDEs, and optimization problems, we recommend:

- **Julia:** The SciML (Scientific Machine Learning) ecosystem, led by Chris Rackauckas. It includes `DifferentialEquations.jl`, `DiffEqFlux.jl`, neural operators, adjoint sensitivity tools, and highly optimized PDE solvers.
- **Python:** The NeuroMANCER library developed at PNNL (Jan Drgona et al.), which provides a unified differentiable programming framework for control, optimization, PINNs, and operator learning.

From Geometry and Dynamics to Learning Systems

Chapter 4 traced a unifying geometric and dynamical perspective on modern deep learning. We saw that SGD behaves not merely as an optimization routine but as a *stochastic dynamical system* whose trajectories tend toward wide, stable valleys of the loss landscape; that architectures such as CNNs, ResNets, and Neural ODEs implicitly *steer computations onto low-dimensional manifolds*; and that deep networks perform a kind of *structured dimensionality reduction* as information flows across layers.

Across all examples—loss-landscape exploration, skip connections as discretized ODE solvers, Neural ODEs as continuous-depth models, and PCA analyses of CNN activations—the core message is that **deep learning works because learning dynamics and architecture jointly impose powerful geometric biases**. These biases guide solutions toward smooth, low-complexity representations that generalize beyond the training set.

This geometric–dynamical lens prepares us for the more advanced themes of the upcoming chapters, where differential geometry, variational principles, optimal transport, and stochastic processes will become the organizing framework for understanding generative models and the mathematics of modern AI.

Roadmap: How Chapter 4 Leads into Chapters 5,6,7,8,9

The ideas developed in Chapter 4 serve as conceptual foundations for the remainder of the book. Here we briefly summarize how the main themes of this chapter — representation learning, optimization dynamics, and continuous-depth architectures — naturally flow into the topics that follow.

From deterministic feature maps to probabilistic models (Chapter 5). In Chapter 4 we treated neural networks as deterministic maps $x \mapsto f_\theta(x)$ learned from data. To reason about *uncertainty* in predictions, random initialization, SGD noise, and generalization, we must place these constructions into a probabilistic framework. Chapter 5 develops this framework: probability spaces, random variables, multivariate Gaussians, empirical distributions, and change-of-variables. These tools underlie:

- viewing neural outputs as random variables, not just point estimates;
- interpreting stochastic gradient methods as operating on random losses;
- understanding normalizing flows as invertible neural maps between probability measures.

From low-dimensional manifolds to information and compression (Chapter 6). Section 4.3.2 demonstrated empirically that deep networks concentrate data on low-dimensional manifolds and perform strong nonlinear compression. Chapter 6 builds a quantitative language for this behavior: entropy, mutual information, KL divergence, and cross-entropy. These notions are then used to:

- formalize training losses (cross-entropy) already used for classification in Chapter 4;
- reinterpret autoencoders and U-Net as information-theoretic encoders and decoders;
- introduce the information bottleneck viewpoint on deep representations and compression.

From Neural ODEs and SGD noise to stochastic processes (Chapter 7). The ResNet and Neural ODE sections linked deep networks to time-discretized and continuous ODEs, and the SGD discussion highlighted the role of noise and flat minima. Chapter 7 turns these intuitions into stochastic-process language: Brownian motion, diffusion, Markov chains, and MCMC. This allows us to:

- treat noisy gradient dynamics as stochastic processes in parameter space;
- view score-based diffusion and denoising as time-reversed stochastic dynamics;
- connect auto-regressive models and transformers to Markov and Markov-like chains.

From feedforward networks to energy-based and graphical models (Chapter 8). Chapter 4 focused on feedforward discriminative networks trained by backpropagation. Chapter 8 broadens the picture to *energy-based* models and graphical models, where the central object is a probability distribution

$$p_\theta(x) \propto e^{-E_\theta(x)}.$$

This chapter revisits themes from Chapter 4 — representation, optimization, and decoding — in new guises:

- neural decoding of error-correcting codes extends the simple decoding example in Section 4.3.1;
- variational autoencoders (VAEs) combine neural networks with probabilistic latent-variable models, anticipating the diffusion-based generative models of Chapter 9;
- restricted Boltzmann machines and graph neural networks connect layer-wise neural computations to inference on graphs.

From architectures to a unifying generative and control perspective (Chapter 9). Finally, Chapter 9 synthesizes the book’s main threads. The neural architectures of Chapter 4, the probabilistic tools of Chapter 5, the information-theoretic view of Chapter 6, the stochastic processes of Chapter 7, and the energy-based models of Chapter 8 come together to:

- develop score-based diffusion models and their bridge versions as continuous-depth, noise-driven analogues of deep networks;
- reinterpret GANs and VAEs as special cases or limits of diffusion-like constructions;

- connect reinforcement learning, Markov decision processes, and the path-integral diffusion (PID) framework to generative modeling and control.

Readers are encouraged to revisit the neural-network examples of Chapter 4 as they proceed: the same ideas — representation, dynamics, noise, and structure — will reappear in progressively richer mathematical forms throughout Chapters 5–9.

Chapter 5

Probability and Statistics

Probability Theory vs. Statistics

At its core, **probability theory** provides a mathematical framework for **modeling uncertainty**. It allows us to quantify randomness, describe the behavior of random variables, and analyze probability distributions that govern real-world stochastic processes. In contrast, **statistics** is concerned with analyzing data — often referred to in modern contexts as **data science** — wherein we use observed samples to infer underlying distributions, test hypotheses, and build predictive models.

In AI, probability theory forms the foundation of probabilistic models such as Bayesian networks, variational autoencoders, normalizing flows, and diffusion models. Meanwhile, statistical methods enable learning from data, optimizing model parameters, and validating results through statistical inference.

This book blends probability theory and statistics into a unified perspective, emphasizing their interplay in the context of generative AI. The structure of this chapter reflects this integration, treating both theoretical foundations and practical applications holistically.

Why Probability Matters in Deep Learning

Chapter 4 showed that modern neural networks — CNNs, ResNets, Neural ODEs and Transformers — learn powerful representations by gradually deforming data through compositions of trainable maps. Chapter 5 now shifts perspective: instead of studying transformations of *deterministic inputs*, we study transformations of *probability distributions*.

This conceptual shift from geometry of features to geometry of *densities* is what makes normalizing flows, variational inference, and diffusion models possible. Probability is therefore not an optional appendix to deep learning; it is the mathematical engine behind modern generative AI.

Uncertainty in Generative AI

Generative AI must grapple with multiple sources of uncertainty, requiring probabilistic and statistical tools to address challenges in model design, data interpretation, and computational

feasibility:

- **Model uncertainty:** Probabilistic models such as normalizing flows, hidden Markov models, and diffusion models must account for inherent randomness in data generation. Some probabilistic frameworks are application-specific, incorporating structural features such as Poisson rates (e.g., event modeling) or sparsity in covariance matrices (e.g., high-dimensional settings).
- **Data uncertainty:** Real-world training data is often incomplete, noisy, or biased. This motivates statistical tools such as empirical distributions, Kernel Density Estimation (KDE), Maximum Likelihood Estimation (MLE), and confidence intervals — a few of the many techniques introduced in this chapter.
- **Computational uncertainty:** Many probabilistic models are analytically intractable, requiring approximation schemes such as Monte Carlo sampling, variational inference, and reparameterization methods. Later chapters build these techniques into full generative AI pipelines.

Why This Chapter (in the Book)?

The preceding chapters developed the *geometric*, *architectural*, and *optimization*-based foundations of neural networks. However, generative AI ultimately requires reasoning about *probability distributions*, not just deterministic features.

Chapter 5 provides the mathematical language for:

- measuring distances between distributions (KL divergence, entropy);
- transforming distributions via smooth maps (change-of-variables);
- modeling high-dimensional uncertainty (joint distributions, covariance);
- understanding universal phenomena such as the Central Limit Theorem;
- studying extreme statistics relevant for risk, robustness, and anomaly detection.

These tools will be essential for:

- variational inference and VAEs (Chapter 6,
- information theory and compression principles in generative modeling (Chapter 7),
- stochastic processes and diffusion models (Chapter 8,
- the unifying synthesis of generative frameworks (Chapter 9).

In short: Chapter 5 is where the mathematics of uncertainty enters the generative story.

Organization of the Chapter

This chapter is structured to gradually build intuition, formal definitions, and applications:

- **Section 5.1: Primer on Probability Spaces and Random Variables** introduces probability spaces, random variables, expectations, and moments, establishing the core theoretical machinery.
- **Section 5.2: Transforming Probability Distributions** discusses change-of-variable formulas, pushforward distributions, empirical distributions, and leads directly into the introduction of normalizing flows — a key class of deep generative models.
- **Section 5.3: Multivariate Random Variables** extends probability to multiple dimensions, covering joint densities, independence, conditional distributions, and the multivariate Gaussian — the central object of high-dimensional modeling.
- **Section 5.4: From Aggregate Behavior to Rare Events.** This section develops a unified view of distributional limits. We begin with the Central Limit Theorem, which explains the emergence of Gaussian structure in sums of random variables and provides essential convergence and tail bounds. We then examine regimes where Gaussian approximations break down: the *rare-event limit*, where summing Bernoulli variables leads to the Poisson distribution and point-process models; and the *extreme-value limit*, where the behavior of maxima (rather than sums) gives rise to universal extreme-value laws. Together, these results form a toolkit for understanding fluctuations, anomalies, and worst-case behavior in modern machine learning systems.

We begin by introducing relevant foundational material from a combined applied mathematics and AI perspectives¹. For a rigorous measure-theoretic treatment, the classical text *Probability With Martingales* by David Williams [34] is recommended.

5.1 Primer for Probability Spaces & Random Variables

Probability provides the mathematical language for uncertainty. All models used in modern AI — from simple classifiers to deep generative models such as VAEs, GANs, Diffusion Models, and Transformers — manipulate or transform probability distributions in one form or another. Whether we *sample* noise, *estimate* likelihoods, or *push forward* distributions through learned maps, the underlying machinery rests on the foundations introduced in this section.

This chapter therefore begins with a brief mathematical primer: probability spaces, random variables, distributions, expectations, and transformations of variables. These ingredients will be reused throughout the chapter and will also motivate the computational notebooks that accompany the text.

¹Applied mathematics wise this chapter, along with the following chapters of the book, incorporates material from the author’s recent book *Principles and Methods of Applied Mathematics* [33].

5.1.1 Probability Spaces: The Foundation

A *probability space* formalizes randomness through a triple

$$(\Omega, \mathcal{F}, P),$$

where:

- Ω is the **sample space** — the set of all possible outcomes.
- \mathcal{F} is a **σ -algebra** of subsets of Ω whose elements are called *events*. It satisfies:
 - If $A \in \mathcal{F}$ then $A^c \in \mathcal{F}$.
 - If $A_i \in \mathcal{F}$ for $i \geq 1$, then $\bigcup_i A_i \in \mathcal{F}$.
 - Consequently, $\bigcap_i A_i \in \mathcal{F}$.
- $P : \mathcal{F} \rightarrow [0, 1]$ is a **probability measure** satisfying the Kolmogorov axioms:

$$P(\Omega) = 1, \quad P(A) \geq 0, \quad P(A \cup B) = P(A) + P(B) \text{ if } A \cap B = \emptyset.$$

Example 5.1.1 (Coin Toss). *For a single fair-coin toss:*

$$\Omega = \{\text{Head}, \text{Tail}\}, \quad \mathcal{F} = 2^\Omega = \{\emptyset, \{\text{Head}\}, \{\text{Tail}\}, \Omega\},$$

and

$$P(\text{Head}) = P(\text{Tail}) = \frac{1}{2}, \quad P(\emptyset) = 0, \quad P(\Omega) = 1.$$

A biased coin with parameter ρ simply modifies the measure:

$$P(\text{Head}) = \rho, \quad P(\text{Tail}) = 1 - \rho,$$

while leaving Ω and \mathcal{F} unchanged.

Exercise 5.1.1 (A Probability Space in Coding Theory). *Three information bits are encoded with one parity check and transmitted over a **Binary Erasure Channel (BEC)** with erasure probability ϵ .*

Construct the probability space:

1. Define the sample space Ω of all received 3-bit patterns including erasures (ϵ).
2. Define a natural σ -algebra \mathcal{F} of decoding-relevant events.
3. Construct a probability measure P consistent with BEC erasures.

Hint: *Probabilities factor over bit positions; a received bit is either correct (probability $1 - \epsilon$) or erased (probability ϵ).*

5.1.2 Random Variables

A **Random Variable** (RV) is a measurable function

$$X : \Omega \rightarrow \mathbb{R},$$

assigning a numerical value to each outcome.

Example 5.1.2 (Rolling a Die). *For $\Omega = \{1, \dots, 6\}$, the natural random variable is $X(\omega) = \omega$. Here X is discrete, supported on $\{1, \dots, 6\}$.*

Random variables may be:

- **Discrete:** e.g., outcomes of a die, coin flips, syndrome bits in decoding.
- **Continuous:** e.g., Gaussian noise injected into a neural network layer.

Notation. Uppercase letters denote random variables (X, Y), lowercase letters denote realizations (x, y). We write

$$P_X(x) = P(X = x)$$

for Probability Mass Function (PMF) of discrete RVs and

$$p_X(x)$$

for Probability Density Functions (PDFs) of continuous RVs.

The **Cumulative Distribution Function** (CDF) of X is

$$F_X(x) = P(X \leq x).$$

For discrete RVs it is a step function; for continuous RVs it is differentiable with $p_X(x) = F'_X(x)$.

Sampling Notation. We write

$$X \sim P_X$$

to indicate that the random variable X is generated according to the probability distribution P_X . To *sample* from a distribution means to produce one or more numerical realizations of X whose empirical behavior reflects the underlying law P_X . In practice, sampling corresponds to running a (possibly deterministic or randomized) algorithm that outputs values which are distributed according to the specified probability model.

For example, we may write

$$X \sim \text{Bernoulli}(\rho), \quad X \sim \text{Poisson}(\lambda), \quad X \sim \mathcal{N}(\mu, \sigma^2),$$

to denote that draws of X take the value 1 with probability ρ , count rare events with mean λ , or follow a Gaussian bell curve with mean μ and variance σ^2 , respectively.

Throughout the rest of the chapter (and later in the book), “generating samples” refers to using computational procedures (e.g., NumPy’s random module, inversion sampling, rejection sampling, or later, Markov-chain or diffusion-based samplers) to obtain independent realizations X_1, X_2, \dots whose aggregate statistics approximate those of the theoretical distribution P_X .

5.1.3 Expectation and Moments

The **expectation** of X is

$$\mathbb{E}[X] = \begin{cases} \sum_x x P_X(x), & \text{discrete,} \\ \int_{-\infty}^{\infty} x p_X(x) dx, & \text{continuous.} \end{cases}$$

More generally, the n -th moment is $\mathbb{E}[X^n]$, and the variance is

$$\text{Var}(X) = \mathbb{E}[X^2] - (\mathbb{E}[X])^2.$$

Example 5.1.3 (Moment Generating Function). *The Moment Generating Function (MGF)*

$$M_X(t) = \mathbb{E}[e^{tX}]$$

encodes all moments through differentiation:

$$\mathbb{E}[X^n] = \frac{d^n}{dt^n} M_X(t) \Big|_{t=0}.$$

Exercise 5.1.2 (Poisson Moments via MGF). *For $X \sim \text{Poisson}(\lambda)$:*

1. Compute $M_X(t) = \mathbb{E}[e^{tX}]$.
2. Use differentiation to extract $\mathbb{E}[X]$ and $\mathbb{E}[X^2]$.
3. Show that $\text{Var}(X) = \lambda$.

Exercise 5.1.3 (Gaussian Integral and a Useful Identity). (a) Evaluate the Gaussian integral

$$I = \int_{-\infty}^{\infty} e^{-t^2} dt$$

by computing I^2 in polar coordinates.

(b) For $X \sim \mathcal{N}(\mu, \sigma^2)$, use (a) to show

$$\mathbb{E}[X^2] = \sigma^2 + \mu^2.$$

5.1.4 Data–Driven Probability: Empirical Distributions

In modern machine learning, distributions rarely appear in closed form. Instead, we often have *samples* and must construct empirical approximations to probability laws. The accompanying notebook `Empirical-Distributions-1D.ipynb` demonstrates the key ideas through several one-dimensional examples.

Example 5.1.4 (Empirical PMF and CDF from Samples). *Given samples $x_1, \dots, x_N \sim P_X$, one builds:*

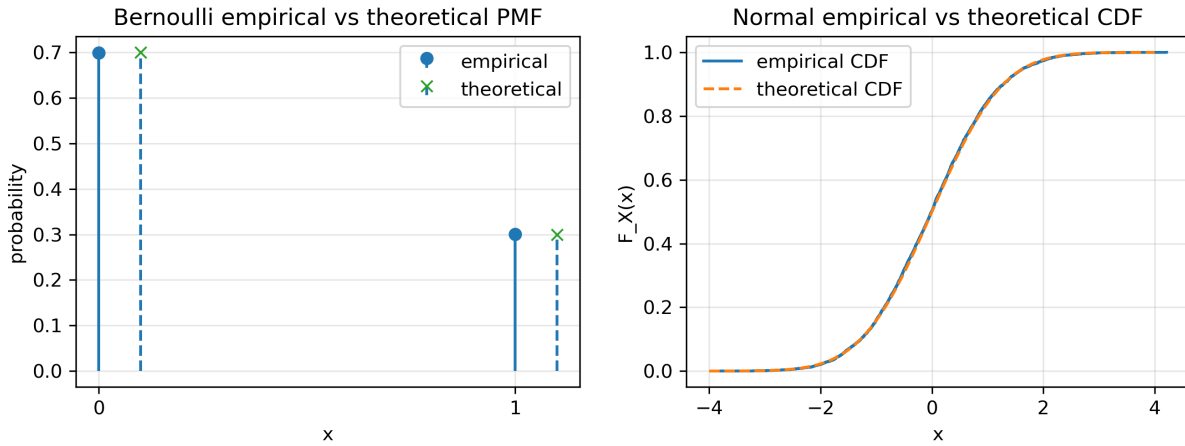


Figure 5.1: Empirical vs. theoretical (left) PMF for a Bernoulli random variable and (right) CDF for a Gaussian random variable – the staircase curve is the empirical CDF; the smooth curve is the analytic CDF, as generated by `Empirical-Distributions-1D.ipynb`.

- an empirical PMF gives the probability of a discrete variable equaling a specific value simply via normalized counts,

$$\hat{P}_{emp}(x) = \frac{1}{N} \sum_{i=1}^N \delta(x_i, x),$$

where $\delta(a, b)$ is the Kronecker δ – unity if $a = b$ and zero otherwise.

- an empirical Cumulative Distribution Function (CDF) is

$$\hat{F}_{emp}(x) = \frac{1}{N} \sum_{i=1}^N \mathbf{1}\{x_i \leq x\}.$$

Left panel of Fig. 5.1 shows the empirical and theoretical PMFs for a Bernoulli random variable. Right panel of Fig. 5.1 shows the empirical and theoretical CDFs for a Gaussian random variable, illustrating how the empirical CDF converges to the true CDF as N grows.

Exercise 5.1.4 (Empirical Convergence and the Law of Large Numbers). Using the notebook `Empirical-Distributions-1D.ipynb`:

1. For Bernoulli, Poisson, and Normal distributions, generate Independent Identically Distributed – i.i.d. – samples and compute the running sample mean

$$\hat{m}_N = \frac{1}{N} \sum_{i=1}^N X_i$$

as a function of N .

2. Plot \hat{m}_N versus N on a log scale and compare with the true mean, as in Fig. 5.2.
3. Explain how these plots illustrate the Law of Large Numbers.

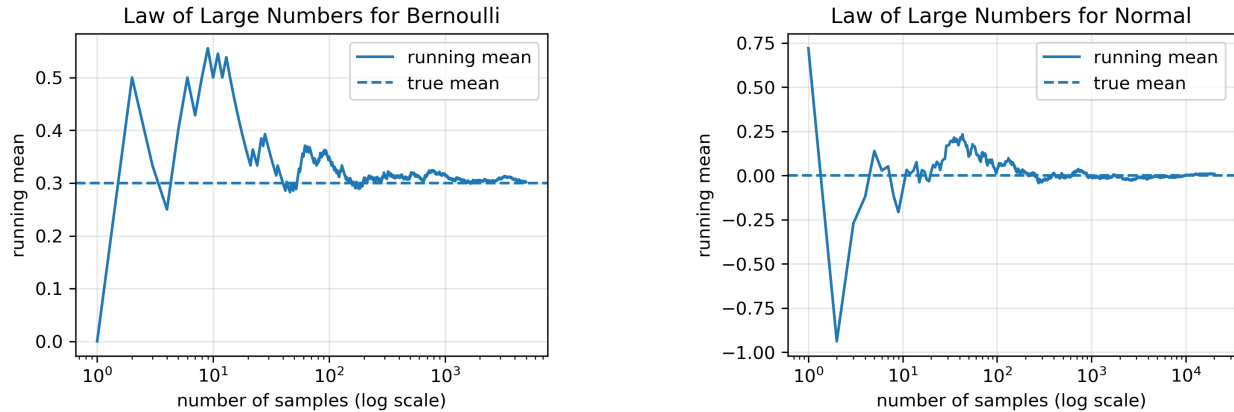


Figure 5.2: Law of Large Numbers in action: running sample mean for Bernoulli (left) and Normal (right) distributions converging toward the true mean. Generated by `Empirical-Distributions-1D.ipynb`.

5.1.5 Transformations of Random Variables

Later in this chapter we will study *change of variables*, *pushforward distributions*, and *normalizing flows*. The notebook `Transformations-1D.ipynb` illustrates these topics computationally.

Example 5.1.5 (Deterministic Transformations $Y = g(X)$). *If X has PDF p_X and $Y = g(X)$ is a smooth, monotone transformation, then*

$$p_Y(y) = p_X(g^{-1}(y)) \left| \frac{d}{dy} g^{-1}(y) \right|.$$

The notebook implements and visualizes three cases:

- *affine map* $Y = aX + b$,
- *nonlinear squaring* $Y = X^2$,
- *saturating nonlinearity* $Y = \tanh(X)$.

Fig. 5.3 shows a multi-panel summary of these transformations, comparing empirical histograms with analytic densities where available.

Exercise 5.1.5 (Comparing Nonlinear Transformations). *Using `Transformations-1D.ipynb`:*

1. *For $X \sim \mathcal{N}(0, 1)$, numerically compare the empirical distribution of $Y = X^2$ with the analytic density obtained via change of variables.*
2. *Repeat for $Y = \tanh(X)$ with different input variances, and discuss how saturation affects the output distribution.*
3. *Comment on how local stretching/compression of the map g is reflected in the shape of p_Y .*

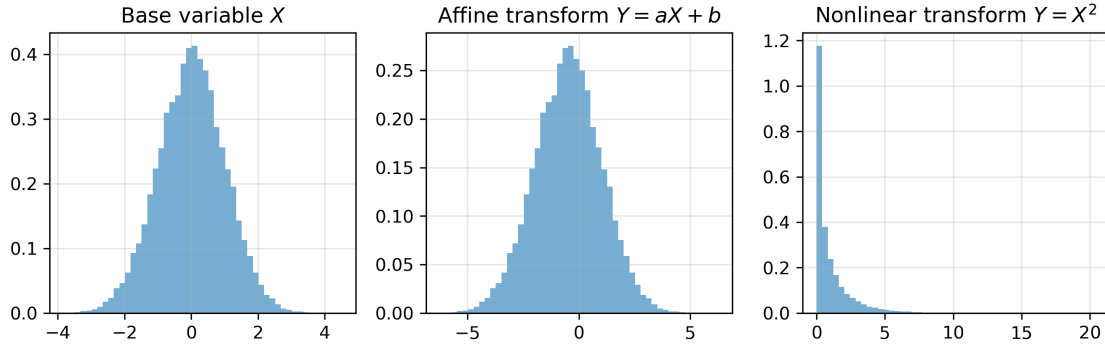


Figure 5.3: Multi-panel view of one-dimensional transformations $Y = g(X)$: base variable X , affine transform $Y = aX + b$, and nonlinear squaring $Y = X^2$. Generated by `Transformations-1D.ipynb`.

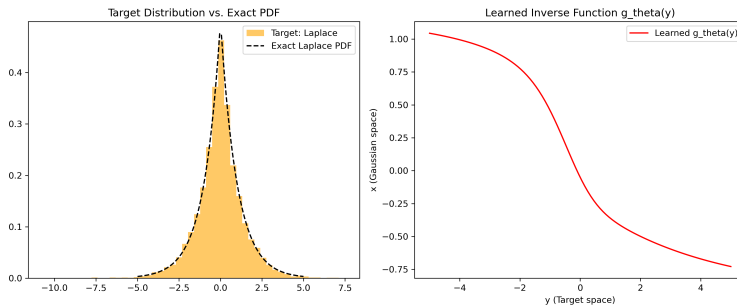


Figure 5.4: A simple one-dimensional normalizing flow: a learned inverse map g_θ pushes samples from a non-Gaussian target back to a standard Gaussian base. Generated by `Normalizing-Flow-1D.ipynb`.

5.1.6 A First Normalizing Flow in 1D

Modern generative models frequently construct complex target distributions by transforming simple base distributions through *invertible* maps (flows). The notebook `Normalizing-Flow-1D.ipynb` implements a simple instance of this idea in one dimension.

Example 5.1.6 (Learning an Inverse Map with a Normalizing Flow). *Let Y be a non-Gaussian target variable (e.g., Laplace), and let $Z \sim \mathcal{N}(0, 1)$ be a standard Gaussian. A one-dimensional normalizing flow learns an invertible map f_θ such that $f_\theta(Z)$ has the same law as Y , or equivalently an inverse map g_θ that sends Y back to Z .*

The notebook trains g_θ by minimizing a KL-based objective derived from the change-of-variables formula. Fig. 5.4 shows the learned inverse transform and its effect on the distribution of the transformed samples.

Exercise 5.1.6 (Extending the 1D Flow). *Modify `Normalizing-Flow-1D.ipynb` to:*

1. *Change the target distribution (e.g., heavier tails or multimodal).*
2. *Increase the depth or width of the neural network implementing g_θ .*

3. Compare the quality of the learned inverse map and the match to the Gaussian base for different architectures.

Relate your observations to the theoretical change-of-variables formula introduced earlier.

5.2 Transforming Probability Distributions

In the previous section, *Primer for Probability Spaces & Random Variables*, we introduced probability spaces, random variables, their distributions, and empirical approximations. Here we build on that material and ask:

How do probability distributions change when we transform, approximate, or learn them?

We focus on three tightly connected themes:

- the **change-of-variables** formula for deterministic transformations $Y = f(X)$,
- **empirical** and **smoothed** (regularized) distributions,
- **normalizing flows**, which learn invertible transformations between simple and complex distributions.

Each topic is presented in the now familiar pattern: material → example → exercise.

5.2.1 Change of Variables in One Dimension

Let X be a continuous random variable with PDF $p_X(x)$, and let $Y = f(X)$ be a deterministic transformation. From the viewpoint of Section 5.1, the transformation f induces a new random variable Y on the same probability space, and we would like to express the PDF p_Y of Y in terms of p_X and f .

If f is differentiable and possibly *not* one-to-one, the **change-of-variables formula** in one dimension reads

$$p_Y(y) = \sum_{\text{all pre-images } x: f(x)=y} p_X(x) \left| \frac{dx}{dy} \right|. \quad (5.1)$$

The sum runs over all solutions x of the equation $f(x) = y$. When f is strictly monotone, there is a single pre-image and the sum reduces to a single term. When f is not injective (e.g., $f(x) = x^2$), multiple pre-images contribute.

Example 5.2.1. Squaring a Standard Normal: $Y = X^2$ Let

$$X \sim \mathcal{N}(0, 1), \quad p_X(x) = \frac{1}{\sqrt{2\pi}} e^{-x^2/2}.$$

Consider the nonlinear transformation

$$Y = X^2.$$

For $y > 0$ the equation $y = x^2$ has two solutions $x = \pm\sqrt{y}$, and

$$\frac{dx}{dy} = \pm \frac{1}{2\sqrt{y}}.$$

Applying (5.1):

$$\begin{aligned} p_Y(y) &= p_X(\sqrt{y}) \left| \frac{d}{dy} \sqrt{y} \right| + p_X(-\sqrt{y}) \left| \frac{d}{dy} (-\sqrt{y}) \right| \\ &= \frac{1}{\sqrt{2\pi}} e^{-y/2} \frac{1}{2\sqrt{y}} + \frac{1}{\sqrt{2\pi}} e^{-y/2} \frac{1}{2\sqrt{y}} \\ &= \frac{1}{\sqrt{2\pi y}} e^{-y/2}, \quad y > 0. \end{aligned}$$

Thus $Y = X^2$ has a chi-square distribution with one degree of freedom. Its tail decays exponentially in y , so for large y it resembles an exponential distribution. This is the analytic counterpart of the numerical experiment with $Y = X^2$ in the notebook *Transformations-1D.ipynb* which we already used in the preceding Section.

Exercise 5.2.1. Other Transformations of a Gaussian Let $X \sim \mathcal{N}(0, 1)$.

1. Define $Y = e^X$. Use (5.1) to derive the PDF of Y and identify its distribution.
2. Define $Z = |X|$. Compute the PDF of Z using the two pre-images $\pm z$.
3. Compare your analytic PDFs with numerical histograms produced in *Transformations-1D.ipynb*. Comment on how well the empirical distributions match the analytic densities.

5.2.2 From Spiky to Smooth: Kernel Density Estimation

In many applications, we do not know p_X explicitly. Instead, we observe N i.i.d. samples

$$x_1, \dots, x_N \sim p_X.$$

Then – and re-phrasing what we discussed in the previous Section – the **empirical distribution** is the discrete measure

$$p_{\text{emp}}(x) = \frac{1}{N} \sum_{i=1}^N \delta(x - x_i), \tag{5.2}$$

where $\delta(\cdot)$ is the Dirac delta-function ²

²The **Dirac δ-function** is not a function in the classical sense but a *distribution* (or *generalized function*) acting on test functions. Formally, it is defined as the linear functional satisfying

$$\int_{-\infty}^{\infty} \delta(x - x_0) \varphi(x) dx = \varphi(x_0) \quad \text{for all smooth test functions } \varphi.$$

Intuitively, $\delta(x - x_0)$ is “infinitely peaked” at x_0 with total mass 1, and zero elsewhere. The concept was introduced by P. A. M. Dirac in the 1930s in the context of quantum mechanics, where such objects naturally arise when describing point sources, impulses, or eigen-states of continuous spectra. Rigorous mathematical foundations were later provided through the theory of distributions developed by Schwartz.

While (5.2) is statistically sound, it is extremely irregular: it consists of spikes at the observed samples and is not directly suitable as a smooth model. A standard way to obtain a smooth approximation is **Kernel Density Estimation** (KDE), which replaces each delta with a smooth kernel:

$$p_{\text{KDE}}(x) = \frac{1}{N} \sum_{i=1}^N K_h(x - x_i), \quad (5.3)$$

where $K_h(\cdot)$ is a smoothing kernel with bandwidth $h > 0$. A common choice is the Gaussian kernel

$$K_h(x) = \frac{1}{\sqrt{2\pi h^2}} \exp\left(-\frac{x^2}{2h^2}\right).$$

Small h yields a nearly spiky estimate (low bias, high variance), while large h produces a very smooth but potentially biased estimate.

Regularization Viewpoint. The transition from P_{emp} to P_{KDE} can be interpreted as *regularization*: instead of fitting every sample exactly with a delta spike, we enforce additional structure (smoothness) in our estimate. Similar ideas appear when we learn parametric transformations f_θ or g_θ between distributions and penalize overly complex maps.

Example 5.2.2. Regularized Transformation Fit Consider a parametric map $f_\theta : \mathbb{R} \rightarrow \mathbb{R}$ (e.g., a small neural network) that takes samples from X and aims to match a target distribution P_Y (known only through samples). A typical regularized loss has the form

$$\mathcal{L}(\theta) = \mathbb{E}_{X \sim P_{\text{emp}}} [d(f_\theta(X), Y)] + \lambda R(\theta),$$

where:

- $d(\cdot, \cdot)$ is a data-fit or discrepancy term between $f_\theta(X)$ and target samples Y ;
- $R(\theta)$ is a regularizer (e.g., weight decay, smoothness penalty) that discourages overly complex transformations;
- $\lambda > 0$ balances fit and regularization.

This structure foreshadows what we will do in normalizing flows, where f_θ or g_θ must be invertible and sufficiently smooth.

Exercise 5.2.2. Empirical vs. Smoothed Estimates Using *Empirical-Distributions-1D.ipynb* as a template:

1. Draw $N = 5000$ samples from a distribution with exponential tails, e.g.,

$$p_X(x) \propto e^{-|x|}, \quad x \in \mathbb{R}.$$

2. Plot the empirical histogram and overlay the true PDF (up to normalization).
3. Implement a Gaussian-kernel KDE (5.3) with several bandwidths h . Compare the KDE curves to the empirical histogram and to the target PDF.
4. Discuss the bias-variance trade-off as h varies. Which values of h give the most visually and quantitatively reasonable approximation?

5.2.3 From Gaussian to Arbitrary Distributions: Normalizing Flows

Example 5.2.1 showed how a *fixed* nonlinear transformation can turn a simple Gaussian into a non-Gaussian distribution. In many AI applications, we want the reverse: given samples from a complex target distribution, we want to *learn* a map that relates it to a simple base distribution such as a standard Normal. This is the idea behind **normalizing flows**³.

We typically:

- choose a simple base variable $Z \sim \mathcal{N}(0, 1)$,
- learn an invertible map f_θ such that $Y = f_\theta(Z)$ matches a target distribution,
- or equivalently learn an inverse map $g_\theta = f_\theta^{-1}$ that sends target samples Y back to the base Z .

Change of Variables for Flows. If f_θ (or g_θ) is differentiable and invertible, the one-dimensional change-of-variables formula gives

$$p_Y(y) = p_Z(g_\theta(y)) |\partial_y g_\theta(y)|, \quad g_\theta = f_\theta^{-1}.$$

In many flow models we minimize a Kullback–Leibler divergence between the transformed distribution and a reference (see also Section 6.2.3), leading to loss functions of the form

$$\mathcal{L}(\theta) = \mathbb{E}_{Y \sim P_Y} \left[\underbrace{\frac{1}{2} g_\theta(Y)^2}_{\text{Gaussian energy}} + \underbrace{\log |\partial_y g_\theta(Y)|}_{\text{Jacobian term}} \right] + R(\theta), \quad (5.4)$$

where $R(\theta)$ is a regularizer.

Example 5.2.3. Gaussian–Laplace Matching via an Inverse Flow Consider a Laplace target

$$Y \sim \text{Laplace}(0, 1), \quad p_Y(y) = \frac{1}{2} e^{-|y|},$$

and a base $Z \sim \mathcal{N}(0, 1)$. We seek an inverse map g_θ such that $g_\theta(Y) \approx Z$ in distribution.

- **Analytic inverse via CDFs.** The CDF of the Laplace distribution is

$$F_Y(y) = \begin{cases} \frac{1}{2} e^y, & y < 0, \\ 1 - \frac{1}{2} e^{-y}, & y \geq 0, \end{cases}$$

while the CDF of Z is $\Phi(z)$. Matching CDFs, $F_Y(y) = \Phi(z)$, gives an exact inverse map

$$g(y) = \Phi^{-1}(F_Y(y)).$$

³The term *flow* emphasizes that the transformation f_θ transports probability mass in a structured, continuous, and invertible manner, analogous to the flow of particles under a deterministic dynamical system, where distributions evolve according to a pushforward induced by the map

- **Learned inverse.** In `Normalizing-Flow-1D.ipynb`, we parametrize g_θ by a small neural network and minimize (5.4) using samples from $Y \sim \text{Laplace}(0, 1)$. A successful training run produces g_θ that closely approximates g , and transformed samples $g_\theta(Y)$ that are nearly standard Normal.

This simple one-dimensional flow illustrates how learned transformations connect the measure-theoretic change-of-variables formula of Section 5.1 to practical generative modeling.

Exercise 5.2.3. Experimenting with the 1D Normalizing Flow Using `Normalizing-Flow-1D.ipynb`:

1. Train an inverse flow g_θ for the Laplace target as in the example above. Visualize:
 - the map $y \mapsto g_\theta(y)$,
 - histograms of $g_\theta(Y)$ compared to the standard Normal PDF.
2. Compare $g_\theta(y)$ to the analytic inverse $g(y) = \Phi^{-1}(F_Y(y))$. How close are they, and where do discrepancies appear?
3. Change the target distribution to a heavier-tailed law, e.g.,

$$p_Y(y) \propto (1 + y^2)^{-\alpha}, \quad \alpha > 1,$$

and repeat the experiment. Comment on how tail behavior affects training and the learned map.

5.2.4 Normalizing Flows and Optimal Transport (Preview)

In the standard normalizing-flow setup, an invertible map is trained so that its pushforward distribution matches the data distribution. In Section 5.2.3 we saw how likelihood-based training (or, equivalently, minimizing a KL divergence) ensures that the *final* distribution produced by the flow is correct. However, nothing in that formulation explicitly controls *how far* individual points move under the learned transformation.

This raises the following guiding question:

Can we encourage flows that move samples “as little as possible” while still matching the target distribution?

This question connects normalizing flows to the mathematical field of **Optimal Transport** (OT), which studies the most efficient way to move mass between two probability distributions. Although we will postpone the formal definition of transport costs and Wasserstein distances until Chapter 6, it is useful to preview how OT-style ideas arise naturally in flow-based generative modeling.

Transport-Based Viewpoint (Conceptual). Given a source distribution P_X and a target distribution P_Y , one may ask for a map T that pushes P_X onto P_Y while minimizing the average “movement cost” $c(X, T(X))$. In OT, a common choice is a quadratic cost $c(x, y) = \|x - y\|^2$, favoring transport plans that displace points minimally. A likelihood-trained normalizing flow seeks a correct pushforward, but does not address the magnitude of pointwise displacements.

Regularizing Flows Toward Minimal Transport. One way to introduce OT flavor into normalizing flows is to augment the standard loss with a *transport penalty*:

$$\mathcal{L}_{\text{OT}}(\theta) = \mathbb{E}_{X \sim P_X}[-\log p_Y(T_\theta(X))] + \lambda \mathbb{E}_{X \sim P_X}[\|X - T_\theta(X)\|^2].$$

The first term is the likelihood objective familiar from Section 5.2.3 (and fully developed via KL divergence in Chapter 6). The second term favors transformations that resemble those arising in Optimal Transport, and encourages minimal displacement among plausible maps.

Flow Matching and Continuous-Time Limits (Preview). Recent generative-modeling methods (e.g., *flow matching*) build continuous-time interpolations between P_X and P_Y by training time-dependent vector fields. These approaches blur the line between normalizing flows and diffusion-based models, and often exhibit strong connections to transport geometry. We will revisit these ideas in Chapter 9, where score-based diffusion models, probability–flow ODEs, and flow matching appear as continuous-time analogues of the invertible transformations studied in this chapter.

How This Fits into Later Chapters.

- In Chapter 6 we develop a systematic framework for *comparing distributions*, including KL divergence and, later, *Wasserstein distances*, which measure the minimal transport cost between distributions. These distances formalize the intuitive “minimal movement” principle hinted at above.
- In Chapter 9 we return to the geometry of probability transformations through score-based diffusion models and probability–flow ODEs. There we encounter *flow matching*, an OT-inspired method that constructs generative models by matching infinitesimal transports rather than static maps.
- The empirical and parametric tools introduced in Section 5.2 reappear there as building blocks for these continuous-time generative frameworks.

5.3 Multivariate Random Variables

The previous sections developed probability theory in the univariate setting: probability spaces, random variables, empirical distributions, change-of-variables, and simple transformations such as those used in normalizing flows. However, most real-world systems — from generative AI models to physical networks, financial portfolios, and sensor arrays — involve *multiple* interacting random variables. This section extends the framework to the multivariate case.

We introduce:

- Random vectors and their joint and marginal distributions;
- The notion of independence for collections of random variables;
- Algebraic and linear operations on multivariate random variables;

- The structure and special closure properties of multivariate Gaussians;
- Empirical multivariate statistics and sampling in higher dimensions, including non-Gaussian examples.

The multivariate setting is the foundation for later chapters: in Chapter 6 we compare multi-dimensional distributions using KL divergence and Wasserstein distance, and in Chapters 7–9 we study stochastic processes, diffusion models, and probability flows that operate on high-dimensional spaces.

5.3.1 Random Vectors, Joint Distributions, and Independence

A **random vector** is a collection of random variables defined on a common probability space. Formally, a d -dimensional random vector is

$$X = (X_1, \dots, X_d)^\top : \Omega \rightarrow \mathbb{R}^d.$$

Its law is a probability distribution on \mathbb{R}^d .

Joint Distributions. For discrete-valued X , the *joint PMF* is

$$P_X(x_1, \dots, x_d) = P(X_1 = x_1, \dots, X_d = x_d).$$

For continuous-valued X , the *joint PDF* $p_X(x)$ satisfies, for any rectangle $A_1 \times \dots \times A_d$,

$$P(X_1 \in A_1, \dots, X_d \in A_d) = \int_{A_1} \dots \int_{A_d} p_X(x_1, \dots, x_d) dx_d \dots dx_1.$$

Marginals. The distribution of a single coordinate X_i is obtained by summing or integrating out the others. For example, for a continuous X ,

$$p_{X_i}(x_i) = \int_{\mathbb{R}^{d-1}} p_X(x_1, \dots, x_d) dx_1 \dots dx_{i-1} dx_{i+1} \dots dx_d.$$

More generally, any subset of coordinates forms a lower-dimensional random vector with its own joint law.

Independence. Random variables X_1, \dots, X_d are *mutually independent* if their joint distribution factorizes:

$$P_X(x_1, \dots, x_d) = \prod_{i=1}^d P_{X_i}(x_i)$$

in the discrete case, or

$$p_X(x_1, \dots, x_d) = \prod_{i=1}^d p_{X_i}(x_i)$$

in the continuous case. Intuitively, knowing any subset of coordinates does not change our beliefs about the others.

Mean Vector and Covariance Matrix. The *mean* (or expectation) of a random vector X is

$$\mu = \mathbb{E}[X] = \begin{bmatrix} \mathbb{E}[X_1] \\ \vdots \\ \mathbb{E}[X_d] \end{bmatrix}.$$

The *covariance matrix* Σ is the $d \times d$ matrix with entries

$$\Sigma_{ij} = \text{Cov}(X_i, X_j) = \mathbb{E}[(X_i - \mu_i)(X_j - \mu_j)].$$

Diagonal entries are variances; off-diagonal entries measure linear dependence between coordinates.

Example 5.3.1. Joint, Marginal, and Independence in 2D Let (X_1, X_2) take values in $\{0, 1\}^2$ with joint probabilities

$$P_X(0, 0) = \frac{1}{4}, \quad P_X(0, 1) = \frac{1}{4}, \quad P_X(1, 0) = \frac{1}{4}, \quad P_X(1, 1) = \frac{1}{4}.$$

Then

$$P_{X_1}(0) = P_{X_1}(1) = \frac{1}{2}, \quad P_{X_2}(0) = P_{X_2}(1) = \frac{1}{2},$$

and $P_X(x_1, x_2) = P_{X_1}(x_1)P_{X_2}(x_2)$, so X_1 and X_2 are independent.

If instead $P_X(0, 0) = P_X(1, 1) = \frac{1}{2}$ and $P_X(0, 1) = P_X(1, 0) = 0$, the marginals are still Bernoulli with parameter $\frac{1}{2}$, but $P_X(x_1, x_2) \neq P_{X_1}(x_1)P_{X_2}(x_2)$. Here X_1 and X_2 are perfectly correlated: $X_1 = X_2$ almost surely.

Exercise 5.3.1. Construct an example of a 3-dimensional random vector (X_1, X_2, X_3) such that:

- all pairwise marginals (X_i, X_j) have the same distribution,
- but the three variables are not mutually independent.

Describe the joint PMF explicitly and check the factorization property.

5.3.2 Algebraic and Linear Operations on Random Vectors

Algebraic operations on random vectors are defined coordinate-wise. For example, for two random vectors $X, Y \in \mathbb{R}^d$,

$$Z = X + Y$$

is the random vector with coordinates $Z_i = X_i + Y_i$. Scalar multiples and more general linear combinations are defined similarly.

Expectations and Covariances under Linear Maps. If $Y = AX + b$ for a deterministic matrix A and vector b , then

$$\mathbb{E}[Y] = A\mathbb{E}[X] + b, \quad \text{Cov}(Y) = A \text{Cov}(X) A^\top.$$

These identities hold for *any* distribution of X (not just Gaussian).

The distributional shape, however, is generally *not* preserved. Summing or transforming non-Gaussian variables typically yields a different functional form. Multivariate Gaussians are special because many such operations stay within the same family; this is one reason they are so ubiquitous in probabilistic modeling.

Example 5.3.2. Sum and Scaling of Independent Gaussians Let $X_1, X_2 \sim \mathcal{N}(0, 1)$ be independent.

Sum. Define $Z = X_1 + X_2$. Using convolution of independent densities,

$$p_Z(z) = \int_{\mathbb{R}} p_{X_1}(x) p_{X_2}(z - x) dx = \frac{1}{\sqrt{4\pi}} e^{-z^2/4},$$

so $Z \sim \mathcal{N}(0, 2)$. The sum of independent Gaussians is again Gaussian.

Scaling. For a constant a , define $W = aX_1$. A 1D change of variables gives

$$p_W(w) = \frac{1}{|a|} p_{X_1}\left(\frac{w}{a}\right) = \frac{1}{\sqrt{2\pi a^2}} e^{-w^2/(2a^2)},$$

so $W \sim \mathcal{N}(0, a^2)$. Again, we remain in the Gaussian family.

Exercise 5.3.2. Let X_1, X_2 be independent with a common Laplace (double-exponential) distribution

$$p_{X_i}(x) = \frac{1}{2} e^{-|x|}.$$

1. Show that $Y = X_1 + X_2$ does not have a Laplace distribution by computing its PDF (via convolution) explicitly.
2. Compare the shape of p_Y to a Gaussian and to a Laplace; which tails are heavier?
3. Contrast this with the Gaussian example above. What does this say about the closure of distribution families under summation?

5.3.3 Multivariate Gaussian Distributions

A d -dimensional random vector X is Gaussian (or Normal) if it has density

$$p_X(x) = \frac{1}{(2\pi)^{d/2} |\Sigma|^{1/2}} \exp\left\{-\frac{1}{2}(x - \mu)^\top \Sigma^{-1}(x - \mu)\right\},$$

with mean $\mu \in \mathbb{R}^d$ and covariance matrix $\Sigma \succ 0$.

Among all distributions on \mathbb{R}^d , the multivariate Gaussian is particularly special because it is *closed* under many natural operations:

- marginalization (dropping coordinates),
- conditioning on linear observations,
- linear transformations $Y = AX + b$,
- summation of independent Gaussian vectors.

For general distributions these operations typically leave the original family, but for Gaussians they remain Gaussian. This “invariance under linear operations” is a major reason why Gaussians are so analytically tractable and so widely used.

Marginalization. Partition X into two blocks:

$$X = \begin{bmatrix} X_1 \\ X_2 \end{bmatrix}, \quad \mu = \begin{bmatrix} \mu_1 \\ \mu_2 \end{bmatrix}, \quad \Sigma = \begin{bmatrix} \Sigma_{11} & \Sigma_{12} \\ \Sigma_{12}^\top & \Sigma_{22} \end{bmatrix}.$$

Then

$$X_1 \sim \mathcal{N}(\mu_1, \Sigma_{11}), \quad X_2 \sim \mathcal{N}(\mu_2, \Sigma_{22}).$$

Conditioning. The conditional distribution of X_1 given $X_2 = a$ is Gaussian:

$$X_1 | X_2 = a \sim \mathcal{N}(\mu_{1|2}, \Sigma_{1|2}),$$

with

$$\mu_{1|2} = \mu_1 + \Sigma_{12}\Sigma_{22}^{-1}(a - \mu_2), \quad \Sigma_{1|2} = \Sigma_{11} - \Sigma_{12}\Sigma_{22}^{-1}\Sigma_{12}^\top.$$

This is a concrete instance of Bayes’ rule in the Gaussian setting and will reappear in various guises (Kalman filters, Gaussian processes, linear Bayesian inference).

Linear Transformations and Sums. If $Y = AX + b$ with $A \in \mathbb{R}^{m \times d}$ and $b \in \mathbb{R}^m$, then

$$Y \sim \mathcal{N}(A\mu + b, A\Sigma A^\top).$$

In particular, if $X^{(1)}, X^{(2)}$ are independent with $X^{(k)} \sim \mathcal{N}(\mu^{(k)}, \Sigma^{(k)})$, then

$$X^{(1)} + X^{(2)} \sim \mathcal{N}(\mu^{(1)} + \mu^{(2)}, \Sigma^{(1)} + \Sigma^{(2)}).$$

Example 5.3.3. Gaussian Conditioning in Practice Consider

$$X = \begin{bmatrix} X_1 \\ X_2 \end{bmatrix} \sim \mathcal{N}\left(\begin{bmatrix} 0 \\ 0 \end{bmatrix}, \begin{bmatrix} 2 & 1 \\ 1 & 1 \end{bmatrix}\right).$$

From the formulas above,

$$\mu_{1|2} = 0 + 1 \cdot 1^{-1} \cdot (1 - 0) = 1, \quad \Sigma_{1|2} = 2 - 1 \cdot 1^{-1} \cdot 1 = 1,$$

so

$$X_1 | X_2 = 1 \sim \mathcal{N}(1, 1).$$

Such conditioning formulas underpin Bayesian linear regression, Kalman filtering, and Gaussian process prediction.

Exercise 5.3.3. Prove the marginalization, conditioning, and linear-transformation properties stated above by completing the Gaussian integrals and manipulations. Then verify them numerically by sampling from a chosen multivariate Gaussian and estimating:

- empirical marginals,
- empirical conditionals $X_1 | X_2 \in [a, a + \Delta]$,
- empirical distributions of linear transforms $Y = AX + b$.

Compare your empirical estimates with the analytical predictions as the sample size grows.

5.3.4 Empirical Multivariate Statistics

The empirical distribution and Law of Large Numbers experiments of Section 5.1 extend naturally to higher dimensions. Given i.i.d. samples

$$x_1, \dots, x_N \in \mathbb{R}^d,$$

we define the **sample mean** and **sample covariance** as

$$\hat{\mu} = \frac{1}{N} \sum_{i=1}^N x_i, \quad \hat{\Sigma} = \frac{1}{N} \sum_{i=1}^N (x_i - \hat{\mu})(x_i - \hat{\mu})^\top.$$

By the multivariate Law of Large Numbers,

$$\hat{\mu} \rightarrow \mu, \quad \hat{\Sigma} \rightarrow \Sigma \quad \text{almost surely as } N \rightarrow \infty.$$

Multivariate sampling reveals geometric phenomena not present in 1D: concentration of measure, anisotropy, correlated directions, and, for non-Gaussian data, multimodality and heavy tails. The accompanying Jupyter/Python notebook `Empirical-Multivariate.ipynb` implements these constructions and generates the figures used in this subsection. It can be used to:

- Visualize scatter plots and covariance ellipses in 2D;
- Track convergence of $\hat{\mu}$ and $\hat{\Sigma}$;
- Study the effects of correlations and linear transforms (whitening, PCA-like decorrelation);
- Compare Gaussian and non-Gaussian (mixture and heavy-tailed) clouds of points.

Example 5.3.4. Gaussian vs. Non-Gaussian Clouds in 2D

We compare three models for $X \in \mathbb{R}^2$.

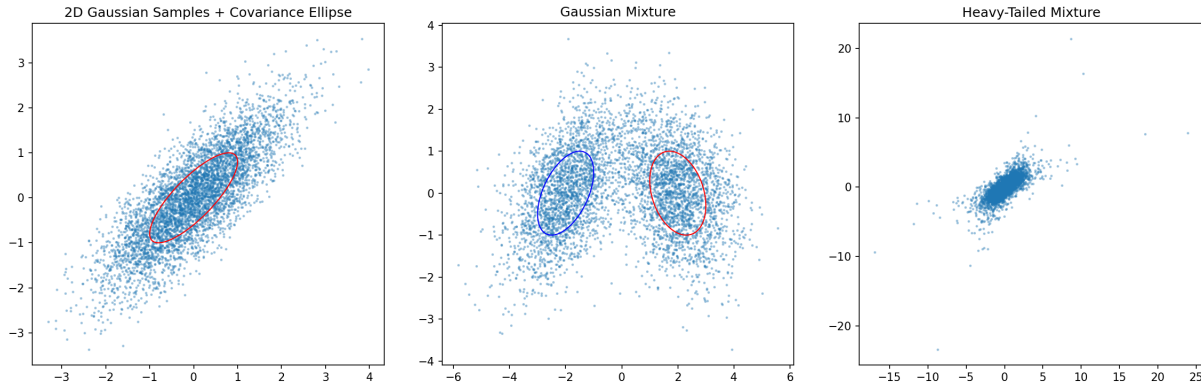


Figure 5.5: Left: Correlated Gaussian: samples and empirical covariance ellipse. Center: Two-component Gaussian mixture: bimodal cloud with a single covariance ellipse. Right: Heavy-tailed mixture: outliers and extended tails despite a finite covariance.

- **Correlated Gaussian.**

$$X^{(G)} \sim \mathcal{N}\left(\begin{bmatrix} 0 \\ 0 \end{bmatrix}, \begin{bmatrix} 1 & 0.8 \\ 0.8 & 1 \end{bmatrix}\right).$$

Scatter plots show an elongated elliptical cloud. As N grows, the empirical $\hat{\mu}$ and $\hat{\Sigma}$ converge to the true mean and covariance, and the covariance ellipse closely matches the visible level sets (left panel of Fig. 5.5).

- **Mixture of two Gaussians.**

$$X^{(M)} \sim \frac{1}{2} \mathcal{N}\left(\begin{bmatrix} -m \\ 0 \end{bmatrix}, I_2\right) + \frac{1}{2} \mathcal{N}\left(\begin{bmatrix} m \\ 0 \end{bmatrix}, I_2\right),$$

with $m > 0$ and I_2 the 2×2 identity. The scatter plot reveals two well-separated clusters. The empirical covariance still converges, but it cannot capture the multimodal structure: the covariance ellipse is centered between the modes and misses the “two-bump” shape (center panel of Figure 5.5).

- **Heavy-tailed mixture.** We modify the second component so that one coordinate follows a heavy-tailed distribution (e.g. a Student- t with a small number of degrees of freedom). The resulting cloud exhibits more extreme points and more spread in the heavy-tailed direction. The covariance still exists and converges, but it hides the frequency and severity of outliers (right panel of Fig. 5.5).

This contrast illustrates both the usefulness and the limitations of second-order statistics: for Gaussians, mean and covariance essentially describe the distribution; for more complex laws, they are only part of the story.

Exercise 5.3.4. Using the accompanying notebook *Empirical-Multivariate.ipynb*:

1. Generate samples from the correlated Gaussian and the two-component Gaussian mixture described in the example. Reproduce left and right panels of Fig. 5.5.

2. For the correlated Gaussian, compute $\hat{\mu}$ and $\hat{\Sigma}$ for increasing N and track their convergence. Compare your convergence curves (see notebook).
3. Plot covariance ellipses and overlay them on scatter plots. For the mixture, comment on what the covariance “sees” and what it misses.
4. Apply a whitening transform – see https://en.wikipedia.org/wiki/Whitening_transformation – based on $\hat{\Sigma}$ and visualize the transformed samples. Are the whitened Gaussians approximately isotropic? What happens to the mixture after whitening? (See also other notebook figures.)
5. Replace one of the components with a heavy-tailed distribution (e.g. Laplace or a Student- t) and repeat. How do heavy tails manifest in sample covariance and in the scatter plots? Compare your results to right panel of Fig. 5.5.

5.4 From Aggregate Behavior to Rare Events

In earlier sections we examined how single random variables behave and how simple transformations (e.g. affine maps) affect their distributions. We now turn to a deeper and more universal question:

What happens when we combine many random variables?

Three classical asymptotic regimes appear again and again in probability, statistics, physics, and modern AI:

1. **Aggregating many small contributions** leads to the *Central Limit Theorem* (Gaussian limit).
2. **Aggregating many rare events** leads to the *Poisson limit*.
3. **Aggregating extreme outcomes** leads to *extreme-value limits* (Gumbel, Fréchet, Weibull).

These regimes complement one another: they describe limit behaviors not of a single variable, but of *collections* of variables, each producing a different form of universality.

The accompanying notebook `Aggregate-Rare-Events.ipynb` illustrates all of these regimes numerically and saves the figures used throughout this section into the `figs-final/chapter5/` folder.

We begin with the most famous result — the Central Limit Theorem (CLT) — and gradually broaden its scope and limitations.

5.4.1 The Central Limit Theorem: Weak Form

Earlier in the chapter we saw that sums of independent Gaussian variables remain Gaussian. The remarkable fact is that *even non-Gaussian* variables, when aggregated in large numbers, produce Gaussian-like behavior.

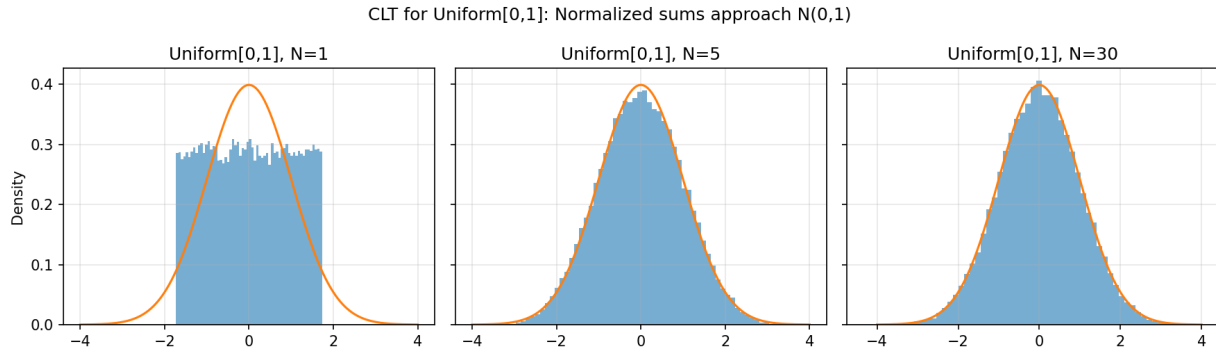


Figure 5.6: CLT for sums of i.i.d. Uniform[0, 1] variables: histograms of normalized sums for increasing N , overlaid with the standard Gaussian density. Generated by `Aggregate-Rare-Events.ipynb`.

Let X_1, \dots, X_N be i.i.d. with mean μ and variance $\sigma^2 < \infty$. Define the normalized sum

$$Z_N = \frac{X_1 + \dots + X_N - N\mu}{\sqrt{N\sigma^2}}.$$

The **Central Limit Theorem** (CLT) states:

$$Z_N \xrightarrow{d} \mathcal{N}(0, 1) \quad \text{as } N \rightarrow \infty.$$

In words:

Large sums of independent finite-variance variables become Gaussian.

This is a cornerstone of statistical modeling: many phenomena appear Gaussian not because their components are Gaussian, but because they are *aggregations of many (uncorrelated or weakly-correlated) contributions*. In the language of Section 5.1, we are looking at the distribution of a function of many i.i.d. samples from a fixed probability space.

Stronger versions. Beyond convergence in distribution, there are “almost sure” refinements (e.g. invariance principles), but the weak form suffices for most applications in applied math and AI.

Example 5.4.1. CLT in Action: Sums of Non-Gaussian Inputs

Let X_i be i.i.d. uniform on $[0, 1]$. For each N , form the normalized sum Z_N and plot its histogram alongside the standard Gaussian density. Even though the uniform law is far from Gaussian, the histograms of Z_N quickly resemble the bell curve as N grows.

Figure 5.6 shows this effect for several values of N . A similar experiment with exponential inputs is shown in Figure 5.7: despite the strong skew of the exponential law, the normalized sums again converge visually to a Gaussian.

The notebook `Aggregate-Rare-Events.ipynb` constructs these panels and can be extended with Quantile-Quantile (Q-Q) plots – see https://en.wikipedia.org/wiki/Q%25E8%2593Q_plot – or empirical CDF overlays to further quantify convergence in distribution.

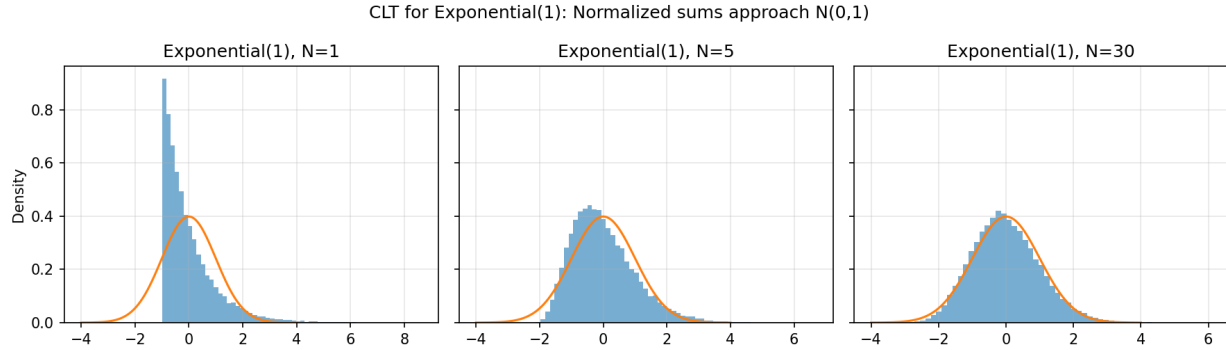


Figure 5.7: CLT for sums of i.i.d. exponential variables: strong skew in the one-variable distribution, but Gaussian behavior emerges for normalized sums. Generated by `Aggregate-Rare-Events.ipynb`.

Exercise 5.4.1. Using `Aggregate-Rare-Events.ipynb` as a template or starting from scratch, pick one non-Gaussian distribution (e.g. exponential, uniform, Bernoulli) and simulate normalized sums Z_N . For increasing N :

1. Plot histograms of Z_N and overlay the standard Gaussian density.
2. Add Q–Q plots or empirical CDFs to visualize convergence in distribution.
3. Compare convergence rates across different input distributions by inspecting how quickly the histograms and Q–Q plots align with the Gaussian reference.

5.4.2 Large Deviations: Tail Form of the CLT

While the CLT describes the *typical* fluctuations of order \sqrt{N} , we may also ask:

How likely are atypically large deviations?

Large deviation theory provides the answer. Under mild assumptions,

$$\mathbb{P}\left(\frac{1}{N} \sum_{i=1}^N X_i = x\right) \approx \exp(-N \Phi^*(x)),$$

where Φ^* is the **Cramér rate function**. It is convex, non-negative, and minimized at $x = \mu$. Thus the probability of extreme deviations decays *exponentially in N* . This complements the CLT: the CLT describes central fluctuations, while large deviation theory describes rare events far in the tails.

Example 5.4.2. Rare Averages Are Exponentially Unlikely

Consider $X_i \sim \text{Bernoulli}(1/2)$ and the sample average $\bar{X}_N = \frac{1}{N} \sum_{i=1}^N X_i$. The notebook estimates

$$\mathbb{P}(\bar{X}_N \geq 0.7)$$

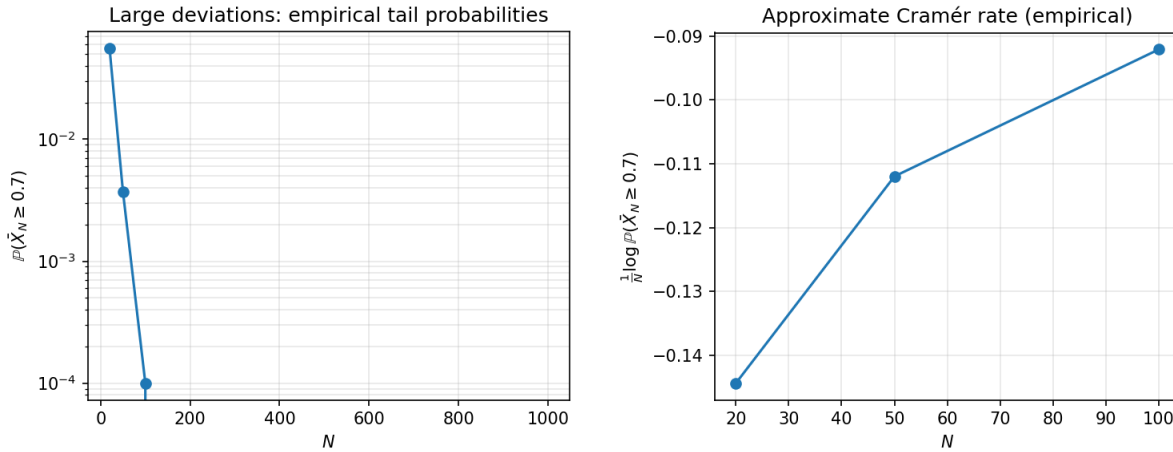


Figure 5.8: Left: Empirical tail probabilities $\mathbb{P}(\bar{X}_N \geq 0.7)$ for Bernoulli(1/2) averages, plotted versus N on a log scale. Right: Scaled log-probabilities $\frac{1}{N} \log \mathbb{P}(\bar{X}_N \geq 0.7)$ approaching a negative constant, illustrating a Cramér-type rate. Generated by `Aggregate-Rare-Events.ipynb`.

for increasing N . Left panel of Fig. 5.8 shows the empirical tail probabilities on a log scale, while the right panel plots

$$\frac{1}{N} \log \mathbb{P}(\bar{X}_N \geq 0.7)$$

versus N . The approximate linear decay in the log-probabilities and the convergence of the scaled log-probabilities to a negative constant provide (an early) numerical evidence for an exponential $\exp(-N\Phi^*(x))$ law.

Even moderate deviations (e.g. $\bar{X}_N \approx 0.6$) become exponentially unlikely as N grows; the figures make this suppression visually apparent.

Exercise 5.4.2. Using `Aggregate-Rare-Events.ipynb` or your own code:

1. For a chosen distribution (e.g. Bernoulli, uniform, or exponential), empirically estimate $\mathbb{P}(\frac{1}{N} \sum X_i \geq x)$ for several values of $x > \mu$.
2. Plot the tail probabilities on a log scale as a function of N and check whether the decay appears exponential.
3. Compute $\frac{1}{N} \log \mathbb{P}(\frac{1}{N} \sum X_i \geq x)$ and compare empirical slopes to theoretical Cramér-rate predictions where available.

5.4.3 When CLT Fails: Heavy Tails and Stable Laws

The CLT requires $\text{Var}(X) < \infty$. If the variance is infinite, the normalized sum *does not* converge to a Gaussian. Heavy-tailed distributions — often encountered in practice — can violate this assumption.

A distribution with power-law tails

$$p_X(x) \sim C |x|^{-(\alpha+1)}$$

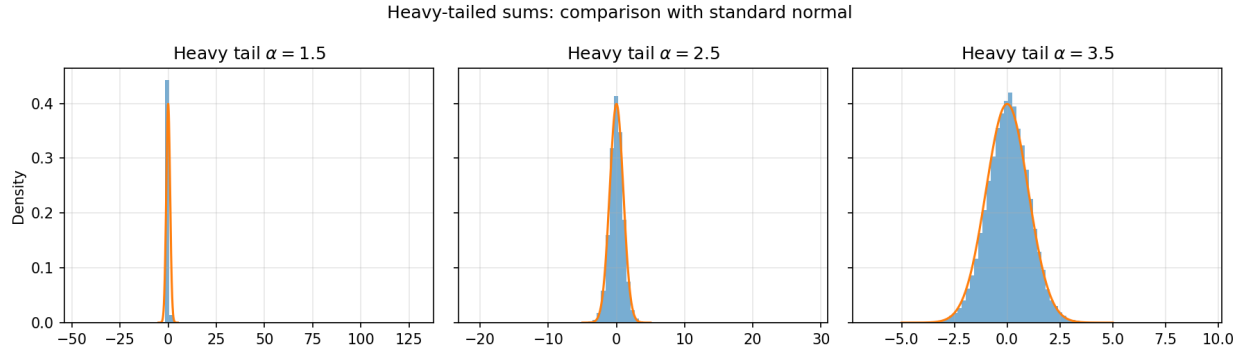


Figure 5.9: Normalized sums from finite-variance (Gaussian) vs. heavy-tailed inputs, with Gaussian reference density. Heavy tails persist under aggregation, illustrating breakdown of the CLT and emergence of non-Gaussian stable behavior. Generated by `Aggregate-Rare-Events.ipynb`.

has finite variance only if $\alpha > 2$. For $0 < \alpha \leq 2$, the variance diverges and Gaussian behavior disappears.

Instead, sums converge to a **stable distribution**, of which the Gaussian ($\alpha = 2$) is just one special case.

Example 5.4.3. Sums of Heavy-Tailed Variables

The notebook compares normalized sums of i.i.d. Gaussian and heavy-tailed variables with the same mean (zero), using histograms and Gaussian overlays. In the Gaussian case, the histograms rapidly become bell-shaped. In the heavy-tailed case, Figure 5.9 shows that even for large N , the distribution retains pronounced tails and outliers, clearly deviating from the Gaussian reference.

A particularly extreme case is the Cauchy distribution, which is stable with tail exponent $\alpha = 1$: if X_i are i.i.d. Cauchy, then $S_N = X_1 + \dots + X_N$ remains Cauchy for all N .

Exercise 5.4.3. Consider random variables with PDF

$$p(x) = \frac{C}{(1 + |x|)^{\alpha+1}}.$$

1. Show that $\mathbb{E}[X^2] < \infty$ if and only if $\alpha > 2$.
2. Using `Aggregate-Rare-Events.ipynb` as a guide, numerically simulate normalized sums for $\alpha = 1.5, 2.5, 3.5$ and compare histograms to the Gaussian density.
3. For $\alpha \leq 2$, verify that normalized sums do not resemble Gaussian distributions and discuss how the heavy tails manifest in the histograms and in occasional large outliers.

5.4.4 Rare Events in Many Trials: The Poisson Limit

The CLT describes the regime where many small contributions accumulate and the variance (of the sum) grows without bound (while variance of the mean – normalized sum – converge to a constant). A completely different universal behavior appears when we have:

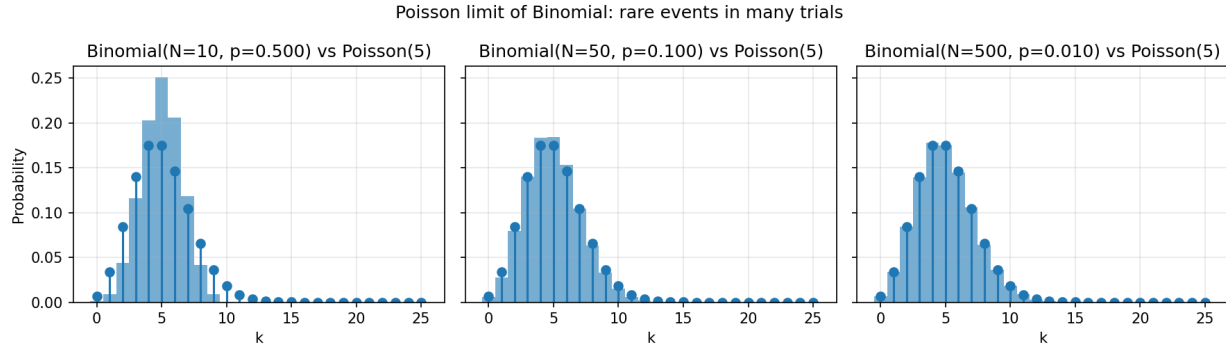


Figure 5.10: Poisson limit of binomial counts: binomial histograms for increasing N (with $\lambda = N\rho$ fixed) compared to the $\text{Poisson}(\lambda)$ PMF. Generated by `Aggregate-Rare-Events.ipynb`.

Many trials, but extremely rare successes.

Let $X_i \sim \text{Bernoulli}(\rho)$ and $S_N = \sum_{i=1}^N X_i$. If we let $N \rightarrow \infty$ while keeping $\lambda = N\rho$ fixed, then

$$S_N \xrightarrow{d} \text{Poisson}(\lambda).$$

This is the **Poisson limit theorem**: the universal distribution of counts of rare, nearly independent events.

Relation to the CLT. The appearance of the Poisson limit should not be interpreted as a failure of the Central Limit Theorem. Rather, the CLT is simply *not entered* in this regime. Indeed, while the CLT requires the variance of the sum to grow without bound, here we have

$$\text{Var}(S_N) = N\rho(1 - \rho) \approx \lambda,$$

which remains finite as $N \rightarrow \infty$.

Thus, the Poisson limit and the CLT correspond to two distinct scaling regimes: the CLT describes the accumulation of many *non-negligible* contributions, leading to diverging variance, whereas the Poisson limit captures the statistics of *rare events*, where the expected number of successes and the variance remain $\mathcal{O}(1)$ even as the number of trials grows.

Example 5.4.4. Modeling Defects in a Large-Scale Process

In `Aggregate-Rare-Events.ipynb` we generate samples from $\text{Binomial}(N, \rho)$ with $\rho = \lambda/N$ and fixed λ . Fig. (5.10) compares the resulting histograms to the $\text{Poisson}(\lambda)$ PMF for increasing N . Already for moderate N , the binomial histograms lie almost exactly on top of the Poisson bars.

A concrete interpretation: if a machine produces a defective part with probability 0.001, then after inspecting $N = 1000$ parts, $S_N \sim \text{Binomial}(1000, 0.001)$ is well-approximated by $\text{Poisson}(1)$, greatly simplifying probability calculations.

Exercise 5.4.4 (Quantifying and Stress-Testing the Poisson Approximation). Fix $\lambda = 5$ and let $\rho = \lambda/N$.

1. **Quantitative accuracy.** Using `Aggregate-Rare-Events.ipynb`, estimate the distance between $\text{Binomial}(N, \lambda/N)$ and $\text{Poisson}(\lambda)$ as N varies. Choose at least one quantitative metric, for example:

- total variation distance,
- KL divergence,
- maximum absolute difference of PMFs.

Plot this distance versus N and identify its scaling behavior.

2. **Beyond visual agreement.** Show that visual overlap of histograms can be misleading. For a fixed N , identify regions of the support (e.g. the tails) where the Poisson approximation is systematically biased, even when the bulk appears accurate.
3. **Dependence on λ .** Repeat the analysis for $\lambda = 1, 5, 20$. How does the required N for a given accuracy threshold depend on λ ? Provide an explanation based on the underlying binomial variance and skewness.
4. **Model misspecification.** Suppose the defect probability is not exactly $\rho = \lambda/N$, but instead $\rho = \lambda/N + \delta_N$ with $\delta_N = \mathcal{O}(N^{-1/2})$. Empirically study how sensitive the Poisson approximation is to such misspecification and discuss practical implications for modeling real systems.
5. **Connection to large deviations (conceptual).** Explain why the Poisson approximation captures typical fluctuations of S_N but may fail to accurately represent extremely rare events. Relate your observations to large-deviation scaling discussed elsewhere in the chapter.

5.4.5 Beyond Sums: Extreme Value Theorems

Summation is only one way to aggregate many random variables. Another fundamental operation is taking the **maximum** or **minimum**. The limiting behavior is quite different from the CLT and depends strongly on tail characteristics.

Let $M_N = \max(X_1, \dots, X_N)$. Properly rescaled, M_N converges (in distribution) to one of three classical extreme-value laws:

- **Gumbel** (light-tailed distributions such as exponential, Gaussian),
- **Fréchet** (heavy-tailed power laws),
- **Weibull** (bounded distributions).

Sums produce Gaussian universality; maxima produce extreme-value universality.

Example 5.4.5. Universality of Extreme-Value Limits

The notebook `Aggregate-Rare-Events.ipynb` simulates maxima $M_N = \max\{X_1, \dots, X_N\}$ for three representative families of i.i.d. random variables, chosen to illustrate the three universality classes of extreme-value theory:

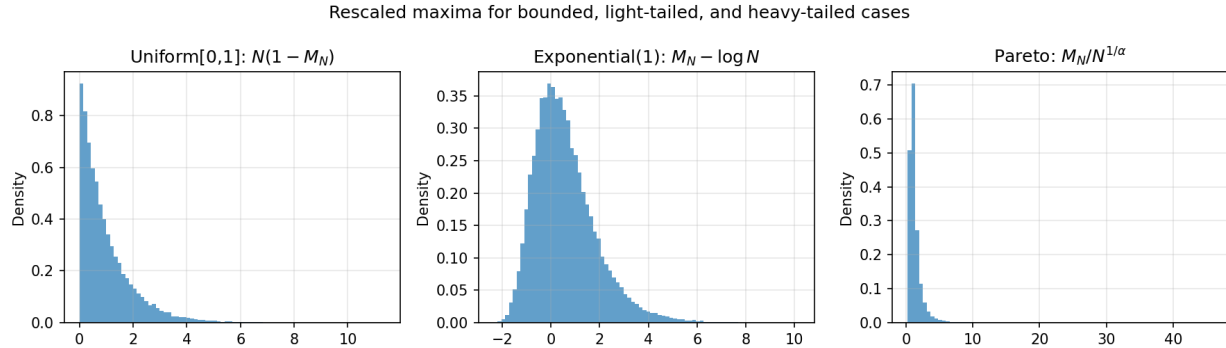


Figure 5.11: **Rescaled maxima in the three universality classes of extreme-value theory.** *Left:* bounded support ($\text{Uniform}[0,1]$), showing exponential fluctuations near the upper boundary (Weibull class). *Middle:* light-tailed exponential variables, exhibiting Gumbel fluctuations after logarithmic centering. *Right:* heavy-tailed Pareto variables, where algebraic rescaling yields a Fréchet limit. Generated by `Aggregate-Rare-Events.ipynb`.

- **Bounded support (Uniform[0,1]).** Since $M_N \uparrow 1$, the relevant fluctuations are those of the distance to the boundary. The left panel of Fig. 5.11 shows that

$$N(1 - M_N) \xrightarrow{d} \text{Exp}(1),$$

an instance of the Weibull extreme-value class.

- **Light-tailed (Exponential).** For exponentially distributed variables, maxima grow logarithmically with sample size. The middle panel shows that

$$M_N - \log N \xrightarrow{d} \text{Gumbel},$$

the canonical limit for light-tailed distributions.

- **Heavy-tailed (Pareto).** For Pareto variables with tail exponent α , the maximum scales algebraically. The right panel demonstrates that

$$\frac{M_N}{N^{1/\alpha}} \xrightarrow{d} \text{Fréchet},$$

reflecting dominance by a few extreme observations.

Together, these three cases show that the statistics of extremes fall into universality classes entirely different from both Gaussian (CLT-type) and Poisson (rare-event count) limits.

Exercise 5.4.5 (Beyond Simulation: Understanding Extreme-Value Universality). Using `Aggregate-Rare-Events.ipynb` as a starting point, go beyond the demonstrations in the example.

1. **Scaling diagnostics.** For each of the three distributions (Uniform, Exponential, Pareto), empirically verify that the chosen centering and scaling are necessary:

- Show that alternative scalings (e.g. incorrect powers of N or missing centering) do not collapse the histograms.
 - Quantify convergence by measuring distances (e.g. KS or Wasserstein) to the limiting Weibull, Gumbel, or Fréchet laws.
2. **Finite-size effects.** Investigate how large N must be before the asymptotic regime becomes accurate in each class. Which universality class converges slowest, and why?
 3. **Tail sensitivity.** For the Pareto case, vary the tail exponent α .
 - How does the scaling $N^{1/\alpha}$ change?
 - How does decreasing α alter the dominance of a single extreme observation?
 4. **Connection to learning systems (conceptual).** Consider a learning system where the loss over a dataset is governed by the maximum error rather than the mean.
 - Which extreme-value class is most relevant for adversarial robustness?
 - How would heavy-tailed noise or data corruptions affect worst-case performance?

Why These Universality Classes Matter for AI

The three asymptotic regimes developed in this section — Gaussian (CLT) limits, Poisson rare-event limits, and extreme-value limits — are not merely abstract probability results. They arise naturally in modern AI systems and provide principled guidance for modeling, algorithm design, and risk control.

- **Gaussian (CLT) regime and SGD noise.** In large-scale learning with mini-batch stochastic gradient descent (SGD), each parameter update aggregates many weakly dependent sample-wise gradients. By a CLT-type argument, the resulting update noise is often well-approximated as *Gaussian*, which underlies continuous-time diffusion and Langevin interpretations of training dynamics.

Practical implication. This scaling perspective motivates treating the mini-batch size as a *control parameter*: small batches induce high-variance, exploration-enhancing noise, while large batches reduce noise and favor stability and convergence. Diffusion-based views of optimization make this tradeoff explicit and inform principled choices of batch size, learning rate, and noise injection. These ideas will reappear when we model training as stochastic dynamics in Chapters 7 and 9.

- **Poisson regime and rare events in reinforcement learning.** In many reinforcement-learning and safety-critical settings, rewards, failures, or constraint violations are *rare* rather than small. Counts of such events over many episodes fall naturally into a Poisson regime, where variability is dominated by *event counts* rather than averages.

Practical implication. Recognizing a Poisson scaling shifts algorithmic emphasis from variance reduction to *event discovery*: exploration strategies, importance

sampling, and off-policy evaluation must be designed to reliably observe and model rare but consequential outcomes. This perspective also clarifies why naive Gaussian approximations can fail catastrophically in sparse-reward or safety-constrained RL.

- **Extreme-value regime and risk-sensitive modeling.** In many real-world AI applications, performance is determined not by typical behavior but by *worst-case* or near-worst outcomes: maximum load in networks, largest perception error, tail losses in finance, or failure under distribution shift.

Practical implication. Extreme-value scaling laws dictate how maxima grow with system size and data volume, informing the design of risk-sensitive objectives such as Value-at-Risk (VaR), Conditional VaR, robust training, and adversarial defenses. Importantly, extreme-value analysis reveals that tail behavior can remain unstable even when averages appear well-controlled, motivating explicit modeling of tails rather than reliance on mean-based metrics alone.

Takeaway. Together, these three universality classes provide a conceptual map for uncertainty in AI systems: *Gaussian* fluctuations govern aggregate noise and diffusion approximations, *Poisson* statistics describe sparse and count-based phenomena, and *extreme-value* laws control risk and failure. This taxonomy will recur throughout the book as we connect stochastic processes, information theory, and generative AI under a unified mathematical framework.

Chapter 6

Entropy and Information Theory

Why Entropy and Information Theory?

Entropy first appeared in **thermodynamics** as a measure of disorder and irreversibility in physical systems. Shannon’s fundamental insight was that the same mathematical structure captures the *uncertainty* of an information source. This bridge from physics to **information theory** transformed entropy into one of the central concepts of modern probability, statistics, machine learning, and generative AI.

In this chapter we adopt the information-theoretic viewpoint:

- **Entropy** quantifies uncertainty and the minimal number of bits needed to encode a random variable.
- **Kullback–Leibler (KL) divergence** measures how one probability distribution differs from another, forming the basis of likelihood-based training, variational inference, and normalizing flows.
- **Mutual information** quantifies how much knowledge of one variable reduces uncertainty about another, playing a central role in representation learning, bottleneck architectures, and the analysis of neural networks.

These notions did not arise from AI, but they now underpin almost every modern generative model:

- In **diffusion models**, entropy controls the trade-off between randomness and structure during denoising.
- In **variational autoencoders (VAEs)**, KL divergence shapes the latent distribution and regularizes the encoder.
- In **score-based and flow-matching models**, divergences between probability flows guide the training dynamics.

Although KL divergence dominates classical optimization-based approaches, it behaves poorly when distributions lie on low-dimensional manifolds or have non-overlapping support. This motivates the introduction of **Wasserstein distances**, which measure how probability *mass* must move in space and provide a more geometric notion of discrepancy; these will be previewed in this chapter and explored more deeply in later chapters.

Connector to the Rest of the Book. This chapter builds directly on the probability and sampling foundations established in Chapter 5. It introduces the quantitative language needed for the next stages of the book:

- **Stochastic processes** (next chapter), where entropy and KL measure complexity of paths and clarify connections between sampling, diffusion, and control.
- **Variational methods, VAEs, and normalizing flows**, where KL and cross-entropy become primary training objectives.
- **Diffusion models, flow matching, and optimal transport**, where Wasserstein geometry and score-based dynamics reveal deep structural connections.

Our goal in this chapter is therefore twofold: (1) to introduce the core information-theoretic quantities that govern uncertainty and information transfer, and (2) to prepare the conceptual groundwork for the generative modeling frameworks developed in the subsequent chapters.

6.1 Conditional Probability and Bayes' Rule

Modern AI systems operate under uncertainty: sensors are noisy, labels are imperfect, and environments are only partially observed. Whether it is a **self-driving car** estimating its position from noisy GPS and LiDAR data, or a **medical AI** diagnosing a disease from imperfect tests, such systems must continually update their beliefs in light of new evidence. This process is formalized by **conditional probability** and **Bayes' rule**. In this section we:

- Define conditional and joint probabilities, and derive Bayes' theorem;
- Interpret the key components: *prior*, *likelihood*, *posterior*, and *evidence*;
- Work through a concrete, fully discrete toy example (disease–test);
- Connect to simple AI-style classifiers (Bayesian filtering, Naïve Bayes).

6.1.1 Conditional Probability, Joint Laws, and Bayes' Rule

Let A and B be events in a probability space. The **conditional probability** of A given B is

$$\mathbb{P}(A | B) = \frac{\mathbb{P}(A \cap B)}{\mathbb{P}(B)}, \quad \mathbb{P}(B) > 0. \quad (6.1)$$

This tells us how to update our belief in A after learning that B has occurred. Rearranging gives the **multiplication rule**

$$\mathbb{P}(A \cap B) = \mathbb{P}(A | B) \mathbb{P}(B) = \mathbb{P}(B | A) \mathbb{P}(A). \quad (6.2)$$

Equating the two expressions for $\mathbb{P}(A \cap B)$ yields **Bayes' rule**:

$$\mathbb{P}(A | B) = \frac{\mathbb{P}(B | A) \mathbb{P}(A)}{\mathbb{P}(B)}, \quad \mathbb{P}(B) = \sum_a \mathbb{P}(B | A = a) \mathbb{P}(A = a). \quad (6.3)$$

The terms have standard names in Bayesian modeling:

$\mathbb{P}(A)$	prior (belief before seeing B),
$\mathbb{P}(B A)$	likelihood (data model),
$\mathbb{P}(A B)$	posterior (updated belief),
$\mathbb{P}(B)$	evidence or marginal likelihood.

In AI applications we often write $A = X$ (hidden state, class, parameter) and $B = Z$ (observation, feature, measurement), so that

$$\mathbb{P}(X | Z) \propto \mathbb{P}(Z | X) \mathbb{P}(X),$$

where the proportionality constant is the evidence $\mathbb{P}(Z)$.

6.1.2 Discrete Bayes in a Toy Medical Diagnosis Model

To see Bayes' rule in action, consider a simple medical diagnosis problem. Both the (hidden) disease state and the observed test outcome are modeled as binary random variables:

$$D \in \{0, 1\}, \quad T \in \{0, 1\},$$

where

$$D = 1 \text{ means "sick"}, \quad D = 0 \text{ means "healthy"},$$

and

$$T = 1 \text{ means "test positive"}, \quad T = 0 \text{ means "test negative".}$$

We specify:

- **A prior prevalence:**

$$\mathbb{P}(D = 1) = \pi, \quad \mathbb{P}(D = 0) = 1 - \pi;$$

- **A likelihood model for the test:**

Sensitivity:	:	$\mathbb{P}(T = 1 D = 1) = s,$
Specificity:	:	$\mathbb{P}(T = 0 D = 0) = c.$

Thus,

$$\mathbb{P}(T = 1 | D = 0) = 1 - c, \quad \mathbb{P}(T = 0 | D = 1) = 1 - s.$$

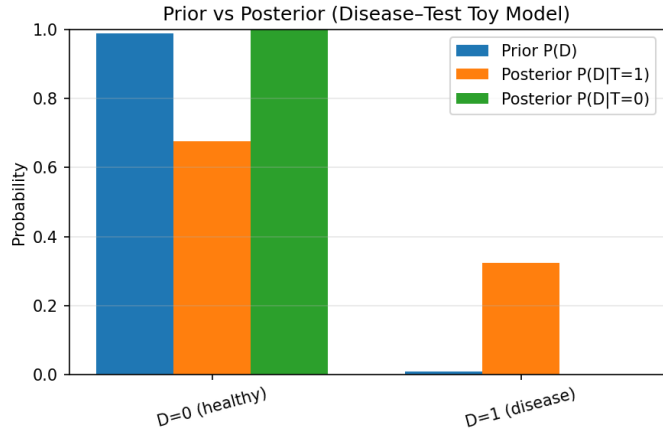


Figure 6.1: Prior vs. posterior probabilities in the toy disease–test model. Even an accurate test yields only moderate posterior probability when the disease is rare.

Example 6.1.1 (Positive Test for a Rare Disease). *Fix*

$$\pi = 0.01, \quad s = 0.95, \quad c = 0.98,$$

so the disease is rare, but the test is quite accurate. Bayes' rule gives

$$\begin{aligned} \mathbb{P}(T = 1) &= s\pi + (1 - c)(1 - \pi), \\ \mathbb{P}(D = 1 | T = 1) &= \frac{s\pi}{\mathbb{P}(T = 1)}. \end{aligned}$$

Even with high sensitivity and specificity, the posterior $\mathbb{P}(D = 1 | T = 1)$ may remain far from 1, because the prior prevalence π is very small.

Fig. 6.1 shows a bar plot of the prior prevalence and the posterior probability after observing a positive test.

The notebook `Bayes-Toy-Discrete.ipynb` implements this model, computes the posterior using Bayes' rule, and generates Fig. 6.1 automatically.

6.1.3 Exploring Test Quality: Sensitivity and Specificity

The same notebook also explores how the posterior $\mathbb{P}(D = 1 | T = 1)$ changes when we vary the *test quality* parameters while keeping the disease prevalence π fixed.

For example, we may sweep the sensitivity s from 0.5 to 0.99 while holding specificity c fixed, or vice versa. In each case, we recompute

$$\mathbb{P}(D = 1 | T = 1) = \frac{s\pi}{s\pi + (1 - c)(1 - \pi)},$$

and display the resulting curve.

Fig. 6.2 shows a typical result: improving sensitivity or specificity increases the posterior probability, but the effect is asymmetric when the disease is rare. Understanding these relationships is crucial for designing and interpreting diagnostic tests.

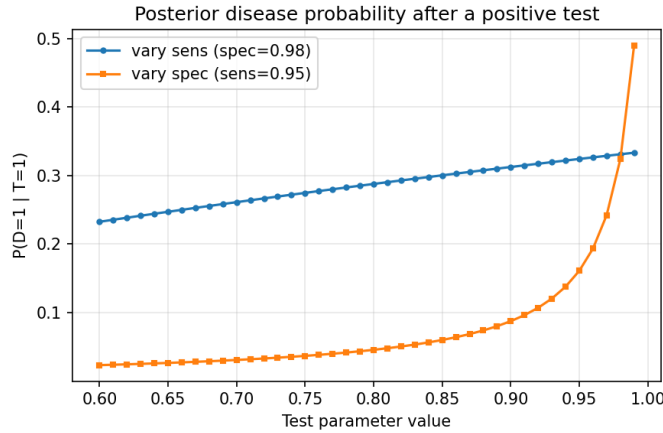


Figure 6.2: Posterior probability $\mathbb{P}(D = 1 \mid T = 1)$ as a function of test sensitivity s (with specificity c fixed). The notebook `Bayes-Toy-Discrete.ipynb` produces this figure.

Exercise 6.1.1 (Discrete Bayesian Inference Toy). *Using the notebook `Bayes-Toy-Discrete.ipynb`:*

1. *Implement the disease–test model with parameters (π, s, c) and verify numerically:*

- *the prior $\mathbb{P}(D)$,*
- *the likelihood $\mathbb{P}(T \mid D)$,*
- *the evidence $\mathbb{P}(T = 1)$,*
- *the posterior $\mathbb{P}(D = 1 \mid T = 1)$.*

2. *Reproduce the bar plot in Fig. 6.1 comparing prior and posterior probabilities.*

3. *Sweep test quality parameters:*

- *vary sensitivity $s \in [0.5, 0.99]$ with specificity c fixed;*
- *optionally vary specificity c with sensitivity fixed.*

Generate a plot like Fig. 6.2. Comment on how improving each parameter affects the posterior.

4. *Optional: Compare which improvement (sensitivity vs. specificity) has a larger effect when the disease is rare vs. common.*

6.1.4 From Naïve Bayes to Neural Networks

The toy example in the previous subsection illustrated how Bayes’ rule updates a prior belief in light of new evidence. We now move to a setting more directly connected to modern machine learning – *classification of images* – one already familiar from earlier chapters. Here, the goal is to infer a latent class label C (e.g., a digit $0, \dots, 9$) from observed features F extracted from the image.

Although state-of-the-art classifiers use neural networks, the probabilistic structure underlying Bayes' rule remains the same:

$$\mathbb{P}(C | F) \propto \mathbb{P}(C) \mathbb{P}(F | C).$$

To illustrate we consider an example of a small MNIST experiment connecting three perspectives:

1. A **Naïve Bayes classifier**, which assumes conditional independence of pixel features given the class.
2. A **neural network classifier**, which learns a likelihood model $\mathbb{P}(C | F)$ directly from data.
3. **Evaluation tools** – confusion matrices and calibration curves—that will return in later sections when we discuss KL divergence and cross-entropy.

Example 6.1.2 (Naïve Bayes vs Neural Network for MNIST). *Given an image represented as a vector of discrete pixel intensities, Naïve Bayes models the likelihood as*

$$\mathbb{P}(F | C = c) = \prod_{i=1}^d \mathbb{P}(F_i | C = c),$$

treating individual pixels as conditionally independent. This assumption is unrealistic for image data – but surprisingly effective as a baseline, and invaluable as a conceptual stepping stone toward more flexible models.

A small neural network trained by minimizing cross-entropy learns a much richer representation. Its predictions

$$\hat{p}(C | F)$$

can be compared to Naïve Bayes using two complementary visualizations:

- a **confusion matrix**, showing where each model makes mistakes;
- a **calibration (reliability) curve**, comparing predicted probabilities to empirical frequencies.

These quantitative tools also prepare us for the next sections, where we connect entropy, KL divergence, and cross-entropy to empirical performance.

The notebook `Bayes-MNIST-NaiveBayes.ipynb` implements:

- training a small neural network on MNIST,
- training a Naïve Bayes classifier,
- computing confusion matrices, shown in Fig. (6.3), and calibration curves, shown in Fig. (6.4)

This notebook will be reused later when we introduce KL divergence and cross-entropy, since the predictions of both models provide natural examples of probability distributions to compare.

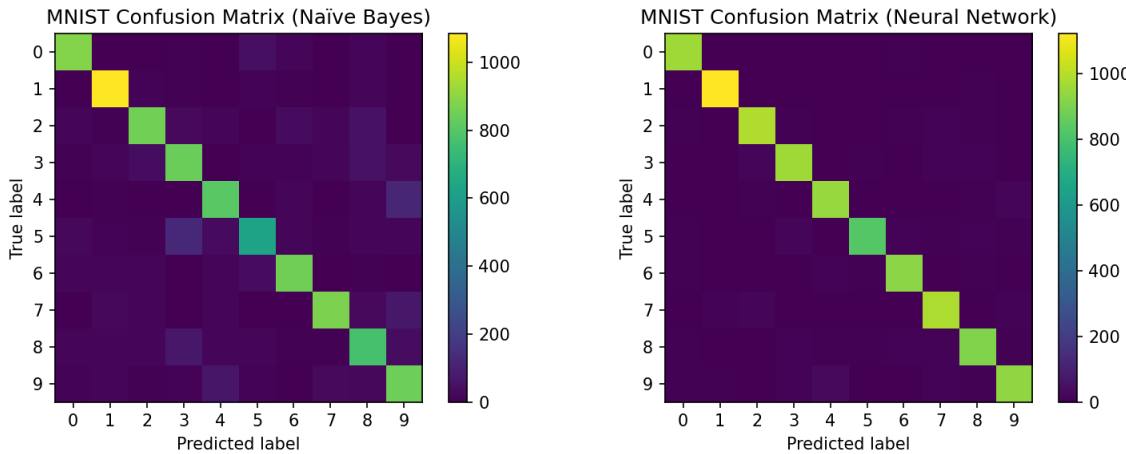


Figure 6.3: Example confusion matrices for the naïve Bayes (left) and neural network classifier (right).

Exercise 6.1.2 (Diagnosing Model Failures: Feature Dependence, Calibration, and KL Analysis). *Using the notebook `Bayes-MNIST-NaiveBayes.ipynb`, perform a deeper investigation of why Naïve Bayes underperforms compared to the neural network, and how the two models differ as probabilistic predictors.*

1. **Identify systematic failure modes.** Using the confusion matrices in Fig. 6.3, choose two pairs of digits that Naïve Bayes confuses much more often than the neural network (e.g. (3, 5) or (4, 9)).

For each selected pair:

- Visualize several misclassified images.
- Overlay (or display side-by-side) the Naïve Bayes class-conditional mean images, i.e. $\mathbb{E}[F | C = c]$.
- Explain which pixel dependencies break the Naïve Bayes independence assumption and lead to the observed errors.

2. **Calibration vs confidence.** Using the calibration curves in Fig. 6.4, select probability bins where:

- the neural network is overconfident, and
- Naïve Bayes is underconfident.

For each bin:

- inspect several test images whose predicted probability lies in that bin,
- report the empirical accuracy,
- comment on whether the miscalibration is due to poor likelihood modeling, insufficient capacity, or noisy training labels.

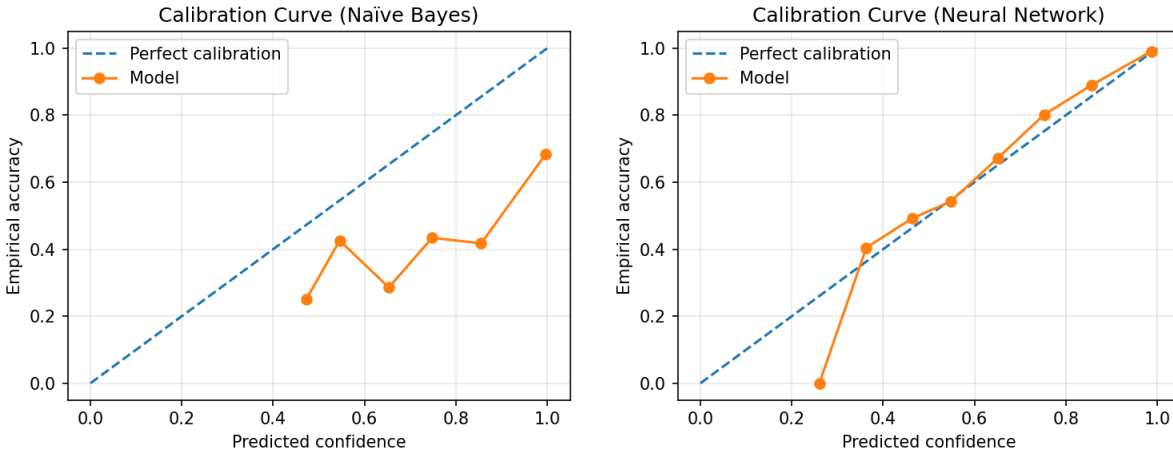


Figure 6.4: Example calibration (reliability) curves for the naïve Bayes (left) and for the neural network classifier (right). The gap between the curves and the diagonal indicates miscalibration.

3. **Per-sample KL divergence (preview of Section 6.2.3).** For every test image, compute the KL divergence between the two model predictions:

$$D_{\text{KL}}\left(p_{\text{NN}}(\cdot \mid F) \parallel p_{\text{NB}}(\cdot \mid F)\right).$$

Then:

- plot a histogram of these KL values,
- identify the images with the largest KL divergence,
- inspect them visually and explain why Naïve Bayes and the NN disagree so strongly.

(This KL analysis will be revisited later, when we study divergence-based training objectives.)

4. **Optional: selective feature removal.** Choose a pair of digits that Naïve Bayes confuses. Remove (mask) a small set of informative pixels (e.g. central strokes), retrain both models, and compare:

- changes in confusion rates,
- changes in calibration error,
- changes in the KL divergence distribution.

Discuss whether the neural network is more robust to missing / corrupted features than Naïve Bayes.

6.2 Entropy: Quantifying Uncertainty

Entropy in AI serves two primary roles:

- **Measuring Uncertainty:** The entropy of a probability distribution quantifies how uncertain or unpredictable a system is. High entropy corresponds to greater randomness, while low entropy suggests more certainty.
- **Guiding Learning and Decision-Making:** Many AI models – such as **variational autoencoders (VAEs)**, **generative adversarial networks (GANs)**, and **diffusion models** – explicitly optimize entropy-based loss functions to balance structure and randomness.

For example:

- In **reinforcement learning**, entropy regularization ensures that agents explore diverse strategies.
- In **generative models**, entropy helps control randomness in data generation, making outputs more varied or precise.

6.2.1 Definition and Interpretations of Entropy

For a discrete random variable X with probability mass function $P(X)$, the (Shannon) entropy is

$$H(X) = - \sum_{x \in \mathcal{X}} P(x) \log P(x). \quad (6.4)$$

For a continuous random variable, the *differential* entropy is

$$H(X) = - \int p(x) \log p(x) dx. \quad (6.5)$$

Entropy admits several complementary interpretations:

- **Uncertainty measure.** A uniform distribution has maximal entropy; a deterministic distribution has zero entropy.
- **Expected information content.** Entropy is the expected number of nats (or bits) required to encode a sample drawn from P .
- **Decision-theoretic perspective.** In reinforcement learning, entropy regularization helps balance exploration and exploitation.

Example 6.2.1 (Entropy of Class Distributions). *A classification dataset consists of samples (X, Y) , where Y is the discrete class label. The entropy of the class distribution,*

$$H(Y) = - \sum_{y \in \mathcal{Y}} P_Y(y) \log_2 P_Y(y),$$

quantifies class imbalance and the inherent label uncertainty.

For MNIST, which contains ten digit classes that are nearly uniformly represented, the theoretical entropy is

$$H(Y) = \log_2 10 \approx 3.32 \text{ bits.}$$

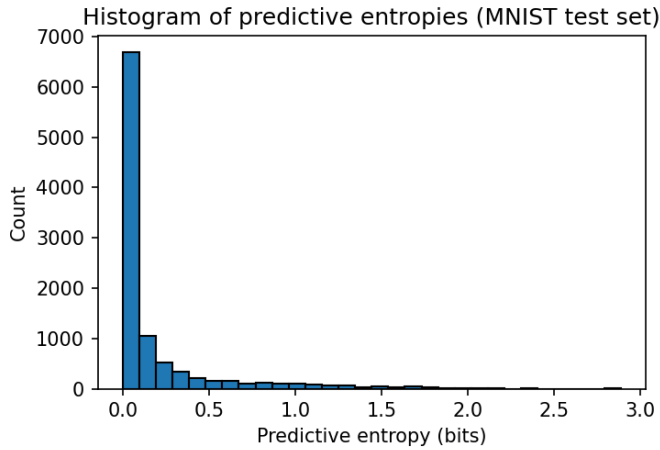


Figure 6.5: Histogram of predictive entropies $H_{\text{pred}}(x)$ for MNIST test images. Most predictions are low-entropy (high confidence), but a nontrivial tail highlights ambiguous digits.

Given a classifier producing a predictive distribution $\hat{p}(y | x)$ for each input x , the predictive entropy

$$H_{\text{pred}}(x) = - \sum_{y \in \mathcal{Y}} \hat{p}(y | x) \log \hat{p}(y | x)$$

measures the model's uncertainty on that particular example. Low entropy = confident prediction; high entropy = ambiguity or model uncertainty.

The `Entropy-Classification-Experiment-torch.ipynb` notebook computes this predictive entropy over the MNIST test set and visualizes its distribution in Fig. 6.5. The bulk of the mass lies near zero—indicating confident predictions—while a visible tail corresponds to challenging or visually ambiguous digits.

High- and low-entropy examples. *To further interpret predictive entropy, the notebook displays the test samples with the lowest and highest entropy values.*

- **Lowest entropy:** clean, prototypical digits for which the classifier confidently assigns nearly all probability mass to one class.
- **Highest entropy:** ambiguous or atypical digits, often resembling multiple classes (e.g., 4 vs. 9, 3 vs. 5).

Representative grids generated by the notebook are shown in Figs. 6.6.

Exercise 6.2.1 (Entropy in Data and in Predictive Models). *Using the notebook `Entropy-Classification-Experiment.ipynb`:*

1. **Dataset entropy.** *Compute the class entropy $H(Y)$ for MNIST and for any user-constructed imbalanced variant (e.g., subsample the digit “1” by a factor of 10). How does class imbalance affect entropy?*

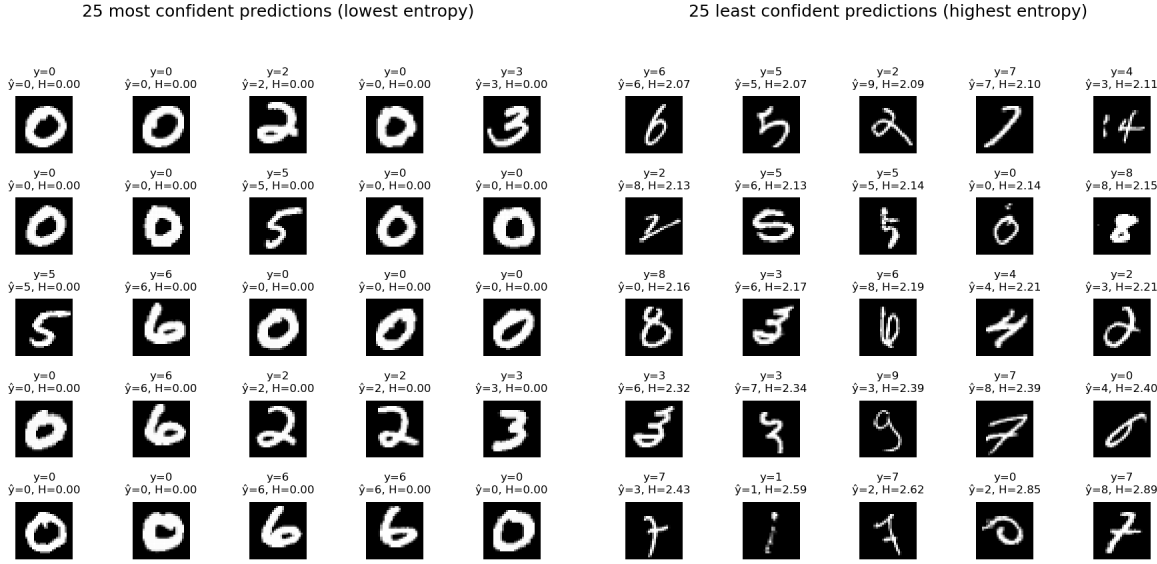


Figure 6.6: MNIST test samples with *lowest* (left) and *highest* (right) predictive entropy. These prototypical digits with lowest predictive entropy lead to highly confident (near-delta) predictions; while images correspondent to highest predictive entropy are visually ambiguous, leading the classifier to distribute its probability mass across multiple plausible classes.

2. **Predictive-entropy vs. accuracy.** Split the test set into correctly and incorrectly classified samples. Compare the predictive-entropy histograms for the two groups. Does higher entropy correlate with errors?
3. **Extreme cases.** Identify test samples with (i) maximum predictive entropy and (ii) minimum predictive entropy. Display the images and their predicted distributions. Explain why the model is (un)certain.
4. **Optional: temperature scaling.** Apply temperature scaling $p_T(y \mid x) \propto p(y \mid x)^{1/T}$ for several values of T . Analyze how predictive entropy changes and relate this to calibration behavior (see Section 6.2.3).

6.2.2 Mutual Information

Mutual information quantifies the amount of information shared between two random variables X and Y . It measures how much knowing Y reduces uncertainty about X and vice versa. The mutual information is defined as:

$$I(X; Y) = H(X) - H(X \mid Y), \quad (6.6)$$

where $H(X)$ is the entropy of X and $H(X \mid Y)$ is the conditional entropy of X given Y . This formulation makes it clear that mutual information represents the reduction in uncertainty about X after observing Y .

Equivalently, mutual information can be expressed as:

$$I(X; Y) = \sum_{x,y} P(x, y) \log \frac{P(x, y)}{P(x)P(y)}, \quad (6.7)$$

which shows that mutual information measures the divergence between the joint distribution $P(X, Y)$ and the product of the marginal distributions $P(X)P(Y)$. If X and Y are independent, then $P(X, Y) = P(X)P(Y)$, leading to $I(X; Y) = 0$.

Intuition and Visualization: Mutual information can be intuitively understood using **Venn diagrams** in an information-theoretic sense. The entropy of X and Y can be visualized as two overlapping sets, where the overlap represents their shared information.

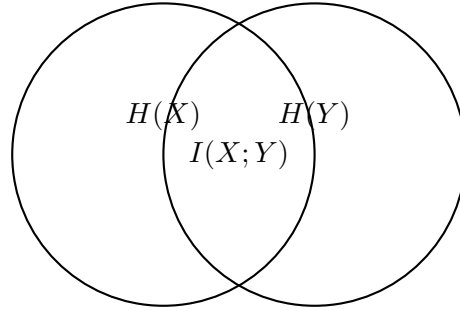


Figure 6.7: Mutual information $I(X; Y)$ as the intersection of entropy $H(X)$ and $H(Y)$.

In the diagram shown in Fig. (6.7: The left circle represents $H(X)$, the uncertainty in X ; The right circle represents $H(Y)$, the uncertainty in Y ; The overlapping area represents $I(X; Y)$, the mutual information, i.e., the reduction in uncertainty about one variable given the other; The non-overlapping parts correspond to the conditional entropies $H(X | Y)$ and $H(Y | X)$.

Example 6.2.2. Example: Coin Flip with Noise: Consider a scenario where we flip a fair coin (X) but then communicate the result through a noisy channel (Y) where there is a 10% chance that the transmitted value is incorrect: If there were no noise, $I(X; Y) = H(X)$ because knowing Y would fully determine X ; If the noise were extreme (randomizing Y completely), then $I(X; Y) = 0$, as Y contains no information about X .

Exercise 6.2.2. Computing Mutual Information for a Simple Distribution: Consider a binary random variable X that takes values $\{0, 1\}$ with equal probability, and another random variable Y that is a noisy observation of X , with error probability p . That is,

$$P(Y = X) = 1 - p, \quad P(Y \neq X) = p.$$

Compute:

1. The entropies $H(X)$ and $H(Y)$.
2. The conditional entropy $H(X | Y)$.

3. The mutual information $I(X; Y)$.

How does $I(X; Y)$ behave as p varies?

Exercise 6.2.3. Mutual Information Between Images and Classifier Predictions (MNIST) Extend the notebook `Entropy-Classification-Experiment.ipynb` to numerically explore mutual information between the true class label Y and the classifier's predictive distribution $\hat{p}(y | x)$ on MNIST.

Recall that for discrete variables,

$$I(Y; \hat{Y}) = H(Y) - H(Y | \hat{Y}),$$

and that for a probabilistic classifier we may approximate

$$H(Y | X = x) \approx - \sum_y \hat{p}(y | x) \log \hat{p}(y | x) = H_{\text{pred}}(x),$$

the predictive entropy already computed in the notebook.

In this exercise:

1. **Estimate the conditional entropy.** Using the predictive entropies computed over the MNIST test set, estimate

$$H(Y | X) \approx \mathbb{E}_{x \sim \text{test set}} [H_{\text{pred}}(x)].$$

2. **Compute the mutual information.** Using the empirical class entropy $H(Y)$ already computed in the notebook and your estimate of $H(Y | X)$, compute

$$I(Y; X) \approx H(Y) - H(Y | X).$$

Interpret this quantity: how many bits of class information does the trained classifier typically “recover” from an image?

3. **Per-class analysis.** For each digit $y \in \{0, \dots, 9\}$, compute the class-conditional average predictive entropy

$$\mathbb{E}[H_{\text{pred}}(X) | Y = y].$$

Visualize these ten values as a bar plot. Which digits have the lowest uncertainty? Which have the highest? Relate this to the geometry of the digit classes (e.g., 1 vs. 8).

4. **High-information vs. low-information images.** Identify:

- the 25 images with lowest predictive entropy (highest information);
- the 25 with highest predictive entropy (lowest information).

Display both grids (similar to earlier entropy visualizations). Comment on visual patterns: Do high-information images look more prototypical? Are low-information images ambiguous or unusually shaped?

5. **Optional: Comparing models.** Train a second classifier (e.g. a deeper MLP or a CNN) in the same notebook. Repeat items 1–4 for both models. Compare the mutual-information estimates:

$$I_{\text{MLP}}(Y; X) \quad \text{vs.} \quad I_{\text{CNN}}(Y; X).$$

Does the better-performing model recover more information about the label?

This exercise connects mutual information to practical classifier behavior: $H(Y)$ reflects dataset uncertainty, $H(Y | X)$ reflects residual model uncertainty, and their difference quantifies how much information a trained classifier extracts from each image.

6.2.3 KL Divergence: Comparing Distributions

The **Kullback–Leibler (KL) divergence** quantifies how much one probability distribution P differs from another Q . For a discrete variable with support \mathcal{X} , it is defined as

$$D_{\text{KL}}(P \| Q) = \sum_{x \in \mathcal{X}} P(x) \log \frac{P(x)}{Q(x)}. \quad (6.8)$$

- $D_{\text{KL}}(P \| Q) = 0$ iff $P = Q$ almost everywhere.
- Larger values indicate increasing dissimilarity between P and Q .

KL divergence is not a metric. KL divergence does not satisfy symmetry or the triangle inequality:

1. **Non-symmetry:** $D_{\text{KL}}(P \| Q) \neq D_{\text{KL}}(Q \| P)$.
2. **No triangle inequality.**
3. **Non-negativity:** $D_{\text{KL}}(P \| Q) \geq 0$.

Thus KL divergence is best interpreted as a *directed measure of information loss* when approximating a “true” distribution P with a model Q .

Classifier outputs as distributions. A K -class classifier maps each input F to a probability vector $p(\cdot | F)$. If two models—here a Neural Network (NN) and a Naïve Bayes classifier (NB)—produce distributions $p_{\text{NN}}(\cdot | F)$ and $p_{\text{NB}}(\cdot | F)$ the KL divergence provides a natural way to measure how strongly they disagree on each input.

Example 6.2.3 (KL Divergence Between Naïve Bayes and NN on MNIST). *Continuing the MNIST experiment of Subsection 6.1.4, the notebook Bayes-MNIST-NaiveBayes.ipynb computes, for every test image F , the predictive distributions*

$$p_{\text{NB}}(\cdot | F), \quad p_{\text{NN}}(\cdot | F),$$

and the directed divergences

$$D_{\text{KL}}(p_{\text{NN}}(\cdot | F) \| p_{\text{NB}}(\cdot | F)), \quad D_{\text{KL}}(p_{\text{NB}}(\cdot | F) \| p_{\text{NN}}(\cdot | F)).$$

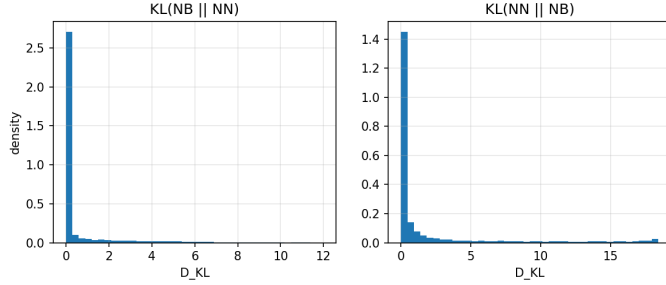


Figure 6.8: Histogram of $D_{\text{KL}}(p_{\text{NN}}(\cdot | F) \| p_{\text{NB}}(\cdot | F))$ over the MNIST test set. A heavy tail indicates inputs on which the neural network and Naïve Bayes produce substantially different predictive distributions.

A first global summary is provided by the histogram of $D_{\text{KL}}(p_{\text{NN}} \| p_{\text{NB}})$ over the test set, shown in Fig. 6.8. Most KL values are small—the two models usually agree as probabilistic predictors—but the distribution exhibits a clear tail corresponding to inputs on which the models diverge significantly.

Exercise 6.2.4 (KL Divergence and Model Disagreement on MNIST). Using the (extended) notebook `Bayes-MNIST-NaiveBayes.ipynb`:

1. **Global statistics.** Compute the mean KL divergences

$$\overline{D}_{\text{KL}}^{\text{NN} \parallel \text{NB}} = \mathbb{E}\left[D_{\text{KL}}(p_{\text{NN}}(\cdot | F) \| p_{\text{NB}}(\cdot | F))\right],$$

and

$$\overline{D}_{\text{KL}}^{\text{NB} \parallel \text{NN}} = \mathbb{E}\left[D_{\text{KL}}(p_{\text{NB}}(\cdot | F) \| p_{\text{NN}}(\cdot | F))\right].$$

Comment on which direction is larger and why the asymmetry arises.

2. **Condition on correctness.** Partition the test set into four groups:

- both models correct,
- only NN correct,
- only NB correct,
- both models wrong.

For each group, compute the mean KL divergence in both directions. How does KL divergence correlate with model accuracy and disagreement?

3. **Per-class disagreement.** For each true digit $c \in \{0, \dots, 9\}$, compute the mean $D_{\text{KL}}(p_{\text{NN}} \| p_{\text{NB}})$ over all test images with label c and visualize the ten values as a bar plot. Which digits show the strongest disagreement between models? Relate your findings to the confusion matrices from Fig. 6.3.
4. **Optional: inspect high- KL examples.** Extend the notebook to select a small set of images with the largest values of $D_{\text{KL}}(p_{\text{NN}} \| p_{\text{NB}})$. For each such image, display:

- the input image,
- the top predicted probabilities from both models.

Qualitatively describe what types of digits lead to large KL divergence (e.g., visually ambiguous digits, digits with unusual stroke patterns, etc.).

KL divergence as an optimization objective. Beyond post-hoc comparison of predictors, KL divergence also appears directly in training objectives. In normalizing flows (Section 5.2), one minimizes a KL divergence between the data distribution and a transformed base distribution, leading to loss functions of the form

$$\mathcal{L}(\theta) = \mathbb{E}_{Y \sim P_Y} [g_\theta(Y)^2 + \log|J_{g_\theta}(Y)|], \quad (6.9)$$

where g_θ is a learned transform and $J_{g_\theta}(Y)$ is its Jacobian determinant. Later chapters will connect these KL-based objectives to maximum likelihood and cross-entropy in generative models.

6.2.4 Cross-Entropy and Its Connection to KL Divergence

The **cross-entropy** between two discrete distributions P and Q (with common support \mathcal{X}) is defined as

$$H(P, Q) = - \sum_{x \in \mathcal{X}} P(x) \log Q(x). \quad (6.10)$$

It quantifies how “surprised” we would be, on average, if data generated from the true distribution P were encoded or predicted using the model distribution Q .

Cross-entropy is intimately connected to KL divergence. Using the entropy of P ,

$$H(P) = - \sum_x P(x) \log P(x),$$

we have the identity

$$D_{\text{KL}}(P \| Q) = H(P, Q) - H(P). \quad (6.11)$$

Since $H(P)$ does not depend on Q , minimizing the cross-entropy $H(P, Q)$ with respect to Q is equivalent to minimizing the KL divergence $D_{\text{KL}}(P \| Q)$. This is the conceptual reason why **cross-entropy is the standard loss function in modern classification and generative modeling**.

Why “cross”-entropy? Entropy $H(P)$ measures the intrinsic uncertainty of a *single* distribution P . Cross-entropy $H(P, Q)$ combines two distributions:

- the true distribution P ,
- the predictive or model distribution Q .

It asks: *How many bits would we need to encode samples from P using a code optimized for Q instead of P ?* This mismatch cost is exactly the KL divergence plus the irreducible entropy of P .

Cross-entropy in modern AI. Cross-entropy appears in several core learning pipelines:

- **Neural networks.** For a one-hot label y and predictive distribution \hat{p} , the loss

$$\mathcal{L}_{\text{CE}} = - \sum_{y_i} \log \hat{p}_i$$

promotes high probability on the correct class.

- **Language models.** Next-token prediction is trained with cross-entropy, equivalent to maximum likelihood.
- **Normalizing flows.** Flow models minimize KL divergence between the data distribution and a transformed base distribution; this reduces to a cross-entropy term plus a Jacobian correction.
- **Importance sampling and adaptive sampling.** Cross-entropy is central to the *cross-entropy method* of Rubinstein, where one iteratively updates a parametric distribution by minimizing cross-entropy to a set of high-reward samples.

Empirical cross-entropy vs. KL divergence. Cross-entropy has a crucial practical advantage over KL divergence:

- KL divergence $D_{\text{KL}}(P \parallel Q)$ requires evaluating $\log P(x)$, which is impossible when P is available only through samples (empirical distribution).
- Cross-entropy $H(P_{\text{emp}}, Q) = -\frac{1}{N} \sum_{i=1}^N \log Q(x_i)$ is always well-defined, because it involves only $\log Q(x)$.

Thus cross-entropy provides a stable, tractable substitute for KL when the “true” distribution is empirical (a sum of delta functions). This is why maximum-likelihood training of neural networks reduces to minimizing empirical cross-entropy.

Exercise 6.2.5 (Cross-Entropy, Entropy, and KL Divergence). *This exercise connects analytic calculations with empirical evaluations using the distributions saved by the notebook Bayes-MNIST-NaiveBayes.ipynb.*

1. **Entropy calculations.** Compute the entropy of:

- a uniform distribution over 4 categories;
- a “peaked” 4-category distribution $(0.9, 0.0333, 0.0333, 0.0333)$;
- the Gaussian $N(0, 1)$ (use the analytic formula).

2. **KL divergence calculations.** Compute:

- $D_{\text{KL}}(N(\mu_1, \sigma^2) \parallel N(\mu_2, \sigma^2))$;
- $D_{\text{KL}}(\text{Laplace}(0, 1) \parallel N(0, 1))$ numerically on a grid.

3. **Empirical cross-entropy on MNIST.** Using the predictive distributions saved in the notebook:

- compute the empirical cross-entropy of the Naïve Bayes predictions relative to the true labels;
- compute the empirical cross-entropy of the neural network predictions relative to the true labels;
- compare these values and relate them to the confusion matrices in Fig. 6.3.

4. **Cross-entropy vs. KL divergence (empirical).** For each test image F , compute

$$-\log p_{\text{NN}}(y \mid F), \quad -\log p_{\text{NB}}(y \mid F),$$

where y is the true label. Compare the distributions of these two per-sample losses to the KL-based disagreement analysis from Subsection 6.2.3. Discuss:

- why cross-entropy can be computed directly from true labels,
- why KL between model predictions requires two full distributions,
- how the two diagnostics provide complementary information.

5. **Optional: replacing cross-entropy by KL in training.** Modify the MNIST neural network so that it is trained with the loss

$$\mathcal{L}_{\text{KL}} = D_{\text{KL}}(y_{\text{onehot}} \parallel p_{\text{NN}}(\cdot \mid F)),$$

which is numerically identical to cross-entropy. Verify this equivalence in code and compare learning curves.

6.2.5 Wasserstein Distance: Geometry of Probability Distributions

KL divergence and cross-entropy quantify how one distribution differs *informationally* from another. But there are important situations where these quantities behave poorly:

- KL divergence becomes infinite when the supports do not overlap;
- small translations of a distribution can cause large KL divergence;
- neither KL nor cross-entropy reflect the *geometry* of the space in which samples live.

The **Wasserstein distance** – also called **Earth-Mover Distance** (EMD) – addresses these limitations by measuring the *cost of transporting mass* from one distribution to another. Rather than comparing probabilities pointwise, Wasserstein distance compares distributions according to how difficult it is to move probability mass across the underlying space.

Definition (1-Wasserstein distance). For two probability distributions P and Q on \mathbb{R}^d ,

$$W_1(P, Q) = \inf_{\gamma \in \Gamma(P, Q)} \mathbb{E}_{(X, Y) \sim \gamma} [\|X - Y\|],$$

where $\Gamma(P, Q)$ is the set of all couplings (joint distributions) with marginals P and Q . Intuitively: $W_1(P, Q)$ is the minimum amount of “work” required to transport mass from P to match Q , using Euclidean distance as the cost of moving unit mass.

Higher-order Wasserstein distances W_p are defined analogously.

Why Wasserstein? A geometric metric. Wasserstein distances:

- are true metrics on distributions;
- remain finite even when supports do not overlap;
- behave smoothly under translations and deformations of distributions;
- incorporate the geometry of data (important for images, audio, embeddings).

In modern AI this geometric sensitivity is crucial:

- *Generative Adversarial Networks* (GANs) utilize Wasserstein distance as a metric to avoid gradient collapse;
- *Diffusion models* implicitly minimize Wasserstein-type objectives;
- *Optimal transport (OT)* provides the mathematical foundation for alignment, matching, barycenters, and flow-based generative models.

Thus Wasserstein distance is the “right” metric whenever one cares about *how* distributions differ in space, not just *whether* they differ.

Closed-form case: 1D and Gaussian measures. For one-dimensional distributions with cumulative distribution functions F_P and F_Q ,

$$W_1(P, Q) = \int_0^1 |F_P^{-1}(u) - F_Q^{-1}(u)| du.$$

For Gaussian distributions in \mathbb{R}^d ,

$$W_2^2(\mathcal{N}(m_1, \Sigma_1), \mathcal{N}(m_2, \Sigma_2)) = \|m_1 - m_2\|^2 + \text{Tr}\left(\Sigma_1 + \Sigma_2 - 2(\Sigma_2^{1/2} \Sigma_1 \Sigma_2^{1/2})^{1/2}\right),$$

reflecting both the shift in means and the mismatch in covariance geometry. These closed forms motivate the following example.

Example 6.2.4 (Wasserstein Distance Between Simple Distributions). Consider three Gaussian distributions on \mathbb{R} :

$$P_1 = \mathcal{N}(0, 1), \quad P_2 = \mathcal{N}(2, 1), \quad P_3 = \mathcal{N}(0, 4).$$

For one-dimensional distributions, the W_1 (earth-mover) distance admits the closed-form quantile formula

$$W_1(P, Q) = \int_0^1 |F_P^{-1}(u) - F_Q^{-1}(u)| du.$$

Applying it to the three Gaussians gives

$$W_1(P_1, P_2) = 2, \quad W_1(P_1, P_3) = \frac{2}{\sqrt{\pi}} \approx 1.128.$$

These values highlight an essential geometric aspect of Wasserstein distance:

- Shifting a Gaussian by 2 units requires transporting mass by exactly 2, hence $W_1(P_1, P_2) = 2$.
- Increasing variance spreads mass but does not require a uniform shift, resulting in a smaller cost for $W_1(P_1, P_3)$.

By contrast, KL divergence reacts strongly to changes in variance, so it judges P_3 to be far more dissimilar from P_1 than P_2 — the opposite of the Wasserstein ordering.

The accompanying notebook `Wasserstein-1D-Gaussians.ipynb`:

- samples from each distribution,
- computes empirical Wasserstein distances using `scipy`,
- compares empirical estimates to the theoretical values above,
- visualizes:
 1. histograms of samples,
 2. quantile functions $F^{-1}(u)$,
 3. absolute quantile gaps $|F_P^{-1}(u) - F_Q^{-1}(u)|$ whose integral is W_1 .

Representative outputs are shown in Fig. (6.9).

Exercise 6.2.6 (Exploring Wasserstein Geometry). Using the notebook `Wasserstein-1D-Gaussians.ipynb`:

1. Compute empirical $W_1(P_i, P_j)$ for all three pairs and compare to theoretical values.
2. Plot the quantile functions $F_{P_i}^{-1}(u)$ and the absolute transport distance $|F_{P_i}^{-1}(u) - F_{P_j}^{-1}(u)|$.
3. Replace one Gaussian by a heavy-tailed Laplace distribution. How does W_1 compare to KL divergence in this case?
4. (**Advanced**) Fit a small neural network that transports samples from P_1 to P_2 by minimizing empirical W_1 . Visualize how the learned map behaves.

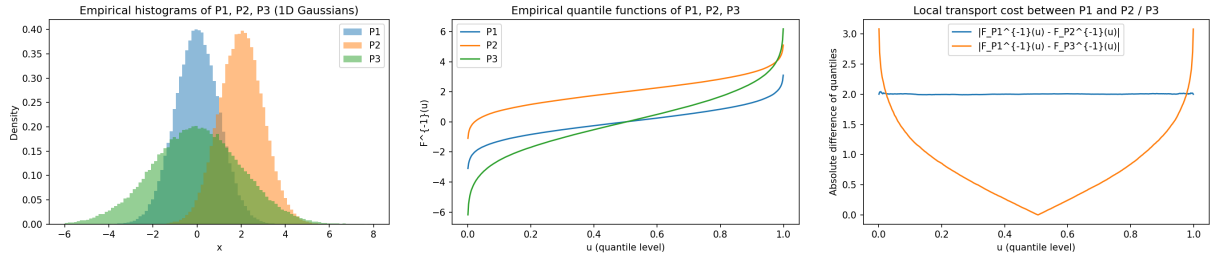


Figure 6.9: Left: Histograms of samples from P_1 , P_2 , and P_3 . The shift in the mean of P_2 and the increased spread of P_3 are clearly visible. Center: Quantile functions of the three Gaussians. In 1D, the Wasserstein distance equals the area between these curves. The constant horizontal shift between P_1 and P_2 explains why $W_1(P_1, P_2) = 2$. Right: Pointwise transport cost $|F_{P_i}^{-1}(u) - F_{P_j}^{-1}(u)|$ ($i = 1, 2, 3$). The shaded area under each curve equals the Wasserstein distance. The cost curve for the variance change (P_3) is smaller overall, matching the fact that $W_1(P_1, P_3) < W_1(P_1, P_2)$.

Forward Look: Optimal Transport and Flow Matching

The Wasserstein distance discussed here is only the beginning of a broader story. Optimal transport (OT) provides a geometric framework for comparing and transforming probability distributions, and its ideas reappear in increasingly sophisticated forms throughout modern generative modeling.

In the *Synthesis Chapter 9*, we return to OT in two deeper contexts:

- **Continuous-time OT maps and flows**, which offer principled ways to morph one distribution into another through dynamical systems;
- **Flow matching**, a recent family of generative-model training objectives that align learned vector fields with OT-inspired transport flows.

These constructions reveal how classical OT geometry underlies diffusion models, normalizing flows, and score-based generative methods. The simple 1D examples in this chapter serve as a conceptual anchor for the more general and powerful OT machinery developed later.

6.3 Information Theory and Neural Networks

Information theory provides a rigorous language for describing how neural networks *store*, *compress*, *transmit*, and *transform* information. Although originally developed for communication systems, Shannon’s framework now underpins many of the most important principles in modern deep learning, from representation learning and model capacity to generalization and robustness.

This section develops the interplay between **entropy**, **compression**, and **expressivity** in neural networks. We connect the information-theoretic quantities introduced in the previous section (entropy, KL divergence, cross-entropy, mutual information, Wasserstein distance)

to the mechanics of neural networks as learning and inference systems.

Shannon's foundational theorems—the **Source Coding Theorem** and the **Channel Coding Theorem**—establish fundamental limits on data compression and reliable communication. These limits have concrete implications for deep learning: how efficiently networks can encode inputs, how much information must pass between layers, and what constraints govern representation bottlenecks.

In the subsections that follow, we examine:

- how entropy and compression relate to the capacity and architecture of neural networks;
- how mutual information illuminates the role of intermediate representations;
- how information bottlenecks (explicit and implicit) shape generalization;
- how modern generative models leverage information-theoretic objectives.

The goal is not only to present classical theorems, but to show how they *actively structure the learning dynamics and representational geometry of neural networks*.

6.3.1 Source Coding Theorem (Lossless Compression)

The **Source Coding Theorem** — Shannon's fundamental result on lossless compression — establishes the ultimate limit on how efficiently data from a probabilistic source can be encoded.

For a discrete memoryless source producing a random variable X with Probability Mass Function (PMF) $P(X)$, the *minimum achievable average code length per symbol* under any lossless encoding scheme is asymptotically bounded below by the **Shannon entropy**

$$H(X) = - \sum_x P(x) \log_2 P(x).$$

In other words, no lossless compression algorithm can achieve an average rate smaller than $H(X)$ bits per symbol, and conversely, Shannon proved that one *can* in principle construct codes whose rate approaches $H(X)$ arbitrarily closely when encoding long sequences of i.i.d. samples.

Compression viewpoint. Entropy thus quantifies the *irreducible information content* of the source. Any redundancy in the data (non-uniform probabilities, correlations, structure) can be exploited by a good encoder to reduce the average number of bits needed. But once all redundancy has been removed, the entropy barrier $H(X)$ cannot be crossed without introducing loss.

Asymptotic and non-constructive nature. While the theorem characterizes the optimal rate, it is not itself a coding algorithm. It guarantees existence but does not provide explicit codes, and its optimality statements hold only in the limit of infinite sequence length. Practical compression methods — e.g., Huffman coding, arithmetic coding, and dictionary-based schemes such as Lempel–Ziv — approximate the theoretical optimum for finite sequences.

Example 6.3.1 (Huffman Coding and Near-Optimal Compression). Consider a source that emits four symbols $\{A, B, C, D\}$ with probabilities

$$P(A) = 0.5, \quad P(B) = 0.25, \quad P(C) = 0.15, \quad P(D) = 0.1.$$

A fixed-length binary code requires 2 bits per symbol. A Huffman code assigns shorter codes to more probable symbols:

$$A \rightarrow 0, \quad B \rightarrow 10, \quad C \rightarrow 110, \quad D \rightarrow 111.$$

The expected code length becomes

$$L = 0.5(1) + 0.25(2) + 0.15(3) + 0.1(3) = 1.75 \text{ bits.}$$

The entropy of the source is

$$H(X) = - \sum_x P(x) \log_2 P(x) \approx 1.72 \text{ bits.}$$

Thus the Huffman code comes very close to Shannon's theoretical lower bound, illustrating how entropy quantifies the best possible lossless compression.

Classical vs. Learned Compression

Classical source coding constructs explicit prefix-free bit strings that minimize average code length. In contrast, **neural networks perform learned compression**:

- autoencoders learn low-dimensional latent representations that approximately satisfy the spirit of source coding,
- Variational Autoencoders (VAEs) explicitly trade off compression and reconstruction using KL divergence,
- modern generative models learn latent spaces whose dimensionality and entropy reflect the underlying data complexity.

Although the mechanisms differ, the organizing principle is the same: *entropy places fundamental limits on how concisely data can be represented*. Later subsections return to this viewpoint when discussing the information bottleneck, latent-variable models, and generative compression.

- Exercise 6.3.1** (Designing and Evaluating Optimal Codes).
1. Compute the entropy $H(X)$ for the four-symbol distribution in the example.
 2. Construct the Huffman code and verify its expected length L .
 3. Modify the distribution (e.g. make it more skewed or more uniform) and repeat the entropy and code-length calculations. How does the gap $L - H(X)$ behave?
 4. For a longer discrete source where the alphabet is moderately large (e.g. 20 symbols), numerically generate random pmfs and compare Huffman code lengths to entropy across many trials. What empirical patterns emerge?

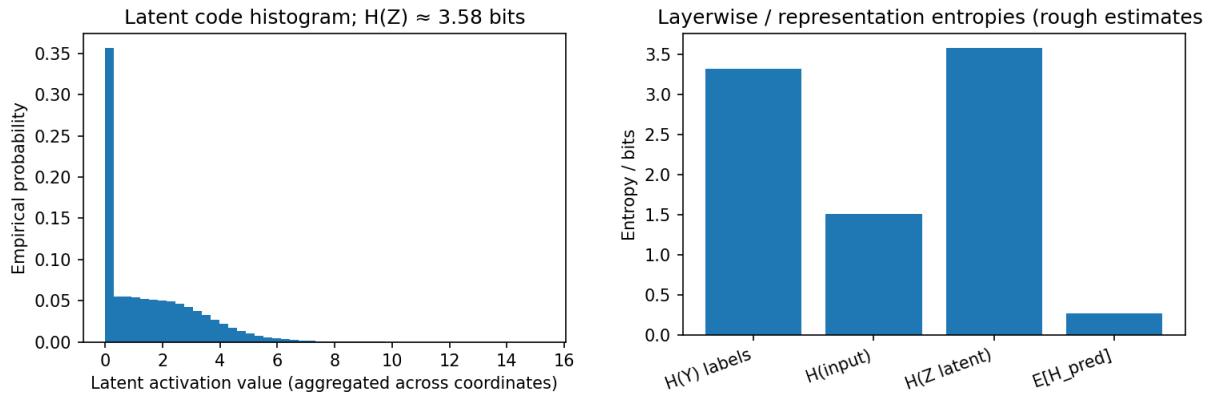


Figure 6.10: Left: Histogram of latent activations in the final hidden layer and empirical entropy estimate $H(Z)$ obtained by binning (Gaussian Model Mixture). The entropy typically decreases compared to raw inputs, indicating task-dependent compression. Right: Layerwise entropy estimates $H(Z_i)$ for a small MNIST CNN. Early layers retain high entropy (broad feature variability), while deeper layers compress toward the label entropy $H(Y)$, consistent with a learned encoding pipeline.

6.3.2 Neural Networks as Encoding Schemes

Neural networks can be understood not only as function approximators – the viewpoint of Chapter 4 – but also as **learned encoding schemes** in the sense of Shannon’s source coding theory. A standard feed-forward classifier performs a sequence of transformations

$$X \longrightarrow Z \longrightarrow Y,$$

where X is the raw input, Z is an internal representation (latent encoding), and Y is the predicted label distribution. From an information-theoretic perspective, the entropy $H(Z)$ measures how much information the network retains about the input after encoding it at a given layer.

For a well-trained classifier, one expects that the deepest representation extracts precisely the information needed for classification:

$$H(Z_{\text{deep}}) \approx H(Y),$$

so that the representation is neither too redundant (overly large entropy) nor too compressed (discarding task-relevant information).

This new viewpoint aligns neural networks with classical source coding: the network acts as a learned encoder whose latent space Z must preserve just enough information to determine the label Y , analogous to optimal lossless compression constrained by the downstream task.

Example 6.3.2 (Estimating Encoding Entropy in a Neural Network). *Consider a small CNN trained on MNIST. For each test image:*

1. Extract latent vectors from a designated hidden layer.
2. Discretize the activations (e.g., via binning or by fitting a Gaussian mixture model).

3. Estimate the entropy

$$H(Z) = - \sum_z P_Z(z) \log_2 P_Z(z).$$

4. Compare $H(Z)$ to $H(Y)$. Well-trained models typically satisfy $H(Z) \approx H(Y)$ in deep layers, while earlier layers retain superfluous variability.

The `entropyNN.ipynb` notebook automates this workflow, producing Figs. 6.10.

Exercise 6.3.2 (Layer-wise Entropy and Information Flow in Neural Networks). Train a small CNN on MNIST or CIFAR-10 and analyze its internal representations as follows:

1. **Activation extraction:** For a fixed test set, record activations from each hidden layer Z_1, Z_2, \dots, Z_L .
2. **Entropy estimation:** Discretize each activation tensor (per neuron or jointly via PCA) and compute empirical entropies $H(Z_i)$.
3. **Comparison with label entropy:** Compute the class entropy $H(Y)$. Identify layers for which $H(Z_i)$ approaches $H(Y)$.
4. **Analysis:** Plot $H(Z_i)$ vs. depth. Discuss how compression emerges across layers, and relate your findings to generalization and robustness.

Compression, Redundancy, and Generalization

Neural networks walk a fine line between two extremes:

- **Redundancy** (under-compression): Large $H(Z)$ means the network preserves too much input variability, increasing the risk of overfitting.
- **Over-compression:** If $H(Z)$ becomes smaller than $H(Y)$, task-relevant information may be destroyed, harming accuracy.
- **Effective encoders:** Good classifiers typically compress representations so that $H(Z_{\text{deep}}) \approx H(Y)$, echoing the optimality principle of Shannon's source coding theorem.

This perspective also underlies the *information bottleneck* principle and sets the stage for later discussions of variational autoencoders (VAEs) and diffusion models.

6.3.3 Autoencoders and Nonlinear Compression

Classical dimensionality-reduction methods such as PCA or SVD provide *linear* compression: they represent data as linear combinations of a small number of orthogonal directions. Many datasets encountered in modern machine learning—images, speech, trajectory data, molecular conformations—contain nonlinear geometric structure that cannot be captured efficiently by linear projections.

A **nonlinear autoencoder** addresses this limitation by learning an *encoder–decoder pair*:

$$X \longrightarrow Z \longrightarrow \hat{X},$$

where:

- the **encoder** maps a high-dimensional input X to a compressed latent representation Z ,
- the **decoder** reconstructs an approximation \hat{X} of the original input.

The reconstruction loss is typically

$$\mathcal{L}_{\text{AE}} = \mathbb{E}_X \left[\|X - \hat{X}\|^2 \right],$$

and the user chooses the *bottleneck size* $\dim(Z)$, which determines the compression ratio. From an information-theoretic point of view, an autoencoder is a *learned compression scheme*. The latent entropy $H(Z)$ provides a quantitative measure of how much information the autoencoder retains after compression:

$$H(Z) \approx \text{bits needed to represent the latent code } Z.$$

A smaller bottleneck or stronger regularization often leads to smaller entropy — but may also degrade reconstruction quality.

Example 6.3.3 (Entropy of Autoencoder Latent Codes). *The accompanying notebook `autoencoder-entropy.ipynb` trains a small autoencoder on MNIST with a configurable bottleneck dimension.*

For a trained model, the notebook performs:

1. **Encoding.** Compute latent vectors $Z = f_\theta(X)$ for the whole test set.
2. **Discretization.** Each latent coordinate is binned into a small number of intervals (e.g., 20–50 bins per dimension), producing a discrete empirical distribution P_Z .
3. **Entropy estimation.** The latent entropy is approximated by:

$$H(Z) \approx - \sum_z P_Z(z) \log_2 P_Z(z).$$

4. **Comparison across bottleneck sizes.** The notebook repeats this procedure for

$$\dim(Z) \in \{8, 16, 32, 64\}.$$

This produces the curve $\dim(Z) \mapsto H(Z)$, which illustrates how compression strength controls the information content of the representation.

Representative outputs appear in Figs. 6.11.

This experiment makes the abstract quantity $H(Z)$ concrete and shows how autoencoders perform nonlinear compression in practice.

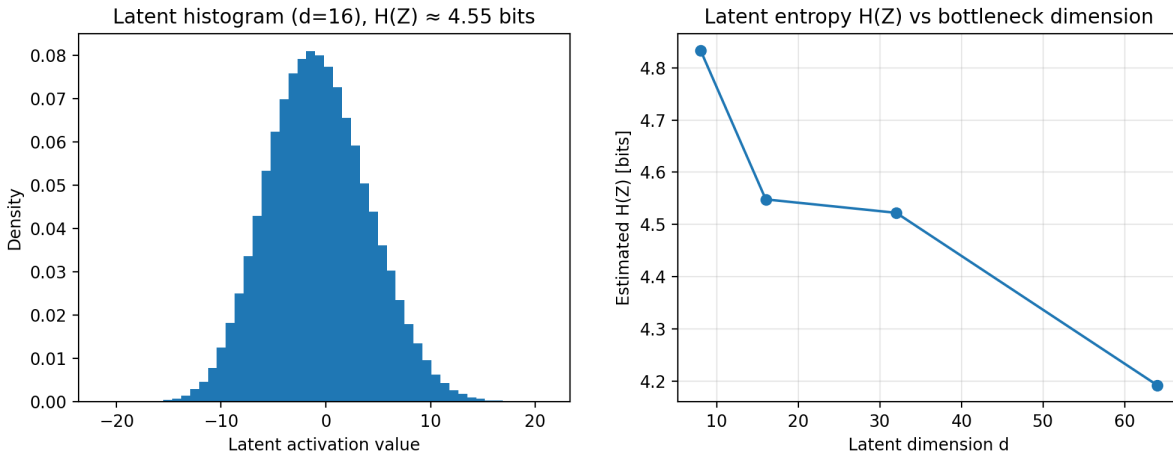


Figure 6.11: Left: Histogram of latent activations for a trained autoencoder (for a chosen bottleneck size), together with the estimated latent entropy $H(Z)$. Increasing compression tends to concentrate activations and reduce entropy. Right: Estimated latent entropy $H(Z)$ as a function of bottleneck dimension. Larger bottlenecks retain more information; smaller bottlenecks enforce stronger compression.

Exercise 6.3.3 (Entropy and Compression in Autoencoders). *Using the notebook `autoencoder-entropy.ipynb`:*

1. Train autoencoders with bottleneck dimensions $d \in \{8, 16, 32, 64\}$.
2. For each model, extract latent representations Z of the MNIST test set and estimate the latent entropy $H(Z)$.
3. Plot $H(Z)$ as a function of d , as in Fig. 6.11.
4. Compare reconstruction errors across bottleneck sizes. How does the trade-off between compression and reconstruction quality manifest?
5. Discuss whether the autoencoder is overcompressing (too little information retained) or undercompressing (latent space carries unnecessary redundancy).

From Autoencoders to Variational and Flow-Based Models

Autoencoders illustrate the core idea of *learned compression*. In later chapters we will see two major generalizations:

- **Variational Autoencoders (VAEs):** introduce an explicit probabilistic model for latent variables Z , with KL divergence controlling information flow.
- **Flow-based Models and Diffusions:** treat the encoder as an invertible map, enabling exact likelihoods and connecting learned representations to optimal transport.

Both perspectives refine and extend the basic compression viewpoint developed in this subsection.

6.3.4 The Information Bottleneck Principle and U-Net as a Non-linear Compressor

A unifying perspective on feature extraction and representation learning in neural networks is provided by the **Information Bottleneck** (IB) principle [35]. Given an input X , an encoded representation Z , and a task variable Y , the IB objective seeks a representation that is both *minimal* (removing irrelevant information about X) and *sufficient* (retaining task-relevant structure):

$$\min_{p(z|x)} I(X; Z) - \beta I(Z; Y),$$

where $I(\cdot; \cdot)$ denotes mutual information and $\beta > 0$ controls the trade-off between compression and predictive usefulness. Although computing $I(X; Z)$ and $I(Z; Y)$ exactly is challenging in high dimensions, the IB principle provides an intuitive conceptual framework: *good representations discard nuisance variability while preserving the information needed for the task.*

U-Net as an Architectural Information Bottleneck. The **U-Net** architecture [36], originally proposed for biomedical image segmentation, offers a vivid architectural example of the bottleneck principle in action. A U-Net consists of three main components:

- a **contracting path** (encoder) that repeatedly downsamples and compresses spatial structure,
- a **bottleneck layer** of reduced spatial extent and increased channel depth,
- an **expanding path** (decoder) that upsamples and combines compressed features with high-resolution skip connections from the encoder.

The encoder compresses X into a low-resolution latent representation Z , enforcing an implicit information bottleneck. The skip connections mitigate excessive information loss by reintroducing fine spatial detail during decoding. Thus, a U-Net simultaneously exhibits the two competing pressures emphasized by IB: *compress aggressively in the bottleneck, yet preserve task-relevant information* needed for accurate reconstruction or segmentation.

Example 6.3.4 (U-Net Compression Effects on MNIST Reconstruction). *The accompanying notebook `UNet-MNIST-light.ipynb` trains two lightweight U-Nets on MNIST with significantly different compression strengths:*

$$\text{depth} = 1 \quad (\text{weak compression}), \quad \text{depth} = 3 \quad (\text{strong spatial bottleneck}).$$

The difference in performance, particularly in discarded information, is visualized using the Absolute Error Map $|X - \hat{X}|$, where \hat{X} is the reconstruction.

Compression Discard: Absolute Error Maps

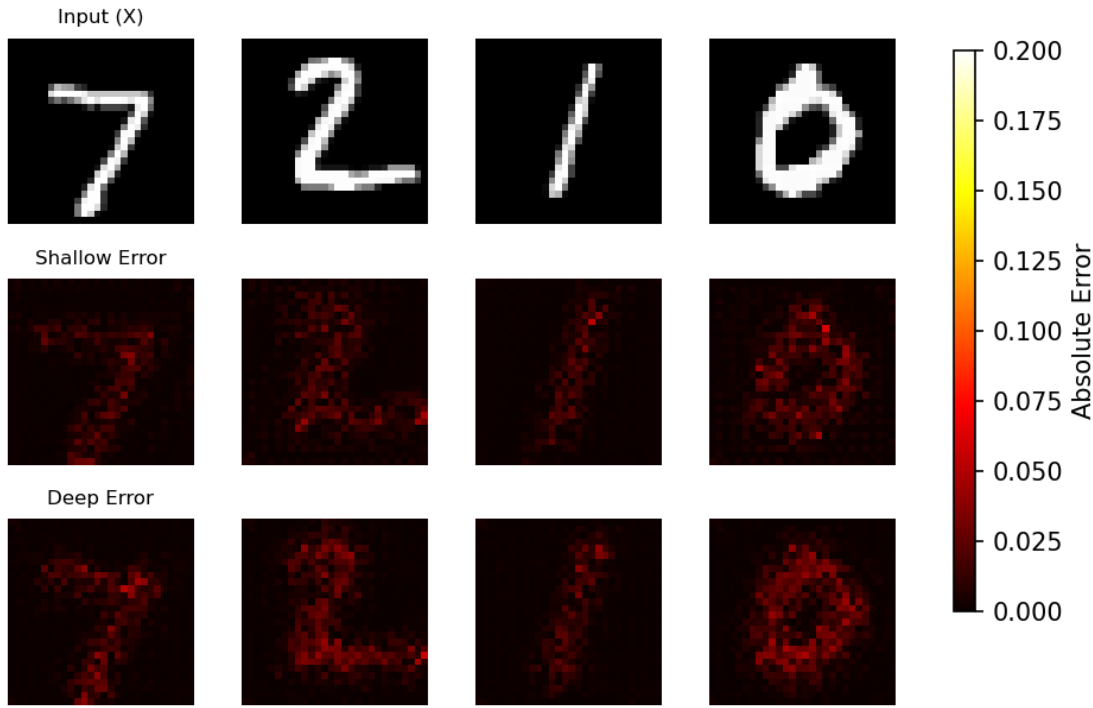


Figure 6.12: Absolute Error Maps ($|X - \hat{X}|$) for two U-Net variants. The top row shows the input X . The middle row shows the error for the shallow (depth = 1) U-Net, which is minimal (less red). The bottom row shows the error for the deep (depth = 3) U-Net, which is significantly higher (more red) and concentrated around the digit boundaries, confirming that the strong bottleneck successfully discarded high-frequency spatial information.

1. **Shallow U-Net (depth = 1):** With no spatial downsampling, the error is minimal, confirming little information loss.
2. **Deep U-Net (depth = 3):** Aggressive spatial downsampling (e.g., to 7×7 features) enforces strong compression, resulting in non-zero error concentrated at the sharp boundaries.
3. **Compression Proxy:** The estimated entropy $H(Z)$ of the latent space (a proxy for $I(X; Z)$) is measurably lower in the depth = 3 model.

Representative results are shown in Fig. 6.12. The depth = 3 network's stronger bottleneck visibly discards more information, producing higher error concentrated on high-frequency details (edges and corners) that are most difficult to represent in a small feature map. This behavior aligns with the IB principle: increasing the strength of the bottleneck reduces $I(X; Z)$, though at the cost of reconstruction fidelity.

Exercise 6.3.4 (Information Bottleneck Behavior in U-Net Architectures). Using the notebook `UNet-MNIST-light.ipynb`:

1. **Vary compression strength:** Train U-Nets of depth $d \in \{1, 2, 3\}$ and record reconstruction losses.
2. **Analyze latent statistics:** Extract the bottleneck activations for each model and plot activation histograms and variances as rough proxies for compression (smaller variance \Rightarrow stronger compression).
3. **Assess IB trade-offs:** For each depth, discuss qualitatively how a proxy for $I(X; Z)$ decreases as compression strengthens, while reconstruction quality (a proxy for $I(Z; Y)$) deteriorates.
4. **Role of skip connections:** Remove or thin out skip connections and examine how reconstruction quality changes. How do skip connections balance compression with preservation of spatial detail?

6.3.5 Channel Coding Theorem and Its Application to Neural Networks

Claude Shannon's **Channel Coding Theorem** establishes a fundamental limit on reliable communication over a noisy channel. If information is transmitted at rate R (bits per channel use) through a channel of capacity

$$C = \max_{P(X)} I(X; Y),$$

then reliable decoding is possible if and only if $R < C$. Above capacity, errors are unavoidable no matter how clever the code.

This viewpoint is surprisingly fruitful when thinking about how information flows through deep neural networks. Each hidden layer can be treated as a *communication channel* transmitting information about the input X toward the target Y :

$$X \rightarrow Z_1 \rightarrow Z_2 \rightarrow \dots \rightarrow Z_L \rightarrow Y.$$

Key analogies:

- **Layer-by-Layer Transmission:** Each hidden layer Z_i passes on a compressed description of X . If compression is too aggressive (a narrow bottleneck), then the next layer cannot reliably recover the features needed for prediction.
- **Noise, Dropout, and Stochasticity:** Regularizers such as dropout act as injected noise, reducing the “effective capacity” of the layer—just as physical noise reduces channel capacity in communication systems.
- **Bottleneck Geometry:** Autoencoders, U-Nets, and classification CNNs all impose information bottlenecks. The channel coding theorem reminds us that these bottlenecks have a *maximum rate* beyond which information simply cannot pass reliably.

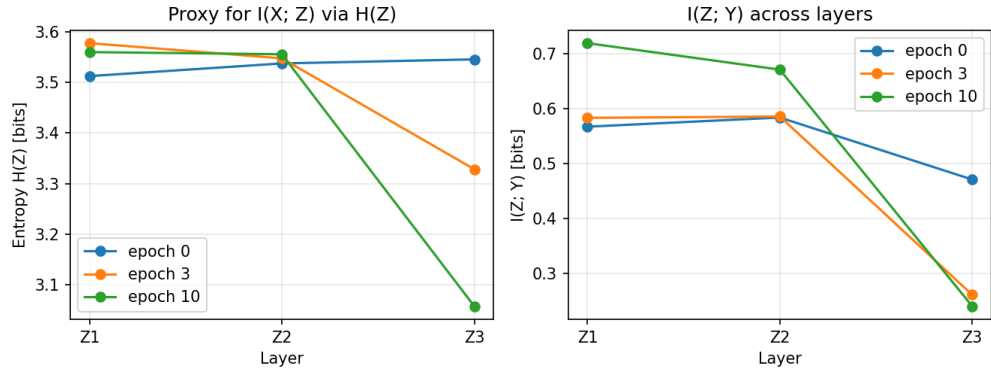


Figure 6.13: Information flow across layers in the MNIST CNN from Example 6.3.5. The left panel shows the entropy $H(Z_i)$ of scalar summaries of the intermediate layers Z_1, Z_2, Z_3 at epochs 0, 3, 10, serving as a rough proxy for $I(X; Z_i)$. The right panel shows the estimated mutual information $I(Z_i; Y)$ with the labels. As training proceeds, deeper layers compress (entropy decreases) while becoming more predictive (larger $I(Z_i; Y)$), illustrating a capacity-like bottleneck effect analogous to channel coding.

Information as a Conserved Quantity

From the channel-coding perspective, the “job” of a neural network is not to preserve *all* information about the input, but rather to preserve precisely the subset relevant for the task. Training gradually pushes intermediate representations Z_i toward states that carry high mutual information with Y , while shedding irrelevant variability in X . This creates a natural lens through which to view the dynamics of representation learning.

Example 6.3.5 (Information Flow in a CNN Viewed as a Noisy Channel). *To make this analogy concrete, we consider a small convolutional neural network trained on MNIST, instrumented so that the intermediate activations*

$$Z_1, Z_2, Z_3$$

are available during evaluation. We approximate the entropy $H(Z_i)$ (as a proxy for $I(X; Z_i)$) and the mutual information $I(Z_i; Y)$, using histogram-based estimators applied to simple scalar summaries of each layer.

The accompanying Jupyter notebook `CNN-MNIST-channel.ipynb` provides a full implementation: training, activation extraction, entropy estimation, mutual information diagnostics. The output of the notebook—summarized in Fig. 6.13 — reveals several characteristic information-flow patterns:

- **Early layers** exhibit relatively high entropy, reflecting sensitivity to many fine-grained pixel-level variations present in the input.
- **With increasing depth,** the representations undergo visible compression: the entropy $H(Z_i)$ decreases across layers. At the same time, the mutual information with the

labels, $I(Z_i; Y)$ increases from epoch 0 to epoch 10, indicating that deeper layers discard irrelevant input variability while increasingly aligning their representations with the task-relevant structure.

- **Dropout as channel noise:** repeating the experiment with larger dropout rates reduces the achievable $I(Z_i; Y)$, demonstrating a clear “capacity-like” limitation: noisier layers function as lower-capacity channels, restricting the amount of label-relevant information that can be reliably transmitted downstream.

This experiment operationalizes the channel coding theorem intuition: a layer of limited capacity (narrow, noisy, or both) cannot transmit arbitrary amounts of information, but it can be trained to transmit precisely the information relevant for classification.

Exercise 6.3.5 (Tracking Mutual Information Through Layers and Epochs). Using the provided notebook `CNN-MNIST-channel.ipynb`, carry out the following steps:

1. Train the supplied CNN for 10 epochs with dropout $p = 0.3$.
2. Extract the intermediate activations Z_1, Z_2, Z_3 at epochs 0, 3, 10 and estimate:

$$H(Z_i), \quad I(Z_i; Y),$$

using the histogram-based estimators implemented in the notebook.

3. Plot and compare the curves (already generated by the notebook):

$$H(Z_i) \quad \text{and} \quad I(Z_i; Y)$$

across layers and epochs. Does the entropy generally decrease with depth? Does $I(Z_i; Y)$ increase, indicating a sharpening of class-specific information?

4. Repeat the experiment with a different dropout rate (e.g. $p = 0.0$ or $p = 0.5$). Compare how the noise level affects the ability of deeper layers to preserve predictive information. Is there evidence of a “capacity limit” analogous to Shannon’s theorem?

Relate your findings to the communication-channel view of neural networks. In particular, interpret where in your model the “bottleneck” lies and how training adapts the internal code to operate below the effective channel capacity.

6.3.6 Efficient Memory and Neural Network Storage

Efficient memory and robust retrieval are essential for understanding both *generalization* and *memorization* in neural networks. A well-trained network must faithfully store task-relevant structure while discarding irrelevant detail. This tension between **memorization** and **compression** mirrors classical communication systems, where reliable transmission requires coding schemes adapted to the channel’s limited capacity.

Memorization vs. Compression as an Information-Theoretic Trade-Off

Over-parameterized networks can memorize the entire training set — including idiosyncratic noise — yet successful generalization requires compressing away most of this information. From an information-theoretic viewpoint, a neural network acts much like a channel encoder: it must map high-dimensional data to lower-capacity internal representations. Too much memorization leads to overfitting; too much compression destroys useful signal. Balancing the two is central to modern deep learning.

Associative Memory and Hopfield Networks. Classical **Hopfield networks** [37] provide an early model of associative memory, storing patterns as stable attractors in a dynamical system. For a binary state vector $\mathbf{x} \in \{-1, +1\}^n$ and weight matrix $W \in \mathbb{R}^{n \times n}$, the system evolves to minimize the energy

$$E(\mathbf{x}) = -\frac{1}{2} \mathbf{x}^\top W \mathbf{x} + \sum_i b_i x_i.$$

With **Hebbian learning** [38],

$$W_{ij} \propto \langle x_i x_j \rangle,$$

the network stores training patterns as energy minima. Given a corrupted input $\mathbf{x}^{(0)}$, the iterative update

$$x_i^{(t+1)} = \text{sgn}\left(\sum_j W_{ij} x_j^{(t)} + b_i\right)$$

drives the state toward a nearby attractor, recovering the original memory. This process is reminiscent of *error correction*: the dynamics undo a small amount of noise by converging to a stored pattern.

Modern Hopfield Networks. Recent work [39, 40] has generalized the Hopfield energy function to support exponentially many attractors, enabling associative retrieval modules to be embedded within contemporary deep networks. These modern Hopfield systems offer:

- high-capacity memory storage,
- fast content-based retrieval,
- and compatibility with architectures such as Transformers.

They can be viewed as adaptive lookup tables governed by energy minimization, blending neuroscience-inspired dynamics with modern AI computation.

Hebbian vs. Linear Codes. An enduring question is how associative memories compare with engineered error-correcting codes:

- **Hopfield networks** store patterns in distributed weights and retrieve them from partial or corrupted cues, but lack explicit guarantees on correction radius or worst-case decoding.

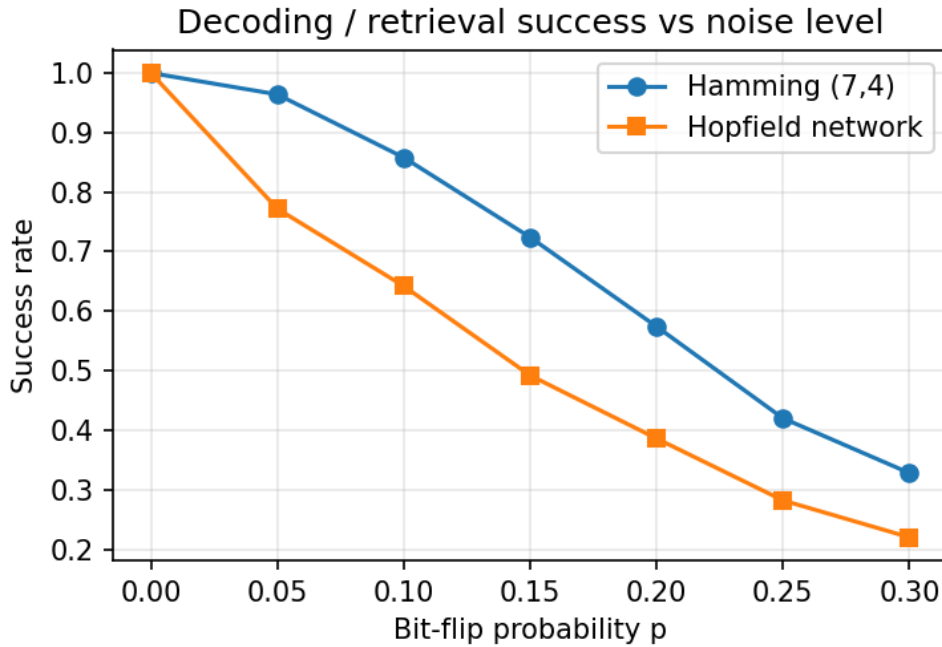


Figure 6.14: Retrieval success rates for the (7, 4) Hamming decoder (top curve) and a Hopfield network storing two corresponding 7-bit codewords (bottom curve), as a function of bit-flip noise level p . Hamming decoding maintains near-perfect accuracy for small noise levels due to its guaranteed single-error correction radius, whereas Hopfield retrieval succeeds frequently but degrades more rapidly with increasing noise.

- **Linear codes** (e.g., Hamming codes) provide formal distance guarantees and maximum-likelihood decoding, ensuring reliable correction under specific noise models.

Associative memory is flexible and brain-inspired; linear codes are rigid but provably reliable.

Example 6.3.6 (Encoding and Retrieval: Hamming Code vs. Hopfield Network). **Linear Code (Hamming).** The classical (7, 4) Hamming code maps a 4-bit message $\mathbf{m} \in \{0, 1\}^4$ into a 7-bit codeword $\mathbf{c} = \mathbf{m}G \pmod{2}$ using a generator matrix G . Decoding is performed by computing the syndrome $H\mathbf{c}$ via a parity-check matrix H , which identifies and corrects any single-bit error. Thus, for small noise levels, the Hamming code provides formal recovery guarantees.

Hopfield Associative Memory. A Hopfield network stores binary patterns as stable attractors of an energy function. Storing a 7-bit pattern $\mathbf{x}^* \in \{-1, +1\}^7$ amounts to forming

$$W = \mathbf{x}^*(\mathbf{x}^*)^\top,$$

(optionally normalized and with zero diagonal). Given a noisy initialization $\mathbf{x}^{(0)}$, the asynchronous update rule

$$x_i^{(t+1)} = \text{sgn}\left(\sum_j W_{ij} x_j^{(t)}\right)$$

drives the state toward a nearby attractor, thereby performing noise-correction. However, unlike the Hamming code, Hopfield retrieval has no rigorous correction radius: for larger

noise levels or when multiple patterns are stored, the dynamics may converge to the wrong attractor or a spurious fixed point.

Empirical Comparison. The accompanying notebook *Hopfield-vs-Hamming.ipynb* stores only two Hamming codewords in the Hopfield network (to avoid overloading the $n = 7$ system) and evaluates retrieval success under random bit-flip noise $p \in [0, 0.3]$. The results, summarized in Fig. 6.14, show:

- For **small noise**, Hamming decoding succeeds with probability nearly 1, while Hopfield retrieval also succeeds frequently but with visibly lower accuracy.
- As **noise increases**, Hamming decoding gradually degrades as multiple-bit errors become likely, whereas Hopfield performance declines more quickly due to limited attraction basins and the possibility of converging to the wrong attractor.
- The comparison illustrates the distinction between engineered error-correcting codes with explicit guarantees and associative memories that rely on energy-based dynamics without worst-case bounds.

Exercise 6.3.6 (Exploring Capacity and Noise Sensitivity in Hopfield Retrieval). *Using the notebook *Hopfield-vs-Hamming.ipynb*:*

1. Repeat the main experiment for different numbers of stored patterns $K \in \{1, 2, 3, 4\}$. For each K , construct a Hopfield network from K Hamming codewords and measure retrieval success under the same noise sweep $p \in [0, 0.3]$.
2. Plot the success curves for each K (overlaid) and compare: how does Hopfield performance deteriorate as more patterns are stored?
3. Estimate the “effective” attraction basin size for each K by identifying the largest p for which retrieval success is above 0.9.
4. Compare your findings with the classical Hopfield capacity $K \approx 0.138n$ for $n = 7$, and contrast this with the strict correction radius of the Hamming code.
5. Discuss: does increasing K cause new spurious attractors? How do empirical results relate to the absence of worst-case guarantees in Hopfield retrieval?

Chapter 7

Stochastic Processes

The preceding chapters developed the mathematical foundations that govern learning via optimization (Ch. 3) and information flow in neural networks (Ch. 4) with probabilistic modeling and latent variables (Ch. 5), and the information-theoretic structure of modern architectures (Ch. 6). These viewpoints emphasized that learning systems operate by *transforming, propagating, and compressing uncertainty*. Stochastic processes provide the natural mathematical language for describing such uncertainty. They are the backbone of sampling, inference, noise injection, model training, and generative mechanisms.

Stochastic processes arise throughout the modern Generative AI ecosystem:

- **Exact and approximate sampling** from distributions is the essence of GenAI, and e.g. central to auto-regressive models, VAEs, EBMs, and diffusion models.
- **Markov chains** underlie both classical Monte Carlo methods and modern architectures such as masked auto-regressive models and token-level Transformers, but it is also a key mathematical ingredient behind diffusion models.
- **Diffusion processes**, with roots from Brownian motion, they are the engines encoding the forward-noising and reverse-de-noising dynamics in score-based diffusion models.
- **Markov Chain Monte Carlo** of various kinds – including and Importance sampling – form the algorithmic bridge between structured (e.g. via graph) mid-size "physical" models and high-dimensional generative modeling.
- **Stochastic differential equations (SDEs)** and their time-reversal laws reappear in the foundations of generative diffusion, Langevin dynamics, energy-based models, and further down the road (discussed in the two last chapters of the book) in path-integral and optimal-transport formulations.

This chapter introduces these stochastic tools in a systematic and unified manner. Each subsection follows a structure already familiar from earlier chapters: concise mathematical development, a worked example with a supporting notebook and figure, and an exercise that extends or stress-tests the ideas. Throughout, short connector boxes highlight how each concept reappears in modern neural generative models and how it prepares us for the energy-based, Langevin, and score-driven frameworks of the following chapters.

Chapter Layout.

- **Section 7.1: Exact Sampling.** Inverse transform sampling and chain-rule sampling as the mathematical foundation of auto-regressive and flow-based models.
- **Section 7.2: Importance Sampling.** Reweighting, proposal mismatch, and effective sample size as precursors to variational inference and gradient-based samplers.
- **Section 7.3: Diffusion and Brownian Motion.** The heat equation, Brownian motion, and the stochastic calculus that underpins diffusion-based generative modeling.
- **Section 7.4: Markov Chains.** Finite-state stochastic dynamics, stationary distributions, and their connection to auto-regressive architectures and sequence models.
- **Section 7.5: MCMC.** Classical Markov-chain sampling algorithms and their limitations, motivating gradient-based and score-based alternatives.
- **Section 7.6: Beyond Markov – Auto-regressive Modeling.** Sequential, conditional, and non-Markovian models that directly connect to Transformers and next-token prediction.

By the end of this chapter, we will have assembled the full stochastic vocabulary required to understand generative diffusion processes, energy-based models, and the path-integral perspective developed in Chapters 8 and 9.

7.1 Exact Sampling

Sampling from probability distributions is a fundamental operation in statistics, Bayesian inference, and generative modeling of AI. **Exact Sampling** refers to methods that produce independent and identically distributed (i.i.d.) samples from a given target distribution without bias and in a finite number of steps – even though potentially exponential number of steps in the system size. Unlike approximate methods such as Markov Chain Monte Carlo (MCMC) – which become exact only asymptotically when the number of samples is sent to infinity – exact sampling techniques ensure that each sample is drawn precisely according to the specified distribution.

7.1.1 Inverse Transform Sampling

Inverse Transform Sampling (ITS) provides an exact and universal method for drawing samples from any one-dimensional distribution with a known cumulative distribution function (CDF). In Section 5.2.3 we saw how invertible maps can transport a simple Gaussian source into complex high-dimensional data distributions. ITS is the *one-dimensional* version of the same idea: instead of transporting a Gaussian, we transport a uniform random variable through the inverse CDF.

Let $U \sim \text{Uniform}(0, 1)$ and let F be the CDF of a target distribution. Then

$$X = F^{-1}(U)$$

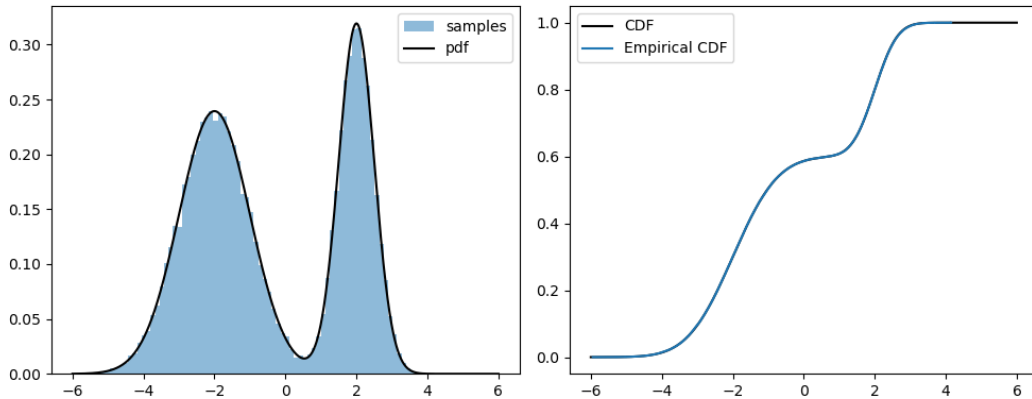


Figure 7.1: Inverse Transform Sampling for a two-component Gaussian mixture. *Left:* target pdf and histogram of ITS samples. *Right:* theoretical CDF $F(x)$ vs. empirical CDF of samples, illustrating exactness. All figures produced by `ITS-1D.ipynb`.

is an exact sample from that distribution. The source need not be Gaussian; any easily sampled base distribution with a well-defined CDF can be used.

Inverse Transform Sampling in Generative AI

In diffusion models, the forward process amounts to repeatedly sampling from Gaussian kernels — an exact operation akin to inverse-CDF sampling. ITS thus provides an instructive toy example of “known” sampling steps that make the forward diffusion analytically tractable. The reverse direction, learned from data, replaces F^{-1} with a neural score model.

Example 7.1.1 (Sampling from a Non-Gaussian Density via ITS). *Consider the Gaussian mixture*

$$p(x) = 0.6 \mathcal{N}(x; -2, 1) + 0.4 \mathcal{N}(x; +2, 0.5^2),$$

a simple non-Gaussian distribution exhibiting multi-modality. We numerically construct its CDF and obtain F^{-1} via interpolation. The ITS procedure is:

$$U \sim \mathcal{U}(0, 1), \quad X = F^{-1}(U).$$

The notebook `ITS-1D.ipynb` computes F , constructs F^{-1} on a fine grid, and generates 50,000 samples. Fig. 7.1 compares the theoretical density with the empirical histogram and shows the agreement between theoretical and empirical CDFs.

Exercise 7.1.1 (Inverse CDF Sampling for Arbitrary Densities). *Use the notebook `ITS-1D.ipynb` as a template.*

1. Replace the Gaussian mixture with a heavy-tailed distribution (e.g., Student- t). Numerically construct its CDF and inverse CDF.
2. Generate 100,000 samples and compare the empirical CDF to the theoretical CDF.

3. Quantify accuracy using either the Kolmogorov–Smirnov distance or KL divergence between the empirical histogram and the true density.

Comment on how numerical errors in F^{-1} interpolation affect sample quality.

Why is ITS only a 1D method? Inverse Transform Sampling relies on the fact that in one dimension the *CDF is an invertible scalar function*:

$$F(x) = \mathbb{P}(X \leq x) \Rightarrow X = F^{-1}(U), U \sim \mathcal{U}(0, 1).$$

The construction works because $F : \mathbb{R} \rightarrow [0, 1]$ is monotone and invertible almost everywhere. In higher dimensions, however, there is no canonical multivariate analogue of a CDF that yields an equally simple inverse map.

For a random vector $\mathbf{X} \in \mathbb{R}^d$ the CDF is

$$F(\mathbf{x}) = \mathbb{P}(X_1 \leq x_1, \dots, X_d \leq x_d),$$

which is a *scalar* function on \mathbb{R}^d . Such an F cannot be inverted to produce a d -dimensional sample: the map $F : \mathbb{R}^d \rightarrow [0, 1]$ collapses all d degrees of freedom into a single number. Recovering \mathbf{X} from $U \in [0, 1]$ would require an inverse map from a scalar to a vector, which is impossible without supplying additional structure.

Higher-dimensional ITS via the chain rule. Note that there is one natural way to generalize ITS to multivariate distributions: apply ITS to *each conditional distribution* in the chain-rule factorization

$$p(x_1, \dots, x_d) = p(x_1) p(x_2 | x_1) \cdots p(x_d | x_{1:d-1}).$$

Each 1D conditional distribution admits its own inverse CDF,

$$x_i = F_{X_i|X_{1:i-1}}^{-1}(u_i | x_{1:i-1}), \quad u_i \sim \mathcal{U}(0, 1),$$

and this produces an exact sampler.

This is precisely the mechanism underlying:

- auto-regressive flows (MAF, MADE);
- normalizing flows with triangular Jacobians;
- exact direct-sampling models with a partition-function oracle;
- ancestral sampling in graphical models.

In these settings, the multidimensional sampling task reduces to a sequence of one-dimensional inverse-CDF evaluations.

This last remark brings us naturally to the next subsection.

7.1.2 Exact Sampling from Multivariate Distributions via Chain Rule

Exact sampling from a multivariate distribution

$$p(\mathbf{x}) = \frac{1}{Z} f(x_1, x_2, \dots, x_n)$$

is generally computationally difficult because computing the global partition function Z typically requires summing over an exponentially large state space. However, if an oracle is available to compute *partial partition functions*, then the high-dimensional sampling problem decomposes into a sequence of tractable one-dimensional conditional sampling problems.

The chain rule for probabilities gives

$$p(x_1, x_2, \dots, x_n) = p(x_1) p(x_2 | x_1) \cdots p(x_n | x_{1:n-1}).$$

Each conditional takes the form

$$p(x_i | x_{1:i-1}) = \frac{f(x_1, \dots, x_i)}{Z(x_1, \dots, x_{i-1})}, \quad Z(x_{1:i-1}) = \sum_{x_i \in \mathcal{X}} f(x_1, \dots, x_i),$$

where $Z(x_{1:i-1})$ is a partial partition function computed by the oracle. Sampling proceeds sequentially, starting with

$$p(x_1) = \frac{f(x_1)}{Z}, \quad Z = \sum_{x_1 \in \mathcal{X}} f(x_1).$$

Example 7.1.2 (Chain-Rule Sampling in a 2D Toy Model). *Consider the two-dimensional discrete distribution*

$$f(x_1, x_2) = \exp(-x_1^2 - 2x_1x_2 + 0.2x_2^2), \quad x_1, x_2 \in \{-3, -2, \dots, 3\}.$$

The oracle computes

$$Z(x_1) = \sum_{x_2} f(x_1, x_2), \quad Z = \sum_{x_1} Z(x_1).$$

The notebook `ChainRuleSampling-2D.ipynb` draws exact samples via the chain rule, plots the 2D histogram of (x_1, x_2) , and compares it to the normalized $f(x_1, x_2)$. Fig. 7.2 displays the theoretical density and the exact samples obtained by ancestral sampling.

Exercise 7.1.2 (Auto-regressive Sampling in Higher Dimensions). *Extend Example 7.1.2 to dimension $n = 5$.*

1. *Construct a function $f(x_{1:5})$ that factorizes weakly but not trivially (e.g., weak pairwise couplings).*
2. *Use a partial-partition oracle (implemented in Python) to compute $Z(x_{1:i-1})$ for $i = 1, \dots, 5$.*
3. *Produce 20,000 exact samples and visualize all pairwise marginals.*
4. *Compare the empirical marginals to the analytically normalized distribution.*

Comment on computational cost and how it scales with dimension.

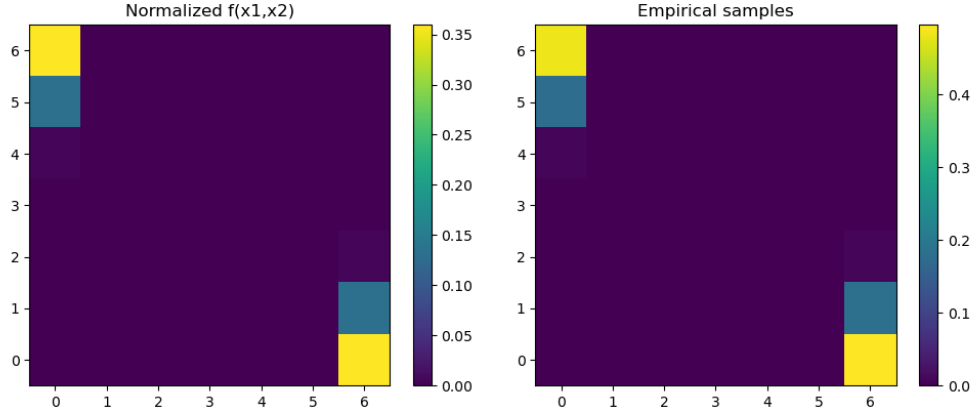


Figure 7.2: Exact ancestral sampling from the 2D toy distribution in Example 7.1.2. *Left:* heat map of the normalized $f(x_1, x_2)$. *Right:* empirical histogram of (x_1, x_2) samples obtained by the chain-rule method. Figures produced by `ChainRuleSampling-2D.ipynb`.

Chain-Rule Sampling and Auto-regressive Generative Models

This exact ancestral-sampling procedure mirrors the structure of auto-regressive models used in sequence modeling and Transformers. Given the past (x_1, \dots, x_{i-1}) , the model produces a conditional distribution over x_i . Exact chain-rule sampling is possible only when partial partition functions are tractable; in high-dimensional settings, this limitation motivates approximate versions such as masked auto-regressive flows and neural auto-regressive Transformers.

7.2 Importance Sampling and its Applications

Sampling efficiently from complex distributions is a core challenge in computational statistics, Bayesian inference, and generative modeling. **Importance Sampling (IS)** provides a principled, unbiased way to compute expectations with respect to a target distribution $p(x)$ by instead drawing samples from a simpler proposal distribution $q(x)$ and reweighting the samples.

7.2.1 General Formulation of Importance Sampling

Suppose we wish to compute

$$\mathbb{E}_p[f(x)] = \int f(x)p(x) dx,$$

but sampling from p is difficult. Let q be a tractable proposal distribution whose support covers that of p . Rewriting the expectation:

$$\mathbb{E}_p[f(x)] = \int f(x) \frac{p(x)}{q(x)} q(x) dx,$$

and drawing samples $x_i \sim q$, we obtain the *importance sampling estimator*

$$\widehat{\mathbb{E}}_p[f] = \frac{1}{N} \sum_{i=1}^N w(x_i) f(x_i), \quad w(x_i) = \frac{p(x_i)}{q(x_i)}.$$

This estimator is unbiased and consistent provided $q(x) > 0$ whenever $p(x) > 0$.

A well-chosen proposal q should place mass in regions where p is large, so that the weights $w(x)$ are stable and have low variance. Poor choice of q leads to heavy-tailed weight distributions and unstable estimates.

Example 7.2.1 (Estimating a Rare-Event Probability). *Consider estimating the rare event probability*

$$P(X > 3) = \int_3^\infty p(x) dx, \quad X \sim \mathcal{N}(0, 1).$$

Direct Monte Carlo is inefficient: with 10^5 samples we expect only about 135 hits in $x > 3$. We introduce a proposal distribution

$$q(x) = \mathcal{N}(3, 1),$$

which places much more mass in the rare-event region. The IS estimate becomes:

$$P(X > 3) \approx \frac{1}{N} \sum_{i=1}^N w(x_i), \quad w(x_i) = \frac{p(x_i)}{q(x_i)}, \quad x_i \sim q.$$

The notebook `ImportanceSampling-RareEvent.ipynb` simulates this experiment and produces Fig. 7.3 showing:

- the target density and the shifted proposal,
- Monte Carlo vs. IS estimate as N increases,
- a dramatic reduction in estimator variance under IS.

7.2.2 Importance Sampling for Posterior Estimation

In Bayesian inference, the target distribution is a posterior

$$p(\theta | y) \propto p(y | \theta)p(\theta),$$

which is often known only up to a normalizing constant. Importance sampling allows us to estimate posterior expectations using samples $\theta_i \sim q(\theta)$ from a convenient proposal. Weights are

$$w(\theta_i) = \frac{p(y | \theta_i)p(\theta_i)}{q(\theta_i)}.$$

Normalizing weights

$$\tilde{w}_i = \frac{w(\theta_i)}{\sum_{j=1}^N w(\theta_j)}$$

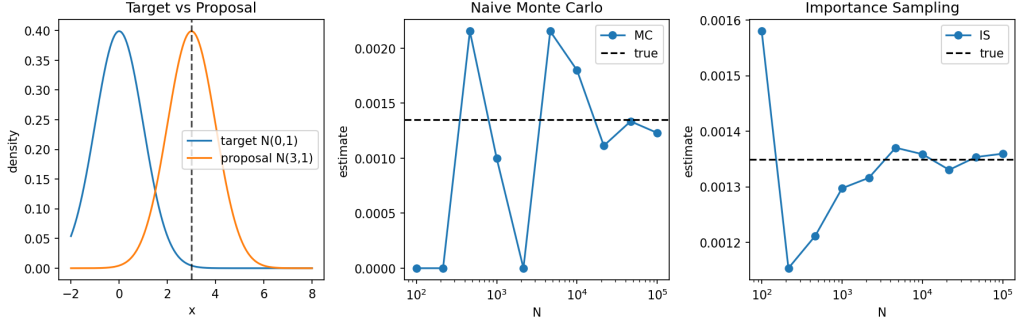


Figure 7.3: Importance sampling for the rare-event probability $P(X > 3)$. *Left:* target density p and proposal q . *Middle:* Monte Carlo estimator using $x_i \sim \mathcal{N}(0, 1)$. *Right:* IS estimator with $x_i \sim \mathcal{N}(3, 1)$, showing orders of magnitude lower variance. All generated by `ImportanceSampling-RareEvent.ipynb`.

yields the self-normalized IS estimator

$$\mathbb{E}_{p(\theta|y)}[f(\theta)] \approx \sum_{i=1}^N \tilde{w}_i f(\theta_i).$$

Example 7.2.2 (Posterior Estimation in a Gaussian Model). *Let the model be*

$$y \mid \theta \sim \mathcal{N}(\theta, 1), \quad \theta \sim \mathcal{N}(0, 10), \quad y = 3.$$

The posterior is Gaussian but we pretend it is unknown in order to test IS. We use a Gaussian proposal

$$q(\theta) = \mathcal{N}(\mu_q, \sigma_q^2), \quad (\mu_q, \sigma_q^2) = (2, 2),$$

and compute weights

$$w(\theta) = \frac{\exp\left(-\frac{1}{2}(y - \theta)^2\right) \exp\left(-\frac{\theta^2}{20}\right)}{\exp\left(-\frac{(\theta - \mu_q)^2}{2\sigma_q^2}\right)}.$$

The notebook `ImportanceSampling-GaussianPosterior.ipynb` evaluates:

- weighted posterior mean and variance estimates,
- the weight distribution and its heavy-tailed behavior,
- the effective sample size (ESS):

$$\text{ESS} = \frac{(\sum_i w_i)^2}{\sum_i w_i^2},$$

a key diagnostic of proposal quality.

Fig. 7.4 compares the true posterior to the IS approximation.

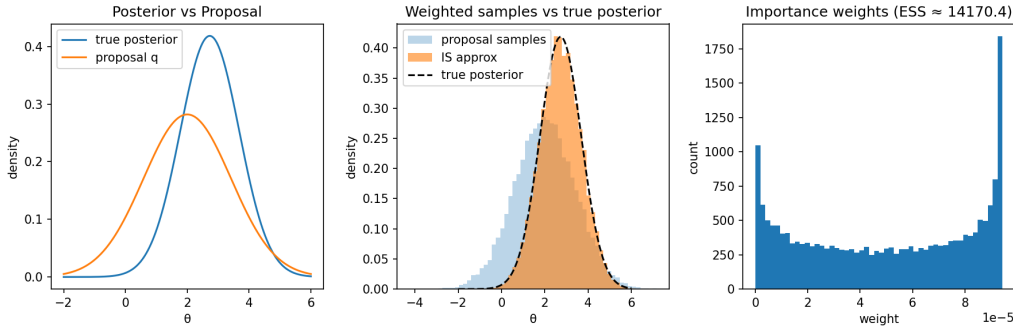


Figure 7.4: Importance sampling for the Gaussian posterior in Example 7.2.2. *Left:* true posterior density and proposal q . *Middle:* weighted sample histogram approximating the posterior. *Right:* importance weights and resulting ESS. Figures produced by `ImportanceSampling-GaussianPosterior.ipynb`.

Importance Sampling in Generative AI

Importance sampling illustrates fundamental limitations of sampling in high-dimensional spaces: proposal mismatch causes weight degeneracy and vanishing ESS. This curse of dimensionality motivates Markov-chain methods (Section 7.5), Langevin dynamics, and ultimately the score-based diffusion samplers used in modern generative models. Many training objectives in diffusion models and VAEs can be interpreted as reducing the mismatch between the learned model and the target distribution, thereby improving IS-like efficiency.

Exercise 7.2.1 (Diagnostics and Proposal Design in Importance Sampling). *Use the notebook `ImportanceSampling-GaussianPosterior.ipynb` as a base.*

- Experiment with several proposals $q(\theta)$ by varying (μ_q, σ_q^2) . For each choice, compute the weight histogram, ESS, and the IS estimate of the posterior mean.*
- Plot ESS as a function of the proposal variance and identify the optimal region. Compare with intuition from KL divergence between q and the posterior.*
- Modify the example so that the likelihood is heavy-tailed (e.g. using a Student- t model). Study how importance weights behave and how ESS changes.*
- Discuss the failure mode of IS in moderate dimension ($d = 10$), where even mildly mismatched proposals produce $ESS \ll 1$.*

Summarize the regimes where IS is effective and where alternative sampling methods (MCMC, SDE-based methods, diffusion models) are necessary.

7.2.3 Adaptive Importance Sampling and the Cross-Entropy Method

Importance Sampling (IS) is effective only when the proposal distribution $q(x)$ places mass in the same regions as the target $p(x)$. When the mismatch is large, weights become

heavy-tailed and the effective sample size (ESS) collapses. *Adaptive Importance Sampling (AIS)* aims to fix this by iteratively *adapting* the proposal distribution to better approximate the target.

A powerful and widely used AIS framework is the **Cross-Entropy (CE) Method**, introduced by Rubinstein [41, 42]. Originally developed for rare-event simulation and combinatorial optimization, CE has become a pillar of adaptive Monte Carlo methods, reinforcement learning, sequence design, and modern generative modeling (e.g., adaptive proposal training, energy-based model sampling).

Goal of Adaptive IS

Suppose we want to evaluate

$$\mathcal{I} = \mathbb{E}_p[f(x)]$$

but sampling directly from p is difficult. We choose a parametric proposal family $q_\theta(x)$ and seek parameters θ^* such that q_θ approximates the optimal IS proposal

$$q^*(x) \propto |f(x)|p(x),$$

which in general is intractable.

AIS updates θ iteratively from

$$\theta_{t+1} \leftarrow \arg \max_{\theta} \mathbb{E}_{q_{\theta_t}} \left[w_{\theta_t}(x) \log q_{\theta}(x) \right], \quad w_{\theta_t}(x) = \frac{p(x)}{q_{\theta_t}(x)}.$$

This is equivalent to minimizing the KL divergence

$$\theta_{t+1} = \arg \min_{\theta} D_{\text{KL}}(q^* \parallel q_{\theta}),$$

and can be viewed as a weighted maximum-likelihood update.

Let us adopt general CE method – discussed in Section 6.2.4 – to Importance Sampling. In the CE method, the update is expressed through the *cross-entropy*

$$\text{CE}(q^*, q_{\theta}) = -\mathbb{E}_{q^*}[\log q_{\theta}(x)].$$

Since q^* is unknown, we approximate expectations with weighted samples $x_i \sim q_{\theta_t}$.

A defining feature of the CE method is that the weights are constructed from *elite samples*. For rare-event probability estimation, the elite set corresponds to the top ρ -quantile of the likelihood ratio, or equivalently, the set of samples that fall in the rare region.

Let E_t be the elite set at iteration t :

$$E_t = \{x_i : S(x_i) \geq \gamma_t\},$$

where $S(x)$ is a score function (e.g. indicator of a rare event) and γ_t is the empirical ρ -quantile threshold. The CE update becomes a maximum-likelihood fit:

$$\theta_{t+1} = \arg \max_{\theta} \sum_{x_i \in E_t} \log q_{\theta}(x_i).$$

Thus CE re-fits q_{θ} to the elite samples at every iteration, gradually shifting mass toward the regions where $p(x)$ is large.

Example 7.2.3 (Adaptive IS via CE for Fitting a Target Distribution). *To illustrate the mechanics of Adaptive Importance Sampling (AIS) and the Cross-Entropy (CE) update, we consider a clean, well-controlled setting where the goal is to adapt a Gaussian proposal distribution toward a known target. This avoids the instability of rare-event optimization and shows clearly how adaptive IS reduces weight variance and improves ESS.*

Setup. Let the target be

$$p(x) = \mathcal{N}(2, 0.75^2),$$

and let the proposal family be

$$q_{\theta}(x) = \mathcal{N}(\mu, \sigma^2).$$

We begin with a poor initial guess, for example

$$(\mu_0, \sigma_0) = (0, 3).$$

AIS / CE Update. At iteration t :

1. Draw samples $x_i \sim q_{\theta_t}$.
2. Compute importance weights

$$w_i = \frac{p(x_i)}{q_{\theta_t}(x_i)}, \quad \tilde{w}_i = \frac{w_i}{\sum_j w_j}.$$

3. Perform a weighted maximum-likelihood update:

$$\mu^{(w)} = \sum_i \tilde{w}_i x_i, \quad (\sigma^2)^{(w)} = \sum_i \tilde{w}_i (x_i - \mu^{(w)})^2.$$

4. Apply smoothing:

$$\mu_{t+1} = \alpha \mu^{(w)} + (1 - \alpha) \mu_t, \quad \sigma_{t+1}^2 = \alpha (\sigma^2)^{(w)} + (1 - \alpha) \sigma_t^2,$$

with $\alpha \in (0, 1)$ and a small variance floor to avoid degeneracy.

This update decreases the KL divergence $D_{\text{KL}}(p\|q_{\theta})$ and improves the quality of the proposal. The accompanying notebook `AdaptiveIS-CE-fitGaussian.ipynb` implements this procedure. Figure 7.5 shows:

- **Proposal evolution:** (μ_t, σ_t) moves smoothly from a broad, misaligned initial proposal toward the true target.
- **Weight stabilization:** the variance of the normalized weights decreases over iterations.
- **ESS improvement:** the effective sample size increases significantly as the proposal approaches the target.

This example demonstrates the core principle of AIS: iteratively adapting the proposal sharply reduces weight degeneracy, increasing sampling efficiency.

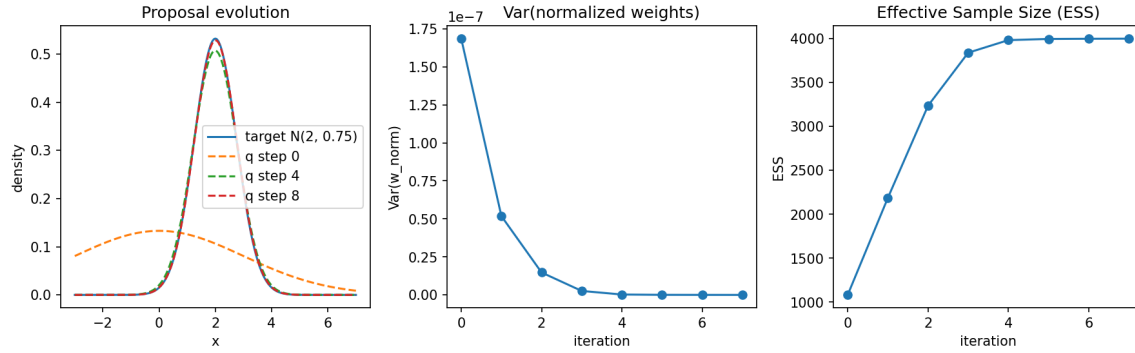


Figure 7.5: Adaptive Importance Sampling using the Cross-Entropy update applied to fitting a Gaussian target $p(x) = \mathcal{N}(2, 0.75^2)$. *Left:* evolution of the proposal densities over iterations. *Middle:* variance of normalized importance weights decreases. *Right:* ESS increases substantially as the proposal improves. Figures generated by `AdaptiveIS-CE-fitGaussian.ipynb`.

Exercise 7.2.2 (Adaptive IS for a Non-Gaussian Target). *Implement AIS and CE for sampling a heavy-tailed target distribution*

$$p(x) \propto \frac{1}{1+x^2}, \quad x \in \mathbb{R},$$

using a Gaussian proposal family $q_\theta = \mathcal{N}(\mu_t, \sigma_t^2)$.

- (a) Derive the weighted MLE update for (μ_t, σ_t^2) .
- (b) Implement the CE version where elite samples replace weights. Compare convergence behavior.
- (c) Track and plot ESS over iterations. Describe how AIS improves proposal quality.
- (d) Discuss why heavy-tailed targets can destabilize AIS and how CE (elite re-fitting) partially mitigates such instability.

Adaptive Importance Sampling in Modern AI

AIS and the CE method appear implicitly throughout modern generative modeling:

- In diffusion models, optimal proposal schedules minimize a KL objective structurally identical to CE.
- In reinforcement learning, policy-gradient and trajectory-optimization schemes (e.g. CEM-RL) directly descend the CE objective.
- In energy-based and score-based models, AIS is used to calibrate and refine approximate samplers.

Viewed broadly, AIS provides the conceptual bridge between classical IS and the adaptive, KL-driven training procedures that dominate contemporary generative AI.

7.3 Diffusion and Brownian Motion

Diffusion processes form the mathematical backbone of modern generative models based on noise injection and gradual denoising, including *score-based models* and *Denoising Diffusion Probabilistic Models (DDPMs)*. In these models, data are progressively transformed into noise by a forward diffusion process and then reconstructed by learning how to reverse that diffusion.

This section develops the theory of diffusion from first principles. We proceed in the following steps:

1. Introduce Brownian motion as the canonical continuous-time stochastic process with independent Gaussian increments.
2. Derive the diffusion (heat) equation from Brownian motion using both path integrals and Chapman–Kolmogorov consistency.
3. Generalize diffusion by introducing drift through a potential, leading to Langevin dynamics and the Fokker–Planck equation.
4. Interpret diffusion as convolution with the heat kernel and connect this viewpoint to discrete approximations used in generative AI.

These ideas will culminate in a conceptual bridge to diffusion-based generative models, where learning the reverse-time dynamics enables sampling from complex data distributions.

7.3.1 Diffusion from Brownian Motion

Brownian motion is the simplest nontrivial continuous-time stochastic process and serves as the universal scaling limit of random walks. Its defining properties — independent increments, Gaussian fluctuations, and Markovian evolution — make it the natural “base process” for forward diffusion in generative models. In score-based and diffusion probabilistic models, the forward process is precisely a Brownian motion (possibly with time-dependent variance), while the learning problem focuses on approximating the reverse-time dynamics.

Consider the simplest case of Brownian motion, where a particle diffuses with no advection. The stochastic differential equation (SDE) for Brownian motion is given by ¹

$$dX_t = \sqrt{2D} dW_t, \quad (7.1)$$

where

¹The Wiener process, named after Norbert Wiener, provides the first rigorous mathematical formulation of Brownian motion. Although Brownian motion had been observed since the 19th century and modeled statistically by Einstein and Smoluchowski, it was Wiener who, in the early 1920s, defined the continuous-time stochastic process that now bears his name. His construction used functional analysis to describe the probability space of continuous paths, formalizing properties such as continuity, Gaussian increments, and the Markov property. Wiener’s 1923 paper [43] introduced “differential space,” and in 1924 in [44] he clarified the link between Brownian motion and harmonic analysis — laying the groundwork for modern stochastic calculus and the path-space approach to diffusion.

- X_t is the position of the particle at time t ;
- D is the diffusion coefficient;
- W_t is the standard Wiener process (or Brownian motion).

The Wiener process W_t is defined by the properties:

1. $W_0 = 0$;
2. W_t has independent increments;
3. The increment $W_{t+\epsilon} - W_t$ is normally distributed with mean 0 and incremental variance ϵ :

$$W_{t+\epsilon} - W_t \sim \mathcal{N}(0, \epsilon) \quad (7.2)$$

As we see below this translates into accumulation of variance over time:

$$\text{Var}(\sqrt{2D} W_t) = 2D t.$$

7.3.2 From the Stochastic Differential Equation to the Path Integral

To connect the stochastic differential equation (SDE) description of Brownian motion with the path integral representation, we begin by discretizing the SDE and examining the resulting probability distribution over paths.

Recall that the SDE for Brownian motion is given by Eq. (7.1). We discretize the time interval $[0, t]$ into N steps of size $\epsilon = t/N$ each, and define $X_n = X(n\epsilon)$, $n = 1, \dots, N$. The increment of the Wiener process satisfies Eq. (7.2) which implies that:

$$X_{n+1} - X_n \sim \mathcal{N}(0, 2D\epsilon).$$

Therefore, the transition probability density from X_n to X_{n+1} is given by the Gaussian:

$$p(X_{n+1}|X_n) = \frac{1}{\sqrt{4\pi D\epsilon}} \exp\left(-\frac{(X_{n+1} - X_n)^2}{4D\epsilon}\right).$$

The joint probability density for the full trajectory $\{X_1, \dots, X_{N-1}\}$ is:

$$p(X_1, \dots, X_{N-1}) \propto \left(\prod_{n=1}^{N-1} \frac{1}{\sqrt{4\pi D\epsilon}} \right) \exp\left(-\sum_{n=0}^{N-1} \frac{(X_{n+1} - X_n)^2}{4D\epsilon}\right),$$

and thus the marginal probability density of observing $X_N = x$ given $X_0 = x_0$ – thus marginalized over x_1, \dots, x_{N-1} is

$$p(x_N|x_0) \approx \int \left(\prod_{n=1}^{N-1} \frac{dX_n}{\sqrt{4\pi D\epsilon}} \right) \exp\left(-\sum_{n=0}^{N-1} \frac{(X_{n+1} - X_n)^2}{4D\epsilon}\right).$$

Recognizing the exponent as a Riemann sum approximation of an integral, we transition to the continuum limit:

$$\sum_{n=0}^{N-1} \frac{(X_{n+1} - X_n)^2}{\epsilon} \rightarrow \int_0^t \left(\frac{dX(\tau)}{d\tau} \right)^2 d\tau.$$

Thus, we arrive at the so-called *path integral*, also called Feynman-Kac, formulation²:

$$p(x_t | x_0) = \int_{X(0)=x_0}^{X(t)=x_t} \mathcal{D}[X] \exp \left[-\frac{1}{4D} \int_0^t \left(\frac{dX(\tau)}{d\tau} \right)^2 d\tau \right],$$

where $\mathcal{D}[X]$ denotes the path integral measure defined as the continuum limit of the finite-dimensional product of Gaussian integrals.

From Path Integral to Diffusion. Using the notation introduced earlier in this subsection, we now derive the diffusion equation starting from the path integral formulation. The marginal probability density can be written as the continuum limit of a discrete sum over intermediate positions:

$$p_t(x) = \lim_{N \rightarrow \infty} \int dX_1 \cdots dX_{N-1} \prod_{n=0}^{N-1} K(X_{n+1}, X_n; \epsilon),$$

where the short-time propagator K is given by:

$$K(X_{n+1}, X_n; \epsilon) \approx \frac{1}{\sqrt{4\pi D\epsilon}} \exp \left[-\frac{(X_{n+1} - X_n)^2}{4D\epsilon} \right].$$

This Gaussian kernel encodes the transition probability for a diffusing particle over a single time step of duration ϵ .

Marginalization over Intermediate Times. The product

$$\prod_{n=0}^{N-1} K(X_{n+1}, X_n; \epsilon)$$

²The Feynman-Kac formula is a foundational result linking stochastic processes and partial differential equations (PDEs), uniting ideas from physics and probability. Physicist Richard Feynman introduced the path integral formulation in quantum mechanics during the 1940s as a way to compute quantum amplitudes by summing over all possible trajectories, each path weighted by a complex exponential of the classical action. Around the same time, mathematician Mark Kac developed a probabilistic method for solving parabolic PDEs by computing expectations over Brownian motion trajectories. Kac's work, particularly his 1949 paper, provided a rigorous mathematical foundation for interpreting solutions to the Schrödinger and heat equations as averages over stochastic paths — a viewpoint deeply rooted in the earlier work of Norbert Wiener. In fact, Kac's construction built directly on Wiener's rigorous definition of Brownian motion and his development of path-space integration in the early 1920s. The resulting Feynman-Kac formula can be seen as a synthesis: while Feynman's path integrals were originally heuristic and formal in the physics tradition, Kac's use of Wiener integrals provided the analytical machinery to render them precise in imaginary (Euclidean) time. Today, this formulation is a cornerstone of mathematical physics, quantitative finance, and generative modeling via stochastic differential equations. See Wiener (1923, 1924) [43, 44], Kac (1949)[45], and Feynman & Hibbs (1965)[46].

can be interpreted as a chain of conditional transition probabilities. The marginal probability $P(X_N = x, t \mid X_0 = x_0)$ is computed by integrating over all intermediate positions X_1, \dots, X_{N-1} , which embodies the structure of the Chapman–Kolmogorov equation³:

$$p_t(x) = \int dX' p_{t-\epsilon \rightarrow t}(x \mid X') p_{t-\epsilon}(X').$$

Derivation of the Diffusion Equation. We analyze the small-time limit of the Chapman–Kolmogorov relation:

$$p_{t+\epsilon}(x) = \int_{-\infty}^{\infty} dX' K(x, X'; \epsilon) p_t(X').$$

Expanding $p_t(X')$ about x via Taylor series:

$$p_t(X') = p_t(x) + (X' - x) \frac{\partial p_t(x)}{\partial x} + \frac{(X' - x)^2}{2} \frac{\partial^2 p_t(x)}{\partial x^2} + \dots,$$

and applying standard Gaussian integrals:

$$\begin{aligned} \int_{-\infty}^{\infty} \frac{dX'}{\sqrt{4\pi D\epsilon}} \exp\left[-\frac{(x - X')^2}{4D\epsilon}\right] &= 1, \\ \int_{-\infty}^{\infty} \frac{(X' - x) dX'}{\sqrt{4\pi D\epsilon}} \exp\left[-\frac{(x - X')^2}{4D\epsilon}\right] &= 0, \\ \int_{-\infty}^{\infty} \frac{(X' - x)^2 dX'}{\sqrt{4\pi D\epsilon}} \exp\left[-\frac{(x - X')^2}{4D\epsilon}\right] &= 2D\epsilon, \end{aligned}$$

we find:

$$p_{t+\epsilon}(x) \approx p_t(x) + D\epsilon \frac{\partial^2 p_t(x)}{\partial x^2}.$$

Taking the limit $\epsilon \rightarrow 0$ yields the **diffusion equation**:

$$\frac{\partial p_t(x)}{\partial t} = D \frac{\partial^2 p_t(x)}{\partial x^2},$$

which is a deterministic Partial Differential Equation (PDE) describing the time evolution of the probability density $p_t(x)$ in one spatial dimension.

Example 7.3.1 (Brownian Motion and the Heat Equation in One Dimension). *Consider the Brownian motion*

$$dX_t = \sqrt{2D} dW_t, \quad X_0 = 0,$$

whose marginal density satisfies the heat equation

$$\partial_t p_t(x) = D \partial_x^2 p_t(x), \quad p_0(x) = \delta(x).$$

³This integral identity is attributed to Sydney Chapman and Andrey Kolmogorov, who independently formalized the evolution of probability distributions under Markovian dynamics. Chapman's work (circa 1928) laid the foundation in statistical mechanics, while Kolmogorov's 1931 axiomatization of probability theory gave the result its modern mathematical rigor. The resulting identity — a recursive composition of transition probabilities — now serves as a central organizing principle in stochastic processes, underpinning both forward and backward equations in diffusion and Markov chains.

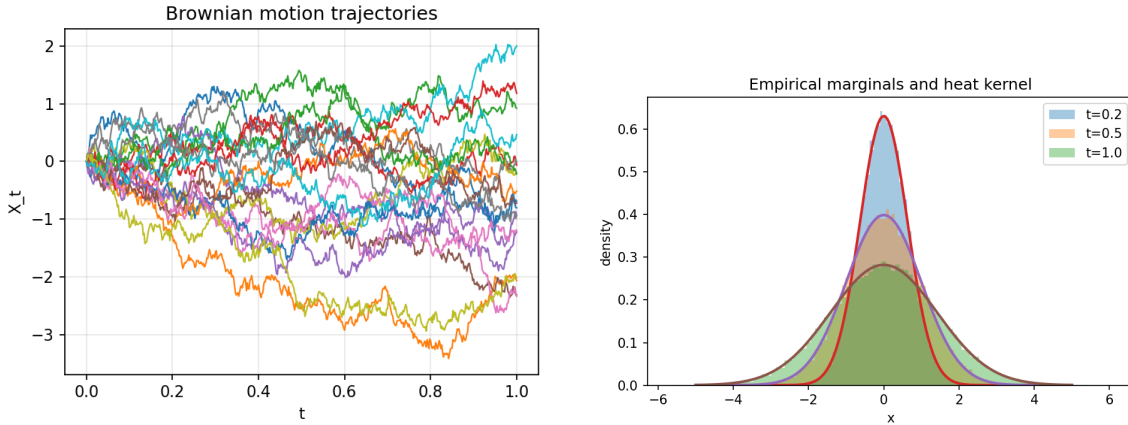


Figure 7.6: Brownian motion and diffusion. *Left:* sample trajectories of 1D Brownian motion generated via Euler–Maruyama discretization. *Right:* empirical marginal distributions at increasing times, compared with the analytic heat kernel solution of the diffusion equation. Figures generated by `BrownianMotion-and-HeatEquation.ipynb`.

The analytic solution is the heat kernel:

$$p_t(x) = \frac{1}{\sqrt{4\pi Dt}} \exp\left(-\frac{x^2}{4Dt}\right),$$

which is simply a Gaussian whose variance grows linearly with time.

A standard numerical method for simulating Stochastic Differential Equations (SDEs) is the Euler–Maruyama scheme⁴. We implement it by discretizing time as $t_k = k\Delta t$ and approximating the SDE by

$$X_{k+1} = X_k + \sqrt{2D} \Delta W_k, \quad \Delta W_k \sim \mathcal{N}(0, \Delta t),$$

or equivalently

$$X_{k+1} = X_k + \sqrt{2D \Delta t} \xi_k, \quad \xi_k \sim \mathcal{N}(0, 1).$$

The accompanying notebook `BrownianMotion-and-HeatEquation.ipynb` illustrates three complementary viewpoints:

- **Path space:** simulated Brownian trajectories using Euler–Maruyama;
- **Marginals:** empirical histograms at multiple times compared to the analytic heat kernel;
- **PDE evolution:** numerical solution of the heat equation via convolution with the Gaussian kernel (FFT-based).

⁴The Euler–Maruyama method is the stochastic analogue of the classical Euler method for ordinary differential equations. It was introduced by Gisiro Maruyama in 1955 as a rigorous discretization scheme for stochastic differential equations driven by Wiener processes. Maruyama showed that replacing infinitesimal Wiener increments dW_t by Gaussian random variables $\sqrt{\Delta t} \xi_k$, with $\xi_k \sim \mathcal{N}(0, 1)$, yields a convergent approximation to the true stochastic process. The method is named in analogy with the deterministic Euler scheme and is now a cornerstone of numerical stochastic analysis and simulation-based modeling.

These three perspectives — trajectories, probability densities, and PDEs — are mathematically equivalent and form the foundation of diffusion-based generative modeling.

Exercise 7.3.1 (Brownian Motion with Absorbing and Reflecting Boundaries). Consider standard Brownian motion

$$dX_t = \sqrt{2D} dW_t, \quad X_0 = x_0 \in (0, L),$$

but now confined to an interval $[0, L]$.

Discrete simulation. Use the Euler–Maruyama update

$$X_{k+1} = X_k + \sqrt{2D \Delta t} \xi_k, \quad \xi_k \sim \mathcal{N}(0, 1),$$

and impose the boundary condition after each step, according to the cases below. Extend the notebook `BrownianMotion-and-HeatEquation.ipynb` accordingly.

- (a) **Absorbing boundary at 0 and L.** Declare a trajectory killed (absorbed) when it first exits the interval. Simulate many trajectories and estimate:

- the survival probability

$$S(t) = \mathbb{P}(\tau > t), \quad \tau = \inf\{t \geq 0 : X_t \notin (0, L)\},$$

- the empirical distribution of the first passage time τ ,
- the probability of exiting through the right endpoint $\mathbb{P}(X_\tau = L)$.

- (b) **Reflecting boundary at 0 and L.** Modify the simulation so that paths are reflected at the boundaries: whenever a step proposes $X_{k+1} < 0$ set $X_{k+1} \leftarrow -X_{k+1}$, and whenever $X_{k+1} > L$ set $X_{k+1} \leftarrow 2L - X_{k+1}$. Simulate trajectories and estimate the marginal density $p_t(x)$ at multiple times. What distribution do you observe as $t \rightarrow \infty$?

- (c) **Compare the two cases.** For absorbing boundaries, mass disappears over time (trajectories are killed), while for reflecting boundaries, total probability is conserved. Explain how this is visible in your simulation outputs (histograms and $S(t)$).

- (d) **Bonus: PDE and boundary conditions.** Let $p_t(x)$ denote the density of X_t . Argue that in both cases the interior evolution is still governed by the diffusion equation

$$\partial_t p_t(x) = D \partial_x^2 p_t(x), \quad x \in (0, L),$$

but the boundary conditions differ:

- absorbing boundary: $p_t(0) = p_t(L) = 0$ (Dirichlet),
- reflecting boundary: $\partial_x p_t(0) = \partial_x p_t(L) = 0$ (Neumann).

Give a short intuitive explanation in terms of probability flux.

Implementation note. For (a), keep track of the first time a path leaves $(0, L)$; for (b), implement reflection step-by-step. Use the same Δt , number of trajectories, and time horizons in both cases so that comparisons are meaningful.

Generalization to Higher Dimensions. The above derivation assumes $x \in \mathbb{R}$, i.e., motion in a one-dimensional spatial domain. However, the formalism generalizes naturally to higher dimensions, where $x \in \mathbb{R}^d$, for arbitrary spatial dimension $d = 1, 2, \dots$. In this setting, the first derivative ∂_x becomes the gradient ∇ , and the second derivative ∂_x^2 is replaced by the Laplacian operator:

$$\Delta = \sum_{i=1}^d \frac{\partial^2}{\partial x_i^2}.$$

Accordingly, the diffusion equation in higher dimensions becomes:

$$\frac{\partial p_t(x)}{\partial t} = D \Delta p_t(x),$$

where now $\nabla p_t(x)$ is a vector field, and $\Delta p_t(x)$ captures the spatial spread of probability mass across dimensions.

In summary – by discretizing time, we expressed the path integral as a product of transition kernels and marginalized over intermediate positions. Through the Chapman–Kolmogorov identity and a Taylor expansion of the probability density, we derived the diffusion equation in the continuous limit. This derivation illustrates the deep connection between the stochastic microscopic dynamics (in the form of random trajectories) and the deterministic macroscopic PDE that governs the evolution of marginal distributions.

7.3.3 Generalization: Diffusion with Drift Induced by a Potential

We now generalize the diffusion process by introducing a drift term governed by the gradient of a potential function $U(x)$. This leads to the following Stochastic Differential Equation (SDE):

$$dX_t = -\nabla U(X_t) dt + \sqrt{2D} dW_t, \quad (7.3)$$

where $\nabla U(X_t)$ is shorthand for $\nabla_X U(X)$ evaluated at $X = X_t$. This equation is commonly referred to as the *Langevin equation*⁵.

In this setting, the time evolution of the probability density $p_t(x)$ is governed by the *Fokker–Planck equation*⁶:

$$\frac{\partial p_t(x)}{\partial t} = \nabla_x \cdot (\nabla U(x) p_t(x)) + D \nabla^2 p_t(x).$$

In the *stationary state*, defined by the condition $\partial_t p_t^{(\text{st})}(x) = 0$, and assuming the system satisfies the so-called *detailed balance* (DB) condition – i.e., the probability flux vanishes –

⁵Named after Paul Langevin, who in 1908 proposed this equation to describe the stochastic dynamics of particles immersed in a fluid, combining deterministic drag with random thermal fluctuations. Langevin's formulation extended earlier work on Brownian motion by introducing a force term, thereby opening the path to modern theories of nonequilibrium statistical mechanics.

⁶The equation is named after Adriaan Fokker and Max Planck. Fokker derived a form of the equation in his study of Brownian motion under external forces, while Planck had earlier obtained a similar equation describing radiation and entropy in statistical physics. The modern name reflects their combined contributions to the theory of stochastic processes and statistical mechanics.

we have:

$$-\nabla_x U(x) p_t^{(\text{st})}(x) - D \nabla_x p_t^{(\text{st})}(x) = 0.$$

(This notion of detailed balance will be generalized in the next section to the case of discrete-time Markov chains, where time and space are discrete.)

Rewriting the above equation yields:

$$\nabla_x p_t^{(\text{st})}(x) = -\frac{1}{D} \nabla_x U(x) p_t^{(\text{st})}(x).$$

Integrating both sides leads to the stationary distribution:

$$p_t^{(\text{st})}(x) = \frac{1}{Z} \exp\left(-\frac{U(x)}{D}\right),$$

which is known as the *Boltzmann, Gibbs, or Boltzmann–Gibbs distribution*, where Z is the *partition function* ensuring normalization:

$$Z = \int_{\mathbb{R}^d} \exp\left(-\frac{U(x)}{D}\right) dx.$$

Ornstein–Uhlenbeck Process: A Solvable Langevin Model

A particularly important special case of the Langevin equation arises when the potential is quadratic,

$$U(x) = \frac{\lambda}{2}x^2,$$

which yields a linear drift. The resulting SDE,

$$dX_t = -\lambda X_t dt + \sqrt{2D} dW_t, \quad (7.4)$$

is known as the *Ornstein–Uhlenbeck (OU) process*⁷.

The corresponding Fokker–Planck equation is

$$\frac{\partial p_t(x)}{\partial t} = \frac{\partial}{\partial x} (\lambda x p_t(x)) + D \frac{\partial^2 p_t(x)}{\partial x^2}.$$

Exact Solution and Stationarity. If $X_0 = x_0$, the OU process admits an explicit solution:

$$X_t = x_0 e^{-\lambda t} + \sqrt{2D} \int_0^t e^{-\lambda(t-s)} dW_s,$$

from which one finds

$$\mathbb{E}[X_t] = x_0 e^{-\lambda t}, \quad \text{Var}(X_t) = \frac{D}{\lambda} (1 - e^{-2\lambda t}).$$

⁷The Ornstein–Uhlenbeck process was introduced in 1930 by Leonard Ornstein and George Eugene Uhlenbeck as a refinement of Brownian motion that incorporates mean-reverting dynamics [47]. Their motivation was to model the velocity of a Brownian particle subject to linear friction, extending earlier work by Einstein and Langevin. Because of its linear drift and Gaussian noise, the OU process is exactly solvable and has since become a standard model in physics, finance, biology, and machine learning.

As $t \rightarrow \infty$, the distribution converges to the stationary Gaussian

$$p^{(\text{st})}(x) = \sqrt{\frac{\lambda}{2\pi D}} \exp\left(-\frac{\lambda x^2}{2D}\right),$$

which is precisely the Boltzmann distribution associated with the quadratic potential $U(x)$.

Conceptual Role. The OU process plays a distinguished role as the simplest nontrivial diffusion with drift:

- it is Gaussian at all times,
- it exhibits exponential relaxation toward equilibrium,
- it provides a local linear approximation to general Langevin dynamics near stable equilibria.

For these reasons, OU-type noise processes are widely used to model regularizing noise in neural networks and as analytically tractable building blocks in diffusion-based generative models.

From Brownian Motion to Score-Based Diffusion Models

Brownian motion (often with drift, e.g. of the Ornstein-Uhlenbeck type) provides the canonical *forward diffusion* used in score-based generative models and DDPMs. As time increases, the data distribution is convolved with Gaussian noise, eventually approaching a simple reference distribution.

Score-based models learn the *score function*

$$\nabla_x \log p_t(x),$$

along this diffusion trajectory. By reversing the diffusion process using this learned score, one can transform noise back into structured data.

Thus, Brownian motion, the heat equation, and Langevin dynamics form the mathematical foundation underlying modern diffusion-based generative AI.

Double-Well Potential

While the Ornstein–Uhlenbeck (OU) process provides an exactly solvable example with a single stable equilibrium, many systems of interest in physics, chemistry, and machine learning exhibit *multiple metastable states*. A double-well potential offers the simplest setting in which diffusion, drift, and noise interact to produce barrier crossing, long correlation times, and nontrivial sampling behavior.

Example 7.3.2 (Langevin Diffusion in a Double-Well Potential). *To illustrate diffusion with drift, consider the one-dimensional Langevin equation*

$$dX_t = -U'(X_t) dt + \sqrt{2D} dW_t,$$

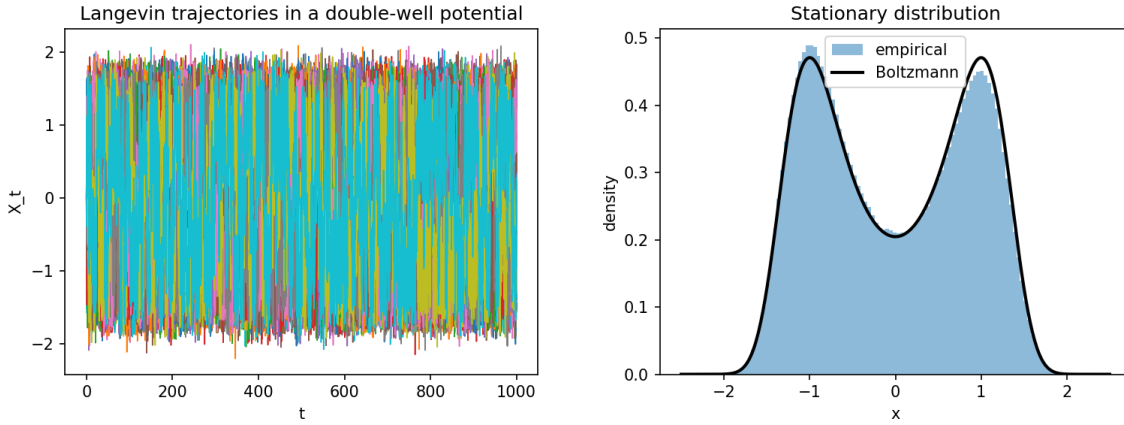


Figure 7.7: Langevin diffusion in a double-well potential. *Left:* sample trajectories showing metastability and noise-induced transitions between wells. *Right:* empirical stationary distribution compared with the analytic Boltzmann–Gibbs density. Figures generated by `Langevin-DoubleWell.ipynb`.

with the double-well potential

$$U(x) = \frac{1}{4}(x^2 - 1)^2.$$

This potential has two stable minima at $x = \pm 1$ separated by an energy barrier at $x = 0$. The stationary distribution predicted by the Fokker–Planck equation under detailed balance is the Boltzmann distribution

$$p^{(\text{st})}(x) \propto \exp\left(-\frac{U(x)}{D}\right),$$

which concentrates near the minima for small D and spreads out as D increases.

The notebook `Langevin-DoubleWell.ipynb` simulates this process using the Euler–Maruyama scheme and visualizes both sample trajectories and empirical marginals. It highlights how stochastic noise enables barrier crossing between the two wells and how long-time averages recover the Gibbs distribution.

Exercise 7.3.2 (Langevin Sampling, Metastability, and Stationarity). Consider the Langevin SDE

$$dX_t = -U'(X_t) dt + \sqrt{2D} dW_t, \quad U(x) = \frac{1}{4}(x^2 - 1)^2.$$

- (a) Derive the associated Fokker–Planck equation and verify that the Boltzmann distribution

$$p^{(\text{st})}(x) \propto e^{-U(x)/D}$$

is stationary under detailed balance.

- (b) Implement the Euler–Maruyama scheme and simulate trajectories for different values of the diffusion coefficient D . How does D affect the frequency of transitions between the two wells?

- (c) Estimate the empirical stationary distribution from long-time simulation and compare it to the analytic Boltzmann distribution, as in Fig. 7.7.
- (d) Explain why small D leads to metastability and long correlation times, and relate this to challenges in sampling multimodal distributions.
- (e) (Bonus) Discuss how adding a non-gradient drift term would break detailed balance and change the stationary behavior.

In summary – the derivation + example + exercise presented above demonstrate how the diffusion equation emerges naturally from Brownian motion via the path integral formulation. Extending the model to include a drift term given by the gradient of a potential $U(x)$ leads to the Fokker–Planck equation. The stationary solution under detailed balance conditions yields the Gibbs distribution – a fundamental object in statistical mechanics and machine learning. These ideas will be pivotal in our discussion of diffusion-based generative models, where the interplay of noise, structure, and reversibility enables powerful sampling mechanisms.

From Continuous Diffusion to Discrete Markov Dynamics

The diffusion processes discussed in this section describe stochastic evolution in continuous time and state space. Markov chains provide the discrete counterpart of the same idea: stochastic evolution driven by local transition rules. Many of the concepts introduced above – stationarity, equilibrium, reversibility, and relaxation – reappear in the discrete setting, often with sharper algebraic structure. In fact, continuous diffusions can be viewed as scaling limits of Markov chains, while Markov chains often serve as computational surrogates for diffusions. This discrete–continuous duality will be central for both sampling and learning in the sections that follow.

7.4 Markov Chains

Section 7.3 focused on stochastic dynamics evolving in *continuous time* and in *continuous state spaces*, culminating in Brownian motion, Langevin dynamics, and diffusion processes central to modern generative models. We now switch perspective and study stochastic dynamics that evolve in *discrete time* and on *discrete state spaces*. While seemingly simpler, this setting is foundational: it underlies classical sampling algorithms, Markov Chain Monte Carlo (MCMC), dynamic programming, reinforcement learning, and discrete-time formulations of diffusion and denoising used throughout AI. Moreover, this discrete framework is in fact more general: many continuous-time and continuous-state stochastic models arise as scaling limits of appropriately constructed Markov chains.

From a modeling viewpoint, Markov chains can be seen as discrete analogues of diffusions: the infinitesimal generator of a continuous-time process is replaced by a transition matrix, and probability flow is described by matrix multiplication rather than differential operators. In practice, many AI systems operate natively in discrete time – iterations of an algorithm, layers of a neural network, or token updates in language models – making Markov chains a natural and indispensable abstraction.

A *Markov chain* is a discrete-time stochastic process $\{X_n\}_{n \geq 0}$ with a finite (or countable) state space \mathcal{S} that satisfies the *Markov property*:

$$P(X_{n+1} = j \mid X_n = i, X_{n-1} = i_{n-1}, \dots, X_0 = i_0) = P(X_{n+1} = j \mid X_n = i),$$

for all n and all states $i_0, i_1, \dots, i_{n-1}, i, j \in \mathcal{S}$. That is, *the future depends on the past only through the present state*.

The dynamics of a Markov chain are fully specified by its *transition matrix* P , where $P(i, j) = P(X_{n+1} = j \mid X_n = i)$, and each row of P sums to one.

Basic Examples

- **Two-State Chain.** Consider two states A and B with transition matrix

$$P = \begin{pmatrix} 0.8 & 0.2 \\ 0.3 & 0.7 \end{pmatrix}.$$

This chain is irreducible and aperiodic, and therefore converges to a unique stationary distribution.

- **Three-State Cycle.** For

$$P = \begin{pmatrix} 0 & 1 & 0 \\ 0 & 0 & 1 \\ 1 & 0 & 0 \end{pmatrix},$$

every state is reachable from every other, but the chain is periodic (period 3) and does not mix unless randomness (e.g., self-loops) is added.

- **Linear Chain.** States arranged on a line with nearest-neighbor transitions provide a simple discrete analogue of one-dimensional diffusion and will reappear in MCMC and graphical models.

Stationarity, Mixing, and Ergodicity

A Markov chain is called *stationary* if its transition probabilities do not depend on time. If the chain is irreducible and aperiodic, it is *ergodic*: regardless of the initial condition, the distribution of X_n converges to a unique stationary distribution π as $n \rightarrow \infty$.

In algorithmic and AI contexts, the speed of this convergence – quantified by the *mixing time*—is often more important than stationarity itself. Efficient samplers, optimizers, and generative models rely on chains that mix rapidly.

7.4.1 Global Balance and Detailed Balance

For a stationary chain with transition matrix P and stationary distribution π , *global balance* requires

$$\pi(j) = \sum_{i \in \mathcal{S}} \pi(i)P(i, j), \quad j \in \mathcal{S}.$$

A stronger condition is *detailed balance*:

$$\pi(i)P(i,j) = \pi(j)P(j,i), \quad i, j \in \mathcal{S},$$

which implies reversibility. Detailed balance is convenient and widely used in MCMC, but it is not mandatory – many modern generative and diffusion-based algorithms intentionally break it to accelerate mixing or encode an arrow of time.

Example 7.4.1. *Toy Discrete Diffusion for Image Intensities* Consider a toy model for the forward diffusion of image intensities. Let the state space be $\mathcal{S} = \{0, 1, 2\}$, representing dark, medium, and bright pixels. Define a discrete-time Markov chain with transition matrix

$$P = \begin{pmatrix} 0.8 & 0.15 & 0.05 \\ 0.2 & 0.6 & 0.2 \\ 0.1 & 0.2 & 0.7 \end{pmatrix}. \quad (7.5)$$

This chain is irreducible and aperiodic, hence ergodic, but it is not reversible: there exists no distribution π satisfying detailed balance $\pi(i)P(i,j) = \pi(j)P(j,i)$. The violation of detailed balance reflects the non-equilibrium nature of the forward diffusion process used in generative models.

Starting from a sharply peaked initial distribution (a clean pixel), repeated application of P gradually spreads probability mass across states, effectively injecting noise. Fig. 7.8 illustrates this mixing behavior. All computations and figures in this example are generated in the

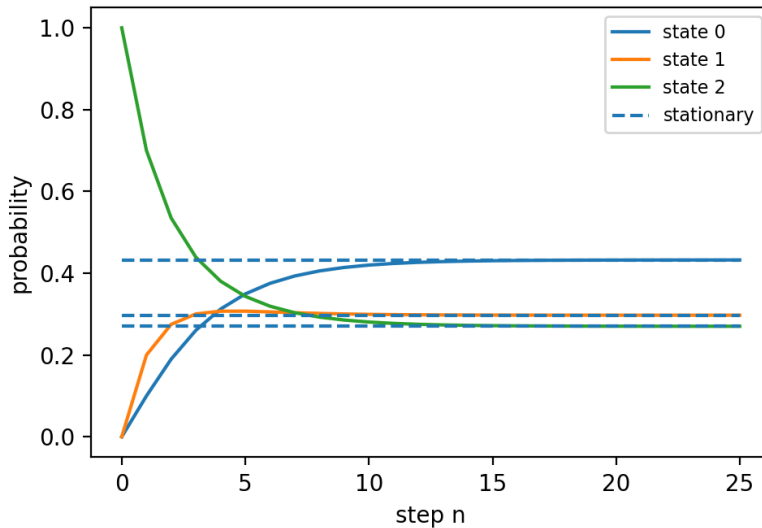


Figure 7.8: Evolution of state probabilities for the toy Markov-chain diffusion model, showing convergence toward the stationary distribution.

accompanying Jupyter notebook `MC_Toy_Diffusion.ipynb`.

Exercise 7.4.1. *Discrete Diffusion, Mixing, and Simulation* Using the notebook `MC_Toy_Diffusion.ipynb` as a starting point:

- (a) Verify irreducibility and aperiodicity of the chain defined by (7.5).
- (b) Compute the stationary distribution numerically and confirm global balance.
- (c) Starting from each pure state, simulate the evolution of the distribution and estimate the mixing time.
- (d) Modify the transition matrix to enforce detailed balance with respect to the same stationary distribution. Compare the mixing behavior with the original chain.

This exercise highlights how discrete-time Markov chains provide a minimal yet powerful laboratory for understanding diffusion, irreversibility, and sampling in AI.

In the next section, we will build on these ideas by introducing MCMC methods that leverage detailed balance to ensure convergence to a specified distribution.

7.4.2 Perron–Frobenius Theorem, Spectral Gap, and Mixing on Graphs

Let $P \in \mathbb{R}^{n \times n}$ be a row-stochastic matrix with nonnegative entries. If P is *ergodic* – that is irreducible and aperiodic – then Perron–Frobenius implies: (i) $\lambda_1 = 1$ is a simple dominant eigenvalue, and (ii) there exists a unique stationary distribution $\pi \succ 0$ such that $\pi^\top P = \pi^\top$. Moreover, the convergence rate of $p^{(k)} = p^{(0)}P^k$ to π is controlled by

$$\text{gap} = 1 - |\lambda_2|,$$

where $|\lambda_2|$ is the second largest eigenvalue magnitude of P . A small gap corresponds to slow mixing (long memory), whereas a large gap corresponds to rapid mixing.

The Perron–Frobenius theorem is most informative when the state space is moderately large: then the spectrum of P is rich and the *spectral gap* becomes a tangible diagnostic of mixing speed. This viewpoint is also directly relevant to AI, because many algorithms can be interpreted as repeated application of a diffusion operator on a graph: PageRank, label propagation, and message passing in Graph Neural Networks (GNNs).

Example 7.4.2. *Graph Diffusion: Slow vs. Fast Mixing and the Spectrum* Consider a lazy random walk on a graph $G = (V, E)$ with $|V| = n$ nodes: with probability $1/2$ the walk stays put, and with probability $1/2$ it moves to a uniformly chosen neighbor. This defines an ergodic Markov chain with transition matrix P .

We compare two graphs with the same number of nodes:

- **Cycle graph (slow mixing).** A lazy random walk on an n -cycle has many eigenvalues close to 1, producing a small spectral gap and slow convergence.
- **Expander-like graph (fast mixing).** A lazy random walk on a random d -regular graph typically has a much larger spectral gap and mixes rapidly.

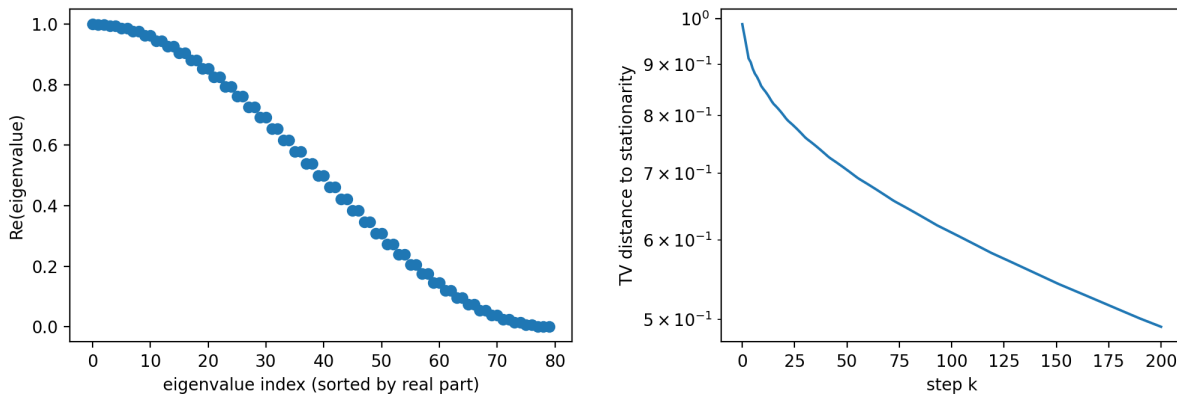


Figure 7.9: Cycle graph. Left: there are many eigenvalues close to 1, indicating a small spectral gap. Right: slow decay of total variation distance to stationarity (slow mixing).

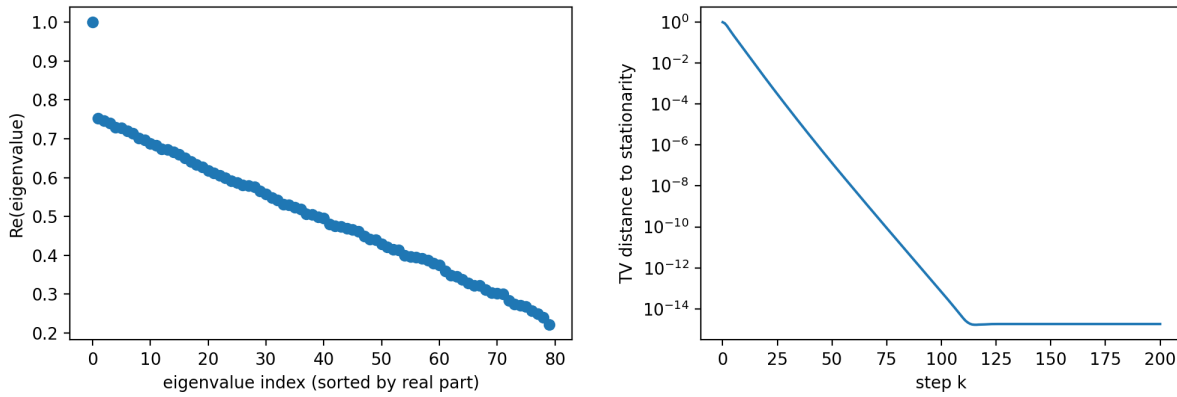


Figure 7.10: Random d -regular graph. Left: a gap between 1 and other eigenvalue is $O(1)$. Right: rapid decay of total variation distance (fast mixing).

Figs. 7.9 vs. Fig. 7.10 compare the spectra (left panels) and convergence to stationarity – measured by total variation distance (right panel). These diagnostics are exactly what one needs in AI practice: repeated application of a graph diffusion operator (as in label propagation or GNN message passing) will over-smooth representations on graphs with a large spectral gap, while graphs with a small gap preserve local structure longer.

All computations and figures are generated in the accompanying notebook `PF_GraphSpectrum_Mixing.ipynb`.

Exercise 7.4.2. Spectral Gap: Analytic vs. Empirical Perspectives

In Example 7.4.2, we compared two Markov chains on graphs with the same number of nodes: a cycle graph and a random regular graph. Both chains are ergodic, yet their spectral properties and mixing behavior are dramatically different.

(a) **Analytic case (cycle).** For the lazy random walk on an n -cycle with transition matrix

$$P(i, j) = \begin{cases} \frac{1}{2}, & j = i, \\ \frac{1}{4}, & j = i \pm 1 \pmod{n}, \\ 0, & \text{otherwise,} \end{cases}$$

derive analytic formula for the eigenvectors of P . Analyze what happens with the spectral gap in the limit $n \rightarrow \infty$.

- (b) **Empirical case (random regular graph).** Using the notebook `PF_GraphSpectrum_Mixing.ipynb`, compute the spectrum of the lazy random walk on a random d -regular graph of the same size. Why is an analytic eigenvalue formula no longer available in this case?
- (c) **Comparison.** Compare the spectral plots and mixing curves of the two chains. Relate the presence or absence of a spectral gap to the observed convergence rates.
- (d) **Interpretation for AI.** In graph-based learning and message-passing algorithms, repeated application of a diffusion operator $H^{(k+1)} = PH^{(k)}$ is common. Explain why graphs with a large spectral gap tend to exhibit rapid over-smoothing, while graphs without a gap preserve structure over many iterations.
- (e) **Takeaway.** Summarize what this example illustrates about the role of analytic solutions versus numerical diagnostics in studying stochastic processes for AI.

Spectrum, Mixing, and the Emergence of Directionality

The spectral gap quantifies how fast a Markov process forgets its initial condition. Yet, many processes of interest in AI and physics are not merely about forgetting — they are about directed evolution, goal-seeking behavior, or irreversible flows of information. This motivates a shift in perspective: from equilibrium properties governed by spectra to time-directed dynamics governed by value functions and recursion. The next subsection makes this shift explicit by reframing Markov evolution through the lens of dynamic programming and the arrow of time.

7.4.3 Arrow of Time and Dynamic Programming

A defining feature of Markov chains is their *forward* temporal evolution: the state at the next time depends only on the present state and not on the full history. This “memoryless” property allows stochastic systems to be simulated step by step, progressing naturally from past to future.

At the same time, many fundamental algorithmic ideas in probability, optimization, and AI — including dynamic programming and reinforcement learning — adopt a seemingly opposite perspective. They solve problems by starting from a *terminal condition* in the future and propagating information *backward* in time. Reconciling these two viewpoints — forward stochastic evolution versus backward computational recursion — lies at the heart of the *arrow of time* in dynamic programming (DP).

Computational insight. If one were to enumerate all possible trajectories of a Markov chain over T time steps, the number of scenarios would typically grow exponentially with T . Dynamic programming circumvents this combinatorial explosion by exploiting the Markov property: instead of tracking full paths, it propagates *marginal distributions* or *value functions* through one-step recursions. As a result, the computational cost scales linearly with the time horizon (or as $O(\text{states} \times T)$ in discrete settings), yielding an enormous gain in efficiency.

Forward vs. Backward Evolution

A discrete-time Markov chain is defined by random variables

$$X_0, X_1, X_2, \dots,$$

satisfying

$$P(X_{n+1} = x \mid X_n, X_{n-1}, \dots, X_0) = P(X_{n+1} = x \mid X_n).$$

This conditional independence supports a *forward-in-time* generative procedure: given X_n , we sample X_{n+1} , then X_{n+2} , and so on.

In contrast, dynamic programming methods — such as Bellman’s principle of optimality, shortest-path algorithms, and reinforcement learning — compute quantities of interest by working *backward* from a final time T . Once a terminal cost or reward is specified, the Markov property enables a backward recursion that determines optimal costs, policies, or expected values at earlier times. This coexistence of forward stochastic evolution with backward computational inference encapsulates the arrow-of-time phenomenon in DP.

Bellman Recursions

The DP principle applies both to probabilistic *marginalization* and to *optimization*. In the latter case, one typically considers a Markov Decision Process (MDP), where actions influence transitions.

Marginalization. Let P be the transition matrix of a Markov chain. Then the distribution evolves forward as

$$p_{n+1}(x) = \sum_y P(y, x) p_n(y).$$

This recursion propagates uncertainty forward in time, but it can also be inverted or conditioned when future distributions are known.

Optimization (MDPs). In an MDP with reward function $r(x, a)$ and discount factor $\gamma \in (0, 1]$, the value function satisfies Bellman’s equation

$$V_n(x) = \max_{a \in \mathcal{A}(x)} \left\{ r(x, a) + \gamma \mathbb{E}[V_{n+1}(X_{n+1}) \mid X_n = x, a] \right\},$$

(or a minimization variant for cost). Although the system evolves forward, optimal values are typically computed backward from a terminal condition V_T , illustrating the intrinsic forward–backward duality.

Example 7.4.3 (Forward–Backward Duality on a Network). Consider a small network with probabilistic transitions and edge costs. Starting from an initial node, the Markov chain induces a forward evolution of state probabilities. At the same time, the minimum expected cost to reach a target node can be computed by backward dynamic programming.

Left panel of Fig. 7.11 shows forward propagation of probabilities over time, while the right panel shows backward propagation of the cost-to-go function. Both computations rely on the same transition structure, yet proceed in opposite temporal directions. All figures are

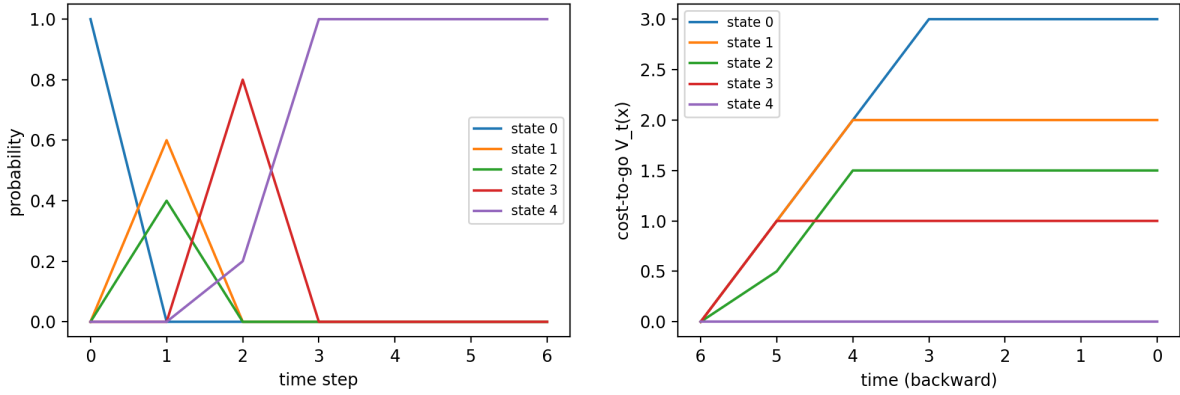


Figure 7.11: Left: Forward evolution of state probabilities in a Markov chain. Right: Backward dynamic programming – cost-to-go functions propagated from the terminal time.

generated in the accompanying notebook `DP_Arrow_of_Time.ipynb`.

Exercise 7.4.3 (Forward vs. Backward Computation). Using the notebook `DP_Arrow_of_Time.ipynb` as a starting point:

- (a) Modify the transition probabilities and observe how the forward distribution changes over time.
- (b) Modify the edge costs and recompute the backward cost-to-go functions.
- (c) Introduce a discount factor $\gamma < 1$ and study its effect on the backward recursion.
- (d) Compare the numerical effort required for forward simulation versus backward dynamic programming as the horizon T increases.

Discuss how the forward–backward duality illustrated here underlies reinforcement learning, shortest-path algorithms, and backpropagation through time in neural networks.

7.5 Markov Chains Meet Sampling: MCMC

Markov Chain Monte Carlo (MCMC) methods generate samples from a complex target distribution by constructing a Markov chain whose stationary distribution matches the target. Two paradigmatic instances are *Gibbs sampling* and *Metropolis–Hastings* (MH). In AI,

MCMC is particularly natural for *energy-based models*, where the probability of a configuration is defined implicitly via an energy function and a typically intractable partition function. A representative example is the Ising model on a graph and its bipartite specialization known as a *Restricted Boltzmann Machine* (RBM).

Unlike direct sampling, MCMC produces a *correlated* sequence X_0, X_1, \dots since each state is obtained from the previous one. Practical use therefore introduces three standard notions: (i) *burn-in*, discarding an initial transient before the chain reaches its stationary regime; (ii) *mixing time*, the time scale on which correlations decay; and (iii) optionally, *thinning*, keeping only every k -th sample. (Thinning is not always necessary; it is best viewed as a convenience for reducing storage and correlation in downstream estimates.)

7.5.1 Gibbs Sampling (Warm-up: Ising / RBM Conditionals)

Gibbs sampling updates variables by sampling from their conditional distributions given all others. This circumvents direct sampling from the full joint distribution.

Illustrative example: Ising model. Consider an Ising model on a graph $\mathcal{G} = (\mathcal{V}, \mathcal{E})$, with spins $x_i \in \{-1, +1\}$ on nodes $i \in \mathcal{V}$, and energy

$$E(x) = - \sum_{(i,j) \in \mathcal{E}} J_{ij} x_i x_j - \sum_{i \in \mathcal{V}} h_i x_i, \quad p(x) = \frac{1}{Z} \exp(-E(x)).$$

The conditional distribution of one spin is local:

$$p(x_i | x_{\mathcal{N}(i)}) = \frac{1}{1 + \exp\left(-2x_i\left(\sum_{j \in \mathcal{N}(i)} J_{ij} x_j + h_i\right)\right)}, \quad \mathcal{N}(i) := \{j : (i, j) \in \mathcal{E}\}.$$

Algorithm 1 summarizes Gibbs sampling in this setting.

7.5.2 Metropolis–Hastings (Local Moves and Detailed Balance)

Metropolis–Hastings proposes a candidate $x' \sim q(\cdot | x)$ and accepts it with probability

$$\alpha(x, x') = \min\left\{1, \frac{p(x')q(x | x')}{p(x)q(x' | x)}\right\}.$$

This acceptance rule enforces detailed balance (and hence stationarity) without requiring the partition function Z . This makes MH especially attractive for energy-based models, where Z is typically intractable.

7.5.3 Restricted Boltzmann Machines as Bipartite Ising Models

A Restricted Boltzmann Machine (RBM) is an energy-based model on a bipartite graph with visible units v and hidden units h . Its energy is commonly written as

$$E_\theta(v, h) = -b^\top v - c^\top h - v^\top Wh, \quad \theta = (W, b, c),$$

Algorithm 1 Gibbs Sampling for the Ising Model

Require: Graph $\mathcal{G} = (\mathcal{V}, \mathcal{E})$ with couplings $\{J_{ij}\}$ and external fields $\{h_i\}$; initial configuration $x_i^{(0)} = \{x_i^{(0)} \in \{-1, +1\} : i \in \mathcal{V}\}$; number of iterations T .

- 1: **for** $t = 0, 1, \dots, T - 1$ **do**
- 2: **for** each node $i \in \mathcal{V}$ (in any order or randomly) **do**
- 3: Compute the local field:

$$H_i = \sum_{j \in \mathcal{N}(i)} J_{ij} x_j^{(t)} + h_i.$$

- 4: Update the spin:

$$x_i^{(t+1)} = \begin{cases} +1, & \text{with probability } \frac{1}{1+\exp(-2H_i)}, \\ -1, & \text{with probability } \frac{\exp(-2H_i)}{1+\exp(-2H_i)}. \end{cases}$$

- 5: **end for**
 - 6: **end for**
 - 7: **return** Final configuration $s^{(T)}$.
-

Algorithm 2 Metropolis–Hastings Sampling for the Ising Model

Require: Graph $\mathcal{G} = (\mathcal{V}, \mathcal{E})$ with couplings $\{J_{ij}\}$ and external fields $\{h_i\}$; initial configuration $x^{(0)}$; number of iterations T .

- 1: **for** $t = 0, 1, \dots, T - 1$ **do**
- 2: Randomly select a node $i \in \mathcal{V}$.
- 3: Propose a flip of its spin: $x'_i = -x_i^{(t)}$; let x' be the resulting configuration.
- 4: Compute the energy difference:

$$\Delta E = E(x') - E(x^{(t)}).$$

- 5: Accept x' with probability

$$\alpha = \min\left\{1, \exp(-\Delta E)\right\}.$$

- 6: **if** $U(0, 1) < \alpha$ **then**
 - 7: Set $x^{(t+1)} = x'$.
 - 8: **else**
 - 9: Set $x^{(t+1)} = x^{(t)}$.
 - 10: **end if**
 - 11: **end for**
 - 12: **return** Final configuration $x^{(T)}$.
-

and the joint distribution is $P_\theta(v, h) \propto \exp(-E_\theta(v, h))$. The bipartite structure implies that the conditional distributions factorize:

$$P_\theta(h | v) = \prod_j \sigma(c_j + (W^\top v)_j), \quad P_\theta(v | h) = \prod_i \sigma(b_i + (Wh)_i),$$

where $\sigma(x) = 1/(1 + e^{-x})$. Hence RBMs admit efficient *block Gibbs* sampling by alternating $h \sim P_\theta(h | v)$ and $v \sim P_\theta(v | h)$.

7.5.4 Gibbs vs. Local MH (Glauber-Style) in an RBM

For RBMs, block Gibbs makes structured moves (entire layers), while a local MH scheme makes small, localized moves by flipping a single bit in either the visible or hidden layer. The latter is often called *Glauber-style* dynamics in the physics literature, and can be viewed as a “local MH” algorithm with a symmetric single-bit-flip proposal.

Example 7.5.1 (Two MCMC samplers for the same RBM). *The notebook RBM_MCMC_Samplers.ipynb compares:*

- **Block Gibbs:** one step is $v \rightarrow h \rightarrow v$, using the RBM conditional factorization.
- **Local MH (Glauber-style):** propose a single-bit flip in either v or h and accept/reject based on the energy difference.

To diagnose convergence and mixing, the notebook plots – shown in Fig. (7.12) – (i) the running mean of the energy (after burn-in), and (ii) an energy autocorrelation curve. If both chains have reached the same stationary regime, their long-run mean energy should agree, while their autocorrelation decay reveals different mixing behavior.

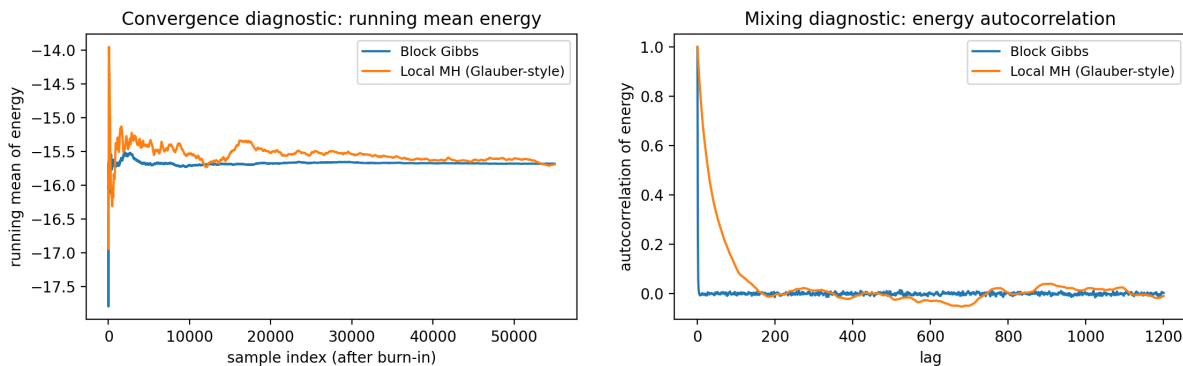


Figure 7.12: Left: Running mean energy (after burn-in) for block Gibbs and local MH sampling of the same RBM. Right: Energy autocorrelation as a simple mixing diagnostic for the two samplers.

Exercise 7.5.1 (Extend the RBM MCMC notebook). *Extend RBM_MCMC_Samplers.ipynb as follows:*

- (a) Implement a **non-local MH proposal** (e.g., flip a random block of k bits, or flip a whole visible vector v conditioned on a partially resampled hidden state). Report acceptance rate versus k , and discuss the trade-off between move size and acceptance.
- (b) Add at least one additional mixing diagnostic (e.g., autocorrelation of a chosen visible bit, or the integrated autocorrelation time of the energy trace).
- (c) Compare the three samplers (block Gibbs, local MH, your non-local MH) by producing a single summary figure (e.g., three autocorrelation curves on one plot, or three running-mean traces).

7.5.5 Contrastive Divergence: Truncated MCMC for Learning

When MCMC is used inside learning of an energy-based model, one often cannot afford to run a chain to equilibrium for each parameter update. Hinton's *Contrastive Divergence* (CD) algorithm [48] replaces the intractable expectation under the model distribution by a short Gibbs chain initialized at data. This yields a biased but often effective learning rule, especially when the model is already close to the data distribution.

Example 7.5.2 (Contrastive Divergence on a toy dataset). *The notebook*

RBM_Contrastive_Divergence.ipynb trains a small RBM on a synthetic binary dataset with two dominant modes, comparing CD-1 and CD-10. It reports in Fig. (7.13) a reconstruction-style proxy and an energy-contrast statistic (data vs. negative phase) across epochs.

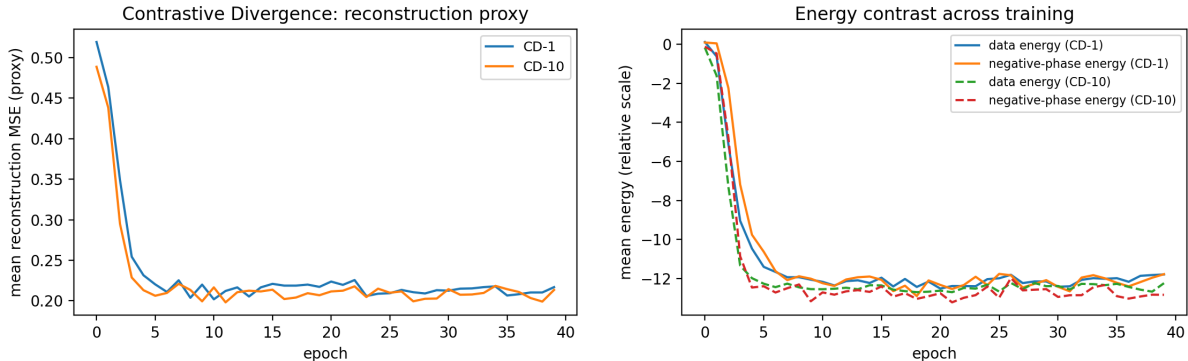


Figure 7.13: Left: Training diagnostics for CD- k : a reconstruction-style proxy for CD-1 vs. CD-10. Right: Energy contrast across training: mean energy of data-anchored positive phase vs. negative phase.

Exercise 7.5.2 (CD- k as truncated MCMC). *Starting from* *RBM_Contrastive_Divergence.ipynb*:

- (a) Vary $k \in \{1, 2, 5, 10, 20\}$ and produce a single figure comparing the training curves. What changes as k increases? Which effects look like reduced bias vs. simply increased cost?

- (b) Replace the two-mode dataset by a dataset with three modes, and repeat the experiment. Comment on whether CD-1 remains effective.
- (c) (Optional.) Implement Persistent CD (PCD): maintain a persistent negative-phase chain across parameter updates. Compare its behavior to CD-k on the same dataset.

From State-Based Sampling to History-Based Generation

Markov Chain Monte Carlo methods construct stochastic dynamics on a fixed state space whose stationary distribution matches a target law. Modern generative models often depart from this paradigm. In auto-regressive models, the “state” is no longer a fixed configuration but the entire history of previously generated symbols. Sampling becomes generation, equilibrium is replaced by sequence likelihood, and reversibility is lost by design. Despite this conceptual shift, auto-regressive models remain stochastic processes – and many of the ideas developed in this chapter reappear in disguised form. This motivates the final section, where Markovian ideas are extended to expanding state spaces.

7.6 Beyond Markov via Auto-Regressive Modeling

Classical Markov chains evolve on a fixed state space, with the future depending only on the current state. In contrast, modern auto-regressive generative models — most prominently transformers (see Section 1.1.5) — generate sequences one token at a time, conditioning on the entire previously generated history. Formally, the state at time t is

$$s_t = (x_1, x_2, \dots, x_t),$$

and the next-token distribution is

$$P(x_{t+1} | s_t) = P(x_{t+1} | x_1, \dots, x_t).$$

Therefore the joint probability of a length- T sequence factorizes according to the chain-rule formula (recall Section 7.1.2)

$$P(x_1, \dots, x_T) = \prod_{t=1}^T P(x_t | x_1, \dots, x_{t-1}).$$

From a probabilistic standpoint, auto-regressive models can still be interpreted as Markov processes — but with a crucial twist: the state space *grows with time*. Each new token extends the state, producing a non-stationary Markov process whose transition kernel changes dimension at every step.

7.6.1 Randomness in Next-Token Generation

Although auto-regressive models output a full probability distribution over the next token, generation requires selecting a single realization. This is achieved via sampling schemes that inject controlled randomness into the process.

1. **Greedy and temperature sampling.** Greedy decoding selects the most likely token. More generally, probabilities can be interpreted via energies $E(w) = -\log P(w \mid s_t)$ and rescaled by a temperature $T > 0$:

$$P_T(w \mid s_t) = \frac{e^{-E(w)/T}}{\sum_{w'} e^{-E(w')/T}}.$$

Low temperature yields near-deterministic behavior, while higher temperature increases stochasticity.

2. **Top- k sampling.** Sampling is restricted to the k most probable tokens, renormalizing their probabilities.
3. **Nucleus (top- p) sampling.** Sampling is restricted to the smallest token set whose cumulative probability exceeds a threshold $p \in (0, 1)$, yielding a dynamic truncation of the state space.

All three methods modify the effective transition kernel of the auto-regressive process, balancing coherence and diversity.

7.6.2 Auto-Regressive Models as Expanding Markov Chains

Viewed through the lens of Markov chains, auto-regressive generation can be summarized as:

- **State evolution:** $s_{t+1} = s_t \oplus x_{t+1}$.
- **Markov property (revisited):** x_{t+1} depends only on s_t , but the dimension of s_t grows with t .

This expanding-memory viewpoint connects auto-regressive transformers with the Markov framework developed earlier (Sections 7.4, 7.5), while highlighting why classical notions such as stationarity and fixed transition matrices no longer apply directly.

Example 7.6.1 (Autoregressive feedback as an expanding Markov process). *To make the “expanding-state Markov” viewpoint concrete, we consider an explicitly auto-regressive toy generator in which the next-token distribution depends on the realized history. This mirrors a key structural feature of transformers: the next-step logits are context-dependent, hence the transition kernel changes along the generated trajectory.*

Transformer viewpoint (context-dependent logits). *In a causal transformer, the next-token distribution is produced from the hidden state $h(s_t)$ computed from the prefix $s_t = (x_1, \dots, x_t)$:*

$$P(x_{t+1} = w \mid s_t) = \text{softmax}(Wh(s_t) + b)_w,$$

so the logits $\ell_t(w) = (Wh(s_t) + b)_w$ are a learned function of the entire history. This is Markovian in the expanding state s_t , but not a classical stationary Markov chain because the state dimension grows with t .

Toy autoregressive model (interpretable surrogate for logits). We replace the learned map $s_t \mapsto h(s_t)$ by a simple, interpretable summary of the prefix. Let the vocabulary be finite, $\mathcal{V} = \{0, 1, \dots, V - 1\}$. Given the prefix s_t , define token counts $c_t(w) = \sum_{k=1}^t \mathbb{1}\{x_k = w\}$ and specify next-token logits by

$$\ell_t(w) = \ell_0(w) + \lambda \frac{c_t(w)}{t} - \eta \mathbb{1}\{w = x_t\}.$$

Here $\ell_0(w)$ is a heavy-tailed base logit profile (mimicking the long-tailed next-token probabilities often observed in language models), $\lambda \geq 0$ controls context feedback (tokens that have appeared in the prefix become more likely), and $\eta \geq 0$ is an optional repetition penalty discouraging immediate repeats. The auto-regressive transition is then

$$P(x_{t+1} = w \mid s_t) = \text{softmax}(\ell_t)(w), \quad s_{t+1} = s_t \oplus x_{t+1}.$$

This is genuinely auto-regressive (history-dependent) and Markovian in the expanding state s_t . Importantly, because the next-token distribution depends on the realized history, a sampling heuristic does not merely affect a single step: it changes the prefix and thereby changes all future transition kernels.

Notebook experiment. The notebook `AR_Contextual_Dynamics.ipynb` simulates this process and compares how sampling heuristics shape the trajectory via feedback (see Fig. (7.14)):

- **Entropy of the transition kernel:** $H_t = \mathbb{H}(P(x_{t+1} \mid s_t))$, quantifying randomness of the next-token step.
- **Realized diversity:** fraction of distinct tokens observed in the prefix.
- **Degeneration proxy:** cumulative repetition rate $\frac{1}{t} \sum_{k=2}^t \mathbb{1}\{x_k = x_{k-1}\}$, which captures repetition loops.

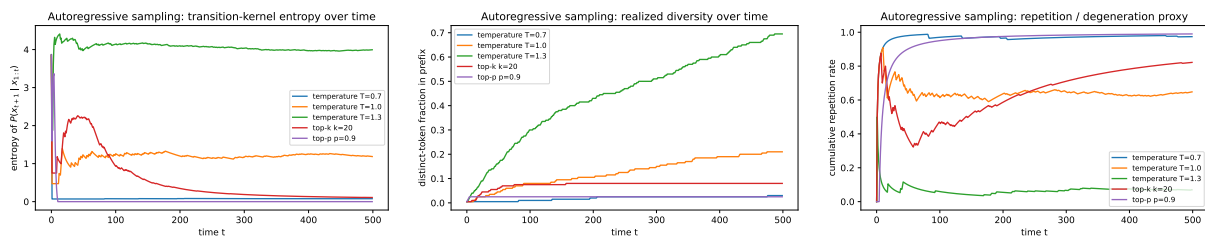


Figure 7.14: Left: Entropy of the autoregressive next-token distribution $P(x_{t+1} \mid s_t)$ over time for different sampling strategies. Because logits depend on the realized history, sampling affects the entire future evolution (not just a single step). Center: Realized diversity over time (fraction of distinct tokens observed so far). Truncation-based schemes (top- k , top- p) and temperature can produce qualitatively different diversity trajectories once feedback is present. Right: Cumulative repetition rate as a simple degeneration proxy. Strong feedback combined with low temperature can induce self-reinforcing collapse into repetition.

Exercise 7.6.1 (Auto-regressive feedback, sampling, and degeneration). Starting from `AR_Contextual_Dynamics.ipynb`:

- (a) **Feedback strength vs. sampling.** Vary λ over a suitable range (e.g., $\lambda \in \{0, 2, 4, 6, 8\}$) and reproduce Figures 7.14 for at least two sampling schemes (e.g., temperature sampling with two values of T , and top- k with two values of k). Describe how increasing feedback changes the long-run behavior.
- (b) **Stationarity vs. non-stationarity.** Explain why this process is Markovian in the expanding state s_t , yet not a stationary Markov chain on a fixed state space. Which quantity in the model explicitly depends on t ?
- (c) **Repetition penalty.** Enable the last-token penalty ($\eta > 0$) and compare repetition curves with and without the penalty. For fixed λ , identify a regime where repetition is significantly reduced while entropy and diversity remain comparable.
- (d) **Connecting back to transformers.** Relate the toy logits $\ell_t(w)$ to transformer logits $\ell_t(w) = (Wh(s_t) + b)_w$. Which aspects of transformer behavior are captured by the toy feedback term, and which are not?

This final section completes the chapter’s arc: from sampling, stochastic processes to classical Markov chains with fixed state spaces, through MCMC and energy-based sampling, to modern autoregressive generative models whose Markovian structure evolves dynamically with time.

From Stochastic Dynamics to Energy-Based Inference

This chapter introduced stochastic processes as mechanisms for sampling, exploration, and generation. In many AI models, however, stochastic dynamics are not the end goal but a tool for inference and learning in structured probability distributions. Chapter 8 builds on this foundation by focusing on energy-based and graphical models, where distributions are specified implicitly via energies rather than transition rules. The sampling techniques developed here –diffusion, MCMC, and truncated dynamics – will reappear as computational engines for inference, likelihood estimation, and learning.

Chapter 8

Energy Based (Graphical) Models

From Energies to Inference Dynamics to Learning

Chapter 7 developed *stochastic dynamics* — Markov chains, diffusions, and MCMC — as mechanisms for sampling and exploring high-dimensional spaces. In this chapter we shift perspective. Rather than starting from dynamics, we take as primary object a *structured probability distribution*, specified implicitly by an energy function and a graph of interactions. A generic energy-based model has the form

$$p_\theta(x) = \frac{1}{Z_\theta} \exp(-E_\theta(x)), \quad Z_\theta := \sum_x \exp(-E_\theta(x)) \quad (\text{or } \int \exp(-E_\theta(x)) dx), \quad (8.1)$$

where the energy E_θ decomposes into local terms encoded by a graph or factor graph. Such representations make locality, conditional independence, and compositional structure explicit — features that are central to probabilistic modeling, unsupervised learning, and modern generative AI.

Computation reintroduces time. Although (8.1) is a static specification, essentially every practical task with energy-based and graphical models requires an auxiliary *inference dynamics*. Computing marginals, conditional distributions, or Maximum A-Posteriori (MAP) states entails running an algorithm over time: iterative message passing (belief propagation), optimization over variational families (mean-field or structured variational inference), or stochastic sampling (Gibbs/Metropolis–Hastings). The efficiency of these procedures is governed by the same notions — mixing time, spectral gaps, ergodicity — introduced in Chapter 7. In this sense, inference transforms a static energy landscape into an algorithmic dynamical system.

Two pillars: inference and learning. The chapter is organized around two tightly coupled themes:

- **Inference:** given a model p_θ , compute quantities of interest such as marginals $p_\theta(x_i)$, conditional distributions $p_\theta(x_{\mathcal{H}} | x_{\mathcal{O}})$, or a MAP configuration $\arg \max_x p_\theta(x)$. This includes directed models (Bayesian networks, Hidden Markov Models), undirected models (Markov random fields), and their factor-graph representations, together with Belief Propagation (BP), variational methods, and MCMC as computational engines.

- **Learning:** fit parameters θ (and sometimes graph structure) from data. For energy-based models, maximum-likelihood learning leads to gradients of the form “data expectation minus model expectation,” where the latter requires sampling or approximate inference. The need to approximate these expectations motivates truncated or biased dynamics, such as *contrastive divergence* in Restricted Boltzmann Machines.

Energy as a unifying concept. The term *energy* borrows intuition from physics, where it quantifies the cost of a configuration and governs dynamics via variational principles. As discussed earlier in Chapter 2, energy functionals underlie classical ODEs, while in Chapter 7 they give rise to Boltzmann–Gibbs distributions through ergodic stochastic dynamics (Langevin, Fokker–Planck, Perron–Frobenius theory). In probabilistic AI, energy plays an analogous role: it defines a scalar landscape over configurations (images, binary variables, graph states), with lower energy corresponding to higher probability. This duality – energy as both a physical and statistical construct – forms the foundation of energy-based models.

Inference-first viewpoint. A central theme of this chapter is the duality between inference and learning. While in practice models are trained first and then deployed for inference, our exposition proceeds in the opposite direction. We begin with inference – how a model is queried, sampled, or used to solve downstream tasks—and then turn to learning. This is not merely a pedagogical choice but reflects a deeper principle: the requirements of inference largely determine which models are learnable and which learning objectives are computationally meaningful. Learning, in this view, is designed around the inference procedures the model must ultimately support.

Why this matters for generative AI. Energy-based and graphical models provide a flexible language for representing complex distributions even when the normalization constant Z_θ is unknown or intractable. They make it possible to encode structure, constraints, and prior knowledge explicitly, while delegating computation to inference dynamics. At the same time, their computational bottlenecks—slow-mixing equilibrium samplers and intractable partition functions – expose the limits of classical approaches.

Looking ahead. These limitations motivate the developments in Chapter 9, where generative modeling is reframed in terms of *non-equilibrium (non-autonomous)* stochastic dynamics, such as score-based diffusions and controlled stochastic processes. From this perspective, the present chapter serves as a conceptual hinge: it highlights both the expressive power of energy-based representations and the computational pressures that lead naturally to diffusion-based and control-inspired generative frameworks.

8.1 Inference

Inference is the computational engine that turns a probabilistic model into actionable predictions, samples, or decisions. Given a structured distribution – often specified by an energy or graphical factorization – the goal of inference is to compute quantities such as marginal



Figure 8.1: Conceptual roadmap for inference in Graphical Models (GM). Graph structure induces algorithmic inference dynamics, which in turn determine computational complexity and approximation quality.

probabilities, conditional distributions given evidence, expectations, or most probable configurations.

Fig. 8.1 summarizes the organizing principle of this section: structural assumptions encoded by a graph determine which inference algorithms are feasible, and these algorithms define the trade-off between accuracy and computational complexity.

The central challenge is computational: for general graphical models, exact inference typically scales *exponentially* with system size. This combinatorial explosion renders exact methods impractical beyond small or specially structured models, motivating a broad spectrum of approximate inference algorithms. Understanding the trade-off between inference quality and computational complexity is therefore essential for modern AI systems.

This section introduces inference through the lens of *graphical models*, emphasizing how structural assumptions enable efficient algorithms – and where those assumptions break down. We begin with a concise overview of graphical models, then focus on two paradigmatic families: Bayesian Networks and Hidden Markov Models. These examples highlight how inference, dynamic programming, and probabilistic modeling interact.

8.1.1 Graphical Models

Graphical Models (GMs) provide a unifying framework for representing high-dimensional probability distributions via graphs that encode conditional independence structure (see also Section 10.2 of [33]). Nodes correspond to random variables, while edges encode direct probabilistic dependencies.

From the perspective of inference, GMs are valuable because they:

- **Expose factorization structure**, reducing exponential complexity where possible.
- **Enable algorithmic inference**, such as message passing, dynamic programming, or structured sampling.
- **Provide modularity**, allowing local computations to be reused globally.

Common inference tasks include:

- **Sampling** from the model distribution.
- **Marginalization and conditioning**, i.e. computing $p(X_i)$ or $p(X_i | \mathbf{e})$.
- **MAP inference**, identifying the most probable configuration.

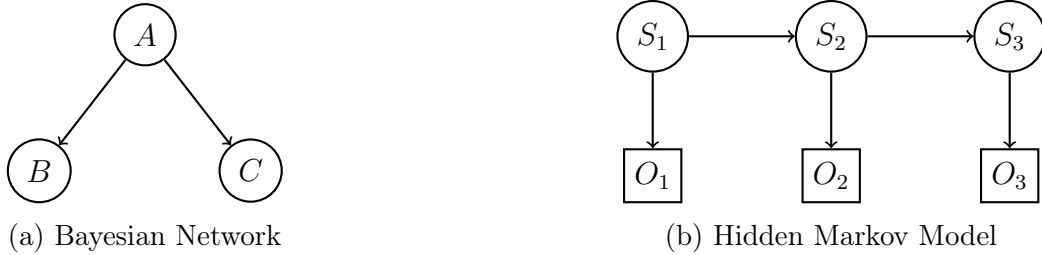


Figure 8.2: Directed acyclic graph (DAG) representations of the Graphical Models (GMs) used in the inference Examples 8.1.1, 8.1.2. *Left:* a Bayesian Network where conditioning on B induces backward inference to the parent A and forward inference to the sibling C . *Right:* a Hidden Markov Model, where the Markov structure of hidden states enables efficient sequential inference via dynamic programming.

Many Graphical Models (GM) introduced earlier — such as the Ising model and Restricted Boltzmann Machines (Section 7.5) — are undirected GMs. Here we broaden the scope and focus on two directed and temporally structured families that admit particularly clear inference algorithms.

Bayesian Networks (Directed Acyclic Graphs)

A Bayesian Network (BN) is a Directed Acyclic Graph (DAG) whose nodes represent random variables and whose edges encode conditional dependencies. The joint distribution over X_1, \dots, X_n factorizes as

$$P(X_1, \dots, X_n) = \prod_{i=1}^n P(X_i | \text{Pa}(X_i)),$$

where $\text{Pa}(X_i)$ denotes the parents of node X_i .

This factorization transforms global inference problems into combinations of local conditional distributions. Unlike undirected models, Bayesian Networks naturally encode *directionality* and are frequently interpreted causally.

Example 8.1.1 (Bayesian Network Inference and Evidence Propagation). *Consider a simple Bayesian Network with three binary variables A, B, C and directed edge $A \rightarrow B$ and $A \rightarrow C$ – see Fig. (8.2a). The joint distribution factorizes as*

$$P(A, B, C) = P(A) P(B | A) P(C | A).$$

Despite its simplicity, this network already illustrates a central feature of inference in graphical models: conditioning on evidence induces nonlocal effects that propagate through the graph structure.

The accompanying notebook `Inference_Graphical_Models_Informative.ipynb` implements this model and performs exact inference by enumeration. Rather than focusing on a single marginal, the notebook visualizes how observing $B = 1$ modifies the posterior distributions of both the parent variable A (backward propagation) and the sibling variable C (forward propagation).

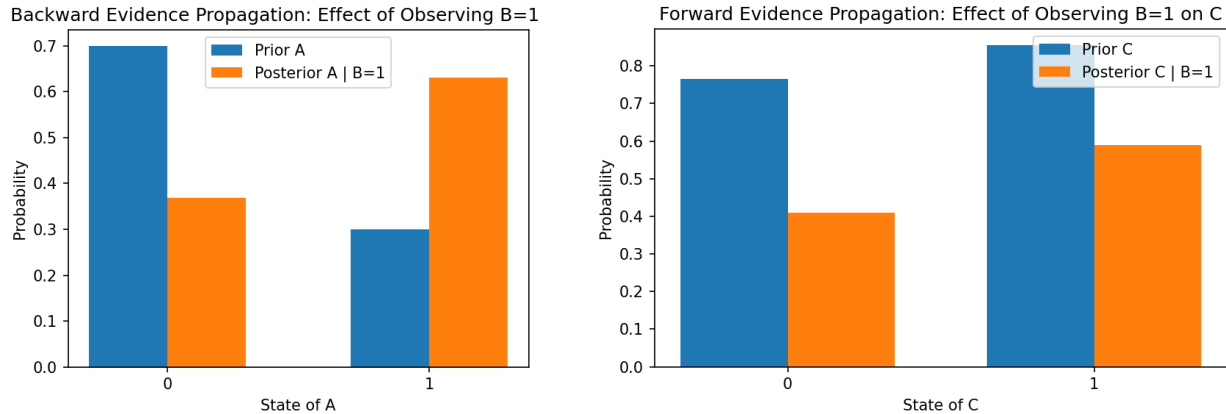


Figure 8.3: Evidence propagation in a Bayesian Network after conditioning on $B = 1$. *Left:* backward propagation to the parent variable A . *Right:* forward propagation to the child variable C . Both effects arise solely from the factorization structure of the joint distribution.

Figs. 8.3 make this effect explicit. Figure on the left panel of Figs. 8.3 compares the prior distribution of the parent variable A with its posterior distribution after conditioning on the observation $B = 1$, illustrating backward propagation of evidence through the graph. Figure on the right panel of Figs. 8.3 shows the corresponding change in the distribution of the sibling variable C , demonstrating forward propagation of evidence from B through their shared parent. Although only B is observed, the conditional structure encoded by the network induces nonlocal updates of belief over unobserved variables, highlighting how Bayesian Networks support structured probabilistic reasoning via local conditional probabilities.

Exercise 8.1.1 (Extending Bayesian Network Inference). Using the notebook `Inference_Graphical_Models_Informative.ipynb` as a baseline:

1. **Higher-order dependencies.** Extend the network by adding a fourth binary variable D with parents (A, B, C) , and define the conditional probabilities $P(D | A, B, C)$.
2. **Inference under partial observations.** Implement conditioned inference to compute posterior distributions such as $p(A, C | B = 1, D = 0)$. Visualize how evidence at D further reshapes beliefs over upstream variables.
3. **Exact vs. approximate inference.** Approximate the same conditional distributions using sampling-based methods. Compare their accuracy with exact enumeration as the number of variables grows.
4. **Scalability and limitations.** Discuss why exact enumeration becomes infeasible for larger networks, and relate your observations to the need for approximate inference methods (e.g. variational inference or MCMC) introduced later in this chapter.

Hidden Markov Models and Dynamic Programming

Hidden Markov Models (HMMs) specialize Bayesian Networks to sequential data. A hidden state S_t evolves according to a Markov chain, while observations O_t are emitted conditionally

on the current state – see Fig. (8.2b). The joint distribution factorizes as

$$P(S_{1:T}, O_{1:T}) = P(S_1) \prod_{t=2}^T P(S_t | S_{t-1}) \prod_{t=1}^T P(O_t | S_t).$$

Crucially, inference in HMMs – filtering, smoothing, and decoding – can be solved efficiently using *dynamic programming*, connecting directly to the forward–backward perspective introduced in Section 7.4.3.

Example 8.1.2 (HMM Filtering (Forward Inference)). *The notebook*

Inference_Graphical_Models.ipynb implements a simple Hidden Markov Model (HMM) for a two-state “weather” process. The hidden state $S_t \in \{\text{Sunny, Rainy}\}$ evolves as a Markov chain with transition matrix $P(S_t | S_{t-1})$, and each observation $O_t \in \{\text{Umbrella, No Umbrella}\}$ is generated from the emission model $P(O_t | S_t)$.

A central inference task is filtering: computing the posterior belief over the current hidden state given observations seen so far,

$$\alpha_t(s) := P(S_t = s | O_{1:t}), \quad s \in \{\text{Sunny, Rainy}\}.$$

Filtering is obtained by the forward (dynamic-programming) recursion

$$\alpha_t(s) \propto P(O_t | S_t = s) \sum_{s'} \alpha_{t-1}(s') P(S_t = s | S_{t-1} = s'),$$

followed by normalization so that $\sum_s \alpha_t(s) = 1$.

Figure 8.4 (generated by the notebook) plots $\alpha_t(\text{Sunny})$ and $\alpha_t(\text{Rainy})$ versus time. Each update corresponds to incorporating a new observation and propagating beliefs forward through the transition model. The plot therefore makes the filtering recursion visible as an evolving belief state driven by data.

Exercise 8.1.2 (Sequential Inference in HMMs). Using the HMM code in *Inference_Graphical_Models.ipynb* as your baseline:

1. **Sensitivity to model parameters.** Modify the transition matrix or the emission probabilities and regenerate Figure 8.4. Describe how stronger persistence (larger $P(S_t = S_{t-1})$) or noisier emissions affect the sharpness and stability of the beliefs.
2. **Viterbi decoding vs. filtering.** Implement Viterbi decoding to compute the MAP hidden-state path $\arg \max_{s_{1:T}} P(S_{1:T} = s_{1:T} | O_{1:T})$, and compare it with filtering. In particular, explain why the most likely path need not correspond to choosing the most likely state at each time separately.
3. **Connection to dynamic programming.** Write down the forward recursion you implemented (filtering) and the recursion used by Viterbi. Explain how both are dynamic programs enabled by the Markov property, connecting to the discussion in Section 7.4.3.

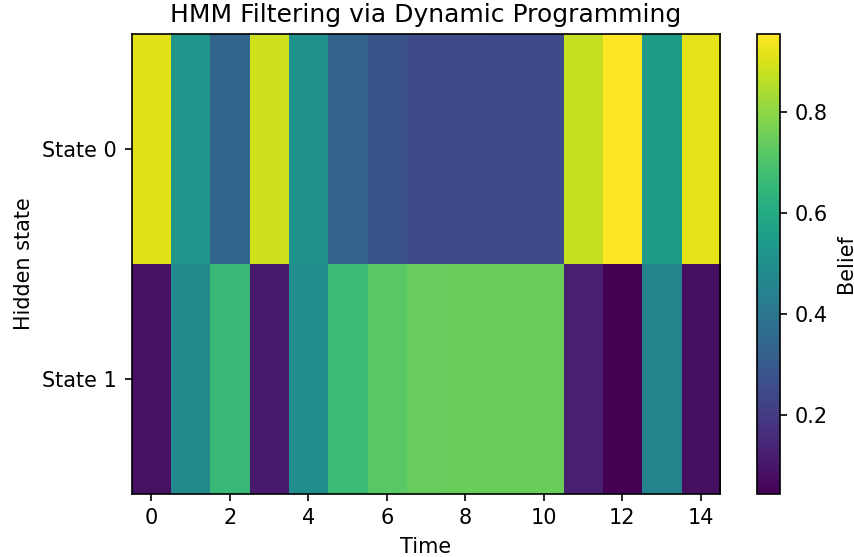


Figure 8.4: HMM filtering (forward inference). The curves show posterior beliefs $\alpha_t(s) = P(S_t = s | O_{1:t})$ for the two hidden states as observations arrive sequentially.

8.1.2 Variational Methods

Having already discussed exact approaches — for instance, by leveraging the chain rule for exact sampling or by relying on asymptotically exact Markov Chain Monte Carlo (MCMC) methods — we now acknowledge that the majority of inference tasks in high-dimensional models are formidable. In such cases, exponential complexity often makes these exact approaches computationally prohibitive. To cope with these challenges, *variational inference* provides a practical route by recasting inference as an optimization task. Specifically, one chooses a tractable family of distributions and seeks to approximate the true (often intractable) posterior distribution by minimizing a divergence measure (such as KL divergence) between the two. This approach not only yields computational efficiency but also offers a systematic way to balance approximation quality with speed.

Below, we summarize the variational approaches following closely the material from [49], also reviewed in [33], specifically in Section 10.2.

From Posterior Inference to an Optimization Problem

Let x denote the variables of interest (e.g. spins in an Ising model or bits in a decoding problem) and define the *posterior*

$$p(x) = \frac{\tilde{p}(x)}{Z}, \quad Z = \sum_x \tilde{p}(x).$$

In Bayesian language the term *posterior* simply signals that this distribution already contains *all* information currently available – the prior couplings, external fields and any observations – whereas the *prior* would describe our beliefs before seeing those observations. We call $p(x)$

intractable because the partition function Z cannot be computed (or even tightly approximated) in polynomial time for realistic system sizes, making exact normalization or direct sampling infeasible and motivating approximate-inference techniques.

Variational inference posits a **surrogate** (variational) distribution $q(x|\theta)$ – which we may also call **belief** distribution or just belief – selected from a tractable parametric family, and seeks to find the parameters θ that minimize the Kullback–Leibler (KL) divergence

$$\text{KL}(q(x|\theta) \| p(x)) = \sum_x q(x|\theta) \log \frac{q(x|\theta)}{p(x)}, \quad (8.2)$$

or equivalently to maximize the corresponding **Evidence-Based Lower Bound** (ELBO). This setup recasts inference into a familiar optimization framework that can often be tackled via gradient-based or message-passing methods.

Evidence-Based Lower Bound (ELBO)

To clarify why minimizing (8.2) yields a lower bound on the log-partition function (or log-evidence), let us provide a concise proof of the relevant inequality rather than merely recalling it. Suppose we wish to evaluate

$$\log \sum_x \tilde{p}(x).$$

By multiplying and dividing by any other distribution $q(x)$, we can rewrite this as

$$\log \sum_x \tilde{p}(x) = \log \sum_x q(x) \frac{\tilde{p}(x)}{q(x)}.$$

Now let us introduce a distribution $q(x)$ and note that $\sum_x q(x) = 1$ by definition. Applying Jensen's inequality to the concave function $\log(\cdot)$, we obtain

$$\log \sum_x q(x) \frac{\tilde{p}(x)}{q(x)} \geq \sum_x q(x) \log \left[\frac{\tilde{p}(x)}{q(x)} \right]. \quad (8.3)$$

Proof by Jensen's Inequality. Let $\{w(x)\}$ be nonnegative weights such that $\sum_x w(x) = 1$. Define $f(z) = \log(z)$ as our concave function. Then, by Jensen's inequality,

$$f\left(\sum_x w(x) z_x\right) \geq \sum_x w(x) f(z_x).$$

Identifying $w(x) = q(x)$ and $z_x = \frac{\tilde{p}(x)}{q(x)}$, we see $z_x \geq 0$ and $\sum_x w(x) z_x = \sum_x q(x) \frac{\tilde{p}(x)}{q(x)} = \sum_x \tilde{p}(x)$, which is precisely the quantity inside the log on the left-hand side. Hence the inequality (8.3) follows directly.

Rearranging to See the ELBO. From (8.3), rearrange terms to find that

$$\log \sum_x \tilde{p}(x) \geq \sum_x q(x) \log \tilde{p}(x) - \sum_x q(x) \log q(x).$$

Note that $\sum_x q(x) \log \tilde{p}(x) - \sum_x q(x) \log p(x)$ can be rewritten using the definition of KL divergence:

$$\sum_x q(x) \log \tilde{p}(x) - \sum_x q(x) \log p(x) = -\text{KL}(q \parallel p) + (\text{constant}),$$

where the constant depends on the normalization constant for $\tilde{p}(x)$ – that is the partition function, Z . Consequently, minimizing $\text{KL}(q \parallel p)$ is equivalent to maximizing the right-hand side, which we identify as the *evidence-based lower bound* (ELBO). In other words, $-\text{KL}(q \parallel p)$ is a lower bound to the log-partition function, and the distribution $q(x)$ that attains the minimum KL divergence provides the best such lower bound within the chosen variational family.

Thus, the objective $\text{KL}(q(x) \parallel \tilde{p}(x))$ represents a practical target for approximate inference in situations where directly computing or maximizing $Z = \sum_x \tilde{p}(x)$ (the partition function) is infeasible.

Example 8.1.3 (ELBO Tightness on a Toy Posterior). *The inequality (8.3) is often stated abstractly; the notebook `VI_ELBO_Toy.ipynb` visualizes it in the simplest nontrivial setting: a two-state model $p(x) \propto \exp(\beta x)$ with $x \in \{-1, +1\}$ and a one-parameter variational family $q_\theta(x = +1) = \theta$.*

Fig. 8.5 visualizes the variational decomposition of the log-partition function in a simple two-state energy-based model. The curve labeled $\text{ELBO}(\theta)$ shows how the evidence lower bound depends on the variational parameter $\theta = q(x = +1)$. As required by construction, $\text{ELBO}(\theta)$ lies below the constant line $\log Z$ for all values of θ , and becomes tight at the value of θ that coincides with the true posterior marginal.

The same figure also displays the Kullback–Leibler divergence $\text{KL}(q_\theta \parallel p)$. This quantity is non-negative and vanishes precisely at the same optimal value of θ where the ELBO attains its maximum. Moving away from this optimum, the ELBO decreases while the KL divergence increases, signaling a progressively poorer variational approximation.

Crucially, the figure makes explicit the exact identity

$$\log Z = \text{ELBO}(\theta) + \text{KL}(q_\theta \parallel p),$$

which holds for all θ . Thus, although the ELBO and KL curves vary in opposite directions as functions of θ , their sum remains constant and equal to $\log Z$. This decomposition highlights the fundamental variational trade-off: tightening the ELBO is achieved solely by reducing the divergence between the surrogate distribution q_θ and the true target distribution p , rather than by modifying the underlying normalization constant.

Exercise 8.1.3 (ELBO and KL in a One-Parameter Variational Family). *Use `VI_ELBO_Toy.ipynb` as a baseline.*

1. *Vary β (e.g. $\beta \in \{0.2, 0.8, 1.5, 3.0\}$). How does the maximizing θ^* move as β increases? Interpret θ^* as the best approximation of $p(x = +1)$.*
2. *Numerically verify that $\log Z - \text{ELBO}(\theta) = \text{KL}(q_\theta \parallel p) \geq 0$ for all θ and all β you tested.*
3. *Replace the family q_θ by a two-parameter family on $x \in \{-1, 0, +1\}$ (e.g. q_{θ_+, θ_0}). Reproduce the same three-way relationship between $\log Z$, ELBO, and KL.*

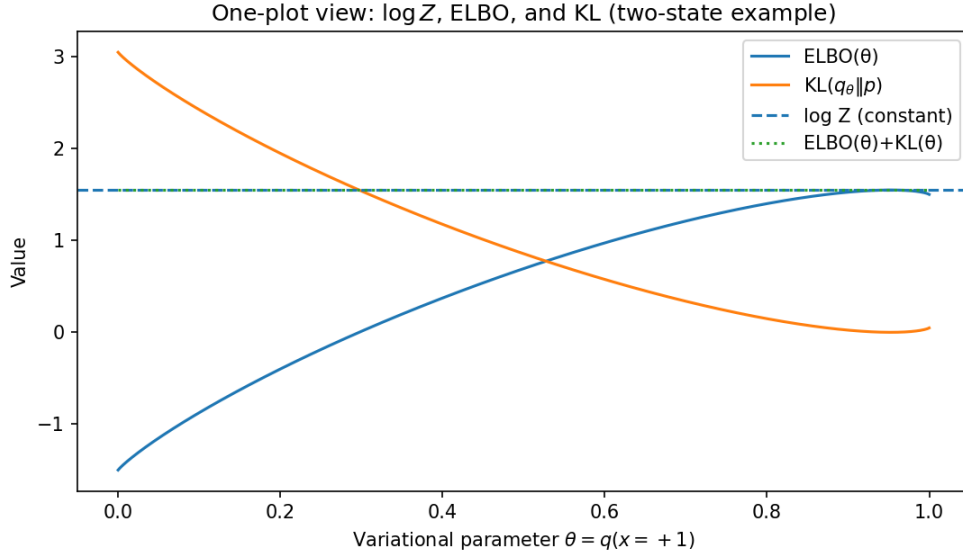


Figure 8.5: Variational decomposition of the log-partition function in a two-state energy-based model. The $\text{ELBO}(\theta)$ curve lies below the constant $\log Z$ for all values of the variational parameter $\theta = q(x = +1)$ and becomes tight at the true posterior marginal. The KL divergence $\text{KL}(q_\theta \| p)$ is non-negative, vanishes at the same optimum, and compensates the ELBO so that $\text{ELBO}(\theta) + \text{KL}(q_\theta \| p) = \log Z$ identically. The opposing deformation of the ELBO and KL curves visualizes how variational inference trades approximation error against bound tightness. Produced by `VI_ELBO_Toy.ipynb`.

Mean-Field Approximation on the Ising Model

Let us now illustrate Eq. (8.2) by specializing the variational surrogate $q(x)$ to a specific choice known as the *mean-field* (MF) ansatz.

Why “Mean-Field”? The name “mean-field” traces back to physics, where the original intuition emerged from treating each spin or particle as if it experiences only an *average* (mean) effect from all other particles instead of fully capturing detailed fluctuations or correlations. In statistical mechanics, this approximation often becomes asymptotically exact in the so-called thermodynamic limit, where the size of the system grows unbounded and collective behavior can be effectively captured by averaged interactions.

Consider the Ising model – introduced earlier in Section 7.5) on a graph $\mathcal{G} = (\mathcal{V}, \mathcal{E})$, where each node $i \in \mathcal{V}$ has a spin variable $x_i \in \{-1, +1\}$. The joint distribution, up to a normalization constant, is given by

$$p(x) \propto \exp\left(\sum_{(i,j) \in E} J_{ij} x_i x_j + \sum_{i \in V} h_i x_i\right). \quad (8.4)$$

A particularly simple variational ansatz is the *mean-field* approximation:

$$q(x) = \prod_{i \in V} q_i(x_i), \quad (8.5)$$

where each spin is treated as if it were statistically independent, having its own one-site marginal $q_i(x_i)$. In practice, one often parameterizes $q_i(x_i)$ in terms of the *magnetization* $m_i \in [-1, 1]$, via

$$q_i(x_i = +1) = \frac{1+m_i}{2}, \quad q_i(x_i = -1) = \frac{1-m_i}{2}.$$

KL Divergence under Mean-Field. Substituting (8.5) into the KL-divergence objective (8.2) and recalling that $p(x) \propto \exp(\sum_{(i,j)} J_{ij}x_i x_j + \sum_i h_i x_i)$, one obtains

$$\text{KL}(q \| p) = \sum_x \left(\prod_i q_i(x_i) \right) \log \left[\frac{\prod_i q_i(x_i)}{\exp(\sum_{(i,j)} J_{ij}x_i x_j + \sum_i h_i x_i)} \right] + (\text{const}).$$

Rewriting in terms of expectations over the single-site marginals $q_i(x_i)$ yields the well-known *mean-field self-consistency equations*:

$$m_i = \tanh(h_i + \sum_{j \in \partial i} J_{ij} m_j), \quad \forall i \in V, \quad (8.6)$$

where ∂i denotes the set of neighbors of node i in the graph. Solving (8.6) numerically provides a stationary point in the variational parameters $\{m_i\}$, hence yielding the mean-field approximation $q(x)$. Because this approximation factorizes all spins, it typically underestimates true correlations $\langle x_i x_j \rangle$, especially when the couplings J_{ij} are large or the graph contains loops.

Exactness and Thermodynamic Limit. In finite-size systems, mean-field is rarely exact, since real-world (or simulated) spins exhibit correlations that the product ansatz omits. However, in certain limiting regimes – for instance, as the system size $|V| \rightarrow \infty$ with suitably weak or dense couplings – the mean-field description can become asymptotically exact. Theoretical aspects of such regimes are discussed extensively in the literature on statistical physics, e.g., [50] and [49]. In practice, mean-field often serves as a fast baseline or initialization method before more refined approaches are used.

In what follows, we will see how one can improve upon this factorized approximation by allowing small subsets of variables (e.g., pairs) to be jointly modeled, leading to Belief Propagation and the Bethe approximation.

Example 8.1.4 (Mean-Field on a Loopy Ising Grid: What It Gets Right (and Wrong)). *Mean-field replaces a correlated posterior by a product distribution (8.5), yielding fast but biased marginals. The notebook `MeanField_Ising_3x3.ipynb` compares mean-field fixed points to exact enumeration on a 3×3 Ising grid (a small loopy graph where exact sums are still feasible). Left panel of Fig. 8.6 compares exact and mean-field magnetizations $m_i = \mathbb{E}[x_i]$. Center panel of Fig. 8.6 visualizes the correlation error $\Delta_{ij} = \langle x_i x_j \rangle_{\text{exact}} - \langle x_i x_j \rangle_{\text{MF}}$, highlighting that a fully factorized surrogate systematically misses loop-induced dependencies. Finally, right panel of Fig. 8.6 shows how mean-field accuracy degrades as the coupling strength increases.*

Exercise 8.1.4 (When Does Mean-Field Break?). *Use `MeanField_Ising_3x3.ipynb` as a baseline.*

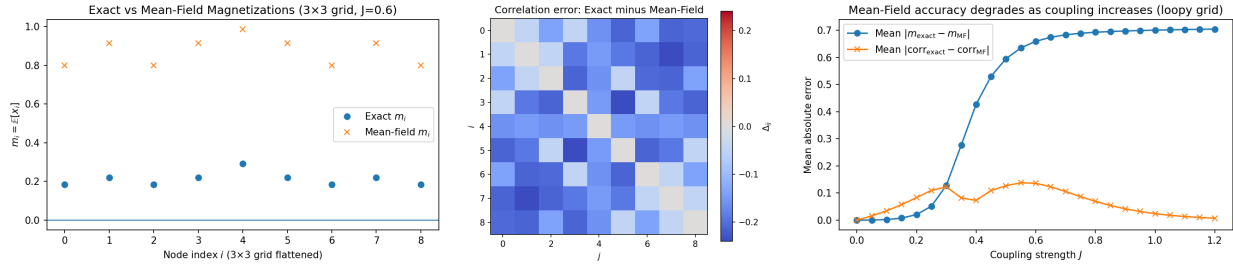


Figure 8.6: Left: Exact vs. mean-field magnetizations m_i on a 3×3 Ising grid. Center: Correlation error heatmap $\Delta_{ij} = \langle x_i x_j \rangle_{\text{exact}} - \langle x_i x_j \rangle_{\text{MF}}$. Mean-field cannot represent these correlations because $q(x)$ factorizes. Right: Mean-field error vs. coupling strength J on a loopy grid. Produced by `MeanField_Ising_3x3.ipynb`.

1. Repeat the coupling sweep in the right panel of Fig. 8.6 but change the graph: (i) a chain (tree), (ii) a grid (loopy), (iii) a fully connected graph with rescaled couplings. Compare regimes in which mean-field is accurate.
2. In the loopy grid, increase the external field at one node and re-run the experiments. How does symmetry breaking affect convergence and accuracy?
3. Replace the fixed-point solver by gradient descent on the mean-field free energy. Compare stability and speed.

Belief Propagation (BP): Factorization via Marginals

A more refined variational method is Belief Propagation (BP), sometimes called the Bethe approximation. Instead of factorizing over single nodes, one factorizes over small subsets (e.g., edges) in a factor graph. For the Ising model in (8.4), one treats each edge $(i, j) \in E$ as a two-site factor, thereby incorporating pairwise correlations:

$$q(x) = \prod_{(i,j) \in E} q_{ij}(x_i, x_j) / \prod_{i \in V} q_i(x_i)^{d_i - 1}, \quad (8.7)$$

where $q_{ij}(x_i, x_j)$ is the two-site marginal and $q_i(x_i)$ is the single-site marginal, with d_i the degree of node i . The exponents $(d_i - 1)$ in the denominator compensate for multiple over-counting in the product of pairs.

Exactness on a Tree. When the underlying graph G is a tree (i.e. loop-free), the Bethe or BP factorization (8.7) is *exact*, yielding the true posterior. A simple way to see this is by inductively constructing the solution from smaller trees:

1. *Base case (single node).* If $|V| = 1$, there are no edges. In this trivial graph, the Bethe factorization reduces to a single-site marginal $q_i(x_i)$ that must match the exact posterior. No overcounting arises, so exactness is manifest.
2. *Inductive step (adding a leaf).* Assume exactness for any tree with $n - 1$ nodes. Consider a tree with n nodes and $n - 1$ edges. Pick any leaf node ℓ whose only neighbor

is k . In the BP factorization, the edge term $q_{\ell k}(x_\ell, x_k)$ couples only these two sites, while all other edges remain unaffected. One can remove ℓ and its edge to reduce the problem to a tree with $n - 1$ nodes. By the induction hypothesis, the factorization there is exact. Restoring ℓ and its single edge then amounts to adding a single factor $q_{\ell k}(x_\ell, x_k)$ and the single-site term $q_\ell(x_\ell)$. A counting argument shows that ℓ 's contribution is accounted for *exactly once* in the product of pairwise marginals, once the single-site marginal $q_\ell(x_\ell)$ is included with exponent $(d_\ell - 1) = 0$. Thus consistency with the exact posterior is preserved.

3. *Consequence.* Repeating this leaf-removal argument from base up to a tree of any size $|V|$ confirms that the Bethe factorization perfectly reconstructs the exact distribution. In more physical terms, there is no “overcounting” on a loop-free graph, and so the Bethe free-energy functional coincides with the true free energy.

Consequently, on a tree, solving for q_{ij} and q_i that minimize the Bethe free energy yields the unique exact solution for $p(x)$. This underlies why belief propagation (BP) is guaranteed to converge to the exact marginals on trees.

BP Equations on the Ising Model: Message-Passing View. The resulting BP algorithm – sometimes also called the *sum-product* algorithm – can be expressed in terms of messages that pass between nodes along edges. For an edge (i, j) , let $m_{i \rightarrow j}(x_j)$ be the (unnormalized) *message* from node i to j , capturing i 's beliefs about x_j . One may derive the following iterative updates:

$$m_{i \rightarrow j}(x_j) \leftarrow \sum_{x_i \in \{-1, +1\}} \exp(J_{ij} x_i x_j + h_i x_i) \prod_{k \in \partial i \setminus j} m_{k \rightarrow i}(x_i), \quad (8.8)$$

where $\partial i \setminus j$ denotes neighbors k of i except for j . Once these messages converge, one obtains the single-site marginals via

$$q_i(x_i) \propto \exp(h_i x_i) \prod_{k \in \partial i} m_{k \rightarrow i}(x_i),$$

and the pairwise marginals from $q_i(x_i)q_j(x_j)$ times an additional factor from $J_{ij}x_i x_j$. As shown above when the graph is a tree, convergence to the unique exact marginals is guaranteed. However for graphs with loops, BP – in this context often called **loopy belief propagation** as applied to graphs with loops – typically provides a good approximation. The BP can also be corrected systematically by accounting for contributions of loops – see [49] and references therein for more details.

Example 8.1.5 (BP: Exact on Trees, Approximate on Loopy Graphs). *Belief Propagation (BP) is guaranteed to be exact on trees, while on loopy graphs it becomes an approximation whose quality depends on coupling strength, loop structure, and numerical damping. The notebook `BP_Tree_vs_Loopy_Ising.ipynb` compares BP on a random tree with BP on a graph obtained by adding a few extra edges (creating short loops) while keeping the same node set. Left panel of Fig. 8.7 plots the BP residual (maximum message change) as a function of iteration. Center panel of Fig. 8.7 compares BP and exact magnetizations, and Right panel of Fig. 8.7 summarizes the marginal error for tree vs. loopy cases.*

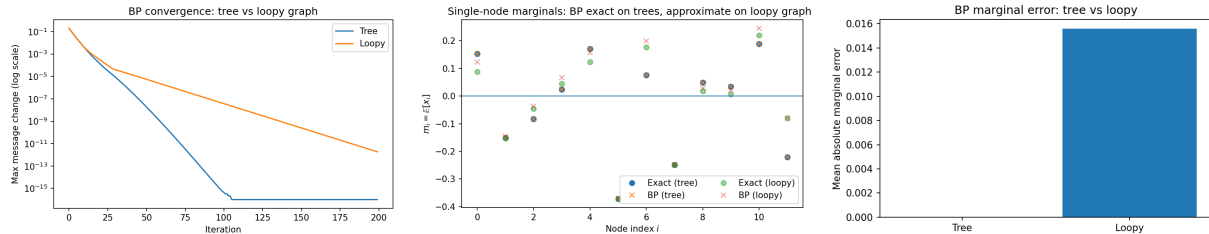


Figure 8.7: Left: BP convergence residual vs. iteration – tree vs. loopy graph. Center: single-node marginals: BP exact on trees, approximate on loopy graph. Right: Mean absolute marginal error for BP – tree vs. loopy. Produced by `BP_Tree_vs_Loopy_Ising.ipynb`.

Exercise 8.1.5 (BP on a Cycle: Analytic Structure and Numerical Stabilization). Use `BP_Tree_vs_Loopy_Ising.ipynb` as a baseline.

1. Replace the random loopy graph by a simple n -cycle (ring). For homogeneous coupling J and homogeneous field h , analyze the symmetry of BP fixed points and derive a reduced (one- or two-parameter) message update.
2. Implement BP on the cycle and compare with exact enumeration for small n . How do the BP marginals depend on J and h ?
3. Add damping and experiment with different damping factors. In which regimes does damping improve convergence?
4. (Optional) Compare with mean-field on the same cycle and discuss which approximation is more accurate and why.

From Variational Inference to Amortized Inference

Throughout this section we have viewed inference as an *optimization problem* over probability distributions, typically formulated via KL divergence minimization or ELBO maximization. Classical algorithms such as mean-field methods and belief propagation solve this optimization *iteratively*, producing approximate posteriors on a case-by-case basis.

A recurring limitation of this approach is computational: each new instance requires running a (possibly expensive) inference algorithm to convergence. This observation motivates a shift in perspective: rather than repeatedly *solving* the variational problem, one may attempt to *learn the inference map itself*. Neural networks provide a natural mechanism for such *amortized inference*, where a single forward pass replaces many iterations of an inference algorithm.

The following subsections illustrate this idea in two complementary settings: structured discrete models (LDPC decoding) and continuous latent-variable models (variational auto-encoders).

8.1.3 Neural Decoding of Low-Density Parity-Check Codes

This subsection illustrates how *variational inference*, *belief propagation (BP)*, and *neural parameterization* come together in a concrete and practically important task: decoding Low-Density Parity-Check (LDPC) codes from noisy channel observations. We begin by formulating LDPC decoding as inference in a factor graph and recalling its variational interpretation via BP. We then show how the resulting beliefs can be *amortized* by neural networks trained end-to-end, replacing per-instance iterative message passing by a single forward evaluation.

LDPC Codes, Channel Model, and Posterior

An LDPC code of length n is defined by a sparse parity-check matrix $H \in \{0, 1\}^{m \times n}$. A binary vector $x \in \{0, 1\}^n$ is a valid codeword if

$$Hx = 0 \pmod{2},$$

with arithmetic over GF(2). Each parity constraint involves only a small subset of bits, leading naturally to a bipartite factor graph with *bit nodes* and *check nodes*.

We assume transmission over an additive white Gaussian noise (AWGN) channel. Bits are mapped to BPSK symbols $\mu_{x_i} \in \{-1, +1\}$ and observed as

$$y_i = \mu_{x_i} + z_i, \quad z_i \sim \mathcal{N}(0, \sigma^2).$$

Given the channel output y , the posterior distribution over codewords is

$$p(x | y) \propto \prod_{c=1}^m \mathbf{1}(H_{c,:}x = 0 \pmod{2}) \prod_{i=1}^n \exp\left(-\frac{(y_i - \mu_{x_i})^2}{2\sigma^2}\right).$$

The parity constraints induce strong, nonlocal dependencies, making exact inference intractable for realistic blocklengths.

Belief Propagation as Variational Inference

Belief propagation can be interpreted as minimizing the KL divergence between the true posterior $p(x | y)$ and a structured variational family of Bethe type:

$$q^{(\text{bp})}(x) = \prod_{c=1}^m q_c(x_c) \prod_{i=1}^n q_i(x_i)^{1-d_i}, \tag{8.9}$$

where $q_c(x_c)$ are check-node beliefs, $q_i(x_i)$ are bit-node beliefs, and d_i is the degree of bit i in the factor graph. The exponents correct for overcounting of single-site marginals.

Minimizing $\text{KL}(q^{(\text{bp})} \| p(\cdot | y))$ under normalization and marginal-consistency constraints yields the BP fixed-point equations. Classical BP solves this optimization implicitly by iterative message passing.

Neuralized and Amortized Belief Approximation

Rather than running BP iterations separately for each new observation y , we may *amortize inference* by learning a direct map from channel outputs to beliefs. Concretely, we parameterize the local beliefs by neural networks:

$$q_i(x_i | y_i) = \text{NN}_\theta^{(\text{bit})}(x_i, y_i), \quad q_c(x_c | y_c) = \text{NN}_\theta^{(\text{check})}(x_c, y_c),$$

with shared parameters θ . These networks are trained on synthetic (x, y) pairs to approximate a reference inference procedure (exact enumeration for very small codes, or BP-based targets).

Approximate consistency between bit and check beliefs is enforced through a soft penalty, leading to the training objective

$$\min_{\theta} \text{KL}(q_\theta \| p) + \lambda \sum_c \sum_{i \in \text{vars}(c)} \left\| \sum_{x_c \setminus x_i} q_c(x_c | y_c) - q_i(x_i | y_i) \right\|_1.$$

This construction preserves the factor-graph structure and scales far better than a single global neural surrogate $q_\theta(x | y)$, whose complexity grows exponentially.

Relation to Graph Neural Network- (GNN-) Based Decoders

Neuralized BP naturally connects to graph neural network (GNN) extensions of message passing for LDPC decoding, such as [51], where messages or update rules are learned rather than fixed. While such architectures can outperform classical BP in certain regimes, our focus here is conceptual: demonstrating how inference itself can be learned and amortized.

Example 8.1.6 (Amortized Neural Decoding of a Toy LDPC Code). *The notebook `NN-BP-LDPC.ipynb` implements the above construction for a small LDPC code transmitted over an AWGN channel. The neural network learns an inference operator*

$$y \longmapsto \{q_\theta(x_i = 1 | y)\}_{i=1}^n,$$

approximating bit-wise posterior beliefs produced by exact inference or BP.

To obtain an informative single-instance visualization, the notebook plots posterior means in the BPSK (spin) representation,

$$s_i := 1 - 2x_i \in \{-1, +1\}, \quad \mathbb{E}[s_i | y] = 1 - 2p(x_i = 1 | y) \in [-1, 1].$$

This representation encodes both the inferred bit value (sign) and confidence (magnitude). Fig. 8.8 compares, for the same received word y , (i) exact posterior means, (ii) BP estimates after a fixed number of iterations, and (iii) neural predictions obtained in a single forward pass. A non-zero transmitted codeword is used to avoid a degenerate visualization and to highlight how different inference methods separate bit hypotheses under uncertainty.

Importantly, the neural decoder is not expected to systematically outperform well-tuned BP in accuracy: BP already solves the Bethe variational problem. The advantage lies in amortization: inference becomes a single evaluation rather than an iterative algorithm.

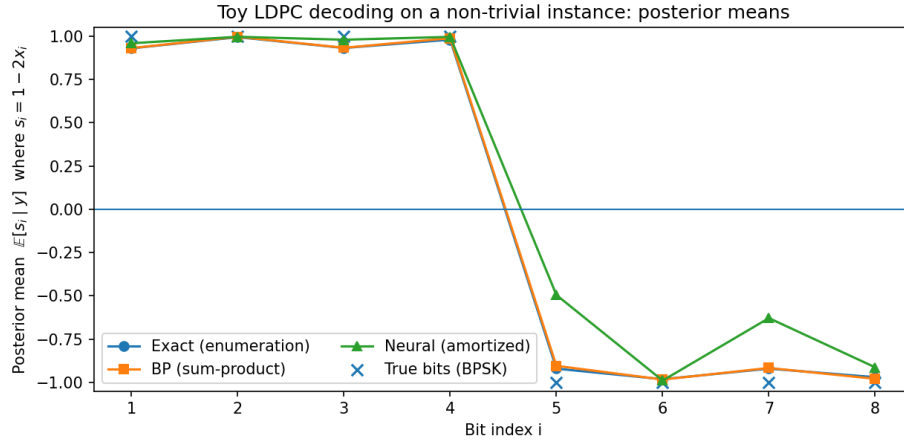


Figure 8.8: Posterior means for a toy LDPC code on a non-zero transmitted codeword. Shown are exact enumeration, belief propagation, and an amortized neural approximation. Posterior means are plotted in the BPSK/spin representation $s_i = 1 - 2x_i$, where sign indicates the inferred bit and magnitude indicates confidence.

Exercise 8.1.6 (Amortized Inference vs. Iterative Decoding). *Using the notebook `NN-BP-LDPC.ipynb`:*

1. Compare inference time of the neural decoder with BP as the number of BP iterations increases. When does amortization become advantageous?
2. Test the neural decoder at noise levels σ not seen during training. How robust is the learned inference map?
3. Train the network to mimic BP outputs after a small, fixed number of iterations. How does this affect accuracy and stability?
4. Conceptually distinguish learning to decode from learning to approximate inference. In which settings might the latter be preferable?

Inference Algorithms as Learnable Maps

The neuralized LDPC decoder illustrates a general principle: classical inference algorithms can be reinterpreted as structured, differentiable maps from observations to beliefs. In belief propagation, this map is implemented by hand-crafted message updates derived from a variational objective. In the neural formulation, the same objective is retained, but the update rules are replaced by trainable function approximators.

This viewpoint blurs the traditional distinction between *inference* and *learning*. Inference becomes a parametric object that can be optimized from data, while learning is guided not only by predictive accuracy but by the internal consistency of inferred probability distributions.

Variational auto-encoders take this idea one step further: rather than approximating a specific inference algorithm, they learn a global inference model jointly with a

generative model, using the ELBO as a unifying objective.

8.1.4 Variational Auto-Encoders

Earlier in this section we formulated inference in Graphical Models (GM) as an optimization over probability distributions, governed by KL divergences and variational objectives. *Variational Auto-Encoders (VAEs)* extend this paradigm to deep latent-variable models, combining variational inference with Neural Network (NN) parameterizations. Introduced by Kingma and Welling [52], VAEs were at the start of modern generative modeling and thus provided a direct bridge from classical Bayesian inference to neural generative architectures.

Latent-Variable Models and Variational Inference

VAEs are based on a latent-variable generative model

$$p_{\theta}(x, z) = p_{\theta}(z) p_{\theta}(x | z),$$

where $x \in \mathbb{R}^d$ denotes observed data, $z \in \mathbb{R}^m$ is a latent variable, and θ parametrizes both the prior and the likelihood. Learning proceeds by maximizing the marginal likelihood $p_{\theta}(x) = \int p_{\theta}(x, z) dz$, which is generally intractable due to the integral over z .

As in Section 8.1.2, variational inference introduces a tractable surrogate $q_{\phi}(z | x)$ and optimizes the Evidence Lower Bound (ELBO)

$$\mathcal{L}(\theta, \phi; x) = \mathbb{E}_{q_{\phi}(z|x)}[\log p_{\theta}(x | z)] - \text{KL}(q_{\phi}(z | x) \| p_{\theta}(z)),$$

which satisfies $\mathcal{L}(\theta, \phi; x) \leq \log p_{\theta}(x)$. Maximizing the ELBO simultaneously trains the generative model and learns an approximate posterior.

Neural Parameterization: Encoder and Decoder

In a VAE, both components of the variational construction are parameterized by NNs:

- **Encoder (approximate posterior).** The encoder maps data to a latent distribution,

$$q_{\phi}(z | x) = \mathcal{N}(\mu_{\phi}(x), \Sigma_{\phi}(x)),$$

with mean and (typically diagonal) covariance predicted by a NN.

- **Decoder (generative model).** The decoder – represented with another NN – maps latent variables back to data space,

$$p_{\theta}(x | z) = \mathcal{N}(\hat{x}_{\theta}(z), \sigma_x^2 I),$$

or another suitable likelihood depending on the data type.

Training relies on the reparameterization trick $z = \mu_{\phi}(x) + \Sigma_{\phi}^{1/2}(x) \epsilon$, $\epsilon \sim \mathcal{N}(0, I)$, which allows gradients to propagate through stochastic sampling.

Example 8.1.7 (1D-Latent VAE on a 2D Ring). *The notebook `Ring_VAE_1D_Latent.ipynb` illustrates VAEs on a controlled geometric example: a noisy ring in \mathbb{R}^2 ,*

$$x = (R \cos \theta, R \sin \theta) + \varepsilon, \quad \theta \sim \text{Unif}[0, 2\pi), \quad \varepsilon \sim \mathcal{N}(0, \sigma_{\text{data}}^2 I_2).$$

The model uses a one-dimensional latent $z \in \mathbb{R}$, deliberately introducing a mismatch between the topology of the data manifold (a circle) and the latent space (a line).

Fig. (8.9) summarizes the learned generative behavior. The left panel shows reconstructions obtained by encoding each data point, sampling from $q_\phi(z | x)$, and decoding. The right panel shows unconditional generations produced by sampling $z \sim \mathcal{N}(0, 1)$ and decoding. Together, the panels visualize the ELBO trade-off: the reconstruction term aligns decoded points with the observed ring, while the KL term regularizes the latent space so that sampling from the prior produces plausible data. (Couple of clarifying remarks are in order: (1) In this low-dimensional and well-matched setting, reconstructions and prior samples appear visually similar. This reflects successful alignment between the aggregate posterior and the latent prior, rather than a redundancy of the visualization. (2) Although the latent prior $z \sim \mathcal{N}(0, 1)$ is a one-dimensional Gaussian cloud, the learned decoder maps this line nonlinearly into data space. The ring structure therefore emerges as the image of the Gaussian under the decoder, not as a property of the latent distribution itself.)

Learned latent geometry. *Fig. (8.10) plots the encoder mean $z = \mu_\phi(x)$ against the true polar angle θ of each data point. The latent coordinate varies approximately monotonically with θ , demonstrating that the VAE has discovered a meaningful one-dimensional representation of the ring. However, a sharp jump appears at one location. This discontinuity is unavoidable: a continuous, one-to-one mapping from a circle to a line cannot exist without a cut. The VAE therefore chooses a branch cut, analogous to unwrapping an angular variable. The location of the jump is not fixed a priori and reflects spontaneous symmetry breaking during training.*

Why the ring is clean and incomplete. *Both reconstructed and generated samples in Fig. (8.9) concentrate on a clean (thin) ring and leave a small angular segment underrepresented. This behavior is expected and reflects two fundamental aspects of the VAE formulation. First, with a Gaussian likelihood $p_\theta(x | z) = \mathcal{N}(\hat{x}_\theta(z), \sigma_x^2 I)$, the decoder is trained to predict the conditional mean $\hat{x}_\theta(z) = \mathbb{E}[x | z]$. As a result, both reconstructions and prior-based generations visualize denoised manifold means; the observational noise present in the data would reappear only if one explicitly samples from the likelihood distribution. Second, a one-dimensional latent space cannot globally parametrize a circular manifold. The VAE therefore introduces an implicit “cut” in latent space, mapping most of the ring to the high-density region of the Gaussian prior and sacrificing a small angular segment. The location of this gap is arbitrary and depends on initialization, but its presence is a topological consequence of representing a periodic structure with a non-periodic latent variable.*

Exercise 8.1.7 (VAE geometry and the ELBO trade-off). *Using `Ring_VAE_1D_Latent.ipynb`:*

1. *Vary the KL weight β and study how reconstruction quality and prior samples change. Relate your observations to the ELBO terms.*

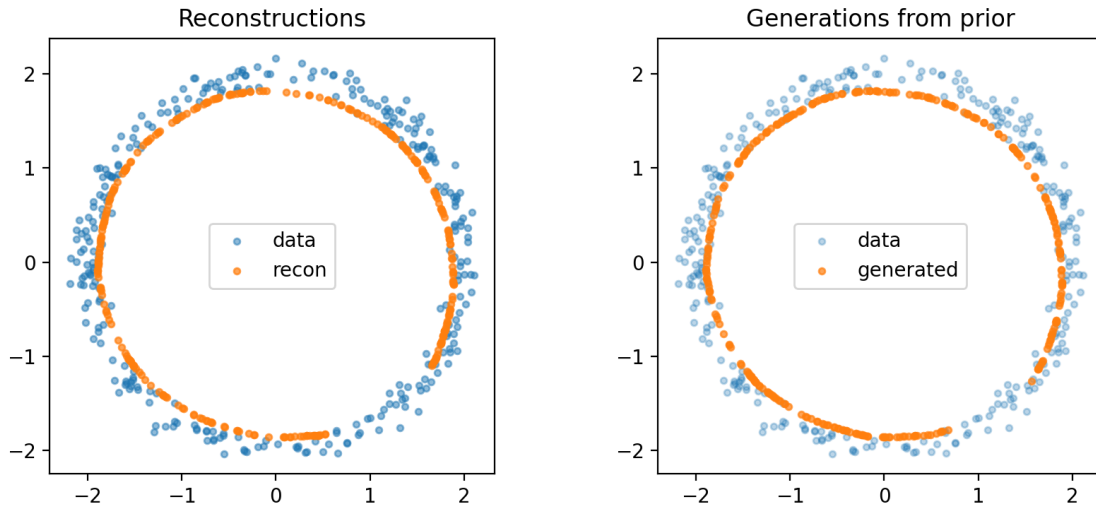


Figure 8.9: 1D-latent VAE trained on a noisy 2D ring. **Left:** reconstructions (encode \rightarrow sample $z \rightarrow$ decode). **Right:** generations from the prior $z \sim \mathcal{N}(0, 1)$. The figure visualizes the balance between reconstruction fidelity and latent regularization imposed by the ELBO.

2. Explain why a globally continuous latent coordinate is impossible in Fig. 8.10. How would the plot change if the latent dimension were increased to $z \in \mathbb{R}^2$?
3. Inspect the posterior variance near the latent jump. Why does increased uncertainty appear precisely at the branch cut?

Additional diagnostics. Extend the exercise as follows:

1. **Likelihood sampling.** Modify the generation step to sample from the likelihood, $\tilde{x} = \hat{x}_\theta(z) + \sigma_x \epsilon$, $\epsilon \sim \mathcal{N}(0, I)$. Compare the resulting samples with Fig. 8.9 and explain how observational noise reappears and why it was absent in the original plots.
2. **Latent dimensionality.** Increase the latent dimension from $z \in \mathbb{R}$ to $z \in \mathbb{R}^2$ and retrain the VAE. Reproduce the reconstruction and generation figures. Explain why the angular gap disappears and how this relates to the topology of the data manifold.
3. **Effect of the KL weight.** Repeat the experiment for several values of the KL weight β . Describe how increasing β changes (i) the sharpness of the reconstructed ring, (ii) the size of the missing angular region, and (iii) the quality of prior-based samples. Relate your observations to the trade-off between reconstruction fidelity and latent regularization in the ELBO.

Bridge to Chapter 9: From Latent Variables to Generative Dynamics

The models studied in this section share a common structure: they define probability distributions implicitly through optimization principles (KL divergence, ELBOs, or variational free energies) and rely on approximate inference to make these distributions usable in practice. Whether implemented by message passing, neural amortization, or

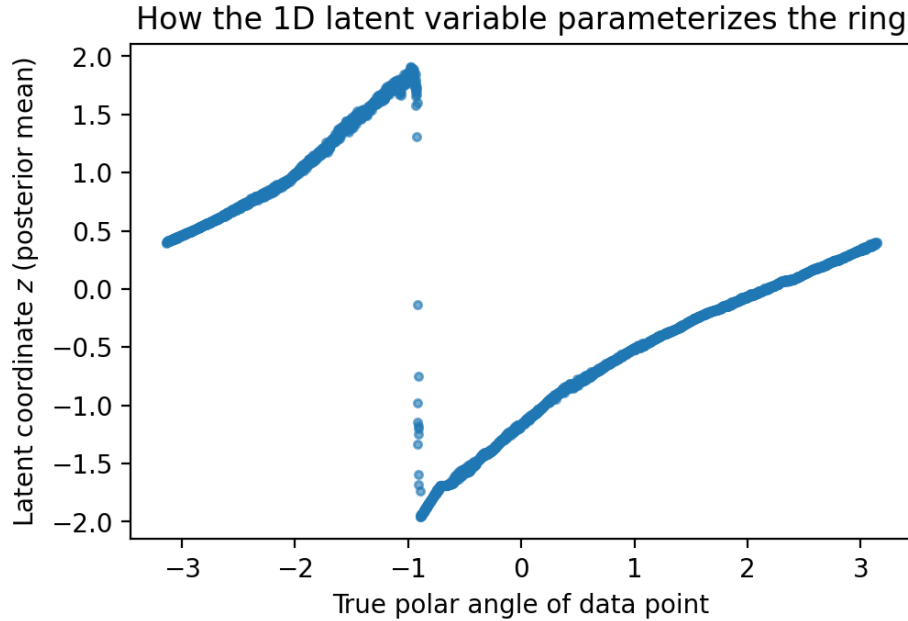


Figure 8.10: Encoder mean $z = \mu_\phi(x)$ versus the true polar angle θ of points on the ring. The approximately monotone relation shows that the VAE has learned a meaningful 1D coordinate. The discontinuity reflects the topological mismatch between a circular data manifold and a linear latent space.

encoder-decoder architectures, inference remains a central computational bottleneck. Chapter 9 revisits these ideas from a dynamical perspective. Instead of approximating a static posterior or latent-variable model, we will construct *non-equilibrium stochastic processes* whose time marginals interpolate between simple reference distributions and complex data distributions. Score-based diffusion models and Schrödinger bridge formulations can be viewed as continuous-time analogues of the variational principles introduced here, replacing latent variables by stochastic trajectories and inference by time reversal.

Seen from this angle, variational auto-encoders form a conceptual midpoint: they retain latent variables but already point toward generative models defined by learned dynamics rather than explicit normalization.

8.2 Learning

This section delves into how one can infer or learn an underlying Graphical Model (GM) directly from data. We focus on methods relevant to *Energy-Based Models (EBMs)*, touching on both conceptual underpinnings and efficient algorithms. The exposition closely mirrors discussions in Sections 10.3 of [33] and 9.2 of [49], as well as the notes introduced in earlier sections of this text. The goal is to reveal how statistical learning, i.e. reconstructing the GM from data, is conceptually intertwined with inference (partition function, marginals,

sampling) and can inherit its computational difficulties. We outline both the core theory and the common approximations crucial for modern AI.

8.2.1 Likelihood

This subsection develops likelihood-based learning for Energy-Based and Graphical Models. Whereas Section 8.1 assumed a fixed model and focused on inference (marginals, partition functions, sampling), here the model parameters themselves must be learned from data. A recurring theme is that learning and inference are inseparable: likelihood optimization requires expectations under the model, and therefore inherits the computational challenges of inference.

Learning as Inference in Disguise

In Energy-Based Models, maximizing likelihood requires computing model expectations. These expectations are exactly the objects studied in inference (Section 8.1). As a result, learning EBMs is computationally hard for the same reasons inference is hard.

Sufficiency of Empirical Moments in the Exponential Family

We begin with a general principle underlying likelihood-based learning in EBMs: *empirical moments are sufficient statistics*. Although the Ising model offers the most familiar example, the argument applies to arbitrary exponential-family models, including categorical, count-based, and continuous-variable graphical models.

Exponential-family representation. A probability distribution over $x = (x_1, \dots, x_N) \in \mathcal{X}^N$ belongs to the exponential family if it can be written as

$$P_\theta(x) = h(x) \exp(\theta^\top T(x) - A(\theta)), \quad A(\theta) = \log Z(\theta), \quad (8.10)$$

where $\theta \in \mathbb{R}^d$ are canonical parameters, $T(x) \in \mathbb{R}^d$ are sufficient statistics (node and factor terms in a GM), and $A(\theta)$ is the log-partition function.

Likelihood and empirical moments. Given i.i.d. samples $\{x^{(\ell)}\}_{\ell=1}^M$, the log-likelihood is

$$\log \mathcal{L}(\theta) = \sum_{\ell=1}^M \log P_\theta(x^{(\ell)}) \quad (8.11)$$

$$= M \theta^\top \hat{T}_M - MA(\theta), \quad \hat{T}_M = \frac{1}{M} \sum_{\ell=1}^M T(x^{(\ell)}). \quad (8.12)$$

All dependence on the dataset enters exclusively through the empirical moments \hat{T}_M . Once these are computed, the raw data are no longer needed for likelihood-based learning.

Moment-matching condition. Taking derivatives yields

$$\nabla_{\theta} \log \mathcal{L}(\theta) = M(\hat{T}_M - \mathbb{E}_{\theta}[T(x)]). \quad (8.13)$$

Thus, maximum likelihood learning enforces *moment matching*:

$$\mathbb{E}_{\theta}[T(x)] = \hat{T}_M. \quad (8.14)$$

Example 8.2.1. • *Ising model:* $T(x)$ consists of node terms x_i and edge terms $x_i x_j$.

- *Gaussian model:* $T(x) = (x, xx^{\top})$ encodes mean and covariance.

- *Categorical GM:* $T(x)$ includes indicator functions for clique configurations.

In all cases, learning reduces to matching empirical and model moments.

Why Likelihood Learning is Hard

Computing $\mathbb{E}_{\theta}[T(x)]$ requires summing or integrating over all configurations $x \in \mathcal{X}^N$. For high-dimensional graphical models this is intractable, making exact maximum likelihood learning impractical except in very special cases.

Approximate likelihood methods. To circumvent the partition function, practical learning algorithms rely on:

- sampling-based approximations (MCMC, Langevin dynamics),
- variational bounds on $A(\theta)$,
- local objectives such as pseudo-likelihood,
- alternative criteria such as score matching or contrastive divergence.

We now illustrate one such alternative in a concrete low-dimensional setting.

Example: Score Matching for a Two-Dimensional Energy Model

Score matching provides a way to train unnormalized models without evaluating the partition function. Instead of matching probabilities, it matches their gradients with respect to the data.

Example 8.2.2 (Score Matching in Two Dimensions: Geometry of the Learned Score). *We consider a synthetic dataset in \mathbb{R}^2 generated from a mixture of Gaussians. Our goal is to learn an unnormalized density*

$$P_{\theta}(x) \propto e^{-E_{\theta}(x)},$$

where $E_{\theta}(x)$ is a shallow neural network representing the energy landscape.

Instead of maximum likelihood, which would require evaluating the partition function, we train the model using score matching. The score-matching objective reads

$$\mathcal{L}_{\text{SM}}(\theta) = \mathbb{E}_{x \sim \text{data}} \left[\frac{1}{2} \|\nabla_x E_{\theta}(x)\|^2 + \Delta_x E_{\theta}(x) \right], \quad (8.15)$$

and depends only on derivatives of the energy with respect to the input x . Crucially, the partition function does not appear.

Why this objective? To interpret the objective (8.15), recall that for an energy-based model $P_\theta(x) \propto e^{-E_\theta(x)}$, the score of the model distribution is

$$\nabla_x \log P_\theta(x) = -\nabla_x E_\theta(x).$$

Score matching seeks to align this model score with the (unknown) score of the data distribution, $\nabla_x \log P_{\text{data}}(x)$, by minimizing the squared L^2 distance between the two vector fields:

$$\mathcal{J}(\theta) = \frac{1}{2} \int \|\nabla_x \log P_\theta(x) - \nabla_x \log P_{\text{data}}(x)\|^2 P_{\text{data}}(x) dx. \quad (8.16)$$

This quantity is known as the Fisher divergence.

Crucially, although (8.16) appears to involve the unknown data score, it can be rewritten in a tractable form. By expanding the square, discarding terms independent of θ , and integrating the remaining expression by parts (under standard decay assumptions at infinity), one arrives exactly at Eq. (8.15).

The structure of this objective (8.15) admits a direct geometric interpretation. The gradient term $\frac{1}{2}\|\nabla_x E_\theta(x)\|^2$ controls the overall magnitude and regularity of the learned score field, while the Laplacian term $\Delta_x E_\theta(x)$ encodes local curvature, encouraging the score to point toward regions of high data density. Together, these terms enforce that $-\nabla_x E_\theta(x)$ approximates both the direction and local geometry of increasing probability mass.

In this way, score matching replaces likelihood maximization – which depends on the global normalizing constant – by a purely local, differential variational principle. This makes it particularly well suited for continuous, unnormalized models and naturally connects learning to stochastic dynamics such as Langevin sampling and diffusion.

Left panel of Fig. 8.11 shows the training data: samples from a two-component Gaussian mixture. The multi-modal structure is simple but nontrivial, making it a useful testbed for energy-based learning.

After training, we evaluate the learned score

$$s_\theta(x) = -\nabla_x E_\theta(x)$$

on a grid in \mathbb{R}^2 . Right panel of Figure 8.11 visualizes this vector field.

Several important features are worth noting:

- The score vectors point toward regions of high data density, illustrating that the model has learned the gradient of the log-density rather than the density itself.
- Around each mode, the vector field behaves approximately like a linear attractor, consistent with the local Gaussian structure of the data.
- Away from the data manifold, the score field extrapolates smoothly, providing meaningful directions even in low-density regions.

This geometric viewpoint clarifies why score-based learning is powerful: it directly learns the directions of probability flow, which are precisely the quantities required for Langevin sampling and diffusion-based generation.

The accompanying notebook `ScoreMatchingEnergy_Renewed.ipynb` implements the full pipeline: data generation, score-matching training, vector-field visualization.

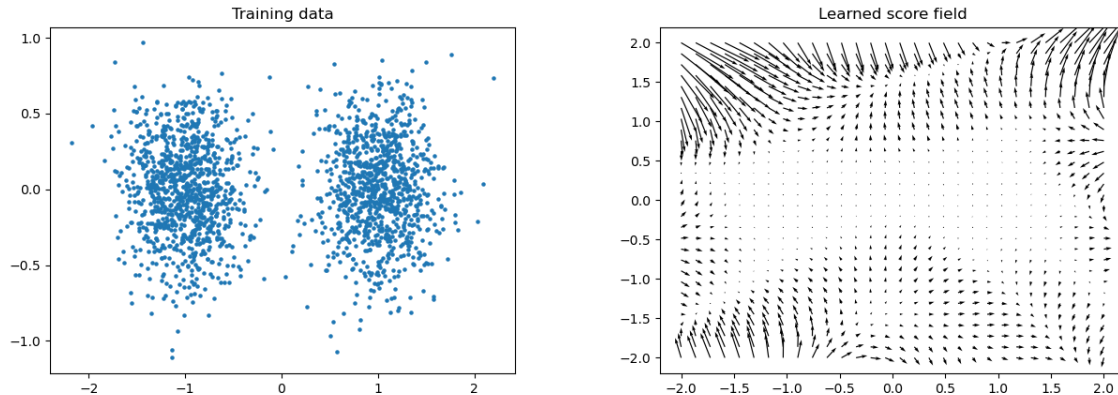


Figure 8.11: Training data – shown on the left – a two-dimensional mixture of two Gaussians. The goal of learning is not merely to fit a classifier, but to recover a vector score field $-\nabla_x E_\theta(x)$ – shown on the right. Arrows point toward regions of high data density. Near each Gaussian mode, the vector field contracts inward, indicating local stability of probability mass.

Exercise 8.2.1 (From Score Learning to Generative Sampling). *Starting from `ScoreMatchingEnergy_Renewed.ipynb`, carry out the following steps. The tasks are ordered by increasing conceptual and computational difficulty.*

1. **Langevin Sampling (Warm-up).** Implement overdamped Langevin dynamics

$$x_{k+1} = x_k - \eta \nabla_x E_\theta(x_k) + \sqrt{2\eta} \xi_k, \quad \xi_k \sim \mathcal{N}(0, I),$$

starting from isotropic Gaussian noise. Visualize the generated samples and compare them to the training data.

2. **Stability and Hyperparameters.** Systematically vary the step size η and number of iterations. Identify regimes where: (i) sampling collapses to a single mode, (ii) sampling diverges, (iii) sampling approximately recovers both modes. Explain these behaviors using the geometry of the score field.
3. **Denoising Score Matching.** Replace score matching with denoising score matching (DSM) at a fixed noise level σ . Compare the learned score fields for different σ . How does added noise change smoothness, stability, and extrapolation?
4. **Annealed Sampling.** Implement annealed Langevin dynamics using a decreasing noise schedule. Compare sample quality and mode coverage against the fixed-noise case.
5. **Challenging Extension: Dynamical Interpretation.** Interpret Langevin sampling as a discretization of a stochastic differential equation. Empirically investigate how the learned score field defines an effective potential landscape:
 - Identify approximate fixed points of the dynamics.

- Linearize the score field near a mode and estimate local contraction rates.
- Discuss how these quantities relate to the curvature of the underlying energy.
- Relate your findings to the Ornstein–Uhlenbeck process from Section 7.3.3.

Bridge to Score-Based Diffusion Models

Score matching and Langevin sampling provide a static view of learning unnormalized models. Chapter 9 shows how multi-scale denoising scores naturally lead to reverse-time diffusions and modern score-based generative models.

8.2.2 Local Methods: Pseudo-Log-Likelihood and Interaction Screening

Likelihood-based learning of graphical models becomes computationally infeasible at scale, as it requires repeated evaluation of the partition function or its gradient. In this subsection, we study *local learning methods* that bypass global normalization by exploiting conditional independence and neighborhood structure. Two representative approaches are *Pseudo-Log-Likelihood* (PLL) and *Interaction Screening* (IS) [53, 54, 49].

Local Learning Philosophy

Local methods replace global likelihood maximization by a collection of independent, node-wise learning problems. Each node is trained using only its conditional distribution given its neighbors, completely avoiding the evaluation of the global partition function.

A two-stage perspective. Throughout this subsection, we adopt a unified *two-stage view* of local learning:

1. **Structure discovery:** identify the neighborhood of each node (i.e., recover the graph) using sparse, local objectives;
2. **Weight refinement:** once the graph is fixed, re-estimate interaction strengths without sparsity penalties to reduce bias.

This separation mirrors classical ideas in statistical model selection and proves particularly effective in high-dimensional graphical models.

Pseudo-Log-Likelihood

The pseudo-log-likelihood replaces the joint log-likelihood by a sum of local conditional log-probabilities:

$$\mathcal{L}_{\text{PLL}}(\theta) = \sum_{a \in \mathcal{V}} \sum_{s=1}^S \log P_\theta(x_a^{(s)} | x_{\setminus a}^{(s)}), \quad (8.17)$$

where $x_{\setminus a}$ denotes all variables except x_a . For exponential-family graphical models, these conditional distributions admit closed-form expressions.

Ising specialization. For an Ising model with parameters θ_a, θ_{ab} ,

$$P(x_a = 1 | x_{\setminus a}) = \frac{\exp(\theta_a + \sum_{b \in \mathcal{N}(a)} \theta_{ab} x_b)}{1 + \exp(\theta_a + \sum_{b \in \mathcal{N}(a)} \theta_{ab} x_b)}. \quad (8.18)$$

Thus, maximizing \mathcal{L}_{PLL} reduces to solving $|\mathcal{V}|$ independent logistic regression problems—one per node.

Interpretation: Pseudo-likelihood transforms global graphical-model learning into a collection of interpretable local regressions. Nonzero regression coefficients directly indicate edges, making PLL a natural tool for structure recovery.

Interaction Screening

Interaction Screening (IS) adopts a complementary viewpoint. Rather than maximizing conditional likelihoods, IS constructs *local surrogate objectives* whose minimizers recover the correct neighborhoods under suitable conditions.

For each node a , one solves a regression problem of the form

$$\min_{\theta_a, \theta_{ab}} \mathbb{E}_{\text{emp}} \left[(x_a - \sigma(\theta_a + \sum_b \theta_{ab} x_b))^2 \right] + \lambda \sum_b |\theta_{ab}|, \quad (8.19)$$

where $\sigma(\cdot)$ is the sigmoid function. The ℓ_1 penalty promotes sparsity, enabling reliable neighborhood screening even when the number of variables is large.

Theoretical Guarantees. Under standard assumptions (incoherence, sufficient samples), both PLL and IS are *consistent* and *sparsistent*: they recover the correct edge set with high probability, even in regimes where global maximum likelihood is computationally infeasible.

Example 8.2.3 (Two-Stage Structure and Weight Recovery in an Ising Model). *We now illustrate the two-stage local-learning paradigm using a controlled Ising experiment. We consider an Ising model on a 4×4 grid ($N = 16$ nodes), where all true edges have equal magnitude and random signs. This construction removes ambiguities associated with vanishingly weak interactions and isolates algorithmic effects.*

Stage one: structure recovery. *Using a collection of i.i.d. samples generated by Gibbs sampling, we apply both PLL and IS with ℓ_1 regularization to obtain local interaction scores. The final graph is reconstructed by retaining the top $E = 24$ undirected edges (rank-based selection).*

Fig. 8.12, generated in the notebook `Ising_PLL_IS_TwoStage.ipynb`, compares the ground-truth Ising model with the results of pseudo-log-likelihood (PLL) and interaction screening (IS) learning using a deviation-from-truth visualization. At the first (screening) stage, both methods recover the interaction graph exactly: all true edges are identified and no spurious edges appear. The figure goes further by displaying, on the recovered edges, the deviations of the estimated couplings from their true values after the second, unpenalized refit stage. This representation reveals that PLL and IS not only recover identical graph structure, but also produce reasonably accurate interaction strengths.

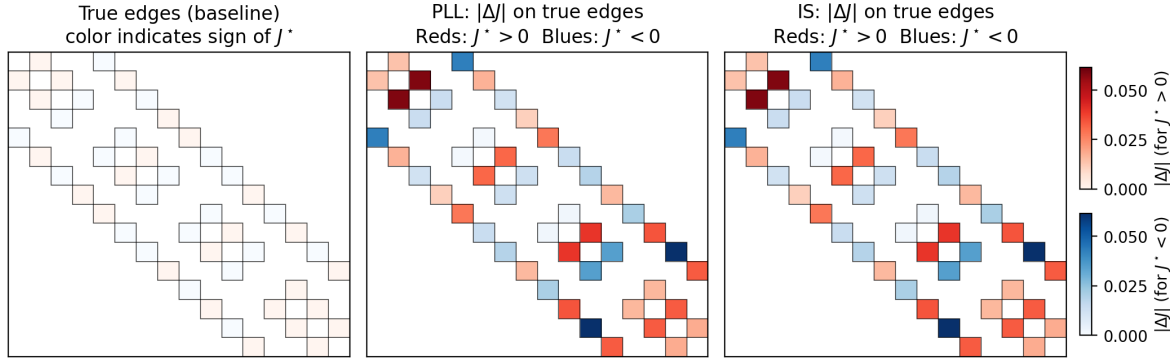


Figure 8.12: Structure and weight recovery in a 4×4 Ising model. Left: true interaction graph, with color indicating the sign of the ground-truth couplings ($J^* > 0$ in red, $J^* < 0$ in blue). Middle: pseudo-log-likelihood (PLL) recovery, showing deviations $\Delta J = \hat{J} - J^*$ on true edges after the second (unpenalized) refit stage. Right: interaction screening (IS) recovery, shown in the same deviation-from-truth representation. Color intensity encodes the magnitude $|\Delta J|$, while black outlines mark the true edges. Both methods recover the exact graph at the screening stage; this figure highlights the remaining (small) weight-estimation errors and their spatial structure.

Optimization behavior. An important practical distinction between PLL and IS emerges at the level of optimization. Fig. 8.13 compares the convergence of the ℓ_1 -regularized node-wise objectives for a representative node. While both methods ultimately recover the correct neighborhood structure, interaction screening converges substantially faster than pseudo-log-likelihood. This behavior is consistent with the simpler geometry of the IS objective, which relies on a squared-loss surrogate, in contrast to the logistic loss underlying PLL. As a result, IS can be advantageous in large-scale or time-sensitive settings, where rapid screening of candidate interactions is required before more refined estimation.

Stage two: weight refinement. Fixing the recovered graph, we refit interaction strengths using unpenalized node-wise logistic regression. This second stage substantially reduces the bias introduced by ℓ_1 regularization. While finite-sample effects prevent exact recovery of coupling values, the refined estimates closely track the true interactions and improve systematically with increasing data.

Exercise 8.2.2 (Extending Local Learning Beyond the Baseline: Structure, Strength, and Sample Complexity). Starting from the accompanying notebook *Ising_PLL_IS_TwoStage.ipynb*:

1. **Sample-size scaling.** Repeat the experiment for increasing numbers of samples. Quantify how edge recovery and weight error improve with data.
2. **Heterogeneous interactions.** Modify the model so that edge strengths are drawn from a distribution with varying magnitudes. Which edges become hardest to recover, and why?
3. **Beyond grids.** Replace the grid by a random sparse graph or a small-world topology. Compare recovery behavior across graph families.

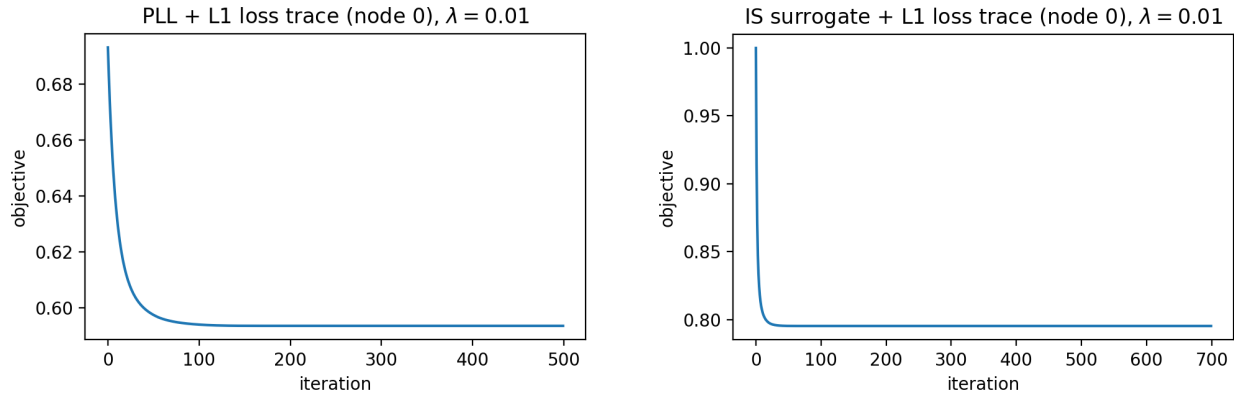


Figure 8.13: Convergence behavior of local screening objectives at the first stage. Left: pseudo-log-likelihood (PLL) objective with ℓ_1 regularization for a representative node. Right: interaction screening (IS) surrogate objective with ℓ_1 regularization for the same node. Both objectives converge to stable minima, but IS exhibits significantly faster convergence, reflecting its simpler squared-loss structure compared to the logistic loss used in PLL.

4. **Two-stage design.** Experiment with alternative screening rules in stage one (e.g., varying E , adaptive thresholds, or hybrid PLL-IS screening). How sensitive is the second-stage refinement to screening errors?
5. **Open-ended.** Can you design a local objective that outperforms both PLL and IS in the low-sample regime? Justify your proposal empirically.

Connection to Modern Energy Based Models (EBMs)

Local learning methods anticipate key ideas in modern energy-based models: they prioritize scalable, neighborhood-level objectives over global normalization and naturally support sparsity, modularity, and parallel training.

8.2.3 Restricted Boltzmann Machines: Learning with Latent Variables

Restricted Boltzmann Machines (RBMs) have already appeared several times in this text, most notably in Sections 7.5.3, 7.5.4, and 7.5.5, where they served as a concrete and instructive example for introducing Gibbs sampling, block updates, and Contrastive Divergence as a truncated MCMC scheme. In those earlier sections, the emphasis was deliberately algorithmic: RBMs were used as a convenient testbed for understanding *how* sampling works and *why* short-run Markov chains can be effective in practice.

We now return to RBMs from a different and complementary perspective. Rather than treating them primarily as an object of inference or sampling, we use RBMs here as a *learning model* – a minimal yet expressive example of how unnormalized energy-based models with latent variables can be trained from data. This shift in viewpoint places RBMs squarely within the broader theme of this section: learning graphical models and energy-based models when exact likelihood-based methods are computationally infeasible.

In particular, RBMs allow us to examine, in a controlled setting, the interaction between three central ideas developed throughout this chapter: (i) likelihood gradients expressed as differences of expectations, (ii) latent-variable representations that act as learned features, and (iii) approximate learning rules based on short-run MCMC. While all of these ingredients were already present implicitly in earlier sections, our goal here is to make their *learning interpretation* explicit and to connect RBMs to the general framework of local, approximate, and sampling-driven learning methods discussed above.

With this motivation in mind, we briefly recall the RBM model and notation before turning to its learning dynamics and representative examples.

A *Restricted Boltzmann Machine (RBM)* is an undirected, bipartite energy-based model over *visible* variables $v \in \{0, 1\}^n$ and *hidden* variables $h \in \{0, 1\}^m$. It can be viewed as a special case of the Ising model on a bipartite graph, but with an important algorithmic advantage: the absence of intra-layer edges makes the conditional laws factorize, enabling efficient block updates.

Energy and conditionals. The RBM energy is

$$E_\theta(v, h) = -v^\top Wh - b^\top v - c^\top h, \quad \theta = (W, b, c), \quad (8.20)$$

and the joint distribution is $P_\theta(v, h) \propto \exp(-E_\theta(v, h))$. Because the graph is bipartite, both conditionals factorize:

$$P_\theta(h | v) = \prod_{j=1}^m \sigma((W^\top v + c)_j), \quad P_\theta(v | h) = \prod_{i=1}^n \sigma((Wh + b)_i),$$

where $\sigma(x) = 1/(1 + e^{-x})$.

Why RBMs matter in a learning chapter

RBM are a minimal setting where three core learning themes meet: (i) *unnormalized* energy models (the partition function is intractable), (ii) *latent variables* and representation learning (hidden units act as learned features), and (iii) *sampling-driven* learning rules (negative-phase expectations are approximated by short MCMC runs).

Likelihood gradient: positive vs. negative phase. For a training sample v , the log-likelihood gradient has the characteristic difference-of-expectations form

$$\nabla_\theta \log P_\theta(v) = \underbrace{\mathbb{E}_{P_\theta(h|v)}[\nabla_\theta(-E_\theta(v, h))]}_{\text{positive phase (data-anchored)}} - \underbrace{\mathbb{E}_{P_\theta(v,h)}[\nabla_\theta(-E_\theta(v, h))]}_{\text{negative phase (model)}}, \quad (8.21)$$

where the negative phase is expensive because it requires sampling from the model. This is precisely where short-run MCMC enters.



Figure 8.14: RBM on Bars-and-Stripes. Left: training data samples. Middle: learned features (columns of W reshaped as images). Right: model samples produced by block Gibbs sampling. The RBM learns reusable features and composes them to generate new structured samples.

Contrastive divergence (CD) and the role of truncated MCMC. We do *not* repeat the CD- k procedure here. A detailed discussion of CD as *truncated MCMC inside learning* is given in Section 7.5.5, together with diagnostic plots and an implementation notebook (`RBM_Contrastive_Divergence.ipynb`) ¹.

Expectation Maximization (EM) perspective. Because the hidden variables h are latent, RBM learning naturally invites comparison with the Expectation–Maximization (EM) framework. The E-step is tractable due to the bipartite structure, as expectations under $P_\theta(h \mid v)$ factorize. However, unlike classical latent-variable models such as Gaussian mixtures or HMMs, the M-step would require expectations under the *model distribution* $P_\theta(v, h)$, which are intractable.

From the present learning perspective, this observation is crucial: it explains why RBMs occupy an intermediate position between classical EM-based models and modern energy-based models. Contrastive Divergence and related sampling-based approximations can be viewed as practical substitutes for the missing exact M-step, completing the link between latent-variable learning and truncated MCMC introduced earlier.

Example 8.2.4 (RBM as a feature learner on a Bars-and-Stripes dataset). *We train a small RBM on the Bars-and-Stripes dataset, where each data point is a binary $H \times W$ image reshaped into $v \in \{0, 1\}^{HW}$. Although simple, this dataset has strong combinatorial structure: valid images consist of coherent horizontal or vertical patterns, which must be captured through local couplings in the energy function.*

Fig. 8.14 summarizes the outcome. The left panel shows representative training samples. The middle panel visualizes learned hidden features by reshaping selected columns of W into $H \times W$ images. The right panel shows samples generated from the trained RBM via block Gibbs sampling. Even in this minimal setting, one observes the characteristic RBM behavior: hidden units specialize into reusable pattern templates, and sampling recombines them into realistic configurations.

The accompanying notebook `RBM_BarsStripes_Renewed.ipynb` generates the dataset, trains the RBM using CD- k (with an option for persistent chains), and produces the figures.

¹Conceptually, CD replaces the intractable negative-phase expectation in (8.21) by a short Gibbs chain initialized at data. This produces a biased gradient, but often a useful descent direction at a fraction of the cost.

What is being learned? The Bars-and-Stripes dataset does not define a complete target probability distribution. Rather, it provides a finite set of configurations illustrating latent constraints (e.g., row or column coherence). The goal of learning is therefore not memorization of the observed (ground truth) samples, but the construction of an energy landscape whose low-energy region captures this shared combinatorial structure.

Formally, after training the RBM defines a model distribution

$$P_\theta(v) = \frac{1}{Z_\theta} \sum_h \exp(-E_\theta(v, h)), \quad (8.22)$$

from which samples are generated by block Gibbs dynamics. This model distribution should be contrasted with the empirical distribution $\hat{P}_{\text{emp}}(v) = \frac{1}{S} \sum_{s=1}^S \delta(v - v^{(s)})$, which places all its mass on the observed samples and cannot generate novel patterns.

Learning does not aim to reproduce \hat{P}_{emp} . Instead, Contrastive Divergence reshapes the energy so that configurations consistent with the latent constraints lie in extended low-energy regions. As a result, the RBM creates an **inductive bias** and assigns nonzero probability to many unseen but structurally valid configurations, which is precisely what is observed in the generated samples.

In summary, the RBM is not learning to resample the dataset; it is learning a probability law whose typical samples obey the same structural rules as the data, while supporting combinatorial generalization beyond it.

Exercise 8.2.3 (Extending RBM learning beyond the baseline notebook). Starting from `RBM_BarsStripes_Renewed.ipynb`:

1. **Warm-up (model capacity).** Vary the number of hidden units m and report when the RBM begins to (i) miss entire pattern families (underfit) versus (ii) memorize rare configurations (overfit). Support your conclusions with a small panel of learned filters and generated samples.
2. **CD- k bias-cost tradeoff.** Compare CD- k for $k \in \{1, 5, 10, 20\}$ at fixed compute budget (e.g., fixed number of Gibbs transitions total). Which regime improves sample quality most per unit cost?
3. **More challenging (persistent negative phase).** Implement Persistent CD (PCD) by maintaining a persistent set of negative-phase particles. Compare PCD to CD- k using a quantitative metric (e.g., held-out pseudo-likelihood, or a simple pattern-constraint violation rate for Bars-and-Stripes).
4. **Open-ended (connect forward).** Replace the binary dataset by a real-valued toy dataset (e.g., noisy bars with continuous intensities) and implement a Gaussian–Bernoulli visible layer. Discuss what changes in the conditional sampling step and why this anticipates modern continuous-data generative models.

Generalization via Latent Energy Landscapes

The Bars-and-Stripes example highlights a central mechanism behind generalization in energy-based generative models. The RBM does not attempt to reproduce the empirical distribution supported on the training samples. Instead, through its hidden layer, it learns an *energy landscape* whose low-energy regions correspond to a family of configurations satisfying shared structural constraints.

From this perspective, generalization arises because learning identifies *extended low-energy sets* rather than isolated probability spikes. Latent variables introduce degrees of freedom that allow the model distribution to interpolate, recombine, and extrapolate beyond the observed data. Generated samples need not coincide with training examples, yet remain plausible because they lie within the same low-energy manifold. This viewpoint suggests a broader interpretation of neural generative models: hidden layers do not merely parametrize densities, but implicitly define constraint-satisfying regions of configuration space. Sampling then explores these regions stochastically, producing novel yet structured outcomes.

At the same time, this raises a natural question that will be central in the next chapter. In modern diffusion and score-based models, one often speaks of sampling from a *target data distribution*, seemingly without an explicit energy function. Where, then, is the analogue of the learned energy landscape? Is it replaced by a learned score field, a time-dependent family of effective energies, or something else entirely?

We return to this question in Chapter 9, where diffusion models will be shown to recover an energy-based interpretation in a dynamic and implicit form.

8.2.4 From Graphical Models to Graph Neural Networks

In Section 8.1.2 we developed inference in Graphical Models (GMs) using explicit probabilistic structure: energies, factor graphs, and analytically derived message-passing algorithms such as mean-field (MF) and belief propagation (BP). In Section 8.1.3, we took a first step beyond classical inference by showing how a *specific inference algorithm* – BP for LDPC codes – can be unfolded, parameterized, and improved through learning.

The goal of the present subsection is conceptually different. Here, we move from *learning parameters within a known inference scheme* to *learning the inference procedure itself*. Graph Neural Networks (GNNs) represent this shift: rather than implementing a prescribed probabilistic update rule, they learn task-dependent message-passing dynamics directly from data. This transition marks the emergence of *amortized inference* on graphs.

Graph Structure as Prior Knowledge. In many scientific and engineering problems, data are not i.i.d. but organized by relational, spatial, or physical constraints. Graphs encode this structure explicitly: nodes represent degrees of freedom, while edges encode interaction, conditional dependence, or information flow. Graphical models exploit this structure probabilistically via energies or conditional distributions; GNNs exploit it algorithmically by constraining how information propagates during learning.

This distinction is subtle but crucial. In GMs, the graph determines *what inference should*

compute. In GNNs, the graph determines *where information is allowed to flow*, while the computation itself is learned.

Message Passing: From Inference Rules to Learned Updates. Let $G = (V, E)$ be an undirected graph with $|V| = n$. In a pairwise GM, inference proceeds by iteratively exchanging analytically defined messages along edges, as in MF or BP. In contrast, a GNN layer implements a learned message-passing operation of the form

$$h_i^{(t+1)} = \sigma \left(W_0 h_i^{(t)} + \sum_{j \in \mathcal{N}(i)} W_1 h_j^{(t)} \right), \quad (8.23)$$

where $h_i^{(t)} \in \mathbb{R}^d$ is a latent embedding of node i at layer t .

Eq. (8.23) closely resembles the update structure of MF (Eq. 8.6) and BP (Eq. 8.8), but the interpretation is different. MF and BP propagate *probabilistic beliefs* whose semantics are fixed by the model. GNNs propagate *learned embeddings* whose semantics are determined implicitly by the training objective. Thus, while Section 8.1.3 learned parameters inside a fixed inference rule, GNNs learn the rule itself.

Ising-Inspired Viewpoint. Consider a binary labeling problem on a graph, with node labels $y_i \in \{-1, +1\}$ governed by the Ising energy

$$E(\mathbf{y}) = - \sum_{(i,j) \in E} J_{ij} y_i y_j - \sum_i h_i y_i. \quad (8.24)$$

Mean-field inference replaces the discrete variables y_i by continuous local magnetizations and iteratively minimizes a variational free energy derived from (8.24), yielding an explicit update rule with a probabilistic interpretation.

In a GNN-based approach, inference is instead realized as a learned dynamical system. Node embeddings $h_i^{(t)}$ evolve according to a parameterized message-passing rule, for example

$$h_i^{(t+1)} = \sigma \left(W_1 h_i^{(t)} + \sum_{j \in \mathcal{N}(i)} J_{ij} W_2 h_j^{(t)} + b_i \right), \quad (8.25)$$

which is structurally reminiscent of a single mean-field iteration, but no longer tied to probabilistic consistency. Stacking layers corresponds to unrolling this learned inference dynamics for a fixed number of steps T .

Objective Conditioned on the Inference Dynamics. Training the GNN amounts to optimizing the parameters $\theta = \{W_1, W_2, b, \dots\}$ so that the final embeddings $h^{(T)}$ produced by (8.25) agree with the observed labels. Concretely, one minimizes a task-driven objective of the form

$$\mathcal{L}(\theta) = \sum_{i \in V_{\text{obs}}} \ell(h_i^{(T)}, y_i) + \lambda \sum_{(i,j) \in E} \|h_i^{(T)} - h_j^{(T)}\|^2, \quad (8.26)$$

where $\ell(\cdot, \cdot)$ is a supervised loss applied directly to the final node embeddings.

Crucially, the minimization of (8.26) is *conditioned on* the inference dynamics (8.25). Unlike classical inference, the update rule is not obtained by minimizing the energy explicitly; instead, the parameters of the dynamics are learned end-to-end so that the resulting fixed-depth evolution produces embeddings that minimize the task objective.

The crucial distinction from Section 8.1.3 is that neither the update equation (8.25) nor its objective is derived from probabilistic consistency or likelihood maximization. Both are learned end-to-end from data, driven solely by task performance.

Example 8.2.5 (Learned vs. Analytical Inference on an Ising Grid). We consider a single sample from a binary Ising model defined on an $n \times n$ grid graph with interaction strength $\beta > 0$ and no external field. A random subset of node labels is revealed and held fixed.

We compare three inference strategies on the same instance:

1. **Mean-Field (MF):** Iterative variational inference with clamped observed nodes.
2. **Belief Propagation (BP):** Max-product message passing to approximate a MAP configuration.
3. **Graph Neural Network (GNN):** A message-passing neural network trained on the observed nodes of this single instance.

Fig. 8.15 visualizes the inferred configurations. The accompanying notebook `gnn_vs_gm_grid.ipynb` reproduces this figure and allows systematic variation of grid size, interaction strength, and label sparsity.

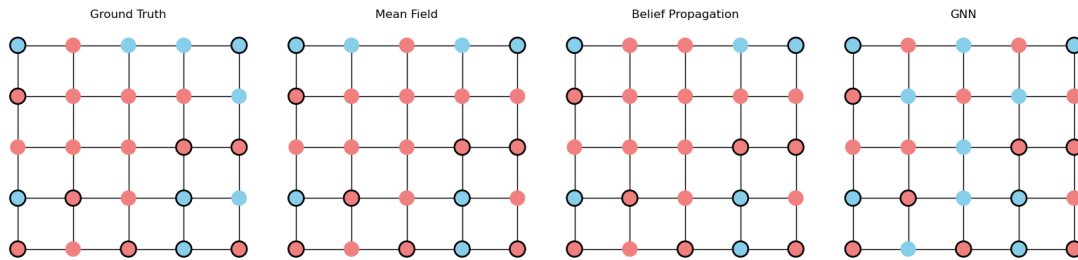


Figure 8.15: **Inference on a Single Ising Sample from a 5×5 Grid.** The ground truth configuration is generated using Gibbs sampling from the Ising model with interaction parameter β and no external field. Mean-field (MF), belief propagation (BP), and a graph neural network (GNN) are applied to infer hidden labels from partial observations.

Exercise 8.2.4 (Scaling, Noise, and Learned Message Passing). Starting from the notebook `gnn_vs_gm_grid.ipynb`:

1. Increase the grid size and study how MF, BP, and GNN accuracy scale with system size.
2. Add noise to the observed labels and compare robustness across methods.

3. Replace uniform couplings by random Gaussian edge weights and retrain the GNN.
4. Analyze whether the learned GNN dynamics more closely resemble MF or BP as interaction strength varies.

From Explicit Inference to Amortized Solvers

Graphical-model inference computes beliefs or samples for a *single instance* of a specified probabilistic model, typically by iterative optimization or message passing. In contrast, a trained GNN represents an *amortized solver*: its parameters θ encode a reusable inference procedure that can be applied across many instances, without re-solving a variational or optimization problem from scratch.

Seen through this lens, the development across this chapter (Sections 8.1 and 8.2) traces a progressive shift in how inference is represented and executed: Exact inference → Variational inference → Neuralized inference → Amortized, learned inference.

This viewpoint extends naturally to generative modeling on graphs and beyond. GNNs can be interpreted as discrete-time, graph-based learned dynamics, providing a conceptual bridge to the continuous-time generative models introduced in Chapter 9. From this perspective, diffusion models emerge as the infinite-dimensional, continuous, and stochastic analogues of amortized inference on structured spaces, unifying inference, learning, and generation within a single dynamical framework.

Recommended Additional Readings. Foundational connections between graphical models, energy minimization, and Graph Neural Networks are articulated in the Graph Convolutional Network of Kipf and Welling [55], which explicitly links message passing to Laplacian-based regularization. Physics-informed neural operators, such as the Fourier Neural Operator [56], extend these ideas to PDE-governed systems and continuous domains. Input Convex Neural Networks [57] provide a complementary energy-based perspective by enforcing convexity of learned objectives, enabling efficient and stable optimization.

Chapter 9

Synthesis

From Discrete Inference to Continuous-Time Generative Dynamics

Chapter 8 revealed a recurring theme: inference is most naturally viewed as an *iterative dynamical process*. Across graphical models, variational methods, neuralized message passing, and graph neural networks, inference appeared as a sequence of updates that progressively transform local information into global structure.

Chapter 9 builds directly on this observation. Here, we elevate inference from a discrete iteration to a *continuous-time stochastic dynamics*, and show how modern generative models can be understood as learned flows on high-dimensional spaces. This shift prepares the ground for unifying inference, learning, and generation within a single variational-dynamical framework.

Over the past decade, generative modeling has undergone a sequence of transformative developments. Early frameworks such as Variational Autoencoders (VAEs) and Generative Adversarial Networks (GANs) introduced powerful latent-variable and implicit-generation paradigms. More recently, Diffusion Models (DMs) – and in particular Score-Based Diffusions (SBDs) – have emerged as the state of the art, offering remarkable sample quality, stability, and scalability.

Beyond their empirical success, diffusion models have brought with them a conceptual shift. A growing body of work has shown that many pre-diffusion generative models can be reinterpreted as special or limiting cases within a broader diffusion-based framework. This observation motivates the structure of the present chapter.

Score-Based Diffusions as a Starting Point. We begin in Section 9.1 with Score-Based Diffusion Models. In this framework, generation is formulated through two coupled stochastic processes: a forward-time process that incrementally corrupts ground-truth samples by adding noise, and a reverse-time process that removes noise to generate new data. The central learned object is the *score function*—the gradient of the log-density – which parameterizes the drift of the reverse-time stochastic differential equation and is typically approximated by a neural network.

Bridge Diffusions and Conditioned Dynamics. Section 9.1.1 introduces a complementary but closely related class of models: Bridge Diffusions. Rooted in optimal transport and Schrödinger bridge theory, these models also employ a forward diffusive corruption process. However, their reverse dynamics are fundamentally different: they are *conditioned* processes that connect prescribed endpoint distributions. The resulting stochastic bridges transport samples from a simple prior (often Gaussian) to a complex data distribution, again through a learned drift represented by a neural network.

Unifying Generative Models through Diffusion. By introducing score-based and bridge diffusion models early in the chapter, we set the stage for a unified perspective on generative modeling. In Section 9.2, we return to earlier approaches—including VAEs and GANs—and reinterpret them through the lens of diffusion, revealing them as special cases or limiting regimes of a more general, geometrically grounded framework. This synthesis clarifies theoretical connections between models and highlights opportunities for hybrid generative constructions.

Beyond Equilibrium: Dynamics, Decisions, and Control. Section 9.3 probes *non-equilibrium learning dynamics* through the lens of statistical-physics phase transitions. After revisiting the U-turn diffusion model of [58], which captures memorization–forgetting trade-offs, we show how high-dimensional generative diffusions can undergo sharp transitions in sample quality and mode coverage, and we outline open mathematical questions connecting these phenomena to spin-glass theory.

Section 9.4 provides a concise primer on Markov Decision Processes (MDPs) as the calculus of sequential decision making. We review value–policy duality, Bellman operators, and entropy-regularized reinforcement learning, and discuss how physics-inspired viewpoints—such as control-as-inference—enrich classical Reinforcement Learning (RL) and already underpin large-scale fine-tuning in modern Gen-AI systems.

Diffusion as Control and Transport. In Section 9.5, we explicitly merge the diffusion and decision making viewpoints. Starting from Stochastic Optimal Control and Path-Integral Diffusion (PID), and following [59], we identify a sequence of increasingly integrable regimes in which score-based diffusion admits a control interpretation—or, conversely, where reinforcement learning can be viewed as a diffusion process. This synthesis yields new algorithmic perspectives that inherit the strengths of both paradigms.

Section 9.6 reframes Generative Flow Networks (GFNs) [60] as samplers over *decision trajectories* rather than over raw data. We introduce Decision Flow [61] as an integrable, diffusion-like extension of GFNs, and argue that the choice of time—artificial versus physical—is itself a modeling decision that affects diversity, credit assignment, and computational cost.

Outlook and Path Forward. The chapter concludes in Section 9.7 with a forward-looking synthesis of ongoing directions—space–time and PID diffusions, decision flows, and controlled generative dynamics—and a “grand unification” outlook. Here, diffusion models, auto-regressive architectures, and reinforcement learning are positioned as limiting cases of

a single mathematical framework, opening new avenues for controllable generation, adaptive scientific simulation, and principled exploration in high-dimensional spaces.

9.1 Score-Based Diffusion Models

From Iterative Inference to Stochastic Flows

Chapter 8 repeatedly framed inference as an iterative dynamical process: message passing in graphical models, variational updates, neural decoding, and amortized GNN inference. Score-based diffusion models represent the continuous-time limit of this idea, where inference and generation are realized as stochastic flows on data space.

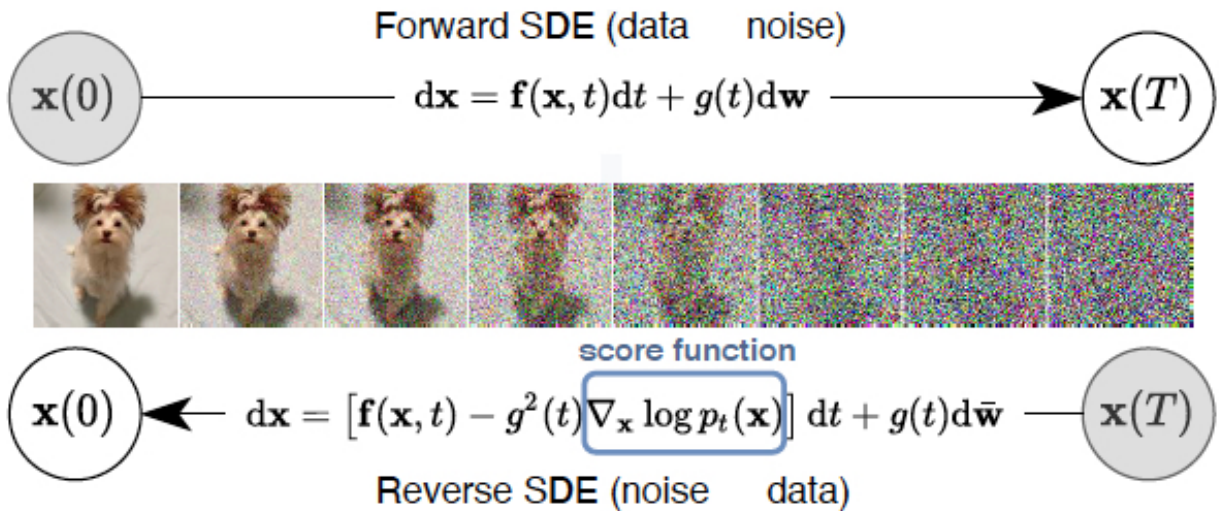


Figure 9.1: **Score-Based Diffusion Modeling** (adapted from [62]). A forward-time diffusion progressively corrupts data with noise. A neural network learns the score (log-density gradient) at each noise level. The reverse-time dynamics use this learned score to iteratively denoise and generate new samples.

Generative modeling can be viewed as the final stage of the classical AI cycle: acquiring ground-truth data, constructing a model, and *generating* new samples. In modern generative AI, this last stage is central, and *score-based diffusion* (SBD) models have emerged as a particularly powerful and flexible framework.

The key innovation of SBD models is the introduction of an auxiliary time variable and the explicit use of stochastic differential equations (SDEs). Generation is formulated as the time-reversal of a stochastic noising process. What distinguishes SBDs from earlier generative approaches is the role of the *score function* – the gradient of the log-density – which directly governs the reverse-time dynamics.

Historically, SBDs unify two complementary strands: denoising diffusion probabilistic models (DDPMs) [63, 64] and score matching with Langevin dynamics [62]. Their synthesis is most

naturally expressed in continuous time, enabling a clean theoretical formulation via reverse-time SDEs.

Forward and Reverse SDEs

Following [65], consider time-indexed random vectors $x_t, y_t \in \mathbb{R}^d$ governed by the forward and reverse SDEs

$$\textbf{Forward: } dx_t = f(x_t, t) dt + g(x_t, t) dw_t, \quad t \in [0, T], \quad (9.1)$$

$$\textbf{Reverse: } dy_t = \left(f(y_t, t) - \nabla \cdot G(y_t, t) - G(y_t, t) s(y_t, t) \right) dt + g(y_t, t) d\bar{w}_t, \quad (9.2)$$

where $G = gg^\top$ and $s(x_t, t) = \nabla_{x_t} \log p(x_t, t)$ is the score of the forward marginal distribution. The forward process maps the data distribution p_{data} to a simple reference distribution p_T (typically Gaussian) by progressively adding noise. Crucially, the forward dynamics are usually chosen independently of the data. The reverse process reconstructs samples by following a drift field determined by the score.

Theoretical Foundation: Fokker–Planck and Anderson’s Theorem

Applying the Fokker–Planck formalism (Chapter 7) to Eqs. (9.1)–(9.2) yields forward and backward PDEs for the same marginal density $p(x, t)$. Concretely, the forward and reverse processes induce the following Fokker–Planck equations for the common marginal density $p(x, t)$:

$$\partial_t p = -\nabla_i(f_i p) + \frac{1}{2}\nabla_i \nabla_j(G_{ij} p), \quad (9.3)$$

$$\partial_t p = -\nabla_i \left[(f_i - \nabla_j G_{ij} - G_{ij} s_j) p \right] - \frac{1}{2}\nabla_i \nabla_j(G_{ij} p), \quad (9.4)$$

where repeated indices are summed. Requiring that the two equations describe the *same* time-marginal $p(x, t)$ for all $t \in [0, T]$ uniquely fixes the reverse drift in Eq. (9.2). This observation, due to Anderson [66], provides the theoretical principle underlying score-based diffusion: the reverse dynamics are not postulated, but *derived* from marginal consistency.

Finite-Time Effects. Exact equivalence of marginals holds in the limit $T \rightarrow \infty$. In practice, finite-time effects are important; their role is explored later in Section 9.3.1 via the U-turn diffusion model [58].

Deterministic Alternative and Freedom in Reverse Dynamics. Marginal consistency does not require stochastic reversibility. This observation leads to deterministic probability-flow ODEs [65], which reproduce the same marginals while violating detailed balance at the path level.

More generally, the requirement of marginal consistency leaves considerable freedom in the choice of reverse-time dynamics. The stochastic reverse SDE in Eq. (9.2) corresponds to a particular realization in which the reverse diffusion strength matches that of the forward

process. In this special case, one may interpret the construction as a *non-autonomous, non-equilibrium extension of detailed balance*, generalizing the steady-state notion of detailed balance introduced in Chapter 7.

However, matching path measures is not required for correct generation. Deterministic alternatives, such as the probability-flow ODE [65], eliminate stochasticity altogether while preserving the same time-marginal densities. In these more general settings, forward and reverse processes share the same marginals but differ in their transition statistics: cross-time correlations are no longer related, and detailed balance does not hold even in a dynamical sense. Score-based diffusion thus highlights a key conceptual point: *it is marginal consistency, not microscopic reversibility, that underlies correct generation*.

Brownian Diffusion and Beyond

A particularly transparent instantiation sets

$$f(x_t, t) = 0, \quad g(x_t, t) = \sqrt{2\beta_t} I. \quad (9.5)$$

In this case the score admits a closed-form expression in terms of the empirical dataset, bypassing explicit simulation of the forward process and simplifying both analysis and training. While Brownian diffusion provides the simplest analytically tractable choice, many other *integrable* linear forward processes have been explored in the literature. Prominent examples include Ornstein–Uhlenbeck diffusions, as well as variance-preserving and variance-exploding stochastic differential equations, which underlie widely used models such as Denoising Diffusion Probabilistic Models (DDPM) [64], the Variance-Preserving SDE (VPSDE) [65], and the Variance-Exploding SDE (VESDE) [62].

More recent constructions go beyond isotropic noise injection while preserving analytical tractability. By maintaining linearity of the forward dynamics, these models retain closed-form transition kernels yet encode richer inductive biases through structured drift or anisotropic diffusion thus aligning the noising process with the geometry of the data manifold and empirically yielding sharper and more faithful generations without sacrificing analytical tractability. Examples enriching the forward (and induced reverse) dynamics while retaining a controlled structure include: Schrödinger-bridge diffusions that preserve tractable transition kernels while imposing endpoint constraints [67], critically damped (second-order) Langevin diffusions that improve stability of the resulting reverse-time flows [68], diffusion processes adapted to non-Euclidean geometry via Riemannian structure [69], symmetry-preserving (equivariant) diffusions that hard-wire group invariances into the stochastic flow [70] and space–time diffusions with Laplacian or graph-based drift terms [71].

From this perspective, the choice of forward diffusion is no longer innocent: it determines the geometry of path space and shapes the class of admissible reverse-time controls, a theme that will be formalized in Sections 9.5 and 9.6.

Training via Denoising Score Matching

The score network s_θ is trained minimizing the denoising score-matching objective

$$\mathcal{L}_{\text{DSM}}(\theta) = \mathbb{E} \left[\frac{\lambda(t)}{2} \|\nabla_{x_t} \log p(x_t | x_0) - s_\theta(x_t, t)\|^2 \right],$$

which encourages accurate estimation of the conditional score across noise levels. While denoising score matching is the most common training objective, alternative formulations have been explored. These include sliced score matching, score matching with annealed noise levels, likelihood-based objectives derived from the probability-flow ODE, and hybrid losses combining reconstruction and score terms [62, 65, 72]. These variants trade statistical efficiency, stability, and computational cost, while preserving the same underlying reverse-time dynamics.

Inference and Sampling

Generation proceeds by simulating the reverse SDE (9.2) from $t = T$ to $t = 0$, initialized with a sample from the reference distribution p_T . In practice, this reverse-time evolution is implemented using a time discretization scheme, most commonly the Euler–Maruyama method, as introduced earlier in Chapter 7. The learned score field provides the drift that steers trajectories toward high-density regions of the data distribution while stochastic noise ensures adequate exploration.

Beyond Euler–Maruyama, a variety of numerical schemes have been investigated to improve stability and efficiency. These include higher-order stochastic solvers, predictor–corrector methods, and deterministic ODE solvers applied to the probability-flow formulation [65]. In particular, adaptive step-size integrators for ordinary differential equations can significantly reduce computational cost during sampling, especially at low noise levels where the dynamics become stiff [73, 74].

In practice, generation is approximate in several respects: the reverse process is initialized at a finite T rather than $T = \infty$, the SDE is discretized in time, and only a finite number of samples is used to estimate expectations. Nevertheless, the framework admits a clear hierarchy of limits: as $T \rightarrow \infty$, the time discretization step vanishes, and the number of samples grows, *score-based diffusion recovers the exact target distribution*.

Key Takeaway: Score-based diffusion replaces explicit likelihoods by learned drift fields. Generation succeeds not because forward and reverse paths coincide, but because their time-marginal distributions do.

Example 9.1.1 (Score-Based Diffusion on a 3×3 Grid Graph). We illustrate the above construction on a synthetic 3×3 grid dataset. The companion notebook `02-SGM-with-SDE-9grid.ipynb`, also producing Figs. (9.2, 9.3) implements the forward SDE, trains a score network, and simulates the reverse-time dynamics.

Three diagnostic visualizations are emphasized: (i) comparison of ground-truth and generated samples (left panel of Fig. (9.2)), (ii) representative reverse time trajectories (right panel of Fig. (9.2)) and (iii) evolution of trajectories and score fields over time (Fig. (9.3)). These figures provide intuition for how learned score fields guide generation.

Specifically, the figures show how initially unstructured noise is progressively shaped by the learned score field into coherent samples, how individual trajectories concentrate near high-density regions, and how the score field sharpens and aligns with the data geometry as the noise level decreases.

Exercise 9.1.1 (Reverse Noise and Stability). Starting from the notebook `02-SGM-with-SDE-9grid.ipynb`:

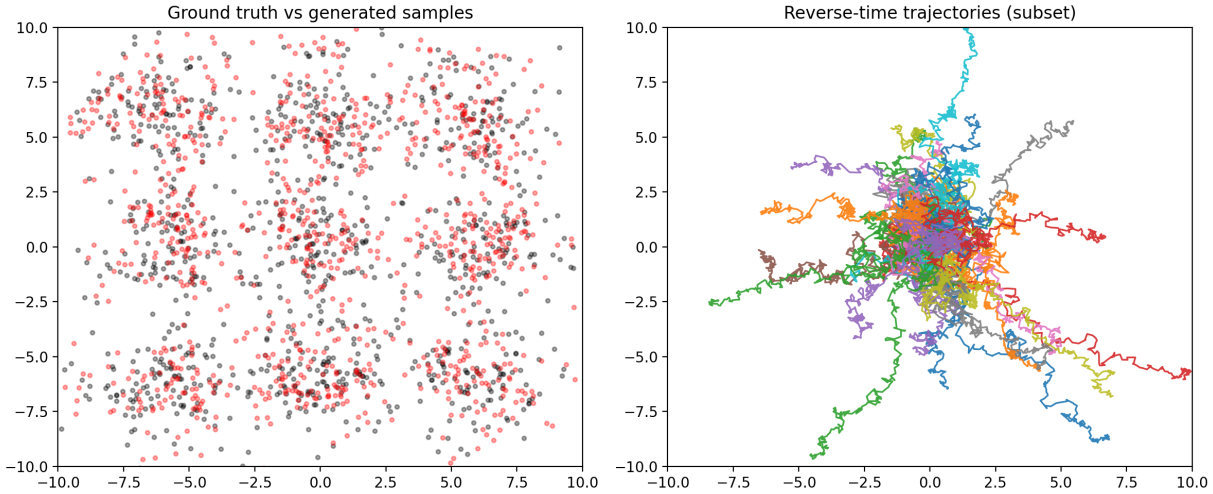


Figure 9.2: Score-Based Diffusion on a 3×3 grid: samples and trajectories. *Left:* ground-truth (GT) samples from the target distribution (black) overlaid with samples generated by the learned reverse-time diffusion (red). *Right:* several representative reverse-time trajectories, initialized from the reference distribution at $t = T$ and evolved toward $t = 0$ using the learned score field. The figure illustrates the basic mechanism of score-based generation: a learned drift guides noisy initial conditions toward high-density regions of the data distribution.

1. **Reverse noise sensitivity.** Vary the diffusion strength in the reverse process while keeping the forward process fixed. Quantify sample quality and stability using visual diagnostics and simple divergence measures.
2. **Discretization effects.** Study how the number of reverse-time steps affects convergence and trajectory smoothness. Identify regimes where numerical instability appears.
3. **Deterministic vs. stochastic reversal.** Implement the probability-flow ODE and compare its samples and trajectories to those obtained from the stochastic reverse SDE.
4. **Theoretical analysis (advanced).** Using the Fokker–Planck equations, explain why marginal distributions remain correct under these modifications, even though pathwise statistics differ.

Bridge to Control and Transport

Score-based diffusion constructs generative dynamics by learning the drift of a stochastic process. In the following sections, we reinterpret this drift as a control field and connect diffusion models to stochastic optimal control and transport.

9.1.1 Bridge Diffusion

Standard score-based diffusion models rely on the asymptotic limit $T \rightarrow \infty$, in which the forward noising process loses memory of its initial condition and converges to a simple

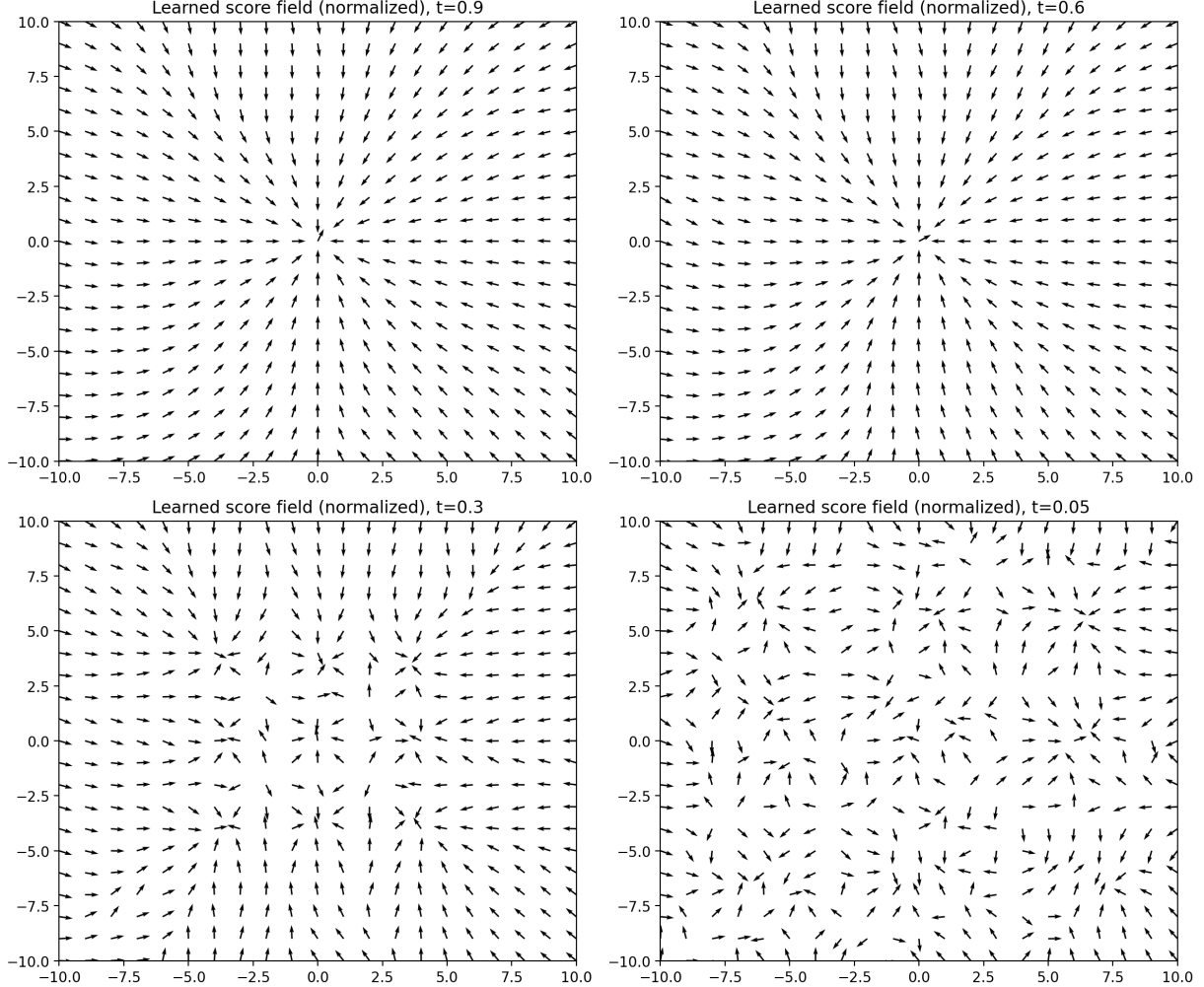


Figure 9.3: Time evolution of the learned score field. The panels visualize snapshots of the learned score vector field $s_\theta(x, t) \approx \nabla_x \log p(x, t)$ at several noise levels (times) along the diffusion. At larger t (higher noise), the score field is smoother and less structured; as $t \rightarrow 0$ the field sharpens and aligns with the geometry of the target distribution, providing a drift that concentrates probability mass near the data manifold.

reference distribution. In practice, however, generation is carried out at finite time horizons, and the terminal distribution $p(x(T))$ only approximately forgets its pre-history.

This raises a natural question: *Can one enforce an exact, prescribed terminal distribution at a finite diffusion horizon?* Bridge diffusions provide a principled affirmative answer. Rather than relying on asymptotic mixing, they modify the dynamics so that the stochastic process is explicitly conditioned on its endpoint.

Schrödinger Bridges

Consider a general stochastic differential equation

$$dx(t) = f(t, x(t)) dt + \sqrt{G(t, x(t))} dw_t, \quad (9.6)$$

with associated forward and backward Fokker–Planck operators

$$\left(\partial_t - \hat{\mathcal{L}}_t^* \right) p(x(t) | x(0)) = 0, \quad \hat{\mathcal{L}}_t^* = -\nabla \cdot f + \frac{1}{2} \nabla_i \nabla_j G_{ij}, \quad (9.7)$$

$$\left(\partial_t + \hat{\mathcal{L}}_t \right) p(x(1) | x(t)) = 0, \quad \hat{\mathcal{L}}_t = f \cdot \nabla + \frac{1}{2} G_{ij} \partial_i \partial_j. \quad (9.8)$$

A *Schrödinger bridge* modifies this dynamics by conditioning the process to reach a prescribed terminal state or distribution at $t = 1$. The conditioned process can be constructed via a Doob h -transform, leading to the *bridge SDE*

$$dx(t) = \left(f(t, x) + G(t, x) \nabla_x \log p(x(1) | x(t)) \right) dt + \sqrt{G} dw_t. \quad (9.9)$$

The additional drift term acts as a *time-dependent guidance field* that steers trajectories toward the desired endpoint while preserving stochastic exploration. Unlike score-based diffusion, where guidance emerges implicitly through time reversal and long-time mixing, bridge diffusion enforces endpoint constraints explicitly and at finite horizon.

Historical and Conceptual Context

Doob h -Transform. The modification of the drift in Eq. (9.9) is an instance of the classical Doob h -transform [75] (see also [76] - an excellent pedagogical reference), a general construction that conditions a Markov process on a future event. Let $\hat{\mathcal{L}}_t$ denote the generator of the original diffusion, and let $h(x, t)$ be a positive space–time harmonic function satisfying

$$(\partial_t + \hat{\mathcal{L}}_t) h(x, t) = 0.$$

The Doob-transformed generator is

$$\hat{\mathcal{L}}_t^{(h)} \phi = \frac{1}{h} \hat{\mathcal{L}}_t(h\phi),$$

which induces an additional drift proportional to $\nabla_x \log h(x, t)$. Choosing $h(x, t) = p(x(1) | x(t))$ recovers exactly the bridge drift in Eq. (9.9). Thus, bridge diffusion arises from a systematic conditioning principle, not an ad hoc modification.

Schrödinger’s Question. The term *Schrödinger bridge* traces back to a pair of seminal papers by Erwin Schrödinger (1931–1932) [77, 78], written shortly after his foundational contributions to quantum mechanics. Schrödinger asked a classical probabilistic question: given two probability distributions observed at different times, what is the *most likely stochastic evolution* of a large ensemble of particles consistent with these observations?

His answer was to condition a reference diffusion – he was working primarily with Brownian motion – on both its initial and terminal distributions. The resulting process interpolates between the two marginals while minimally perturbing the underlying dynamics in relative entropy. In modern terms, Schrödinger bridges solve an entropy-regularized transport problem.

Connection to Optimal Transport. This perspective reveals a deep connection to optimal transport [79, 80]. Classical Wasserstein transport (see Section 6.2.5) seeks deterministic maps that move one distribution to another at minimal cost. Schrödinger bridges introduce entropic regularization, admitting stochastic transport paths. As the noise level vanishes, Schrödinger bridges converge to Wasserstein geodesics; at finite noise, they interpolate between diffusion and transport. Thus, bridge diffusion can be viewed as a *regularized transport of probability density over time*, a theme that will reappear later in this chapter in the context of stochastic optimal control and path-integral transport.

Take-Home Message: Why Bridge Diffusion?

Score-based diffusion relies on asymptotic mixing to generate samples from a target distribution. Bridge diffusion replaces this asymptotic viewpoint with explicit endpoint conditioning, allowing distributional constraints to be enforced exactly at finite time. The resulting dynamics remain stochastic, yet are guided by time-dependent fields that coordinate trajectories toward a global objective. Schrödinger bridges thus form a natural interface between diffusion, optimal transport, and control—a perspective developed further in the chapter that follow.

Bridge Score. In practice, the conditional density $p(x(1) | x(t))$ is not available analytically. Analogously to score-based diffusion, one introduces the *bridge score*

$$\nabla_x \log p(x(1) | x(t)),$$

which can be approximated from data or represented by neural networks. This enables bridge-modified diffusions that exactly match prescribed terminal distributions even at finite horizon [67, 71].

Example 9.1.2 (Schrödinger Bridge on a One-Dimensional Gaussian Mixture). We illustrate bridge diffusion in a minimal one-dimensional setting. The forward dynamics are Brownian motion starting from a bimodal initial distribution, while the terminal distribution is prescribed to be a single Gaussian at $t = 1$.

The companion notebook `03-SchrBridge-1D.ipynb` contrasts two processes on the same finite horizon: (i) unconstrained diffusion, in which trajectories spread freely under noise, and (ii) bridge diffusion, in which an additional drift progressively steers trajectories to satisfy the terminal constraint.

Fig. 9.4 visualizes this contrast. Although both processes originate from identical initial conditions, only the bridge diffusion exhibits coordinated behavior at the terminal time.

Fig. 9.5 visualizes the time-dependent bridge drift field, making the Doob conditioning mechanism explicit. For the Brownian reference process considered here, the bridge drift is affine in the state variable, resulting in families of straight, parallel lines at each fixed time. The narrow spread of the drift field at early times reflects weak sensitivity to the terminal constraint when $T - t$ is large, while the progressive widening of the band as $t \rightarrow T$ indicates the increasing influence of the endpoint condition. Concurrently, the clockwise rotation (steepening) of the lines encodes the divergence of the feedback gain $1/(T - t)$, revealing how the

bridge dynamics apply increasingly strong corrections to ensure arrival at the prescribed terminal distribution. This simple structure is a hallmark of Gaussian bridges; in more general settings, the linear bands deform into nonlinear, state-dependent guidance fields.

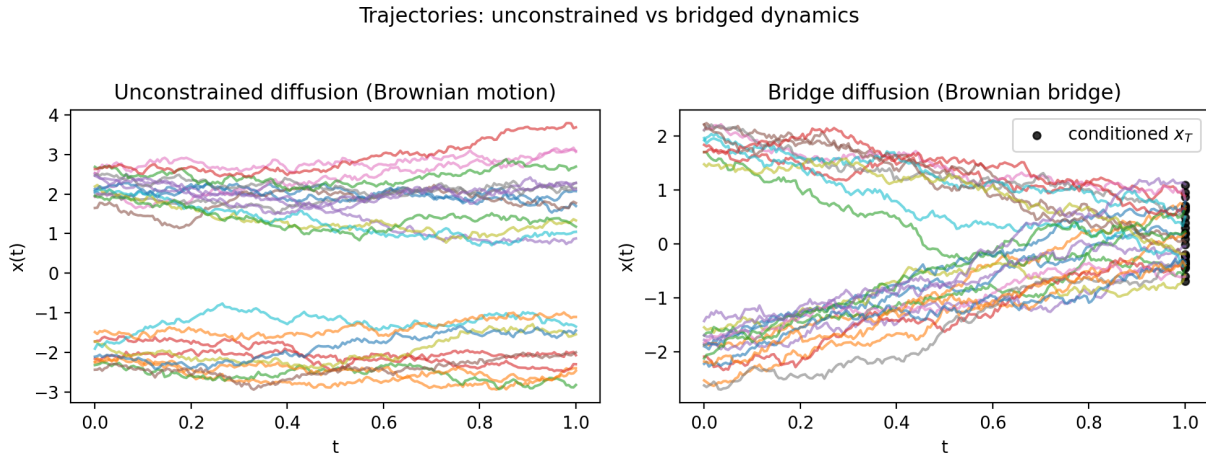


Figure 9.4: **Trajectories under unconstrained diffusion and Schrödinger bridge dynamics.** *Left:* unconstrained Brownian diffusion starting from a bimodal initial distribution. *Right:* Schrödinger bridge trajectories conditioned to reach a prescribed terminal distribution at $t = 1$ (black markers). The bridge drift acts as a time-dependent guidance field that steers trajectories toward the endpoint while preserving stochastic exploration.

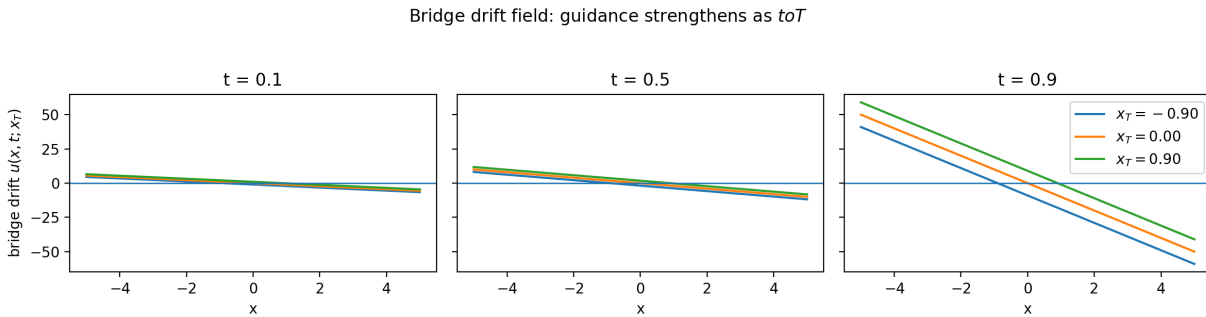


Figure 9.5: Time-dependent bridge drift field. Snapshots of the guidance field $G\nabla_x \log p(x(1) | x(t))$ at several times, illustrating how endpoint conditioning manifests as a control-like force that intensifies as $t \rightarrow 1$.

Exercise 9.1.2 (Exploring Bridge Diffusions). Starting from the notebook `03-SchrBridge-1D.ipynb`:

1. Replace the terminal Gaussian by a bimodal distribution and study how trajectories split.
2. Compare bridge diffusion with score-based diffusion for the same finite horizon T .

3. Interpret the bridge drift as a time-dependent control field and identify the corresponding running cost.
4. (Conceptual) Consider the vanishing-noise limit and explain how Schrödinger bridges relate to Wasserstein optimal transport geodesics.

9.2 A Unified View: Generative Models as Diffusions

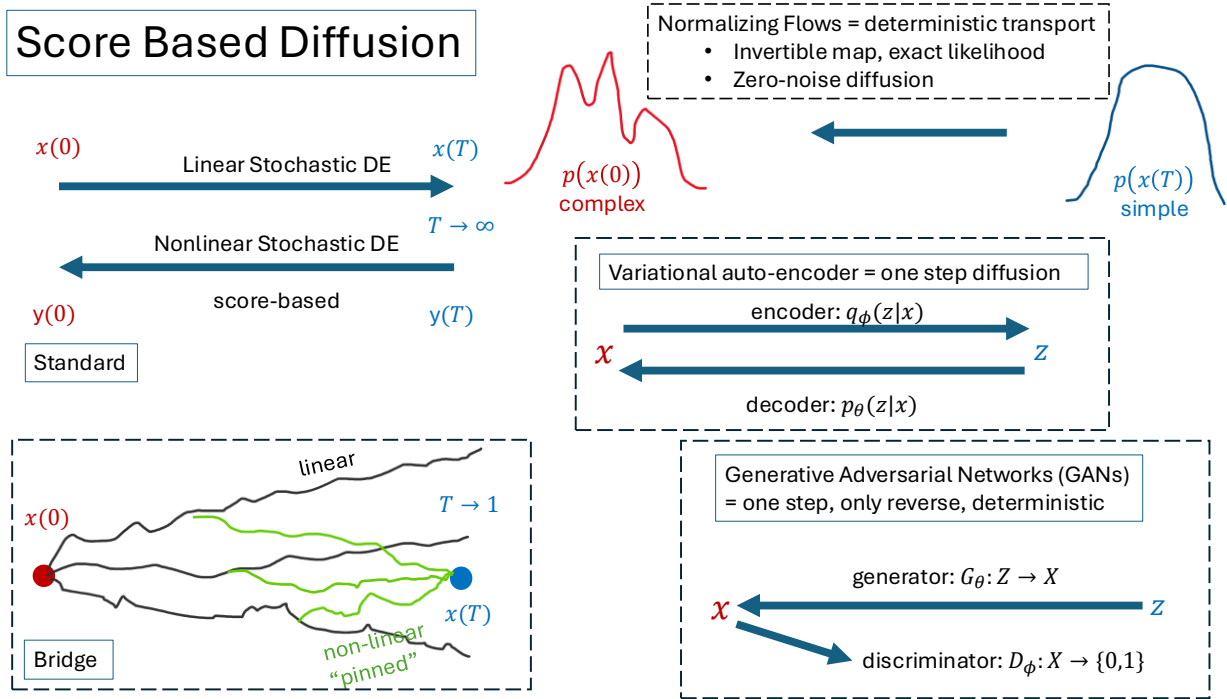


Figure 9.6: A unifying landscape of generative models viewed through the lens of diffusion and transport. Classical paradigms – GANs, normalizing flows, and VAEs – emerge as structured limits of diffusion-based models, obtained by removing noise, collapsing time horizons, or amortizing inference. Score-based and bridge diffusions occupy the most general position, allowing stochastic, time-extended, and entropy-regularized transport. See also Table 9.1.

This section develops a unifying perspective in which modern generative models are interpreted as *transport processes from a simple reference distribution to a complex data distribution*. The key message – expressed in Fig. (9.6) and Table (9.1) – is that diffusion-based models provide the most general and flexible realization of this idea, with earlier paradigms appearing as special or limiting cases.

The organizing principle is the introduction (or removal) of three structural elements: *time*, *noise*, and *entropy regularization*. Score-based diffusions and Schrödinger bridges—introduced in the previous section – combine all three, yielding stochastic, time-extended, and variationally grounded transport. By selectively simplifying this structure, one recovers classical models.

Roadmap. In the subsections that follow, we reinterpret foundational generative paradigms as special cases of diffusion:

- In Section 9.2.1, we show that **Generative Adversarial Networks** (GANs) correspond to *deterministic, single-step transport maps*, interpretable as the zero-noise, zero-time-horizon limit of diffusion and Schrödinger bridge models.
- In Section 9.2.2, we place **normalizing flows** as deterministic, invertible, multi-step transport processes. They realize continuous-time transport via ordinary differential equations and can be viewed as the noise-free counterpart of probability-flow diffusion models.
- In Section 9.2.3, we reinterpret **Variational Auto Encoders** (VAEs) as short-horizon, amortized stochastic diffusions in latent space. Hierarchical VAEs discretize diffusion paths, while deeper constructions approach continuous-time latent diffusion.

From this perspective, diffusion models subsume GANs, flows, and VAEs, combining their strengths while mitigating their limitations in mode coverage, robustness, and scalability. This viewpoint sets the stage for the subsequent sections, where diffusion is further connected to stochastic optimal control, path-integral formulations, and decision-making models.

Table 9.1: Generative models viewed as transport and diffusion processes.

Model	Noise	Time Horizon	Likelihood	Interpretation
GANs	None	Single step	No	Deterministic Transport Map
Normalizing Flows	None	Multi-step ODE	Yes	Invertible Deterministic Transport
VAEs	Yes	Short Discrete	Approx.	Amortized Stochastic Transport
Score-Based Diffusions	Yes	Long Continuous	Yes	Stochastic Diffusion with Learned Score
Schrödinger Bridges	Yes	Finite Continuous	Yes	Entropy-Regularized Stochastic Transport

9.2.1 GANs as Implicit Diffusion Models

Generative Adversarial Networks (GANs), introduced by Goodfellow et al. [81], were among the first deep generative models capable of producing high-fidelity samples in complex data domains. Historically, GANs were developed independently of diffusion models and without explicit probabilistic dynamics. Nevertheless, from the perspective developed in this chapter, GANs can be reinterpreted as a highly degenerate limit of diffusion-based generative modeling.

Classical GAN Formulation. A GAN consists of two competing neural networks:

- a *generator* $G_\theta : \mathcal{Z} \rightarrow \mathcal{X}$ that maps latent noise $z \sim \mathcal{N}(0, I)$ to the data space;
- a *discriminator* $D_\phi : \mathcal{X} \rightarrow [0, 1]$ that attempts to distinguish generated samples from real data.

Training proceeds via the min–max objective

$$\min_{\theta} \max_{\phi} \mathbb{E}_{x \sim p_{\text{data}}} [\log D_\phi(x)] + \mathbb{E}_{z \sim p(z)} [\log(1 - D_\phi(G_\theta(z)))]. \quad (9.10)$$

GANs as One-Step Deterministic Reverse Diffusions. Although GANs lack an explicit forward noising process, the generator implements a deterministic transport

$$z \sim \mathcal{N}(0, I) \longmapsto x = G_\theta(z),$$

which can be interpreted as a *single-step reverse diffusion with zero noise*. In the language of Schrödinger bridges, GANs correspond to the $\varepsilon \rightarrow 0$ limit of entropy-regularized transport, where stochastic exploration vanishes and the generative process collapses to a deterministic map.

GANs, Scores, and Optimal Transport. When trained with Integral Probability Metrics (e.g. Wasserstein or MMD), GANs implicitly align gradients of log-densities [82]. In this sense, GANs approximate score information indirectly, despite never modeling the score explicitly. From the modern viewpoint, GANs can be seen as learning a single optimal transport map between prior and data distributions – without intermediate states, time, or stochasticity.

Example 9.2.1 (GAN as Deterministic Transport (Zero–Noise Diffusion Limit)). We illustrate how a Generative Adversarial Network (GAN) implements a deterministic transport map from a simple latent distribution to a complex data distribution, corresponding to the zero–noise, one–step limit of diffusion and Schrödinger bridge models.

The companion notebook `gan_as_deterministic_transport.ipynb` produces Fig. 9.7, which visualizes three complementary aspects of this interpretation.

Left Panel of Fig. 9.7: GAN-like sample matching. The left panel overlays samples from the target distribution (a nonconvex, multi-modal distribution shown in black) with samples generated by a trained GAN generator (colored). Here “GAN-like” means that the generator is trained via an Integral Probability Metric (IPM), enforcing distributional agreement without explicit likelihoods or forward noising. While the generated samples capture the global multi-modality, they exhibit noticeably sharper, nonconvex boundaries than the target. This behavior is characteristic of deterministic transport: probability mass is pushed forward without stochastic smoothing, often leading to overly crisp or geometrically distorted support.

Middle Panel of Fig. 9.7:: Deterministic transport map. *The middle panel makes determinism explicit by visualizing the map $z \mapsto G_\theta(z)$ itself. Each latent point is mapped to exactly one output point, and trajectories appear as straight line segments. This is not an artifact: it is the intended behavior of GANs. Unlike diffusion or bridge models – where a single initial condition generates an ensemble of stochastic paths – GANs learn a single, deterministic flow line per latent input. This highlights their interpretation as a zero-noise, single-step reverse diffusion.*

Right Panel of Fig. 9.7:: Optimization signal. *The right panel shows the training curve of the objective – Maximum Mean Discrepancy. Its overall decrease (not fully monotonic, with spikes, but persistent) confirms convergence of the learned transport. Crucially, this objective enforces only endpoint consistency between generated and target distributions, not pathwise or dynamical consistency – again underscoring the contrast with diffusion-based models.*

Conceptual takeaway. *Together, the three panels show that GANs realize a deterministic, zero-noise limit of generative diffusion: they transport a prior to data in a single step, with no intermediate stochastic exploration. This explains both their strengths (sharp samples, fast generation) and their limitations (mode dropping, geometric rigidity), and situates GANs as a singular corner of the broader diffusion–transport framework developed in this chapter.*

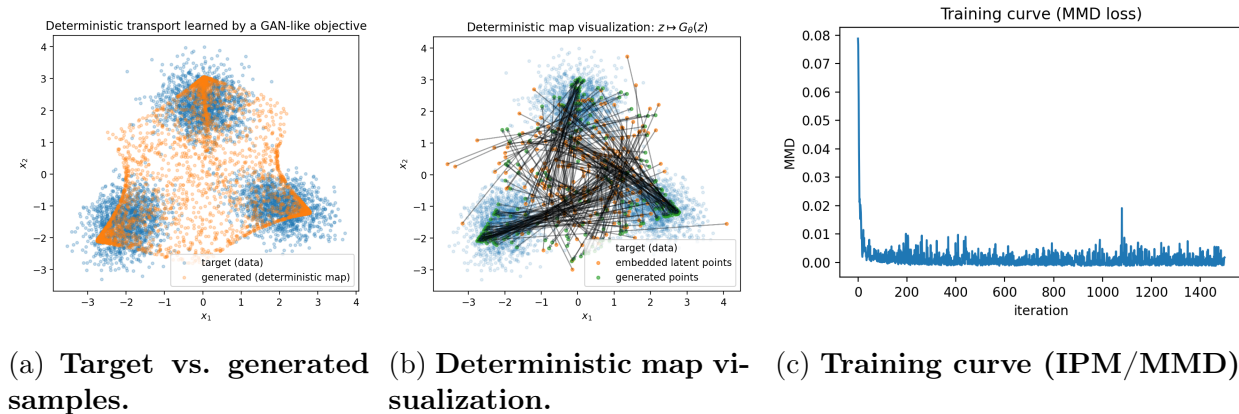


Figure 9.7: **GAN as deterministic transport (one-step, zero-noise reverse diffusion).** *Left:* *Sample matching*—the learned generator implements a one-step deterministic pushforward map that transforms a simple prior into a multi-modal target distribution (overlay of target and generated samples). *Middle:* *Determinism*—visualization of the map $z \mapsto G_\theta(z)$: each latent point maps to exactly one output, in contrast to diffusion/bridge models where stochasticity yields families of trajectories. *Right:* *Optimization signal*—the Integral Probability Metric objective – here, Maximum Mean Discrepancy with the Gaussian kernel $k(x, x') = \exp\left(-\frac{\|x-x'\|^2}{2\sigma^2}\right)$ – decreases during training, confirming convergence of the learned transport.

Exercise 9.2.1 (GANs as Zero–Noise Schrödinger Bridges). This exercise explores GANs as the deterministic, zero–noise limit of bridge diffusions, using both analysis and the companion notebook `gan_as_deterministic_transport.ipynb`.

1. **Zero–Noise Limit of Bridge Dynamics (Analytical).** Consider the Schrödinger bridge SDE

$$dx(t) = \left(f(t, x) + \varepsilon \nabla_x \log p(x(1) | x(t)) \right) dt + \sqrt{\varepsilon} dw_t.$$

Show formally that as $\varepsilon \rightarrow 0$, stochastic paths concentrate on deterministic trajectories minimizing the action functional. Explain how the resulting dynamics reduce to a deterministic transport map $x(0) \mapsto x(1)$, and relate this limit to classical optimal transport.

2. **Empirical Determinism vs. Stochasticity (Computational).** Using the notebook, compare:

- the deterministic map $z \mapsto G_\theta(z)$ learned by the GAN, and
- a stochastic Schrödinger bridge or diffusion model trained on the same target distribution.

Visualize multiple trajectories starting from the same initial point. Confirm empirically that GANs admit a single trajectory per input, while bridge/diffusion models generate ensembles.

3. **Geometry of the Generated Support.** In Fig. 9.7 (left panel), the GAN-generated samples exhibit sharper, more nonconvex boundaries than the target distribution. Explain why deterministic transport tends to preserve sharp features and may distort geometry. How does stochastic exploration in diffusion or bridge models mitigate this effect?

4. **Discriminator vs. Bridge Score (Conceptual).** In Schrödinger bridges, endpoint constraints are enforced via the bridge score $\nabla_x \log p(x(1) | x(t))$. In GANs, the discriminator provides a gradient signal enforcing $p_G \approx p_{\text{data}}$. Compare these two mechanisms:

- What quantity is being optimized or constrained in each case?
- Why does the GAN discriminator enforce the constraint only at the endpoint, not along trajectories?

5. **Beyond GANs.** Discuss how adding a small amount of noise to the GAN generator – e.g. by injecting noise at intermediate layers—would move the model away from the zero–noise limit. Would this make the model closer to a bridge diffusion or a score-based diffusion? What trade-offs would you expect in sample quality and diversity?

From GANs to Normalizing Flows: Determinism Made Explicit

GANs realize the *most singular* limit of diffusion-based generative modeling: a deterministic, one-step transport from a simple prior to data, obtained as the zero-noise limit of a Schrödinger bridge. However, this determinism comes at a price: the transport map is implicit, generally non-invertible, and does not admit a tractable likelihood. Normalizing Flows occupy the next point along this spectrum. They retain determinism and zero noise, but replace adversarial training by *explicitly invertible* maps with computable Jacobians. In this sense, flows can be viewed as *multi-step, structured deterministic diffusions*, where the reverse-time dynamics are resolved exactly rather than learned implicitly.

The following subsection formalizes this connection, positioning normalizing flows as deterministic, invertible counterparts of diffusion and bridge models—and as a critical link between GANs, VAEs, and stochastic diffusion frameworks.

9.2.2 Normalizing Flows as Deterministic Transport

Normalizing flows – which we started to discuss in Sections 5.2.3 and 5.1.6 – provide an explicit, likelihood-based framework for generative modeling grounded in *invertible deterministic transport*. They occupy a crucial conceptual position between GANs and diffusion models: like GANs, flows implement deterministic maps from noise to data; like diffusion models, they admit a precise probabilistic interpretation and exact density evaluation.

Why “Normalizing”? The term *normalizing flow* reflects the construction of complex data distributions by successively *normalizing* them into a simple reference distribution (typically a standard Gaussian) through a sequence of invertible transformations. Each transformation preserves total probability mass while reshaping the density, and the overall likelihood is computed exactly via the change-of-variables formula.

Historically, this idea traces back to early work on nonlinear independent component analysis and density estimation [83], with modern neural realizations appearing in models such as NICE [84], RealNVP [85], and Glow [86].

Classical Formulation. A normalizing flow defines a diffeomorphism

$$x = f_\theta(z), \quad z \sim \mathcal{N}(0, I),$$

so that the data density is given exactly by

$$\log p_X(x) = \log p_Z(z) - \log |\det \nabla f_\theta(z)|.$$

In practice, f_θ is constructed as a composition of simple invertible maps with tractable Jacobians, allowing exact maximum-likelihood training.

Flows as Continuous-Time Transport ODEs. In the continuous-depth limit, normalizing flows converge to neural Ordinary Differential Equations (ODEs),

$$\frac{dx_t}{dt} = v_\theta(t, x_t),$$

which deterministically transport probability mass from the prior to the data distribution. The associated log-density evolves according to a continuity equation, making flows a concrete realization of *deterministic optimal transport* in continuous time.

Relation to Diffusion Models. Normalizing flows can be understood as the *zero-noise limit* of diffusion-based generative models. In particular, the *probability flow ODE* associated with score-based diffusion produces exactly the same time marginals as the stochastic reverse-time SDE, while eliminating randomness entirely. From this perspective, diffusion models strictly generalize flows by reintroducing stochasticity, entropy regularization, and non-invertible dynamics, which often improves robustness and mode coverage in high-dimensional settings.

Position in the Generative Landscape. Normalizing flows extend GANs by replacing adversarial, implicit matching with explicit likelihood optimization and invertibility. At the same time, they remain a restricted subclass of diffusion models, corresponding to deterministic, invertible transport with zero noise. This places flows at a mathematically clean – but algorithmically constrained – corner of the diffusion zoo illustrated in Fig. 9.6.

Exercise 9.2.2 (From GAN Transport to Normalizing Flows). *This exercise builds directly on the GAN example and notebook `gan_as_deterministic_transport.ipynb`.*

1. **Invertibility vs. Implicit Transport.** Identify why the GAN generator learned in the example does not admit a tractable inverse or likelihood. Which properties of normalizing flows address these limitations?
2. **Upgrading the GAN Map.** Modify the GAN generator by replacing it with a simple invertible architecture (e.g. affine coupling layers). Train the model using maximum likelihood instead of an adversarial loss. Compare:
 - sample quality,
 - geometric distortion of the support,
 - training stability.
3. **Deterministic Paths vs. Stochastic Exploration.** Compare the learned flow trajectories with those produced by a diffusion or Schrödinger bridge model trained on the same target distribution. Which modes are better covered, and why?
4. **Conceptual.** Explain why enforcing invertibility constrains expressiveness. Discuss how diffusion models relax this constraint while retaining probabilistic consistency.

From Normalizing Flows to VAEs

Normalizing flows achieve exact likelihoods through invertible deterministic transport, but this requirement severely restricts architectural flexibility. Variational Autoencoders relax invertibility by introducing latent-variable models and amortized inference, trading exact likelihoods for scalable, probabilistic encoders and decoders.

The next subsection revisits VAEs from this unified diffusion perspective, showing how latent-variable models interpolate between deterministic flows and fully stochastic diffusion processes.

9.2.3 Variational Autoencoders as Diffusion Models

Variational Autoencoders (VAEs) [87, 52] – which we started to discuss in Section 8.1.4 – combine latent-variable graphical models with amortized inference. Unlike GANs and normalizing flows, VAEs explicitly model stochastic transitions and therefore occupy an intermediate position between deterministic transport and full diffusion models.

Classical VAE Objective. Given a latent prior $p(z) = \mathcal{N}(0, I)$, VAEs optimize the ELBO

$$\mathcal{L}(\theta, \phi; x) = \mathbb{E}_{q_\phi(z|x)}[\log p_\theta(x|z)] - D_{\text{KL}}(q_\phi(z|x)\|p(z)), \quad (9.11)$$

balancing reconstruction accuracy and regularization toward the prior.

VAEs as Short-Horizon Diffusions. A VAE defines two stochastic maps

$$x \xrightarrow{q_\phi} z, \quad z \xrightarrow{p_\theta} x,$$

which can be interpreted as a single forward and reverse diffusion step. Hierarchical VAEs extend this to multiple latent layers, effectively discretizing a diffusion process in latent space. As the number of layers increases, this construction converges toward continuous-time latent diffusion.

VAE and Modern Diffusion Models

From the diffusion perspective, VAEs differ in two key respects: (i) the encoder and decoder are trained jointly (amortized inference), and (ii) the diffusion horizon is short. Score-based models remove both constraints, learning time-dependent scores over long horizons and achieving superior coverage and sample quality.

Example 9.2.2 (Latent Diffusion via a Two-Layer VAE on a Ring). We illustrate how diffusion-like dynamics can be embedded into a latent-variable model using a simple synthetic ring dataset. The companion notebook `ring_vae_latent_diffusion_comparison.ipynb` compares two models trained on identical data: (i) a standard Variational Autoencoder (VAE) with a single latent decoding step, and (ii) an extended model in which the decoder is augmented by an additional stochastic latent stage, forming a short latent reverse diffusion.

Fig. 9.8 diagnoses a well-known limitation of classical VAEs. The left panel shows reconstructions obtained by encoding data points and decoding them back. These reconstructions faithfully preserve the ring structure, indicating that the amortized inference model has learned a good representation of the data manifold. However, the right panel reveals a mismatch at generation time: samples obtained by decoding latent variables drawn from the prior are overly concentrated, forming a thin ring with reduced variability. This illustrates a fundamental gap between reconstruction quality and generative fidelity in single-step latent-variable models.

Fig. 9.9 demonstrates how introducing a diffusion-like mechanism in latent space addresses this issue. The left panel reproduces the baseline VAE generations, while the right panel shows samples produced by the two-layer latent decoder. Here, latent variables are progressively denoised through an intermediate stochastic stage before decoding. The resulting samples exhibit increased thickness and more uniform coverage of the target ring, while maintaining competitive reconstruction accuracy. Even this minimal extension – adding a single additional latent diffusion step – substantially improves generative diversity.

Taken together, these figures make explicit how diffusion generalizes amortized inference. A standard VAE corresponds to a single-step stochastic map from latent space to data, whereas the two-layer model approximates a short reverse diffusion. This example provides a concrete, low-dimensional illustration of the broader theme of this chapter: introducing time, stochasticity, and iterative structure into generative models fundamentally enhances their expressive power.

Exercise 9.2.3 (Exploring Latent Diffusion Depth and Generative Tradeoffs). This exercise builds directly on the example and the companion notebook `ring_vae_latent_diffusion_comparison.ipynb`. Your goal is to systematically investigate how introducing diffusion-like structure in latent space affects representation, generation, and stability.

1. **Latent Geometry and Amortized Inference.** Using the trained baseline VAE, visualize the encoder means $\mu_\phi(x)$ in latent space.

- Verify that the encoder learns a ring-like latent geometry.
- Explain why this geometry is well suited for reconstruction but problematic for generation from the isotropic prior $p(z) = \mathcal{N}(0, I)$.
- Relate your observations to Fig. 9.8.

2. **Depth as Discrete Diffusion Time.** Extend the decoder to include multiple stochastic latent stages,

$$z_K \rightarrow z_{K-1} \rightarrow \cdots \rightarrow z_1 \rightarrow x,$$

with fixed Gaussian noise injected at each step.

- Treat the number of latent stages K as a discrete diffusion depth.
- Compare generated samples for $K = 1, 2, 3$.
- At what depth do improvements in sample diversity saturate?

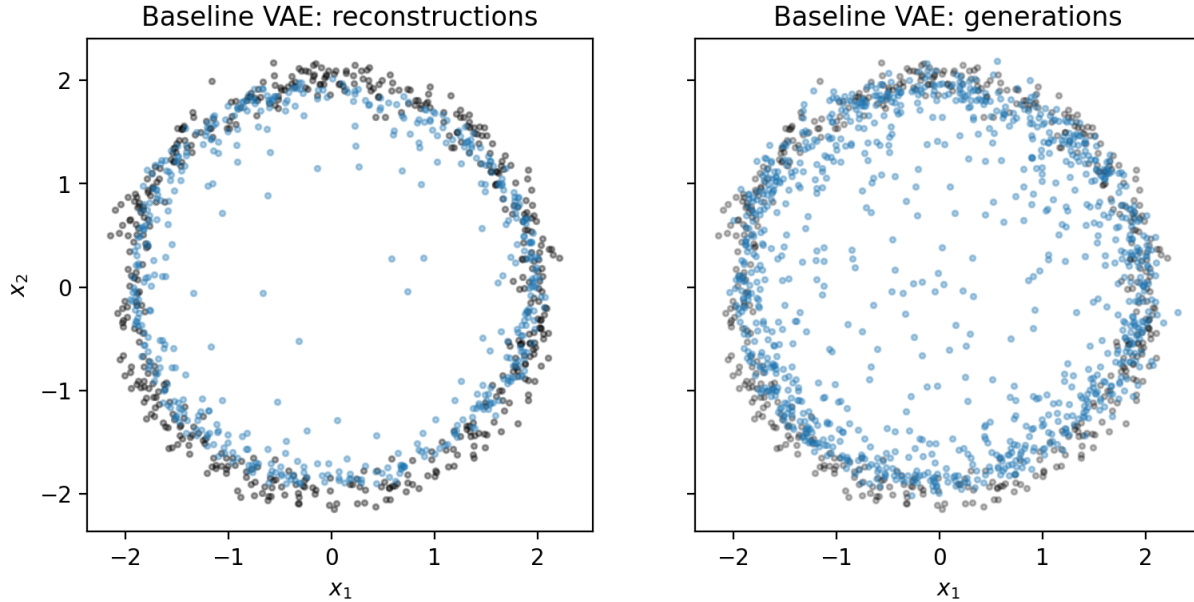


Figure 9.8: Baseline VAE: reconstructions versus generations. *Left:* reconstructions of test data (shown black) obtained by encoding samples into latent space and decoding them back (shown blue). The ring structure is preserved, indicating that the amortized inference model captures the data manifold accurately. *Right:* samples generated by decoding latent variables drawn from the prior $p(z) = \mathcal{N}(0, I)$ (shown blue). Although the topology is approximately correct, the generated ring is noticeably thinner and exhibits reduced variability. This illustrates a fundamental limitation of single-step latent-variable models: good reconstruction does not necessarily imply faithful generation from the prior.

3. Reconstruction–Diversity Tradeoff. For each latent depth K , evaluate:

- reconstruction error (e.g. MSE),
- sample diversity (e.g. radial variance or pairwise distance statistics).

Plot reconstruction error versus diversity and discuss the tradeoff. How does increasing diffusion depth move the model along this curve?

4. Noise Scheduling and Stability. Replace the fixed latent noise variance by a schedule β_k .

- Compare constant, increasing, and learned noise schedules.
- Identify regimes where training becomes unstable.
- Relate these observations to the role of noise schedules in score-based diffusion models.

5. Conceptual Synthesis. Explain how the multi-layer latent decoder approximates a reverse-time diffusion process in latent space.

- In what sense is the baseline VAE a single-step diffusion?

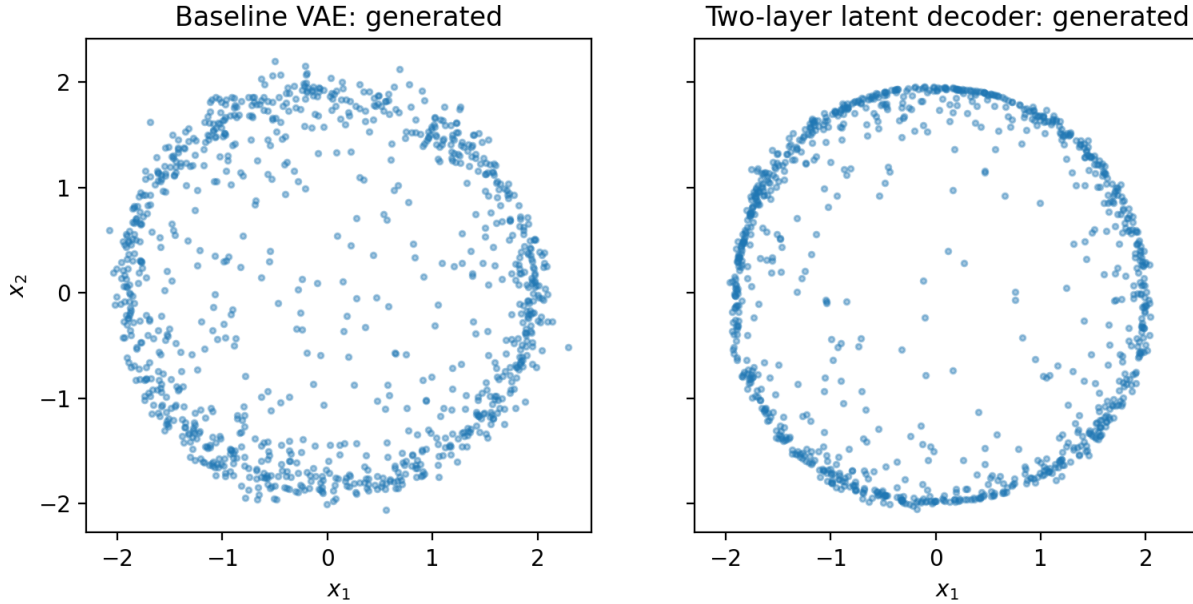


Figure 9.9: Latent diffusion improves generative diversity. *Left:* samples generated by the baseline VAE decoder from the latent prior, reproducing the thin-ring pathology seen in Fig. 9.8. *Right:* samples generated by a two-layer latent decoder, where an additional stochastic latent step progressively denoises samples before decoding. The resulting distribution exhibits increased thickness and improved coverage of the target ring. This experiment demonstrates how introducing a short reverse diffusion in latent space mitigates prior mismatch and bridges the gap between amortized inference and high-quality generation.

- How does increasing depth move the model closer to score-based diffusion?
- Which limitations of VAEs remain even after adding latent diffusion?

From Generative Models to Nonequilibrium Dynamics

In this section, we have reframed a broad class of generative models – GANs, normalizing flows, VAEs, and diffusion models – as instances of *transport in probability space*, differing primarily in how randomness, conditioning, and reversibility are incorporated. What emerges is a common structural theme: generation is realized as a *dynamical process*, often far from equilibrium, that progressively reshapes distributions through learned flows, drifts, and noise schedules. Diffusion models make this dynamical nature explicit, but it is already latent in adversarial training, variational inference, and deterministic transport.

This perspective invites a deeper question: *What governs the qualitative behavior of these dynamics as model dimension, noise strength, or time horizon vary?* In particular, when and why do generative diffusions exhibit abrupt changes in sample quality, diversity, or memorization—phenomena reminiscent of *phase transitions* in statistical physics?

The next section adopts this viewpoint explicitly. By treating generative diffusions as nonequilibrium stochastic systems, we analyze transitions (or their smoother version – transients), metastability, and scaling behavior, drawing connections to statistical physics interpretations of learning dynamics.

9.3 Diffusion Models and Dynamic Phase Transitions

A central theme of this chapter has been that generative models can be viewed as dynamical systems evolving in an abstract time variable. In diffusion-based generative models, this “time” is not merely a bookkeeping device: it acts as a genuine *control parameter* that governs the qualitative behavior of the dynamics. As time, noise level, or protocol parameters are varied, the system may undergo abrupt and reproducible changes in its macroscopic behavior. These changes are not metaphorical. They are measurable through well-defined observables and, in high-dimensional regimes, take the form of sharp dynamical phase transitions.

In this section, we develop this viewpoint by synthesizing three complementary perspectives: (i) the U-Turn diffusion construction as an empirical probe of trained models [58]; (ii) recent theoretical analyses of diffusion dynamics in high dimension [88, 89]; and (iii) concrete low-dimensional experiments that clarify what survives—and what does not—outside the asymptotic regime. The unifying message is simple: *diffusion time plays the role of a control parameter, and U-Turn diffusion provides an algorithmic microscope for resolving the associated dynamical regimes.*

9.3.1 U-Turn Diffusion as a Dynamical Probe

U-Turn diffusion [58] modifies a pre-trained score-based diffusion model by interrupting the forward noising process at an intermediate time $T_u < 1$, and immediately reversing the dynamics from that same state. Concretely, one samples

$$x(0) \rightarrow x(T_u)$$

using the forward diffusion, and then initializes the reverse-time SDE at $x(T_u)$ to produce a backward trajectory

$$x(T_u) \rightarrow y(0).$$

The U-Turn parameter T_u therefore controls how deeply the system is allowed to enter the noisy regime before being pulled back by the learned score field.

Varying T_u exposes distinct dynamical regimes that are largely hidden in standard end-to-end sampling. Empirically, three characteristic behaviors are observed:

- **Short-time regime (memorization-dominated).** For sufficiently small T_u , the backward trajectory returns to a state that remains close to the original sample that seeded the forward process. The dynamics are strongly influenced by local nonlinear structure in the score function.

- **Intermediate regime (metastable interpolation).** As T_u increases, the backward dynamics lose sensitivity to the individual training sample while still retaining information about the broader data manifold. In this regime, the effective score field becomes approximately affine, and sample diversity grows rapidly.
- **Long-time regime (speciation).** Beyond a second characteristic time scale, backward trajectories preferentially collapse into different semantic basins or classes, indicating a qualitative change in generative behavior.

These regimes are not defined by visual inspection alone. They can be diagnosed using quantitative observables such as trajectory auto-correlations, divergence from reference paths, and transition probabilities between semantic modes. From this perspective, U-Turn diffusion is best viewed not as a new generative model, but as an *experimental protocol* for interrogating the dynamics of an existing one.

9.3.2 Dynamic Phase Transients and High-Dimensional Theory

The phenomenology revealed by U-Turn diffusion aligns closely with recent theoretical analyses of diffusion dynamics in high-dimensional data spaces [88, 89]. In these works, diffusion models are studied in an asymptotic regime where dimension, data complexity, and noise interact in a controlled manner. Within this framework:

- The **memorization (or collapse) transition** corresponds to the onset of trajectory attraction toward individual data points, analogous to condensation into metastable states in glassy physical systems.
- The **speciation transition** corresponds to a symmetry-breaking phenomenon in which trajectories resolve global structure and separate into distinct macroscopic basins.
- These transitions are associated with sharp changes in spectral properties of data correlation operators and in information-theoretic quantities such as excess entropy.

Crucially, in the high-dimensional limit these transitions are predicted to be *sharp*: small changes in time or noise parameters lead to discontinuous changes in macroscopic observables. This justifies the language of dynamic phase transitions in a precise, non-metaphorical sense.

Example 9.3.1 (U-Turn Dynamics in a 9-Mode Gaussian Mixture). *To ground these ideas, we now turn to a deliberately simple example: a two-dimensional mixture of nine Gaussian modes arranged on a 3×3 grid, implemented in the notebook `02-SGM-with-SDE-9grid.ipynb`. Although this system is far from the high-dimensional regime assumed in theory, it serves as a clean testbed for illustrating what U-Turn diagnostics measure—and what their limitations are.*

A particularly informative observable is the probability that a backward trajectory returns to its original mode. Averaging this probability uniformly over all source modes yields the scalar diagnostic

$$P_{\text{same}}(T_u) = \mathbb{E}_i[\Pr(\text{mode}(y(0)) = i \mid \text{mode}(x(0)) = i)].$$

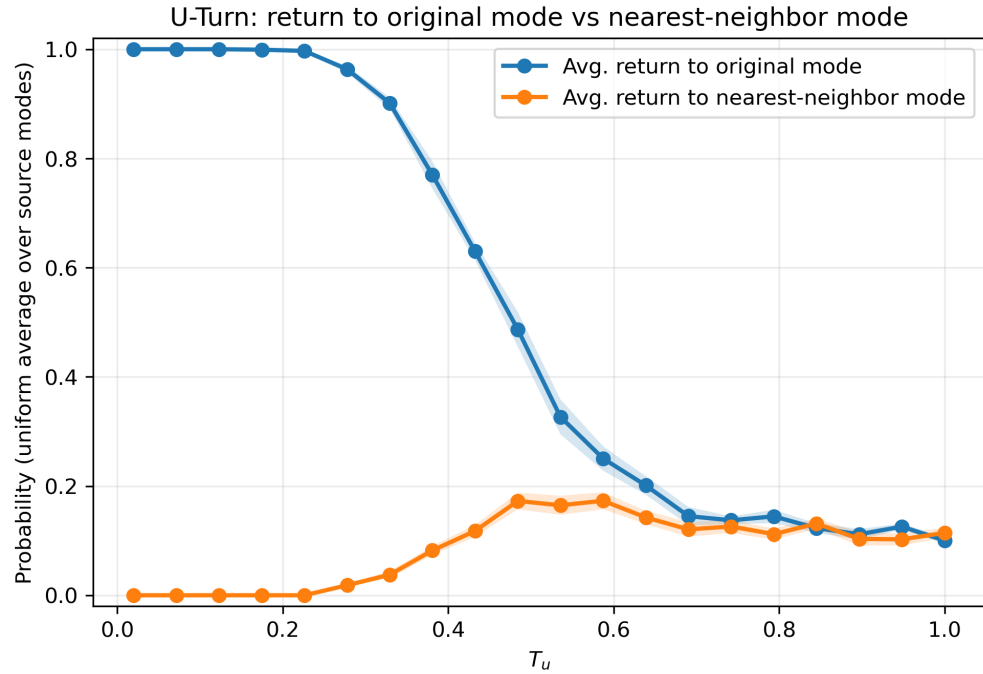


Figure 9.10: U-Turn diagnostics for a 9-mode Gaussian mixture. The solid curve shows the average probability that a backward trajectory returns to the same mode that seeded the forward process, while the second curve shows the average probability of returning to a nearest-neighbor mode. As the U-Turn time T_u increases, the return-to-self probability decays smoothly, while the return-to-neighbor probability exhibits a broad maximum. In this low-dimensional setting, both curves evolve continuously, illustrating transient dynamical regimes rather than sharp phase transitions.

Complementarily, one may track the probability of returning to a neighboring mode, which captures the onset of inter-mode transitions.

Fig. 9.10, produced within the notebook `04-UTurn-9grid_analysis.ipynb`, illustrates these quantities as functions of T_u . Two observations are essential. First, the return-to-self probability decays smoothly rather than discontinuously. Second, the return-to-neighbor probability exhibits a broad and relatively low maximum rather than a sharp peak. In other words, we observe transients, not true phase transitions. Both curves converge to the same asymptotic behavior at sufficiently large T_u .

This behavior is expected. Within each Gaussian mode, individual samples are already extremely close in Euclidean distance, making it difficult to resolve a distinct memorization transition. Speciation, while present, manifests as a gradual redistribution of probability mass rather than a sharp symmetry-breaking event. The example therefore serves as a controlled demonstration of a key principle: the sharpness of dynamic phase transitions is intrinsically tied to dimensionality and data complexity.

9.3.3 Perspective and Open Directions

U-Turn diffusion provides a versatile and model-agnostic probe of generative dynamics. Its real power emerges when combined with systematic diagnostics and with models operating in regimes where high-dimensional theory is expected to apply. Several open directions naturally follow.

Exercise 9.3.1 (U-Turn Diffusion — Further Explorations¹). *Consider a multi-class generative setting, starting from the 9-mode Gaussian mixture and progressively increasing dimensionality or structural complexity (number and hierarchy of modes). Investigate the following:*

1. *How do return-to-self and return-to-neighbor probabilities sharpen as dimension, mode separation, or sample size increases?*
2. *How do the locations and ordering of dynamical regimes change under different forward noise schedules or reverse-time diffusion coefficients?*
3. *Can U-Turn diagnostics be used to automatically identify semantic basins or to self-classify generated samples?*
4. *At what point do smooth transients give way to sharp, reproducible transitions? How do these thresholds scale with dimension?*
5. *Propose and explore observables that could serve as order parameters for dynamic phase transitions in diffusion models.*

Key Takeaway: Time as a Control Parameter

Diffusion time is not a passive index—it is a control parameter that governs qualitative changes in generative behavior. U-Turn diffusion makes this fact operational by turning time into an experimentally accessible knob.

Across both theory and experiment, three conclusions emerge:

- Diffusion models exhibit *distinct dynamical regimes*—memorization, interpolation, and speciation—that can be diagnosed through measurable observables.
- In high-dimensional regimes, these regime changes become *sharp dynamical phase transitions*, analogous to symmetry breaking and condensation phenomena in statistical physics.
- In low-dimensional or weakly separated settings, the same mechanisms persist but manifest as *smooth transients rather than true transitions*.

From this perspective, U-Turn diffusion is best understood as an *algorithmic microscope*: it does not alter the trained model, but reveals how generative structure emerges, disappears, and reorganizes as a function of time. This viewpoint sets the stage for the next step – treating diffusion, and more generally generative modeling,

¹Although framed as an exercise, this is intended—like several others in this chapter – as an invitation to research.

not only as a generator, but as a controllable dynamical system, where time, noise, and guidance act as levers for decision-making, optimization, and control.

9.4 From Markov Decision Processes to Reinforcement Learning

How this section fits?

This section serves as a conceptual and mathematical bridge between the diffusion-based generative models developed earlier in the chapter and the control- and transport-based viewpoints introduced next.

Historically, *Reinforcement Learning (RL)* emerged as a data-driven realization of *stochastic optimal control*: Bellman recursion provides the discrete-time backbone, while its continuous-time limit leads to Hamilton–Jacobi–Bellman (HJB) equations. Under additional structural assumptions, these equations admit exact linearizations and path-integral representations, which will become central in subsequent sections. From a modern perspective, RL also underlies the rapid growth of *agentic AI* systems – agents that plan, act, evaluate outcomes, and re-plan in closed feedback loops. While such systems are often implemented using large neural networks and generative models, their operational logic remains rooted in policy improvement, value estimation, and controlled stochastic dynamics.

The purpose of this section is therefore *not* to provide a full tutorial on RL, but to extract the minimal set of concepts needed to:

- connect Bellman-style decision making to continuous-time stochastic control,
- reinterpret agentic behavior as structured control over trajectory distributions,
- and prepare the ground for viewing diffusion models as controllable dynamical systems, unified with RL through optimal control and transport principles.

In the previous sections, we examined stochastic processes and their Markovian specializations, where the future evolution depends only on the present state (the Markov property). We now introduce *Markov Decision Processes (MDPs)*, a framework for *controlled* Markov processes — i.e., settings in which an agent selects actions that influence both state transitions and associated costs or rewards. We then connect MDPs to *Reinforcement Learning (RL)*, which provides data-driven methods for solving MDPs when the transition model and/or reward structure are not available in closed form. The present section is intentionally succinct and focuses only on the elements that will be reused in subsequent sections, where we reinterpret modern generative modeling through the lenses of stochastic optimal control and transport. For a comprehensive treatment of RL, see [90, 91] and references therein.

9.4.1 Markov Decision Processes

An MDP generalizes a Markov chain by allowing an *action* a to be chosen at each step. Formally, an MDP is defined by:

- **States:** a set \mathcal{S} .
- **Actions:** a set \mathcal{A} (discrete or continuous, depending on the problem).
- **Transition probabilities:** for each (s, a) , a distribution $p(s' | s, a)$ over next states.
- **Reward function:** $r(s, a)$, specifying immediate reward (or negative cost) after taking action a in state s (some formulations use $r(s, a, s')$).

A trajectory of length T is

$$s_0, a_0, s_1, a_1, \dots, s_{T-1}, a_{T-1}, s_T,$$

where actions are sampled from a *policy* π :

$$\pi(a | s) = \text{Prob}(\text{take action } a | \text{current state } s).$$

Goal: Optimal Policy. Given an MDP, one typically seeks a policy π^* that *maximizes* expected cumulative reward. A common objective is the discounted return

$$J(\pi) = \mathbb{E}_\pi \left[\sum_{t=0}^{\infty} \gamma^t r(s_t, a_t) \right], \quad (9.12)$$

where $\gamma \in [0, 1]$ is a discount factor, and thus

$$\pi^* = \arg \max_{\pi} J(\pi). \quad (9.13)$$

Value Functions and the Bellman Equations. The *value function* $V^\pi(s)$ is the expected return starting in state s and following policy π :

$$V^\pi(s) = \mathbb{E}_\pi \left[\sum_{t=0}^{\infty} \gamma^t r(s_t, a_t) \right] \quad \text{where } s_0 = s.$$

It satisfies the *Bellman equation*

$$V^\pi(s) = \mathbb{E}_{a \sim \pi(\cdot | s)} \left[r(s, a) + \gamma \sum_{s'} p(s' | s, a) V^\pi(s') \right], \quad (9.14)$$

and the optimal value function V^* satisfies the *Bellman optimality equation*

$$V^*(s) = \max_{a \in \mathcal{A}} \left\{ r(s, a) + \gamma \sum_{s'} p(s' | s, a) V^*(s') \right\}.$$

Solving these equations – via dynamic programming (DP) when the model is known, or via data-driven approximations otherwise – yields an optimal decision rule.

Historical Note: Bellman, Kantorovich, and the Birth of Dynamic Programming. Richard Bellman introduced the principle of optimality and formulated the DP recursion [92] at RAND in the 1950s. Almost in parallel (independently, and somewhat earlier), Leonid Kantorovich developed foundational methods for resource allocation and multi-stage planning [93, 94]. Both viewpoints converge around recursive decompositions of sequential decision problems, laying groundwork for MDP theory in control and AI.

Example 9.4.1 (Bellman's DP for a Simple Two-State MDP.). *Consider an MDP with two states, S_1 and S_2 , and two actions available in each state:*

$$\mathcal{A}(S_1) = \{\text{Action A, Action B}\}, \quad \mathcal{A}(S_2) = \{\text{Action C, Action D}\}.$$

Assume $\gamma \in (0, 1)$ and the following rewards and transitions:

- **State S_1 :** Action A: $r(S_1, A) = 1$, with $P(S_1 | S_1, A) = 0.5$, $P(S_2 | S_1, A) = 0.5$. Action B: $r(S_1, B) = 0$, with $P(S_2 | S_1, B) = 1.0$.
- **State S_2 :** Action C: $r(S_2, C) = 2$, with $P(S_1 | S_2, C) = 0.6$, $P(S_2 | S_2, C) = 0.4$; Action D: $r(S_2, D) = 0$, with $P(S_1 | S_2, D) = 0.2$, $P(S_2 | S_2, D) = 0.8$.

The Bellman optimality equations read

$$\begin{aligned} V^*(S_1) &= \max \left\{ 1 + \gamma [0.5V^*(S_1) + 0.5V^*(S_2)], \gamma V^*(S_2) \right\}, \\ V^*(S_2) &= \max \left\{ 2 + \gamma [0.6V^*(S_1) + 0.4V^*(S_2)], \gamma [0.2V^*(S_1) + 0.8V^*(S_2)] \right\}. \end{aligned}$$

A standard DP method is value iteration: initialize $V_0(S_1), V_0(S_2)$, and update V_{k+1} by applying the right-hand side until convergence. The optimal policy π^* selects the maximizing action in each state.

9.4.2 Reinforcement Learning

In *Reinforcement Learning (RL)*, the MDP formalism is retained but the agent typically does *not* assume explicit knowledge of $p(s' | s, a)$ and/or $r(s, a)$. Instead, the agent collects trajectory data $\{(s_t, a_t, r_t, s_{t+1})\}$ and learns a policy π that improves expected return. Modern RL combines MDP structure with function approximation (notably neural networks), enabling scalable control in high-dimensional environments; see [90, 95, 96].

Value and Advantage. In addition to $V^\pi(s)$, it is customary to define the state-action value function

$$Q^\pi(s, a) = \mathbb{E}_\pi \left[\sum_{t=0}^{\infty} \gamma^t r(s_t, a_t) \mid s_0 = s, a_0 = a \right],$$

and the *advantage*

$$A^\pi(s, a) = Q^\pi(s, a) - V^\pi(s).$$

These objects will reappear later when we connect RL to stochastic optimal control and to probability reweighting on path space.

A Minimal RL Picture (brief). A canonical value-based algorithm is *Q-learning*, which iteratively updates an estimate \hat{Q} using sampled transitions. Policy-based methods instead parameterize $\pi_\theta(a|s)$ and update θ to improve $J(\pi_\theta)$; in practice, the advantage A^π is used to reduce variance. We do not develop these methods further here, since our primary interest is the *structural* link between (i) Bellman recursion, (ii) continuous-time stochastic control, and (iii) generative modeling viewed as controlled stochastic dynamics.

Key Takeaways from “Classic” MDP and RL (for later reuse).

- MDPs formalize sequential decisions in Markovian environments via $(\mathcal{S}, \mathcal{A}, p, r)$ and a policy π .
- Bellman recursion expresses optimality through a local-to-global dynamic-programming principle.
- RL is a data-driven route to the same objects (policies/values) when the model is unknown, frequently using NN function approximation.

9.4.3 Agentic AI as Iterated Planning and Policy Improvement

The rapid growth of *agentic AI* (tool-using systems, planning–execution loops, self-evaluation and re-planning) can be viewed, mathematically, as repeated applications of the same principles introduced above: (i) construct a surrogate objective, (ii) produce candidate actions/trajectories, (iii) evaluate them via value/reward signals (often learned), and (iv) update a policy or planner. In this sense, agentic workflows operationalize Bellman-style decomposition and RL-style policy improvement, while increasingly leveraging modern generative models as proposal mechanisms. We now propose two small-scale mini-projects (example followed by an exercise) that make this connection concrete and will be directly reused in Section 9.4.4 and in the planning-as-sampling discussion later in the chapter.

Example 9.4.2 (Agentic Re-Planning on a Stochastic GridWorld). **Setup – Control as Inference.** Consider an 8×8 GridWorld with walls and obstacles. An agent starts from a fixed cell and aims to reach a designated goal cell. At each discrete time step, the agent selects an intended action $a \in \{\text{left, right, up, down}\}$. The environment executes the intended action with probability $1 - \rho$, and replaces it by a uniformly random action with probability ρ , modeling stochastic slippage. The immediate reward is

$$r(s, a) = \begin{cases} +1, & \text{if the next state is the goal,} \\ -c, & \text{otherwise,} \end{cases} \quad c > 0.$$

This simple environment is deliberately chosen to isolate the effects of uncertainty, planning horizon, and re-planning, rather than function approximation or representation learning. We compare three conceptually aligned controllers: (i) soft dynamic programming, (ii) sampling-based planning via trajectory reweighting, and (iii) an explicitly agentic re-planning loop.

Method A: Soft Value Iteration. We compute an entropy-regularized value function using soft Bellman backups (log-sum-exp over actions), yielding a Boltzmann policy

$$\pi(a | s) \propto \exp(Q(s, a)/\tau),$$

with temperature $\tau > 0$. This method represents a classical (infinite-horizon) control solution, regularized to encourage exploration and robustness under uncertainty.

Method B: Energy-Based Planner. Candidate trajectories $\tau = (s_0, a_0, \dots, s_T)$ are sampled from a simple proposal (e.g. random rollouts), and assigned importance weights

$$w(\tau) \propto \exp\left(\sum_{t=0}^{T-1} r(s_t, a_t)\right).$$

The first action of the highest-weighted trajectory (or a weighted vote among the top- m trajectories) is executed. This realizes control as inference: planning is performed by reweighting trajectories in path space rather than by value recursion.

Method C: Agentic Re-Planning Loop. During interaction, the agent estimates the slippage probability ρ online from observed discrepancies between intended and executed actions. Every k steps, the planner is re-run using the current estimate $\hat{\rho}$. This produces a minimal observe–update–plan–act loop, characteristic of agentic systems.

Observed behavior and interpretation. Fig. 9.11 summarizes the compute–quality tradeoff, while Fig. 9.12 provides representative qualitative behavior:

- **Method A (soft DP)** is stable but conservative. Even after tuning, it optimizes an entropy-regularized, effectively infinite-horizon objective, which does not necessarily maximize the probability of goal-reaching within a fixed horizon. Cautious detours and occasional dithering are therefore diagnostic of the objective mismatch, rather than an implementation defect.
- **Method B (trajectory reweighting)** improves monotonically with compute budget. As more trajectories are sampled, reweighting concentrates probability mass on goal-reaching plans, illustrating the effectiveness of trajectory-level inference.
- **Method C (agentic re-planning)** is most robust at moderate uncertainty. By repeatedly updating its internal model and re-planning, it turns open-loop planning into closed-loop decision making, correcting course after slips.

Advantage of adaptivity (mechanistic view). The adaptive mechanism in Method C is isolated in Fig. 9.13, which shows a single episode: the trajectory (colored by time) together with the online estimate $\hat{\rho}_t$. Early behavior reflects an initial, imperfect model of slippage; as discrepancies accumulate, $\hat{\rho}_t$ shifts and the re-planning step induces a qualitative change in the chosen actions. Thus, behavior changes because the internal model changes, which is the essence of adaptivity.

A reference implementation and reproducible figures are provided in `N9_4A_agentic_replanning.ipynb`.

Exercise 9.4.1 (Trajectory Based – Diffusion Inspired – RL). These exercises are designed to guide the reader from classical dynamic programming toward a trajectory-based, diffusion-inspired view of control.

1. **Soft Bellman backup.** Write the soft Bellman backup for $V(s)$ using log-sum-exp over actions. Show explicitly that the resulting greedy policy is Boltzmann in $Q(s, a)$ with temperature τ . Discuss how the limit $\tau \rightarrow 0$ recovers standard (hard) value iteration.

2. **Trajectory reweighting as inference.** Implement Method B using a simple proposal distribution over trajectories. Compare two action-selection rules: (i) selecting the first action of the single best trajectory, and (ii) computing a weighted vote over first actions among the top- m trajectories. Relate this procedure to importance sampling and to path-integral control.
3. **Finite vs infinite horizon.** Explain why Method A optimizes an infinite-horizon objective while success is measured by finite-time goal reaching. Modify the implementation to use a finite-horizon soft DP and compare the resulting behavior.
4. **Agentic adaptation.** Propose an estimator $\hat{\rho}_t$ for the slippage probability based on observed transitions. Study how performance depends on the re-planning period k . In particular, identify regimes (in ρ) where frequent re-planning is beneficial or unnecessary.
5. **Toward diffusion-based control.** Interpret Method B as sampling from an unnormalized path distribution on trajectories. Suggest how a diffusion model over trajectories could replace the proposal distribution (e.g. by learning a trajectory prior and sampling via reverse-time denoising), and discuss what training data would be required.

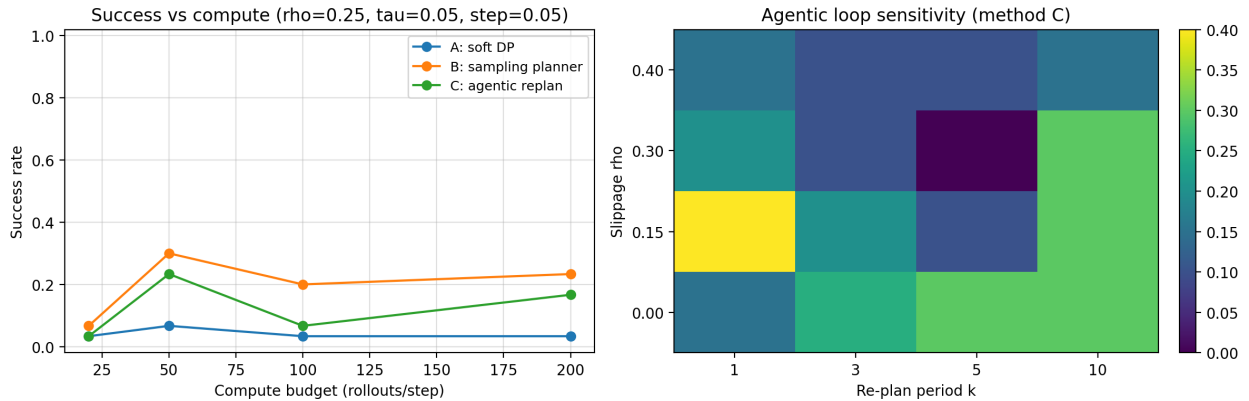


Figure 9.11: Agentic re-planning on a stochastic GridWorld. Left: success rate versus compute budget (number of planning rollouts or backups). Soft value iteration (A) is stable but conservative under a fixed horizon, reflecting entropy-regularized infinite-horizon optimization. Sampling-based planning via trajectory reweighting (B) improves monotonically with compute, as higher-quality plans are discovered. Agentic re-planning (C) is most robust at moderate uncertainty, benefiting from repeated observe–update–plan cycles. Right: sensitivity of the agentic re-planning loop (Method C) to environmental uncertainty ρ and re-planning period k . Each pixel shows empirical success rate, estimated from stochastic simulations. The irregular structure reflects the discrete and stochastic nature of finite-horizon planning under uncertainty. Rather than indicating a smooth monotone trend, the plot should be read as a regime map: adaptivity provides clear benefits in some high-uncertainty settings, while in low-uncertainty regimes performance is relatively insensitive to re-planning frequency. (Produced by N9_4A_agentic_replanning.ipynb.)

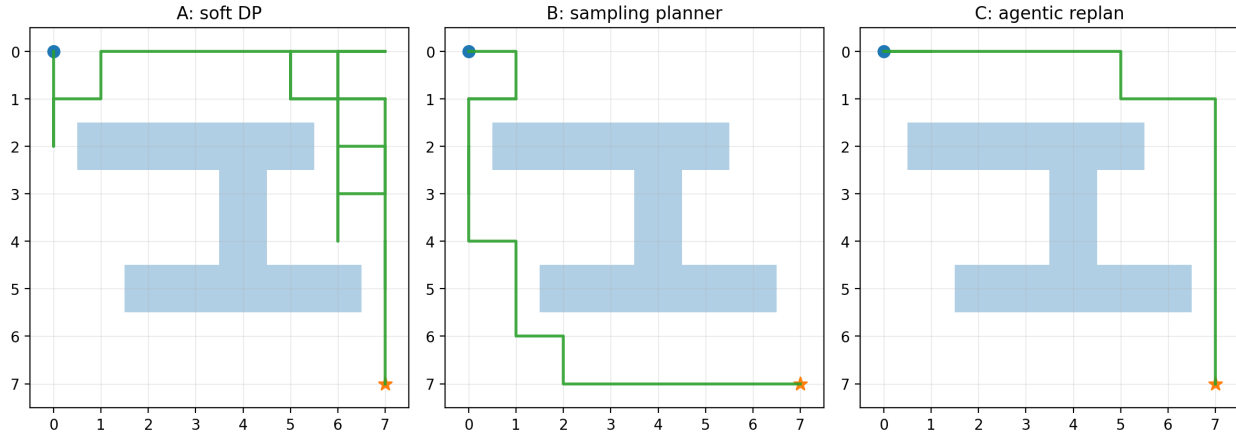


Figure 9.12: Representative trajectories for Methods A/B/C on the same GridWorld instance. Method A (soft DP) can exhibit conservative detours due to entropy regularization and objective mismatch (infinite-horizon value vs finite-horizon success). Method B selects a plan via trajectory reweighting. Method C re-plans online and is typically able to correct after slips.

Example 9.4.3 (Preference-Driven Policy Improvement as KL-Regularized Control). *Example 9.4.2 implemented control-as-inference by exponentially reweighting trajectories in a finite-horizon planning problem. Here we keep the setting even simpler (may call it a contextual bandit²) and move the same idea to the policy level: we exponentially tilt a reference policy using a learned surrogate reward, while controlling the update size via a KL penalty. Conceptually, both examples implement the same primitive:*

reweight by $\exp(score)$ subject to a normalization/regularization constraint,

but applied to different objects: trajectories in A versus per-context action distributions in B.

Setup (contextual bandit with preferences). Consider a small contextual bandit with contexts $s \in \mathcal{S}$ and actions $a \in \mathcal{A}$. The agent does not observe numeric rewards. Instead, in a given context s it may be shown two actions (a, a') and receives a binary preference signal

$$(a \succ a') \quad \text{or} \quad (a' \succ a),$$

interpreted as a noisy comparison of latent utilities. This preference-only interface is the minimal abstraction behind modern preference optimization pipelines in generative AI (e.g., RLHF Reinforcement Learning from Human Feedback (RLHF) and Direct Preference Optimization (DPO)³.

²Bandit, or multi-armed bandit, is a simplified yet fundamental RL problem where an agent repeatedly chooses from several actions ("arms" to maximize rewards, learning the best strategy by balancing to explore unknown options and exploiting known good ones, all without state changes – thus, sometimes called stateless MDP.

³The two are key methods for aligning Large Language Models (LLMs) with human preferences using preference data without needing a separate reward model.

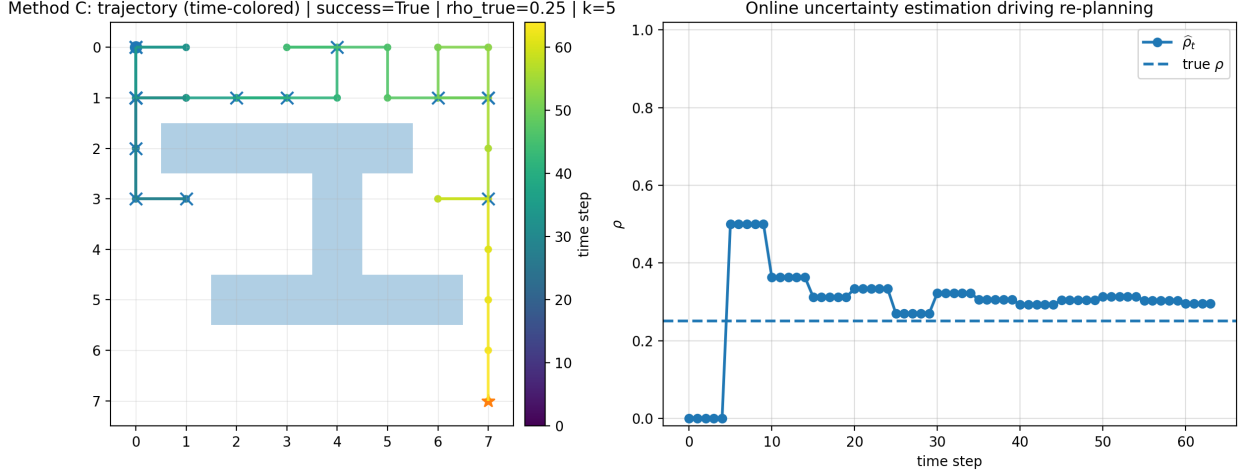


Figure 9.13: Mechanistic view of adaptivity in Method C. (*Left*) A single agentic episode: the trajectory is colored by time; \times -markers indicate slip events. (*Right*) The online estimate $\hat{\rho}_t$ of the slippage probability compared with the true ρ . As $\hat{\rho}_t$ changes, re-planning induces a qualitative change in actions, demonstrating that behavior adapts because the internal model is updated.

Step 1: Fit a preference model. We learn a surrogate reward $\hat{r}_\phi(s, a)$ from pairwise comparisons using a logistic (Bradley–Terry) model:

$$\mathbb{P}_\phi(a \succ a' \mid s) = \sigma(\hat{r}_\phi(s, a) - \hat{r}_\phi(s, a')), \quad \sigma(x) = \frac{1}{1 + e^{-x}},$$

by maximum likelihood on a dataset of comparisons.

Step 2: KL-regularized policy improvement (multiplicative weights). Starting from a reference policy $\pi_0(\cdot \mid s)$ (uniform in the notebook), we perform KL-regularized improvement by exponential tilting:

$$\pi_{k+1}(\cdot \mid s) \propto \pi_k(\cdot \mid s) \exp(\eta \hat{r}_\phi(s, \cdot)), \quad (9.15)$$

where $\eta > 0$ controls the update strength. This update can be viewed as a mirror-descent / proximal step in policy space, and it is the bandit analogue of “soft” (entropy-regularized) policy iteration.

Notebook `N9_4B_preference_KL.ipynb` implements the full loop and produces: (i) regret vs iteration (computed w.r.t. the latent ground-truth reward table in this synthetic experiment); (ii) the per-iteration KL step $\text{KL}(\pi_{k+1} \parallel \pi_k)$ (an explicit diagnostics for update size); (iii) calibration of the learned preference model on held-out comparisons.

Interpretation and lesson. Even in this minimal setting, the experiment exhibits a robust pattern: once a reasonably calibrated preference model is learned, the exponential-tilt update (9.15) yields a stable sequence of policies that improves performance while keeping successive policies close in KL. This is the same structural mechanism that will reappear later in generative modeling: use exponential reweighting to bias a baseline distribution toward preferred outcomes, while a KL term prevents destructive updates.

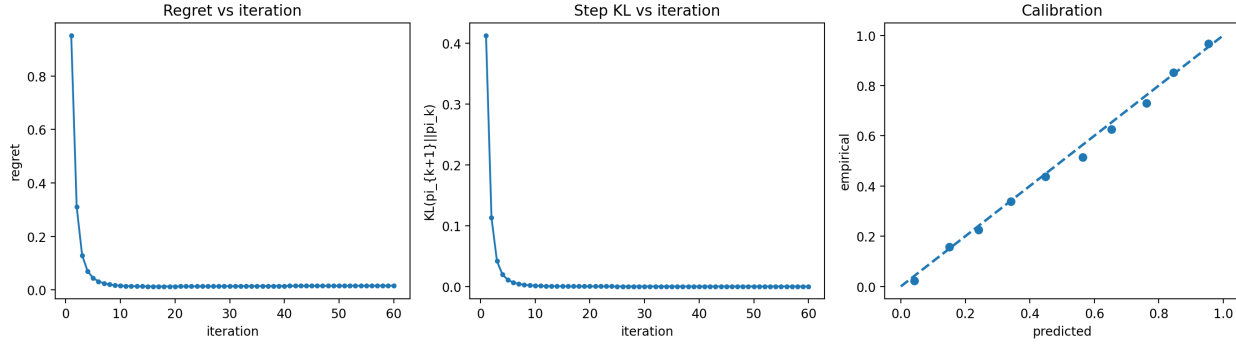


Figure 9.14: Preference-driven policy improvement as KL-regularized control. *Left:* regret decreases rapidly across iterations, indicating that repeated KL-regularized updates concentrate mass on high-utility actions. *Middle:* $\text{KL}(\pi_{k+1} \parallel \pi_k)$ shrinks with k , showing that the policy iteration naturally anneals its step size as it approaches a fixed point. *Right:* reliability (calibration) plot for the preference model: predicted preference probabilities track empirical frequencies on held-out comparisons, supporting the use of \hat{r}_ϕ as a surrogate reward for policy improvement. (Produced by `N9_4B_preference_KL.ipynb`.)

Exercise 9.4.2 (Preference Optimization and KL-Control). *The goal of these exercises is to connect preference-based learning to the broader “control-as-inference” theme of the chapter, and to relate the two examples above.*

1. **Derive the KL-prox form.** Show that the update

$$\pi_{k+1}(\cdot | s) \propto \pi_k(\cdot | s) \exp(\eta \hat{r}_\phi(s, \cdot))$$

is the solution of a KL-regularized maximization problem of the form

$$\pi_{k+1}(\cdot | s) = \arg \max_{\pi(\cdot | s)} \left\{ \mathbb{E}_{a \sim \pi(\cdot | s)} [\hat{r}_\phi(s, a)] - \frac{1}{\eta} \text{KL}(\pi(\cdot | s) \parallel \pi_k(\cdot | s)) \right\}.$$

Interpret η as an inverse “trust-region” weight.

2. **Noise, data, and calibration.** In the notebook `N9_4B_preference_KL.ipynb`, vary (i) the number of comparisons and (ii) the preference noise level. Quantify how calibration degrades and how this impacts regret and convergence. When does the policy improvement step amplify model miscalibration?
3. **Step-size control via KL.** Fix a preference model and vary η . Identify a regime where regret decreases quickly but $\text{KL}(\pi_{k+1} \parallel \pi_k)$ becomes large. Propose a simple adaptive rule for η_k that targets a desired KL per iteration.
4. **Bridge to Example 9.4.2,** where we reweighted trajectories by $\exp(\sum_t r_t)$. Explain how approach of Example 9.4.3 can be viewed as the one-step (bandit – that is without reward) analogue of that construction. What changes when the reweighted object is a full path distribution rather than a per-context action distribution?

5. *Toward diffusion/PID-style updates.* Interpret the exponential tilt as defining an unnormalized distribution over actions. Suggest how one could replace explicit normalization by a learned generative model of actions (or action sequences), and how KL-regularized improvement would translate into training objectives for such a generator.

What Do These Examples Really Teach Us? At a superficial level, Examples 9.4.2 and 9.4.3 demonstrate familiar technical tools: sampling, exponential reweighting, and KL-regularized updates. However, taken together, they illustrate something more fundamental about the role of control, inference, and learning inside modern generative AI.

Both examples implement the same mathematical primitive: *tilting a reference distribution by an exponential of a score, subject to normalization or KL control.* In Example 9.4.2, this primitive acts on *trajectory distributions*, yielding planning-as-inference and agentic replanning under uncertainty. In Example 9.4.3, it acts on *policy distributions*, producing preference-driven improvement without access to numeric rewards. These are not ad hoc tricks, but concrete instantiations of a unifying variational principle:

optimize expected utility while remaining close to a baseline distribution.

From the perspective of generative modeling, this principle is central. Diffusion models, path-integral control, entropy-regularized RL, and modern preference-optimization methods all rely on controlled deformation of probability measures via exponential reweighting. What differs is *what* is being reweighted (noise paths, action sequences, policies, or samples), and *how* the baseline distribution is represented (analytically, by simulation, or by a neural generator).

Crucially, Example 9.4.2 reveals that agentic behavior does not require sophisticated architectures: it emerges when inference, planning, and model updating are coupled in a closed loop. Example 9.4.3 shows that even in the absence of explicit rewards, structured feedback (preferences) combined with KL-regularized updates is sufficient to drive stable policy improvement. Together, these examples expose the mathematical continuity between generative modeling and reinforcement learning: both are instances of *controlled probabilistic inference*.

This exponential reweighting and optimization perspectives naturally brings a question – can it be justified by a universal variational principle? We will answer this question affirmatively in the next Section.

9.4.4 Maximum Entropy Reinforcement Learning

The exponential reweighting constructions encountered in the previous examples naturally raise the question: *is there a principled variational framework in which stochastic policies of Gibbs form emerge as optimal solutions, rather than being imposed by design?* The answer is affirmative. One such framework is provided by *Maximum Entropy Reinforcement Learning* (MaxEnt RL), introduced in [97] and further developed in subsequent work. Importantly, MaxEnt RL is not an isolated construction: it is closely related to earlier formulations of *Linearly Solvable MDPs* (LS-MDP) [98, 99] and to *Path-Integral Control* (PIC) [100]. These

connections will play a central role in the following sections, where we develop Path Integral Diffusion (PID) and Sampling Decisions (SD) as a unifying framework.

From reward maximization to entropy-regularized control. Recall from Section 9.4.1 that in a standard discounted MDP the objective is to maximize

$$J(\pi) = \mathbb{E}_\pi \left[\sum_{t=0}^{\infty} \gamma^t r(s_t, a_t) \right].$$

MaxEnt RL modifies this objective by augmenting it with an entropy term that explicitly favors stochasticity:

$$J_{\text{MaxEnt}}(\pi) = \mathbb{E}_\pi \left[\sum_{t=0}^{\infty} \gamma^t (r(s_t, a_t) + \alpha \mathcal{H}(\pi(\cdot|s_t))) \right], \quad (9.16)$$

where $\mathcal{H}(\pi(\cdot|s)) = -\mathbb{E}_{a \sim \pi(\cdot|s)}[\log \pi(a|s)]$ is the policy entropy and $\alpha > 0$ is a temperature parameter controlling the trade-off between reward and randomness.

This objective can be interpreted as seeking policies that achieve high reward while remaining as *uninformative* (high entropy) as possible, subject to that constraint. Equivalently, it penalizes overly deterministic policies unless strongly justified by reward.

Soft value functions and the soft Bellman recursion. Define the *soft* state-value and state-action value functions by

$$\begin{aligned} V^\pi(s) &= \mathbb{E}_{a \sim \pi(\cdot|s)} \left[Q^\pi(s, a) - \alpha \log \pi(a|s) \right], \\ Q^\pi(s, a) &= r(s, a) + \gamma \mathbb{E}_{s' \sim p(\cdot|s, a)} [V^\pi(s')]. \end{aligned} \quad (9.17)$$

Formally, the “soft” formulation replaces hard reward maximization by an exponential averaging operation: instead of maximizing $Q^\pi(s, a)$ over actions, one maximizes over stochastic policies $\pi(\cdot|s)$ a reward–entropy trade-off.

Specifically, for each state s , the optimal policy solves the per-state variational problem

$$\pi^*(\cdot|s) = \arg \max_{\pi(\cdot|s)} \left\{ \mathbb{E}_{a \sim \pi(\cdot|s)} [Q^*(s, a)] - \alpha \mathcal{H}(\pi(\cdot|s)) \right\}. \quad (9.18)$$

The corresponding optimal value function V^* satisfies the *soft Bellman optimality equation*

$$V^*(s) = \alpha \log \int_{\mathcal{A}} \exp \left(\frac{1}{\alpha} (r(s, a) + \gamma \mathbb{E}_{s' \sim p(\cdot|s, a)} V^*(s')) \right) da, \quad (9.19)$$

where the integral is replaced by a sum in the discrete-action case.

Compared to the classical Bellman equation, the hard max is replaced by a *log-sum-exp*, producing a smooth approximation that preserves optimality while enabling analytic characterization of the optimal policy.

Gibbs form of the optimal policy. A central result of [97] is that the optimal MaxEnt policy admits an explicit Gibbs (Boltzmann) form:

$$\pi^*(a|s) = \frac{1}{Z(s)} \exp\left(\frac{1}{\alpha} Q^*(s, a)\right), \quad Z(s) = \int_{\mathcal{A}} \exp(Q^*(s, a)/\alpha) da. \quad (9.20)$$

Thus, instead of *selecting* the action that maximizes $Q^*(s, a)$, the agent *samples* actions from a Gibbs distribution whose “energy” is $-Q^*(s, a)$.

From this viewpoint, MaxEnt RL replaces deterministic optimization by *sampling from an energy-based policy*. The temperature α controls the sharpness of this distribution: as $\alpha \rightarrow 0$, π^* concentrates on the maximizer of Q^* and classical RL is recovered.

Variational characterization (and proof sketch). The Gibbs form (9.20) is not an ad hoc modeling choice. Rather, it follows directly from a universal variational principle. Specifically, for each state s , the optimal MaxEnt policy is the solution of the KL-regularized optimization problem

$$\pi^*(\cdot|s) = \arg \max_{\pi(\cdot|s)} \left\{ \mathbb{E}_{a \sim \pi}[Q^*(s, a)] - \alpha \text{KL}(\pi(\cdot|s) \parallel \text{Unif}(\mathcal{A})) \right\}, \quad (9.21)$$

where $\text{Unif}(\mathcal{A})$ denotes distribution of action uniform over the allowed action’s set. Taking first-order optimality conditions under the normalization constraint $\int \pi(a|s) da = 1$ yields

$$\pi^*(a|s) \propto \exp(Q^*(s, a)/\alpha),$$

recovering exactly the Gibbs policy in (9.20). More generally, replacing the uniform distribution by an arbitrary reference policy leads to the same exponential tilting structure. This variational derivation makes explicit the universal mechanism already encountered in earlier examples: *exponential reweighting of a reference distribution under a KL constraint* \square .

Example 9.4.4 (MaxEnt RL in a 2D Multi-Goal Environment (multi-modality by Gibbs policies)). *This example is a didactic re-creation of the “2D multi-goal” illustration (Fig. 1) from [97], designed to visualize a key MaxEnt mechanism: optimal stochastic policies can be genuinely multi-modal, and their modes are explained by a Gibbs (Boltzmann) structure in action space.*

Environment. The state is a 2D position $s = (x, y) \in \mathbb{R}^2$. Actions are bounded velocities $a \in [-1, 1]^2$, and dynamics are

$$s_{t+1} = s_t + \Delta t a_t.$$

We place four symmetric goals g_i (at the cardinal directions) and define a mixture-of-Gaussians reward

$$r(s) = \sum_{i=1}^4 \exp\left(-\frac{\|s-g_i\|^2}{2\sigma^2}\right).$$

This landscape has multiple “equally good” directions near the origin and between goals.

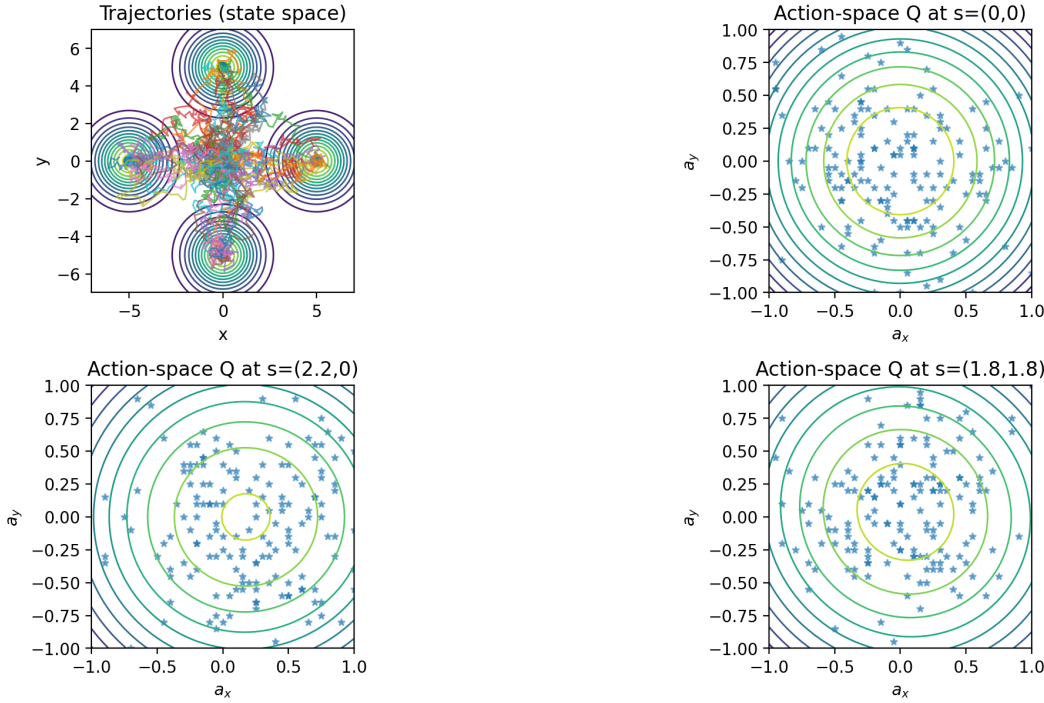


Figure 9.15: MaxEnt RL in a 2D multi-goal environment (didactic re-creation inspired by Fig. 1 of [97]). *Top-left:* reward landscape (contours) with sample trajectories starting at the origin under a Gibbs policy $\pi(a|s) \propto \exp(Q(s, a)/\alpha)$, illustrating mode coverage. All trajectories are run for a sufficiently long horizon ($T = 80$) so that commitment to a single goal occurs; diversity is observed across rollouts rather than within individual paths. *Top-right:* action-space slice $Q(s, \cdot)$ at $s = (-2, 0)$ with actions sampled from $\pi(\cdot|s)$ (stars). *Bottom-left:* action-space slice at $s = (0, 0)$. *Bottom-right:* action-space slice at $s = (2.5, 2.5)$. Across the three action panels, the sampled actions visualize how the MaxEnt policy distributes probability mass over multiple promising directions when several goals are comparably good.

Soft Q and Gibbs policy (MaxEnt structure). In MaxEnt RL (Section 9.4.1–MaxEnt), the optimal policy has the Gibbs form

$$\pi^*(a | s) \propto \exp(Q^*(s, a)/\alpha),$$

where $\alpha > 0$ is the entropy temperature. To keep this example lightweight (no neural-network training and no full dynamic programming), we use a finite-horizon, one-step look-ahead surrogate

$$Q(s, a) = r(s') + \gamma V_{\text{proxy}}(s') - \frac{\lambda}{2} \|a\|^2, \quad s' = s + \Delta t a,$$

where V_{proxy} is a smooth log-sum-exp potential over the same set of goals. The proxy does not represent a learned value function; its sole purpose is to shape the local action–value landscape so that multiple future directions can be simultaneously attractive. In this setting, MaxEnt RL makes explicit a key qualitative phenomenon: when several futures are comparably good, the optimal policy is genuinely stochastic and exhibits multi-modal structure in action space. Fig. 9.15 reports two complementary diagnostics:

- State space (trajectories): *multiple rollouts starting from $s_0 = (0, 0)$ under the same Gibbs policy $\pi(a | s) \propto \exp(Q(s, a)/\alpha)$. Although the dynamics are deterministic, the policy is stochastic by design, so different rollouts commit to different goals. With a sufficiently long rollout horizon, each individual trajectory eventually reaches a single goal, while diversity is expressed across trials rather than within a single path. This behavior is the control-theoretic analog of a generative model that samples from a multi-modal distribution.*
- Action space (local structure): *level sets of $Q(s, a)$ over $a \in [-1, 1]^2$ at three representative states, with actions sampled from $\pi(\cdot | s)$ overlaid. Near a given goal, the action distribution is effectively unimodal, reflecting a single dominant direction of improvement. Between goals, several directions are comparably favorable, and the MaxEnt policy assigns probability mass to multiple modes. Locally, the soft action-value function is approximately quadratic in a , leading to an elliptic geometry of iso-contours and Gaussian-like Gibbs factors around preferred actions.*

A reference implementation (CPU-friendly, no training) is provided in `N9_4C_maxent_multigoal.ipynb`.

Exercise 9.4.3 (MaxEnt multi-modality, temperature, and the path-space analogy). We pose questions which are meant to connect MaxEnt RL to the section theme of sampling by exponential reweighting.

1. **Temperature controls mode selection.** Using the notebook, vary α over a range (e.g. 0.1 to 1.0). Describe (and quantify) how the distribution of final goals changes. Identify a regime where the policy collapses to near-deterministic behavior.
2. **From Q-modes to policy modes.** Pick a state s “between two goals” and plot $\pi(a | s)$ (as a heatmap over the action grid). Verify that the modes of π align with the dominant maxima of $Q(s, \cdot)$.
3. **Reward geometry vs policy geometry.** Vary σ (width of the Gaussian bumps). Explain how narrowing/widening the reward wells changes (i) the contour geometry in state space and (ii) the number and sharpness of modes in action space.

MaxEnt and Generative Modeling

MaxEnt RL provides a principled answer to the question raised earlier: exponential reweighting arises naturally from a variational principle that balances expected utility against informational cost. In this sense, policies in MaxEnt RL are *generative objects*: they define probability distributions over actions (or trajectories) from which decisions are sampled rather than deterministically chosen.

Therefore the remainder of this chapter develops a complementary viewpoint: rather than treating generative modeling and RL as separate toolkits to be combined heuristically, we show how both can be organized under a unified *stochastic control / transport* umbrella. In particular, the continuous-time limit of Bellman recursion leads to Hamilton–Jacobi–Bellman (HJB) equations; under structural assumptions (e.g.

linearly-solvable SOC), HJB admits a Hopf–Cole transform and yields path-integral formulations. These path-integral constructions can not only be viewed akin to exponential corrections/re-weighting we have discussed in this section in the context of RL – but will become the main conceptual bridge to diffusion-based generative modeling highlighted in the following sections.

Further Reading

RL → Better Generation. RL-guided fine-tuning of diffusion models is an active area; see, e.g., [101, 102, 103, 104] and references therein.

Generation → Better RL. Generative models can serve as planners, policy parameterizations, or curriculum generators in RL; see, e.g., [105] for a survey and pointers to recent developments.

9.5 Path–Integral Diffusion: Synthesis of Diffusion and Reinforcement Learning

Why fuse diffusion with reinforcement learning? The preceding sections highlighted two complementary research directions: (i) how score-based diffusion models benefit from ideas rooted in Reinforcement Learning (RL), stochastic control, and optimal transport; and (ii) how modern RL increasingly adopts continuous-time, stochastic-dynamical viewpoints long familiar from diffusion processes. The natural next step is to *erase the boundary altogether* and view both paradigms through a single optimal-control lens.

This section develops such a synthesis via *Path–Integral Diffusion (PID)* [59]. PID can be read simultaneously as

- an *integrable* subclass of Stochastic Optimal Control (SOC), and
- a diffusion model whose score (and hence sampler) admits a *closed-form representation*, e.g. eliminating the need for a Neural Network (NN) score function/oracle, or at least simplifying the NN representation of the score function in a broad and practically relevant family of settings.

Beyond its algorithmic implications, PID provides a conceptual unification: diffusion sampling becomes controlled stochastic dynamics, while RL planning becomes finite-time probability transport.

A short pre–history of “integrable” stochastic optimal control

The idea that certain SOC problems become *linear* after a nonlinear change of variables traces back to the seminal works of Fleming [106] and Mitter [107]. They observed that, under suitable structural assumptions, the Hamilton–Jacobi–Bellman (HJB) equation admits

a Hopf–Cole transformation that converts the nonlinear HJB equation into a linear backward Kolmogorov (or heat) equation.

Kappen’s formulation of *Path–Integral Control* (PIC) [100] provided the modern and most influential incarnation of this idea. When

- the cost of control efforts (per se) is quadratic,
- the control enters the dynamics additively with the same covariance as the noise, and
- the state–dependent part of the cost appears as an external potential,

PIC reduces SOC to solving a linear parabolic PDE. The optimal policy is then expressed in terms of Green functions of this linear operator, revealing a deep connection to Feynman–Kac path integrals and imaginary–time Schrödinger equations.

Todorov subsequently generalized these ideas to discrete state–space and time, introducing *Linearly–Solvable Markov Decision Processes* (LS–MDPs) [108]. (And we will return to the more general discrete space-time Todorov’s LS-MDP formulation, and even generalize it further beyond Markovian processes, later in the chapter.) In parallel, Chernyak *et al.* [109] improved expressivity of integrable SOC by introducing, in addition to the drift, a *vector (gauge) potential* that preserves linear solvability while enriching the class of admissible dynamics.

In the context of generative modeling, Tzen and Raginsky [110] exploited the simplest integrable SOC structure (PIC without an external potential) to establish convergence guarantees for latent diffusion models. These developments foreshadowed a deeper synthesis between SOC, optimal transport, and modern diffusion–based generative modeling.

9.5.1 From stochastic optimal control to Path–Integral Diffusion

Starting point: Path–Integral Control with drift and gauge. We follow the formulation developed in [59], which builds explicitly on PIC [100] and its generalization with drift and gauge fields [109]. The uncontrolled reference dynamics is augmented by

- an *arbitrary drift* $f(t, x)$,
- a *vector (gauge) potential* $A(t, x)$, and
- a scalar potential $V(t, x)$ entering the running cost.

The controlled stochastic dynamics on $t \in [0, 1]$ is

$$dx_t = (f(t, x_t) + u(t, x_t))dt + dW_t, \quad x_0 = 0, \quad (9.22)$$

where u is the control field.

From terminal cost to terminal distribution. Classical SOC prescribes a terminal cost $\phi(x_1)$. The key conceptual step of PID [59] is to *replace the terminal cost by a terminal distribution constraint*

$$p(x_1) = p_{\text{target}}(x_1). \quad (9.23)$$

Assuming a fixed initial state $x_0 = 0$, it is shown in [59] that this constrained Stochastic Optimal Transport (SOT) problem is *equivalent* to an SOC problem with a uniquely determined terminal cost ϕ that is an explicit functional of p_{target} . This establishes a precise equivalence between SOC and SOT in this setting.

SOC formulation. The equivalent SOC problem minimizes the cost-to-go

$$J(t, x) = \mathbb{E} \left[\int_t^1 \left(\frac{1}{2}|u|^2 + V(s, x_s) + \dot{x}_s^\top A(s, x_s) \right) ds + \phi(x_1) \right], \quad (9.24)$$

subject to (9.22). The value function satisfies the backward HJB equation

$$-\partial_t J = V + \frac{1}{2}\nabla^2 J - \frac{1}{2}|\nabla J + A|^2 + f^\top(\nabla J + A), \quad (9.25)$$

with terminal condition $J(1, x) = \phi(x)$.

The optimal control is

$$u^*(t, x) = -\nabla J(t, x) - A(t, x). \quad (9.26)$$

Hopf–Cole linearization. Applying the Hopf–Cole transform $J = -\log \psi$ converts (9.25) into a *linear* backward Kolmogorov equation. Its Green functions G_- and G_+ fully characterize the optimal dynamics. As a result, the optimal control (equivalently, the score) admits the explicit representation

$$u^*(t, x) = \nabla_x \log(Z(t; x)), \quad Z(t; x) := \int p_{\text{target}}(y) \frac{G_-(t, x; y)}{G_+(1, y; 0)}, \quad (9.27)$$

Backward–inference interpretation. The normalized weight

$$w(y | t, x) = (Z(t; x))^{-1} \propto p_{\text{target}}(y) \frac{G_-(t, x; y)}{G_+(1, y; 0)}, \quad (9.28)$$

defines a bona-fide conditional probability – which allows a transparent interpretation – it is *the posterior distribution of the terminal state $y = x_1$ conditioned on observing $x_t = x$* . According to Eq. (9.27) it is the normalization coefficient of the conditional probability, $Z(t; x)$ – which we also call the partition function, which completely defines the optimal control (score function).

9.5.2 Three levels of integrability

(i) Top level: arbitrary fields. With general (V, f, A) , PID remains formally integrable: if the Green functions can be evaluated (analytically or numerically), sampling reduces to integrating (9.22) with u^* given by (9.27). No neural network is required.

(ii) Mid level: Harmonic PID. If V is quadratic in x and f, A are affine, the Green functions are Gaussian. In this case the optimal drift becomes

$$u^*(t, x) = a(t)x - b(t), \hat{y}(t; x), \quad (9.29)$$

revealing a linear dependence on the predicted terminal state on the *predicted terminal state*

$$\hat{y}(t, x) := \mathbb{E}[y | t, x], \quad (9.30)$$

therefore making explicit the interpretation of PID as a *backward-inference mechanism*.

(iii) Low level: uniform quadratic potential. Setting $f = A = 0$ and $V(x) = \frac{1}{2}\beta|x|^2$ yields the Harmonic PID (H-PID) sampler of [59]. All Green functions and the optimal drift admit closed-form expressions.

In what follows we will mainly focus on discussing integrability of low and mid level.

9.5.3 Sample-based and Importance Sampling Representations

The numerical analysis of [59] focused on two practically distinct regimes:

- (a) *Sample-based targets.* When the target distribution is specified through high-dimensional samples (e.g., images), the optimal control (9.27) is evaluated directly by summation over samples. In this regime, the conditional mean $\hat{y}(t; x) = \mathbb{E}[y | t, x]$ acts as an *order parameter*: as time evolves, it transitions from a noisy, uninformative estimate to a symmetry-broken, mode-selective prediction. This transition is interpreted as a β -dependent *dynamic speciation phase transition*, discussed earlier in Section 9.3, and marks the onset of reliable mode selection in multimodal targets.
- (b) *Energy-based targets.* When the target distribution is specified via an energy function, $p_{\text{target}}(y) \propto \exp(-E(y))$, the integral in (9.27) is approximated using *Universal Importance Sampling* (UIS), where the probe distribution is chosen as the analytically known Green-function ratio, which is Gaussian. In these lower-dimensional settings, $\hat{y}(t; x)$ does not exhibit a sharp symmetry-breaking transition; instead, it appears as a transient predictive quantity that nevertheless enables remarkably early inference of target structure, well before the terminal time.

Both approaches yield excellent reconstruction of the target distribution at terminal time, while exhibiting markedly different transient dynamics as the stiffness parameter β is varied. A common and revealing feature is that the predicted terminal state $\hat{y}(t; x_t)$ is substantially more exploratory than the instantaneous state x_t : at early stages of the dynamics, $\hat{y}(t; x_t)$ frequently visits multiple modes, including those distinct from the mode ultimately realized at the terminal time.

In both regimes, all computations are performed entirely at *inference time*: no neural networks are trained, and no learned score models are employed. This is not an argument against neural networks; rather, PID provides a principled analytic baseline that clarifies which components of the dynamics are already captured in closed form, thereby indicating where lightweight, targeted learning may be most effective. This perspective naturally motivates the challenges posed below.

The study of H-PID in the low-level integrability regime – reported in [59] – was further extended to mid-level integrability regimes:

- In Adaptive Path–Integral Diffusion (AdaPID) [111] we allowed the stiffness parameter β to vary in time, $\beta = \beta(t)$.
- Guided Harmonic PID (GH–PID) – analyzed in [112] – generalizes Harmonic PID further by introducing a guidance centerline a moving quadratic potential $V(t, x) = \frac{1}{2}\beta(t)\|x - \nu(t)\|^2$.

These extensions preserves integrability thus guaranteeing convergence to the target distribution at $t = 1$ while also enabling creative path-level shaping of the dynamics. In the following we present two highlight studies from the papers.

9.5.4 Sensitivity Minimization via Adaptive Path Integral Diffusion

A complementary and physically motivated perspective on adaptive scheduling in PID emerges in [111] from analyzing the *sensitivity* of the optimal velocity field. As argued in [113] and in related work on stochastic interpolants [114, 115], the spatial Lipschitz constant of the control field (score function) plays a central role in distributional stability, discretization error, and numerical robustness of diffusion-based samplers. This motivates minimizing the time-averaged squared gradient of the velocity field.

We define the velocity gradient (optimal-control sensitivity) as

$$\Omega_t(x) := \nabla_x u^*(t, x),$$

and analyze its statistics along sample paths $\{x_t\}_{t \in [0,1]}$. (Which would be called Lagrangian statistics in the fluid mechanics literature.) In the regime of interest – $f = A = 0$ and $V(t, x) = \frac{1}{2}\beta(t)\|x\|^2$, the score function is a gradient field, and $\Omega_t(x)$ reduces to a scalar radial gain controlled by the sensitivity of the predicted terminal map $\hat{y}(t; x)$. This reduction renders $\|\Omega_t\|^2$ a transparent and interpretable proxy for stability and smoothness of the induced transport.

It shown in [111] that sensitivity minimization over piece-wise-constant in time β leads to a *nontrivial optimal stiffness* $\beta_{0 \rightarrow 1}^*$. Optimal dynamics is illustrated in Fig. (9.16) for three different Gaussian Mixture models A consistent qualitative pattern emerges: small stiffness at early times promotes exploration and mode discovery, while increasing stiffness at later times suppresses excessive velocity gradients and stabilizes convergence. Importantly, these adaptive schedules differ across targets, even though corresponding optimal constant- β values are nearly identical.

From a broader perspective, Adaptive PID illustrates how integrability enables principled control over score regularity and numerical stability. Rather than learning the entire velocity field, one designs or learns low-dimensional protocols that regulate sensitivity – suggesting a natural division of labor between analytic structure and lightweight learning.

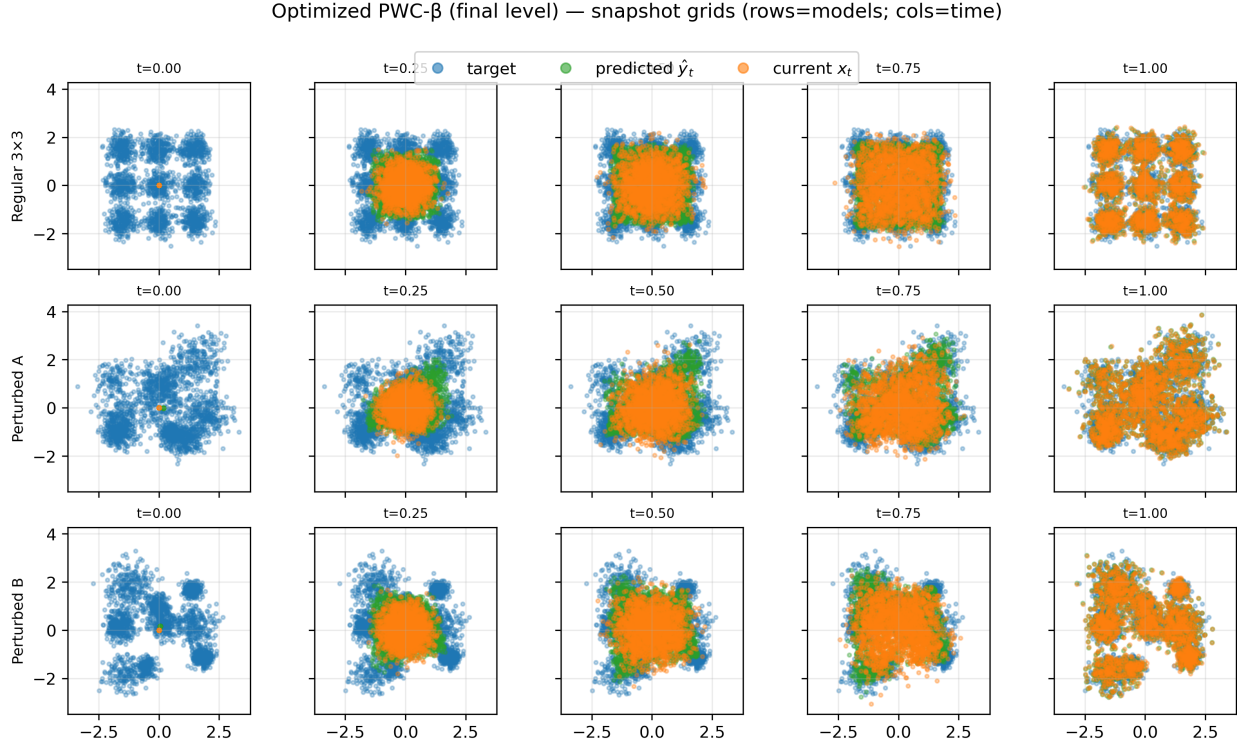


Figure 9.16: **Hierarchical optimization of PWC- $\beta(t)$ schedules.** Qualitative evolution under the optimized schedules: target samples (gray), predicted terminal states $\hat{y}(t; x_t)$ (green), and instantaneous states x_t (orange) at representative time slices. (Notebooks used to generate this and other figures in [111] are available at <https://github.com/mchertkov/AdaPID>.)

9.5.5 Navigation via Guided PID

To illustrate how guidance can be *learned* – rather than hand-designed – within an integrable PID framework, we consider in [112] a simple but representative example: a single two-mode navigation task in a narrow corridor.

We consider $V(t, x) = \frac{1}{2}\beta(t)\|x - \nu(t)\|^2$ fix β_t and optimize the guidance protocol ν_t . The starting point is a smooth “teacher” or *desiderata* centerline, chosen as an S-shaped curve connecting the initial state $x_0 = 0$ to the terminal region. This desiderata path encodes prior geometric knowledge about the task but is not assumed to be optimal.

The guidance ν_t is parameterized as a piecewise-constant (PWC) function in time, and its values are optimized by differentiating through the GH-PID sampler. The optimization objective trades off three effects: (i) adherence of the state trajectories to the desiderata tube, (ii) fidelity of the terminal distribution to the prescribed Gaussian-mixture target, and (iii) smooth deviations from the teacher protocol (see [112] for details). Importantly, the analytic GH-PID structure is preserved throughout: the Green functions and optimal drift are still obtained in closed form, with learning acting only on the low-dimensional protocol parameters.

Fig. 9.17 compares path ensembles generated by GH-PID under three protocols: a straight-axis

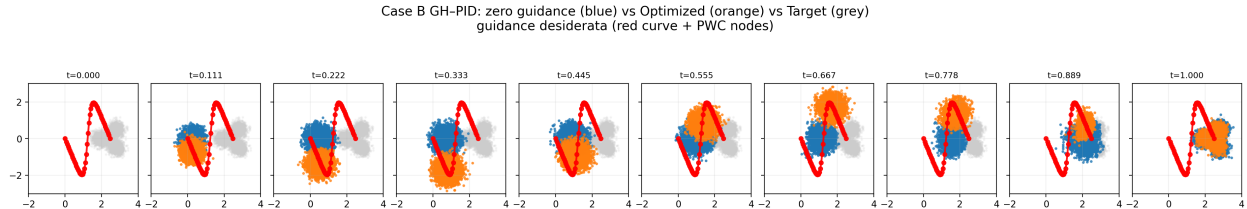


Figure 9.17: GH-PID snapshots under baseline and optimized guidance. Grey dots: samples from the two-mode GMM target. Blue dots: GH-PID cloud driven by a straight-axis baseline guide. Orange dots: GH-PID cloud under the optimized protocol $\nu^*(t)$. The red curve and nodes show the continuous teacher/desiderata S-shaped centerline and its PWC midpoints. Columns correspond to increasing diffusion times $t \in [0, 1]$. The optimized protocol steers trajectories into the S-shaped corridor earlier and maintains tighter adherence to the guided tube, while preserving correct terminal sampling of the target GMM. (Notebooks used to generate this and other figures in [111] are available at <https://github.com/mchertkov/GuidedPID>.

baseline guide, the optimized guide $\nu^*(t)$, and the underlying teacher/desiderata centerline. Each column shows a snapshot at increasing diffusion times $t \in [0, 1]$.

Under the baseline protocol, mass is transported roughly along the corridor axis. The ensemble remains broad, lags behind regions of high curvature, and exhibits delayed modal splitting. In contrast, the optimized protocol bends the cloud into the S-shaped corridor much earlier in time. Trajectories adhere more tightly to the guided tube, and separation into the two terminal modes occurs in a controlled and geometrically aligned manner. Despite these substantial differences in transient geometry, the terminal empirical distribution remains faithful to the target Gaussian mixture.

This example demonstrates that even in a low-dimensional setting, *learning the guidance protocol alone* can substantially reshape path geometry without compromising exact terminal matching. Guided PID thus offers a middle ground between fully analytic samplers and fully learned policies: the stochastic dynamics and score remain integrable, while task-specific structure is injected through lightweight protocol learning.

9.5.6 Open Challenges and Research Directions

The adaptive and guided extensions of Path–Integral Diffusion presented above demonstrate that a substantial degree of control over generative dynamics can be achieved through low-dimensional protocol design, while preserving analytic solvability and exact terminal matching. At the same time, these developments expose several fundamental limitations and opportunities. Rather than posing exercises (as done in all the preceding subsections and sections of the book), we conclude with a small set of open research challenges – intended as calls for collaboration – that point toward a broader and more powerful PID methodology.

Beyond quadratic integrability: controlled loss of solvability. Both AdaPID and GH–PID rely on quadratic (harmonic) path costs in order to retain linear Kolmogorov–Fokker–Planck equations and closed-form Green functions. A central open challenge is to

extend PID beyond purely quadratic potentials while maintaining partial analytic structure. Promising directions include low-rank or piecewise-quadratic potentials, locally quadratic approximations stitched by adaptive interfaces, and perturbative corrections around the harmonic backbone. The goal is not full generality, but a controlled hierarchy in which analytic PID serves as a baseline and nonlinearity is introduced in a principled, interpretable manner.

Protocol learning in high dimension and non-Gaussian targets. The present work focuses on low-dimensional settings with Gaussian-mixture terminal laws, where predicted-state maps and scores admit closed forms. Scaling protocol learning to high dimensions, structured data (images, fields, graphs), and non-Gaussian targets raises both conceptual and computational questions. Key challenges include identifying low-dimensional collective variables for guidance, designing protocol parametrizations that remain expressive yet stable, and combining PID with lightweight learned surrogates for the predicted map $\hat{y}(t; x)$. This direction naturally connects PID to representation learning and dimensional reduction, but under the constraint that terminal correctness and path interpretability be preserved.

Coupling stiffness and geometry: joint adaptive protocols. In AdaPID, adaptation acts on the stiffness schedule β_t , while in Guided PID it acts on the geometry of the guide ν_t . A largely unexplored direction is the joint, coupled adaptation of these two levers. How should confinement and geometry co-evolve in time? Can sensitivity-based diagnostics (e.g. velocity-gradient statistics) be used to trigger geometric reconfiguration of the guide? Understanding such coupled protocols would move PID closer to a true path-planning framework, where exploration, commitment, and geometric bias are negotiated dynamically rather than prescribed a priori.

PID as a variational ansatz for general stochastic optimal transport. More broadly, PID can be viewed as a structured variational family for solving mixed stochastic optimal transport problems with hard terminal constraints and soft path costs. An important open challenge is to clarify the approximation power of this ansatz: which classes of cost functionals can be well approximated by guided harmonic protocols, and which fundamentally cannot? Developing theoretical error bounds, expressivity criteria, and principled diagnostics for failure modes would place PID on firmer footing as a general-purpose tool for non-equilibrium sampling, planning, and control.

Taken together, these challenges outline a research program in which Path-Integral Diffusion evolves from an exactly solvable core into a modular, interpretable, and physics-informed framework for generative modeling and stochastic control.

9.6 Sampling Decisions: Diffusion, Reinforcement Learning and Transformers under one Umbrella

The continuous *Path-Integral Diffusion* (PID) formulation interprets a score-based diffusion model as an *integrable* Schrödinger bridge: a Stochastic Optimal Control (SOC) problem defined on the artificial “noise-scale” $\tau \in [0, 1]$ that smoothly transports the point-source

$x(0) = 0$ to a Gibbs target p_{target} at $\tau = 1$ [59]. The parameter τ , however, is purely algorithmic — it is not the clock that governs the *physical* assembly of the sample.

Sampling Decisions provide a unifying language for restoring physical, causal time to generative modeling. They achieve this by discretizing the generative process into decision stages and formulating sampling as a controlled stochastic evolution. Depending on how the state space is represented, this leads to two closely related but conceptually distinct regimes:

- *Markovian Sampling Decisions*, where the state space is fixed and decisions reweight transitions; and
- *Decision Flow*, where the state grows over time, giving rise to auto-regressive structure.

We begin with the Markovian setting, which admits a fully integrable formulation and serves as a conceptual bridge between Path–Integral Diffusion and auto-regressive models.

9.6.1 Markovian Sampling Decision

We first consider a discrete-time, discrete-state formulation in which the *state space* is fixed – as custom in Markov Decision Flow formulations⁴. Let $x_t \in \mathcal{X}$ denote the system state at time $t = 0, 1, \dots, T$, where \mathcal{X} is a fixed finite or countable set. We are given:

- a *reference (prior) Markov kernel* $P_t^{(\text{ref})}(x' | x)$, encoding baseline dynamics, feasibility, or physical constraints; and
- a *target terminal distribution* $\pi_T(x)$, specified up to normalization by $\pi_T(x) \propto \exp[-E(x)]$.

The objective of *Markovian Sampling Decision* (MSD) is to construct a controlled Markov chain $\{x_t\}_{t=0}^T$ whose terminal distribution matches π_T exactly, while deviating as little as possible from the reference dynamics at intermediate times.

Entropy–regularized control formulation. Among all Markov kernels $P_t(\cdot | \cdot)$ and marginals $\{\pi_t\}$ satisfying

$$\pi_{t+1}(x') = \sum_x \pi_t(x) P_t(x' | x), \quad \pi_0 = \delta_{x_0}, \quad (9.31)$$

we minimize the stochastic control objective

$$\sum_{t=0}^{T-1} \mathbb{E}_{P_t} \left[\text{KL}\left(P_t(\cdot | x) \| P_t^{(\text{ref})}(\cdot | x)\right) \right], \quad (9.32)$$

over transition probabilities P_t under condition that the energy of the terminal distribution is fixed,

$$P_T(x) \propto \exp(-E(x)). \quad (9.33)$$

Notice that the optimization problem is NOT a standard MDP – where the terminal constraint (9.33) would be replaced by addition of the terminal cost $\mathbb{E}_{P_t}[\phi(x)]$, where $\phi(x)$ is a terminal potential, to Eq. (9.32).

⁴This section presents an original formulation. Related ideas appear implicitly in [61], which develops a more general auto-regressive framework that is discussed later in Section 9.6.

Linear solvability. Problem of optimizing (9.32) under Eqs. (9.31,9.33) is *linearly solvable*. As in the case of PID discussed in the previous section we achieve it by first solving the auxiliary problem – one with an arbitrary terminal potential $\phi(x)$ – and then showing that we can choose $\phi(x)$ to fit any terminal energy $E(x)$.

Resolving the “contradiction”: terminal constraint via an equivalent terminal potential. As written, (9.32) is an *entropy-minimal deformation* of the reference path measure, while (9.33) is a *hard marginal constraint*. These two requirements are generically incompatible if one tries to enforce (9.33) by simply adding a terminal *cost* $\phi(x)$ to (9.32). The correct viewpoint (mirroring the PID discussion in Section 9.5) is that (9.33) can be enforced by a *specific, uniquely induced* terminal potential ϕ that depends on both the desired terminal law and the reference dynamics. Concretely, we proceed in two steps:

Step 1: auxiliary LS-MDP with an arbitrary terminal potential. Consider the entropy-regularized control problem

$$\min_{\{P_t, \pi_t\}} \sum_{t=0}^{T-1} \sum_{x \in \mathcal{X}} \pi_t(x) \text{KL}\left(P_t(\cdot | x) \| P_t^{(ref)}(\cdot | x)\right) + \sum_{x \in \mathcal{X}} \pi_T(x) \phi(x), \quad (9.34)$$

subject to the forward consistency constraints (9.31). This is a standard linearly-solvable MDP. Introducing the “desirability” (Hopf–Cole) transform $u_t(x) := \exp[-J_t(x)]$, the optimality conditions reduce to the linear backward recursion

$$u_T(x) = e^{-\phi(x)}, \quad u_t(x) = \sum_{x'} P_t^{(ref)}(x' | x) u_{t+1}(x'), \quad t = T-1, \dots, 0, \quad (9.35)$$

and the optimal controlled kernel is the Doob h -transform

$$P_t^\phi(x' | x) = P_t^{(ref)}(x' | x) \frac{u_{t+1}(x')}{u_t(x)}. \quad (9.36)$$

This is the discrete-time analog of PID’s “Green-function ratio” representation of the optimal drift.

Step 2: choose ϕ so that the terminal marginal matches π_T . Let $\pi_t^{(ref)}$ denote the reference marginals generated by $P_t^{(ref)}$ from $\pi_0 = \delta_{x_0}$:

$$\pi_{t+1}^{(ref)}(x') = \sum_x \pi_t^{(ref)}(x) P_t^{(ref)}(x' | x).$$

Then, for any terminal potential ϕ , the optimal marginals under P_t^ϕ satisfy the exact identity

$$\pi_t^\phi(x) = \frac{u_t(x)}{u_0(x_0)} \pi_t^{(ref)}(x), \quad t = 0, \dots, T. \quad (9.37)$$

Evaluating (9.37) at $t = T$ gives

$$\pi_T^\phi(x) = \frac{e^{-\phi(x)}}{u_0(x_0)} \pi_T^{(ref)}(x). \quad (9.38)$$

Therefore, enforcing the *hard* terminal constraint $\pi_T^\phi := \pi_T$ is achieved by choosing

$$e^{-\phi(x)} \propto \frac{\pi_T(x)}{\pi_T^{(ref)}(x)} \iff \phi(x) = -\log \pi_T(x) + \log \pi_T^{(ref)}(x) + \text{const.} \quad (9.39)$$

In particular, if $\pi_T(x) \propto e^{-E(x)}$, then

$$\phi(x) = E(x) + \log \pi_T^{(ref)}(x) + \text{const.} \quad (9.40)$$

This is precisely the discrete analogue of the PID statement that the terminal distribution constraint induces a uniquely determined terminal cost functional, now expressed explicitly through the *reference* terminal law $\pi_T^{(ref)}$.

Final MSD construction. Combining (9.36) with the induced terminal choice (9.39) yields the MSD kernel in the closed form:

$$P_t^*(x' | x) = P_t^{(ref)}(x' | x) \frac{u_{t+1}(x')}{u_t(x)}, \quad u_T(x) \propto \frac{\pi_T(x)}{\pi_T^{(ref)}(x)}, \quad u_t(x) = \sum_{x'} P_t^{(ref)}(x' | x) u_{t+1}(x'). \quad (9.41)$$

We can thus describe MSD as the Schrödinger bridge on a fixed state space with reference chain $P_t^{(ref)}$ and endpoint constraint π_T ; the optimal dynamics is the Doob transform driven by the backward “desirability” u_t .

Two equivalent representations: backward recursion vs. forward reachability. The MSD construction admits two fully equivalent, and complementary, descriptions. The first is a *backward dynamic-programming* view (linear Bellman / Hopf–Cole recursion), and the second is a *forward reachability* view (reweighting of terminal outcomes reachable under the reference chain). They are discrete counterparts of the two standard PID representations: “backward PDE / Green function” and “forward sampling with a terminal posterior.”

(A) Backward recursion (LS–MDP / Hopf–Cole). Given the terminal tilt

$$u_T(x_T) \propto \frac{\pi_T(x_T)}{\pi_T^{(ref)}(x_T)} \quad \left(\text{equivalently } u_T(x_T) = e^{-\phi(x_T)} \right), \quad (9.42)$$

the desirability is obtained by the linear backward recursion

$$u_t(x) = \sum_{x'} P_t^{(ref)}(x' | x) u_{t+1}(x'), \quad t = T-1, \dots, 0, \quad (9.43)$$

and the optimal kernel is the Doob transform

$$P_t^*(x' | x) = P_t^{(ref)}(x' | x) \frac{u_{t+1}(x')}{u_t(x)}. \quad (9.44)$$

(B) Forward reachability (terminal posterior / smoothing). Define the forward propagator of the reference chain from (t, x) to T ,

$$G_t^{(f)}(x_T | x) := \sum_{x_{t+1:T-1}} \prod_{\tau=t}^{T-1} P_\tau^{(ref)}(x_{\tau+1} | x_\tau), \quad (x_t = x). \quad (9.45)$$

Then the desirability admits the forward convolution representation

$$u_t(x) = \sum_{x_T \in \mathcal{X}} G_t^{(f)}(x_T | x) u_T(x_T) \propto \sum_{x_T \in \mathcal{X}} G_t^{(f)}(x_T | x) \frac{\pi_T(x_T)}{\pi_T^{(ref)}(x_T)}. \quad (9.46)$$

Moreover, this forward view immediately induces a bona-fide conditional distribution over terminal states,

$$w(x_T | t, x) := \frac{G_t^{(f)}(x_T | x) u_T(x_T)}{\sum_{z \in \mathcal{X}} G_t^{(f)}(z | x) u_T(z)} = \frac{G_t^{(f)}(x_T | x) \frac{\pi_T(x_T)}{\pi_T^{(ref)}(x_T)}}{\sum_{z \in \mathcal{X}} G_t^{(f)}(z | x) \frac{\pi_T(z)}{\pi_T^{(ref)}(z)}}, \quad (9.47)$$

which can be interpreted as the *posterior distribution of the terminal state x_T given the current state $x_t = x$* , with the reference dynamics providing the prior reachability and the ratio $\pi_T/\pi_T^{(ref)}$ providing the terminal “likelihood tilt.”

Finally, combining (9.44) with (9.47) yields a compact “one-step lookahead” representation of the optimal kernel:

$$P_t^*(x' | x) = P_t^{(ref)}(x' | x) \frac{\sum_{x_T} G_{t+1}^{(f)}(x_T | x') u_T(x_T)}{\sum_{x_T} G_t^{(f)}(x_T | x) u_T(x_T)}. \quad (9.48)$$

Thus the controlled transition biases moves toward states x' that increase expected terminal alignment under the posterior $w(\cdot | t+1, x')$.

Link to PID’s bona-fide distribution. Eq. (9.47) is the discrete-time/state analogue of the PID conditional weight $w(y | t, x)$ defined in Section 9.5: in both cases one forms a posterior over terminal states by combining (i) *reachability* under the reference process (Green functions / propagators) with (ii) a *terminal tilt* induced by the target distribution. In PID this tilt appears through $p_{\text{target}}(\cdot)$ multiplied by a Green-function ratio; in MSD it appears as the Radon–Nikodym derivative $\pi_T/\pi_T^{(ref)}$. The role of u_t is also identical: it is the normalization (partition function) of this terminal posterior, and it determines the optimal control / optimal transition.

Computational remarks (applies to both views). MSD is exact once either (A) the backward recursion (9.43) or (B) the forward propagator sums in (9.46) are computable. In large-scale settings this becomes practical when: (i) $P_t^{(ref)}$ is sparse/local so backward updates are cheap; (ii) u_t admits a structured approximation (graphical, low-rank, or neural) that preserves the Doob-form (9.44); and/or (iii) one can Monte-Carlo estimate the ratios in (9.48) by sampling terminal outcomes under the reference dynamics and reweighting them by the terminal tilt.

Applications and ongoing work. The Markovian Sampling Decision framework provides a principled, analytically transparent foundation for decision-making problems in which the system evolution is naturally Markovian and the state space is fixed. Applications to practical decision-flow problems with this structure are currently under development by the author

and collaborators, including: (i) neuro-biological modeling, where MSD offers a tractable framework for probabilistic state transitions of neuron signaling; and (ii) energy-systems applications, where reference dynamics encode physical feasibility or operational baselines, and terminal distributions represent desired system configurations or risk-aware outcomes. References to these applications will be included in the living updates once this work is complete.

From Markovian Decisions to Auto-Regressive Sampling

The MSD framework developed above is fully integrable and analytically explicit, but it operates on a *fixed state space*. As a result, it cannot directly represent generative processes in which the object being sampled is *assembled over time*, such as sequences, graphs, images, or combinatorial structures.

To capture such settings, one must allow the state itself to *grow* with time. This introduces an explicit auto-regressive structure, where each decision appends a new component to the partial configuration. In modern machine learning, this paradigm underlies transformer-based generative models.

The next section introduces *Generative Flow Networks* (GFNs), which can be viewed as *transformers without attention*: they generate objects auto-regressively by enforcing probabilistic flow conservation rather than token-level attention mechanisms. GFNs provide the missing auto-regressive ingredient absent from Markovian approaches and form the conceptual bridge to fully fledged Decision Flow models discussed later in this chapter.

9.6.2 Generative Flow Networks in a Nutshell

A *Generative Flow Network* (GFN) [60, 116] produces samples by successively *growing* an object, rather than drawing it in one shot. Let $\sigma = (\sigma_{a_1}, \dots, \sigma_{a_T}) \in \mathcal{X}$ be the final object we wish to draw with probability $\pi_T(\sigma) \propto R(\sigma) = \exp(-E(\sigma))$. A GFN introduces a growth trajectory

$$s_0 = \emptyset \rightarrow s_1 \rightarrow \dots \rightarrow s_T = \sigma, \quad s_t = (a_1, \dots, a_t) \quad (9.49)$$

where s_t records the first t moves, with size gradually increasing in t — like starting from a white image and coloring it pixel-by-pixel, such that $s_t \in \mathcal{X}_t$ and $\mathcal{X}_0 = \emptyset \subset \mathcal{X}_1 \subset \dots \subset \mathcal{X}_T = \mathcal{X}$. A learned *flow* $F_t(s_{t+1} | s_t)$ must satisfy the *trajectory balance* identity so that marginalizing the trajectories recovers π_T . Writing $R(\sigma) = \exp[-E(\sigma)]$ and $Z = \sum_\sigma R(\sigma)$, the constraint reads

$$\prod_{t=0}^{T-1} F_t(s_{t+1} | s_t) = \frac{1}{Z} R(s_T) \prod_{t=1}^T F_{t-1}^\leftarrow(s_{t-1} | s_t), \quad (9.50)$$

where F^\leftarrow denotes the corresponding reverse flow. Eq. (9.50) — *Trajectory Balance* (TB) — generalizes the familiar *Detailed Balance* (DB) of Markov chains and replaces the more restrictive *Global Balance* (GB) condition historically used in Monte Carlo methods (see Sections 7.4, 7.5).

GFN training amounts to minimizing a TB-inspired loss such as

$$\left(\log \frac{Z_\theta}{R(s_T)} + \sum_{t=0}^{T-1} \log \frac{F_t(s_{t+1}|s_t; \theta)}{F_t^\leftarrow(s_t|s_{t+1}; \theta)} \right)^2,$$

over the parameterized flow F_θ toward the exact solution F^* satisfying (9.50). In practice, $\log F_\theta$ is typically parameterized by a neural network trained via stochastic optimization.

Significance Generative Flow Networks (GFN) for Decision Flow (DF) (coming next). GFN supplies a principled, discrete-time recipe for *auto-regressive sampling*. DF retains this construction but replaces the black-box network by a *linearly-solvable control law* — yielding analytic kernels, transparent explanation, and a link to Markov Decision Processes (MDPs) discussed earlier. In that sense, DF can be viewed as an *integrable* white-box extension of the GFN framework, also injecting diffusion modeling into the GFN formalism.

9.6.3 Decision Flow: an Integrable, Auto-Regressive Extension of Markovian Sampling

In Section 9.6.1 we introduced *Markovian Sampling Decision* (MSD): a linearly solvable, fixed-state-space Schrödinger bridge that enforces a prescribed terminal distribution by an entropy-minimal deformation of reference dynamics. MSD already captures the core variational and probabilistic structure underlying Path-Integral Diffusion (PID) in a fully discrete setting.

Decision Flow (DF) extends this construction to the *auto-regressive* regime by allowing the *state space itself to grow in time*. This enlargement converts non-Markovian global objects into Markovian trajectories in an expanded space, thereby introducing the sequential, causal structure that underlies modern generative models.

Sequential construction. We consider sampling from an energy-based distribution

$$\sigma \sim \pi_T(\sigma) \propto \exp[-E(\sigma)], \quad (9.51)$$

where σ is a structured object (e.g., a configuration, sequence, graph, or image). Rather than generating σ in one step, DF constructs it incrementally via a growth trajectory

$$s_0 = \emptyset \rightarrow s_1 \rightarrow \cdots \rightarrow s_T = \sigma, \quad s_t \in \mathcal{X}_t, \quad \mathcal{X}_0 \subset \cdots \subset \mathcal{X}_T. \quad (9.52)$$

Here s_t records the first t growth decisions, rendering the extended process Markovian even though the terminal object σ is not.

A *prior* kernel $p_t^{\text{prior}}(s_{t+1} | s_t)$ encodes admissible growth moves and baseline dynamics, ensuring reachability of all finite-energy terminal states.

Variational formulation. DF inherits the entropy-regularized control principle of MSD, now posed on the growing state space. Among all controlled kernels $p_t(\cdot \mid \cdot)$ and induced marginals π_t , DF minimizes

$$\sum_{t=0}^{T-1} \mathbb{E}_{\pi_t, p_t} \left[\log \frac{p_t(s_{t+1} \mid s_t)}{p_t^{\text{prior}}(s_{t+1} \mid s_t)} \right] + \mathbb{E}_{\pi_T} [\Phi(s_T)], \quad (9.53)$$

subject to forward consistency

$$\pi_{t+1}(s_{t+1}) = \sum_{s_t} \pi_t(s_t) p_t(s_{t+1} \mid s_t), \quad \pi_0 = \delta_\emptyset.$$

As in MSD, the terminal potential Φ is uniquely induced by the desired terminal law $\pi_T(\sigma) \propto e^{-E(\sigma)}$ and the reference dynamics.

Linear solvability and closed-form policy. Introducing the desirability function $u_t(s_t) = \exp[-J_t(s_t)]$, the optimality conditions reduce to the linear backward recursion

$$u_T(s_T) = e^{-E(s_T)}, \quad u_t(s_t) = \sum_{s_{t+1}} p_t^{\text{prior}}(s_{t+1} \mid s_t) u_{t+1}(s_{t+1}), \quad (9.54)$$

and the optimal controlled kernel is the Doob transform

$$p_t^\star(s_{t+1} \mid s_t) = p_t^{\text{prior}}(s_{t+1} \mid s_t) \frac{u_{t+1}(s_{t+1})}{u_t(s_t)}. \quad (9.55)$$

This is the exact auto-regressive analogue of the MSD kernel (Eq. (9.41)), now acting on an expanding state space.

Interpretation. DF may be viewed as a *Schrödinger bridge on a growing configuration space*. The backward pass computes a terminal-aware potential by propagating preferences through reference reachability, while the forward pass samples a trajectory whose endpoint is distributed exactly according to π_T .

The resulting sampler is:

- *exact* (once u_t is known),
- *integrable* (linear Bellman equations),
- *causal and auto-regressive* (one degree of freedom added per step).

Relation to Generative Flow Networks and Transformers. Generative Flow Networks (GFNs) enforce terminal sampling via trajectory balance constraints, typically learned with neural networks. DF can be interpreted as a *white-box, integrable GFN* in which:

- trajectory balance holds analytically,
- flows are derived from a variational principle,

- no learned normalization or partition function is required.

From a modeling perspective, DF implements an auto-regressive generator analogous to a *transformer without attention*: the expanding context s_t renders the next-step decision conditionally independent of the distant past, while the backward potential plays the role of global conditioning.

Relation to diffusion and optimal transport. DF unifies three viewpoints developed throughout this chapter:

1. **Diffusion / PID:** DF is the discrete, growing-state analogue of Path-Integral Diffusion, with u_t playing the role of a conditional expectation over terminal outcomes.
2. **Optimal control:** DF is a linearly solvable MDP with entropy-regularized deviations from reference dynamics.
3. **Optimal transport:** DF transports a trivial initial distribution to π_T along a sequence of admissible growth steps.

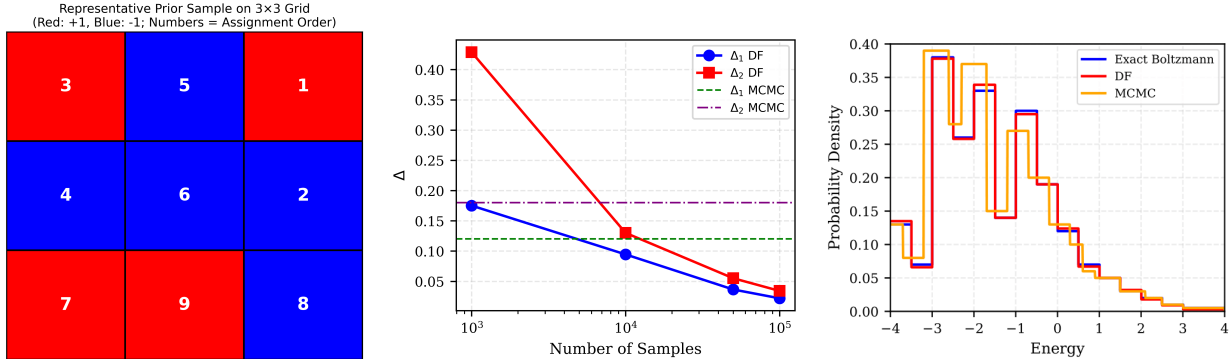


Figure 9.18: **Left:** Typical Decision Flow trajectories on a 3×3 Ising lattice at $\beta = 0.6$ (red/blue = ± 1). Numbers indicate insertion order. **Middle:** Performance of the DF algorithm on a 3×3 planar Ising model. Each bias h_a and interaction J_{ab} is independently drawn from Uniform[−1, 1], and the number of prior samples K equals the number of posterior samples S . The plot displays the discrepancy metrics $\Delta_{1,2}$ using the exact reference, as a function of $S = K$. For comparison, dashed horizontal lines indicate results from Metropolis-Hastings MCMC, where the chain discards the first 2000 burn-in samples and then records every 10th sample from a total of 5000 samples. **Right:** Probability density function of the energy $E(\sigma)$ estimated from DF-generated samples. The density is computed from σ samples produced using the DF algorithm with $K = S = 5 \times 10^4$.

Illustrative example. Fig. 9.18 reproduces a small Ising example from [61], demonstrating that DF achieves accurate energy-based sampling with significantly fewer samples than MCMC, highlighting the practical benefit of integrability and global conditioning.

Outlook and transition. Decision Flow completes the progression

$$\text{PID} \rightarrow \text{MSD} \rightarrow \text{DF},$$

moving from artificial time to physical time, and from fixed to growing state spaces. The remaining ingredient—addressed next—is the fully learned, non-integrable auto-regressive framework embodied by modern Generative Flow Networks and transformers, which trade analytic structure for expressive power.

9.7 Path Forward

Over the preceding sections of this synthesis chapter, we reviewed three paradigms that at first appear distinct yet are becoming increasingly intertwined in modern generative modeling and decision-making:

1. *Score-based diffusion models* (Sections 9.1–9.3), where samples are obtained by inverting a carefully designed stochastic process;
2. *Path-integral control and reinforcement learning* (Sections 9.4–9.5), whose sampling viewpoint emerges from *optimal control*;
3. *Generative Flow Networks (GFNs)* and *(integrable) Sampling Decisions* (Section 9.6), which recast sampling as *decision-making*, i.e. as optimization and control of transition probabilities on directed graphs.

A unifying mathematical language is taking shape — rooted in stochastic optimal control, optimal transport, and the geometry of probability flows — that promises to bridge these paradigms. Constructing a rigorous “dictionary” that links their key objects — score functions, control fields, and flow potentials — remains an outstanding research goal.

9.7.1 Work in Progress (by the author) and Open Directions

While drafting this living book in Spring 2025, I — primarily with Hamidreza Behjoo and, for Sampling Decisions, with Sungsoo Ahn—continued to explore synergies among these models. A partial portfolio of ideas currently under active development is collected below so readers can trace the common thread.

- **U-Turn Diffusion** — building on [59], this minimal modification of score-based diffusion forces trajectories back to the data manifold, enabling faster reverse sampling and offering a dynamical phase-transition interpretation. Key questions:
 - How many phase transitions occur, and how are they linked to latent (possibly discrete) data labels?
 - Which order parameters best capture the transition structure?
 - Can the resulting insights be used to design self-supervised *self-classification* objectives or to regularize diffusion models?

- **Space–Time Bridge Diffusion** — extending [71], this framework employs a Doob transform to create finite-horizon diffusion bridges by *pinning* trajectories at a fixed time. A promising route is to keep the forward process linear in the state space—to retain analytical tractability—while allowing it to be conditioned on observations or summary information about the target distribution. Outstanding tasks:
 - Identify tractable classes of data-conditioned linear processes (and, when needed, controlled departures from linearity);
 - Quantify the trade-off between expressivity and computational cost introduced by the pinning constraints.
- **Path–Integral Diffusion** [59, 111, 112]: this family of *integrable* stochastic-optimal-control (SOC) formulations reduces to a forward–backward pair of linear PDEs yet remains flexible enough to target arbitrary data distributions. Three nested research levels stand out:
 1. *Low-level integrability*: Beyond the Harmonic PID case with quadratic potentials (where integrability mirrors solving a Schrödinger equation in a quadratic well), can we build the scheme on richer families of integrable drift–diffusion processes?
 2. *Mid-level integrability*: Given samples, can neural surrogates (represented by NNs) accurately approximate reversed Green functions and score functions?
 3. *High-level integrability*: How can drifts and vector potentials be tuned or learned to encode additional scientific laws (e.g. conservation laws, constraints, dependencies) or perceptual priors (e.g. aesthetics in images)?
- **Sampling Decisions** — introduced in [61], this framework unifies diffusion, reinforcement learning, and auto-regression. Next milestones:
 - *Domain-specific specialization*: e.g. structural design in materials or real-time control of engineered systems;
 - *Neuralization*: replace analytic transition kernels, score functions, and Green functions with neural surrogates while preserving decision-theoretic guarantees;
 - *Transformer enrichment*: weave more expressive transformer components into the sampling-decision framework, with an emphasis on (sparse) attention mechanisms adapted to the statistics of the data, the underlying energy landscape, or the control objectives. (Compared to diffusion models and classical SOC/RL, a fully developed mathematical theory of transformers is still emerging—but see [117, 118] for notable early progress.)

9.7.2 Further Ideas on a Grand Unification of Generative Models

A number of broader challenges interconnect the topics above:

Scaling Laws: How many samples are needed to guarantee high-quality generation? How does this requirement scale with state-space dimensionality? Can we identify regimes

(dimensionality, energy landscapes, access to structure) in which AI-based samplers provably outperform classical tools such as MCMC for energy-based models?

Mixing Modalities: Which generative tools—among the expanding portfolio—are preferable for (a) discrete, continuous, or mixed spaces, and (b) energy-function, sample-based, or hybrid representations?

From Samples to Policies: How can Sampling Decisions be integrated with model-based RL to produce *policies*, not just trajectories or final samples? Viewed differently: can we fuse Sampling Decisions with broader SOC/RL frameworks to create a *generative control network*?

Physics-informed Learning: How do we weave phenomenological equations, conservation laws, symmetries, and other domain knowledge directly into the sampling procedures discussed above? (See [119] for examples in turbulence.) The challenge is to embed such features without sacrificing generative flexibility.

Outlook. We hope that unifying these threads will yield a cohesive *calculus of decision flows and physics-informed generative controls*: a toolkit that moves fluidly between data-driven modeling, principled control, and decision-centered sampling. A recurring theme is that integrable constructions provide not an alternative to learning, but a principled decomposition: what can be done exactly by physics/control and what should be delegated to lightweight learned surrogates.

9.7.3 Downstream Applications: Where the Mathematics of AI Meets the Real World

The preceding sections of the final chapter of this living book showed *how* we can derive, connect, and sometimes even *unify* diffusion, flow-matching, energy-based, and reinforcement-learning viewpoints. Natural final questions are:

What can we actually build with all this? What are the downstream tasks of generative AI?

These questions are particularly pressing today given the growing asymmetry in compute and data access between major AI companies — focused on training massive foundation models — and the rest of the AI community, including smaller companies, startups, and academic groups. With limited resources, the latter naturally pivot toward opportunities in solving *downstream* problems: fine-tuning, composing, aligning, and deploying powerful models that already exist.

Below is a deliberately **non-technical postcard** of opportunities growing directly out of the ideas developed in this chapter. Each bullet can be seen as an invitation to a project, thesis, or startup.

1. Compositional Generation

- **Composition of Experts.** Building new generative models by combining existing ones: products of experts (PoE) for strong constraint satisfaction [120], classifier-free guidance and general conditioning [121], compositional text-to-image generation via product and mixture rules [122]. Also creative tapestry-style image generation by combining regions under different conditional experts [123].
- **Modality stitching.** Combining distinct modalities (e.g. audio with video, graphs with text) into a coherent generation framework via factor-graph structures. Representative examples include diffusion models for molecules with property captions [124], or conditional latent diffusion as a substrate for structured generation and editing [125].
- **Editable generation *after the fact*.** Score-based diffusion offers *time* as a controllable knob: one can rewind to an intermediate noise level, inject a constraint (e.g. a new text caption or region mask), and then roll forward again [126]. This enables rapid “what-if” loops for art, fashion, drug design, and content personalization.

2. Decision-Aware Generation—Merging Diffusion & Control

- **Planning as inference.** The path-integral view (Section 9.5) allows optimal trajectories to emerge as samples from a guided stochastic process. Applications include human-style motion planning in robotics [127], planning trajectories through a maze (regions with exclusions) [128], and GenAI in supply chain and operations management [129].
- **Data-driven simulators.** Stochastic differential models learned from data can serve as differentiable surrogates for expensive PDE solvers: weather forecasting [130], chip layout placement [131], and aerodynamic shape design [132].
- **Risk-sensitive creativity.** Weighting diffusion paths by user-defined cost potentials (as in Sections 9.5 and 9.6) produces either conservative or exploratory behavior by tuning parameters such as β . To our knowledge, these tools have not yet been widely explored in applications such as portfolio risk management [133], safe reinforcement learning [134], and robust autonomy [135].

3. Scientific Discovery & Inverse Problems

- **Generative surrogates for Bayesian inversion.** Using a diffusion model as a prior and conditioning on partial observations enables fast, amortized Bayesian inversion—applied to MRI image reconstruction [136], seismic tomography [137], and gravitational-wave source inference [138].
- **Symbolic hypothesis engines.** Decoding diffusion latents not into pixels but into symbolic quantitative models (expressed via equations) offers a pathway toward *data-driven scientific discovery*. See [139] for a physics-informed approach and [140] for a large-language-model approach; this direction remains wide open for unified GenAI treatments.

- **Uncertainty-quantified simulators.** Diffusion-based generative models naturally produce full trajectory samples, providing built-in access to uncertainty estimates on outputs [141]; these approaches may be useful across a range of applications.

4. Societal Tooling

- **Alignment with human preferences.** Fine-tuning AI models to human preferences was developed first for transformers and then carried over to diffusion models, which also allow alignment signals to be defined not only on the final sample but also on intermediate steps (see [142] and references therein). This suggests further opportunities—including sampling-decision control—for meeting human performance expectations.
- **Resource-aware AI.** Sparse score models, diffusion pruning, and low-precision samplers offer dramatic gains in energy efficiency, enabling deployment on edge devices and mobile systems [143]. Integration and further development of these ideas within generative and sampling-decision frameworks has tremendous potential.
- **Personalization platforms.** Personalization in GenAI aims to capture and utilize concepts as generative conditions that are not easily describable. Many subject-driven generation methods appear generalizable—see [144] for a review—and better understanding the general trends and developing universal controls is another challenge in the spirit of sampling decisions.

Take-away: The synthesis chapter argued that diffusion, probability flows, energy functions, and control/score fields are *different and synergistic lenses on the same challenge*. We re-framed that unified view as a **toolkit** for applications:

Pretrained foundation model available → Compose experts → Steer paths → Sample solutions,

then deploy the resulting samplers across design, decision-making, science, and society. The mathematics you have learned is therefore not an end-point but a **passport** to whichever downstream application excites you most.

Bibliography

- [1] A. Vaswani, N. Shazeer, N. Parmar, J. Uszkoreit, L. Jones, A. N. Gomez, L. Kaiser, and I. Polosukhin, “Attention Is All You Need,” Dec. 2017, arXiv:1706.03762 [cs]. [Online]. Available: <http://arxiv.org/abs/1706.03762>
- [2] S. Boyd and L. Vandenberghe, *Convex Optimization*. Cambridge University Press, 2004. [Online]. Available: <https://web.stanford.edu/~boyd/cvxbook/>
- [3] Y. Nesterov, *Introductory Lectures on Convex Optimization: A Basic Course*. Springer, 2004. [Online]. Available: <https://doi.org/10.1007/978-1-4419-8853-9>
- [4] L. Bottou, “Large-scale machine learning with stochastic gradient descent,” pp. 177–186, 2010. [Online]. Available: <https://leon.bottou.org/papers/bottou-2010>
- [5] J. Duchi, E. Hazan, and Y. Singer, “Adaptive subgradient methods for online learning and stochastic optimization,” in *Proceedings of the 24th Annual Conference on Learning Theory (COLT)*, 2011.
- [6] T. Tieleman and G. Hinton, “Lecture 6.5—rmsprop: Divide the gradient by a running average of its recent magnitude,” COURSERA: Neural Networks for Machine Learning, 2012, https://www.cs.toronto.edu/~tijmen/csc321/slides/lecture_slides_lec6.pdf.
- [7] D. P. Kingma and J. Ba, “Adam: A method for stochastic optimization,” in *International Conference on Learning Representations (ICLR)*, 2015.
- [8] E. Candes, J. Romberg, and T. Tao, “Robust uncertainty principles: exact signal reconstruction from highly incomplete frequency information,” *IEEE Transactions on Information Theory*, vol. 52, no. 2, pp. 489–509, 2006.
- [9] M. Kurtz, J. Kopinsky, R. Gelashvili, A. Matveev, J. Carr, M. Goin, W. Leiserson, S. Moore, N. Shavit, and D. Alistarh, “Inducing and Exploiting Activation Sparsity for Fast Inference on Deep Neural Networks,” in *Proceedings of the 37th International Conference on Machine Learning*, ser. Proceedings of Machine Learning Research, H. D. III and A. Singh, Eds., vol. 119. PMLR, Jul. 2020, pp. 5533–5543. [Online]. Available: <https://proceedings.mlr.press/v119/kurtz20a.html>
- [10] T. Hoefler, D. Alistarh, T. Ben-Nun, N. Dryden, and A. Peste, “Sparsity in Deep Learning: Pruning and growth for efficient inference and training in neural networks,” Jan. 2021, arXiv:2102.00554 [cs]. [Online]. Available: <http://arxiv.org/abs/2102.00554>

- [11] Z. Wang, “SparseDNN: Fast Sparse Deep Learning Inference on CPUs,” Jul. 2021, arXiv:2101.07948 [cs]. [Online]. Available: <http://arxiv.org/abs/2101.07948>
- [12] M. Grimaldi, D. C. Ganji, I. Lazarevich, and S. Sah, “Accelerating Deep Neural Networks via Semi-Structured Activation Sparsity,” Sep. 2023, arXiv:2309.06626 [cs]. [Online]. Available: <http://arxiv.org/abs/2309.06626>
- [13] DeepSeek-AI, A. Liu, B. Feng, B. Xue, B. Wang, B. Wu, C. Lu, C. Zhao, C. Deng, C. Zhang, C. Ruan, D. Dai, D. Guo, D. Yang, D. Chen, D. Ji, E. Li, F. Lin, F. Dai, F. Luo, G. Hao, G. Chen, G. Li, H. Zhang, H. Bao, H. Xu, H. Wang, H. Zhang, H. Ding, H. Xin, H. Gao, H. Li, H. Qu, J. L. Cai, J. Liang, J. Guo, J. Ni, J. Li, J. Wang, J. Chen, J. Chen, J. Yuan, J. Qiu, J. Li, J. Song, K. Dong, K. Hu, K. Gao, K. Guan, K. Huang, K. Yu, L. Wang, L. Zhang, L. Xu, L. Xia, L. Zhao, L. Wang, L. Zhang, M. Li, M. Wang, M. Zhang, M. Tang, M. Li, N. Tian, P. Huang, P. Wang, P. Zhang, Q. Wang, Q. Zhu, Q. Chen, Q. Du, R. J. Chen, R. L. Jin, R. Ge, R. Zhang, R. Pan, R. Wang, R. Xu, R. Zhang, R. Chen, S. S. Li, S. Lu, S. Zhou, S. Chen, S. Wu, S. Ye, S. Ye, S. Ma, S. Wang, S. Zhou, S. Yu, S. Zhou, S. Pan, T. Wang, T. Yun, T. Pei, T. Sun, W. L. Xiao, W. Zeng, W. Zhao, W. An, W. Liu, W. Liang, W. Gao, W. Yu, W. Zhang, X. Q. Li, X. Jin, X. Wang, X. Bi, X. Liu, X. Wang, X. Shen, X. Chen, X. Zhang, X. Chen, X. Nie, X. Sun, X. Wang, X. Cheng, X. Liu, X. Xie, X. Liu, X. Yu, X. Song, X. Shan, X. Zhou, X. Yang, X. Li, X. Su, X. Lin, Y. K. Li, Y. Q. Wang, Y. X. Wei, Y. X. Zhu, Y. Zhang, Y. Xu, Y. Xu, Y. Huang, Y. Li, Y. Zhao, Y. Sun, Y. Li, Y. Wang, Y. Yu, Y. Zheng, Y. Zhang, Y. Shi, Y. Xiong, Y. He, Y. Tang, Y. Piao, Y. Wang, Y. Tan, Y. Ma, Y. Liu, Y. Guo, Y. Wu, Y. Ou, Y. Zhu, Y. Wang, Y. Gong, Y. Zou, Y. He, Y. Zha, Y. Xiong, Y. Ma, Y. Yan, Y. Luo, Y. You, Y. Liu, Y. Zhou, Z. F. Wu, Z. Z. Ren, Z. Ren, Z. Sha, Z. Fu, Z. Xu, Z. Huang, Z. Zhang, Z. Xie, Z. Zhang, Z. Hao, Z. Gou, Z. Ma, Z. Yan, Z. Shao, Z. Xu, Z. Wu, Z. Zhang, Z. Li, Z. Gu, Z. Zhu, Z. Liu, Z. Li, Z. Xie, Z. Song, Z. Gao, and Z. Pan, “DeepSeek-V3 Technical Report,” Dec. 2024, arXiv:2412.19437 [cs]. [Online]. Available: <http://arxiv.org/abs/2412.19437>
- [14] A. Behrouz, P. Zhong, and V. Mirrokni, “Titans: Learning to Memorize at Test Time,” Dec. 2024, arXiv:2501.00663 [cs]. [Online]. Available: <http://arxiv.org/abs/2501.00663>
- [15] Q. Sun, E. Cetin, and Y. Tang, “\$\\text{Transformer}^2\$: Self-adaptive LLMs,” Jan. 2025, arXiv:2501.06252 [cs]. [Online]. Available: <http://arxiv.org/abs/2501.06252>
- [16] F. Rosenblatt, “The perceptron: A probabilistic model for information storage and organization in the brain,” *Psychological Review*, vol. 65, no. 6, pp. 386–408, 1958.
- [17] M. Minsky and S. Papert, *Perceptrons: An Introduction to Computational Geometry*, 1st ed. Cambridge, MA: MIT Press, 1969.
- [18] Y. LeCun, L. Bottou, Y. Bengio, and P. Haffner, “Gradient-based learning applied to document recognition,” *Proceedings of the IEEE*, vol. 86, no. 11, pp. 2278–2324, 1998, publisher: IEEE.

- [19] A. Krizhevsky, I. Sutskever, and G. E. Hinton, “ImageNet Classification with Deep Convolutional Neural Networks,” in *Advances in Neural Information Processing Systems*, F. Pereira, C. J. Burges, L. Bottou, and K. Q. Weinberger, Eds., vol. 25. Curran Associates, Inc., 2012. [Online]. Available: https://proceedings.neurips.cc/paper_files/paper/2012/file/c399862d3b9d6b76c8436e924a68c45b-Paper.pdf
- [20] G. E. Hinton and R. R. Salakhutdinov, “Reducing the dimensionality of data with neural networks,” *Science*, vol. 313, no. 5786, pp. 504–507, 2006.
- [21] O. Ronneberger, P. Fischer, and T. Brox, “U-Net: Convolutional Networks for Biomedical Image Segmentation,” May 2015, arXiv:1505.04597 [cs]. [Online]. Available: <http://arxiv.org/abs/1505.04597>
- [22] K. He, X. Zhang, S. Ren, and J. Sun, “Deep residual learning for image recognition,” *Proceedings of the IEEE Conference on Computer Vision and Pattern Recognition*, pp. 770–778, 2016.
- [23] R. T. Q. Chen, Y. Rubanova, J. Bettencourt, and D. Duvenaud, “Neural ordinary differential equations,” in *Advances in Neural Information Processing Systems (NeurIPS)*, vol. 31, 2018. [Online]. Available: <https://arxiv.org/abs/1806.07366>
- [24] S. Jastrzebski, Z. Kenton, D. Arpit, N. Ballas, A. Fischer, Y. Bengio, and A. Storkey, “Finding Flatter Minima with SGD,” in *International Conference on Learning Representations (ICLR) Workshop*, 2018. [Online]. Available: <https://openreview.net/forum?id=r1VF9dCUG>
- [25] I. Garg, P. Panda, and K. Roy, “A Low Effort Approach to Structured CNN Design Using PCA,” *IEEE Access*, vol. 8, pp. 1347–1360, 2020, arXiv:1812.06224 [cs]. [Online]. Available: <http://arxiv.org/abs/1812.06224>
- [26] I. E. Lagaris, A. Likas, and D. I. Fotiadis, “Artificial neural networks for solving ordinary and partial differential equations,” *IEEE Transactions on Neural Networks*, vol. 9, no. 5, pp. 987–1000, 1998.
- [27] M. Raissi, P. Perdikaris, and G. Karniadakis, “Physics-informed neural networks: A deep learning framework for solving forward and inverse problems involving nonlinear partial differential equations,” *Journal of Computational Physics*, vol. 378, pp. 686–707, 2019.
- [28] I. G. Kevrekidis, C. W. Gear, and G. Hummer, “Equation-free modeling: Coarse-grained computations for complex dynamical systems,” *SIAM Journal on Scientific Computing*, vol. 24, no. 2, pp. 409–432, 2003.
- [29] M. Schmidt and H. Lipson, “Distilling free-form natural laws from experimental data,” *Science*, vol. 324, no. 5923, pp. 81–85, 2009, available at <https://faculty.washington.edu/morgansn/pmwiki/uploads/Site/schmidt-science2009.pdf>.

- [30] S. L. Brunton, J. L. Proctor, and J. N. Kutz, “Discovering governing equations from data by sparse identification of nonlinear dynamical systems,” *Proceedings of the National Academy of Sciences (PNAS)*, vol. 113, no. 15, pp. 3932–3937, 2016. [Online]. Available: <https://doi.org/10.1073/pnas.1517384113>
- [31] L. Lu, P. Jin, and G. E. Karniadakis, “Learning nonlinear operators via deeponet based on the universal approximation theorem of operators,” *Nature Machine Intelligence*, vol. 3, no. 3, pp. 218–229, 2021.
- [32] Z. Li, N. Kovachki, K. Azizzadenesheli, K. Liu, K. Bhattacharya, A. M. Stuart, and A. Anandkumar, “Fourier neural operator for parametric partial differential equations,” *arXiv preprint arXiv:2010.08895*, 2020. [Online]. Available: <https://arxiv.org/abs/2010.08895>
- [33] M. Chertkov, *Principles and Methods of Applied Mathematics*. World Scientific Publishing Company, 2025. [Online]. Available: <https://www.worldscientific.com/worldscibooks/10.1142/14184>
- [34] D. Williams, *Probability with Martingales*. Cambridge University Press, 1991.
- [35] N. Tishby, F. C. Pereira, and W. Bialek, “The information bottleneck method,” in *Proceedings of the 37th annual Allerton conference on communication, control, and computing*, 2000, pp. 368–377.
- [36] O. Ronneberger, P. Fischer, and T. Brox, “U-net: Convolutional networks for biomedical image segmentation,” *Medical Image Computing and Computer-Assisted Intervention (MICCAI)*, pp. 234–241, 2015.
- [37] J. J. Hopfield, “Neural networks and physical systems with emergent collective computational abilities,” *Proceedings of the National Academy of Sciences*, vol. 79, no. 8, pp. 2554–2558, 1982.
- [38] D. O. Hebb, *The Organization of Behavior: A Neuropsychological Theory*. Wiley, 1949.
- [39] D. Krotov and J. J. Hopfield, “Dense associative memory for pattern recognition,” *Advances in Neural Information Processing Systems*, vol. 29, pp. 1172–1180, 2016.
- [40] ——, “Hierarchical associative memory: Molecules of neuronal computation,” *Philosophical Transactions of the Royal Society B*, vol. 376, no. 1820, p. 20200136, 2021.
- [41] R. Y. Rubinstein, “Optimization of computer simulation models with rare events,” *European Journal of Operational Research*, vol. 99, no. 1, pp. 89–112, 1997.
- [42] R. Y. Rubinstein and D. P. Kroese, *The Cross-Entropy Method: A Unified Approach to Combinatorial Optimization, Monte-Carlo Simulation, and Machine Learning*, ser. Information Science and Statistics. New York: Springer, 2004.

- [43] N. Wiener, “Differential-space,” *Journal of Mathematical Physics*, vol. 2, no. 1, pp. 131–174, 1923.
- [44] ——, “The average value of a functional of brownian motion,” *Proceedings of the National Academy of Sciences*, vol. 10, no. 7, pp. 253–260, 1924.
- [45] M. Kac, “On distributions of certain wiener functionals,” *Transactions of the American Mathematical Society*, vol. 65, no. 1, pp. 1–13, 1949.
- [46] R. P. Feynman and A. R. Hibbs, *Quantum Mechanics and Path Integrals*. New York: McGraw-Hill, 1965, reprinted by Dover Publications, 2010.
- [47] L. Ornstein and G. E. Uhlenbeck, “On the theory of the brownian motion,” *Physical Review*, vol. 36, no. 5, pp. 823–841, 1930.
- [48] G. E. Hinton, “Training Products of Experts by Minimizing Contrastive Divergence,” *Neural Computation*, vol. 14, no. 8, pp. 1711–1800, 2002, publisher: MIT Press.
- [49] M. Chertkov, “INFERLO: Inference, Learning and Optimization with Graphical Models (Living Book, <https://sites.google.com/site/mchertkov/research/living-books>),” 2024. [Online]. Available: <https://sites.google.com/site/mchertkov/research/living-books>
- [50] M. Mezard and A. Montanari, *Information, Physics, and Computation*. Oxford University Press, 2009.
- [51] V. G. Satorras and M. Welling, “Neural Enhanced Belief Propagation on Factor Graphs,” Mar. 2021, arXiv:2003.01998 [cs]. [Online]. Available: <http://arxiv.org/abs/2003.01998>
- [52] D. P. Kingma and M. Welling, “Auto-Encoding Variational Bayes,” Dec. 2022, arXiv:1312.6114 [cs, stat]. [Online]. Available: <http://arxiv.org/abs/1312.6114>
- [53] M. Vuffray, S. Misra, A. Lokhov, and M. Chertkov, “Interaction Screening: Efficient and Sample-Optimal Learning of Ising Models,” in *Advances in Neural Information Processing Systems*, D. Lee, M. Sugiyama, U. Luxburg, I. Guyon, and R. Garnett, Eds., vol. 29. Curran Associates, Inc., 2016. [Online]. Available: https://proceedings.neurips.cc/paper_files/paper/2016/file/861dc9bd7f4e7dd3cccd534d0ae2a2e9-Paper.pdf
- [54] A. Y. Lokhov, M. Vuffray, S. Misra, and M. Chertkov, “Optimal structure and parameter learning of Ising models,” *Science Advances*, vol. 4, no. 3, p. e1700791, Mar. 2018. [Online]. Available: <https://www.science.org/doi/10.1126/sciadv.1700791>
- [55] T. N. Kipf and M. Welling, “Semi-Supervised Classification with Graph Convolutional Networks,” Feb. 2017, arXiv:1609.02907 [cs]. [Online]. Available: <http://arxiv.org/abs/1609.02907>

- [56] Z. Li, N. Kovachki, K. Azizzadenesheli, B. Liu, K. Bhattacharya, A. Stuart, and A. Anandkumar, “Fourier Neural Operator for Parametric Partial Differential Equations,” May 2021, arXiv:2010.08895 [cs]. [Online]. Available: <http://arxiv.org/abs/2010.08895>
- [57] B. Amos, L. Xu, and J. Z. Kolter, “Input Convex Neural Networks,” Jun. 2017, arXiv:1609.07152 [cs]. [Online]. Available: <http://arxiv.org/abs/1609.07152>
- [58] H. Behjoo and M. Chertkov, “U-Turn Diffusion,” *Entropy*, vol. 27, no. 4, 2025. [Online]. Available: <https://www.mdpi.com/1099-4300/27/4/343>
- [59] ——, “Harmonic Path Integral Diffusion,” *IEEE Access*, vol. 13, pp. 42196–42213, 2025. [Online]. Available: <https://ieeexplore.ieee.org/document/10910146/>
- [60] E. Bengio, M. Jain, M. Korablyov, D. Precup, and Y. Bengio, “Flow Network based Generative Models for Non-Iterative Diverse Candidate Generation,” Nov. 2021, arXiv:2106.04399 [cs]. [Online]. Available: <http://arxiv.org/abs/2106.04399>
- [61] M. Chertkov, S. Ahn, and H. Behjoo, “Sampling Decisions,” Mar. 2025, arXiv:2503.14549 [cs]. [Online]. Available: <http://arxiv.org/abs/2503.14549>
- [62] Y. Song and S. Ermon, “Generative Modeling by Estimating Gradients of the Data Distribution,” Oct. 2020, arXiv:1907.05600 [cs, stat]. [Online]. Available: <http://arxiv.org/abs/1907.05600>
- [63] J. Sohl-Dickstein, E. A. Weiss, N. Maheswaranathan, and S. Ganguli, “Deep Unsupervised Learning using Nonequilibrium Thermodynamics,” Nov. 2015, arXiv:1503.03585 [cond-mat, q-bio, stat]. [Online]. Available: <http://arxiv.org/abs/1503.03585>
- [64] J. Ho, A. Jain, and P. Abbeel, “Denoising Diffusion Probabilistic Models,” Dec. 2020, arXiv:2006.11239 [cs, stat]. [Online]. Available: <http://arxiv.org/abs/2006.11239>
- [65] Y. Song, J. Sohl-Dickstein, D. P. Kingma, A. Kumar, S. Ermon, and B. Poole, “Score-Based Generative Modeling through Stochastic Differential Equations,” Feb. 2021, arXiv:2011.13456 [cs, stat]. [Online]. Available: <http://arxiv.org/abs/2011.13456>
- [66] B. D. Anderson, “Reverse-time diffusion equation models,” *Stochastic Processes and their Applications*, vol. 12, no. 3, pp. 313–326, May 1982. [Online]. Available: <https://linkinghub.elsevier.com/retrieve/pii/0304414982900515>
- [67] V. De Bortoli, J. Thornton, J. Heng, and A. Doucet, “Diffusion Schrödinger Bridge with Applications to Score-Based Generative Modeling,” in *Advances in Neural Information Processing Systems*, M. Ranzato, A. Beygelzimer, Y. Dauphin, P. S. Liang, and J. W. Vaughan, Eds., vol. 34. Curran Associates, Inc., 2021, pp. 17695–17709. [Online]. Available: https://proceedings.neurips.cc/paper_files/paper/2021/file/940392f5f32a7ade1cc201767cf83e31-Paper.pdf

- [68] T. Dockhorn, A. Vahdat, and K. Kreis, “Score-Based Generative Modeling with Critically-Damped Langevin Diffusion,” Mar. 2022, arXiv:2112.07068 [stat]. [Online]. Available: <http://arxiv.org/abs/2112.07068>
- [69] V. De Bortoli, E. Mathieu, M. Hutchinson, J. Thornton, Y. W. Teh, and A. Doucet, “Riemannian Score-Based Generative Modelling,” Nov. 2022, arXiv:2202.02763 [cs]. [Online]. Available: <http://arxiv.org/abs/2202.02763>
- [70] E. Hoogeboom, V. G. Satorras, C. Vignac, and M. Welling, “Equivariant Diffusion for Molecule Generation in 3D,” Jun. 2022, arXiv:2203.17003 [cs]. [Online]. Available: <http://arxiv.org/abs/2203.17003>
- [71] H. Behjoo and M. M. Chertkov, “Space-Time Diffusion Bridge,” *IFAC-PapersOnLine*, vol. 58, no. 17, pp. 274–279, 2024. [Online]. Available: <https://linkinghub.elsevier.com/retrieve/pii/S2405896324019360>
- [72] D. P. Kingma, T. Salimans, B. Poole, and J. Ho, “Variational Diffusion Models,” Apr. 2023, arXiv:2107.00630 [cs, stat]. [Online]. Available: <http://arxiv.org/abs/2107.00630>
- [73] C. Lu, Y. Zhou, F. Bao, J. Chen, C. Li, and J. Zhu, “DPM-Solver: A Fast ODE Solver for Diffusion Probabilistic Model Sampling in Around 10 Steps,” Oct. 2022, arXiv:2206.00927 [cs]. [Online]. Available: <http://arxiv.org/abs/2206.00927>
- [74] K. Zheng, C. Lu, J. Chen, and J. Zhu, “DPM-Solver-v3: Improved Diffusion ODE Solver with Empirical Model Statistics,” Oct. 2023, arXiv:2310.13268 [cs]. [Online]. Available: <http://arxiv.org/abs/2310.13268>
- [75] J. L. Doob, *Stochastic Processes*. New York: John Wiley & Sons, 1953.
- [76] S. Särkkä and A. Solin, *Applied Stochastic Differential Equations*, 1st ed. Cambridge University Press, Apr. 2019. [Online]. Available: <https://www.cambridge.org/core/product/identifier/9781108186735/type/book>
- [77] E. Schrödinger, “Über die umkehrung der naturgesetze,” *Sitzungsberichte der Preussischen Akademie der Wissenschaften, Physikalisch-mathematische Klasse*, pp. 412–422, 1931.
- [78] ——, “Über die umkehrung der naturgesetze, ii,” *Sitzungsberichte der Preussischen Akademie der Wissenschaften, Physikalisch-mathematische Klasse*, pp. 144–153, 1932.
- [79] C. Villani, *Optimal Transport: Old and New*. Springer, 2009.
- [80] C. Léonard, “A survey of the schrödinger problem and some of its connections with optimal transport,” *Discrete & Continuous Dynamical Systems - A*, vol. 34, no. 4, pp. 1533–1574, 2014.
- [81] I. J. Goodfellow, J. Pouget-Abadie, M. Mirza, B. Xu, D. Warde-Farley, S. Ozair, A. Courville, and Y. Bengio, “Generative Adversarial Networks,” Jun. 2014, arXiv:1406.2661 [cs, stat]. [Online]. Available: <http://arxiv.org/abs/1406.2661>

- [82] G. Alain and Y. Bengio, “What Regularized Auto-Encoders Learn from the Data Generating Distribution,” Aug. 2014, arXiv:1211.4246 [cs]. [Online]. Available: <http://arxiv.org/abs/1211.4246>
- [83] A. Hyvärinen and E. Oja, “Independent component analysis: Algorithms and applications,” *Neural Networks*, vol. 13, no. 4–5, pp. 411–430, 2000.
- [84] L. Dinh, D. Krueger, and Y. Bengio, “Nice: Non-linear independent components estimation,” in *International Conference on Learning Representations (ICLR)*, 2015, arXiv:1410.8516.
- [85] L. Dinh, J. Sohl-Dickstein, and Y. Bengio, “Density estimation using real NVP,” in *International Conference on Learning Representations (ICLR)*, 2017, arXiv:1605.08803.
- [86] D. P. Kingma and P. Dhariwal, “Glow: Generative flow with invertible 1×1 convolutions,” in *Advances in Neural Information Processing Systems (NeurIPS)*, 2018, arXiv:1807.03039.
- [87] D. P. Kingma and M. Welling, “An Introduction to Variational Autoencoders,” *Foundations and Trends® in Machine Learning*, vol. 12, no. 4, pp. 307–392, 2019, arXiv:1906.02691 [cs]. [Online]. Available: <http://arxiv.org/abs/1906.02691>
- [88] G. Biroli and M. Mézard, “Generative diffusion in very large dimensions,” *Journal of Statistical Mechanics: Theory and Experiment*, vol. 2023, no. 9, p. 093402, Sep. 2023. [Online]. Available: <https://iopscience.iop.org/article/10.1088/1742-5468/acf8ba>
- [89] G. Biroli, T. Bonnaire, V. de Bortoli, and M. Mézard, “Dynamical Regimes of Diffusion Models,” Feb. 2024, arXiv:2402.18491 [cond-mat]. [Online]. Available: <http://arxiv.org/abs/2402.18491>
- [90] R. S. Sutton and A. G. Barto, *Reinforcement Learning: An Introduction (2nd Edition)*. MIT Press, 2018.
- [91] D. P. Bertsekas, *Dynamic Programming and Optimal Control, Vol. I and II*. Athena Scientific, 1995.
- [92] R. Bellman, *Dynamic Programming*. Princeton University Press, 1957.
- [93] L. V. Kantorovich, “Mathematical methods of organizing and planning production,” Leningrad State University Press, 1939, in Russian; partial translations appeared later in various economic journals.
- [94] L. V. Kantorovich and A. G. Zeldovich, *Mathematical Methods of Organizing and Planning Production*. Moscow: State Publishing House of Physical and Mathematical Literature, 1960, in Russian; later English translation by Daniel, M.
- [95] L. P. Kaelbling, M. L. Littman, and A. W. Moore, “Reinforcement learning: A survey,” *Journal of Artificial Intelligence Research*, vol. 4, pp. 237–285, 1996.

- [96] K. Arulkumaran, M. P. Deisenroth, M. Brundage, and A. A. Bharath, “Deep reinforcement learning: A brief survey,” *IEEE Signal Processing Magazine*, vol. 34, no. 6, pp. 26–38, 2017.
- [97] T. Haarnoja, H. Tang, P. Abbeel, and S. Levine, “Reinforcement Learning with Deep Energy-Based Policies,” Jul. 2017, arXiv:1702.08165 [cs]. [Online]. Available: <http://arxiv.org/abs/1702.08165>
- [98] E. Todorov, “Efficient computation of optimal actions,” *Proceedings of the National Academy of Sciences*, vol. 106, no. 28, pp. 11 478–11 483, Jul. 2009. [Online]. Available: <https://pnas.org/doi/full/10.1073/pnas.0710743106>
- [99] K. Dvijotham and E. Todorov, “A Unifying Framework for Linearly Solvable Control,” Feb. 2012, arXiv:1202.3715 [cs, math]. [Online]. Available: <http://arxiv.org/abs/1202.3715>
- [100] H. J. Kappen, “Path integrals and symmetry breaking for optimal control theory,” *Journal of Statistical Mechanics: Theory and Experiment*, p. P11011, 2005.
- [101] K. Black, M. Janner, Y. Du, I. Kostrikov, and S. Levine, “Training Diffusion Models with Reinforcement Learning,” Jan. 2024, arXiv:2305.13301 [cs]. [Online]. Available: <http://arxiv.org/abs/2305.13301>
- [102] Y. Zhang, E. Tzeng, Y. Du, and D. Kislyuk, “Large-scale Reinforcement Learning for Diffusion Models,” Jan. 2024, arXiv:2401.12244 [cs]. [Online]. Available: <http://arxiv.org/abs/2401.12244>
- [103] K. Yang, J. Tao, J. Lyu, C. Ge, J. Chen, Q. Li, W. Shen, X. Zhu, and X. Li, “Using Human Feedback to Fine-tune Diffusion Models without Any Reward Model,” Mar. 2024, arXiv:2311.13231 [cs]. [Online]. Available: <http://arxiv.org/abs/2311.13231>
- [104] S. Shekhar and T. Zhang, “ROCM: RLHF on consistency models,” Mar. 2025, arXiv:2503.06171 [cs]. [Online]. Available: <http://arxiv.org/abs/2503.06171>
- [105] Z. Zhu, H. Zhao, H. He, Y. Zhong, S. Zhang, H. Guo, T. Chen, and W. Zhang, “Diffusion Models for Reinforcement Learning: A Survey,” Feb. 2024, arXiv:2311.01223 [cs]. [Online]. Available: <http://arxiv.org/abs/2311.01223>
- [106] W. H. Fleming, “Exit probabilities and optimal stochastic control,” *Applied Mathematics and Optimization*, vol. 4, no. 1, pp. 329–346, 1977.
- [107] S. K. Mitter, “Non-linear filtering and stochastic mechanics,” in *NATO Advanced Study Institutes Series. Stochastic Systems: The Mathematics of Filtering and Identification and Applications*, vol. 78, 1981, pp. 479–503.
- [108] E. Todorov, “Linearly-solvable Markov decision problems,” in *Advances in neural information processing systems*, vol. 19. MIT Press, 2007, pp. 1369–1376.

- [109] V. Y. Chernyak, M. Chertkov, J. Bierkens, and H. J. Kappen, “Stochastic optimal control as non-equilibrium statistical mechanics: calculus of variations over density and current,” *Journal of Physics A: Mathematical and Theoretical*, vol. 47, no. 2, p. 022001, Dec. 2013, publisher: IOP Publishing. [Online]. Available: <https://dx.doi.org/10.1088/1751-8113/47/2/022001>
- [110] B. Tzen and M. Raginsky, “Theoretical guarantees for sampling and inference in generative models with latent diffusions,” May 2019, arXiv:1903.01608 [cs, math, stat]. [Online]. Available: <http://arxiv.org/abs/1903.01608>
- [111] M. Chertkov and H. Behjoo, “Adaptive Path Integral Diffusion: AdaPID,” Dec. 2025, arXiv:2512.11858 [cs]. [Online]. Available: <http://arxiv.org/abs/2512.11858>
- [112] M. Chertkov, “Generative Stochastic Optimal Transport: Guided Harmonic Path-Integral Diffusion,” Dec. 2025, arXiv:2512.11859 [cs]. [Online]. Available: <http://arxiv.org/abs/2512.11859>
- [113] P. Tsipos, Z. Ren, J. Zech, and Y. Marzouk, “Optimal Scheduling of Dynamic Transport,” Jun. 2025, arXiv:2504.14425 [stat]. [Online]. Available: <http://arxiv.org/abs/2504.14425>
- [114] Y. Chen, E. Vanden-Eijnden, and J. Xu, “Lipschitz-Guided Design of Interpolation Schedules in Generative Models,” Sep. 2025, arXiv:2509.01629 [stat]. [Online]. Available: <http://arxiv.org/abs/2509.01629>
- [115] L. Kunkel, “Distribution estimation via Flow Matching with Lipschitz guarantees,” Sep. 2025, arXiv:2509.02337 [stat]. [Online]. Available: <http://arxiv.org/abs/2509.02337>
- [116] Y. Bengio, S. Lahlou, T. Deleu, E. J. Hu, M. Tiwari, and E. Bengio, “GFlowNet Foundations,” Jul. 2023, arXiv:2111.09266 [cs]. [Online]. Available: <http://arxiv.org/abs/2111.09266>
- [117] B. Geshkovski, C. Letrouit, Y. Polyanskiy, and P. Rigollet, “The emergence of clusters in self-attention dynamics,” May 2023, arXiv:2305.05465 [cs, math, stat]. [Online]. Available: <http://arxiv.org/abs/2305.05465>
- [118] ——, “A mathematical perspective on Transformers,” Feb. 2024, arXiv:2312.10794 [cs, math]. [Online]. Available: <http://arxiv.org/abs/2312.10794>
- [119] M. M. Chertkov, “Mixing artificial and natural intelligence: from statistical mechanics to AI and back to turbulence,” *Journal of Physics A: Mathematical and Theoretical*, vol. 57, no. 33, p. 333001, Sep. 2024. [Online]. Available: <https://iopscience.iop.org/article/10.1088/1751-8121/ad67bb>
- [120] Y. Du and L. Kaelbling, “Compositional Generative Modeling: A Single Model is Not All You Need,” Jun. 2024, arXiv:2402.01103 [cs]. [Online]. Available: <http://arxiv.org/abs/2402.01103>

- [121] J. Ho and T. Salimans, “Classifier-Free Diffusion Guidance,” Jul. 2022, arXiv:2207.12598 [cs]. [Online]. Available: <http://arxiv.org/abs/2207.12598>
- [122] M. Skreta, T. Akhound-Sadegh, V. Ohanesian, R. Bondesan, A. Aspuru-Guzik, A. Doucet, R. Brekelmans, A. Tong, and K. Neklyudov, “Feynman-Kac Correctors in Diffusion: Annealing, Guidance, and Product of Experts,” Mar. 2025, arXiv:2503.02819 [cs]. [Online]. Available: <http://arxiv.org/abs/2503.02819>
- [123] Y. Du, C. Durkan, R. Strudel, J. B. Tenenbaum, S. Dieleman, R. Fergus, J. Sohl-Dickstein, A. Doucet, and W. Grathwohl, “Reduce, Reuse, Recycle: Compositional Generation with Energy-Based Diffusion Models and MCMC,” Sep. 2024, arXiv:2302.11552 [cs]. [Online]. Available: <http://arxiv.org/abs/2302.11552>
- [124] H. Zhu, T. Xiao, and V. G. Honavar, “3M-Diffusion: Latent Multi-Modal Diffusion for Language-Guided Molecular Structure Generation,” Oct. 2024, arXiv:2403.07179 [cs]. [Online]. Available: <http://arxiv.org/abs/2403.07179>
- [125] R. Rombach, A. Blattmann, D. Lorenz, P. Esser, and B. Ommer, “High-Resolution Image Synthesis with Latent Diffusion Models,” Apr. 2022, arXiv:2112.10752 [cs]. [Online]. Available: <http://arxiv.org/abs/2112.10752>
- [126] C. Meng, Y. He, Y. Song, J. Song, J. Wu, J.-Y. Zhu, and S. Ermon, “SDEdit: Guided Image Synthesis and Editing with Stochastic Differential Equations,” Jan. 2022, arXiv:2108.01073 [cs]. [Online]. Available: <http://arxiv.org/abs/2108.01073>
- [127] X. Li, T. Zhao, X. Zhu, J. Wang, T. Pang, and K. Fang, “Planning-Guided Diffusion Policy Learning for Generalizable Contact-Rich Bimanual Manipulation,” Feb. 2025, arXiv:2412.02676 [cs]. [Online]. Available: <http://arxiv.org/abs/2412.02676>
- [128] M. Janner, Y. Du, J. B. Tenenbaum, and S. Levine, “Planning with Diffusion for Flexible Behavior Synthesis,” Dec. 2022, arXiv:2205.09991 [cs]. [Online]. Available: <http://arxiv.org/abs/2205.09991>
- [129] I. Jackson, D. Ivanov, A. Dolgui, and J. Namdar, “Generative artificial intelligence in supply chain and operations management: a capability-based framework for analysis and implementation,” *International Journal of Production Research*, vol. 62, no. 17, pp. 6120–6145, Sep. 2024. [Online]. Available: <https://www.tandfonline.com/doi/full/10.1080/00207543.2024.2309309>
- [130] C. K. Sønderby, L. Espeholt, J. Heek, M. Dehghani, A. Oliver, T. Salimans, S. Agrawal, J. Hickey, and N. Kalchbrenner, “MetNet: A Neural Weather Model for Precipitation Forecasting,” Mar. 2020, arXiv:2003.12140 [cs]. [Online]. Available: <http://arxiv.org/abs/2003.12140>
- [131] V. Lee, M. Nguyen, L. Elzeiny, C. Deng, P. Abbeel, and J. Wawrzynek, “Chip Placement with Diffusion Models,” Mar. 2025, arXiv:2407.12282 [cs]. [Online]. Available: <http://arxiv.org/abs/2407.12282>

- [132] T. Wagenaar, S. Mancini, and A. Mateo-Gabín, “Generative Aerodynamic Design with Diffusion Probabilistic Models,” Sep. 2024, arXiv:2409.13328 [cs]. [Online]. Available: <http://arxiv.org/abs/2409.13328>
- [133] M. Wang and H. Ku, “Risk-sensitive policies for portfolio management,” *Expert Systems with Applications*, vol. 198, p. 116807, Jul. 2022. [Online]. Available: <https://linkinghub.elsevier.com/retrieve/pii/S0957417422002640>
- [134] S. Gu, L. Yang, Y. Du, G. Chen, F. Walter, J. Wang, and A. Knoll, “A Review of Safe Reinforcement Learning: Methods, Theory and Applications,” May 2024, arXiv:2205.10330 [cs]. [Online]. Available: <http://arxiv.org/abs/2205.10330>
- [135] L. Kunze, N. Hawes, T. Duckett, M. Hanheide, and T. Krajník, “Artificial Intelligence for Long-Term Robot Autonomy: A Survey,” Jul. 2018, arXiv:1807.05196 [cs]. [Online]. Available: <http://arxiv.org/abs/1807.05196>
- [136] A. Jalal, M. Arvinte, G. Daras, E. Price, A. G. Dimakis, and J. I. Tamir, “Robust Compressed Sensing MRI with Deep Generative Priors,” Dec. 2021, arXiv:2108.01368 [cs]. [Online]. Available: <http://arxiv.org/abs/2108.01368>
- [137] U. b. Waheed, T. Alkhalfah, E. Haghigat, C. Song, and J. Virieux, “PINNtomo: Seismic tomography using physics-informed neural networks,” Apr. 2021, arXiv:2104.01588 [physics]. [Online]. Available: <http://arxiv.org/abs/2104.01588>
- [138] M. Mould, D. Gerosa, and S. R. Taylor, “Deep learning and Bayesian inference of gravitational-wave populations: Hierarchical black-hole mergers,” *Physical Review D*, vol. 106, no. 10, p. 103013, Nov. 2022. [Online]. Available: <https://link.aps.org/doi/10.1103/PhysRevD.106.103013>
- [139] M. D. Cranmer, R. Xu, P. Battaglia, and S. Ho, “Learning Symbolic Physics with Graph Networks,” Nov. 2019, arXiv:1909.05862 [cs]. [Online]. Available: <http://arxiv.org/abs/1909.05862>
- [140] L. Pan, A. Albalak, X. Wang, and W. Y. Wang, “Logic-LM: Empowering Large Language Models with Symbolic Solvers for Faithful Logical Reasoning,” Oct. 2023, arXiv:2305.12295 [cs]. [Online]. Available: <http://arxiv.org/abs/2305.12295>
- [141] D. Shu and A. B. Farimani, “Zero-Shot Uncertainty Quantification using Diffusion Probabilistic Models,” Aug. 2024, arXiv:2408.04718 [cs]. [Online]. Available: <http://arxiv.org/abs/2408.04718>
- [142] J. Ren, Y. Zhang, D. Liu, X. Zhang, and Q. Tian, “Refining Alignment Framework for Diffusion Models with Intermediate-Step Preference Ranking,” Feb. 2025, arXiv:2502.01667 [cs]. [Online]. Available: <http://arxiv.org/abs/2502.01667>
- [143] X. Yang, D. Zhou, J. Feng, and X. Wang, “Diffusion Probabilistic Model Made Slim,” Nov. 2022, arXiv:2211.17106 [cs]. [Online]. Available: <http://arxiv.org/abs/2211.17106>

- [144] P. Cao, F. Zhou, Q. Song, and L. Yang, “Controllable Generation with Text-to-Image Diffusion Models: A Survey,” Mar. 2024, arXiv:2403.04279 [cs]. [Online]. Available: <http://arxiv.org/abs/2403.04279>